Nonlinear Dynamics of Piecewise-Constant Vorticity Distributions in an Inviscid Fluid.

Numerical Simulations of Some Prototype Flows for the Plane Mixing Layer.

by

PETER A. JACOBS

Department of Mechanical Engineering, University of Queensland,

St. Lucia, Queensland.

A thesis submitted for the degree of Doctor of Philosophy

in the Faculty of Engineering, University of Queensland.

May 1987.

The work presented in this thesis (except as acknowledged in the text) is, to the best of my knowledge and belief, original. This material contained in this thesis has not been submitted previously, either in whole or in part, for a degree at this or any other university.

P. Jacobs

Dedication

This thesis is dedicated to those who endured its production: Juanita, my parents, and Juanita's parents.

Acknowledgements

I acknowledge and am most grateful for the assistance and constant encouragement provided by my supervisor, Dr. D.I. Pullin.

I also thank
(i) the Commonwealth of Australia for providing financial assistance in the form of a Commonwealth Postgraduate Research Award throughout the duration of the project and for computer time provided under ARGS Grant No. F8315031 I;
(ii) the Prentice Computer Centre for providing computing facilities;
(iii) C.S.I.R.O. for providing computer time on their Cyber 205;
(iv) the staff of Mechanical Engineering for many interesting discussions and a pleasant atmosphere in which to work.

Abstract

The method of Contour Dynamics (CD) is applied to several prototype flows typical of the motions found in the transition region of the free shear layer. A derivation of the technique and a numerical implementation is described, suitable for the simulation of quasi-three-dimensional inviscid flows comprising a cylindrically symmetric vorticity field and an imposed stretching-strain field. The aim is to provide accurate evolutionary solutions to the Navier-Stokes' equations, in the limit of infinite Reynolds number (Re), from initial vorticity distributions characteristic of various scales of motion in the shear layer.

These scales of motion are those defined by the strictly two-dimensional temporal shear layer model and by the Corcos-Lin-Sherman (CLS) model (Corcos & Sherman 1984; Corcos & Lin 1984; Lin & Corcos 1984) of the higher order motions. Particular vorticity configurations include

(i) a strictly two-dimensional, streamwise-periodic vortex layer with vorticity of one sign. This models the well known temporal, two-dimensional shear layer.

(ii) an array of finite area vortex regions (FAVRs) with alternating circulation which are embedded in an irrotational, plane strain field aligned so as to stretch the vortex lines. This configuration models the evolution of secondary streamwise vortices (located in the braid region of the shear layer) under the influence of the longitudinal strain provided locally by the rolled-up vortex cores of the two-dimensional temporal shear layer.

(iii) a periodic vortex layer subject to imposed vortex stretching as in *(ii)*. This models some of the aspects of the evolution of finer scales that develop on the secondary vortices.

In a separate but related account we investigate the effect of stretching upon the interaction of two equal, like-signed vortices in close proximity.

Simulations of the two-dimensional layer strongly support the conjecture that the dynamics of the large-scale roll-up is only weakly dependent on Reynolds number. Several case studies illustrate the evolution of the vorticity distribution in which the large-scale flow features are very similar to those produced by previous two-dimensional simulations done at moderate Re and those observed in flow visualization experiments. The influence of the subharmonic perturbation upon the long-time evolution of the strictly two-dimensional layer is found to vary with its relative phase to the fundamental perturbation as noted in previous studies. Examples are presented that illustrate the events of pairing and tearing of two rolled-up cores and also the coalescence of three rolled-up cores. However, there are fine-scale details generated here that are not evident in the moderate Re simulations. These include spiral filaments of rotational fluid which are formed and then wrap around the rolled-up vortex cores. These events generate "spiky" vorticity distributions and also entrain large quantities of irrotational fluid into the layer. Simulations proceed only up until the first such event because we cannot resolve the fine detail that is generated subsequently.

Simulation of secondary streamwise vortices of the shear layer, as in *(ii)* above, provides an interesting example of stretching-strain / vorticity interaction and illustrates a possible single stage of the turbulent energy cascade to smaller-scale motions. For the Re = ∞ cases here, the initial vorticity distribution (elliptical FAVRs) always collapse into compact, nearly-axisymmetric cores surrounded by spiral arms. Although, for very high aspect-ratio vorticity distributions, each secondary vortex may collapse into several smaller nearly-axisymmetric cores.

A stretched periodic shear layer (configuration *(iii)* above) is studied to illustrate the effect of stretching on the interaction of the subharmonic and fundamental perturbations in the limit of Re = ∞. Stretching is found to accelerate the initial roll-up and to enhance the production

of spiral vortex filaments. It slows, but does not prevent, the pairing interaction and, although the rolled-up cores still pair with their nearest neighbours, the simulations are terminated before they approach each other closely.

We also describe some numerical experiments performed to study the effect of stretching strain on the strong interaction of two equal, like-signed vortices in close proximity. It is shown that stretching enhances the coalescence if the line joining the two vortex centres is aligned with the the compressive axis of the strain but inhibits coalescence otherwise.

Publications Arising from this Thesis

[1] Jacobs, P.A. & Pullin, D.I. 1985: "Coalescence of stretching vortices". *The Physics of Fluids*, **28**, 1619-1625.

[2] Jacobs, P.A. & Pullin, D.I. 1986: "Some applications of the method of contour dynamics". Proceedings of the Computational Techniques and Applications Conference (CTAC-85), pp 367-378, Edited by J. Noye & R. May, North-Holland.

[3] Pullin, D.I. & Jacobs, P.A. 1986: "Nonlinear evolution of stretched vortex arrays". *Journal of Fluid Mechanics*, **171**, 377-406.

[4] Jacobs, P.A. & Pullin, D.I. 1986: "Nonlinear dynamics of stretched shear layers". Proceedings of the 9th Australasian Fluid Mechanics Conference, Auckland, N.Z. pp 602-605.

[5] Jacobs, P.A. 1987: "Computer codes for contour dynamics". Report 2/87, Department of Mechanical Engineering, University of Queensland.

[6] Jacobs, P.A. & Pullin, D.I. 1987: "Inviscid vortex modelling of the plane shear layer via Contour Dynamics". To be submitted to *The Physics of Fluids*.

Contents

Appendices

List of Figures

List of Tables

Notation

A_j	area of R_j
a_o	amplitude of perturbation applied to the shear layer
a_2	$= \lambda_2/\delta_2$, aspect ratio of secondary vortex
a	semi-major axis of ellipse
b	semi-minor axis of ellipse
C_j	contour delineating vorticity discontinuity in (x, y)-plane
D/Dt	Lagrangian derivative
D_j	contour delineating vorticity discontinuity in the ξ-plane
d	distance
e	parameter for integration quantities
$e_0..e_3$	abscissa for numerical quadrature
$\underline{F}$	body force
$\underline{f}$	eigenfunction defining the perturbation shape
$g(\zeta)$	singularity distribution around contour C
H	Heavyside step-function
h_j	mean contour separation between contours C_j and C_j, of the shear layer
i	$\sqrt{(-1)}$
$\underline{i},\underline{j},\underline{k}$	unit vectors in the cartesian coordinates
k	wave number
$k_1..k_4$	constants to evaluate computational effort (table 2.1)
L	typical length scale of flow
M	number of nested vortex regions
N_j	number of nodes in the node set defining C_j
N_{max}	upper limit on nodes for each contour
$P_1..P_{10}$	node-adjustment parameters
p	pressure
p_j	length of contour
Q	${}_o\int^t \gamma(t')\, dt'$
q_j	ratio (quotient) *(i)* h_j/h_1, *(ii)* $(r_1)_j/(r_1)_1$
R	magnitude of $\xi = R\, e^{i\theta}$
$(r_1)_j, (r_2)_j$	major, minor axes of initial ellipse for secondary vortex simulations

Re	$= UL/\nu$, Reynolds number
Re_λ	$= \Delta U \lambda_1/\nu$, Reynolds number for primary vortices
Re_δ	$= \Delta U \delta_\omega/\nu$, Reynolds number based on initial vorticity thickness
Re_2	$= \Gamma_2/\nu$, Reynolds number for secondary vortices
R_j	region of constant vorticity
T	equivalent time in the purely two-dimensional simulations (Lundgren's transformation)
T_2	time for braid to reach equilibrium thickness
T_c	$= \lambda^2/\Gamma$, characteristic time for the simulation
T_η	Kolmogorov time-scale
T_n	time for vortex collapse via Neu's strain
T_r	roll-up time-scale for stretched secondary vortices
t	physical time
ΔU	free-stream velocity jump across the shear layer
U_1, U_2	free-stream velocities for the mixing layer
U_c	convection velocity of the mixing layer
$\underline{u}$	vector velocity
u_x, u_y, u_z	velocity components in cartesian coordinates
V_x, V_y	velocity field associated with ω_z
W	$= \Phi + i\,\Psi$, complex potential
$w_0 .. w_3$	weights for numerical quadrature
x, y, z	cartesian coordinates
Y_j	maximum deviation of C_j from $y = 0$
Z	$= X + iY$, complex coordinate of an arbitary point in the (x, y)-plane
α_j	$= \alpha_r + i\,\alpha_i$, perturbation magnitude for C_j
β	(x,y)-plane strain rate
β_2	$= \Gamma_2/\Gamma_1$, relative strength of secondary vortices
Γ_1	circulation of a rolled-up spanwise vortex
Γ_2	circulation of a secondary streamwise vortex
Γ_{comp}	circulation in the computational domain
$\Delta(\Omega_j)$	fractional error in circulation invariant for R_j
γ	(y,z)-plane stretching strain rate
γ_2	dimensionless stretching strain rate for the secondary vortex simulations
γ_3	dimensionless stretching strain rate for the stretched shear layer simulations

$\Delta\omega_m$	$= \omega_m - \omega_{m-1}$, vorticity jump across C_m
η	*(i)* Kolmogorov length scale
	(ii) coordinate in σ-plane
	(iii) $\eta_j(x)$ y-position of C_j
δ_ω	vorticity thickness of the shear layer, $\Delta U/\omega_{max}$
δ_2	vorticity thickness of the *(i)* secondary vortices
	(ii) shear layer braid
ε	*(i)* tolerance, (depends upon context)
	(ii) coordinate in σ-plane
ε_{ni}	tolerance for node insertion
ε_{nd}	tolerance for node deletion
ζ_j	$= x + i\,y$, complex coordinate of a point on C_j
θ	*(i)* argument of $\xi = R\,e^{i\theta}$
	(ii) momentum thickness
κ	curvature
λ_o	wavelength of the initial Kelvin-Helmholtz instability for the shear layer
λ_1	wavelength of the infinitesimal disturbance with highest growth rate
λ_2	wavelength of the secondary vortex array
λ_3	wavelength of the fundamental mode for the stretched shear layer
λ_{comp}	wavelength of the computational domain
ν	kinematic viscosity
ξ	$= \varepsilon + i\,\eta$, complex coordinate
ρ	fluid density
σ	*(i)* $= \sigma_r + i\,\sigma_i$, complex growth rate of layer perturbations
	(ii) radius of vortex blob
	(iii) $= \varepsilon + i\eta$, transformed plane in Lundgren's transformation
τ	$= t/T_c$, nondimensionalized time
τ_{max}	maximum nondimensionalized time reached during simulation
Φ	flow potential
ϕ	phase angle of initial perturbation to shear layer
Ψ	streamfunction
ω_j	z-component of vorticity in R_j
$\underline{\omega}$	vector vorticity

Ω_j	circulation in region R_j
∞	infinity
∇	grad
$\psi\times$	cross product
∂	partial derivative
*	(superscript) complex conjugate
CD	Contour Dynamics
FAVR	finite area vortex region
'	primed quantities are integration variables
O(...)	of order ...
<...>	mean value of ...

Note: The subscripts o and 0 are synonymous.

1.0 INTRODUCTION

Simulation of realistic fluid flows at high Reynolds number is extremely difficult due to the occurrence of turbulence. In this thesis we will use the method of Contour Dynamics, a technique suitable for the simulation of quasi-two-dimensional flow of an inviscid fluid, to calculate the evolution of several prototype flows that typify the structures present in the transition regime of a plane mixing layer.

If we work within the continuum framework for an homogeneous fluid then the well known Navier-Stokes equations describe the motion of the fluid for any given initial and boundary conditions. The solution of these equations is not an easy problem : when attempting direct numerical solutions, we encounter the problems of resolving the large range of time and length scales. The length scales associated with flow range from those associated with the large-scale motions, L, (say, the width of a mixing layer) down to the Kolmogorov length scale, η, of the nonturbulent motions with effective $Re_\eta = O(1)$. If we define the number of degrees-of-freedom for a flow as L/η then this quantity varies as $Re^{3/4}$ for each spatial dimension (Liepmann 1979). Explicit numerical solutions to the governing equations involving such a large range of scales leads to computer memory and processing time requirements that are prohibitive, even for the present generation of supercomputers. Hence, we turn to the study of simplified models in which not all of the flow detail has to be treated explicitly.

The classical approach to the problem of turbulence has been dominated by the statistical view initiated by Osborne Reynolds (1895). Flow quantities are assumed to be composed of a mean component and a superimposed random fluctuation. Substituting these quantities into the Navier-Stokes equations, and averaging with respect to time, results in a set of equations analogous to the Navier-Stokes equations but involving the mean quantities and an extra set of terms

commonly called the Reynolds stresses (Hinze §1.2, 1975). This procedure results in more unknowns than available equations and at some point the system of equations must be completed by introducing a "closure hypothesis". These vary in complexity from a simple eddy-viscosity model relating the Reynolds stresses to the gradients of the time averaged velocities to more complex models involving extra equations governing the transport of the turbulence properties through the flow. One popular closure hypothesis is the k-ε model which has recently been successfully used by Paterson (1986) to compute three-dimensional turbulent flow around buildings. All such models contain one or several parameters that need to be tuned to the flow situation.

Over the past two decades a large body of experimental data has been led to the emergence of a alternative view of turbulent flows. This is the so called "coherent structure" hypothesis which suggests the presence of large individual structures that maintain their coherence for long periods of time and interact in a more deterministic manner than previously thought. Despite the current high profile of coherent structures in turbulence research, there are several new approaches to turbulence currently under study (see e.g., Liepmann 1979; Chapman & Tobak 1985). One of these is the chaotic systems approach (see e.g., Aref 1983). For reviews on the subject of coherent structures in both bounded and free flows see Cantwell (1981) and Hussain (1986).

Early observations of structures, for example the spanwise vortices of the mixing layer, were thought to be unusual and require carefully prepared conditions for their existence. However, recent experiments have produced some very convincing evidence for the existence of coherent structure over a wide range of flow conditions. The now celebrated shadowgraphs of Brown & Roshko (1974) show the persistence of spanwise vortices in a mixing layer at high Re and the photographs of Konrad (1976) (reproduced in figure 1.1) show streamwise streaks which have interpreted by many workers to indicate the presence of streamwise, counter-

rotating vortices superimposed upon the spanwise vortices. As these vortex structures convect with the flow, experiments are best done in a Lagrangian framework and much of the collected evidence has been obtained using very simple flow visualization techniques.

It has been suggested that certain experimentally observed features of turbulent flows may be explained through an understanding of the underlying vortex structure of the flow (see e.g. Corcos 1979; Saffman 1981; Perry 1986). Here the basic surmise is that a turbulent flow may be modelled as a superposition of particular realizations of the vortex evolution which are distinct but structurally similar solutions of the equations of motion. For example, it is now generally accepted that the early growth of the plane mixing layer can be attributed to the progressive amalgamations of the spanwise vortices (Ashurst 1977).

From a computational point of view, the aim is to provide accurate numerical simulations of the nonlinear dynamics of a typical realization as a means of elucidating the various dynamical paths leading to a range of eddy scales which comprise the turbulence. These paths often take the form of nonlinear instabilities which provide mechanisms for the exchange of energy between the different scales of motion.

In this thesis we will take the coherent structure approach and obtain solutions to the Navier-Stokes equations in the $Re = \infty$ limit starting with vorticity distributions that are representative of realistic flow configurations. We will calculate solutions to the (inviscid) Euler equations on the supposition that, for finite times and away form solid boundaries, these solutions will be the same as the limiting solutions to the Navier-Stokes equations as $Re \rightarrow \infty$ starting from the same initial vorticity distribution.

To obtain numerical solutions, we use the Contour-Dynamic (CD) technique (Zabusky, Hughes & Roberts 1979). The CD method may be viewed as a member of the family of boundary-

(a)

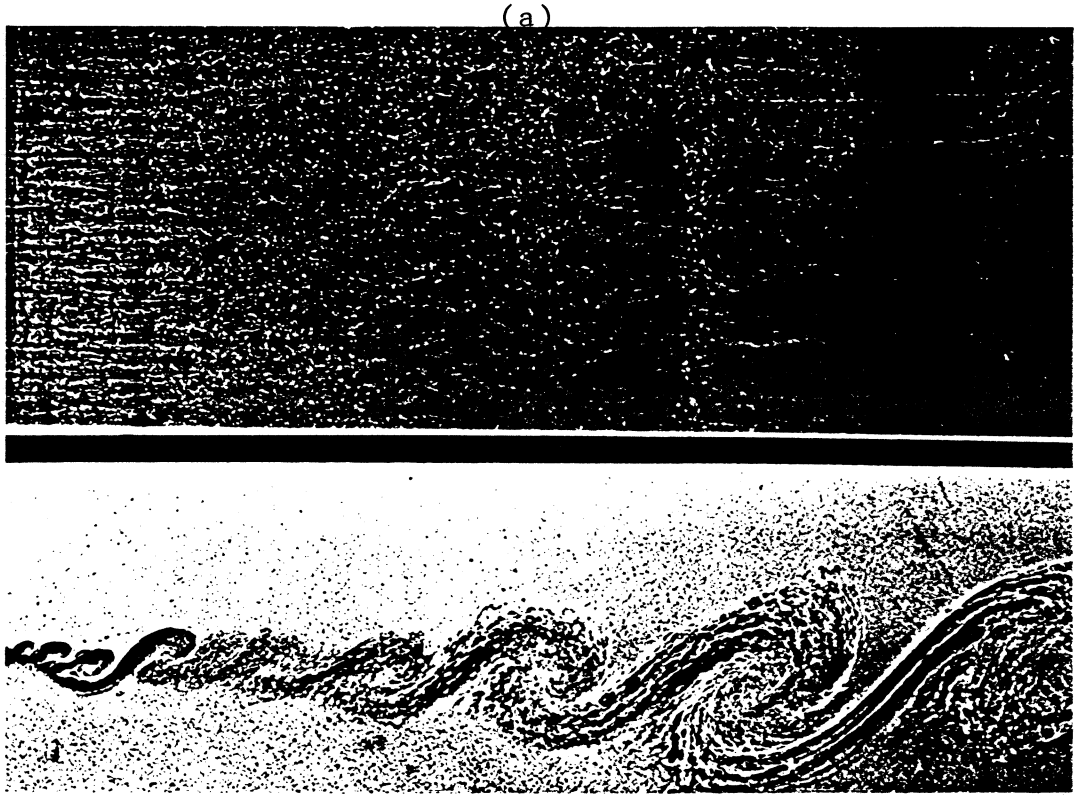

(b)

Figure 1.1: Photograph of the plane mixing layer taken by Konrad (1976).
(a) Plan view of the layer showing streamwise streaks
(b) Spanwise view showing the characteristic rolled-up vortex structures.
See also figure 6.1.

integral methods where the solution to the partial-differential equations is specified in the form of a Green's function. The CD method is suited to the simulation of "almost-continuous" vorticity fields in a two-dimensional flow of an inviscid fluid and, to date, has been restricted to purely two-dimensional flows with strictly uniform vorticity. Most of the simulations presented here use a nested set of vortex regions with piecewise-constant vorticity to approximate a continuous, nonuniform vorticity distribution that is typical of real flows. (See, for example, the experimental measurements of the vorticity of the ensemble averaged flows made by Browand & Weidman 1976 and Oster & Wygnanski 1982.) A three-dimensional, irrotational strain field is also included to model the vortex-stretching effects characteristic of three-dimensional turbulent flows. The nett result is a quasi-three-dimensional simulation technique which can be applied to flows where the vortex dynamics is preferentially two-dimensional (e.g. the pairing of spanwise vortices observed in the mixing layer observed by Winant & Browand 1974) and to flows where the effect of larger-scale motions can be modelled as an ambient strain field (as felt by the streamwise vortices in the braid region of the mixing layer).

As indicated by the example mentioned above, a flow configuration that has been the centre of much attention is the plane mixing layer. This flow occurs naturally in many situations and has provided one of the most striking examples of the large scale or coherent structure. Over the past decade, the cumulative efforts of many workers has led to the emergence of attractive structural models of the mixing layer. One version is the Corcos-Lin-Sherman (CLS) (Corcos & Sherman 1984; Corcos & Lin 1984 and Lin & Corcos 1984) model consisting of a short hierarchy of relatively simple deterministic motions. Each level in the hierarchy is defined as a vorticity field, embedded within and influenced by a larger-scale flow.

To place some of the subsequent discussion in perspective, we will briefly consider the flow configurations of interest. This description will be later expanded in chapter 6 which forms the introduction to the application section of this thesis. The standard laboratory mixing layer (figure 1.2a) is the transition region between two co-flowing parallel streams with different free stream velocities, U_1 and U_2. The layer grows in the streamwise direction and, at any fixed downstream position, its flow properties are roughly periodic in time. Figure 1.1b (Konrad's photograph) shows the nonlinear roll-up of the spanwise vortices in a mixing layer between the two free streams and the subsequent growth of the cross-stream thickness of the layer by the amalgamation of several generations of the spanwise vortices. Another model which has been found to be convenient for numerical simulations is that of the temporal shear layer (figure 1.2b). We define the shear layer as the region between two counter-flowing but parallel streams with velocities $\Delta U/2$ and $-\Delta U/2$ in the x-direction. The shear layer is infinite in extent, periodic in the x-direction and evolves in time. The numerical simulations presented later are based on this temporally evolving shear layer.

In chapter 2 we review the computation of two-dimensional fluid flows via vortex dynamics, and then in chapter 3 describe the method of Contour Dynamics (CD) that is used to calculate the evolution of the prototype flows. This description includes two new extensions to CD : *(i)* modelling a nonuniform vorticity distribution as nested regions of piecewise constant vorticity and *(ii)* the addition of a three-dimensional stretching strain to model the effect of larger scale motions. Chapter 4 describes the numerical implementation of CD while in chapter 5 we compare the CD simulations with both numeric and analytic results obtained from the available literature. Computer codes for this implementation are given in Jacobs [5].

Chapter 6 discusses the prototype flows that have been used to model the motions of the plane mixing layer while

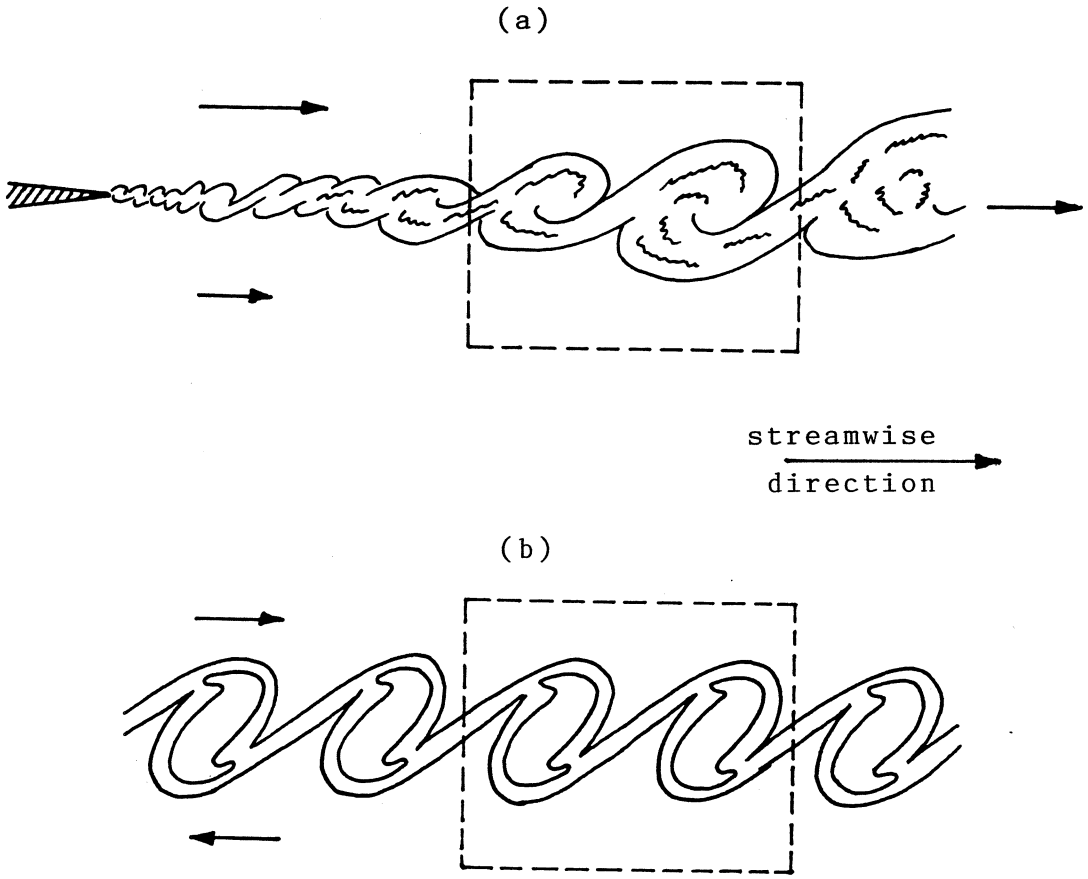

Figure 1.2: (a) Conceptual view of the plane mixing layer.
(b) Conceptual view of spatially periodic shear layer which develops in time.
See also figure 6.2.

applications of CD to prototype flows of the CLS model begin in chapter 7. Chapter 7 contains sample simulations of the strictly two-dimensional layer from which preliminary results were published in Jacobs & Pullin [4] with a more complete account to be published in Jacobs & Pullin [6]. Several cases are presented that illustrate the effect of subharmonic perturbations upon the nonlinear roll-up of the layer.

Chapter 8 contains sample simulations for the evolution of secondary streamwise vortices in the braid region of the shear layer. These results, previously published in Pullin & Jacobs [3], provide an interesting example of stretching strain / vorticity interaction.

In chapter 9 a stretched periodic shear layer is studied as a limiting configuration of the secondary streamwise vortices. Comparisons with the equivalent unstretched shear layers in chapter 7 illustrate the effect of stretching upon the interaction of the subharmonic and fundamental perturbations. Again, preliminary results have appeared in Jacobs & Pullin [4].

Chapter 10 details some numerical experiments that illustrate the effect of an imposed stretching strain field on the strong interaction of two equal, like-signed vortices in close proximity. The results contained in this section have been previously published in Jacobs & Pullin [1] and [2].

2.0 COMPUTATION OF FLUID MOTION VIA VORTEX DYNAMICS

The availability of large scale computing resources has stimulated the study of the nonlinear interactions of vorticity fields flow at effectively infinite Reynolds number. Calculations include both steady state configurations (e.g. Saffman & Szeto 1980, 1981; Saffman & Schatzman 1981; Overman & Zabusky 1982; Dritschel 1985) and their associated linear stability (e.g. Saffman & Schatzman 1982; Dritschel 1985). Fully nonlinear evolutionary-simulations include those by Acton (1976), Ashurst (1977), Zabusky et al (1979), Pullin (1981) and Pozrikidis & Higdon (1986). Here, we will describe the governing equations and some of the "vortex" methods used to obtain particular solutions. These methods characteristically have flow elements consisting of packets of circulation. There have been several extensive reviews of this active area including those by Leonard (1980b, 1985), Saffman & Baker (1979), and Melander, Overman & Zabusky (1986).

2.1 Equations of Motion

The motion of an homogeneous incompressible fluid can be described by the conservation of mass and conservation of linear momentum. In vector notation these take the form

$$\nabla . \underline{u} = 0 \quad , \tag{2.1}$$

$$\frac{D\underline{u}}{Dt} = \underline{F} - \frac{1}{\rho} \nabla p + \nu \nabla^2 \underline{u} \quad , \tag{2.2}$$

respectively, where

$$\nabla \equiv \left[\underline{i} \frac{\partial}{\partial x} + \underline{j} \frac{\partial}{\partial y} + \underline{k} \frac{\partial}{\partial z} \right] \quad , \tag{2.3a}$$

$$\frac{D}{Dt} \equiv \left[\frac{\partial}{\partial t} + u_x \frac{\partial}{\partial x} + u_y \frac{\partial}{\partial y} + u_z \frac{\partial}{\partial z} \right] \quad . \tag{2.3b}$$

Here $\underline{u}$ is the vector velocity

$$\underline{u} = u_x\underline{i} + u_y\underline{j} + u_z\underline{k} \quad , \tag{2.4}$$

where $\underline{i}$, $\underline{j}$, and $\underline{k}$ are the unit vectors in (x, y, z) cartesian coordinates and the subscripts refer to the spatial dimensions. $\underline{F}$, p and ν are the body force per unit mass, fluid static pressure and kinematic viscosity respectively. These are the well known and much studied Navier-Stokes equations in terms of the primitive variables, pressure and velocity. These equations can be normalized by considering a characteristic length, L, and velocity, U, for the flow and defining a Reynolds number as $Re = UL/\nu$.

2.2 Direct Methods of Solution

The most straightforward numerical approach to solving a two-dimensional partial differential equation is to use a finite-difference (FD) method on a rectangular mesh. Such techniques have been applied to both the primitive variable equations (2.1)-(2.2) and the vorticity-stream function equations as discussed in Roache (1976) for example. A key disadvantage to the FD approach is that, in order to eliminate excessive numerical diffusion and dissipation in simulations at high Re, a very fine grid is required. With increasing Re, this very quickly leads to computer memory and processing-time requirements that are beyond the scope of present day supercomputers. For example, consider a three-dimensional simulation of a periodic shear layer modelling the initially two-dimensional instability and growth of the standard laboratory mixing layer during transition to full three-dimensionality. The transition includes (roughly) the first three pairing events of the spanwise vortices and extends for approximately $15\lambda_o$ where λ_o is the wavelength of the initial initial Kelvin-Helmholtz instability of the layer (Jimenez 1983).

To reach this event in the temporally developing shear layer simulation, we might choose a computational domain of length $8\lambda_o$ in the streamwise (x) direction and approximately $4\lambda_o$ in both the cross-stream (y) and spanwise (z) directions. (The simulations in section 7.4 indicate that the final structure spans approximately half its wavelength.) The largest characteristic timescale for the simulation is

$$T_c = \frac{\lambda_o}{\Delta U} \quad , \tag{2.5}$$

where ΔU is the velocity jump across the layer. Although the evolution time depends upon the magnitude of the initial amplitude, we guess that the nonlinear roll-up and third pairing events occur at approximately $1T_c$ and $8T_c$ respectively. The discussion above defines the requirements for the large-scale motions but, to provide accurate evolutionary solutions, we need to resolve all scales of motion down to the Kolmogorov length η and time scale T_η (i.e. those with characteristic Reynolds number $Re_\eta \sim 1$). Following the arguements of Kolmogorov (also discussed in Liepmann 1979), an estimate of the range of length scales in any one dimension is given by

$$\frac{L}{\eta} \sim \left[\frac{LU}{\nu} \right]^{3/4} = Re_L^{3/4} \quad , \tag{2.6}$$

where L is a characteristic length of the large-scale motions, say the length of the computational domain. An estimate of the micro-time scale is given by

$$T_\eta = \frac{\eta}{c} \sim \left[\frac{\nu L}{U^3} \right]^{1/2} \quad , \tag{2.7}$$

where c is the characteristic velocity of the microscale motions. The range of timescales is then

$$\frac{T_c}{T_\eta} = \left[\frac{U\lambda_o}{\nu} \right]^{1/2} = Re_\lambda^{1/2} \quad . \tag{2.8}$$

For a FD solution to the governing primitive variable equations (2.1)-(2.2), a grid over the domain is reguired for the specification of the dependent variables $\underline{u}$ and p. The number of nodes in the streamwise and cross-stream directions is

$$N_x = k_1 \frac{8\lambda_o}{\eta} = 8\ k_1\ Re_\lambda^{3/4} \quad , \tag{2.9a}$$

$$N_y = N_z = k_1 \frac{4\lambda_o}{\eta} = 4\ k_1\ Re_\lambda^{3/4} \quad . \tag{2.9b}$$

The total storage in terms of computer words (8 bytes) is then

$$N_{words} = 4\ N_x\ N_y\ N_z = 512\ k_1^3\ Re_\lambda^{9/4} \quad . \tag{2.10}$$

Each time step involves the inversion of a Poisson equation (2.12) to obtain the pressure and the updating of (2.2). For a fourth order FD method or spectral method each time-step requires

$$N_{ops/step} = (N_x N_y N_z)\ [k_3\ \log_2(N_x N_y N_z) + k_4] \quad , \tag{2.11}$$

operations (Saffman 1977). The number of time steps required for the simulation is

$$N_{time\text{-}steps} = 8\ k_2 \frac{T_c}{T_\eta} = 8\ k_2\ Re_\lambda^{1/2} \quad , \tag{2.12}$$

giving a total operation count

$$N_{total} = (8\ k_2\ Re_\lambda^{1/2}) * (128\ k_1^3\ Re_\lambda^{9/4}) * [k_3\ \log_2(128\ k_1^3\ Re_\lambda^{9/4}) + k_4] \quad . \tag{2.13}$$

Typical values for the constants k_1 to k_4 are given in table 2.1 while estimates for the associated storage and processing-time requirements at various Re are listed in table 2.2. The processing-time is that for a Cyber 205 supercomputer operating at an optimum speed of 200 Mflops (million floating-point operations per second). To place this in perspective with some of the experiments that have been performed, consider the experiments of Winant & Browand (1974) where $Re_\lambda \approx 250$ and the higher speed experiments of Brown & Roshko (1974) with $Re_\lambda \approx 34000$.

There are other grid-based techniques such as the spectral and pseudo-spectral methods based on the expansion of flow variables in terms of Fourier components and orthogonal polynomials. The economy of these methods is that they require fewer grid points than a FD method for similar resolution but the variation of computer processing-time with grid resolution is similar to that for the FD methods (see equation (2.13) and table 2.1). These methods have been reviewed by Orszag & Israeli (1974) with more recent applications described by Melander, Overman & Zabusky (1986). Riley & Metcalfe (1980) used a pseudo-spectral method to simulate the two-dimensional roll-up of the spanwise vortices and the interaction with the first subharmonic at $Re_\lambda \approx 400$, 800 on 64×64 and 128×128 grids. They also performed a three-dimensional simulation of the nonlinear roll-up on a $32 \times 32 \times 33$ grid at $Re_\lambda \approx 200$.

Even if the estimates containied in table 2.2 are in error by several of orders of magnitude (e.g., it may not be necessary to resolve motions at all scales down to $O(\eta)$), they still provide motivation to try to model the small-scale motions in a way that is less demanding of computational effort. Examples include the κ-ε turbulence model that has been successfully used in engineering calculations (e.g. Paterson 1986) and the subgrid-scale modelling (or large-eddy simulations) used, for example, in the channel flow simulations of Moin & Kim (1981, 1985). Those interested in more fundamental studies have often used a vortex method

Table 2.1 : Typical values of constants $k_1 \ldots k_4$ for equations (2.10) and (2.13) defining computational effort. These values are taken from Saffman (1977).

Constant	Computational method	
	4^{th} order FD	Spectral
k_1	5	1
k_2	2	2
k_3	5	25
k_4	90	100

Table 2.2 : Computer storage and processing time required on a Cyber-205 supercomputer for simulations at various Reynolds numbers.

Re_λ	4^{th} order FD method		Spectral method	
	Storage (Mwords)	Processing time	Storage (Mwords)	Processing time
100	2.02×10^3	26.3 hours	16.1	0.58 hours
10^3	3.59×10^5	1.96 years	2.88×10^3	17.6 days
10^4	6.40×10^7	12.5 cent.	5.12×10^5	33.2 years
10^5	1.14×10^{10}	7907 cent.	9.10×10^7	220 cent.

cent. ≡ century

combined with some physical modelling (e.g. the secondary streamwise vortices of the mixing layer embedded in a stretching strain). This is the approach followed in the present study.

2.3 Vortex Methods

It has been noted that flows at high Re are often characterized by compact regions of rotational flow embedded in an irrotational velocity field (see e.g. Batchelor 1962). For flows with no free surface, the equations of motion (2.2) may be recast in terms of the derived variable $\underline{\omega}$ (vorticity) where

$$\underline{\omega} = \nabla \times \underline{u} \quad , \tag{2.14}$$

giving the vorticity transport equation

$$\frac{D\underline{\omega}}{Dt} = [\ \underline{\omega}.\nabla\ ]\ \underline{u} + \frac{1}{Re}\nabla^2\underline{\omega} \quad . \tag{2.15}$$

The left hand side of equation (2.15) represents the rate of change of vorticity following a fluid particle. The second term on the right is the rate of change of $\underline{\omega}$ due to molecular diffusion while the first term describes the effect of the velocity field on $\underline{\omega}$. It represents the extension or contraction of the vortex lines due to the component of $\underline{u}$ parallel to $\underline{\omega}$ and also the the rotation / reorientation of the vortex lines by the component of $\underline{u}$ normal to $\underline{\omega}$. For a purely two-dimensional flow this term is identically zero as there is only one nonzero component of vorticity $\underline{\omega} = \omega_z\underline{k}$ and two nonzero velocity components $\underline{u} = u_x\underline{i} + u_y\underline{j}$.

This vortex description of the flow has the advantage of being compact as we only need to calculate the evolution of $\underline{\omega}$ rather than the entire velocity field and also has the benefit of eliminating pressure as a variable. These advantages, however, are only realized for two-dimensional flows as the

vector streamfunction in three-dimensions adds quite a degree of complexity.

To avoid the limitations of a mesh, several Lagrangian techniques have been developed. These are the vortex methods. In three dimensions they have been applied to phenomena such as the turbulent spot in a boundary layer (Leonard 1980a). Reviews of two- and three-dimensional vortex methods are available in Leonard (1980b) and Leonard (1985) respectively. Generally, the production of fine-scale detail quickly outstrips the computing resources available so only very simple initial configurations have been explored (see e.g. Chorin 1982). We will constrain the flow configurations considered here to be cylindrically-symmetric with only one component of vorticity, ω_z. We note that Saffman & Meiron (1986) have questioned the utility of the three-dimensional equivalent of the two-dimensional point vortex technique owing to its failure to conserve certain invariants of the motion associated with such physical quantities as impulse and angular momentum.

In a purely two-dimensional inviscid flow, the vorticity transport equation (2.15) reduces to

$$\frac{D\omega_z}{Dt} = 0 \quad . \tag{2.16}$$

This means that a fluid particle that initially has a finite vorticity always has that vorticity or, alternatively, that the vortex tubes retain their identity as they move with the fluid. This second feature is also true for three-dimensional flows but there is the added complication of vorticity amplification and reorientation.

The earliest of the vortex methods is the point-vortex technique (Rosenhead 1932). The vorticity distribution is modelled by a discrete set of point-vortices with the local density of these points in a small region approximating $\omega_z(x, y, t)$. The Eulerian velocity field of the flow is identified with the particle velocities of the point-vortices

so that time evolution of the vorticity field is now represented by the particle mechanics of the point-vortices.

There are very few analytic (closed form) solutions for this problem and these are usually for steady state systems such as a pair of equal like-signed vortices rotating about each other or the translating Karman vortex-street. The stability of these configurations to infinitesimal perturbations is readily available in Lamb (1932) but fully nonlinear interactions are, in general, too complicated for analytic study. Instead, numerical simulations have dominated the study of the nonlinear motions of several or many (arrays of) particles.

If we consider a collection of N point-vortices then the velocity calculation is essentially a summation of Green's function solutions to the Poisson equation (2.21). The velocity of particle k is given by the summation

$$\frac{d\zeta_k^*}{dt} = \frac{1}{2\pi i} \sum_{\substack{j=1 \\ j\neq k}}^{N} \frac{\Gamma_j}{(\zeta_k - \zeta_j)} \quad , \qquad (2.17)$$

where $\zeta = x + iy$ is the complex coordinate in the (x, y)-plane and * indicates the complex conjugate. This direct calculation requires $O(N^2)$ operations per time-step and, for large N, it is computationally expensive. Rosenhead (1932) appears to have been the first to use the point-vortex technique as a numerical method by approximating a vortex sheet as a periodic array of point-vortices and computing (by "hand") the nonlinear roll-up of the sheet. He, and more recent workers (e.g., Kadomtsev & Kostomarov 1972), experienced accuracy problems with these calculations. Another early application was the calculation by Abernathy & Kronauer (1962) of the formation of a vortex street from two vortex sheets, again modelled as arrays of point-vortices.

As an approximation to a continuous vorticity distribution, the point vortex method is, at best, a weak solution to the Euler equations (Saffman & Baker 1979, Saffman

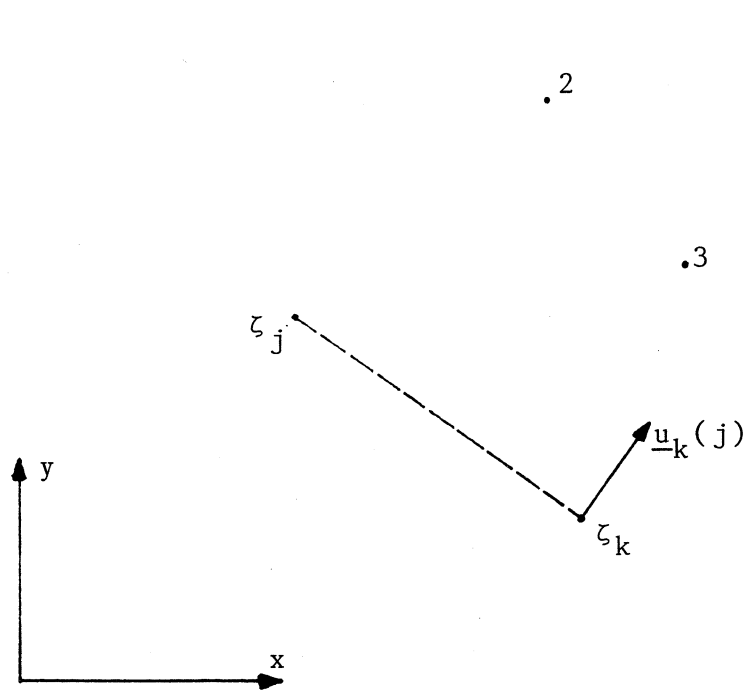

Figure 2.1 : Definition sketch for the point vortex formulation. The velocity of the vortex at ζ_k induced by the vortex at ζ_j is depicted by the vector $\underline{u}_k(j)$. Three other point vortices, labelled 1, 2 and 3, make up the rest of the vorticity distribution.

& Meiron 1986). This vorticity distribution induces an unbounded velocity field (2.11) and numerical procedures experience accuracy problems if the point-vortices approach each other closely. If the velocity field is smoothed then a reasonable approximation to the nonlinear evolution of the original continuous vorticity field may be obtained.

The "vortex blob" method of Chorin (1973) involves the use of a set of nondeformable, finite-area vortex blobs with finite vorticity. The parameters now include the blob strength, position, vorticity distribution and characteristic radius as shown in figure 2.2. A typical axisymmetric vorticity distribution for a single blob is

$$\omega_z = \begin{cases} \omega_1 & r < \sigma \quad , \\ 0 & r \geq \sigma \quad , \end{cases} \tag{2.18}$$

that is, uniform vorticity ω_1 within a radius σ. A vortex blob located at the origin induces a complex velocity

$$u_x - iu_y = \begin{cases} \dfrac{\Gamma}{2\pi i} \dfrac{1}{\zeta} & , \quad |\zeta| \geq 0 \quad , \\ \dfrac{\Gamma}{2\pi i} \dfrac{|\zeta|^2}{\sigma^2} \dfrac{1}{\zeta} & , \quad |\zeta| < 0 \quad , \end{cases} \tag{2.19}$$

where

$$\Gamma = \pi\sigma^2\omega_1 \quad . \tag{2.20}$$

The vorticity distribution has now been "desingularized" and induces a smoother velocity field. There have been a number of large-scale numerical simulations using this method, with several investigating the mixing layer or shear layer. Acton (1976) used 96 vortex blobs positioned on 4 close contours to study the initial rollup and subsequent pairing of vortex regions in a shear layer. In an ambitious calculation, Ashurst (1977) used up to 800 point vortices and 250 hours of processing time on a CDC 6600 (Mflops ≈ 1, Floating Point

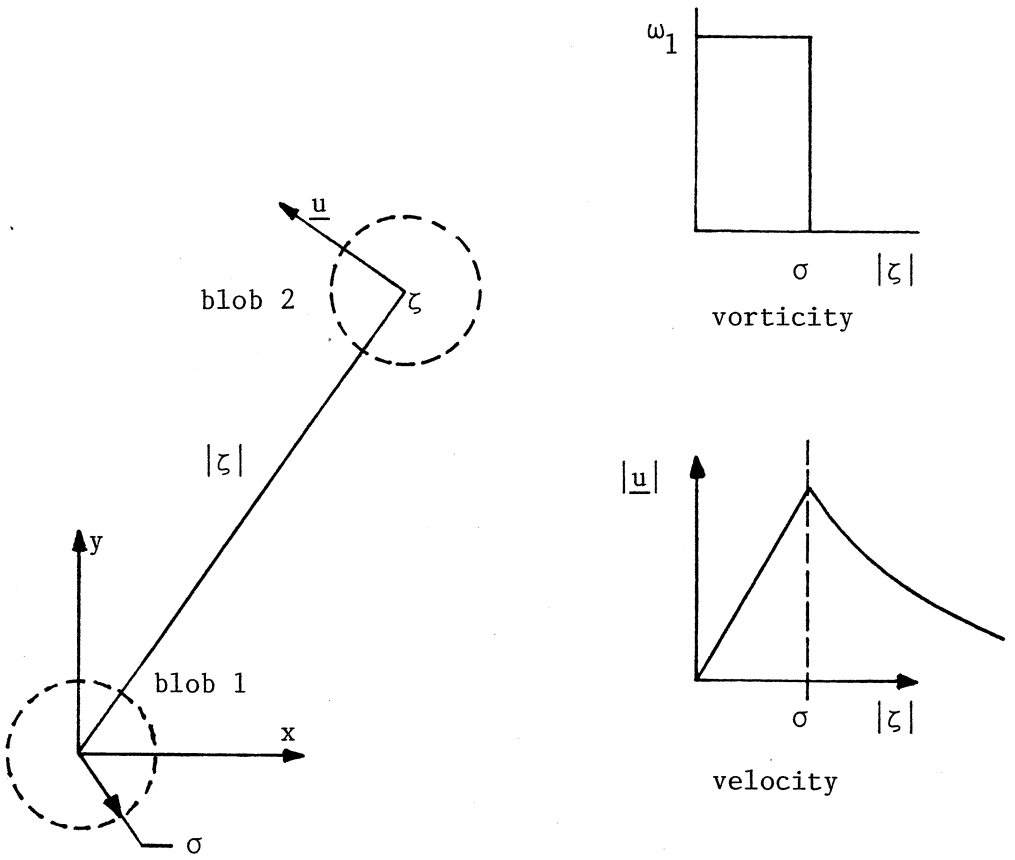

Figure 2.2 : Two interacting vortex blobs. Blob #1 is located at the origin and the induced velocity at the centroid of blob #2 is represented by $\underline{u}$. Inset, the variation of vorticity and magnitude of induced velocity (of blob #1) with distance from the origin.

Systems 1986) to simulate the two-dimensional evolution of a spatially developing mixing layer with the same conditions ($Re_\lambda \approx 250$) as the layer studied by Winant & Browand (1974). He included a random walk component in the velocity (Chorin 1973) to model the effect of viscosity and was also able to emulate the conditions of the Brown & Roshko (1974) mixing layer with $Re_\lambda \approx 34000$.

There are, however, accuracy problems associated with the vortex blob being nondeformable. In simulation of a periodic shear layer using blobs with Gaussian vorticity distributions, Nakamura, Leonard & Spalart (1982) have demonstrated that a blob diameter of order the centre separation (so that the blobs initially overlap) is required to obtain a good approximation to a continuous vorticity distribution. This conflicts with the observations by Christiansen (1973) (see also Jacobs and Pullin [1]) that there are large deformations in the boundaries of finite-area vortex regions (FAVRs) in close proximity. Although the nondeformable nature of the blobs does not invalidate the method's convergence as $\sigma \rightarrow 0$, a more accurate and physically reasonable technique may be obtained by using deformable blobs. One such technique is the "variable-elliptical-vortex" method proposed by Teng (1986) in which the blobs translate, rotate and deform as elliptical shapes.

In an attempt to reduce the processing-time required for large N, Christiansen (1973) proposed an alternate method of calculating the velocities. In this "Cloud-in-Cell" (CIC) technique, the basic variables are still the strengths and positions of the point vortices but the velocity calculation is performed with the aid of a grid. For each time step, vorticity is smoothed onto the grid and then the grid streamfunction, Ψ, is found by solving a discretized form of the relevant Poisson equation

$$\nabla^2\Psi = -\omega_z \ , \qquad (2.21)$$

where

$$u_x = \frac{\partial \Psi}{\partial y} \quad , \quad u_y = - \frac{\partial \Psi}{\partial x} \quad . \qquad (2.22a,b)$$

The grid velocity is obtained by differencing Ψ and then the individual point-vortex velocities are obtained by interpolation. The interpolation is performed consistently so that a vortex does not move in its own velocity field and so that the velocity field induced by each vortex is isotropic. For simple geometries, the inversion of the Poisson equation (2.21) may be done relatively quickly using Fast Fourier Transforms. On an M x M grid, this inversion requires $M^2 \log_2 M$ operations (Temperton 1979) and, when M^2 is typically set to be O(N), the number of operations required per time-step is $O(N \log_2 N)$ plus O(N) operations required for interpolation. As well as this speed advantage, the point-vortex equations have been desingularized by smoothing the vorticity onto the grid. This gives the vortices an effective core size of O(grid spacing) and eliminates the difficult singular behaviour as two point vortices approach closely. However, there is a penalty to be paid in the form of a reduction in solution accuracy.

The CIC method has been used in applications that require large numbers of point-vortices to approximate continuous vorticity distributions. Christiansen (1973) and Christiansen & Zabusky (1973) investigated several case studies including the interactions of two equal FAVRs, the formation of a vortex street from a pair of finite thickness shear layers and, the initial rollup of a spatially periodic free shear layer. More recently, Aref & Siggia (1980) studied the "long-time" evolution (well past the transition region) of a shear layer using 4096 point vortices and an underlying 256 x 256 grid. They performed the same type of computation to study the formation of a vortex street from two perturbed shear layers (Aref & Siggia 1981).

The advantages of vortex methods are that they provide a compact description of the inviscid flow dynamics (especially

in an unbounded domain) and, most importantly, that they are mesh independent. This allows fine-scale motions to develop and convect accurately. However, they require extremely large numbers (N) of point-vortices / vortex blobs to provide a good approximation to a continuous vorticity distribution and the computing time increases rapidly with N.

While the point vortex methods and their variants have been successful in describing the evolution of the largest scales of motion in the two-dimensional free shear layer, they have been less successful in elucidating the dynamical mechanisms which might produce eddy structures on a finer scale. For this purpose it seems necessary to consider a finite and "almost-continuous" distribution of vorticity while simultaneously retaining the mesh free advantages of the vortex techniques. For an inviscid fluid, the simplest and most convenient initial distribution of vorticity is the "generalized step-function" or "piecewise-continuous" distribution where there are several finite-area regions each containing fluid with finite and uniform vorticity. This distribution is "almost-continuous" in the sense that it maintains simple step-discontinuities only on a finite number of curves (contours) in the (x, y)-plane. When the flow is cylindrically-symmetric, the evolution of the vortical regions is completely specified by the motions of the bounding contours. This is the essence of the Contour-Dynamic technique which is formulated in the next chapter.

3.0 CONTOUR DYNAMICS FOR FLUID FLOW

The Contour-Dynamic (CD) technique for the numerical solution of the two-dimensional, inviscid Euler equations for an incompressible fluid (2.16), (2.21) was introduced by Zabusky, Hughes & Roberts (1979) as a modification of the "water-bag" technique used by Berk & Roberts (1970) for simulations of a one-dimensional phase-space, ideal incompressible fluid. The term "water-bag" arises from the nature of the flow evolution. The regions of uniform vorticity evolve as an incompressible fluid in (x, y)-space similar to a blob of water in a perfectly elastic container whose sides are formed by extending the bounding contours in the z-direction.

It is interesting to note the analogy between the vortex flows and the flow of a phase-space fluid (Berk, Nielsen & Roberts 1970). The two-dimensional vorticity equation in physical (x, y)-space is the same as the one-dimensional Vlasov equation for a collisionless plasma in phase (x, v)-space. The fluid vorticity is equivalent to the plasma distribution function and the vortical (action-at-a-distance) interactions are analogous to the long range nonlinear Coulombic interactions of the plasma.

In CD, the initial vorticity field is specified as a piecewise-constant distribution or generalized step-function (Calder & Laframboise 1986). We consider M regions R_j, j=1..M of uniform vorticity ω_j, j=1..M embedded in an unbounded region R_o of irrotational flow (ω_o=0). The R_j j=1..M are bounded by contours C_j delineating the vorticity discontinuities in this piecewise-constant distribution. Figure 3.1 shows a cylindrically-symmetric vorticity distribution (i.e. independent of the z-coordinate) $\underline{\omega} = \omega_z$ (x, y, t) with M = 5, describing two separate FAVRs. The evolution of vorticity field is still governed by the vorticity transport equation (2.15) which, for a purely two-dimensional flow, reduces to Helmholtz's theorem (2.16). This states that fluid particles maintain their vorticity and, when

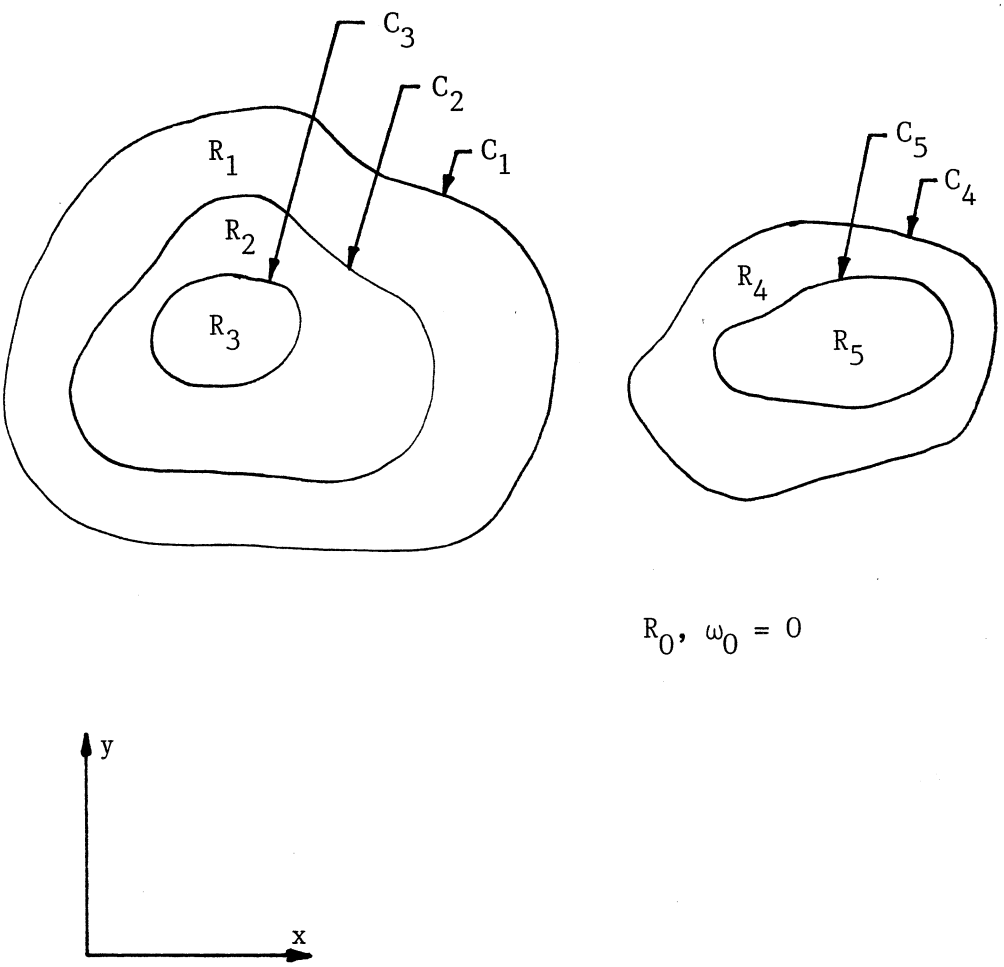

Figure 3.1 : Definion sketch for the Contour-Dynamic formulation. There are two FAVRs consisting of a total of 5 constant vorticity regions $R_1 \ldots R_5$ embedded in an otherwise irrotational flow. The contours $C_1 \ldots C_5$ delineate the discontinuities in the vorticity field.

combined with a continuous velocity field, ensures that particles initially constituting the contours C_j will always be part of the C_j. This means that, to fully describe the evolution of the uniform-vorticity regions R_j, and therefore of the entire flow, we only need to follow the motions of the bounding contours.

The CD method, in principle, provides an accurate solution to the Euler equations (for a piecewise-constant ω_z field) and retains the mesh free advantages of the vortex methods discussed in section 2.3. When compared with the point-vortex or CIC methods, the reduction in dimensionality inherent in the CD method has the advantage of lower computer storage and processing-time requirements for defining the fine-scale motions of FAVRs (at least for moderate times).

CD as an evolutionary technique has been used by Zabusky et al (1979) to study the large surface deformations of two equal, like-signed FAVRs in close proximity. The aim of this study was to elucidate the influence of these deformations on the coalescence phenomena. This flow configuration was previously studied by Christiansen (1973) using the CIC method and will be further discussed in chapter 10 of this thesis. Pullin (1981) used a periodic CD formulation (in terms of complex variables) to study the large-scale motions of a two-dimensional vortex layer near a wall. More recently, Pozrikidis & Higdon (1986) used a periodic formulation to investigate the roll-up of a two-dimensional temporal shear layer. They examined the effect of initial layer thickness and perturbation amplitude upon the final state of the rolled-up layer.

CD has also been used to obtain steady state vorticity configurations with complex-shaped bounding contours. For example, there are the V-states (e.g., Deem & Zabusky 1978; Wu, Overman & Zabusky 1984) which are uniformly rotating (or translating, Pierrehumbert 1980) solutions to the two-dimensional Euler equations. The simplest of these are finite-area generalizations of the pair of equal (or opposite

signed) point-vortices. Dritschel (1985) has studied the more general problem of several FAVRs whose centroids are located at the vertices of a regular polygon. Saffman & Szeto (1980) used a formulation for periodic vorticity distributions to obtain shapes of the FAVRs constituting a linear array of vortices with like circulation. A periodic street of vortices with alternating circulation was studied by Saffman & Schatzman (1981, 1982) as a model of the Karman vortex street.

To date most simulations have used uniform vorticity (M = 1) distributions. However, multiple nested contours were utilized by Jacobs and Pullin [2] and in the application section of this thesis. Recently, an equivalent "multiple-water-bag" technique for plasma simulation has been presented by Calder & Laframboise (1986). Various strategies for extending available simulation times have been suggested by other workers and are discussed in section 5.3 and appendix 2. These include *(i)* contour surgery to remove features of negligible dynamical significance (Dritschel 1986a) *(ii)* inclusion of model dissipative terms such as the tangential regularization of Overman & Zabusky (1983) and *(iii)* desingularization of the equations of motion for the contours as Krasny (1986) has done for the vortex sheet problem.

In the next section we describe a formulation of the CD algorithm for the nonlinear evolution of a single two-dimensional FAVR with piecewise-constant vorticity distribution delineated by a set of nested contours. After describing the CD formulation for purely two-dimensional flows, we add the three-dimensional effect of vortex stretching to produce a quasi-three-dimensional simulation technique. This formulation considers the special case of an external three-dimensional plane strain field superimposed upon the motions of the cylindrically-symmetric vorticity distribution. The effect on the vorticity transport equation (2.15) is to make the term $(\underline{\omega}.\nabla)\underline{u}$ nonzero and, by aligning the extensional axis of the strain with the vortex lines, we produce a vorticity amplification with no reorientation. In some recent turbulence models (see e.g. Lundgren 1982; Perry &

Chong 1982; Corcos & Lin 1984) this local strain is assumed to arise from the average motions of the surrounding three-dimensional flow or larger-scale motions.

3.1 Contour Dynamics for Two-Dimensional Flows

The formulation may proceed by considering an initial vorticity field with only one component of vorticity

$$\underline{\omega} = \omega_z(x, y, t=0)\ \underline{k} \quad , \tag{3.1}$$

with an associated two-dimensional velocity field

$$\underline{u} = V_x\ \underline{i} + V_y\ \underline{j} \quad , \tag{3.2}$$

where ($\underline{i}$, $\underline{j}$, $\underline{k}$) are the unit vectors along the cartesian axes. Using $\nabla.\underline{u} = 0$ for an incompressible fluid and $\underline{\omega} = \nabla \times \underline{u}$ it follows that

$$\frac{\partial V_x}{\partial x} + \frac{\partial V_y}{\partial y} = 0 \quad , \tag{3.3a}$$

$$\omega_z = \frac{\partial V_y}{\partial x} - \frac{\partial V_x}{\partial y} \quad . \tag{3.3b}$$

Hence, V_x and V_y may be derived kinematically from a cylindrically-symmetric vorticity field by solution of the appropriate Poisson equation (2.21). The evolution of the vorticity field must satisfy the vorticity transport equation (2.15) which for a purely two-dimensional flow reduces to (2.16)

$$\frac{D\omega_z}{Dt} = 0 \quad . \tag{2.16}$$

We will now model an initial nonuniform vorticity field in (3.1) by a piecewise-constant distribution defined as

$$\omega_z(x,\ y,\ 0) = \begin{cases} \omega_0(0) = 0 & \text{in } R_0(t=0) \\ \omega_j(0) = \text{const.} & \text{in } R_j(t=0) \quad , \\ & j = 1 \ \ldots \ M. \end{cases} \tag{3.4}$$

for a single isolated FAVR. From this point we drop the z-subscript and refer to the scalar vorticity as ω. In equation (3.4), $R_j(0)$ is an initial domain of the (x, y)-plane bounded by counter-clockwise curves (contours) $C_j(0)$ and $C_{j+1}(0)$, j = 1...M while $R_0(0)$ is an infinite domain containing irrotational fluid. Figure 3.2 shows a single FAVR with piecewise-constant vorticity delineated by a set of nested counter-clockwise running contours C_j counting j = 1, 2 from the outermost contour inwards. The innermost region (here R_2) is simply connected hence, for M regions, there is no C_{M+1}.

The velocity field may be decomposed as a sum of a rotational component and the gradient of a cylindrically-symmetric velocity potential Φ. Consider the single uniform-vorticity FAVR in figure 3.3. The full velocity field is given by

$$\begin{aligned} \underline{u} &= \nabla\Phi_0 && \text{in } R_0 \quad , \\ \underline{u} &= \nabla\Phi_1 - \omega_1 y\underline{i} && \text{in } R_1 \quad . \end{aligned} \tag{3.5}$$

The velocity jump across the contour C_1 due to the rotational flow field is

$$(u_x - iu_y)_{r,1} - (u_x - iu_y)_{r,0} = -\omega_1 y \quad , \tag{3.6}$$

where u_x and u_y are x- and y-components respectively of the velocity field, $i^2 = -1$ and the subscript r refers to the rotational component. Since we require the full velocity field to be continuous, this discontinuity must be cancelled by an equal but opposite discontunuity in $\nabla\Phi$ produced by a distribution of singularities $g(\zeta')$ around C_1. Here $\zeta = x + iy$ is the complex coordinate on C_1 in the (x, y)-plane. The irrotational velocity may then be written as

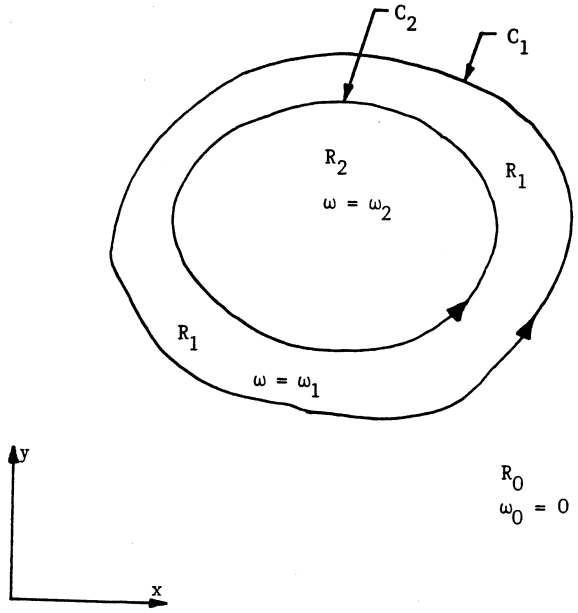

Figure 3.2 : A single nonuniform vorticity FAVR consisting of two nested regions (R_1 and R_2) of uniform-vorticity fluid. These regions are bounded by contours C_1 and C_2 but, with the innermost region (R_2) being simply connected, there is no C_3.

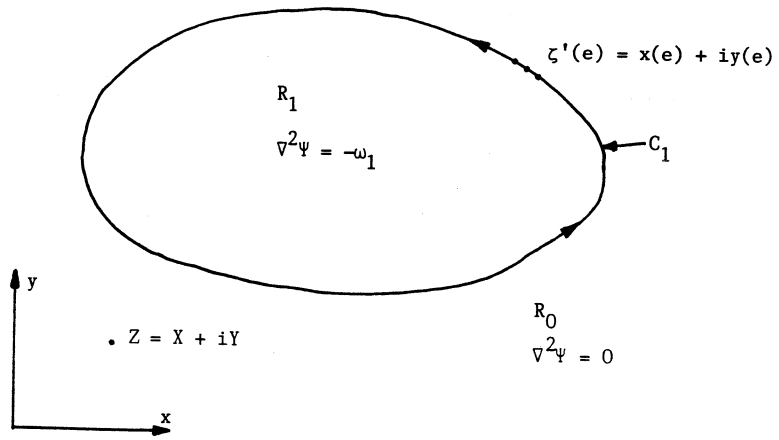

Figure 3.3 : A single uniform-vorticity FAVR embedded in an otherwise irrotational flow field. The velocity field within the contour C_1 is rotational. The point Z is any general point on the ζ-plane while the contour is defined by $\zeta'(e)$ where e is a parameter that varies monotonically around the contour.

$$(u_x - iu_y)_{irr} = \frac{dW}{dZ} = \frac{1}{2\pi i} \oint_{C_1} g(\zeta') \frac{1}{Z - \zeta'} d\zeta' \quad , \qquad (3.7)$$

where primed quantities are integration variables around C_1. Note that, in equation (3.7), the field point $Z = X + iY$ may be in either R_1 or R_0 while ζ' is a point on the contour. The appropriate form of $g(\zeta')$ may be obtained by using the Plemelj formulae (Milne-Thomson §5.596, 1968) which states that the jump in dW/dZ as Z crosses C_1 is

$$\left.\frac{dW}{dz}\right|_{Z \to \zeta_0} - \left.\frac{dW}{dZ}\right|_{Z \to \zeta_1} = -g(\zeta) \quad , \qquad (3.8)$$

where ζ_1 and ζ_0 are points on the R_1 and R_0 sides of C_1 respectively. Adding equation (3.6) to (3.8), and setting the total velocity jump to zero gives

$$g(\zeta') = -\omega_1 y' \quad . \qquad (3.9)$$

Hence, the total velocity field is

$$u_x - iu_y = \frac{-\omega_1}{2\pi i} \oint_{C_1} y' \frac{1}{Z - \zeta'} d\zeta' - H\omega_1 \gamma \quad , \qquad (3.10)$$

where $H = 1$ if Z is within C_1 and $H = 0$ otherwise. Appendix 1 outlines a derivation of equation (3.10) using Green's theorem and shows that the velocity field induced by the FAVR tends to that of a point-vortex as Z becomes large. The integral in equation (3.10) may be decomposed as

$$\oint_{C_1} (Y - y') \frac{1}{Z - \zeta'} d\zeta' - Y \oint_{C_1} \frac{1}{Z - \zeta'} d\zeta'$$
$$\equiv \oint_{C_1} (Y - y') \frac{1}{Z - \zeta'} d\zeta' + 2\pi i Y H \quad . \qquad (3.11)$$

The second integral on the left side of equation (3.11) can be evaluated using residues and when substituted into equation (3.10) produces an expression for the velocity,

$$u_x - iu_y = \frac{\omega_1}{2\pi i} \oint_{C_1} \frac{(Y - y')}{(Z - \zeta')} d\zeta' \quad , \tag{3.12}$$

which is valid both inside, outside and on C_1.

Equation (3.12) may be generalized to evaluate the velocity due to a vortex with domains R_j, $j = 1...M$, of piecewise-constant vorticity ω_j bounded by nested contours C_j as seen in figure 3.2. For C_j, the distribution of singularities equivalent to that in equation (3.9) is

$$g(\zeta') = -(\omega_j - \omega_{j-1})\, y' \quad , \tag{3.13}$$

giving a velocity field

$$u_x - iu_y = \frac{1}{2\pi i} \sum_{m=1}^{M} \Delta\omega_m \oint_{C_m} \frac{(Y - y')}{(Z - \zeta')} d\zeta' \quad , \tag{3.14}$$

where $\Delta\omega_m = \omega_m - \omega_{m-1}$ and the summation is over all nested contours in each FAVR.

The continuous velocity field of equation (3.14) and the Helmholtz theorem (2.16) imply that particles on the bounding contours C_j maintain their identity for all time. Identifying the velocity $d\zeta_j^*/dt$ ($* \equiv$ conjugate) of a material point on C_j with the Eulerian velocity (3.14) we obtain the equation for the evolution of C_j as

$$\frac{d\zeta_j^*}{dt} = \frac{1}{2\pi i} \sum_{m=1}^{M} \Delta\omega_m \oint_{C_m} \frac{(y_j - y_m')}{(\zeta_j - \zeta_m')} d\zeta_m' \quad , \tag{3.15}$$

Note that equation (3.15) is a generic equation for isolated vortex regions and is fully equivalent to the

inviscid Euler equations in two dimensions expressed as an integro-differential equation governing an initial value problem. Particular solutions are obtained numerically (see chapter 4) because the governing equation (3.15) is nonlinear.

3.2 Spatially Periodic Vorticity Configurations

Having discussed isolated vortex regions, we now extend the CD formulation to include the interaction of many vortex regions by considering vorticity configurations which are periodic in the x-direction. Figure 3.4a illustrates a vorticity distribution consisting of an infinite x-wise periodic array of identical FAVRs with centroids located at $x = n\lambda$, $n = -\infty...0...\infty$. Since the configuration is unaffected by a translation of the coordinate system $\pm n\lambda$ in the x-direction, we need consider the evolution of only one FAVR. In the limit of this distribution becoming a "continuous" vortex layer, the contours may be defined as shown in figure 3.4b. To calculate the evolution of the layer, only the evolution of the contours $C^{(1)}$ and $C^{(3)}$ need be followed as $C^{(2)}$ and $C^{(4)}$ form an arbitary boundary between adjacent wavelengths. Note that all wavelengths are constrained to be translated images of the contours in $-\lambda/2 \leq x < \lambda/2$.

Although only uniform vorticity is considered in figures 3.4a and 3.4b, a nonuniform distribution may be introduced and defined via a set of nested contours. For the discrete FAVR array, the C_j take the same form as those in the isolated FAVR case shown in figure 3.1 but, for the periodic layer, they will have the configuration shown in figure 3.5 where a single period of the layer is defined as two regions R_1 and R_2. The contours separating adjacent wavelengths of the layer (i.e., $C_2^{(4)}$ and $C_1^{(4)}$) coincide along the length of the inner contour ($C_2^{(4)}$).

The construction of the Eulerian velocity field proceeds along the same lines as that in section 3.1 but the array of

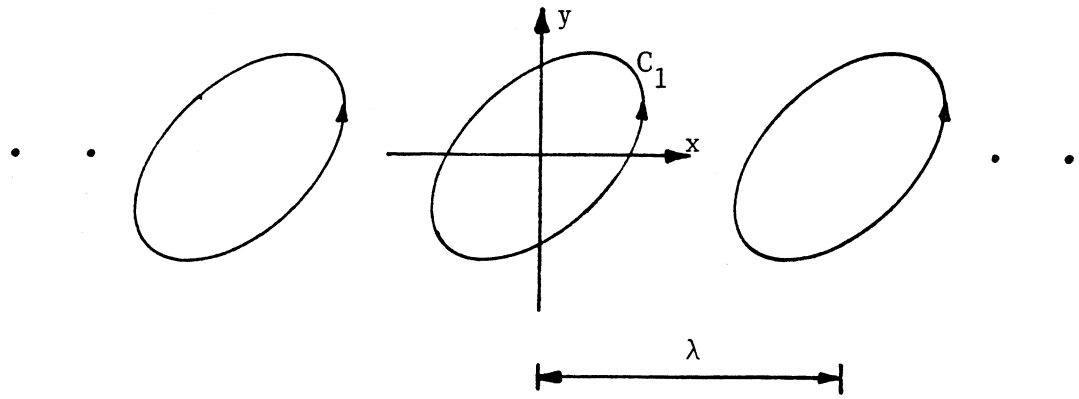

Figure 3.4a : A periodic array of discrete FAVRs. The array extends to $x = \pm\infty$ with wavelength λ. The evolution of only one contour, C_1, needs to be computed as the other elements of the array are constrained to be translated images of this FAVR.

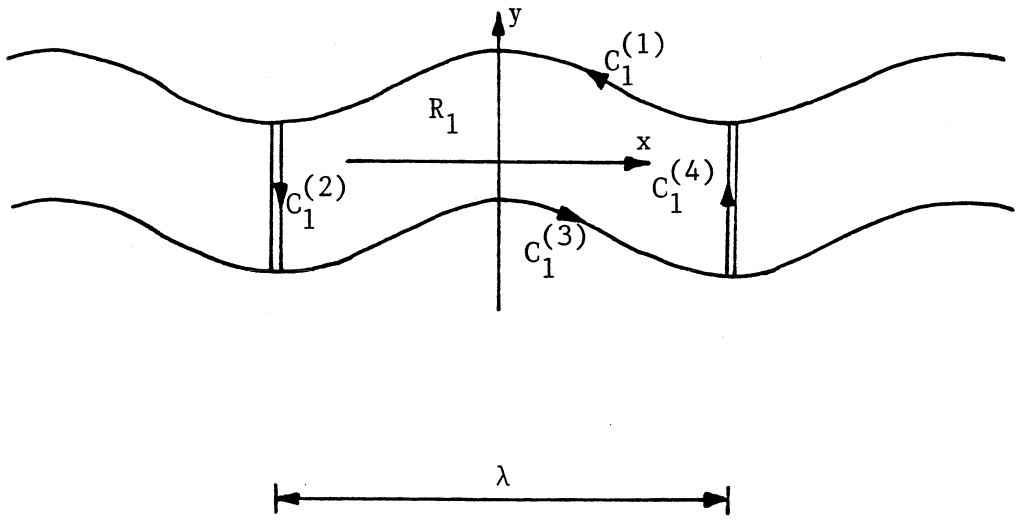

Figure 3.4b : A section of a uniform-vorticity shear layer. The contour C_1 bounding one period, R_1, of the layer is broken into segments $C_1^{(1)}$, $C_1^{(2)}$, $C_1^{(3)}$, and $C_1^{(4)}$. Segments (2) and (4) delineate the boundaries between adjacent wavelengths of the layer.

singularities, with distribution $g(\zeta')$ along one period, produces a complex flow potential for the rotational part of the velocity field

$$W(Z) = \frac{1}{2\pi i} g(\zeta') \sum_{n=-\infty}^{\infty} \ln(Z - \zeta' + n\lambda) \quad . \tag{3.16}$$

This summation converges to

$$W(Z) = \frac{1}{2\pi i} g(\zeta') \ln \left\{ \sin \left[\frac{\pi}{\lambda}(Z - \zeta') \right] \right\} \quad , \tag{3.17}$$

as shown in Milne-Thomson §13.71 (1968). Using this complex potential, and following the arguments of section 3.1, the induced velocity field becomes

$$u_x - iu_y = \frac{1}{2\lambda i} \sum_{m=1}^{M} \Delta\omega_m \oint_{C_m} (Y - y') \cot \left[\frac{\pi}{\lambda} (Z - \zeta') \right] d\zeta' \quad , \tag{3.18}$$

where $\Delta\omega_m = \omega_m - \omega_{m-1}$, the summation is over all nested contours and, for the vortex layer, $C_m = C_m^{(1)} + C_m^{(3)}$. Equation (3.18) is the periodic distribution equivalent of (3.14) and the equivalent CD equation

$$\frac{d\zeta_j^*}{dt} = \frac{1}{2\lambda i} \sum_{m=1}^{M} \Delta\omega_m \oint_{C_m} (y_j - y_m') \cot \left[\frac{\pi}{\lambda} (\zeta_j - \zeta_m') \right] d\zeta_m' \tag{3.19}$$

follows by analogy.

3.3 Vortex Stretching and Contour Dynamics

We will now develop a flow model, in which a three-dimensional strain is superimposed upon a cylindrically-symmetric vortex flow. This may be used to study the effect of strain-induced stretching on the nonlinear self-interaction of the vorticity field (Jacobs & Pullin [1]).

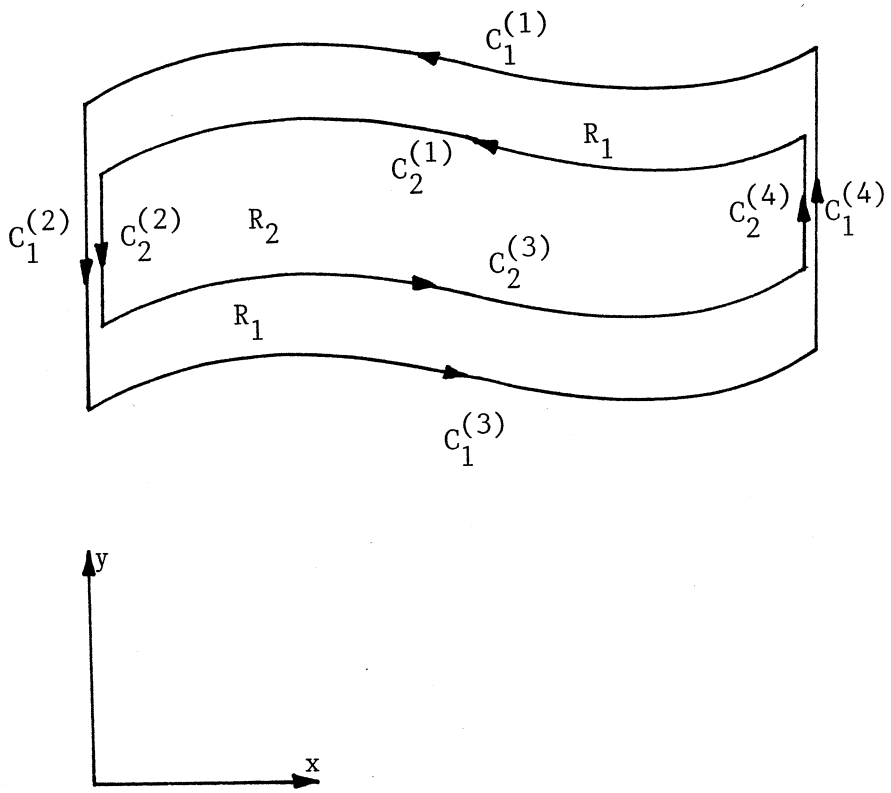

Figure 3.5 : One wavelength of a nonuniform vorticity shear layer consisting of two nested uniform-vorticity regions, R_1 and R_2. The closed contours C_1 and C_2 have been divided into segments superscripted (1) ... (4). Segments (1) and (3) define the layer shape while segments (2) and (4) delineate the arbitary boundaries between adjacent wavelengths of the layer. Segments (2) and (4) need not be vertical straight lines as shown here. Although they are shown to be separate for clarity, segments $C_2^{(2)}$ and $C_2^{(4)}$ actually coincide with $C_1^{(2)}$ and $C_1^{(4)}$ respectively.

The initial vorticity field is that defined in equation (3.1)

$$\underline{\omega} = \omega_z(x, y, t=0)\ \underline{k} \quad , \tag{3.19}$$

but is now embedded in an irrotational strain field

$$\underline{u}_s = -\beta(t)\ x\ \underline{i} + [\beta(t) - \gamma(t)]\ y\ \underline{j} + \gamma(t)\ z\ \underline{k} \quad , \tag{3.20}$$

where $\beta(t)$ and $\gamma(t)$ are arbitary strain rates which are known functions of time. Positive $\gamma(t)$ will stretch the vorticity in the z-direction. This is illustrated in figure 3.6 where the velocity field of the stretching strain is represented by four streamline segments. We shall refer to 3 special cases of interest

(i) plane two-dimensional strain $\gamma(t) = 0$,

(ii) plane three-dimensional stretching strain $\beta(t) = 0$, $\gamma(t) > 0$, and

(iii) pure axisymmetric stretching strain $\beta(t) = \gamma(t)/2$.

The full velocity field is given by

$$\underline{u} = u_x\ \underline{i} + u_y\ \underline{j} + u_z\ \underline{k} \quad , \tag{3.21}$$

where

$$u_x = -\beta(t)\ x + V_x(x, y, t) \quad , \tag{3.22a}$$

$$u_y = [\beta(t) - \gamma(t)]\ y + V_y(x, y, t) \quad , \tag{3.22b}$$

$$u_z = \gamma(t)\ z \quad . \tag{3.22c}$$

Using $\nabla.\underline{u} = 0$ for an incompressible fluid, and defining vorticity as $\underline{\omega} = \nabla \times \underline{u}$, we again obtain the relations (3.3 a,b). Hence, V_x and V_y may be derived kinematically from the vorticity field by solving the Poisson equation

$$\nabla^2\Psi = -\omega \quad , \tag{2.21}$$

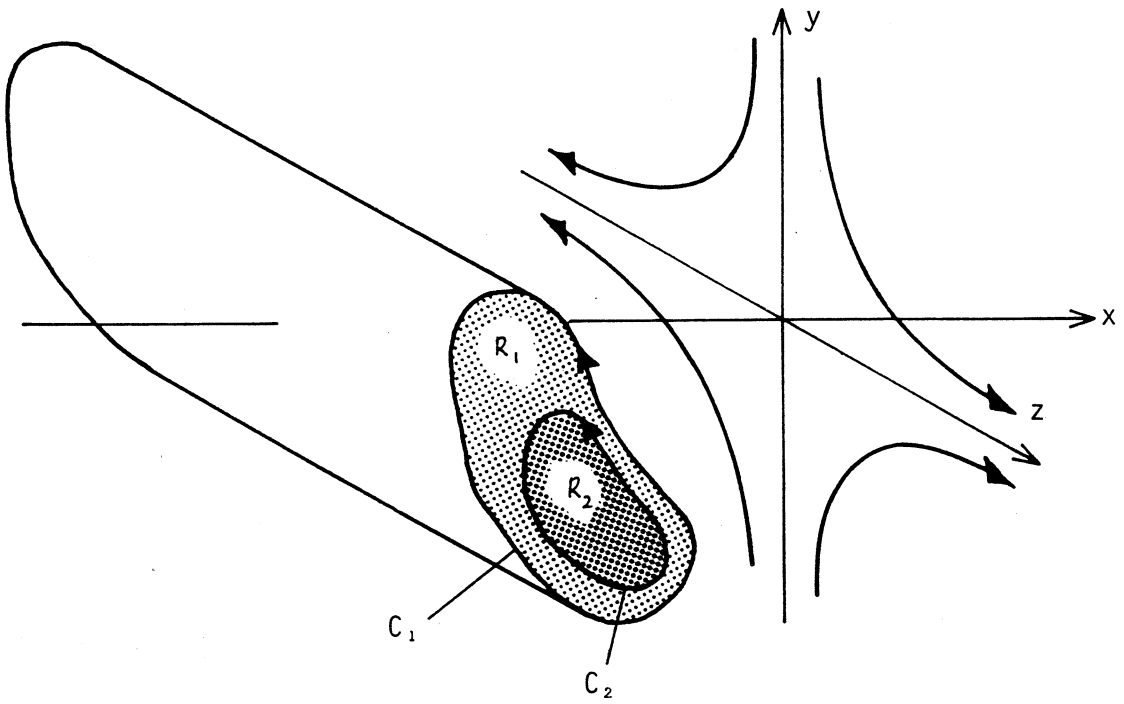

Figure 3.6 : Sectional view of a cylindrically-symmetric FAVR consisting of two regions (R_1 and R_2) of uniform vorticity embedded in a stretching strain field. The four curved streamlines in the (y, z)-plane represent the stretching component of the imposed plane strain field.

The effect of the stretching strain field becomes evident when the components for the vorticity field (3.1) and the total velocity field (3.20) are substituted into the vorticity transport equation (3.15) with Re = ∞ to give

$$\frac{D\underline{\omega}}{Dt} = (\underline{\omega}.\nabla)\underline{u} \quad , \tag{3.23a}$$

which then reduces to

$$\frac{D\omega_z}{Dt} = \gamma(t)\ \omega_z \quad . \tag{3.23b}$$

The solution to equation (3.23b) along particle paths x(t), y(t) is

$$\omega_z[x(t),y(t),t] = \omega_z[x(0),y(0),0]\ \exp[Q(t)] \quad , \tag{3.24a}$$

$$Q(t) = \int_0^t \gamma(t')\ dt' \quad , \tag{3.24b}$$

and $\omega_z[x(0),y(0),0]$ is the initial vorticity. Equations (3.24a, b) represent the intensification of particle vorticity (for $\gamma(t) > 0$) by the z-component of the applied strain field (3.20). Equations (3.23b)-(3.24) show that the vortex-dynamics preserves the initially piecewise-constant property of the vorticity field so that, in the mapping $C_j(0) \rightarrow C_j(t)$, the C_j retain their identity as the material curves that delineate the vorticity discontinuities.

Following the arguments of section 3.1, we then obtain a CD formulation for the evolution of the C_j bounding piecewise-constant regions of vorticity (3.4) embedded in the three-dimensional strain field (3.20) as

$$\frac{\partial \zeta_j^*}{\partial t} = -\beta(t)\, x_j + i\,[\gamma(t) - \beta(t)]\, y_j + \frac{\exp[Q(t)]}{2\pi i} \sum_{m=1}^{M} \Delta\omega_m(0) \oint_{C_m} \frac{y_j - y_m'}{\zeta_j - \zeta_m'}\, d\zeta_m' \quad ,$$

$$j = 1 \ldots M \quad , \qquad (3.25)$$

The equivalent equation governing the evolution of stretched, x-periodic vorticity distributions (for which the two-dimensional form is equation (3.19)) may be written as

$$\frac{\partial \zeta_j^*}{\partial t} = i\,\gamma(t) y_j + \frac{\exp[Q(t)]}{2\lambda i} \sum_{m=1}^{M} \Delta\omega_m(0) \oint_{C_m} (y_j - y_m') \cot\left[\frac{\pi}{\lambda}(\zeta_j - \zeta_m')\right] d\zeta_m' \quad ,$$

$$j = 1 \ldots M \quad . \qquad (3.26)$$

Note that equation (3.26) contains only a plane stretching strain (i.e., special case *(ii)* $\beta = 0$).

As with the purely two-dimensional formulation, the "stretching" model does not allow the creation of vorticity. Hence, the circulation Ω_j of region R_j is an invariant of the flow and, from (3.4) and (3.24), the area A_j enclosed by C_j and C_{j+1} varies as

$$A_j(t) = A_j(0)\, \exp[-Q(t)] \quad . \qquad (3.27)$$

This "stretching" formulation is not unique. Lundgren (1982) has shown that the initial value problem (3.25) may be transformed into an equivalent two-dimensional flow with the change of variables

$$T = \int_0^t \exp[Q(t')]\, dt' \quad , \qquad (3.28a)$$

$$\sigma(T) = \exp[Q(t(T))/2]\ \zeta(t(T)) \quad , \tag{3.28b}$$

in equation (3.25) to give

$$\frac{\partial \sigma_j^*}{\partial t} = -b(T)\ \exp[-Q(t(T))]\ \sigma_j + \frac{1}{2\pi i} \sum_{m=1}^{M} \oint_{C_m} \Delta\omega_m(0)\ \frac{\eta_j - \eta_m'}{\sigma_j - \sigma_m'}\ d\sigma_m' \quad , \tag{3.29}$$

where $\sigma = \varepsilon + i\eta$ and $b(T) = \beta(t(T)) - \gamma(t(T))/2$. This is a strictly two-dimensional flow in the σ-plane (with time variable T), subject to a plane two-dimensional strain with principal axes of strain along the ε and η axes. The physics of the flow is unchanged so that, for the same initial conditions, the vortex boundary in σ at time T has the same shape as the corresponding boundary in ζ at time t but is scaled by the factor $\exp[Q(t)/2]$. For the special case of axisymmetric strain, the equivalent two-dimensional flow is unstrained, that is $b(T) = 0$.

Thus, as an alternative to (3.25), we could use (3.28) to add the effect of stretching on the flow evolution governed by (3.29). There is no computational advantage to be obtained by following this path hence we develop the numerical implementation using equations (3.25) and (3.26) for single FAVRs and periodic vorticity distributions respectively. A comparison of results for a test case computed using both equations (3.25) and (3.29) is presented in section 5.1.

4.0 NUMERICAL IMPLEMENTATION

As discussed in chapter 2, vortex dynamics is an extremely nonlinear problem and, to date, only a few nontrivial analytic solutions to two-dimensional vortex flows are known (e.g. the nondeforming, rotating Kirchoff vortex discussed in Lamb, §159 (1932). One general procedure for obtaining timewise solutions to the CD equations (3.25) and (3.26) is to specify the initial vorticity field and then numerically calculate the subsequent evolution in discrete time-steps. In this chapter, we outline the numerical procedure that we initially applied to equation (3.25) to obtain solutions for single (and paired) isolated vortex regions and, later, to equation (3.26) to obtain solutions for spatially periodic arrays and "continuous" distributions such as the free shear layer. Our aim was to produce a robust and accurate code but the omission of viscous dissipation (in order to directly calculate the the evolution problem in the limit Re = ∞) may lead to an ill-posed or pathologically unstable evolutionary problem. Manifestations of this instability include the formation of cusps and slender filaments on the bounding contours which involve a large computing cost to resolve accurately.

Consider a single FAVR, as shown in figure 4.1, with strain rates $\gamma(t) = \gamma_o$ and $\beta(t) = \beta_o$ as constants. This FAVR is comprised of M = 2 regions R_j, j = 1, 2 with initial areas $A_j(0)$, j = 1, 2, and bounding contours C_j, j = 1, 2. All physical quantities in equation (3.23) are made dimensionless against characteristic length and time-scales. For isolated FAVRs, we choose $[A_1(0)]^{1/2}$ and $[A_1(0)/\Gamma]$ to be our characteristic length and time respectively. This is equivalent to putting $A_1(0) = 1$ and $\Gamma = 1$ (i.e., unit area enclosed by the outer contour and unit circulation of the FAVR) for the computation.

The initial conditions refer to the geometric shapes of the $C_j(0)$ and the values of the $\omega_j(0)$. For each particular vortex configuration to be considered in chapters 7-10, the

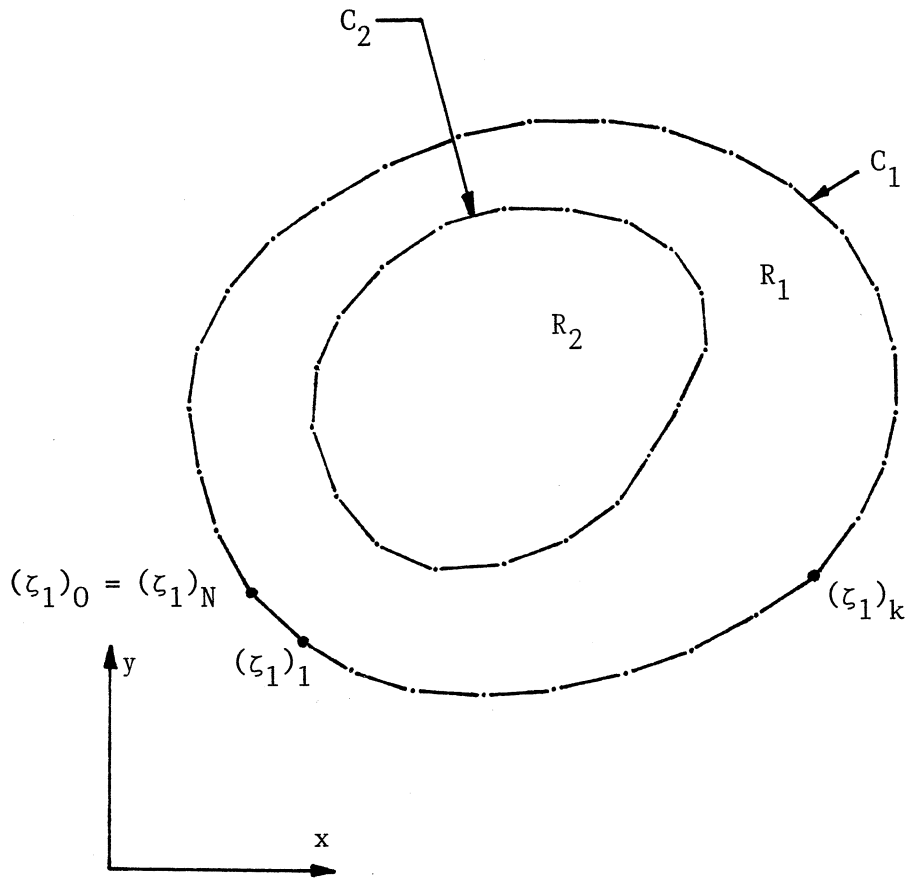

Figure 4.1 : A single FAVR with M = 2. The contours C_j are defined by sets of nodes joined by line segments. To close the contour, node 0 is set equal to node N. The node index (k) progresses anticlockwise around the contours.

initial conditions will be defined at the beginning of the appropriate results section. The initial vorticity profile of the FAVR may be either a uniform distribution (i.e. M = 1) or may be a piecwise-constant profile with nested contours (M > 1). Particular values for $\omega_j(0)$ are chosen to give $|\Gamma| = 1$ in each discrete FAVR or in one period of the continuous shear layer.

There are four major sections to the implementation of the CD equations :

(i) Each continuous contour is discretized by defining it as a set of nodes connected by line-segments. This produces a finite set of ordinary differential equations (ODEs) suitable for a numerical implementation.

(ii) The line integrals, now over each small segment, are evaluated either analytically or by numerical quadrature and are then summed to approximate the integrals on the right hand sides of equations (3.25) and (3.26).

(iii) Having evaluated the right hand side of the CD equation, the solution is stepped forward in time using a standard technique for first order ODEs.

(iv) The node set is (occasionally) updated to ensure that the contour description remains adequate.

The computer codes used in the present work (available in Jacobs [5]) evolved as refinements were made to the numerical implementations of the procedures mentioned in subsections *(i)-(iv)*. The essential features of the major program versions are summarized in table 4.1 and described more fully in the following sections. As we did not have sufficient computing resources to compute all solutions with the most up-to-date implementation, we will give the "code-version" (table 4.1) for each set of results where appropriate.

4.1 Discretization of the Contours

To produce a finite description, we first discretize the contours C_j, j = 1...M, by defining each contour by a set of

Table 4.1 : Features of the major code implementations.

Implementation	Features
A	ζ-plane formulation (isolated FAVRs) straight line interpolating segments analytic integration
B	ξ-plane formulation (x-periodic vorticity) parabolic interpolating segments numerical quadrature only (no analytic patch)
C	ζ-plane formulation (x-periodic vorticity) parabolic interpolating segments numerical quadrature plus analytic patch
D	ζ-plane formulation (x-periodic vorticity) parabolic interpolating segments numerical quadrature only (no analytic patch)

N_j nodes $(\zeta_j)_k$, $k = 0...N_j$, $(\zeta_j)_0 = (\zeta_j)_N$, joined by interpolating line segments. There are $NSEG_j$ segments describing C_j with a local polynomial, interpolated over either two or three nodes, defining each segment. The velocities of the $(\zeta_j)_k$ are then evaluated by summing the contributions of each interpolated segment to the integral in the governing equation (3.23), thus giving a set of 2N

$$N = \sum_{j=1}^{M} N_j(t) \quad , \tag{4.1}$$

ordinary differential equations (ODEs) for the node coordinates, $((x_j)_k, (y_j)_k)$.

Discretizing the C_j and replacing the integral on the right hand side of equation (3.25) as a summation of integrals over the $NSEG_j$ individual segments gives the governing equation for the node coordinates as

$$\left[\frac{dx_j}{dt} \right]_k - i \left[\frac{dy_j}{dt} \right]_k = -\beta_o \, (x_j)_k + i \, [\gamma_o - \beta_o] \, (y_j)_k$$

$$+ \frac{\exp(\gamma_o t)}{2\pi i} \sum_{m=1}^{M} \Delta\omega_m(0) \left\{ \right.$$

$$\left. \sum_{s=1}^{NSEG_m} \int_s \frac{((y_j)_k - y_m')}{((\zeta_j)_k - \zeta_m')} \frac{\partial \zeta_m'}{\partial e'} \, de' \right\} \quad , \tag{4.2}$$

$$k = 1...N_j(t), \; j = 1...M \quad .$$

These segments of the C_j are defined locally by interpolating curves on node subsets with parameter e. For the simulations reported here, we have used either linear linesegments defined by two end points or parabolic curve segments defined over three sequential nodes. Other approaches to the interpolation include circular arcs fitted to subsets of three nodes (Pozrikidis & Higdon 1986) and cubic-splines (Dritschel

1986a). The aim of the higher order methods is to reduce the number of nodes required to adequately resolve the contour. This is an important point as the CD method requires $O(N^2)$ arithmetic operations per time-step (for large N). Adequate resolution is required for conservation of the flow invariants such as the total circulation and also for maintaining contour flexibility. We found that the C_j were inflexible if the segment sizes were significantly larger than the length-scales associated with the velocity variations. Dritschel (1986a) claims that there is also an advantage in having a description (e.g. cubic-spline) that does not introduce discontinuities in the contour curvature. We note that both our linear and parabolic segments do so.

4.2 Integration for Straight Line Segments

The integrand over each segment in equation (4.1) is always bounded but is not well behaved when $(\zeta_j)_k$ approaches C_m (see appendix 3). A fixed rule numerical quadrature over each segment would be relatively straightforward and fast over well behaved sections of the contour but, would not cope with the integrand behaviour for small nonzero values of $|(\zeta_j)_k - (\zeta_m)'|$. Early CD simulations (e.g. Zabusky et al 1979; Pullin 1981) used straight line segments as the integral over each segment could be evaluated in closed form fairly easily. For our isolated vortex and vortex-coalescence simulations, we have chosen to use straight-line segments for the same reasons. The C_j become closed polygons and the governing equations become a set of ODEs

$$\left[\frac{dx_j}{dt}\right]_k - i\left[\frac{dy_j}{dt}\right]_k = -\beta_o(x_j)_k + i\,[\gamma_o - \beta_o]\,(y_j)_k$$

$$+ \frac{\exp(\gamma_o t)}{2\pi i} \sum_{m=1}^{M} \Delta\omega_m(0) \left\{ \sum_{s=1}^{NSEG_m} \left\{ \right.\right.$$

$$\left[- \left((y_j)_k - (y_m)_n \right) + \frac{\left((y_m)_{n+1} - (y_m)_n \right)}{\left((\zeta_m)_{n+1} - (\zeta_m)_n \right)} \left((\zeta_j)_k - (\zeta_m)_n \right) \right]$$

$$* \left[\ln\{G^*((\zeta_j)_k - (\zeta_m)_{n+1})\} - \ln\{G^*((\zeta_j)_k - (\zeta_m)_n)\} \right] + \left[(y_m)_{n+1} - (y_m)_n \right] \Bigg\} \Bigg\} , \tag{4.3a}$$

where

$$\lim_{\substack{(\zeta_j)_k \to (\zeta_m)_n \\ (\zeta_j)_k \to (\zeta_m)_{n+1}}} \{....\} = \left[(y_m)_{n+1} - (y_m)_n \right] , \tag{4.3b}$$

and

$$G^* = \frac{\left[(\zeta_m)_{n+1} - (\zeta_m)_n \right]^*}{\left| (\zeta_m)_{n+1} - (\zeta_m)_n \right|} . \tag{4.3c}$$

Nodes $(\zeta_m)_n$ and $(\zeta_m)_{n+1}$ are the end points of segment s and * ≡ complex conjugate. Figure 4.2 shows a single segment on a section of the contour C_m and the velocity point $(\zeta_j)_k$ on contour C_j. To reduce computing effort, we evaluate the complex logarithms as

$$\ln \{G^*((\zeta_j)_k - (\zeta_m)_{n+1})\} - \ln \{G^*((\zeta_j)_k - (\zeta_m)_n)\}$$

$$= \ln \frac{r_{n+1}}{r_n} + i\theta \, \text{sign}(\Lambda) , \tag{4.4a}$$

$$\theta = \arccos (\Omega) , \tag{4.4b}$$

where

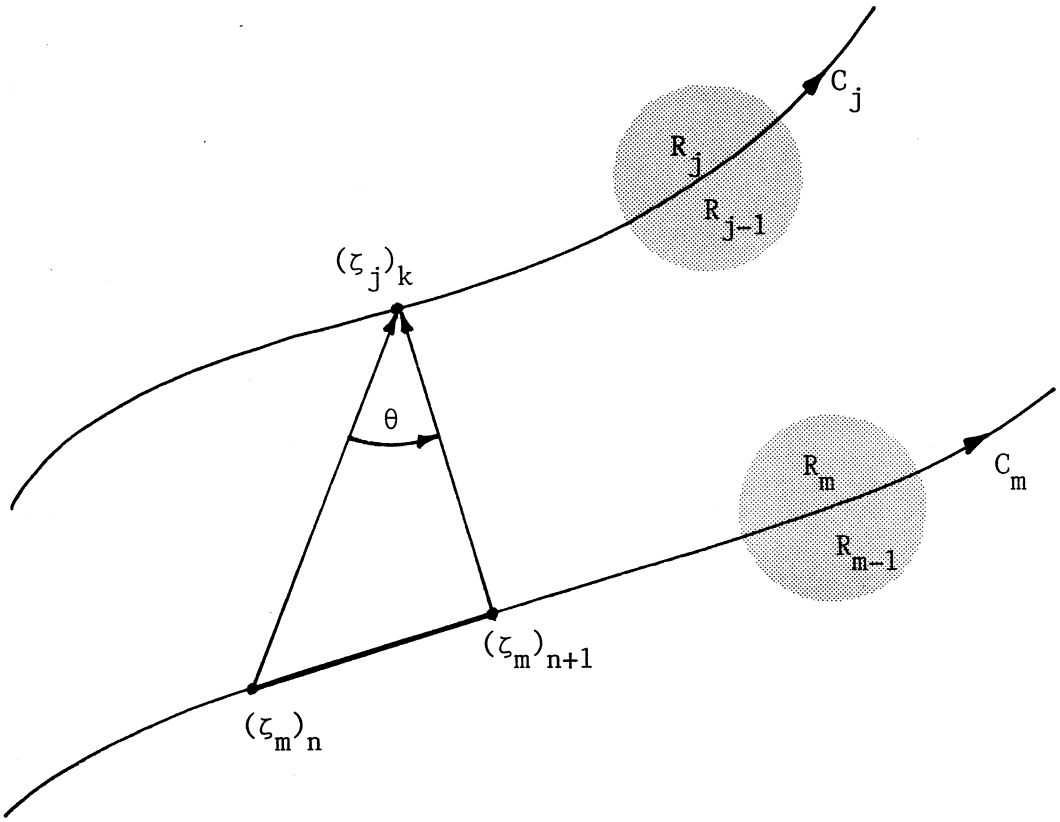

Figure 4.2 : Straight line interpolation over segment $(\zeta_m)_n \rightarrow (\zeta_m)_{n+1}$ on contour C_m. The velocity point is $(\zeta_j)_k$ on contour C_j.

$$\Omega = \{r_n^2 + r_{n+1}^2 - r_s^2\} / (2 r_n\, r_{n+1}) \quad , \tag{4.5a}$$

$$r_n = |(\zeta_j)_k - (\zeta_m)_n| \quad , \tag{4.5b}$$

$$r_{n+1} = |(\zeta_j)_k - (\zeta_m)_{n+1}| \quad , \tag{4.5c}$$

$$r_s = |(\zeta_m)_{n+1} - (\zeta_m)_n| \quad , \tag{4.5d}$$

$$\Lambda = \mathrm{Im}\{[(\zeta_j)_k - (\zeta_m)_n] . \mathrm{conjg}[(\zeta_m)_{n+1} - (\zeta_m)_n]\} \quad , \tag{4.5e}$$

and evaluate the real logarithm and angle using appropriate expansions

$$\ln \frac{r_{n+1}}{r_n} \approx \frac{\chi}{12} (12 + \chi(-6 + \chi(4 - 3\chi))) \quad , \tag{4.6a}$$

$$\theta \approx \Omega_1 (1 + \Omega_1^2/6) \quad , \tag{4.6b}$$

$$\chi = (r_{n+1} - r_n) / r_n \quad , \tag{4.6c}$$

$$\Omega_1 = (1 - \Omega^2)^{1/2} \quad , \tag{4.6d}$$

for large $|(\zeta_j)_k - (\zeta_m)_n|$. Care must be exercised as, with large NSEG, the accumulation of round-off error for each segment may become significant.

Alternatively, we could have used parabolic interpolating segments and a closed form expression as shown in appendix 3 but these are more complex than their linear-segment equivalents. In yet another variation, Dritschel (1986a) used an expansion for small curvature to obtain expressions for his cubic-spline interpolation.

4.3 Implementation for X-Periodic Vorticity Distributions

We now consider a vorticity distribution which is periodic in the x-direction either as an array of FAVRs or as a continuous shear layer. Physical quantities are nondimensionalized by setting one period (i.e. the

computational domain) to 2π and selecting the initial values of the vorticity to give $|\Gamma| = 1$ in one period of the shear layer or within one discrete FAVR in the array. The node set for each C_j is again specified as $(\zeta_j)_k$, $k = 0...N_j(t)$, $j = 1...M$, with $(\gamma_j)_o = (\gamma_j)_N$ (i.e., closed contours) for the array of discrete FAVRs and $(\gamma_j)_o = (\gamma_j)_N \pm \lambda$ (i.e., open contours) for the contours $C_j^{(1)}$ and $C_j^{(3)}$, respectively, of the vortex layer.

The equations of motion for the node coordinates (3.26) become

$$\frac{d(\zeta_j^*)_k}{dt} = i\gamma_o\,(y_j)_k + \frac{\exp(\gamma_o t)}{4\pi i} \sum_{m=1}^{M} \Delta\omega_m(0) \left\{ \sum_{s=1}^{NSEG_m} \int_s [(y_j)_k - y_m'] \cot\left[\frac{1}{2}((\zeta_j)_k - \zeta_m')\right] \frac{\partial \zeta_m'}{\partial e'}\, de' \right\} , \tag{4.7a}$$

$$k = 1...N_j(t), \quad j = 1...M,$$

where the limit of the integrand is

$$\lim_{\zeta_m' \to (\zeta_j)_k} [\text{integrand}] = \frac{\partial y_m'}{\partial e'} , \tag{4.7b}$$

For simplicity, we have only included the (y, z)-component of the three-dimensional plane strain.

In this x-periodic implementation, we choose the interpolating segments to be parabolic curves defined over subsets of three adjacent nodes $[(\zeta_m)_{n-1}, (\zeta_m)_n, (\zeta_m)_{n+1}]$, such that

$$\zeta(e) = Ae^2 + Be + C , \tag{4.8a}$$

$$\zeta(e=0) = (\zeta_m)_n , \tag{4.8b}$$

$$\zeta(e=-1) = (\zeta_m)_{n-1} \quad , \tag{4.8c}$$

$$\zeta(e=1) = (\zeta_m)_{n+1} \quad . \tag{4.8d}$$

Figure 4.3 shows a typical segment with

$$(\zeta_m)_{n-1} = 0.5 - i \quad , \tag{4.9a}$$

$$(\zeta_m)_{n} = 1.0 \quad , \tag{4.9b}$$

$$(\zeta_m)_{n+1} = 1.0 + 2.0i \quad . \tag{4.9c}$$

When we selected the type of interpolation, we were concerned with adequately describing the contour with fewer nodes than was required for linear interpolation. Although the curvature along the segment is continuous and bounded, there are discontinuities at segment boundaries. Dritschel (1986a) considers this to be a disadvantage as it introduces cusps and, possibly, difficult contour behaviour at later times.

The intergrals over the interpolating segments can no longer be obtained in closed form, so we have used a numerical quadrature combined with an "analytic-patch" procedure designed to improve the accuracy in regions where the integrand exhibits difficult behaviour. In particular, we use a 4-point Gauss-Legendre quadrature

$$\int_{-1}^{1} I(e')de' \approx \sum_{i=0}^{3} I(e_i)\, w_i \quad , \tag{4.10}$$

where the w_i are given in table 25.4 of Abramowitz & Stegun (1965). This quadrature had the added feature of eliminating the need to handle the limit (4.7b) where the velocity point coincides with one of the segment nodes (4.8). The method also provided smoother solution contours than Simpson's rule over the same contour-discretization but at the cost of a slight increase in computer processing-time.

The computation of the complex cotangent in equation (4.7a) $O(N^2)$ times per subroutine call is very expensive so it is decomposed into three simpler arithmetic operations using the transformed variable

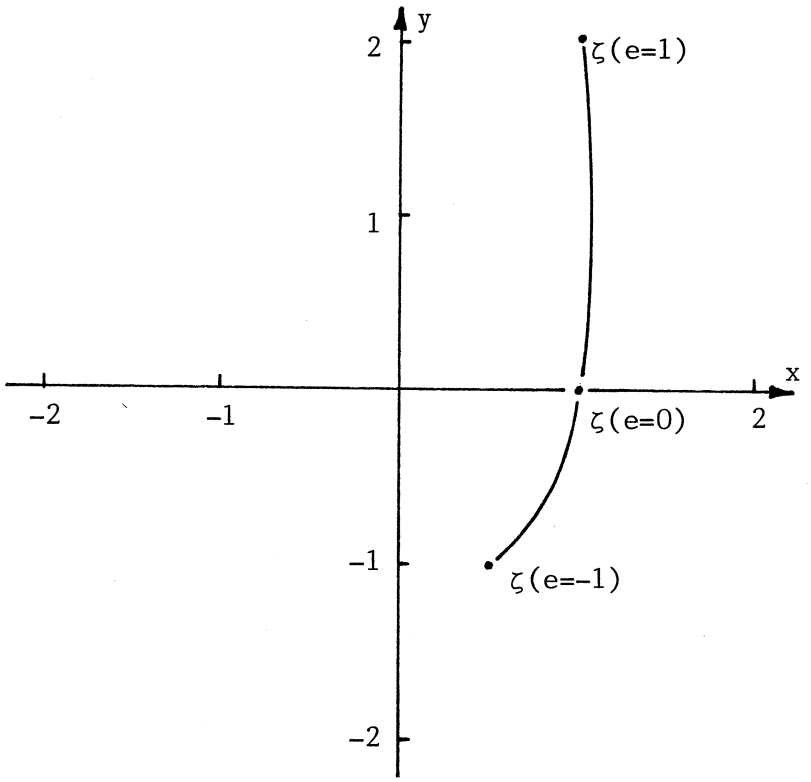

Figure 4.3 : A single parabolic segment $\zeta(e) = Ae^2 + Be + C$ defined by the subset of three nodes

$\zeta(-1) = (\zeta_m)_{n-1} = 0.5 - i$,

$\zeta(0) = (\zeta_m)_n = 1.0$,

$\zeta(1) = (\zeta_m)_{n+1} = 1.0 + 2.0i$.

$$\xi = \exp(-i\zeta) \quad . \tag{4.11}$$

The cotangent term can then be expressed

$$\cot\left[\frac{1}{2}(\zeta - \zeta')\right] = -i\left[\frac{\xi + \xi'}{\xi - \xi'}\right] \quad , \tag{4.12}$$

with the relatively expensive operation of taking the complex exponential in equation (4.11) requiring only O(N) operations (as it is done only once at the beginning of the velocity subroutine).

For the simulation of an array of stretched vortices of alternating sign (the secondary vortices of the CLS heirachy, see chapter 8), we performed the whole calculation in the transformed ξ-plane. This had the advantages that translating (convecting) points always stayed in the computational domain and that the open contours of the shear layer, $C_j^{(1)}$ & $C_j^{(3)}$ in the ζ-plane mapped to the closed contours, in the ξ-plane. Figure 4.4 shows two FAVRs of the periodic array (a) in the ζ-plane and (b) in the ξ-plane where contours C_1, and C_1 map to D_1, and D_1 respectively. Unfortunately, the distortion at large $|y|$ forced the node-adjustment procedure to be done in the ζ-plane thus requiring the transformation (4.11) to be performed at frequent intervals. The equations of motion in the ξ-plane are

$$\frac{-d(\theta_j)_k}{dt} + \frac{i}{(R_j)_k}\frac{d(R_j)_k}{dt} = i\,\gamma_o \ln(R_j)_k + \frac{\exp(\gamma_o t)}{4\pi i}\sum_{m=1}^{M}\Delta\omega_m(0)\left\{\int_{D_m}[\ln(R_j)_k - \ln R_m']\left[\frac{2(\xi_j)_k}{(\xi_j)_k - \xi_m'} - 1\right]\frac{1}{\xi'_m}\frac{d\xi'_m}{de'}\,de'\right\} \quad ,$$

$$k = 1\ldots N_j(t), \quad j = 1\ldots M \quad , \tag{4.13}$$

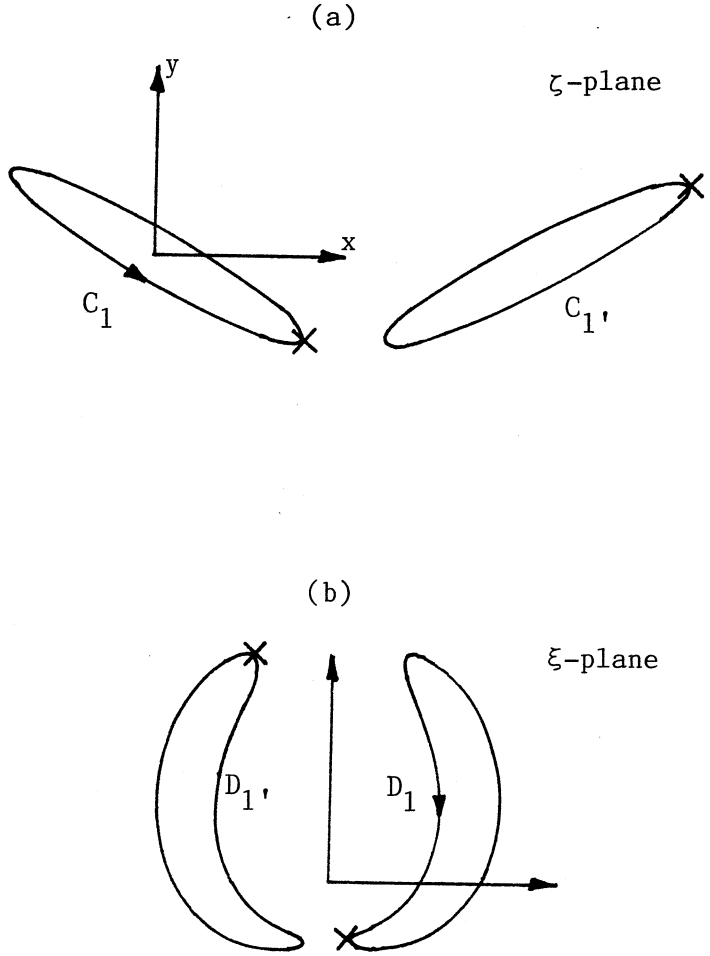

Figure 4.4 : Effect of the transformation $\xi = \exp(-i\zeta)$ on members of the x-periodic FAVR array. Contours C_1 and $C_{1'}$ in the ζ-plane (a) map to contours D_1 and $D_{1'}$, respectively in the ξ-plane (b). The Xs mark corresponding material points in each plane.

where $\xi = R\, e^{i\theta}$ and the integral is now around the transformed contour, D_m. Although the $(y - y')$ term has now been transformed to the more complex $(\ln R - \ln R')$, the logarithms need only be calculated only once per cell (on entry to the velocity subroutine).

As mentioned in section 4.2 and further discussed in appendix 3, the integrand behaves in a weakly singular manner over segments that approach the velocity point, $(\zeta_j)_k$, closely. Dritschel (figure 13, 1986b) illustrated the numerical instability that is related to the inaccurate evaluation of the velocities via a numerical quadrature. Increasing the order of the quadrature delayed the appearance of the instability but did not eliminate it. In appendix 3 we show that the numerical quadrature (4.10) provides an inaccurate estimate of the full integral when contours approach closely. A method for overcoming this problem is also described which we shall refer to as the "analytic patch".

For the implementation of this "analytic-patch", we chose to work with the (simpler) ζ-plane formulation. We decomposed the integrand into a simple part, that varied rapidly but could be integrated analytically, and a slowly varying (but more complex) part that could be accurately integrated with the fixed rule quadrature (4.10). The complexity of implementation for numerical quadrature is fairly insensitive to the style of interpolation and function complexity. The full integrand in (4.7a) has the form

$$I_{total} = (y - y') \cot\left[\frac{1}{2}(\zeta - \zeta')\right] \frac{d\zeta'}{de'} , \qquad (4.14)$$

which, for small $|\zeta - \zeta'|$, may be expanded. Retaining only first order terms, this integrand can be approximated by

$$I_{fast} = 2 \frac{(y - y')}{(\zeta - \zeta')} \frac{d\zeta'}{de'} . \qquad (4.15)$$

For segments on which the full integrand (4.14) is well behaved (i.e. slowly varying), we numerically integrate I_{total} but, on segments where our fixed quadrature rule cannot cope with the rapid variations of this integrand, we integrate

$$I_{slow} = \left\{ (y - y') \cot\left[\frac{1}{2}(\zeta - \zeta')\right] - 2\frac{(y - y')}{(\zeta - \zeta')} \right\} \frac{d\zeta'}{de'} \quad , \tag{4.16}$$

and add the analytically derived value for I_{fast}. This "analytic-patch" procedure is implemented on segments for which

$$\min(\ |(\zeta_j)_k - \zeta_m(e_i)| \ , \ i = 0...3) < \text{segsize} \quad , \tag{4.17a}$$

$$\text{segsize} = |(\zeta_m)_{n+1} - (\zeta_m)_n| + |(\zeta_m)_n - (\zeta_m)_{n-1}| \ , \tag{4.17b}$$

and $(\zeta_j)_k \neq \zeta_m(e)$, $-1 \leq e \leq 1$ (i.e. $(\zeta_j)_k$ is not part of C_m). A check is also made for the images of the velocity point in the wavelengths either side of the computational domain, $(\zeta_j)_k \pm 2\pi$. This criteria was derived from empirical results contained in appendix 3. Although the check on proximity (4.17) is fairly rough and simple, it is still too expensive to compute each time the velocity routine is called. We assume that the nodes do not move too far between calls to the node-adjustment routine and so, on entry to the velocity routine for the first time with a new set of nodes, we store an index of the "close" segments (i.e. those that satisfy equation 4.17) for each node. This information is stored in a large integer "index-array". After summing the numerically integrated contributions of each segment to the velocity of a particular node, we then look up the "index-array" and adjust the contribution of the "close" segments that are listed for this node.

When the "analytic-patch" is to be used, we calculate the value of I_{fast} using either two straight lines approximating the segment (if $|A| < \varepsilon$, $\varepsilon \approx 10 *$ machine precision) or the parabolic segment. The expressions for the straight-line

segments are very similar to those in equation (4.3) while the expressions for the parabolic segment are

$$\int_{-1}^{1} \frac{I_{fast}}{2}\, de = term_1 + coeff_2.term_2 + coeff_3.term_3 \ , \qquad (4.18a)$$

where

$$term_1 = 2(2B_I - A_I B/A) \ , \qquad (4.18b)$$

$$coeff_2 = -T_I + [\, A_I T + B/2\ (-B_I + A_I B/A)\,] \ / \ A \ , \qquad (4.18c)$$

$$term_2 = \ln[(\zeta_j)_k - (\zeta_m)_{n+1}] - \ln[(\zeta_j)_k - (\zeta_m)_{n-1}] \ , \qquad (4.18d)$$

$$coeff_3 = -2B_I T + [2A_I T + B/2\ (-B_I + A_I B/A)]\ B/A \ , \qquad (4.18e)$$

$$term_3 = \frac{1}{\sqrt{(-\Delta)}} \left\{ \ln\left[\frac{-B - 2A - \sqrt{(-\Delta)}}{-B - 2A + \sqrt{(-\Delta)}} \right] - \ln\left[\frac{-B + 2A - \sqrt{(-\Delta)}}{-B + 2A + \sqrt{(-\Delta)}} \right] \right\} \qquad (4.18f)$$

and where

$$\sqrt{(-\Delta)} = (B^2 + 4AT)^{1/2} \ , \qquad (4.18g)$$

$$T = (\zeta_j)_k - (\zeta_m)_n \ . \qquad (4.18h)$$

The subscript I's indicate the imaginary part. Appendix 3 contains a derivation of these expressions along with a description of the logic required to select the correct branches of $term_2$ and $term_3$.

4.4 Integration of the ODEs in Time

The ODE solver utilized was a packaged 4,5th-order Runge-Kutta-Fehlberg routine (RKF45) from the text Forsythe, Malcolm & Moler (1977). This routine uses 6 function evaluations per time step to provide a 5th-order solution and takes sufficiently small steps to maintain a user-specified error tolerance between the 5th-order solution and an estimated 4th-order solution (not explicitly calculated). The single-step truncation error tolerance, ε_{de}, was specified on entry to the

routine and for most calculations was set to 10^{-4}. Some previous CD implementations have used low-order techniques such as the centred-difference leap-frog strategy (see e.g. Zabusky et al 1979; Berk & Roberts 1970) but Nakamura, Leonard & Spalart (1982) demonstrated (in their vortex-blob calculation of a Kirchhoff elliptic vortex) that the effective viscosity (at a time-step $\Delta t \approx 10^{-2}$) for the 1st-order Euler method was $O(1)$ whereas that for a 4th-order Runge-Kutta method was $O(10^{-7})$. Also, we found the RKF45 package convenient as the ODE's (4.3) were already in standard first order form and the truncation errors were handled internally by the package. The routine also had the advantage that it was self-starting (hence, the occasional node adjustments, resulting in a new set of equations did not involve much extra work) and that it could take relatively large time-steps. However, the 6 function evaluations per time-step made the program computationally expensive in situations where the routine was forced to make small steps.

4.5 Node Adjustment

During the evolution of the FAVR, the bounding contours undergo severe local distortion. They may stretch, collapse, form cusps (regions with extremely small radius of curvature) or filaments (localized regions containing little circulation). To enable the discrete contour description to maintain a sufficiently accurate approximation to a continuous contour, the node set must be occasionally refined (or updated). The frequency of updating depends on the rate of contour evolution which, for purely two-dimensional flow, we guess to be approximately constant and, for stretched-vortex cases, to vary as $\exp(\gamma t)$.

The adjustment may take the form of adding and/or deleting nodes from the current node set (see e.g. Berk & Roberts 1970; Pullin 1981) or may involve the parameterization of the contour followed by the generation of a completely new set of nodes (see e.g. Overman & Zabusky 1982; Dritschel

1986a). We have chosen the addition/deletion scheme and have refrained from using a complete or partial node rediscretization approach as we felt that retaining some of the original nodes maintained as true a solution to the CD equations as possible.

Two versions of essentially the same scheme are described in Jacobs & Pullin [1] and (more fully) in Pullin & Jacobs [3]. Specifically, a node was inserted between $(\zeta_j)_k$ and $(\zeta_j)_{k+1}$ on C_j if

$$| (\zeta_j)_{k+1} - (\zeta_j)_k | > \varepsilon_{ni} \quad , \tag{4.19a}$$

$$\varepsilon_{ni} = \max\left[\min\left[\frac{d_{min}}{P_7} , \frac{1}{P_8} \kappa^{-1}, S_{max}, P_9 S_{adj} \right], P_5 \right] , \tag{4.19b}$$

where

$$d_{min} = \max[S_{min}, P_4] \quad , \tag{4.20a}$$

S_{min} = minimum distance of approach of another contour or a "nonadjacent" section of the same contour, (4.20b)

$$\kappa \equiv \text{local curvature} = \frac{\text{Im}\left\{ \frac{\partial \zeta^*}{\partial e} \frac{\partial^2 \zeta}{\partial e^2} \right\}_j}{|\partial \zeta / \partial e|_j^3} \quad , \tag{4.20c}$$

$$S_{max} = \min [(\text{length of } C_j)/P_1 , P_2] \quad , \tag{4.20d}$$

$$S_{adj} = \min [|(\zeta_j)_{k+2} - (\zeta_j)_{k+1}|, |(\zeta_j)_k - (\zeta_j)_{k-1}|] , \tag{4.20e}$$

The new node was placed at e = k + 0.5 by linear interpolation on $[(\zeta_j)_k, (\zeta_j)_{k+1}]$. Cubic interpolation was used for some trials and, although it had higher order accuracy in regions of low curvature-to-segment-length ratio, it was much less

robust than the linear interpolation procedure in cusp-like regions of the C_j where this ratio was large.

The node deletion scheme operated by deleting node $(\zeta_j)_k$ if

$$|(\zeta_j)_{k+1} - (\zeta_j)_k| < \varepsilon_{nd} = \max [P_6, \varepsilon_{ni}/P_{10}] \quad . \tag{4.21}$$

This simple node-deletion procedure was preferred to one involving higher-order interpolation as it reduced the occurrence of slender filaments containing negligible circulation and decreased the tendency for contours to fold back upon themselves. This type of event remains as one of the major problems of the CD technique.

Although the emphasis of the numerical implementation is to remain as faithful as possible to a true solution of the Euler equations, we accept that the low-order linear interpolation procedure for node insertion and the simple deletion scheme are a form of smoothing. However, we attempt to retain as many of the original nodes as possible simply by having a very inefficient node deletion scheme and pay the price of increased computing time. An adjustment scheme based on complete rediscretization of the C_j would probably operate with significantly fewer nodes (e.g. Overman & Zabusky 1982; Dritschel 1986a) but introduces the possibility of suppression of the evolving fine scales through implicit smoothing.

The behaviour of the node adjustment scheme is governed by the empirical parameters P_1 - P_{10}. Parameters P_1, P_2, P_7 P_9, determine the resolution provided by the node set while P_4 - P_6, P_{10} limit the effect of their respective adjustment criteria. As we had to perform calculations with limited computer resources, these parameters were chosen (i.e., tuned to a specific application) so that no single criterion dominated but that the coherence of the contours and accuracy of the flow invariants was maintained. With improvements to the numerical implementation, we were able to relax some of the node-adjustment criteria. For example, the

Table 4.2 : Description of node-adjustment parameters.

Parameter	Description
P_1	minimum number of nodes on the contour
P_2	upper limit (absolute) on node separation
P_3	starting guess for minimum distance calculation
P_4	lower limit to calculated minimum distance
P_5	minimum distance below which a node will not be inserted
P_6	distance below which a node will be removed, regardless
P_7	minimum allowable ratio of intercontour distance over internode distance
P_8	minimum ratio of the radius of curvature over internode distance
P_9	maximum ratio of internode distance on adjacent segments
P_{10}	fraction of recommended internode distance, ε_{ni}, below which a node will be removed

Table 4.3 : Values of node-adjustment parameters. For the secondary vortex calculations (§8), parameters P_4, P_5, and P_6 were scaled with $(A_j)^{\frac{1}{2}}$ so that the C_j are resolved uniformly.

Parameter	Set 1	Set 2	Set 3	Set 4
P_1	40.0	40.0	33.0	40.0
P_2	0.11	0.11	0.15	0.15
P_3	100.0	100.0	100.0	100.0
P_4	0.05	0.035	0.04	0.04
P_5	0.041	0.031	0.021	0.021
P_6	0.02	0.015	0.01	0.01
P_7	0.1	0.1	2.0	1.5
P_8	3.0	4.0	6.0	6.0
P_9	2.0	2.0	4.0	4.0
P_{10}	0.4	0.4	0.333	0.333

value of P_7 was reduced drastically with the inclusion of the "analytic-patch" (see node-parameter sets 1 and 2) thus providing a trade-off between complexity of velocity calculation and numbers of nodes required. We note that the "analytic-patch" procedure did not allow the complete removal of the d_{min}/P_7 constraint in equation (4.19b) as we found that the solution accuracy was sensitive to the "contour flexibility" (see also Dritschel 1986a). Overall, we have achieved an empirical optimization of the node-adjustment parameters and the CD implementation. (We do not believe that the implementation described here represents a global maximum in performance.)

4.6 Monitoring Solution Accuracy

Qualitative checks upon the solution accuracy were made by monitoring the fractional error in the circulation invariants for each uniform-vorticity region

$$\Delta(\Omega_j) \equiv [\exp(\gamma_o t)\, A_j(t) - A_j(0)] \,/\, A_j(0) \quad , \tag{4.22}$$

where $A_j(t)$ is the calculated area of the $R_j(t)$ and γ_o is the dimensionless strain rate. For one application (the secondary vortices in chapter 8), the energy invariant (for $\gamma = 0$) is also monitored. The energy of the array per member (i.e. each FAVR) is defined as

$$E(t) = \frac{1}{2} \int_0^{\lambda/2} \int_{-\infty}^{\infty} (\nabla\Psi)^2 \, dy \, dx \quad , \tag{4.23}$$

$$V_x = \partial\Psi/\partial y \quad , \quad V_y = -\partial\Psi/\partial x \quad , \tag{4.24a,b}$$

where Ψ is a streamfunction satisfying the Poisson equation (2.21). As given by Pullin & Jacobs [3], the energy (4.23) may be written as

$$E(t) = -\frac{1}{2}\exp[Q(t)]\sum_{m=1}^{M}\Delta\omega_m\int_{C_m}[\ldots]\,ds$$

$$+\frac{1}{12}\exp[2Q(t)]\sum_{m=1}^{M}\Delta\omega_m\,[\omega_m(0)+\omega_{m-1}(0)]\int_{C_m}y^3\,dx\quad, \tag{4.25a}$$

$$[\ldots] = \psi\frac{\partial(\Psi^2/2)}{\partial n} - \frac{1}{2}y^2\frac{\partial\Psi}{\partial n}\quad, \tag{4.25b}$$

where $\Psi = 0$ on the line of symmetry midway between two FAVRs ($x = \pm\lambda/2$ in figure 8.2), s is the arc length and n is the inward facing normal on C_m. For $\gamma = 0$, E(t) is an invariant of the vortex evolution, but for $\gamma > 0$, E(t) may be expected to increase due to energy transfer from the imposed strain field to the kinetic energy of the (x, y)-plane motions.

Unfortunately, $\Delta(\Omega_j)$ is fairly insensitive to the fine scale coherence of the C_j (see the end of Section 5.2.1). We found that the most reliable way of testing the accuracy of the method is to demonstrate convergence of the solution contours with respect to the parameters P_1 - P_{10} which determine $N_j(t)$. Such convergence was obtained empirically for the vortex coalescence simulations with M = 1 and separately for the shear layer rollup simulation, again with M = 1. Similar demonstrations for the many contour (M > 1) problems was expensive and difficult to obtain due to the large values of $N_j(t)$ encountered very early in the simulations. However, in figures 5.8 and 5.9 of section 5.2, we show a single example of convergence for the stretched shear layer. As the adjustment parameters are application specific, we will provide an indication of which set of node-parameter values was used in the respective application sections.

5.0 TEST CASES

The numerical implementations of the CD algorithms for both the isolated FAVR and x-periodic vorticity distributions were tested by comparing computed solutions with

(i) previous analytic and numeric solutions;

(ii) distinct but equivalent solutions via Lundgren's transformation (3.28);

(iii) (partially) independent solutions computed with different code-versions;

(iv) solutions computed by the same code-version but having different node resolution.

5.1 Isolated FAVRs with Stretching

The method was tested by considering the evolution of an isolated rectilinear vortex of uniform vorticity, embedded in the three-dimensional strain field (3.20). Analytic solutions for this flow have been obtained by Neu (1984a,b) who has shown that for all γ_o, β_o , an initial elliptical-shaped vortex remains elliptical, thus generalizing the classical rotating Kirchhoff vortex solution (Lamb §159, 1932) which holds for $\gamma_o = \beta_o = 0$. Neu (1984a,b) has obtained three coupled ODE's

$$a = -a\,((\gamma_o - \beta_o)\sin^2\theta + \beta_o\cos^2\theta\,, \tag{5.1a}$$

$$b = -b\,((\gamma_o - \beta_o)\cos^2\theta + \beta_o\sin^2\theta\,, \tag{5.1b}$$

$$\dot{\theta} = \frac{\omega_o \exp(\gamma_o t)\, ab}{(a+b)^2} - \frac{(\gamma_o - 2\beta_o)}{2}\,\frac{(a^2+b^2)}{(a^2-b^2)}\,\sin(2\theta)\,, \tag{5.1c}$$

which govern the length of the semi-major axis, a, the semi-minor axis, b, and the angle between the semi-major axis and the x-axis, θ.

Three examples have been chosen for comparison with Neu's solutions by selecting initial conditions which correspond to oscillation, rotation and infinite planar-elongation of the ellipse for $\gamma_o = 0$, $\beta_o \neq 0$. Neu has presented his solutions for $\gamma_o = 0$ as phase-plane plots of the ellipse aspect ratio, a/b and the angle θ. The initial conditions for the CD calculations were specified by selecting a point in the region of the plot corresponding to one of the three characteristic behaviours for $\gamma_o = 0$. The stretching strain, γ_o was then set to a nonzero value and the vortex evolution calculated using both equations (5.1 a-c) and the CD algorithm (4.3) implemented as code-version A (table 4.1).

Figure 5.1(a)-(c) shows the sequence of frames from the evolution of the three cases. The CD solution is plotted as a solid line with the "X" marking a particular fluid particle. Note that it moves around the contour with the rotating ellipse appearing to the set of nodes as a periodic wave. The analytic solution, obtained by integrating equations (5.1), is plotted as a dashed line and, on the scale of figure 5.1, the difference between the pairs of solutions is not discernible. The times shown on each frame correspond to setting $\omega_1(0) = 1.0$ rather than having unit circulation in the FAVR. In the CD calculation, $N_1 = 30$ initially and no node insertion or removal occurred over the test times as the node-adjustment routine was not active.

Introducing node-adjustment with this case caused some problems with the symmetry of the elliptical contours. It was not simply a matter of inadequate resolution as the same result (to within plotting accuracy) was obtained when doubling the number of nodes, N_1. The particular test case studied had initial axes a = 1.53 and b = 0.208, combined with stretching $\gamma_o = 0.15$. Love (1893) has shown that the (purely two-dimensional) Kirchhoff vortex is unstable to small perturbations for a > 3b. Here, this condition was satisfied and we found that the node-adjustment procedure introduced perturbations to the vortex contour which subsequently grew and destroyed the initial symmetry. The result we obtained

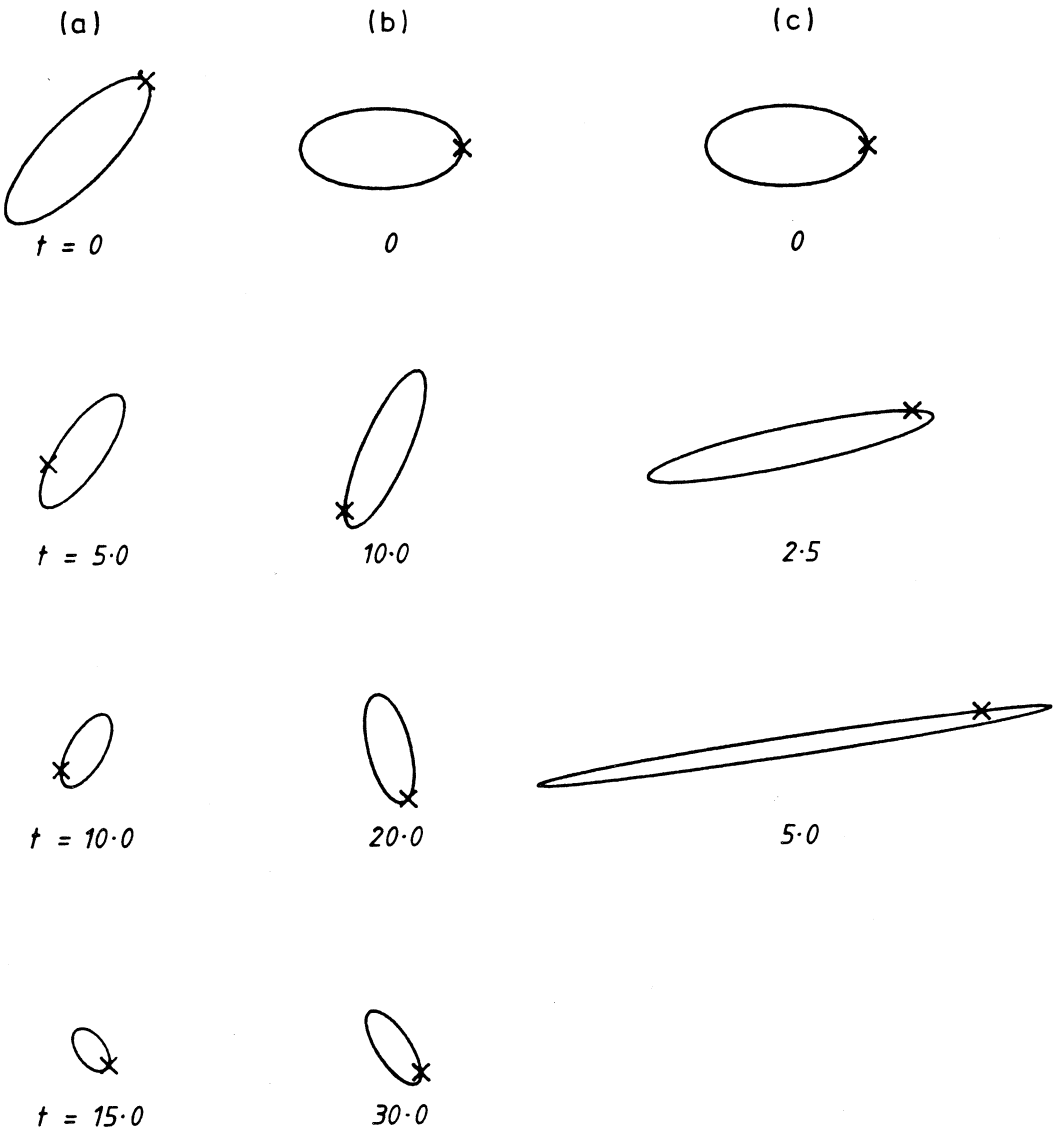

Figure 5.1 : Evolution of isolated uniform vortices in a three-dimensional strain field. X marks a material particle and the times are shown on each drawing. The CD solution is plotted as a solid line with the solution due to Neu (1984) superimposed as a dashed line. The two solutions are indistinguishable on the scale shown. (a) $\gamma_o = 0.15$, $\beta_o = 0.12$, (b) $\gamma_o = 0.05$, $\beta_o = -0.084$, (c) $\gamma_o = 0.05$, $\beta_o = -0.25$

was similar to Dritschel's (1986b) nonlinear evolution of an ellipse with a/b = 6 combined with a two-fold symmetric disturbance which eventually tears the ellipse into two peices (his figure 12a). Despite this short coming of the node adjustment routine, it appears to be adequate for simulations where the growth rate of the (relatively large amplitude) forced perturbation is significantly higher than that excited by the truncation errors introduced via the insertion and deletion nodes. This is the case for the interacting vortex pair and the shear layer configuration.

The second test case that we used was the interaction of a pair of equal, like-signed vortices in close proximity. The unstretched version of this phenomena has previously been studied by Christiansen & Zabusky (1973) using a CIC technique and by Zabusky, Hughes & Roberts (1979) using the CD method. It provides a thorough test of the algorithm as the contours become severely deformed when the FAVRs approach each other closely. We chose flow parameters (diameter $d = (4/\pi)^{1/2}$, centre separation, D = 1.5, 1.7, 1.92 (figures 10.3 - 10.7) to approximately match those of Zabusky et al and found that the results compared well. Physical quantities were scaled to give $\omega_1(0) = 1.0$, $A_1(0) = 1.0$ and $\Gamma = 1.0$ in each FAVR. Final solutions were computed with code-version A and node-parameter set 4 (tables 4.1 and 4.3).

To check the sensitivity of the contour to the variations in N, we repeated several simulations of the two-vortex interaction and varied the node-adjustment parameters P_1 - P_{10}. Figure 5.2 contains an enlarged view of two of the solution frames from the sequence in figure 10.3b, D = 1.50, $\gamma = 0.05$, t = 15, 17.5. In part b, t = 17.5, each FAVR has $N_1 = 435$ and was indistinguishable from the same case with $N_1 = 324$ at t = 17.5. With $N_1 = 160$ at t = 17.5 (part a), the gross features of the vortex regions are unchanged. However, there are small scale irregularities near the centre of the merged structure. Given that the contour shapes converge to smooth curves with increasing N_1, we believe that these spurious features are due to inadequate node resolution. In

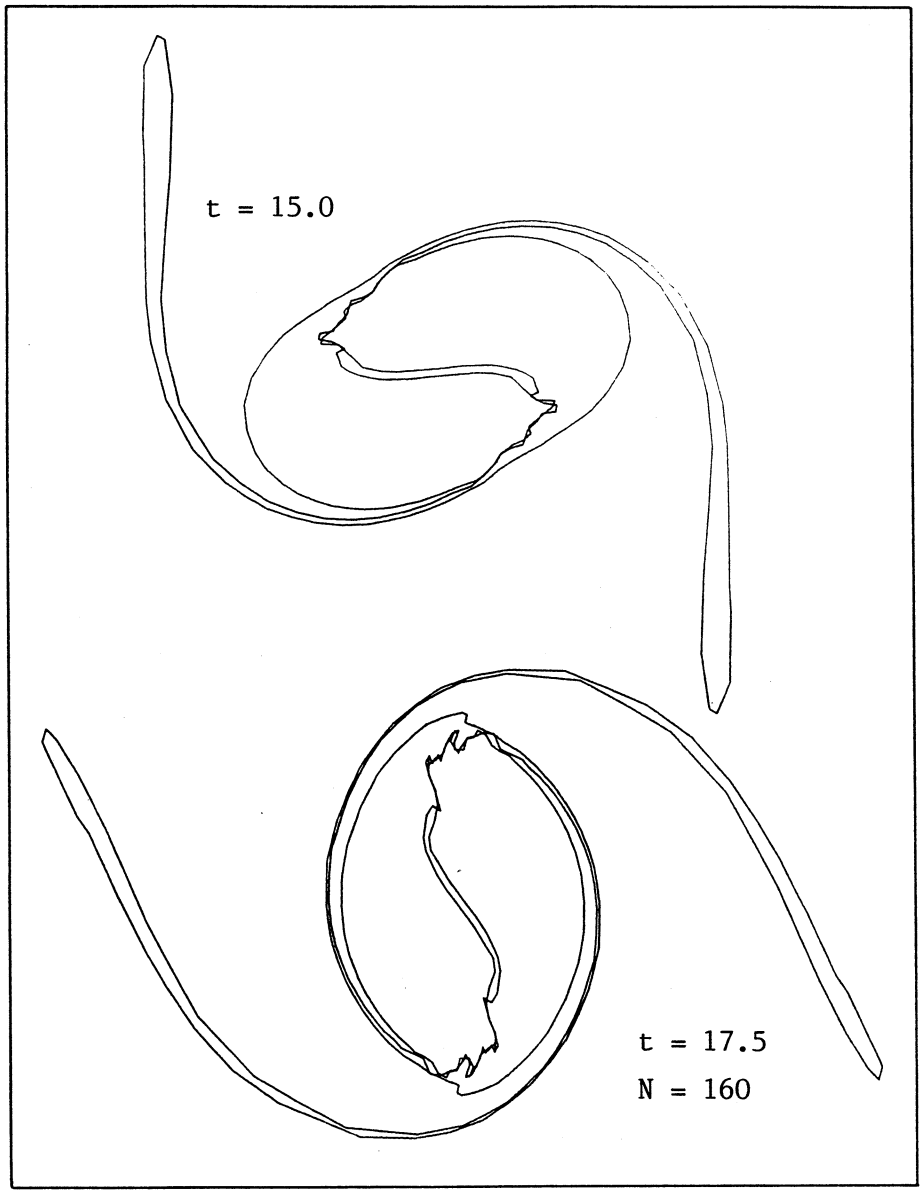

Figure 5.2a : Contour shapes for a low resolution (small N) simulation of two interacting FAVRs, M = 1, D = 1.5, γ = 0.05 (case 2 of § 10). Times and node numbers as shown.

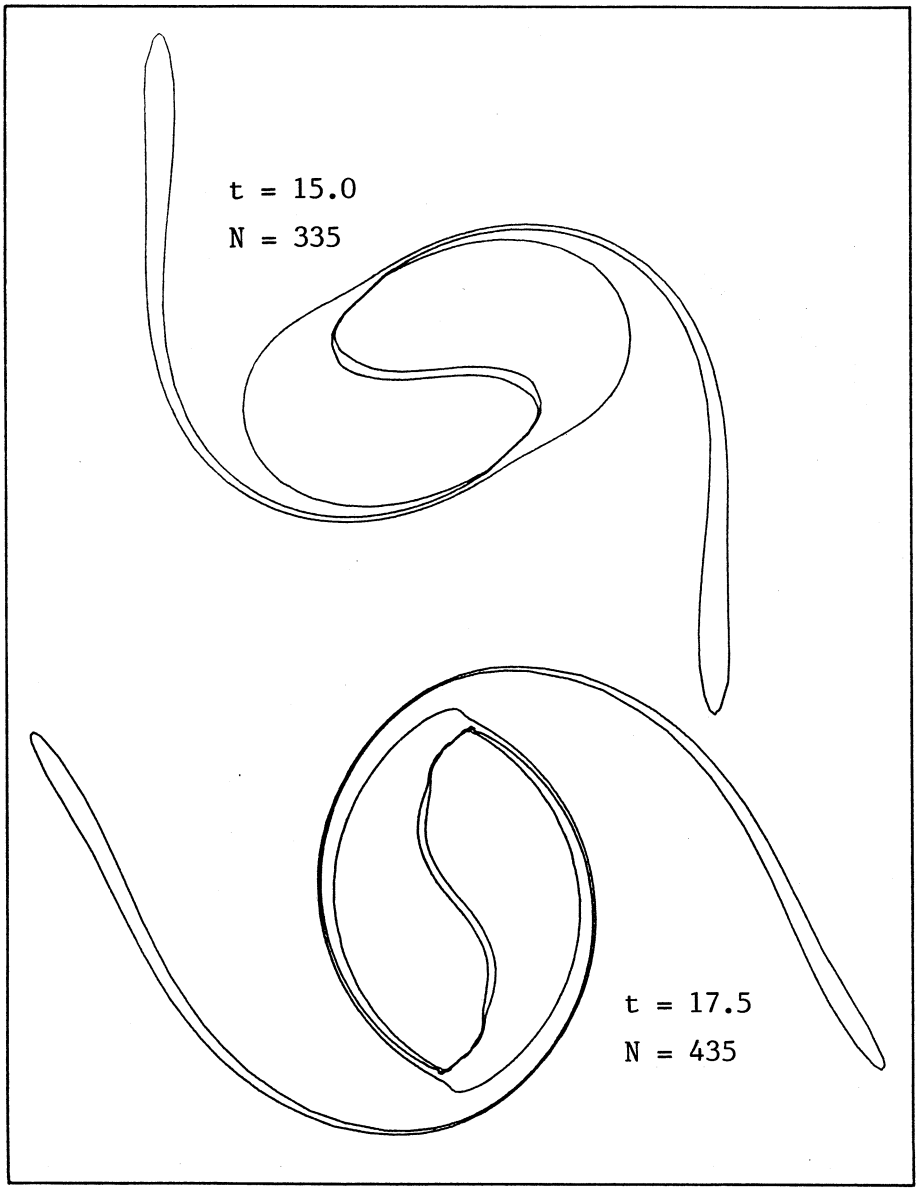

Figure 5.2b : Contour shapes for a high resolution (large N) simulation of two interacting FAVRs (case 2 of §10). The contours have converged to smooth curves with the numbers of nodes shown on the figure.

addition, a local linear stability analysis (similar to that in appendix 5, M = 1) for a layer of irrotational fluid bounded on either side by semi-infinite regions of vortical fluid shows that the flow configuration is stable. In three separate calculations of the case in figure 10.3d (equivalent to the purely two-dimensional flow in figure 5.4), the vortex contour at t = 10.0 was the same (to within plotting accuracy) with N_1 = 87, 139, 227 respectively.

A third test, using the configuration of two interacting FAVRs, involved the comparison of equivalent stretched and unstretched simulations according to Lundgren's (1982) transformation (3.28). We provide two examples in which frames at equivalent times can be directly compared by changing the length scale. Figure 5.3 shows the evolution of a test case with axisymmetric strain γ_o = 0.15, β_o = 0.075. This is the equivalent stretched flow for the purely two-dimensional flow shown in figure 10.3a, D = 1.5. The axisymmetric case shows the stretched simulation time, t, and the equivalent two-dimensional time, T, on each solution frame. For constant $\gamma = \gamma_o$, the time T of the purely two-dimensional evolution is related to the time t of the stretched evolution by

$$T(t) = \frac{1}{\gamma_o} [\, \exp(\gamma_o t) - 1 \,] \quad . \tag{5.2}$$

Figure 5.4 shows the evolution of the vortex pair embedded in an (x, y)-plane strain

$$\beta_o = \frac{\gamma_o/2}{\gamma_o T + 1} \quad , \tag{5.3}$$

so that we have the equivalent two-dimensional case for the plane-stretching flow in figure 10.3d (γ_o = 0.15, β_o = 0, D = 1.5). In both cases (figures 5.3 and 5.4) the contour geometries appear to agree, at least to within plotting accuracy.

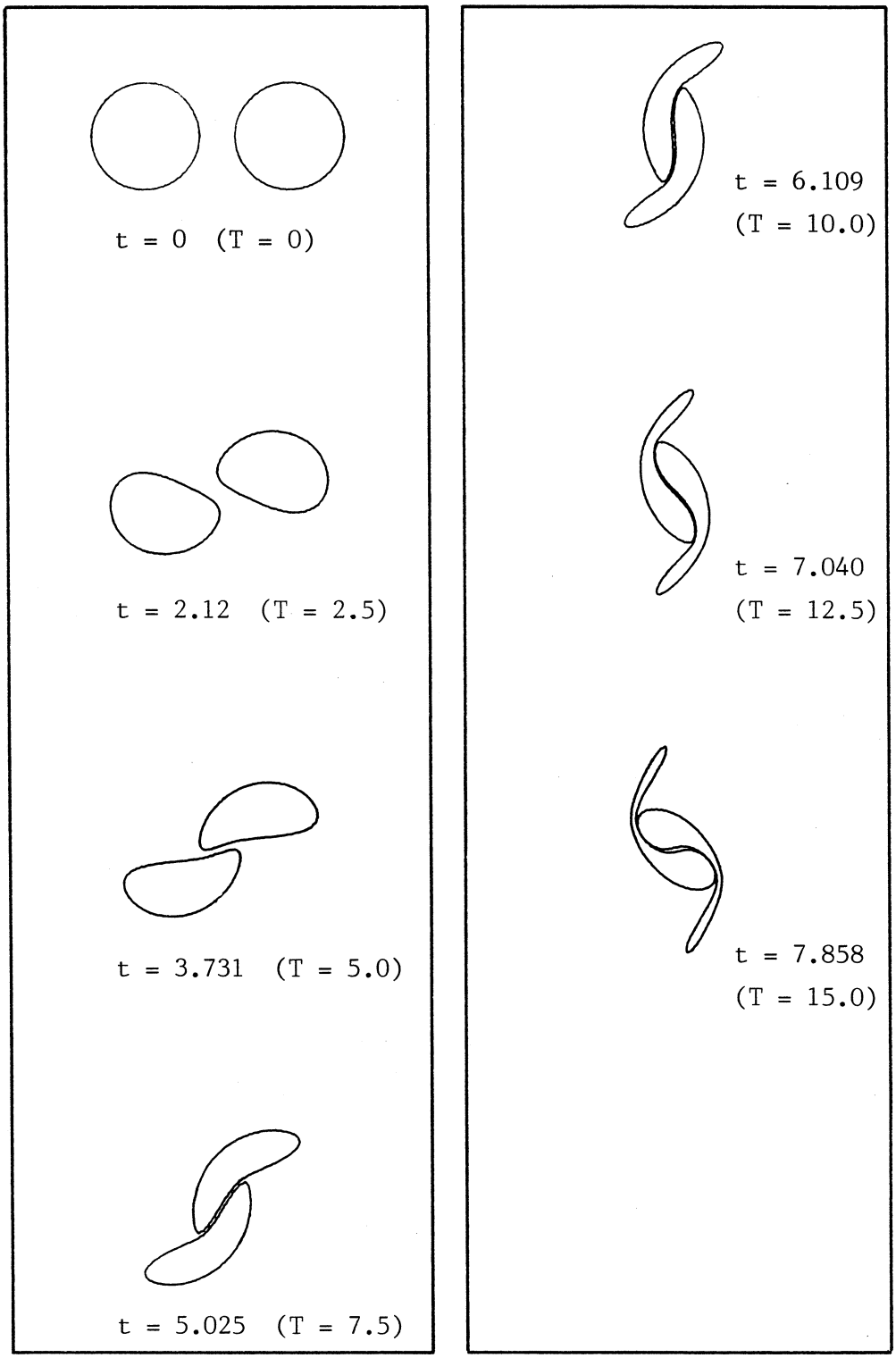

Figure 5.3 : The coalescence of two equal FAVRs in the presence of an axi-symmetric stretching strain field $\gamma = 0.15$, $\beta = 0.075$. The flow configuration is the same as case 1 of §10 ($\gamma = 0$, $\beta = 0$) with initial vortex diameter $d = (4/\pi)^{1/2}$ and separation $D = 1.5$. Times t for the stretched solution as shown. Times T for the purely 2D solution also shown.

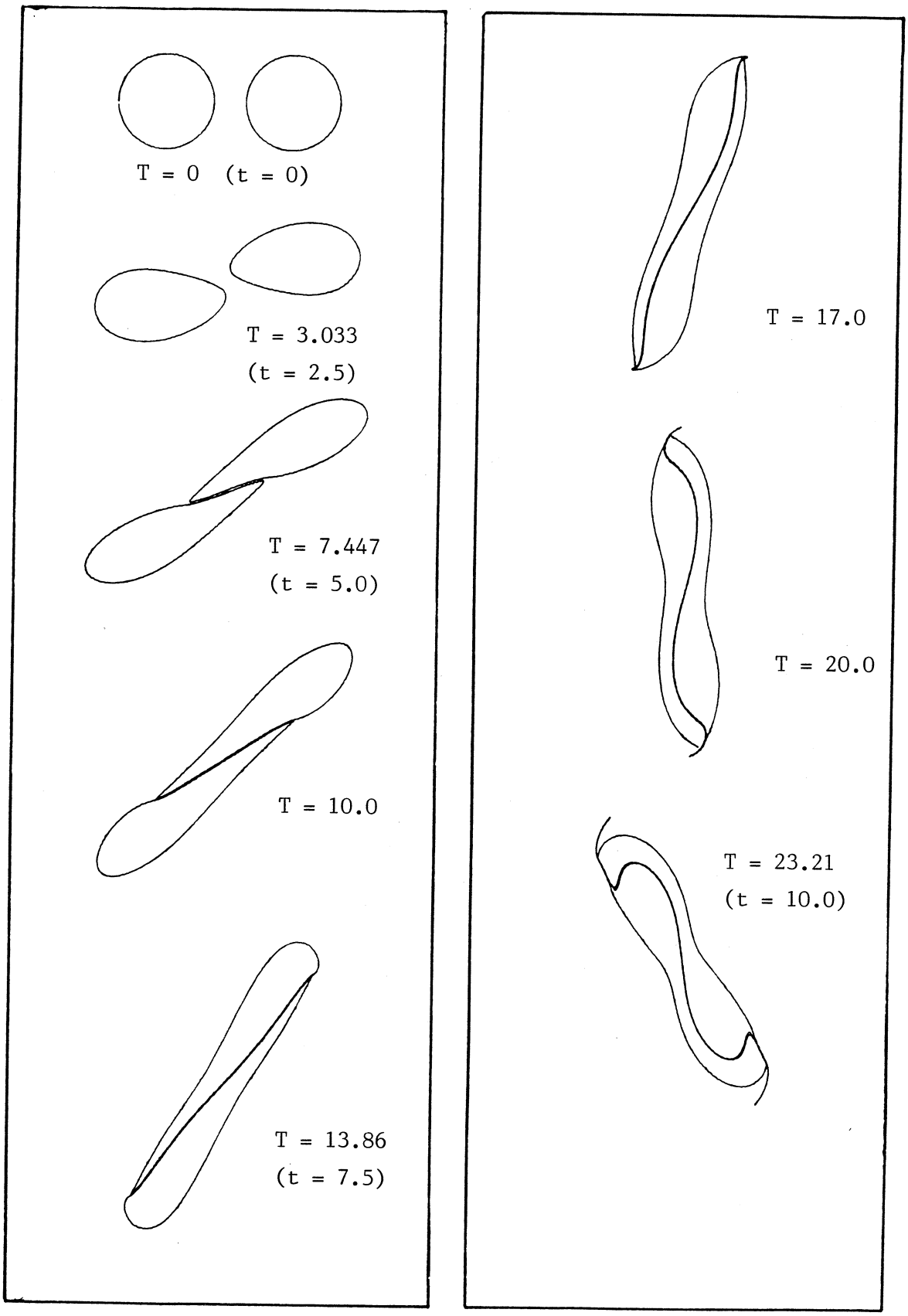

Figure 5.4 : Coalescence of two equal FAVRs in the presence of an (x, y)-plane strain field (5.2). Times T for this pure two-dimensional evolution as shown. Times t for the equivalent stretched flow (case 4 of §10) are also shown.

The favourable comparisons for these vortex pair simulations give us confidence in the stretching CD algorithm and numerical implementation. In chapter 10 we will use the method to study the effect of stretching upon the coalescence phenomena.

5.2 Spatially Periodic Vorticity Distributions

Using symmetries, we are able to study a variety of x-periodic vorticity distributions with the same computer code. Previous CD simulations of periodic flows have been done by Pullin (1981), who studied the dynamics of a uniform-vorticity (M = 1) layer at a wall, and Pozrikidis & Higdon (1986), who simulated the roll-up of a uniform-vorticity (M = 1) shear layer. Here we present two test cases with parameters chosen to match sample calculations from these papers so that the results may be directly compared. We also illustrate some convergence tests for the nonuniform-vorticity shear layer studied in chapters 7 and 9.

5.2.1 Free Shear Layer

Figure 5.5 shows a series of snap shots of an evolving uniform-vorticity shear layer separating two parallel but counter-flowing streams. Solutions were computed using code-version C (table 4.1) and node-parameter set 1 on an IBM 3083 (64-bit precision). Initial contour shape for C_1 is defined by

$$\zeta_1(x) = \frac{2\pi x}{\lambda_1} + i \left\{ \frac{\delta_\omega}{2} + a_0 \sin\left[\frac{2\pi x}{\lambda_1} \right] \right\} \quad , \tag{5.4}$$

with the lower contour C_1' defined as the image

$$\zeta_1'(x) = 2\pi - \zeta_1(2\pi - x) \quad . \tag{5.5}$$

Note that the contours initially below the x-axis are identified with primed subscripts. The layer parameters,

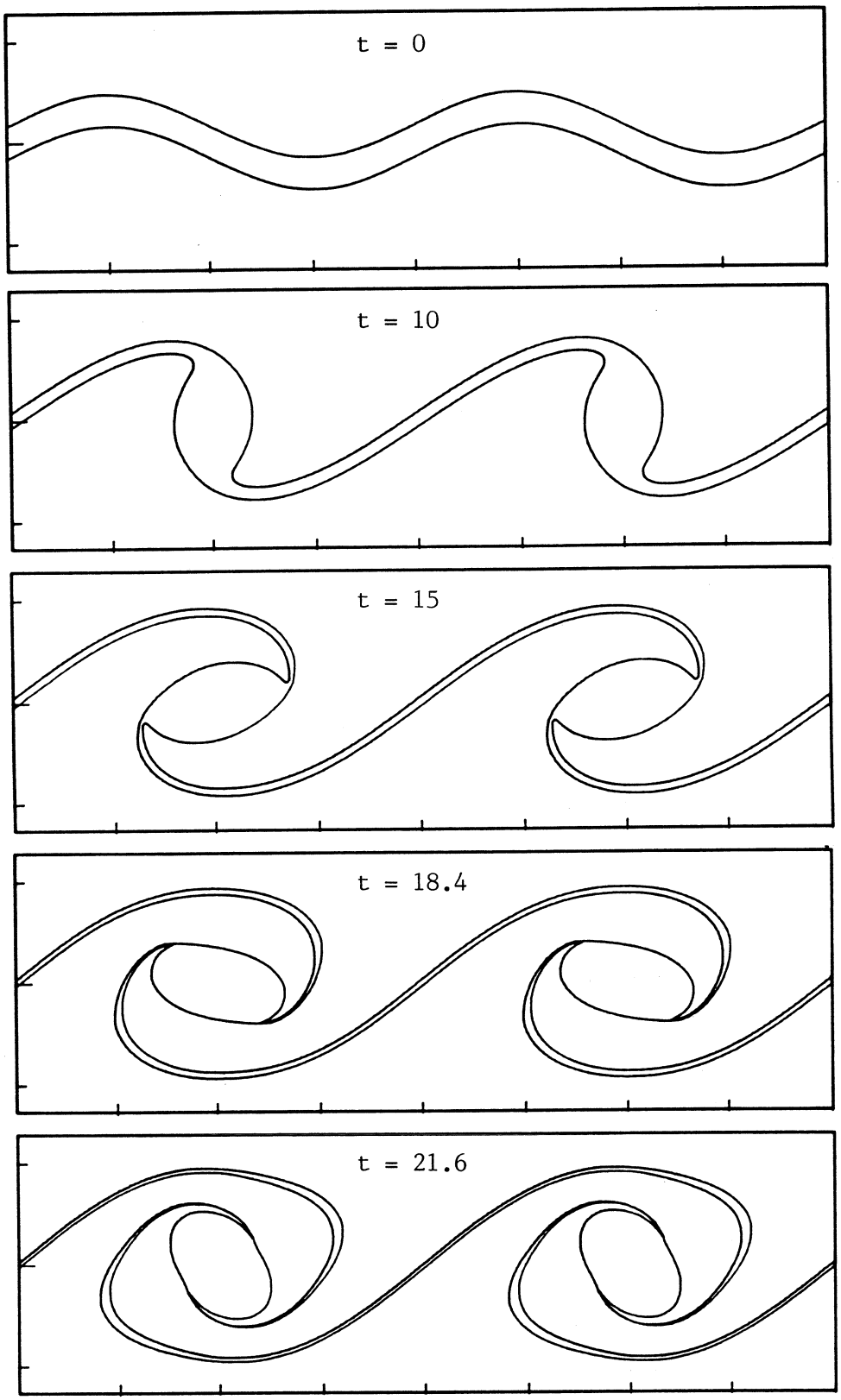

Figure 5.5 : The evolution of a uniform-vorticity shear layer with an initial sinusiodal perturbation. The ratio of layer thickness to perturbation wavelength is $\delta_\omega/\lambda_1 = 1/(4\pi)$ and the perturbation amplitude is $\alpha_0/\lambda_1 = 1/(4\pi)$. Times t as shown.

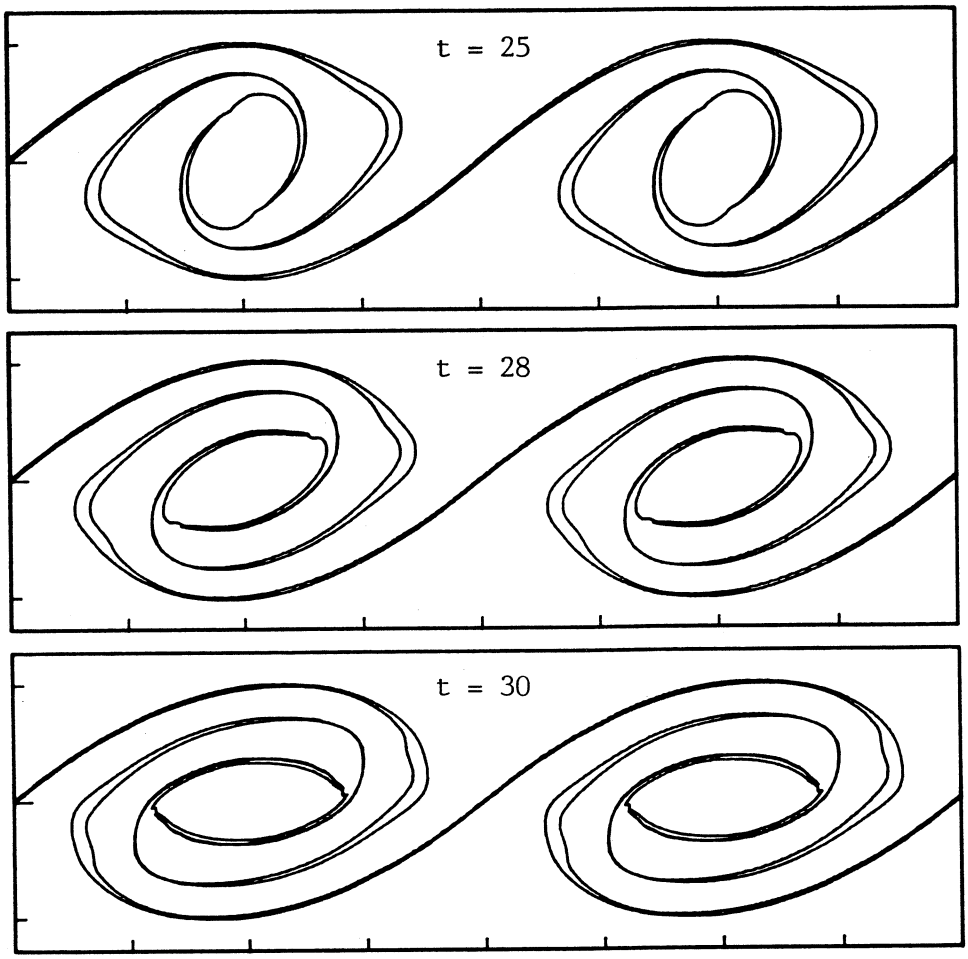

Figure 5.5 continued.

thickness $\delta_\omega/\lambda_1 = 1/(4\pi)$ and initial perturbation amplitude $a_0/\lambda_1 = 1/(4\pi)$, have been chosen to approximate those in figure 10 of Pozrikidis & Higdon (1985). The times included on each frame are scaled to give $\omega_1 = -1.0$. Note that this corresponds to having $\Gamma = -2\pi$ in one wavelength. Agreement between the calculations appears to be very good.

With the node adjustment algorithm trying to maintain good resolution, it is difficult to discern what effect the analytic-patch procedure is having on the solution accuracy. In figure 5.6, we show two magnified views of the shear layer contours at t = 30. The layer evolution in figure 5.6a has been calculated without the analytic patch (code-version D) while in figure 5.6b it has been included (code-version C). It is in regions where the contours approach closely that the integrand behaviour is most difficult and in figure 5.6a, the contour sections labelled (1) and (2) exhibit spurious oscillations that are not evident in the simulation using the analytic-patch procedure (figures 5.6b and 5.5). These oscillations are artifacts of the "noisy" numerical quadrature (4.10, 4.14) in the proximity of the velocity-point. In terms of computational effort, the analytic patch procedure is quite expensive. A 32-bit (not 64-bit) calculation on the IBM 3083 involving 60 nodes and using only the numerical quadrature (4.10) required 0.303 cpu seconds per function call whereas an equivalent calculation including the analytic patch required 0.477 seconds: a 50% increase.

To illustrate the invariance of solutions to the particular CD formulation, figure 5.7 shows two frames at the same simulation time and starting from the same initial conditions (cases 3a and 3 of section 7.4) but computed by two separate codes. The flow is initially a slightly perturbed shear layer between two counter-flowing streams but, unlike the case in figure 5.5, the layer has a nonuniform vorticity distribution approximated by several (M > 1) uniform-vorticity regions. The t = 90 (τ = 4.559) frames here show the vortex structure formed by the coalescence of two adjacent rolled-up vortex cores. Frame (a) was computed with code-version B and

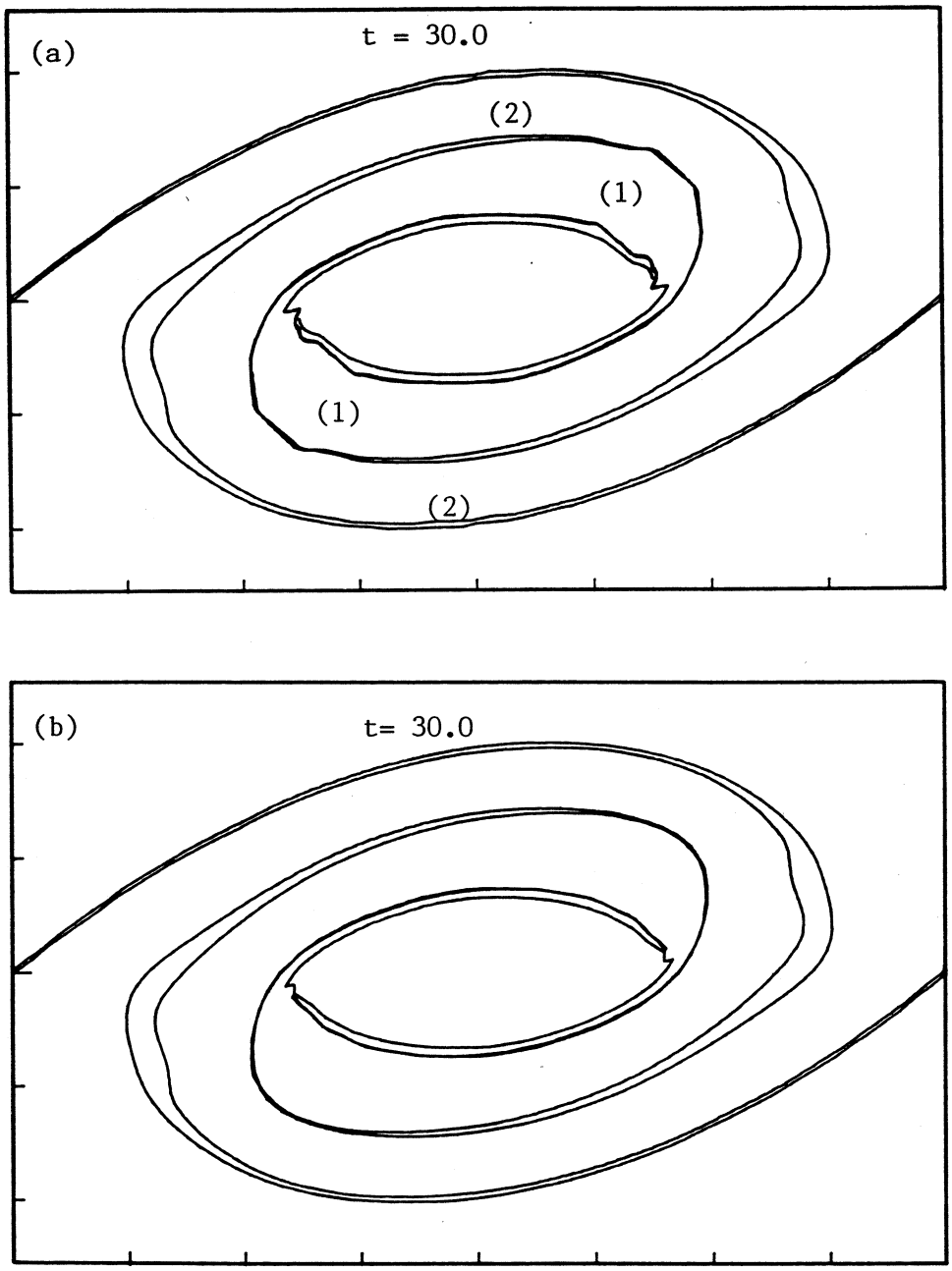

Figure 5.6 : Improvement in the solution accuracy obtained through the use of the "analytic-patch" procedure. Both solutions are from the evolution of a uniform-vorticity shear layer (figure 5.5) at t = 30 computed using 64-bit precision arithmetic. (a) This computation was done without the benefit of the "analytic-patch" procedure (code-version D). Note the artifacts near the region labelled (1) and (2).
(b) Computation with "analytic-patch" (code-version D).

node-parameter set 3 on an IBM 3083 (using 32-bit precision) while frame (b) was computed with code-version C and node-parameter set 1 on a Cyber 205 (using 64-bit precision). There is almost no discernable difference in the large-scale features but frame (b) (analytic patch plus 64-bit precision) has significantly smoother contours.

Figures 5.8, 5.9 give some indication of convergence of the contour shapes with increasing N_j at time t = 70 (τ = 3.546). This configuration is a nonuniform-vorticity shear layer with the same initial vorticity distribution as that in figure 5.7. The difference here is that the layer evolves in the presence of an imposed strain field that stretches the vortex lines and produces a vorticity intensification. Note that the initial condition is therefore not a steady-state solution to the Euler equations. The full history is displayed in figure 9.4 (case 2b of chapter 9). The large scale features for both solutions are almost the same (figure 5.8) but there is an improvement in the contour smoothness where several small-scale features marked in figure 5.9a are not present in the higher resolution simulation of figure 5.9b. Both solutions shown here were computed with code-version C (table 4.1) however the solution in frame (a) used node-parameter set 3 while the solution in frame (b) used node-parameter set 1. Table 5.1 contains the number of nodes on each of the upper contours (C_j, numbered j = 1 to 4 from the outside to the inside) and the circulation errors for the corresponding uniform-vorticity regions. Although the higher resolution case shows a marked improvement in contour smoothness, there has been virtually no change in the fractional error of the circulation invariants. Hence, the monitor based on $\Delta(\Omega_j)$ is a relatively insensitive measure of solution accuracy. It should be noted, however, that the calculation discussed here is an extreme case and, although the solution is losing qualitative accuracy (breaking down), the solutions for smaller values of stretching-strain strength have considerably smoother contours (see figures 9.3 and 9.9).

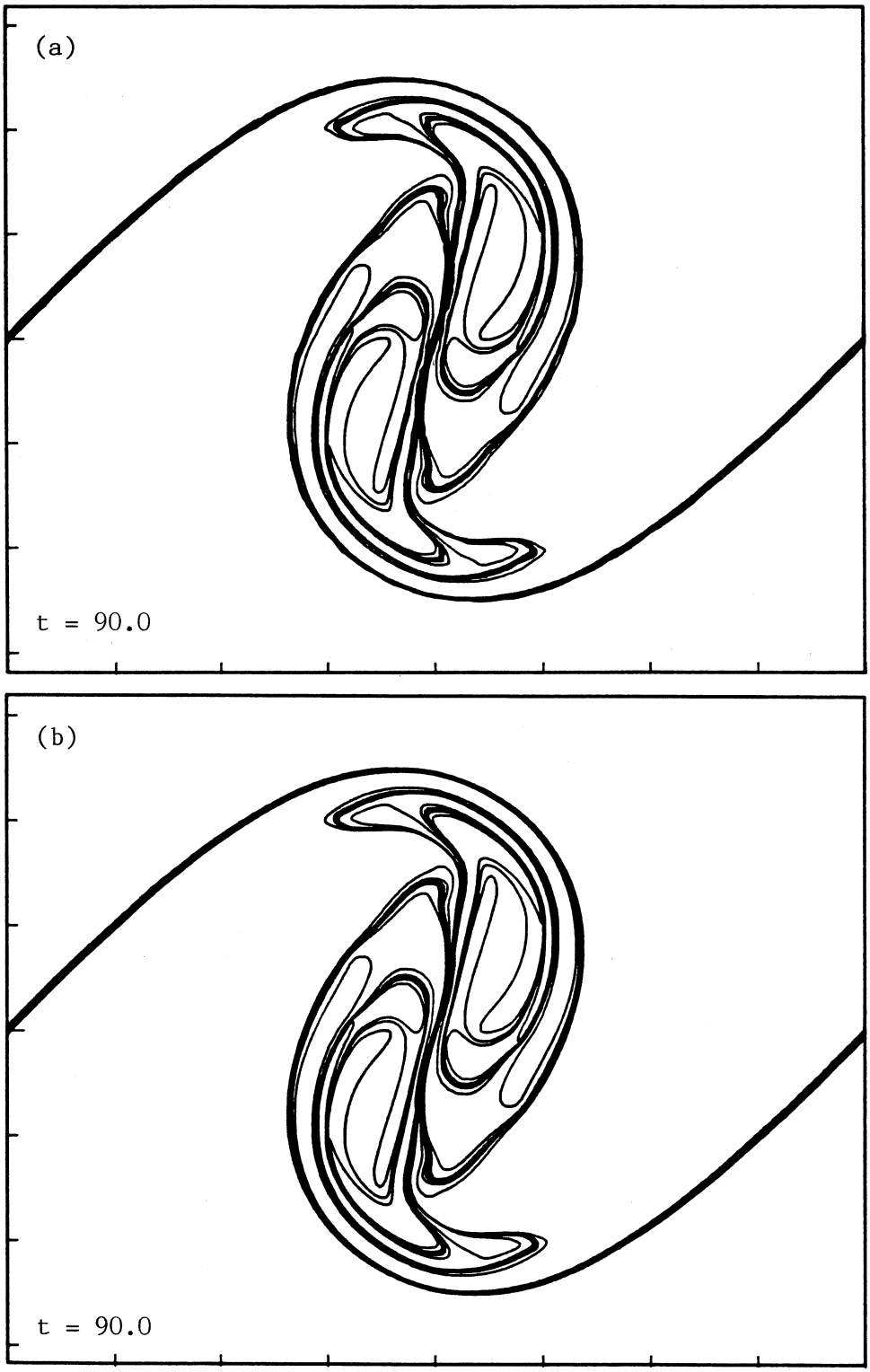

Figure 5.7 : Two independent solutions for the evolution of a non-uniform shear layer; cases 3 and 3a of § 7.4 at time $t = 90$ or $\tau = 4.559$.

(a) Computed with code-version B and node parameter set 3.

(b) Computed with code-version C and node parameter set 1.

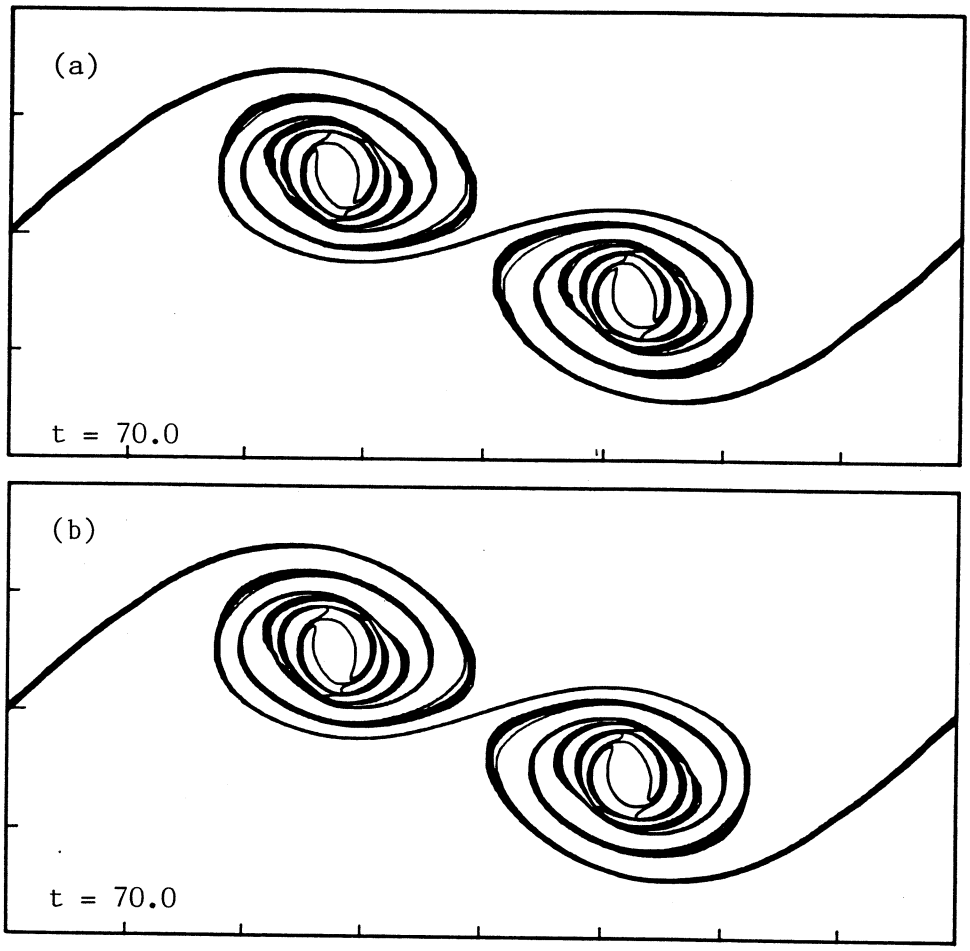

Figure 5.8 : Convergence of contour shape, at fixed time t, with increasing resolution (node numbers). These frames are from two separate calculations of a stretched shear layer with the same numerical code but different node adjustment parameters.

(a) node parameter set 1,

(b) node parameter set 2 (higher resolution).

The tic spacing is $\pi/4$.

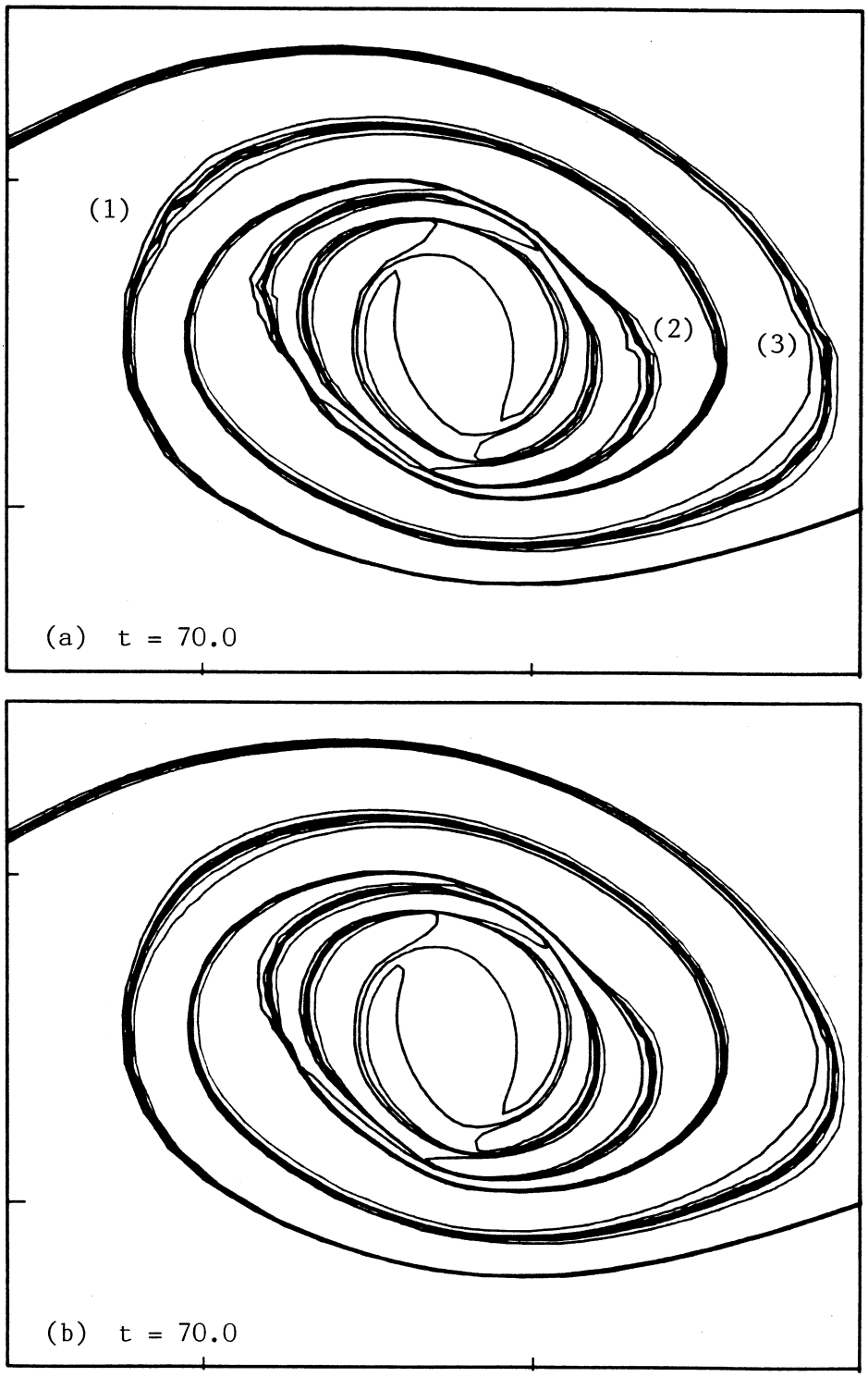

Figure 5.9 : Close-up of figure 5.8 showing convergence of solution contours with increasing resolution. Several small-scale features (labelled (1) - (3)) in frame (a) are not present in the higher resolution computation (b). The tic spacing is $\pi/4$.

Table 5.1 : Number of nodes on upper and lower contours ($N_j=N_{j'}$) and fractional change in circulation $\Delta(\Omega_j)$ for each pair of regions R_j and $R_{j'}$. These figures are for the stretched shear layer with $\gamma=0.015$, cases 2a and 2b of §9.3. The only difference between the calculations is the node parameter set used; set 1 for case 2a and set 2 for case 2b.

j	case 2a		case 2b	
	N_j	$\Delta(\Omega_j)$	N_j	$\Delta(\Omega_j)$
1	387	-0.21×10^{-1}	487	0.21×10^{-2}
2	496	0.89×10^{-2}	641	-0.13×10^{-1}
3	587	-0.19×10^{-1}	748	-0.58×10^{-1}
4	679	-0.41×10^{-1}	862	-0.35×10^{-1}

5.2.2 Shear Layer at a Wall

Figure 5.10 shows the evolution of a constant-vorticity (M = 1) layer at a wall. The influence of a rigid wall is provided by a mirror image R_1, of the vortex region in the x-axis having opposite signed vorticity. Figure 5.11 shows the contour configuration with the C_1, contours delineating the the image regions (denoted by the primed subscripts). The contributions from the vertical sections of the closed contours again cancel but the contributions from the contour sections along the x-axis sum to give an effective contribution

$$(u_x - iu_y)_{wall} = -\omega_1 y \quad . \tag{5.6}$$

The initial contour shape is defined by

$$\zeta_1(x) = \frac{2\pi x}{\lambda} + i\left\{h + a_0 \sin\left[\frac{2\pi x}{\lambda}\right]\right\} \quad , \tag{5.7}$$

with the mean height of the layer, $h/\lambda = 0.25$, and the initial perturbation amplitude, $a_0/\lambda = 0.125$, are chosen to approximate the configuration shown in figure 7 of Pullin (1981). Again, the times are equivalent to having $\omega_1 = -1$. There is good agreement for the large-scale motions but we have obtained smoother solution contours by using more nodes (and computer resources) and a more refined code. Note the "entrainment" or "engulfment" of a nearly closed sliver of irrotational fluid within the layer.

5.3 Contour Breaking and Vortex Filaments

The CD method becomes more expensive as the number of nodes describing the contours increases. To maintain the contour flexibility, the number of nodes required increases roughly with the contour length as shown in figure 5.12. Here we plot (in figure 5.12a) the variation in contour length for the simulation in figure 5.5 in while figure 5.12b we show the

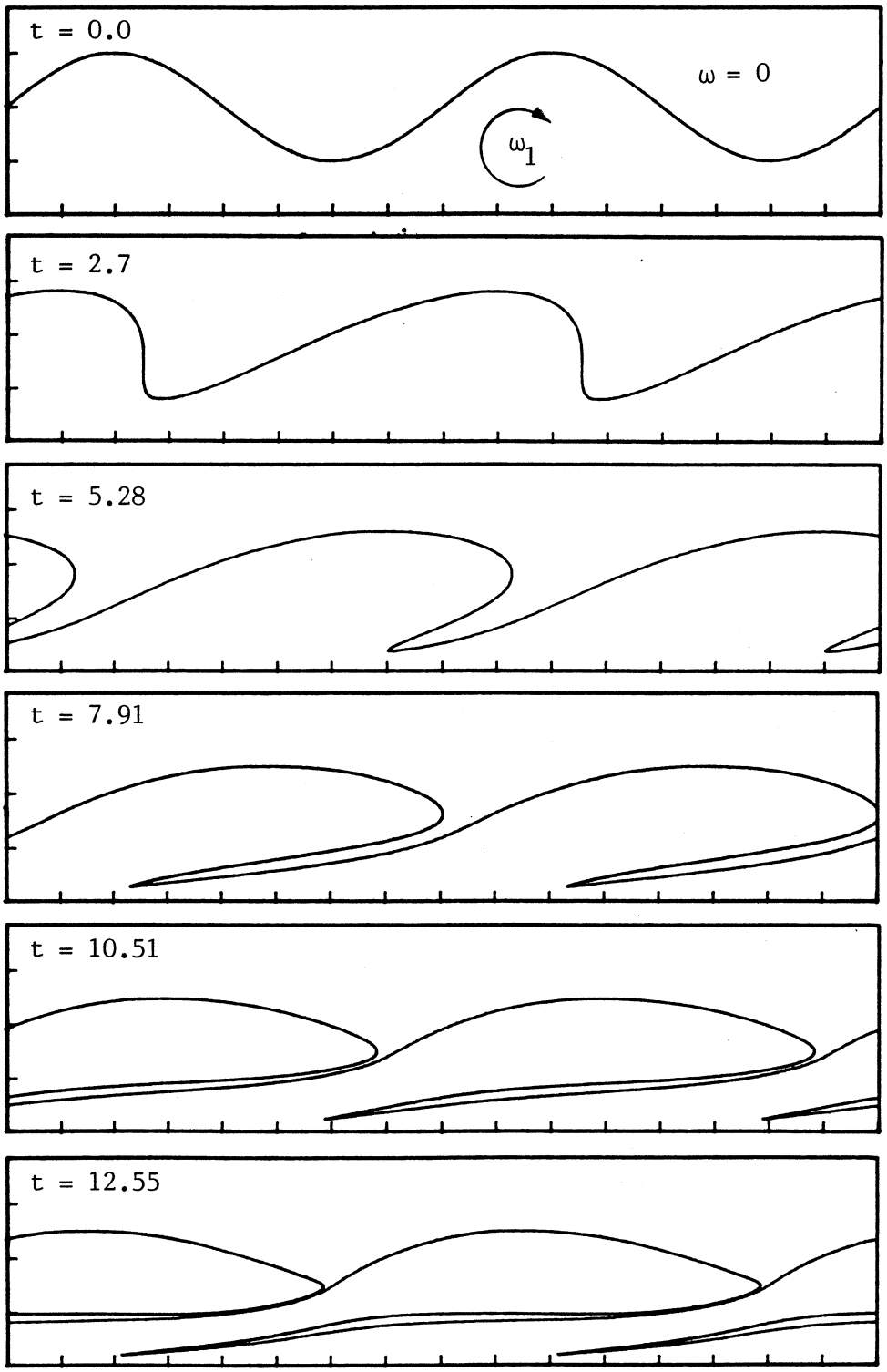

Figure 5.10 : Evolution of a uniform-vorticity layer at a wall (the x-axis). The vorticity is unity and the tic spacing is $\pi/4$.

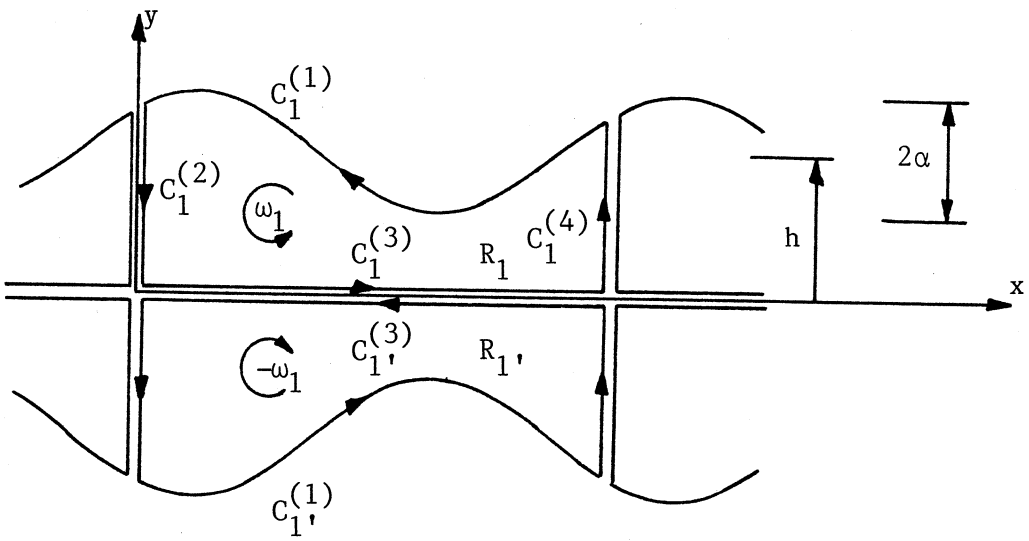

Figure 5.11 : A periodic vorticity layer at a wall. The vortical fluid is bounded by an array of closed contours. One member of this array, C_1, is divided into four segments superscripted (1) - (4). The region R_1, (with opposing vorticity) is the mirror image of the region R_1 in the x-axis. The bounding contour C_1, however, is still defined in the anti-clockwise sense. Mean thickness of the layer and perturbation amplitude are specified by h and α respectively.

corresponding node numbers for the upper contour. The computer processing-time per simulation time-step varies roughly as N^2 (figure 5.13a) because there are nested loops in the velocity calculation. Combined with the increasing numbers of nodes, mostly contained in the filament-like braids joining the rolled-up vortex cores, we have an explosive increase in computer processing-time required as the simulation proceeds (figure 5.13b). Computer-processing time is measured in seconds on a Cyber 205. As long slender filaments containing negligible circulation are characteristic of nearly all of the solutions computed in this thesis, the CD implementations used here (without modification e.g. contour surgery) are not suited to evolutionary problems in the late-time epoch.

Although the filaments illustrated so far have been formed by the stretching of ejected vortex arms or as braids connecting rolled-up vortex cores (figure 5.5), there are other mechanisms for their production. The "breaking" (formation of cusps) of contours and the subsequent filament formation has been observed by Deem & Zabusky (1978) for an isolated uniform- vorticity FAVR and by Overman & Zabusky (1982), Dritschel (1986a), Jacobs & Pullin [1] for interacting FAVRs. Wan (1982) has theoretically investigated the nonlinear stability of circular vortex patches. In figure 5.14 we show the evolution of a Karman vortex-street modelled by two periodic arrays of nonuniform-vorticity FAVRs. As the vortices convect (downstream), large deformations travel around the outer contour, C_1, which eventually (by $t = 40$) breaks and produces a pair of filaments.

The reason for the generation of the filaments is unknown. In some situations, contour-breaking and filamentation may be a genuine feature of the vortex dynamics but, we have included a case in appendix 2 (figure A2.1) in which numerical errors have produced spurious filaments. Once the filaments have formed, there is no in-built mechanism in the CD algorithm to detect their presence but, where filaments are vanishingly thin, (and therefore have negligible global

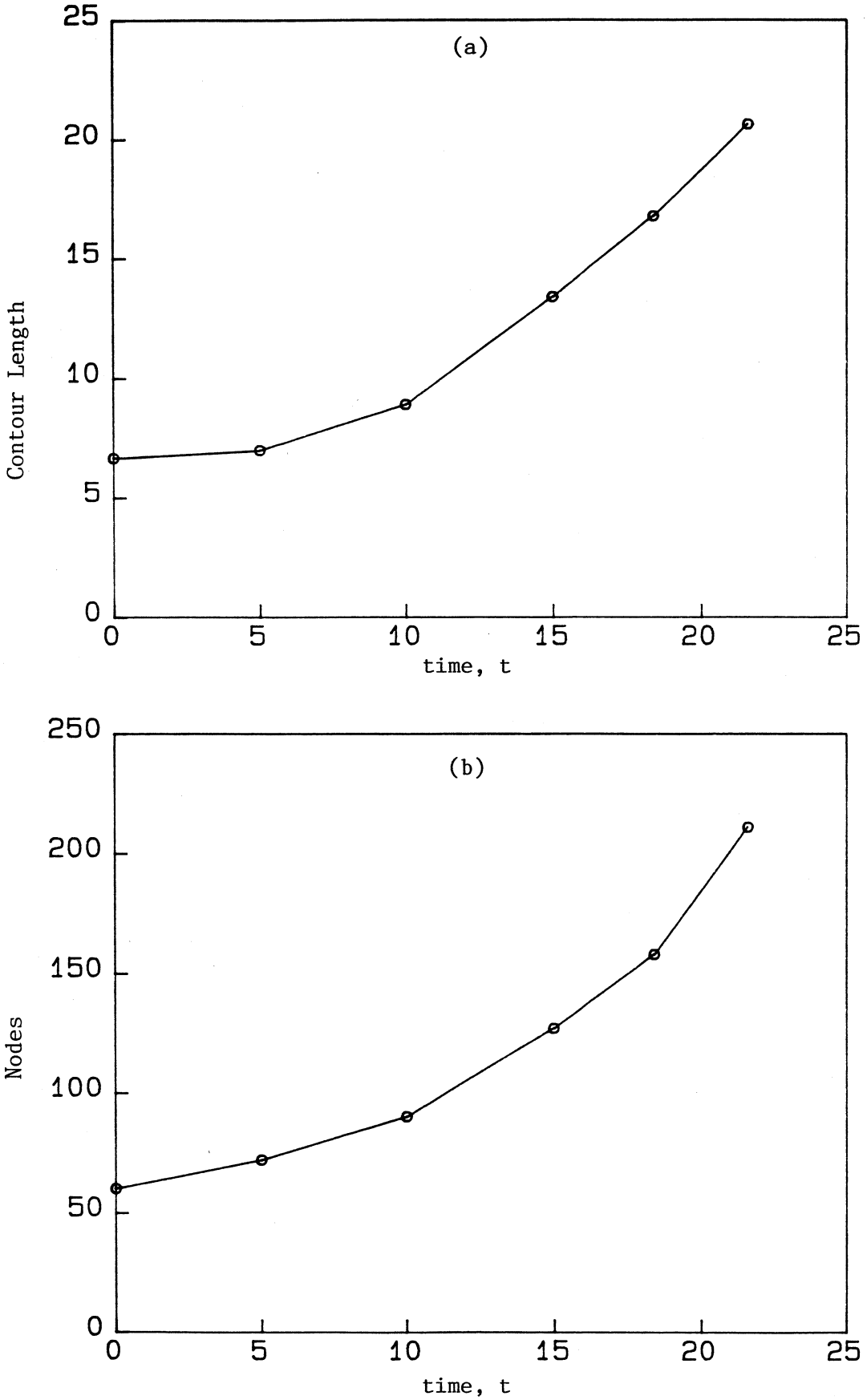

Figure 5.12 : (a) Variation of contour (C_1) length with simulation time t for the uniform vorticity shear layer simulation (figure 5.5). The length of the unperturbed contour is 2π. (b) The number of nodes defining the contour.

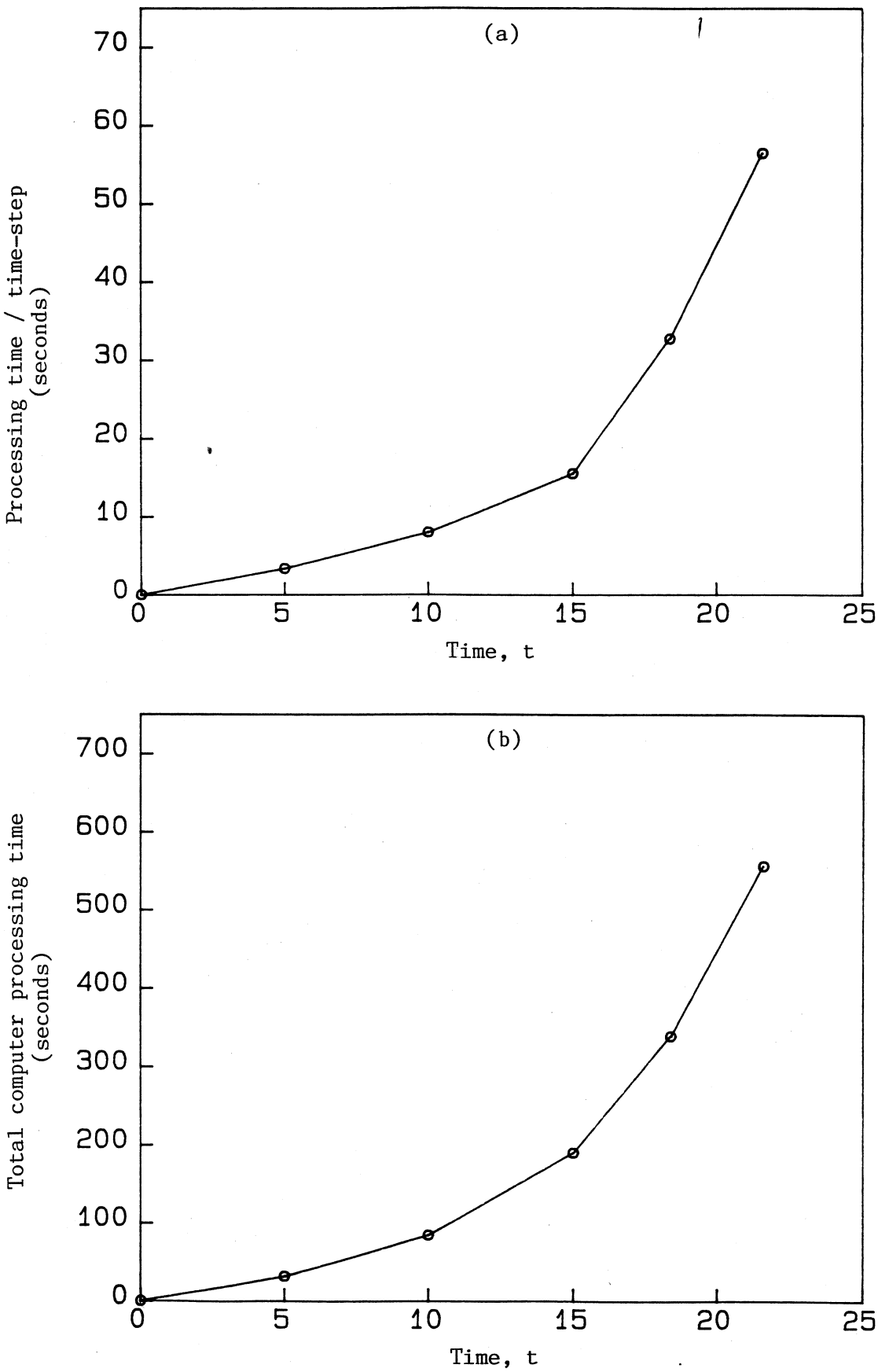

Figure 5.13 : Variation of computer processing time per simulation time time-step for the uniform-vorticity shear layer calculation (figure 5.5). (b) Total computer processing time required to reach the simulation time on the abscissa.

by explicit smoothing or by introduction of model terms in the CD equations (Krasny 1986) would seem to be justified. Dritschel (1986b) has developed a contour surgery technique designed to remove filaments that are dynamically insignificant and allow the computation to proceed to long simulation times with moderate processing time. This approach, however, appears to require some compromises in respect to conserving invariants of the vorticity field (Dritschel 1986a).

The simulation of the Karman vortex-street (figure 5.14) also provided a quantitative check on the CD algorithm via its convection velocity. The circulation of each FAVR is unity while the array period, $\lambda = 2\pi$, and the y-seperation of the FAVR centroids, $h = 1.76$. The major and minor axes of the outer contour C_1 are initially 1.373 and 0.915 respectively, and the regions have the nonuniform (normalized) vorticity profile as specified in table 10.1. At $t = 40$, the measured distance travelled by the FAVR's is 2.22 units giving a convection velocity $U_c = 0.0555$. For a street consisting of point vortices with the same spacing and strength Γ, the convection speed is given by

$$U_c = \frac{\Gamma}{4\pi} \tanh\left[\frac{\pi h}{\lambda}\right] = 0.0562 \quad , \tag{5.8}$$

(Milne-Thomson §13.72, 1968). This is a 1.3 percent difference which (if not a measurement inaccuracy) could be a finite area effect. Saffman & Schatzman (1981) indicate that the steady state uniform-vorticity FAVR street with the same spacing and area ratios ($h/\lambda = 0.280$, $A/\lambda = 0.100$) has a convection speed which is about 2% lower than that for the point-vortex street. Note that this check is rather "weak" in that the vortex centroids in figure 5.14 are located "by eye".

dynamic effect on the vortex motion) their suppression either by explicit smoothing or by desingularization of the CD equations (Krasny 1986) would seem to be justified. Dritschel (1986b) has developed a contour surgery technique designed to remove filaments that are dynamically insignificant and allow the computation to proceed to long simulation times with moderate processing time. This approach, however, appears to require some compromises in respect to conserving invariants of the vorticity field (Dritschel 1986a).

The simulation of the Karman vortex-street (figure 5.14) also provided a quantitative check on the CD algorithm via its convection velocity. The circulation of each FAVR is unity while the array period, $\lambda = 2\pi$, and the y-separation of the FAVR centroids, $h = 1.76$. The major and minor axes of the outer contour C_1 are initially 1.373 and 0.915 respectively, and the regions have the nonuniform (normalized) vorticity profile as specified in table 10.1. At $t = 40$, the measured distance travelled by the FAVR's is 2.22 units giving a convection velocity $U_c = 0.0555$. For a street consisting of point vortices with the same spacing and strength Γ, the convection speed is given by

$$U_c = \frac{\Gamma}{4\pi} \tanh\left[\frac{\pi h}{\lambda}\right] = 0.0562 \quad , \tag{5.8}$$

(Milne-Thomson §13.72, 1968). This is a 1.3 percent difference which (if not a measurement inaccuracy) could be a finite area effect. Saffman & Schatzman (1981) indicate that the steady state uniform-vorticity FAVR street with the same spacing and area ratios ($h/\lambda = 0.280$, $A/\lambda = 0.100$) has a convection speed which is about 2% lower than that for the point-vortex street. Note that this check is rather "weak" in that the vortex centroids in figure 5.14 are located "by eye".

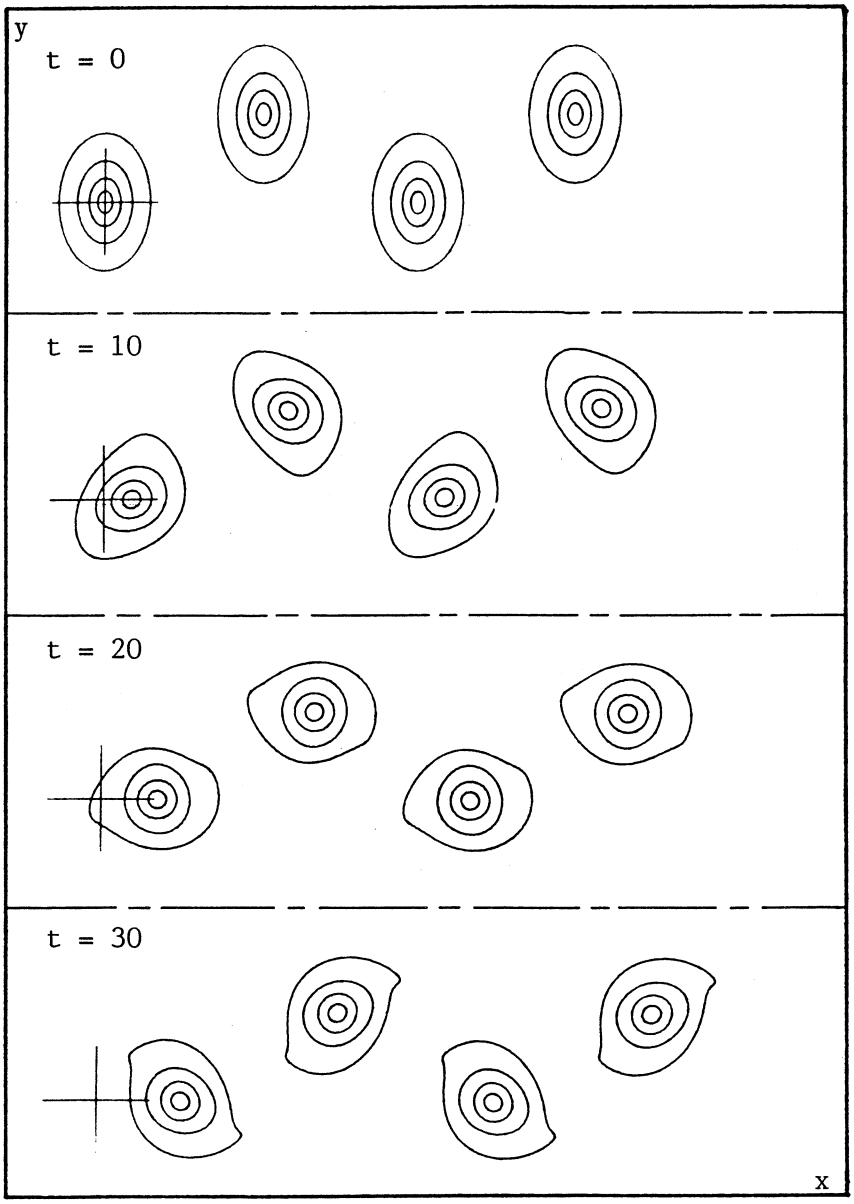

Figure 5.14 : Evolution of a Karman vortex-street. For more details see over page.

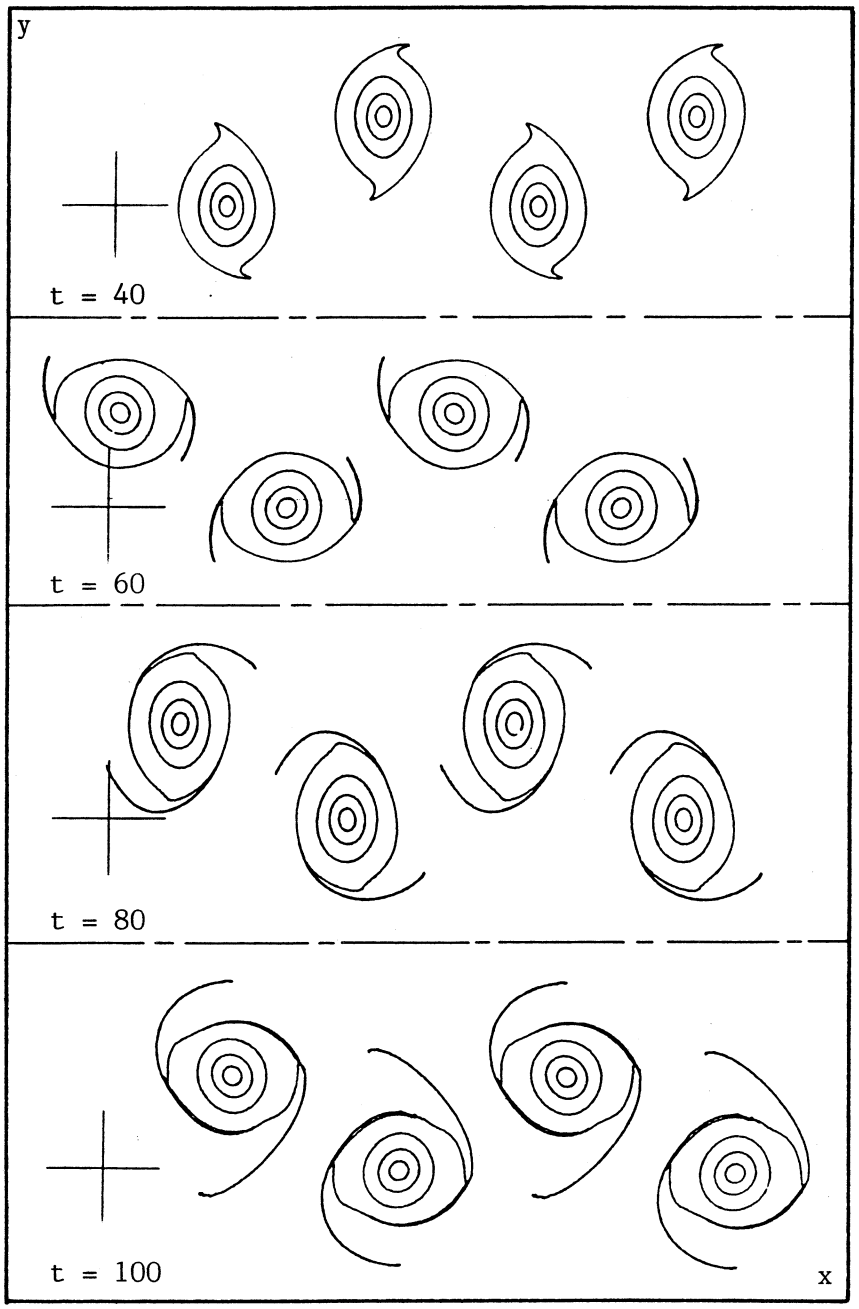

Figure 5.14 : Evolution of a Karman vortex-street of non uniform vorticity FAVRs with unit circulation (upper array). Array period $\lambda = 2\pi$ and y-separation $h = 1.76$. The initial elliptical outer contours, C_1, have major- and minor-axis lengths of 1.373 and 0.915 respectively. Times t as shown. By $t = 40$, two cusps appear to have formed on C_1 and, at later times, vanishingly thin filaments emanate from these points.

6.0 VORTEX MOTIONS OF THE PLANE MIXING LAYER

We now apply the CD technique to some vortex modelling of various eddy scales in the plane mixing layer. This flow is chosen as the large structures that are most apparent (at least in the transition region) in many of the flow visualization studies have been extensively modelled. There is keen interest in such a generic flow and, as a consequence, a large body of literature exists for both experimental and computational studies of the layer. Hence, in the following survey, we will only provide example references rather than an exhaustive list for each point of interest. Ho & Huerre (1984) review some current aspects of mixing layer modelling, with emphasis on hydrodynamic instability concepts, while Hussain (1986) reviews the current state of the coherent structure approach to turbulence modelling.

For the discussion here, we will work within the conceptual framework provided by the coherent structure approach (e.g., Roshko 1976; Liepmann 1979). The resulting flow models will be highly idealized and contain quasi-two-dimensional features that evolve from pure perturbations (rather than random perturbations) to the base flow. The universal existence of such coherent structures is not, however, accepted by all workers (e.g., Chandrsuda et al 1978; Bradshaw 1979). It may be that these features of the flow are artifacts from the early stages of transition in an extremely "clean" layer (i.e., very low free stream turbulence) carefully produced in a laboratory rather than the genuine structure of the fully three-dimensional turbulent flow.

We presuppose the existence of coherent structures within the layer, and restrict our attention to the transition regime by initially considering the development of the quasi-two-dimensional features in sections 6.1 and 6.2. This evolution involves an essentially endless redistribution of the initial spanwise vorticity (Corcos 1979). In sections 6.3 amd 6.4, we describe some of the models of the three-dimensional flow structure that grows on the essentially two-dimensional base

(primary) flow. For the primary flow, we define two Reynolds numbers Re_λ, Re_δ based on the velocity difference ΔU, λ_1 (wavelength of the most unstable perturbation) and θ (initial momentum thickness) respectively.

6.1 Two-Dimensional Features of the Mixing Layer

The mixing layer is the transition region between two parallel, coflowing streams with velocities U_1 and U_2. The traditional view of the mixing layer has been a wedge of fine-scale turbulent motions, growing in cross-stream thickness as the observer moves down-stream. Such blurred images of the fluid motions are typical of the relatively long exposure photographs as shown, for example, in figure 4 of Bernal & Roshko (1986). The layer grows in the cross-stream direction by entraining and mixing nonturbulent free-stream fluid.

More recently, short exposure-time photographs of the mixing layer have shown that large-scale vortical structures (i.e. those with similar spatial dimensions to the width of the layer) exist in the flow over a very wide range of conditions. Examples in the literature have flow conditions ranging from the $Re_\delta \approx 50$ experiments of Winant & Browand (1974) to the $Re_\delta \approx 0.5\times10^4$ experiments of Brown & Roshko (1974). Time-sequences of photographs have shown that the large structures remain coherent over significant times and interact in a deterministic manner. For examples of individual vortex histories, see Brown & Roshko (1974), Roshko (1976) and Hernan & Jimenez (1982). Given the strong evidence for the important role played by the large vortical structures, some workers (e.g. Saffman 1977, 1985; Saffman & Baker 1979; Corcos 1979) believe that the mixing layer behaviour may be better understood through the study of the underlying vortex dynamics.

Figures 6.1a,b are photographs taken by Konrad (1976) looking *(a)* at the plane view of the layer and *(b)* along the span of the layer. The spanwise view is interpreted as

showing the roll-up of the layer into characteristic spanwise structures that convect down-stream with roughly the average velocity of the two streams

$$U_c = \frac{U_1 + U_2}{2} \quad , \tag{6.1}$$

while the plan view shows streamwise streaks due to the three-dimensional motions.

The mixing layer initially undergoes a nonlinear Kelvin-Helmholtz type (primary) instability which redistributes the initial spanwise vorticity into compact, nearly axisymmetric vortex cores whose axes are aligned in the spanwise direction. The layer evolves in the streamwise direction and at any particular down-stream position has roughly periodic properties. At any such point, the layer thickness is related to the spatial dimensions of the spanwise structures.

As the spanwise vortices evolve, they grow in size by ingesting irrotational (free-stream) fluid. Individual vortex histories recorded by Brown & Roshko (1974) and Hernan & Jimenez (1982) indicate that, as the vortices convect down-stream, there is a further concentration of vorticity into fewer, larger but more distantly spaced structures. This redistribution usually occurs in discrete events and appears to be a preferentially two-dimensional process (Winant & Browand 1974; Browand & Troutt 1980, 1985).

Experimental measurements (e.g., Winant & Browand 1974; Lasheras, Cho & Maxworthy 1986) show that the layer thickness increases (approximately) linearly with down-stream distance. To estimate the amount of entrainment required to maintain linear growth, consider the amalgamation of two vortex cores into one. The diameter of a structure containing only the fluid from the two small cores would be roughly $\sqrt{2}$ times the diameter of the small cores. Hence, we require a further factor of $\sqrt{2}$ increase in diameter to be obtained by entrainment of irrotational fluid into the individual vortex

(a)

(b)

Figure 6.1: Photograph of the plane mixing layer taken by Konrad (1976) using a spark shadowgraph technique. This particular figure has been reproduced from figure 146 in Van Dyke (1982).
(a) Plan view showing streamwise streaks.
(b) Spanwise view showing characteristic rolled-up vortex cores. The high speed fluid is in the upper stream.

cores. Hernan & Jimenez (1982) indicate that the bulk of this entrainment occurs between amalgamation events.

The bulk of both experimental evidence (e.g., Winant & Browand 1974; Hernan & Jimenez 1982) and numerical experiments (Acton 1976; Ashurst 1977) strongly suggest that the amalgamation events are dominated by a "pairing" process in which neighbouring vortex cores coalesce to produce a single larger structure. Although the coalescence of two neighbouring vortex cores appears to be most common, it is possible to have three or more cores coalesce into a single structure. For examples of multiple vortex coalescence see Hernan & Jimenez (1982), Winant & Browand (1974) and Ho & Huang (1982). Ho & Huang used a forced mixing layer and, in particular, studied the effect of forcing the layer with subharmonics of the most unstable frequency. They illustrated the sensitivity of the layer to low level forcing and were able to obtain amalgamations of 2, 3 and 4 vortex cores simultaneously by forcing the layer at the appropriate subharmonic frequencies.

Another mechanism of amalgamation, one in which turbulent entrainment plays an important role, was suggested by Moore & Saffman (1975). In this process, the vortex cores of different strengths entrain fluid and grow in size until the spacing cannot be sustained. Once this flow configuration becomes unstable, a "tearing" or "shredding" mechanism redistributes the vorticity of every second core to the slightly larger cores either side. The redistribution is not necessarily equal, so that in the final stages of the process there may be a poor distinction between this process and that of "pairing". However, the end result of larger and more distantly spaced cores is the same. In the experimental data analysed by Hernan & Jimenez (1982) amalgamation by "pairing" occurred 10 times more frequently than amalgamation by "tearing".

6.2 The Temporal Shear Layer Versus the Mixing Layer

Following the "coherent structure" approach, vortex models of the mixing layer have been developed from the interpretations of experimental observations. For example, the nominally two-dimensional mixing layer of figure 6.1b is modelled as an initially thin layer of spanwise vorticity being shed from the trailing edge of the splitter plate (left side of picture). Experiments such as those by Winant & Browand (1974) and Browand & Troutt (1985) indicate that the initial layer evolution is preferentially two-dimensional. Hence, it may be reasonable to study the flow with a purely two-dimensional model consisting of a unidirectional vorticity field.

Another standard computational model is obtained by replacing the vortex dynamics in the window of figure 6.2a with a spatially periodic vorticity distribution which develops in time (figure 6.2b). This is the (spatially periodic) temporal shear layer: a transition region between two parallel counter-flowing streams with velocities $-\Delta U/2$ and $\Delta U/2$ where $\Delta U = U_1 - U_2$. Such a temporal layer provides a computationally economic model as the spatial domain in which the vortex dynamics needs to be explicitly computed is quite compact (e.g., the dashed box in figure 6.2b). The shear layer is related to the mixing layer by the Galilean transformation

$$x = U_c\, t \quad , \tag{6.2}$$

but there are some important differences. The spatially developing mixing layer does not have the symmetry of the shear layer and downstream motions may influence the features of the vortex dynamics in the window (figure 6.2a) thus providing a feedback path for the layer perturbation. This feedback has no analog in the temporal shear layer as a future event cannot influence the present vortex dynamics. One of the few experiments with a temporally evolving layer was

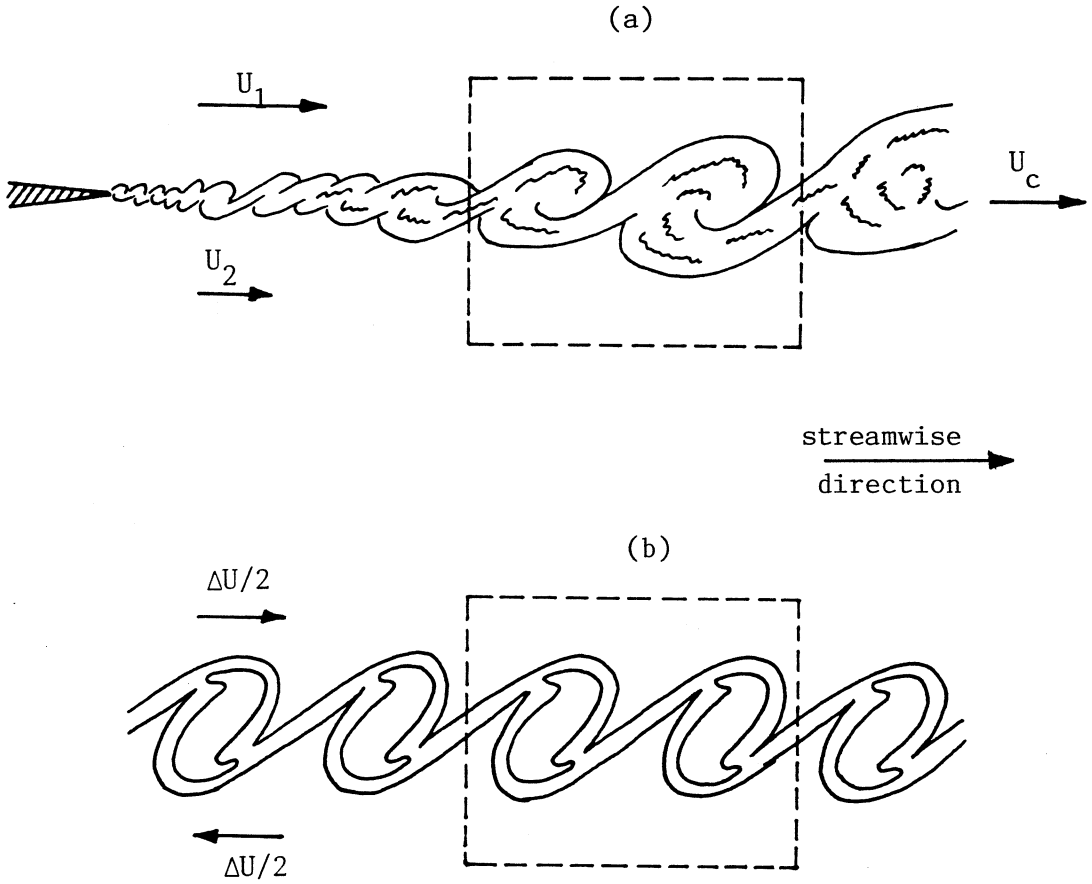

Figure 6.2: (a) Conceptual view of the plane mixing layer showing the spatially developing vorticity field between two parallel streams with velocities U_1 and U_2.
(b) Conceptual view of the two-dimensional, spatially periodic shear layer which develops in time. The "vortex dynamics" of the fluid enclosed in the dashed box (b) models that in box (a).

performed by Thorpe (1971). He used a tilting tank of stably stratified fluid in which the lighter fluid accelerated "uphill" and the heavier fluid accelerated "downhill" thus generating a shear at the interface between the two streams.

Several numerical simulations have been performed using the two-dimensional, spatially developing model (e.g. Ashurst 1977; Davis & Moore 1985; Inoue 1985). These simulations generally used vortex element methods (although Davis & Moore use a finite difference method) and illustrated gross flow features over times equivalent to several life-spans of a typical eddy. Evolutionary histories which were generated closely echoed the available experimental observations. Also, a fully three-dimensional simulation has been performed by Couet & Leonard (1980) (also reported in Couet, Buneman & Leonard 1981) using a three-dimensional extension of the vortex-in-cell algorithm (similar to the CIC method discussed in section 2.3). Simulations using the temporal model include a finite-difference calculation by Patnaik, Sherman & Corcos (1976), a point vortex calculation by Acton (1976), the CIC calculations by Aref & Siggia (1980) and the fully three-dimensional but moderately low Re ($\approx$100) pseudo-spectral calculations of Metcalfe et al (1986). The simulations reported in chapter 7 of this thesis are based on a temporally evolving flow model.

6.3 Three-dimensional Flow Features

The mixing layer motions do not remain two-dimensional as (high-order) three-dimensional instabilities begin to grow on the base flow. Although these instabilities eventually result in the layer motions becoming fully three-dimensional, flow visualization studies (e.g., Lasheras, Cho & Maxworthy 1986) and computational studies (Riley & Metcalfe 1980; Corcos & Lin 1984) indicate that the spanwise coherence and evolution of the primary vortices is only weakly affected. See Roshko (1980) for a review of the three-dimensional motions in the mixing layer.

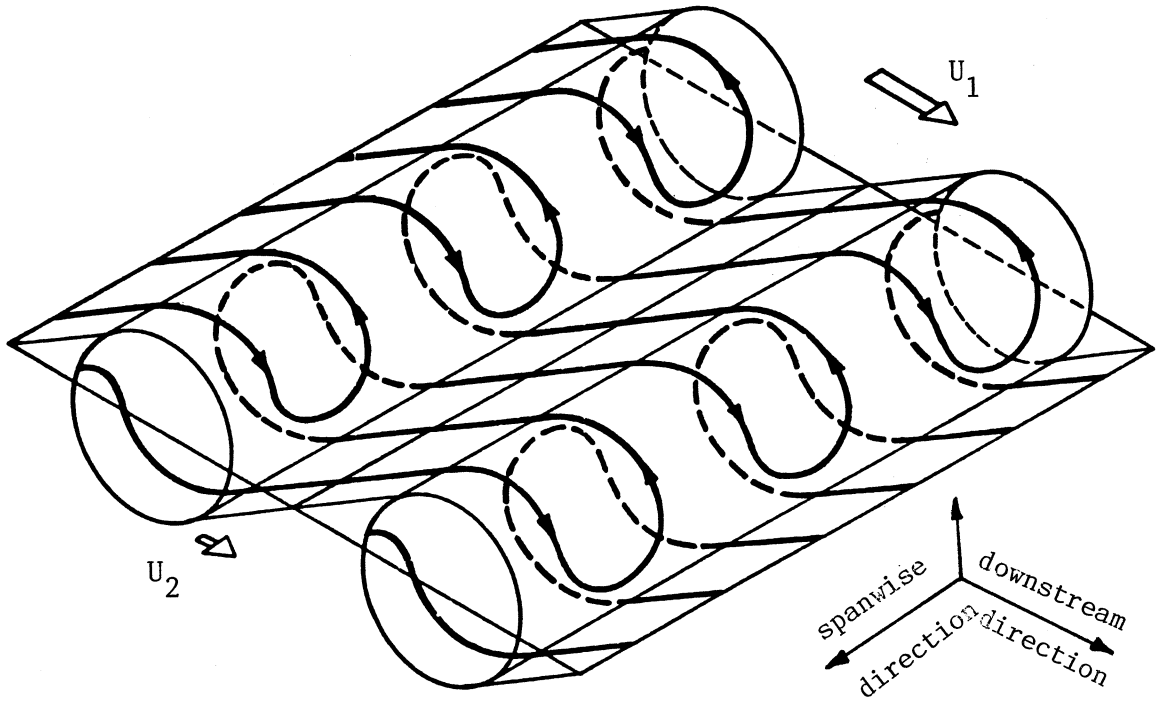

Figure 6.3: An isometric view of the "vortex-skeleton" of the secondary streamwise vortices superimposed on the spanwise vortices. This figure has been reproduced from Bernal's (1981) thesis.

Figure 6.1 (reproduced from Konrad 1976) shows some streamwise streaks in the braid region of the mixing layer. These streaks have been interpreted by Konrad (1976) and Breidenthal (1981) as indicating the existence of a secondary flow structure consisting of an array of counter-rotating, vortices with vorticity in the streamwise direction. This interpretation has been confirmed by the the cross-sectional photographs taken by Bernal (1981) and by computer generated perspective views (Jimenez et al 1985) of the layer produced form the cine film taken by Bernal (1981). Figure 6.3 is a reproduction of Bernal's figure II.18 showing his proposed "vortex skeleton" (a term coined by Perry & Hornung 1984) description of the secondary vortices. In this model, the secondary vortex array is formed as part of a single vortex filament winding back and forth between the high-speed side of one primary vortex and the low-speed side of a second primary vortex immediately up-stream.

These secondary vortices enhance the mixing by further distorting the interface between the two free streams. It is not until higher order instabilities generate even smaller scales of motion than the secondary vortices that there is a catastrophic increase in the interfacial area leading to mixing at the finest scales of motion (Lasheras et al 1986). This event, in which there is an explosive increase in mixing activity, is called the mixing transition (Breidenthal 1981).

The origin of the secondary vortices has been the subject of much interest but has not yet been resolved. Experimental observations by Lasheras et al (1986) indicate that, although the down-stream position at which the interface distortion first becomes evident varies with the up-stream perturbations, the structures always initiate midway along the braids and then propagate into the spanwise vortices. Some workers (e.g., Bernal & Roshko 1986; Lasheras et al 1986) suggest that the secondary vortex structure grows from a genuine flow instability and may be initiated by perturbations introduced

early in the development of the flow (possibly up-stream of the splitter plate).

There are several plausible mechanisms that might generate strong streamwise vorticity from such instabilities. The stability analysis of Benney (1961) predicted the existence of a three-dimensional instability that generated streamwise vorticity. It is clear however that the classical linearized Orr-Sommerfeld instability of the parallel shear layer is not appropriate since the timescale for the growth of the three-dimensional motions is larger than that required for the appearance of the strongly nonlinear features of roll-up and pairing of the two-dimensional spanwise vortices. This led Pierrehumbert & Widnal (1982) to study the inviscid modulational three-dimensional instability of an array of Stuart vortices as a model of the spanwise vortex structure comprising the base flow. They found a "translative" instability that grew over a broad range of spanwise wavelengths that included the streamwise wavelength of the Stuart vortices. Corcos & Lin (1984) argue however that the translative instability is both slower than, and is inhibited by, the pairing instability of the primary vortices. Consequently the assumption of a steady base flow, implicit in the use of the Stuart vortices, is not appropriate to the shear layer evolution. Corcos & Lin (1984) study the origin of the three-dimensional motion at moderate Re as an initial value problem obtained through linearization of the spanwise average of the total velocity field. They found that spanwise periodic perturbations grew to produce non-spanwise vorticity in both the primary vortex cores and the braid regions (where it lies essentially within the braids). Whatever the mechanism, the nett result is the production of streamwise vorticity which is locally tangent to the braids and alternates in sign across the span of the layer.

More recently, Lasheras et al (1986) observed that an isolated disturbance would propagate in the spanwise direction. They described a dynamical mechanism for the formation of the streamwise vortex structure that involved the

spanwise propagation and magnification of disturbances initiated by an isolated perturbation. This mechanism depends upon the stretching and velocity shear across the braid (the midpoint of which is continuously stretched by the velocity field associated with the spanwise vortices). After the structure has been generated it may then settle into a stable configuration consisting of an array of pairs of counter-rotating streamwise vortices. A numerical simulation relevant to this mechanism was performed by Aref & Flinchem (1985) in which solitary waves propagate along a vortex filament embedded in a shear flow. The deformed filament evolves into a form similar in appearance to the spanwise wiggle observed by Breidenthal (1981).

6.4 The Corcos-Lin-Sherman Model

Several highly idealized models have been built from the various interpretations of the observed mixing layer features. One such model is that proposed by Perry (1986) in which the motions of the layer are described by a hierarchy of hair-pin vortices similar in form to the lambda vortices in Perry & Chong's (1982) model of the turbulent boundary layer. All of the vortices start at the trailing edge of the splitter plate and an "inverse cascade" process produces larger-scale structures as the flow develops down-stream.

Motivated by the idea that at least the initial phase of transition occurs as a more or less orderly manner, Corcos-Lin-Sherman (CLS) model the temporal shear layer as a short hierarchy of deterministic motions which interact via a system of identifiable nonlinear instabilities (Corcos & Sherman 1984; Corcos & Lin 1984; Lin & Corcos 1984). Each level of motion in the hierarchy is characterized by a specific vorticity distribution evolving within the ambient strain environment provided by the other scales of motion. Figure 6.4 illustrates the "vortex skeletons" for the first two tiers of these motions. The first tier (or first order motion) is the nominally two-dimensional instability and characteristic

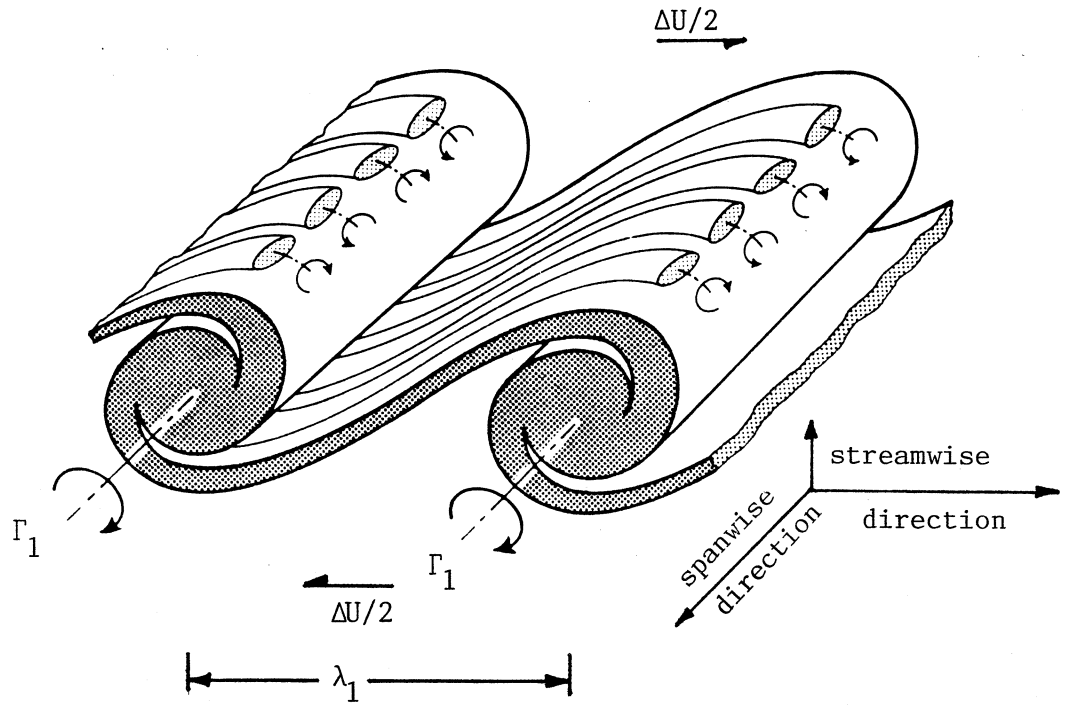

Figure 6.4: The Corcos-Sherman-Lin (CLS) hierarchy of deterministic motions (two tiers shown) modelling the plane turbulent shear layer. The primary vortices (dark shading) are connected by vorticity depleted "braids". Superimposed upon this nominally two-dimensional base flow is the secondary vortex structure depicted by an array of counter-rotating vortices contained within the braid joining two primary vortices. Note that the drawing is not to scale.

roll-up of the layer into spanwise vortex structures (the primary vortices) as mentioned in sections 6.1 and 6.2.

If δ_ω is the initial vorticity thickness of the shear layer, then the fundamental (Kelvin-Helmholtz) instability has a maximum growth rate on a streamwise wavelength $\lambda_1 \approx 7.5\ \delta_\omega$ (Michalke 1964; Miksad 1972). The subsequent nonlinear roll-up of the layer produces an array of vortex cores with circulation

$$\Gamma_1 = \Delta U \lambda_1 \quad , \tag{6.3}$$

on a timescale

$$T_1 = 0(\lambda_1/\Delta U) \quad . \tag{6.4}$$

The braids connecting adjacent vortex cores are embedded in the stretching velocity field induced by the array of vortex cores. For an array of equal strength vortices, the stretching strain strength at the centre of the braid is given approximately by

$$\gamma = \frac{\Delta U \pi}{2\lambda_1} \quad . \tag{6.5}$$

Equation (6.5) is derived from a point-vortex model of the primary vortices as shown in appendix 4. However, for large t, the effects of viscous diffusion will ultimately balance the vorticity intensification induced by stretching. The thickness of the braid, δ_2, might then be expected to approach the Burgers vortex sheet thickness

$$\delta_2 = (2\pi\nu/\gamma)^{1/2} \quad , \tag{6.6}$$

(Burgers 1948) in a time

$$T_2 = 0\left[\frac{1}{\gamma}\left\{\frac{{\delta_1}^2}{{\delta_2}^2} - 1\right\}\right] \quad , \tag{6.7}$$

(Lin & Corcos 1984). For an inviscid fluid, we expect the braid thickness to vary asymptotically as

$$\delta_2 = \exp(-\gamma t) \quad . \tag{6.8}$$

In the experiments of Bernal (1981), Jimenez (1983) (and others) the secondary motions may be interpreted as a structure of counter-rotating streamwise vortices. The stretching strain imposed by the spanwise vortices upon the middle of the braid (represented by the four streamline segments in figure 6.5a) is assumed to be the only connection between the primary and secondary model flows. The imposed strain reorients the streamwise vorticity so that it is aligned with the braid and compresses the braids (in the y-direction of figure 6.5a) so that, within a linearized approximation, the vorticity thickness of the secondary vortices approaches the Burgers vortex-sheet thickness δ_2 in equation 6.6. Hence, in the middle of the braid (where the structures appear to be most coherent), these secondary vortices are modelled as an array of highly flattened, counter-rotating vortices evolving in the local strain environment provided by the spanwise vortices.

Measurements of the spanwise spacing and strength of the secondary vortex structure have been obtained from experiments. Breidenthal (1981) (using flow visualization) suggested that the wavelength of the vortex array $\lambda_2 \approx \lambda_1$ while Jimenez (1983) (using hot-wire techniques) indicated that the strength (circulation) of the individual vortices approached a constant value $\Gamma_2 = \beta_2\Gamma_1$ where $\beta_2 = O(1)$. Later measurements by Jimenez et al (1985) (using flow visualization data) produced similar parameter values. We also define a suitable Reynolds number for the secondary vortices as

$$Re_2 = \Gamma_2/\nu \quad . \tag{6.9}$$

The third tier of deterministic motions is comprised of the small-scale eddies that evolve on the secondary streamwise vortices. For increasing Re_2, the secondary vortices will become very thin (as $\delta_2 \rightarrow 0$) and, on a small scale, the local environment will be similar to that of an infinite vortex layer embedded in a stretching strain field. Such a stretched

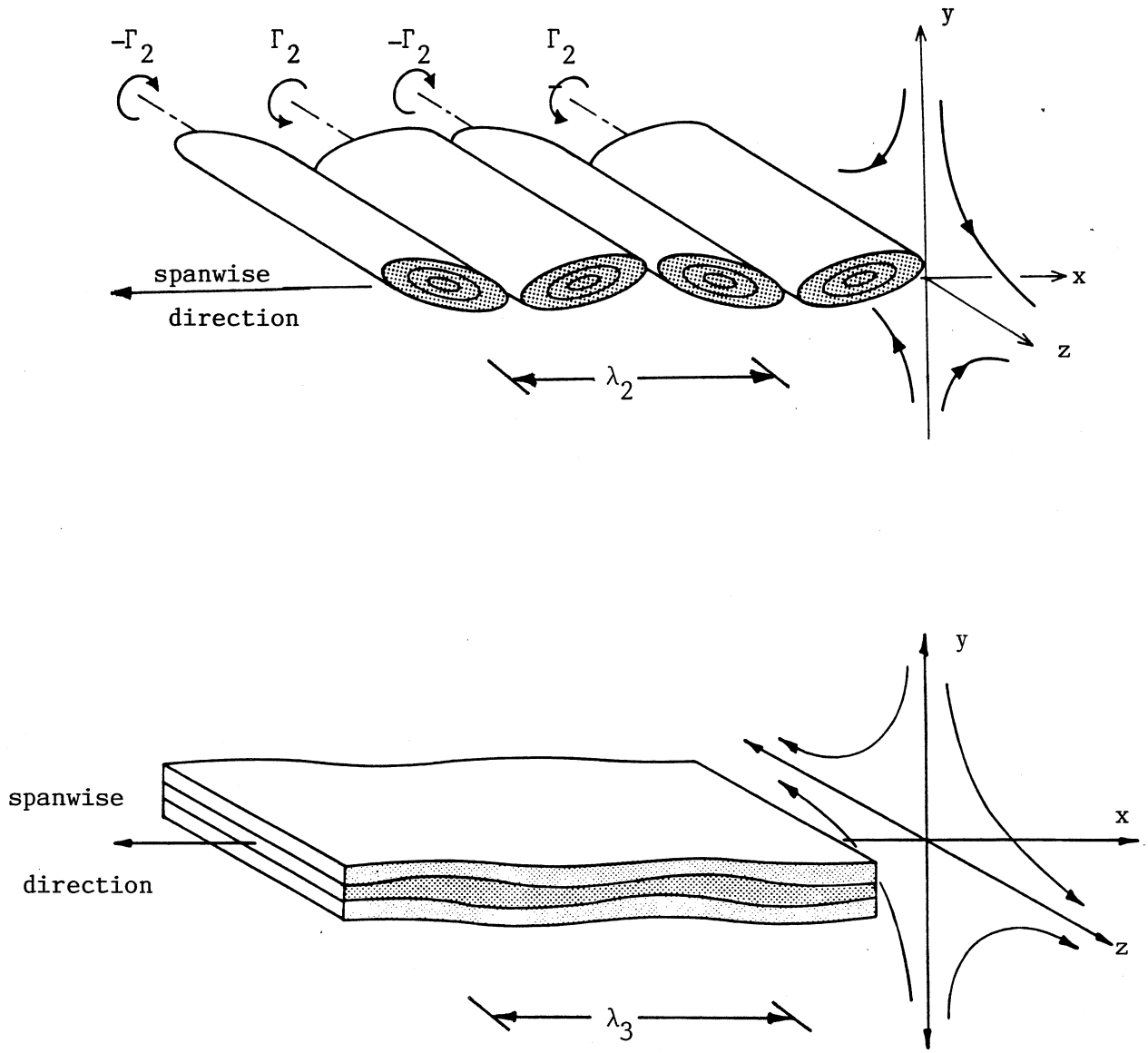

Figure 6.5: (a) Stretched vortex array modelling the secondary vortices in the CLS model.
(b) Stretched vortex layer modelling the tertiary motions in the CLS model.

layer may be expected to be unstable to spanwise perturbations and lead to the production of tertiary motions. Hence, we expect that the evolution of a stretched shear layer, as shown in figure 6.5b, will be relevant to the tertiary motions as the aspect ratio of the secondary vortices $a_2 \rightarrow \infty$. At low Re these motions may not evolve as the viscous diffusion / stretching strain of the vorticity distribution is achieved in a short time but, for $Re_2 \rightarrow \infty$ it might be expected that several tiers of higher order structures will rapidly generate motions needed for the energy cascade to smaller scales characteristic of inertial range turbulence.

In the following chapters we use the CD technique to provide some high resolution vortex histories for the above-mentioned prototype flows at the nominal limit $Re = \infty$. Chapter 7 contains details of the nominally two-dimensional temporal shear layer behaviour (or first order motion), while chapters 8 and 9 describe the simulation results for the secondary vortex array and the stretched shear layer (tertiary motions) respectively. Lastly Chapter 10 treats the interaction of two equal (but otherwise isolated) vortices embedded in a stretching strain field. Figures for each of these sections are included as a "block" following the full text for the chapter.

7.0 PRIMARY MOTION

Numerical simulations of two-dimensional mixing/shear layers have successfully provided structural models and examples of various features observed in experiments. These features include the nonlinear roll-up into compact vortex cores, pairing of vortex structures and resulting growth in thickness of the layer. Aref (1983) reviews the application of vortex element methods to the two-dimensional simulation the mixing/shear layer. Some of the simulations are summarized in table 7.1.

A realistic model of the shear layer would have both a finite thickness (δ) layer and a finite viscosity (ν) fluid. As discussed in section 2.1, the range of Reynolds numbers obtainable in numerical simulations is severely restricted owing to the computational burden of resolving the fine-scale motions. Hence, most computational studies which aim to be relevant to high Re will either use a model in which both $\delta \rightarrow 0$ and $\nu \rightarrow 0$ (a vortex-sheet of zero thickness) or a model having $\delta > 0$ and $\nu \rightarrow 0$ (a finite-thickness vortex layer).

The approximation of the layer as a vortex sheet has been investigated by Damms & Kuchemann (1974), Neu (1984) and Higdon & Pozrikidis (1985) among others. This model is not well defined and there is now substantial evidence which suggests that the evolution of the vortex sheet results in the formation of a singularity in the sheet curvature in a finite time (Moore 1979; see also Krasny 1984). What happens to the sheet evolution beyond the point of singularity formation is still an open question. Note that Moore (1978) has considered a layer of small but finite δ but the relevant equation of motion admits spurious short wave instabilities.

The second approach of keeping δ finite and setting $\nu = 0$ appears to be a well defined limit and may also be a more realistic representation of the early stages of an experimental shear layer. In finding solutions to this model, we suppose that the limiting solution to the Navier-Stokes

equations (in the absence of solid boundaries) as $Re \rightarrow \infty$ (or as $\nu \rightarrow 0$) is equivalent to the solution of the Euler equations starting with the same initial conditions (vorticity field). Hence, we expect that the inviscid simulations in the following discussion will be relevant to the behaviour of the layer as $Re \rightarrow \infty$.

The definition of the vorticity field and the appropriate Reynolds number of the solutions are closely linked with the numerical technique. The simulations of finite-thickness layers have been based on flow models having either *(i)* continuous vorticity distribution at low to moderate Re (finite-difference or spectral methods), *(ii)* discrete vorticity distributions such as a cloud of point-vortices or vortex blobs at $Re = \infty$, or *(iii)* a step-function distribution such as used in the CD method at $Re = \infty$.

The computational effort required for a simulation increases with the required resolution (see section 2.2) and for moderate Re, the evolutionary problems very quickly outstrip the available computing resources. However, several "long-time" numerical simulations have been performed which provide vortex histories over timescales spanning several vortex life-times. Ashurst (1977) used a vortex blob technique in which vortex elements were ejected into the flow at the trailing edge of a splitter plate and were allowed to evolve as they convected downstream. Ashurst showed that the dominant process for the production of the larger structures was by pairing of the smaller cores (or clouds of vortex elements). Aref & Siggia (1980) performed a simulation of the spatially periodic shear layer using the CIC technique with 4096 vortex elements. They provided statistical estimates of the layer properties and suggested that the growth of the cross-stream thickness was due, in part, to the scattering of the vortex cores about the centre line of the layer. Davis & Moore (1985) used a high-order finite-difference method to simulate a spatially developing layer at $Re_\delta = O(10^4)$. The initial conditions at the splitter plate were disturbed with combinations of the primary eigenfunction and its subharmonics

and vortex histories showed examples of pairing and tearing of the vortex cores.

Short time simulations showing the fine details of one amalgamation event have been performed by Patnaik, Sherman & Corcos (1976), Acton (1976) and Riley & Metcalfe (1980). These studies have mainly concentrated on the interaction of fundamental perturbation combined with its first subharmonic. The emphasis on the interaction of just the first subharmonic has been justified by considering the analysis by Pierrehumbert & Widnal (1982) of a flow consisting of an array of Stuart vortices. They showed that, for such a flow, the subharmonic perturbation has the highest growth rate and would be expected to become the dominant influence once the layer has rolled-up into compact cores. Although the simulations of both Riley & Metcalfe (spectral method) and Patnaik et al (using the finite difference method) were limited to $Re_\delta = O(100)$, they still produced vortex-pairing scenarios similar to those produced in the $Re_\delta = \infty$ simulation of Acton (using the point-vortex method). The vortex tearing mechanism was also examined in these simulations and was found to occur over a longer timescale and be weaker than the pairing interaction in cases where both effects were present.

The first Contour-Dynamic simulations (excluding the plasma simulations of Berk, Nielsen & Roberts 1970 showing the equivalent of a combined pairing/tearing interaction) for the inviscid shear layer of finite thickness appear to be those of Pozrikidis & Higdon (1985). They investigated the effect of parameters (i) layer thickness and (ii) amplitude of initial disturbance of a uniform-vorticity shear layer. They found that the initial growth and form of the roll-up process depended on the thickness of the layer, however, the final layer amplitude was consistently limited to about 0.2 of the wavelength of the computational domain, λ_{comp}. We have reproduced some of their results (see e.g. figure 5.5) using the present technique.

In this chapter we will use the inviscid CD formulation for an x-periodic vorticity layer to produce moderate time, high-resolution simulations of shear layer evolution at $Re_\delta = \infty$ without the inherent "graininess" of the vortex element techniques. In particular, we will investigate the evolution of a nonuniform-vorticity layer, defined by a piecewise-constant vorticity distribution, which is initially disturbed by imposing one or more eigenfunction modes, as calculated by a linear analysis (appendix 5), with small but finite amplitudes.

7.1 Flow Configuration

Consider the initial vorticity distribution illustrated in figure 7.1. The two-dimensional vortex layer is periodic in the x-direction, y is the cross-stream direction and z is the spanwise direction (of the shear layer). Only one period $0 \le x \le \lambda_{comp}$ of the computational domain is shown. The vorticity

$$\omega = \omega_z(y)\underline{k} \quad , \tag{7.1}$$

of the undistrubed layer is a piecewise-constant distribution with regions, R_j, j = 1..M, 1'..M' containing fluid with vorticity ω_j in both regions R_j and $R_{j'}$. The primed quantities here indicate contours that are initially below the x-axis. Hence, each contour above the x-axis has a corresponding contour below the axis. The associated velocity field, $u_x(y)$ varies from $+\Delta U/2$, $y > h_1/2$ to $-\Delta U/2$ for $y < -h_1/2$ where h_1 is the average distance between the outer contours C_1 and $C_{1'}$. The contours, C_j, j = 1..M, 1'..M' in the (x, y)-plane delineate the discontinuities of the vorticity profile and are labelled C_1 to C_M, progressing from the top to the middle of the layer (and for the lower contours, $C_{1'}$ to $C_{M'}$). Hence, the regions R_j, j = 1...M-1 are bounded by contours C_j and C_{j+1} with R_M (being the same region as $R_{M'}$) bounded by C_M and $C_{M'}$.

All computations were performed in an x-periodic box of length, $\lambda_{comp} = 2\pi$ containing a total circulation $|\Gamma_{comp}| = 1$. For any particular simulation, the computational domain may contain an integral number (say n) of wavelengths of the fundamental eigenfunction. Hence, for a single rolled-up vortex core $\lambda_1 = (1/n)\ \lambda_{comp}$ and $\Gamma_1 = (1/n)\ \Gamma_{comp}$ giving

$$T_c = \frac{\lambda_1^2}{\Gamma_1} \quad , \tag{7.2a}$$

as the characteristic time for the evolution. For the discussion of results in section 7.4, we find it convenient to normalize the lengths on λ_1 and the times on T_c so that the nondimensional time

$$\tau = t \ / \ T_c \quad . \tag{7.2b}$$

The undisturbed piecewise-constant distribution of $\omega(y)$ has been chosen to approximate a Gaussian distribution

$$\omega(y) = \exp\ [-\rho\ (y/h_1)^2] \quad , \tag{7.3}$$

Figures 7.2a and 7.2b show the vorticity distribution for four regions in the upper half of the layer ($y > 0$) for $M = 4$ and $M = 8$ respectively. (Numeric values for h_j and ω_j are given in tables 7.2a,b). The approximate Gaussian distributions are superimposed as solid curves with values of $\rho = 1.0,\ 1.25$ for $M = 4,\ 8$ respectively. In figure 7.3 we show a comparison of the piecewise-linear velocity profiles (associated with the piecewise-constant vorticity distributions) with the properly-continuous hyperbolic-tangent velocity profile. The differences in appearance between the $M = 4,\ 8$ (especially $M = 8$) profiles and the hyperbolic-tangent profile are barely discernible.

7.2 Growth of Small Perturbations

We will first consider the growth of small-amplitude sinusoidal disturbances superimposed on the mean contours and search for vorticity preserving solutions to the Euler equations for which the contours are perturbed as

$$\eta_j\ (x,\ t) = \frac{h_j}{2} + \alpha_j \exp(i\sigma t) \exp(ikx) \qquad (7.4)$$

$$j = 1...M,\ 1'...M'$$

where $\eta_j(x,\ t)$ is the contour y-coordinate, $\alpha_j = \alpha_{rj} + i\alpha_{ij}$ is the complex amplitude, $k = 2\pi/\lambda$ is the wave number and $\sigma = \sigma_r + i\sigma_i$ is the complex growth rate ($-\sigma_i$ = growth rate, σ_r/k = phase speed). On substituting equation (7.4) and appropriate expressions for the velocity fields into the Euler equations, we can obtain a coupled set of linear algebraic equations which may be solved as an eigenvalue problem with eigenvalue σ and α_j, $j = 1...M,\ 1'...M'$ as part of the associated eigenfunction. Details of this linear stability analysis of the piecewise-constant vorticity profiles are contained in appendix 5.

To obtain a more compact description of the initial contour geometry we define the eigenfunction in vector notation as

$$\underline{\eta}(x,\ t) = \frac{\underline{h}}{2} + \underline{f}^{(M)} \exp(i\sigma\tau) \exp(ikx) \quad , \qquad (7.5)$$

where

$$\underline{\eta} = [\eta_1...\eta_M\ ,\ \eta_{M'}...\eta_{1'}]^T \quad , \qquad (7.6a)$$

$$\underline{h} = [h_1...h_M\ ,\ h_{M'}...h_{1'}]^T \quad , \qquad (7.6b)$$

$$\underline{f}^{(M)} = [\alpha_1...\alpha_M\ ,\ \alpha_{M'}...\alpha_{1'}]^T \quad , \qquad (7.6c)$$

and T represents the transpose.

Figure 7.4 shows the normalized growth rated $(-\sigma_i/\omega_{max})$ for the four vorticity profiles : *(i)* The uniform-vorticity layer M = 1 previously studied by Rayleigh (1880) and more

recently by Pozrikidis and Higdon (1986); *(ii)* The piecewise-constant M = 4 vorticity profile defined in figure 7.2a; *(iii)* The piecewise-constant M = 8 vorticity profile defined in figure 7.2b; and *(iv)* The continuous profile, $\omega_z(y) = \Delta U/2 \cosh(y)$, studied by Michalke (1964). For all profiles, there are unstable perturbations only for a limited range of $k\delta_\omega$ with the upper limit of this range increasing with decreasing ratio δ_ω/h_1. All solutions that have $\sigma_i \neq 0$ also have $\sigma_r = 0$. Hence, unstable disturbances do not progress along the layer.

Considering just the piecewise-constant profiles, figure 7.4 shows that the maximum growth occurs for perturbations with wavelength approximately $7.5\delta_\omega$. Perturbations with wavelengths shorter than about $3\delta_\omega$ for M = 4, 8, and $5\delta_\omega$ for M = 1 are stable while the perturbations of maximum growth rate have $k\delta_\omega = 0.875$ and $k\delta_\omega = 0.857$ for M = 4 and M = 8 respectively. Although the vorticity for these profiles is contained entirely in a relatively thin layer, they provide a close approximation to the perturbation growth rates of the properly-continuous cosh(y) vorticity profile.

In the linear analysis, the shape of the perturbation is calculated as part of the eigenvector but its amplitude is indeterminate. We thus normalize the numerical values for the α_j such that the contour with largest displacement has magnitude $|\alpha| = 1.0$. (The contour of maximum amplitude is invariably the innermost contour C_M , $C_{M'}$). The normalization procedure also imposes a symmetry

$$\alpha_{j'} = - \alpha_j^* \qquad (7.7)$$

where * represents the complex conjugate. This means that, if we rotate the (x, y)-axes π radians about the origin in the physical plane then, the flow configuration is unchanged.

When initializing the contour shapes for the numerical simulations, only the real part is relevant, hence the contour C_j is defined as

$$\eta_j(x) = h_j + a_o \text{ Real } [\alpha_j \exp(i\phi) \exp(ikx)] \quad , \qquad (7.8)$$

where a_o is the initial amplitude of the applied perturbation. For the simulations presented in section 7.4, we will use simple initial contour shapes that consist of only one, two, or three linearly combined eigenfunctions. The fundamental mode is chosen to be the perturbation with maximum rate of growth and is labelled as $f_1^{(M)}$ ($\sigma_i/\omega_{max} \approx 0.192$ for M = 4). In figure 7.4 the fundamental, first subharmonic, and second subharmonic modes for the M = 4 profile are indicated by $f_1^{(4)}$, $f_2^{(4)}$, and $f_3^{(4)}$ respectively. Table 7.3 contains the numeric values for the α_j's in the upper half of the layer (i.e., α_j, j = 1...4) while table 7.4 contains the data defining the fundamental and first subharmonic eigenfunctions for the M = 8 profile.

Figure 7.5 shows the variation of eigenfunction shape for three values of $k\delta_\omega$. Here we plot the contours of the layer disturbed by eigenfunctions $\underline{f}_1^{(4)}$, $\underline{f}_2^{(4)}$, $\underline{f}_4^{(4)}$ with $k\delta_\omega = 0.875, 0.438, 0.219$ respectively. To highlight the difference in shape, each plot has the same wavelength $\lambda = 2\pi$, and a stretched y-axis designed to give the *appearance* of similar vorticity thickness. The fundamental perturbation, $\underline{f}_1^{(4)}$, produces an accumulation of vorticity about the centre of the domain while the smaller $k\delta_\omega$ perturbations, with smaller growth rates, induce a more uniform displacement of the bounding contours.

As the infinitesimally-small perturbations grow independently, they may be combined linearly with any relative phase angle, ϕ, and amplitude ratio. However, Corcos & Sherman (1984) report that an early consequence of nonlinearity in the vortex dynamics is the selection of a dominant wavelength. There is experimental evidence (e.g., Thorpe 1971) to suggest that, early in the evolution, a single wavelength dominates the growth and temporarily inhibits the growth of perturbations having similar wavelengths but with either smaller growth rates (σ_i) or smaller initial amplitudes (α_o).

Figure 7.6 shows the evolution of an M = 4 layer with $\delta_\omega/\lambda_{comp} = 0.0382$ and $N_j(0) = 60$. There is initially no forced perturbation ($a_o = 0$) hence, to within machine precision, the contours were of constant height. The calculation used code-version B (table 4.1), node-parameter set 3 (table 4.3) and was performed with 32-bit precision arithmetic (IBM 3083). Numerical noise, presumably with a wide bandwidth, seems to have been introduced via the finite-precision arithmetic and, by t = 40, the vortex dynamics has produced distinct rolled-up vortex cores and the early stages of a pairing event. Hence, the t = 40 contours indicate the presence of a single dominant wavelength ($k\delta_\omega \approx 0.96$) and its first subharmonic. This wavenumber is close to that of $f_1^{(4)}$ ($k\delta_\omega = 0.875$) and the time for its amplitude to increase by two orders of magnitude $t_d \approx 36$.

We repeated the calculation (figure 7.7) this time using code-version C and 32-bit arithmetic. The layer again rolls-up and the dominant perturbation (evident as a modulation of the vorticity distribution by t = 40) has $k\delta_\omega \approx 1.44$ and $t_d \approx 53$. The first subharmonic ($k\delta_\omega \approx 0.72$) also grows and, by t = 75, produces three merging structures in the computational domain. To isolate the source of the perturbations we *(i)* repeated the calculation using code-version D (i.e. no analytic-patch) with 32-bit precision and *(ii)* tried 64-bit precision with code-version C. The results are summarized in figure 7.8 which shows the t = 60 frames from figure 7.7 and *(i)* and *(ii)* above. In figure 7.8b (case i), the dominant perturbation is only just discernible with an amplitude $a_o/\lambda_{comp} \approx 0.05/2\pi$. In figure 7.8c (case ii), there is no visible evidence that any perturbation has grown. We conclude that, initially, perturbations with effective amplitudes of one or two orders of magnitude larger than the machine-precision have been introduced through the finite-precision arithmetic either in the calculation of the node velocities or in the time-stepping by the differential-equation solver. Although the analytic-patch procedure appears to be the major source of this error, it does not detract form its superiority over the plain numerical

quadrature (4.14) for "nearly touching" contours as illustrated in appendix 3.

Given the evidence for a single wavelength and its subharmonics becoming dominant it seems reasonable to use initial conditions that are simpler than a perturbation with a continuous wavenumber spectrum and have only, say, two or three linearly combined eigenfunctions. Let us consider the superposition of only the fundamental plus first subharmonic eigenfunctions. Leaving aside the amplitude a_o or the value of M, we choose the fundamental (f_1, k = 2) to have a phase $\phi = 0$ and allow the subharmonic (f_2, k = 1) to take the values $\phi = 0, \pi/4, \pi/2$. These are labelled as the pure pairing mode, pairing / tearing mode and the pure tearing mode. The fundamental eigenfunction redistributes the vorticity of the layer by producing two slight accumulations of vorticity as in figure 7.5a while maintaining $\Gamma = 1$ over the computational domain. These accumulations will later become the spanwise vortex cores with spacing λ_1.

The effect of superimposing the eigenfunction f_2 depends upon the value of the relative phase ϕ. Owing to periodicity we need only consider the range $0 < \phi < \pi/2$. For $\phi = 0$, f_2 modulates the y-position of the centroids of the vortex accumulations while keeping their strengths equal. With $\phi = \pi/2$, f_2 modulates the strengths of the vortex accumulations while maintaining their centroids undisturbed, and, with $\phi = \pi/4$, f_2 alters both the accumulation strengths and the positions of their centroids. Other values of ϕ (producing a combination of effects) may be taken anywhere in-between.

Various other perturbations can be obtained by considering combinations of eigenfunctions f_3 and f_4. For example $f_1 + f_3$ will produce a three vortex redistribution while $f_1 + f_2 + f_4$ will produce a four vortex redistribution having two pairs of accumulations.

7.3 *Initial Amplitude*

Ideally, we would like the CD simulation to start from an initial condition that is governed by the linear approximation but which has a large enough amplitude to quickly become nonlinear without great computational expense. As a measure of nonlinearity in the computed solution, we use the difference between a linear calculation and the full nonlinear CD calculation.

Two test cases were chosen to illustrate the effect of initial amplitude upon the short time evolution. As results for both cases are similar, only one set will be presented here. This case corresponds to an initial set of contours (M = 4) defined by

$$\underline{\eta}(x) = \underline{h}/2 + a_o \, \text{Real}(\underline{f}_1^{(4)} e^{i2x} + \underline{f}_2^{(4)} e^{ix}) \quad , \qquad (7.9)$$

where the length of the computational domain $\lambda_{comp} = 2\pi$. Note that the amplitudes of both perturbation components are equal.

Figure 7.7 summarizes the evolutionary calculations by plotting the maximum y-coordinate for each of the contours in the upper half of the layer. For each contour there is a solid line for the full nonlinear CD calculation and a dashed line for the linearized calculation where the contours take the form

$$\underline{\eta}(x, t) = \underline{h}/2 + a_o \, \text{Real} \, [\underline{f}_1^{(4)} \exp(i2x) \exp(i\sigma_1 t) + \underline{f}_2^{(4)} \exp(ix) \exp(i\sigma_2 t)] \quad . \qquad (7.10)$$

Here σ_1 and σ_2 are the complex growth rates of the fundamental and first subharmonic (M = 4) perturbations scaled appropriately with the maximum vorticity (Real(σ) = 0). The evolution for $a_o/\lambda_1 = 0.05/\pi$ is shown on figure 7.9a and, for the first six time-units, the two solutions are the same to within plotted accuracy (±2% for the innermost contour). To check the solution sensitivity, the calculation was repeated for $a_o/\lambda_1 = 0.01/\pi$ (figure 7.9b). After 25 time units, the innermost contour has reached approximately the same height as

the $a_o/\lambda_1 = 0.05/\pi$ case at $t = 0$. The solutions at this point are only just beginning to diverge, thus indicating that the linear solution (7.10) is adequate up to this time. From this experiment we conclude that $a_o/\lambda_1 = 0.05/\pi$ is a reasonable upper-limit to the initial disturbance amplitude for each of the eigenfunctions.

7.4 Simulation Results and Discussion

We now present the results of the simulations of the two-dimensional shear layer for various initial perturbations. Computations have generally performed with code-version C (table 4.1) and with node-parameter sets 1 and 2 (table 4.3) on a CDC Cyber 205 supercomputer (located at C.S.I.R.O). A summary of the full set of simulation results is contained in table 7.5. Selected preliminary calculations (e.g. case 3a) have been presented in Jacobs & Pullin [4].

Computations were started with the vorticity field being defined by contours as defined in section 7.1 and perturbation shapes defined by one or more eigenfunctions as described in section 7.2. The amplitude of the applied perturbation was close to the start of nonlinear interaction (section 7.3). Termination of the computation invariably occurred upon reaching an upper limit set on the computer processing-time allowed per job (approximately 3 hours on the Cyber 205).

In the numerical calculations, we tried to closely approximate the nonuniformities of the fully-continuous vorticity profiles measured in experiments and hence would have preferred to use the M = 8 profile for our "production runs". However, the constraints on memory (2 Mwords on the Cyber 205) and on processing time (CD computational effort varies as $O(N^2)$ as discussed in section 5.2) forced us to compromise and perform the bulk of the simulations with the M = 4 vorticity profile. Sensitivity of the solutions to initial vorticity profile variations was checked by comparing particular M = 4 simulations with a uniform-vorticity (M = 1) layer (case 1) and an M = 8 layer (case 4). A seperate computation case 3a, performed with an independent code (code-version B; table 4.1) indicated that the simulations were broadly insensitive to the numerical implementation of the CD algorithm. See figure 5.7 for a comparison of numerical results.

Where possible (and convenient) we made use of the shear layer symmetries and set the lower contours ($C_{j'}$) to be images of the upper contours, thus halving the computational effort required for the full nonlinear calculation. However, this could only be done for cases where the phase shift of all of the subharmonics was set to zero (cases 1, 2, 3, 3a, 4, 7, 9 of table 7.5). Although case 5 has a similar form of symmetry, it was not implemented in the numerical code.

Numbers of nodes on each contour ranged from $N_j(t=0) = 60$, $j = 1...4$ to typically $N_j(\tau_{max}) = 527, 718, 867, 957$. (These figures are obtained from case 3). The largest number of nodes always occurred on the innermost contours which were invariably the longest. The maximum number of nodes allowed on the Cyber 205 runs was restricted to $N_{max} = 1000$ and, on a 6Mb virtual machine on the University of Queensland IBM3083, was restricted to $N_{max} = 600$. The bulk of this storage was occupied by the integer index-array that recorded the segments that needed the "analytic patch" correction during the velocity calculation (see section 4.4).

Each evolutionary history is presented as a sequence of snapshots of the bounding contours with nondimensional times, τ, increasing down the page. We regard the simulations as quantitatively accurate for times $\tau \leq \tau_{max}$ where, for most cases, τ_{max} is the final time reached by the computation. (The final frame of case 1 (figure 7.10) is an exception.) The contours have been reconstructed from the node sets by joining consecutive nodes by straight line segments. Although parabolic segments have been used in the calculations, the straight segments give a better idea of the segment size and contour resolution obtained.

As well as the pictorial histories, other information presented includes :
(i) length of contour, giving a measure of the interfacial area of the two-dimensional layer and hence mixing. We calculate

$$p_j = \frac{\text{length of contour } C_j}{\#\text{cores in computational domain}.\lambda_1} = \frac{\text{length of contour } C_j}{\lambda_{comp}} \qquad (7.11a)$$

In flows containing a very fast, diffusion-limited reaction (e.g., Breidenthal 1981), the rate of product formation is proportional to the growth rate of the interfacial area. Before the mixing transition, the reaction is restricted to a very thin interface between the two free streams as shown in the laser-induced-fluorescence (LIF) pictures of Koochesfahani & Dimotakis (1986) (reproduced here in figures 7.12a and 7.21c).

(ii) maximum height of contours

$$Y_j = \max |y_j(x)| \quad . \qquad (7.11b)$$

This is an easily obtainable (for CD at least) measure of the layer thickness.

(iii) mean velocity profile

$$\langle u_x \rangle(y) = \frac{1}{\lambda_{comp}} \int_0^{\lambda comp} u_x(x,y)\, dx \quad . \qquad (7.11c)$$

The profile has been evaluated by calculating the average x-velocity $\langle u_x \rangle$ (averaged over 30 x-positions) at N y-positions across the layer.

(iv) vorticity thickness, as a measure of layer thickness

$$\delta_\omega = \frac{\Delta U}{\omega_{max}} = \frac{\langle u_x \rangle_N - \langle u_x \rangle_1}{\langle u_x \rangle_{N/2+1} - \langle u_x \rangle_{N/2}} \quad , \qquad (7.11d)$$

This definition assumes that $\partial U/\partial y|_{max}$ occurs at the midpoint of the layer. Unfortunately this measure was very sensitive to the form of the velocity profile $\langle u_x \rangle$, especially near $y = 0$.

(v) momentum thickness

$$\theta = \int_{-\infty}^{\infty} \left[\frac{1}{4} - \left\{ \frac{\langle u_x \rangle}{\Delta U} \right\}^2 \right] dy \quad . \qquad (7.11e)$$

Being an integral measure, θ was less sensitive to the pecularities of $\langle u_x \rangle$, and more suitable for comparison with experimental results. The numerical quadrature for θ was truncated after the N steps of the calculated velocity profile in *(iii)* above.

(vi) velocity fluctuation intensities

$$\frac{\langle u'_x{}^2 \rangle^{1/2}}{\Delta U} \quad , \quad \frac{\langle u'_y{}^2 \rangle^{1/2}}{\Delta U} \quad ,$$

$$\text{where } \langle u'_x{}^2 \rangle = \frac{1}{\lambda_{comp}} \int_0^{\lambda comp} (u_x - \langle u_x \rangle)^2 \, dx \quad , \qquad (7.11f)$$

$$\langle u'_y{}^2 \rangle = \frac{1}{\lambda_{comp}} \int_0^{\lambda comp} (u_y)^2 \, dx \quad , \qquad (7.11g)$$

and *(vii) Reynolds stresses*

$$\frac{\langle u'_x \, u'_y \rangle^{1/2}}{\Delta U} \quad ,$$

$$\langle u'_x \, u'_y \rangle = \frac{1}{\lambda_{comp}} \int_0^{\lambda comp} (u_x - \langle u_x \rangle) \, u_y \, dx \quad , \qquad (7.11h)$$

and *(viii) local vorticity thickness* of the braid connecting the spanwise vortices

$$\delta_2 = \left[\sum_{j=1}^{M} \omega_j \, (h_j - h_{j+1}) \right] / \omega_M \quad , \qquad (7.11i)$$

where $h_{M+1} = 0$ and h_j, $j = 1...M$ are measured "by hand" from enlarged plots of the solution contours.

7.4.1 Nonlinear Roll-up

We investigated the first stage of the nonlinear evolution by calculating the evolution of a layer disturbed by the fundamental eigenfunction only. Evolution of a uniform-vorticity (M = 1) layer is shown in figure 7.10 and a nonuniform-vorticity (M = 4) layer is shown in figure 7.11. These are cases 1 and 2 respectively in table 7.5. Two wavelengths of the fundamental are shown in each figure. For both, the layer thickness was set to $k\delta_\omega = 0.875$ and the initial perturbation amplitude was set to $\alpha_o/\lambda_1 = 0.05/\pi$. Although this is not the thickness of the uniform-vorticity layer corresponding to maximum initial growth rate, it does allow direct comparison of the effects of nonlinearities of the initial vorticity distribution.

The solutions for both cases have started to degrade by the final times shown in the figures,hence we have not included the final simulation times (reached before exceeding cpu limits). The degradation of this (32-bit precision) computation is in the form of contours crossing and displaying spurious features in the braid region. The reason for this problem is unknown but it did not occur for any of the computations performed with 64-bit arithmetic.

Both of the figures exhibit the same large-scale characteristics. Most of the vorticity has been concentrated into "perturbed-elliptical" vortex cores with only a small amount of circulation left in the braids that spiral around the cores. For the M = 4 case, the fluid in the braids is predominantly the low vorticity fluid. For later times, we expect that the cores will continue to rotate and deform periodically and that the braid wrapped around the cores will be stretched (in-plane) into a tightening spiral.

In figure 7.12, we compare the M = 4, τ = 5.284 vorticity contours and the LIF "picture" taken by Koochesfahani & Dimotakis (1986) of a mixing layer at Re_δ = 1750 (before the mixing transition). The similarity between the two is remarkable. The digital laser-induced-fluorescence (LIF) picture has been produced by concatenating a sequence of scans of the light intensity across the thickness of the layer as the structure was convected past the sensor. A false colour image (reproduced here in black & white) was then formed using digital techniques. In this sense it is not an instantaneous picture of the vortical structure. Also, (i) the flow visualization techniques rely on a passive marker to indirectly tag the vorticity field and (ii) the experimental mixing layer possesses an asymmetry which is noticeable in figure 7.12a. Despite these points, there is a close similarity in features of the CD solution, the LIF picture and also the picture of the forced mixing layer taken by Roberts, Dimotakis & Roshko (1982).

It is interesting to note the migration of the vortical fluid in the braids over the adjacent vortex cores after the roll-up has occurred. In their moderate Re simulations, Corcos & Sherman (1984) observe a relaxation of the vorticity distribution after a "climax" state has been reached. This migration begins to occur at about τ = 5 with the braids taking a shape similar to those in *(i)* the LIF picture (figure 7.12a); *(ii)* the vortex sheet calculations of Krasny (1986, figure 13) and *(iii)* the initial stages of the vortex splitting process observed by Freymuth, Bank & Palmer (1984) for the accelerating flow behind an inclined aerofoil. The spiralling of the braids around the vortex cores entangles irrotational fluid from the free streams in a process that we interpret as entrainment. For a viscous fluid, the vorticity from the spiral arms would diffuse into the irrotational fluid, thus completing the mixing process to the finest-scales of motion.

We also characterize the gross layer evolution by the growth of the interfacial area (contour length) and the growth

of the maximum height reached by the contours (Y_j). These parameters are displayed in figures 7.13 and 7.14 for the M = 1 and M = 4 profiles respectively. The interfacial area, as measured by the contour lengths, is shown in figures 7.13a and 7.14a for the M = 1 and M = 4 cases respectively. Initially there is little growth in the contour length as the vorticity is concentrated into the vortex cores but, as soon as the braids are formed and begin to wrap around the cores, there is a rapid increase in the contour length. The growth rate then approaches a roughly constant value, apparently due to the in-plane stretching of the spiral filaments around the vortex cores. These trends are similar to those observed in the numerical simulations of Pozrikidis & Higdon (1985) and the water tunnel experiments of Breidenthal (1981) although the latter experiments included a mixing enhancement due to three-dimensional motions.

The plots of Y_j versus time indicate that the layer thickness reaches approximately 40%-60% of the (maximum) wavelength λ_1. This is consistent with the results of Pozrikidis & Higdon (1985). These plots (especially 7.14b) also exhibit the low frequency fluctuations in thickness due to the "nutation" of the nearly elliptic vortex cores. This effect was first identified (and the term coined) by Zabusky & Deem (1971) in a CIC simulation of a periodic vortex street. In figure 7.15a we show the variation of momentum thickness with time for the M = 4 simulation. It shows essentially the same features as the Y_j plots with an initial growth during roll-up and oscillations at later times due to the core nutation.

The variation in vorticity thickness, δ_2, of the M = 4 braid midway between the cores is plotted on a logarithmic axis in figure 7.15b. The measured thicknesses are denoted by circles while the broken line indicates the expected asymptotic variation of δ_2 for a model point-vortex array with vortices of strength Γ_1 and spacing λ_1. Once the vorticity layer has collapsed into compact cores (say by τ = 3.040 in figure 7.11) the slope of the δ_2 curve approaches that of the

model (i.e., $d/d\tau[\ln(\delta_2/\lambda_1)] = -\pi/2$). The plot has been truncated at $\tau = 4.053$ owing to the difficulty in accurately measuring the braid thickness beyond this time.

The mean velocity profile for three times during the M = 4 simulation are shown in figure 7.16. For all times shown, the velocity field has maintained similarity with the initial profile. This agrees with the experimental measurements by Winant & Browand (1974) in the nonturbulent region of the mixing layer (reproduced in figure 7.16d). Note that the asymmetry of the experimental measurements is not present in the temporal shear layer simulation here.

In figure 7.17, we compare the velocity fluctuation intensities with the experimental measurements of Ho & Huang (1982) for the forced mixing layer. We have reproduced their figure for the mode I mixing layer which is forced at a frequency near the most unstable frequency resulting in the roll-up of the layer and the temporary suppression of the subharmonic interactions. At x = 11.5cm there is a well defined depression of the x-velocity (longitudinal) fluctuation intensity near the axis of the layer due to the close alignment of the row of vortices. These features compare qualitatively with those for the $\tau = 4.053$ and $\tau = 5.066$ plots of u_x' for the CD simulation. For $x \geq 19.1$cm in the experimental measurements, the comparison is no longer valid as the subharmonic perturbations have grown and merging events have occurred.

7.4.2 Primary Mode Plus First Subharmonic

We now consider simulations of the two-dimensional layer in which the initial disturbance is a linear combination of the fundamental eigenfunction and its first subharmonic. For merging of the primary vortices to occur, both the fundamental plus its subharmonic need to be present. Ho & Huang (1982) have shown that, if the layer is forced by just the fundamental eigenfunction, the subharmonic is suppressed and

merging delayed. Previously Riley & Metcalfe (1980) showed that, if just the subharmonic is present, then the layer will roll-up on a larger wavelength without the merging process. Although the fundamental and subharmonic eigenfunctions may be combined with any relative phase and amplitude, we will investigate only the cases of equal amplitude $\alpha_o/\lambda_1 = 0.05/\pi$ and phase shifts of $\phi = 0$, $\pi/4$ and $\pi/2$. We expect this selection to be representative of the full range of parameters but note that these amplitudes allow the initial domination of the evolution by the fundamental eigenfunction.

First we consider the evolution of the M = 4 nonuniform-vorticity layer with an initial perturbation defined by

$$\underline{\eta}(x) = \underline{h}/2 + 0.05\ \text{Real}[\underline{f}_1\ e^{2ix} + \underline{f}_2\ e^{i\phi x}\ e^{ix}] \quad , \qquad (7.12)$$

with $\phi = 0$. This combination of eigenfunctions leads to a pairing interaction in which two vortex cores (with initial spacing, λ_1) coalesce into a single structure. In figure 7.18, only one wavelength of the computational domain ($\lambda_{comp} = 2\lambda_1$) is shown. At $\tau = 0$ the vorticity distribution has been disturbed to produce two slight accumulations (fundamental) whose centroids have been offset from the x-axis (subharmonic).

The early stage of the nonlinear roll-up is a similar process to that shown for the fundamental alone. However, the growth of the subharmonic has become prominent by $\tau = 2.533$ with the vortex cores approaching each other and beginning to rotate about each other. By $\tau = 4.559$, the vortex cores have coalesced into a single, elongated structure connected to the rest of the array (not shown) by an extremely thin braid. This braid is so fine that we expect its global dynamical effect to be negligible thus justifying the use of a form of contour surgery (Dritschel 1986a) to remove the braids for long-time simulations. Also evident in the final two frames is the initial stage of ejection of vortex arms typical of the coalescence of two equal and otherwise isolated vortices (see

chapter 10; Christiansen & Zabusky 1973; Zabusky, Hughes & Roberts 1979).

Figure 7.19 shows close-ups of sections of the bounding contours at four times during the evolution. The degradation of the contour smoothness is evident as τ increases but, simultaneously, the detail of the vorticity distribution has increased markedly. These fine-scale features are most obvious at $\tau = 5.066$ where the vortex filaments in some places are of the order of the plotting-pen thickness. Although the tracking of these vortex filaments is one of the computational disadvantages of the CD method, the resolution obtained in figures 7.18 and 7.19 could not be obtained with the inherently grainy vortex-element methods.

The sensitivity of the layer evolution to M is tested by performing essentially the same simulation with M = 8 (case 4, table 7.5) shown in figure 7.20. The initial thickness of the layer is slightly different as the maximum growth rate for M = 8 occurs for $k\delta_\omega = 0.857$ according to the linear theory (section 7.2). With the extra contours to be tracked, we could not compute the evolution to the same stage as for the M = 4 case but, up to the time $\tau = 3.799$, the main features of the evolution are very similar. To emphasise this point we directly compare corresponding M = 4 and M = 8 frames at $\tau = 3.546$ in figure 7.21. In the region between the two approaching (M = 8) vortex cores, there are 16 contours plotted in a section of the braid having the width of the plotting pen. Overall, the dynamics are therefore fairly insensitive to the initial vorticity profile. The braid between the pairing structures (i.e. at x = 0) is slightly thicker than for the M = 4 case but, otherwise, the intensification of vorticity gradients is essentially the same. Overlaying the figures 7.21a and 7.21b shows that the difference in the position of the outer contour is only approximately 1% of λ_{comp} ($\approx$2% of λ_1).

The vortex histories produced here are very similar to those generated in other numerical simulations and observed in

experiments. Figure 7.22 shows (a) the τ = 5.066 frame from our M = 4 inviscid simulation, (b) the τ = 3.0 frame from the Re_δ = O(100) simulation by Corcos & Sherman (1984) and (c) the LIF image of vortex coalescence in a plane mixing layer taken by Koochesfahani & Dimotakis (1986). The remarkably similar large-scale features in all three pictures provides supporting evidence for the hypothesis that the large-scale vortex dynamics are only weakly dependent on Re (Zabusky & Deem 1971). This point is echoed by Davis & Moore (1985) who showed that changing the Re_δ for their simulations from 1.4×10^4 to 35 only "smudged" the individual vortex regions without greatly affecting the global dynamics.

By the final times reached, there seems to be less entanglement (entrainment) of irrotational fluid into the vortex structure than for the simulations of the layer with the fundamental eigenfunction (f_1) only. This appears to be consistent with the measurements of Hernan & Jimenez (1982) which showed that the entrainment occurred mainly between pairing events. An explanation for this may be that the entrainment process is relatively slow and that, as noted by Acton (1976), the pairing (and coalescence) process is very rapid, once started.

The growth of the interfacial area for the M = 4 layer, as measured by the contour length, is shown in figure 7.23a. The curves are very similar in form to the corresponding curves in figure 7.14a (fundamental only) except for the earlier starting time for rapid growth. (This is due to the larger initial amplitude for the fundamental eigenfunction in this pairing case.) Even in the presence of the pairing interaction, the growth of the contour length appears to be determined by the roll-up of the spiral filaments about the vortex cores.

The layer thickness, as measured by Y_j is plotted for the M = 4 layer (case 3) in figure 7.23b. The growth is initially similar to that of the fundamental only (case 2), but at later times, the growth is continued in a roughly linear manner

until the thickness is about 70% of the longest allowable wavelength (the computational domain, λ_{comp}). At this point we expect the thickness to begin oscillating as the vortex structure nutates in a similar manner to that in case 2. These features are more clearly evident on the plot of momentum thickness versus time, τ, in figure 7.24a where the reduction in thickness is evident at $\tau \approx 5.5$. The growth rates shown here do not compare well with the experimental measurements of Winant & Browand (1974) for the unforced mixing layer. They show an initial growth that varies roughly as the square root of down-stream distance (equivalent to τ here) and an approximately linear growth after that. Unlike the measurements of the single vortex history here, the experimental measurement of layer thickness is derived from an ensemble average taken over a large number of structures with a statistical distribution of characteristic size and spatial scatter (Roshko 1976, 1980).

Four representative plots of the mean velocity profile during the pairing event are shown in figure 7.25. There is a strong qualitative similarity in the features of these profiles and those of the measurements made by Ho & Huang (1982) for the "mode II" mixing layer which is forced at the first subharmonic of the most amplified frequency. Their data is reproduced in figure 7.25e. Note the difference in the measured profile relative to the hyperbolic-tangent velocity profile for the CD calculations at time $\tau = 4.053$ the vortex centroids approach a maximum displacement from the axis of the layer. This variation is also evident in the experimental measurements at a streamwise position $x = 14.0$ where the mixing layer vortices for both the CD simulation and the experimental measurements are in a roughly similar configuration.

The calculated Reynolds stresses across the thickness of the layer (see figure 7.27) vary during the merging process in a manner similar to the experimental measurements of Oster & Wygnanski (1982) and the computational measurements of Aref & Siggia (1980) and Riley & Metcalfe (1980). The change in sign

of the stresses has been discussed in Ho & Huerre (1984) in terms of the orientation of the merging structure and the associated (induced) velocity field. The stresses are positive and increasing for τ = 2.026, 3.04 while the velocity fluctuations are approaching a maximum but become negative for $\tau \geq 5$ when the merged structure passes through a "climax" state and the velocity fluctuations begin to relax. In the nomenclature of Riley & Metcalfe (1980) this relaxation produces a counter-gradient momentum flux and an associated decrease in the layer momentum thickness (figure 7.24a).

Figure 7.24b shows the value of δ_2 measured at a point on the braid midway between the coalescing structures. Superimposed on the late time section of the curve is a straight (broken) line indicating the asymptotic variation of δ_2 according to the point-vortex model (equations 6.5 and 6.8). The strength and spacing of the model array is $2\Gamma_1$ and $2\lambda_1$ respectively, thus giving a slope $d/d\tau[\ln(\delta_2/\lambda_1)] = -\pi/4$. Note that δ_2, here, decreases at a higher rate in $2.0 < \tau < 3.0$ due to the stronger strain induced by the rolled-up Γ_1 vortices with an initial spacing λ_1. Beyond τ = 4.559, the braid thickness was difficult to measure because the contour description had degraded. When magnified to a scale large enough for thickness measurement, the contours exhibited oscillations with amplitude of order(braid thickness) on a wavelength of order(node spacing). The section of braid between the two approaching vortices is subject to a higher strain and consequently is much thinner than the braid between adjacent vortex pairs (see e.g., figure 7.20).

We now investigate the effects of changing the relative phase, ϕ, between the fundamental and first subharmonic eigenfunction. For small amplitude disturbances, the effects have been discussed in section 7.2 but for the nonlinear evolution the effects are dramatic.

Setting $\phi = \pi/2$ gives the tearing mode in which the vorticity distribution now consists of a large and a small

vorticity concentration with centroids still on the x-axis. Figure 7.28 (case 5, table 7.5) shows the evolution of the layer initially with this distribution. The vorticity from the braid region is now unequally shared in the early stages of roll-up resulting in two vortex cores withsignificantly different strengths (circulations). The process is similar to the "shredding interaction" described by Patnaik, Sherman & Corcos (1976). The larger vortex has $1.2\Gamma_1$ while the smaller core has $0.8\Gamma_1$ where Γ_1 is the nominal circulation of a primary vortex. See figure 7.31 for the variation of vortex core strengths with time. By the final time shown in figure 7.28, the processes of roll-up combined with tearing appear to be complete and the vortical fluid accumulated by the larger core in thick filaments (near the core) are beginning to migrate away and over the top of the smaller vortex core.

The inviscid tearing simulation has different long time behaviour to the moderate Re simulations of Riley & Metcalfe (1980). Although their simulation at $t = 24$ has a very similar vorticity distribution to the CD solutions at $\tau = 4.433$ (as shown in figure 7.27) they indicate that the fluid from smaller vortex will be completely redistributed into the larger cores. However our inviscid simulations suggest that the smaller core is now stable to the tearing instability (Moore & Saffman 1975). As well as looking similar to the simulation containing the fundamental only, the other characteristics of layer evolution are similar. The growth of layer thickness as measured by the maximum contour height Y_j (figure 7.30b) and momentum thickness (figure 7.31a) and the growth of contour length p_j (figure 7.28a) all closely resemble the corresponding plots for the single mode calculation in section 7.4.1.

For any relative phase $0 < \phi \leq \pi/2$, the disturbance may be decomposed into a pairing component and a tearing component. Pairing is the stronger of these two effects (Acton 1976; Riley & Metcalfe 1980; Corcos & Sherman 1984) and so when there is a random combination, we expect the pairing process to occur most frequently as observed by Hernan &

Jimenez (1982). In figure 7.32 we show the evolution of a layer with $\phi = \pi/4$ and $\alpha_o/\lambda_1 = 0.05/\pi$ (case 6, table 7.5). Initially tearing produces two unequal vortex cores which at later times approach each other and coalesce into a single structure in much the same way as the pure pairing case (case 3, figure 7.18). In figure 7.33, we show two examples of the vector velocity field for this combined tearing/pairing case. At $\tau = 3.040$, centres are evident near the vortex centroids and the stagnation points near the braids have become obvious.

7.4.3 Primary Mode Plus Second Subharmonic

The next level of complexity in the interaction of subharmonics is the three-vortex event. Examples of three vortex cores coalescing into a single structure may be found in the experimental observations by Winant & Browand (1974) and Hernan & Jimenez (1982) for the unforced mixing layer and by Ho & Huang (1982) for a forced layer. Numerical simulations by Aref & Siggia (1980) also show multiple vortex events.

In particular, we will consider the evolution of the two-dimensional shear layer with an initial condition

$$\underline{\eta}(x) = \underline{h}/2 + 0.033 \text{ Real}[\underline{f}_1^{(4)} e^{3ix} + \underline{f}_3^{(4)} e^{ix}] , \quad (7.13)$$

The computational domain now contains three wavelengths of the fundamental eigenfunction. Figure 7.34 shows the layer evolution (case 7, table 7.5) up until a time of $\tau = 5.224$. Initially the layer rolls into characteristic cores and, as the subharmonic grows, the two outer cores begin to rotate about and approach the central core. By the final times shown, the vortex cores have merged into a single elongated structure which contains much fine-scale detail, especially in the regions where the braids interact with vortex cores. Inset in the last frame is a section of a photograph taken by Winant & Browand (1974). This photograph shows a three-vortex

structure which is very similar to to that produced in our numerical simulation.

Figure 7.35a is a close-up of one of the outer vortex cores at τ = 5.224. The braids have become extremely thin in places but have still maintained their coherence. There are, however, places where the contour smoothness has degraded substantially. The complexity of the vorticity distribution is illustrated in figure 7.35b which is a vorticity profile along the section through the three vortex cores. The regions indicated by a "*" in the close-up of the structure contain irrotational fluid that has been entangled in the vortical fluid of the braids. This is another example of the entrainment mechanism mentioned in section 7.4.1. Four close-ups of the contour evolution are contained in figure 7.36. As τ increases the contour description degrades more quickly than for case 3 (figure 7.19). Both of these of these computations used node-parameter set 2 but the three-vortex event evolves on a smaller spatial scale. This indicates that, for optimum performance of the CD algorithm, the node parameters need to be tuned to the scales of motions that are expected to evolve.

Figure 7.37a shows the growth of the interfacial area with time. The plots here are almost identical with those from the two-vortex pairing up until τ = 4.0 with rapid growth commencing as soon as the braids were formed. Beyond this time, the growth rate for the three-vortex case (here) is slightly less than that for the two-vortex pairing simulation. The growth of the layer thickness is again shown by both the maximum contour height, Y_j, and the momentum thickness, θ, in figures 7.37b and 7.38 respectively. As would be expected from inspection of vorticity distribution in figure 7.34, the evolution is still in the rapid growth region before the structure reaches its climax. (The axis joining the vortex centroids is not yet aligned with the cross-stream direction.)

7.4.4 *Primary Mode Plus First and Third Subharmonics*

In an attempt to study the first and second amalgamation events using the CD technique, we performed two simulations with an initial perturbation

$$\underline{\eta}(x) = \underline{h}/2 + 0.02\ \text{Real}[\underline{f}_1^{(4)}\ e^{4ix} + \underline{f}_2^{(4)}\ e^{i\phi/2}\ e^{2ix} + \underline{f}_4^{(4)}\ e^{ix}] \quad , \tag{7.14}$$

The computational domain now contains four wavelengths of the fundamental eigenfunction and the initial amplitude $\alpha_o/\lambda_1 = 0.04/\pi$ is 80% of the initial amplitude for case 3 (table 7.5).

Figure 7.39 shows the evolution of the vortex layer for $\phi = 0$ (case 8). There is the characteristic roll-up of the vortex cores followed by the first pairing event which produces two structures very similar to those produced in figure 7.17 (case 3). At time $\tau = 5.066$ the evolution of the structure is not quite as advanced as that in case 3 because the initial disturbance amplitude used here is slightly smaller. The computation was terminated at $\tau = 5.066$ owing to limitations on the available computing resources. Although the effect of $\underline{f}_3$ is beginning to grow by the final time frame, we estimate that the second amalgamation event would not be finished before $\tau \approx 15$ and that the outcome would be similar to the mode IV forced mixing layer of Ho & Huang (1982).

In figure 7.40 we show the early evolution of the layer with $\phi = \pi/2$. This perturbation produces a tearing effect and different sized primary vortex cores labelled (1)-(4) at $\tau = 3.040$. Although the simulation has been terminated at this point we guess that the first concentration event will involve the pairing and coalescence of cores (2) and (3). This may be followed by a coalescence of this larger structure with vortex core (4). Examples of such a two stage coalescence have been observed in the Karman vortex street experiments of Matsui & Okude (1982) and the forced mixing

layer experiments of Ho & Huang (1982). A multi-stage concentration as proposed would lead to the scattering of the vortex cores about the x-axis (and a corresponding growth in layer thickness) in a manner similar to that observed in the numerical CIC simualtions of Aref & Siggia (1980).

7.5 Summary

Using a piecewise-constant vorticity distribution we have been able to qualitatively reproduce, at Re = ∞, some of the interesting features of both forced and unforced mixing layers that have been observed in experiments and previous numerical simulations. In the simulations here the layer vorticity, when initially disturbed by a low amplitude perturbation, is redistributed into compact, nearly-axisymmetric vortex cores. Although the layer evolution appears to be insensitive to the initial vorticity profile, it is extremely sensitive to the composition of the applied disturbance. The combination of the fundamental eigenfunction with its first subharmonic may lead to either the pairing of adjacent vortex cores or the roll-up of the layer into vortex cores of different strengths for the values of $\phi = 0$ and $\pi/2$ respectively. Intermediate values of ϕ will most likely result in the pairing of adjacent vortices of varying strengths. Similarly, disturbing the layer with a combination of the fundamental eigenfunction and its second subharmonic results in the layer roll-up and subsequent interaction of sets of three vortices.

Table 7.1 : Some numerical simulations of two-dimensional mixing/shear layers.

Author	Flow[1] Configuration	Simulation Technique	Re_δ	Comment
Acton 1976	T	point-vortex	∞	Roll-up and pairing
Amsden & Harlow 1964	T	FD, ψ-ω	$\sim$100	Roll-up only
Aref & Siggia 1980	T	CIC	∞	Roll-up, pairings, scattering
Ashurst 1977	S	vortex-blob	$\sim 3\times10^4$	Roll-up, pairings
Christiansen 1973	T	CIC	∞	Roll-up only
Davis & Moore 1985	S	FD, primitive var.	$\sim 10^4$	Roll-up, subharmonics
Inoue 1985	S	vortex blob	∞	
Moore & Saffman 1975	T	point-vortex	∞	Tearing interaction
Nakamura et al 1982	T	vortex-blob	$\sim 10^7$ [2]	Roll-up only
Patnaik et al 1976	T	FD, ψ-ω	$\sim$100	Roll-up, pairing/tearing
Pozrikidis & Higdon 1986	T	CD	∞	Roll-up only
Riley & Metcalfe 1980	T	pseudo-spectral	$\sim$500	Roll-up, pairing/tearing
Tokunaga & Yasui 1985	T	vortex blob	∞	Roll-up, pairing

Notes [1] S = spatially developing mixing layer, T = Temporally developing shear layer

[2] nominally infinite

Table 7.2a : Vorticity profile for the upper half (y > 0) of the M = 4 shear layer, $\lambda_{comp} = 2\pi$, $\delta_\omega/h_1 = 0.6$. Initial vorticity thickness as shown.

δ_ω	j	ω_j	h_j
0.875	1	-0.0498	1.458
	2	-0.117	0.875
	3	-0.158	0.510
	4	-0.182	0.236
0.4375	1	-0.0995	0.729
	2	-0.234	0.437
	3	-0.316	0.255
	4	-0.363	0.118
0.2917	1	-0.150	0.486
	2	-0.315	0.292
	3	-0.475	0.170
	4	-0.546	0.0786
0.2188	1	-0.199	0.365
	2	-0.486	0.219
	3	-0.633	0.128
	4	-0.728	0.0590

Table 7.2b : Vorticity profile for the upper half (y > 0) of the M = 8 shear layer, $\lambda_{comp} = 2\pi$, $\Gamma_{comp} = -1$, $\delta_\omega = 0.429$.

j	ω_j	h_j
1	- 0.0262	0.823
2	- 0.0605	0.7078
3	- 0.1063	0.6008
4	- 0.1631	0.5020
5	- 0.2199	0.4033
6	- 0.2755	0.3127
7	- 0.3360	0.2140
8	- 0.3706	0.1152

Table 7.3 : Complex amplitudes that define the sinusoidal perturbations shapes for the M = 4 shear layer.

j	α_j	
	$f_1^{(4)}$, $(k\delta_\omega = 0.875)$	$f_2^{(4)}$, $(k\delta_\omega = 0.438)$
1	-0.248 - i0.339	-0.194 - i0.652
2	-0.331 - i0.479	-0.211 - i0.772
3	-0.393 - i0.667	-0.206 - i0.883
4	-0.341 - i0.940	-0.137 - i0.991
j	$f_3^{(4)}$, $(k\delta_\omega = 0.292)$	$f_4^{(4)}$, $(k\delta_\omega = 0.219)$
1	-0.143 - i0.762	-0.113 - i0.826
2	-0.151 - i0.842	-0.115 - i0.897
3	-0.137 - i0.931	-0.106 - i0.955
4	-0.0843 - i0.997	-0.0585 - i0.998

Table 7.4 : Complex amplitudes that define the sinusoidal perturbations shapes for the upper half of the layer M = 8.

j	α_j	
	$f_1^{(8)}$, $(k\delta_\omega = 0.857)$	$f_2^{(8)}$, $(k\delta_\omega = 0.429)$
1	-0.220 - i0.315	-0.176 - i0.621
2	-0.248 - i0.355	-0.188 - i0.660
3	-0.276 - i0.397	-0.194 - i0.701
4	-0.306 - i0.448	-0.206 - i0.738
5	-0.339 - i0.511	-0.210 - i0.786
6	-0.370 - i0.595	-0.209 - i0.841
7	-0.386 - i0.735	-0.215 - i0.887
8	-0.329 - i0.994	-0.131 - i0.991

Table 7.5 : Summary of two-dimensional shear layer simulations ($\gamma = 0$). Lengths are in computational units with the wavelength of the computational domain $\lambda_{comp} = 2\pi$. Not all cpu times were available.

Case	δ_ω	$\frac{\lambda_{comp}}{\lambda_1}$	M	Perturbation	Comment
1	0.875	1.0	1	$0.05\ f_1^{(1)}$	roll-up of a uniform vorticity layer
2	0.875	1.0	4	$0.05\ f_1^{(4)}$	roll-up of a nonuniform vorticity layer
3	0.438	2.0	4	$0.05\ f_1^{(4)} + 0.05\ f_2^{(4)}$	roll-up followed by pairing
3a	0.438	2.0	4	as for 3	as for 3 but single precision computation
4	0.438	2.0	8	$0.05\ f_1^{(8)} + 0.05\ f_2^{(8)}$	roll-up followed by pairing
5	0.438	2.0	4	$0.05\ f_1^{(4)} + 0.05\ e^{i\pi/2}\ f_2^{(4)}$	roll-up plus tearing
6	0.438	2.0	4	$0.05\ f_1^{(4)} + 0.05\ e^{i\pi/4}\ f_2^{(4)}$	combined pairing / tearing
7	0.292	3.0	4	$0.033\ f_1^{(4)} + 0.033\ f_3^{(4)}$	three vortex coalescence
8	0.219	4.0	4	$0.02\ f_1^{(4)} + 0.02\ f_2^{(4)} + 0.02\ f_4^{(4)}$	roll-up followed by pairing then a second pairing
9	0.219	4.0	4	$0.02\ f_1^{(4)} + 0.02\ e^{i\pi/2}\ f_2^{(4)} + 0.02\ f_4^{(4)}$	roll-up with tearing followed by pairing

Table 7.5 continued : Summary of two-dimensional shear layer simulations.

Case	Code Version	Node Parameters	Precision (bits)	CPU time (seconds)	T_c	τ_{max}
1	C	1	32	-	39.48	4.559
2	C	1	32	-	39.48	5.826
3	C	2	64	12800	19.74	5.066
3a	B	3	32	-	19.74	4.559
4	C	2	64	13000	19.74	3.799
5	C	1	64	9430	19.74	4.433
6	C	2	64	10800	19.74	4.306
7	C	2	64	12500	13.16	5.224
8	C	2	64	9380	9.87	5.066
9	C	2	32	-	9.87	3.040

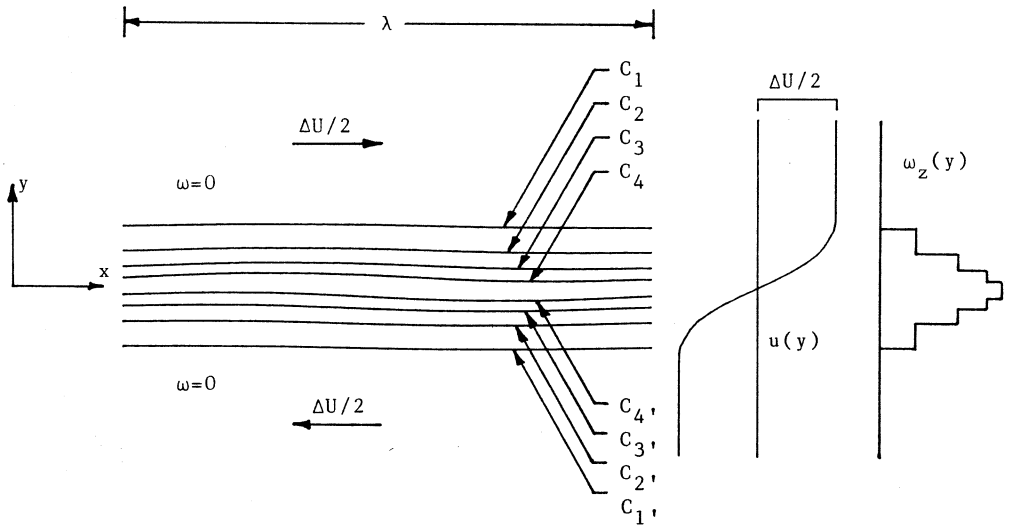

Figure 7.1 : A single wavelength of an x-periodic shear layer consisting of M = 4 uniform-vorticity regions. The bounding contours (primed subscripts indicate contours below the x-axis) are disturbed by a small amplitude perturbation. The associated mean x-velocity field, u(y) and vorticity cross-section are shown to the right.

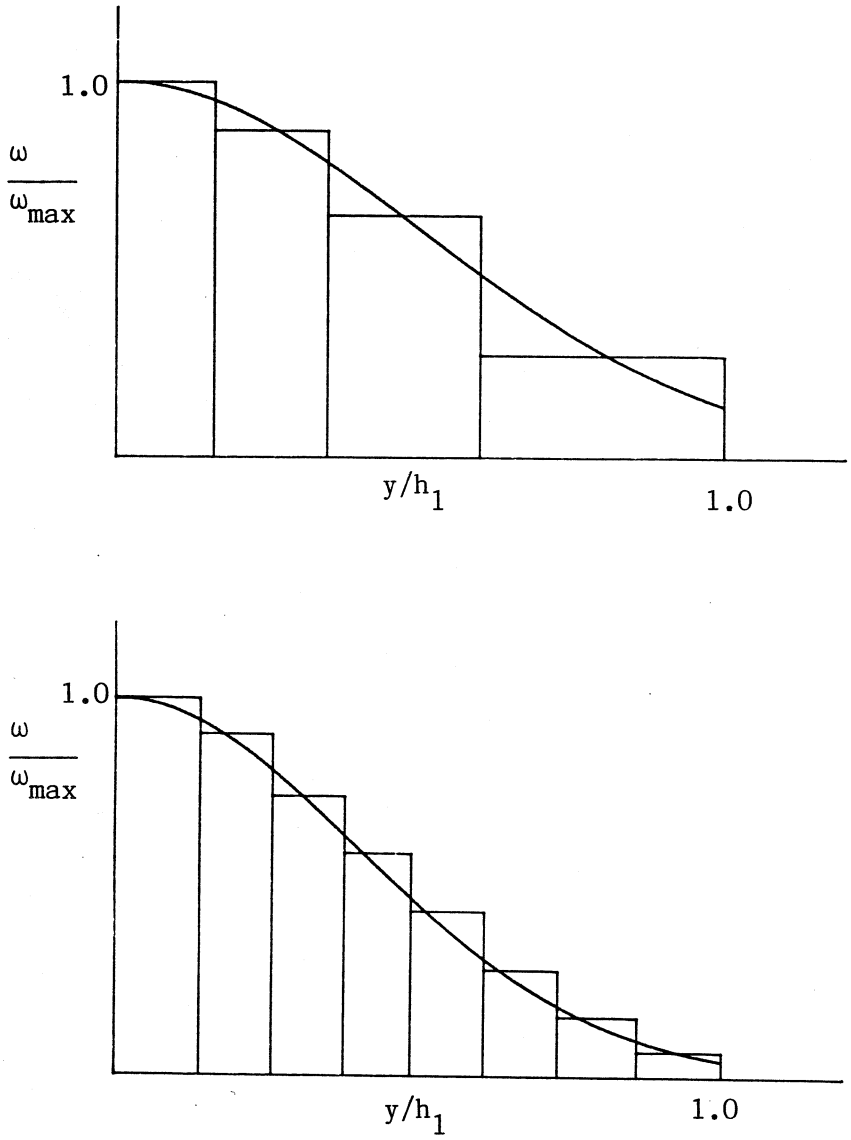

Figure 7.2 : Normalized vorticity distributions for (a) M = 4 and (b) M = 8 piecewise-constant vorticity profiles. The profiles are symmetric in y = 0. The solid curve approximates a Gaussian distribution as defined in equation (7.3).

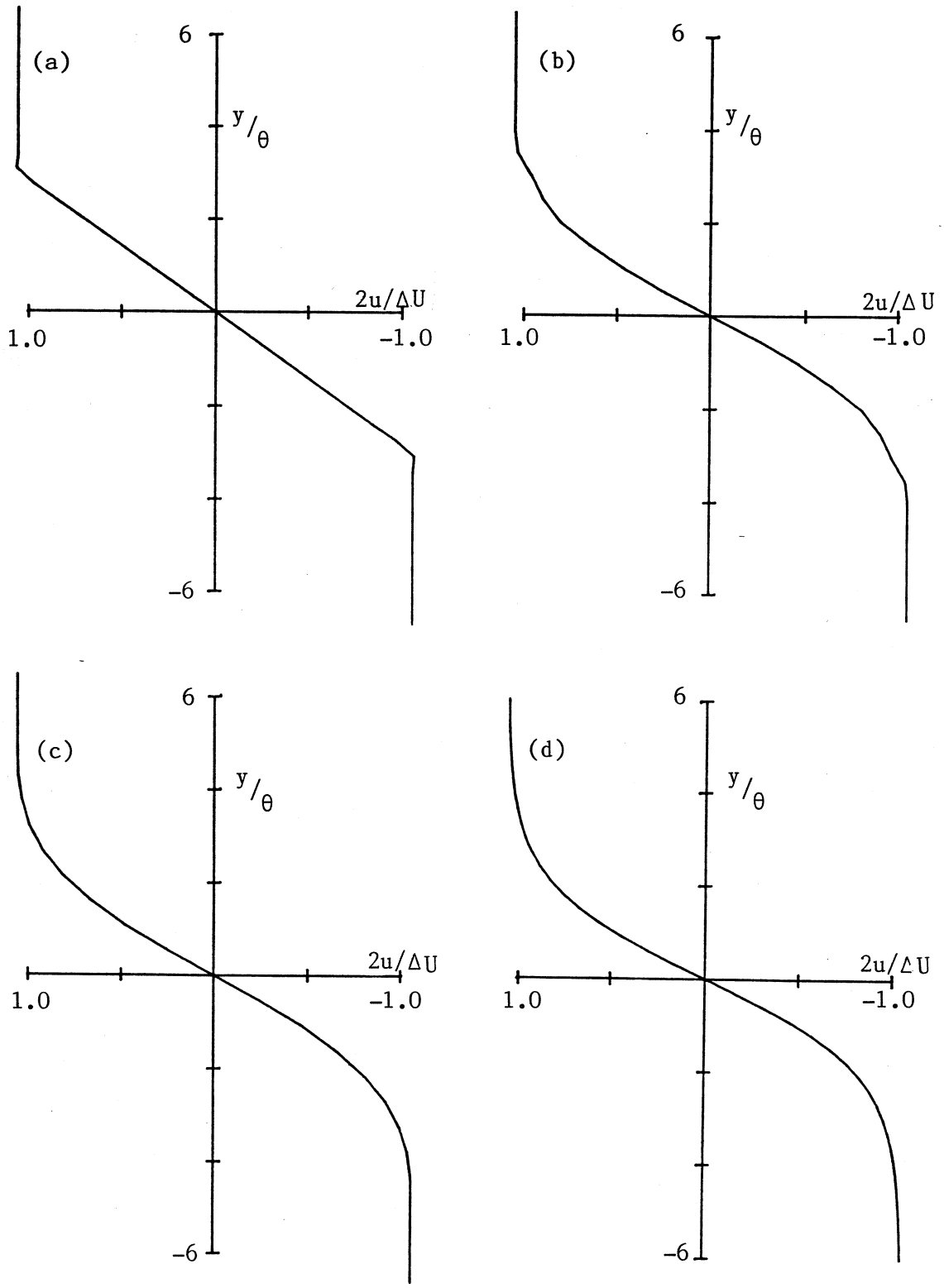

Figure 7.3 : Velocity profiles for the undisturbed shear layer.
(a) M = 1 linear-velocity variation
(b) M = 4 piecewise-linear velocity
(c) M = 8 piecewise-linear velocity
(d) hyperbolic-tangent velocity u = tanh(y)

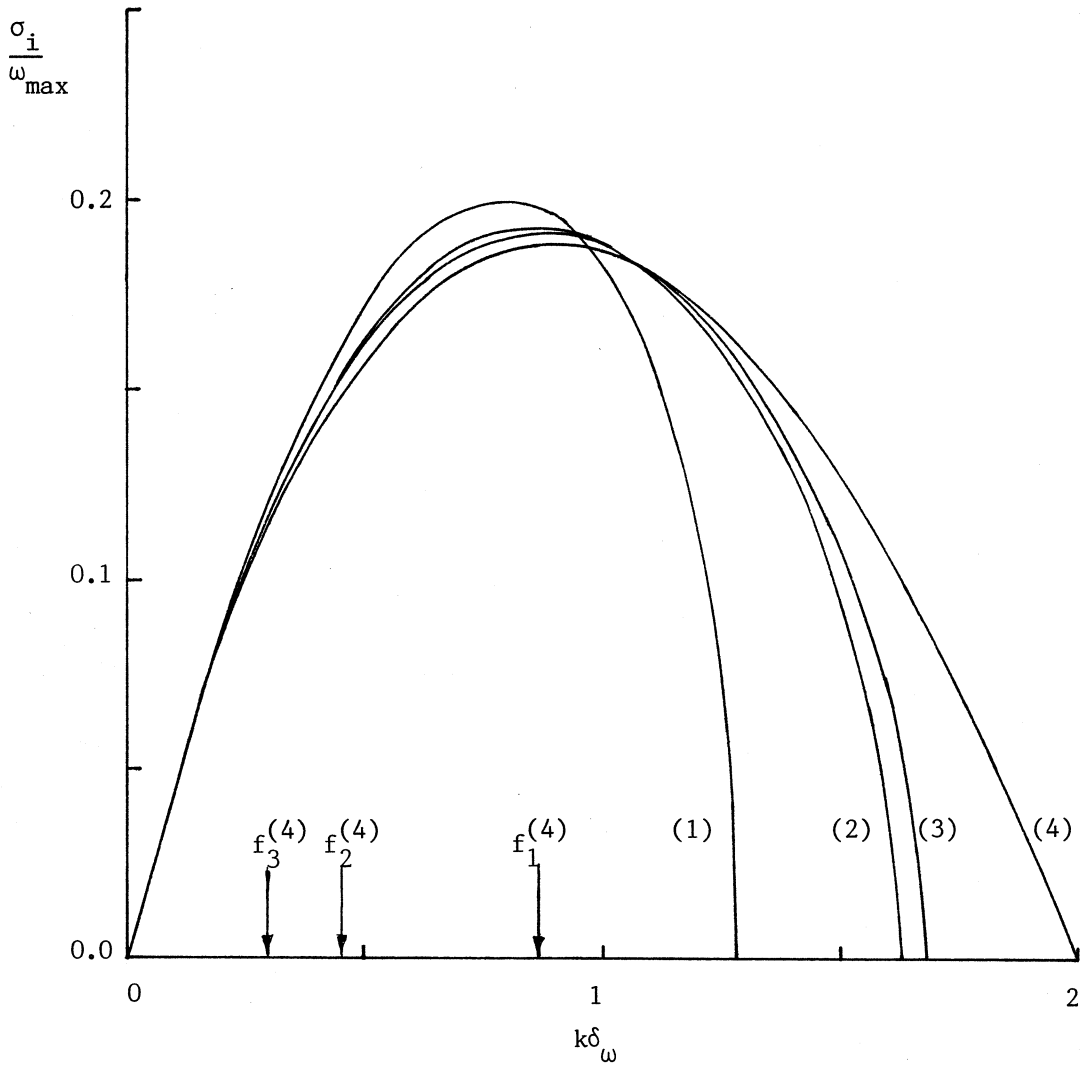

Figure 7.4 : Normalized growth rates for four vorticity distributions.

(1) single region, M = 1, of uniform vorticity

(2) M = 8 piecewise-constant vorticity profile as defined in table 7.3

(3) M = 4 piecewise-constant vorticity profile as defined in table 7.2

(4) the continuous vorticity profile (A5.11) corresponding to the hyperbolic-tangent velocity profile (Michalke, 1964)

The primary mode, first subharmonic, and second subharmonic for the M = 4 vorticity profile are labelled $f_1^{(4)}$ $f_2^{(4)}$ and $f_3^{(4)}$ respectively.

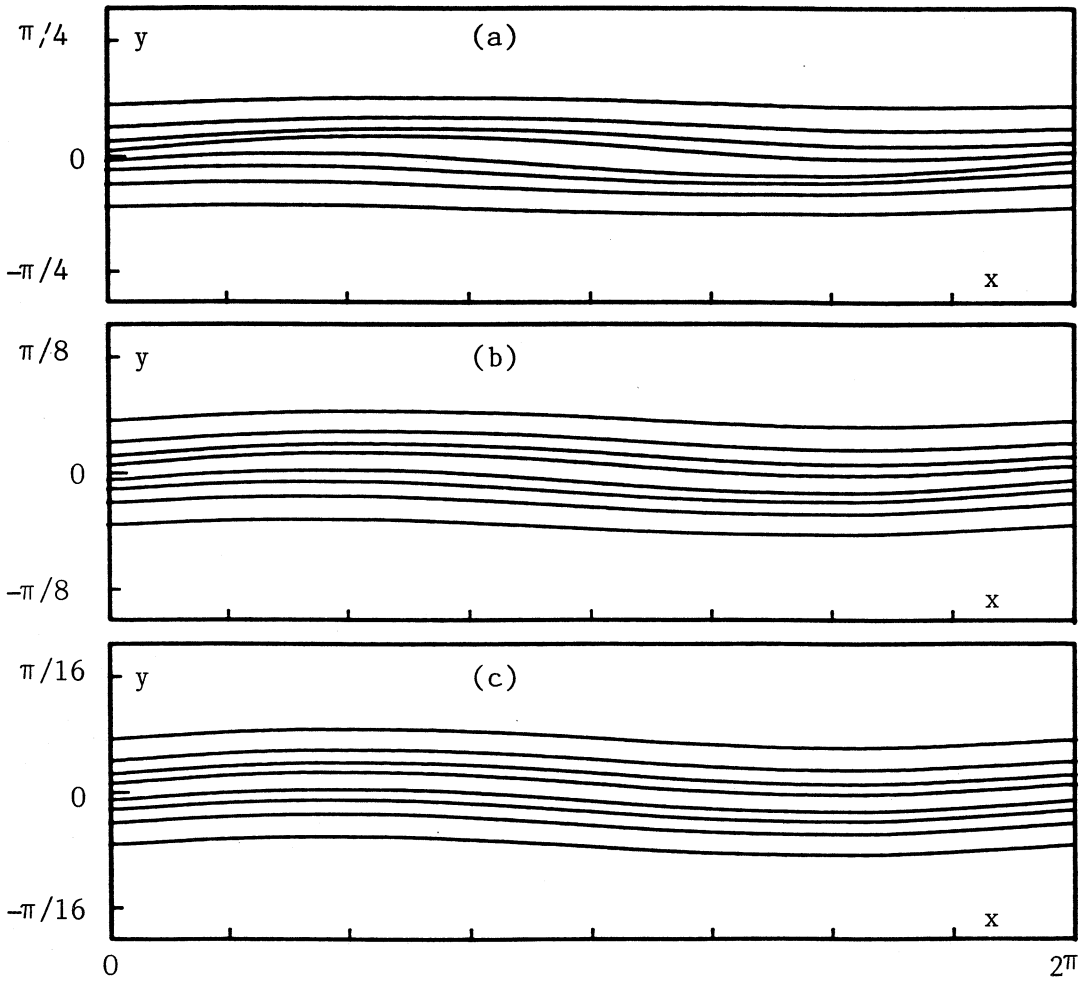

Figure 7.5 : Perturbation shapes for (a) fundamental mode $\underline{f}_1^{(4)}$, (b) first subharmonic $\underline{f}_2^{(4)}$ and (c) third subharmonic $\underline{f}_4^{(4)}$. Note that the y-scale has been expanded by factors of 2 and 4 in parts (b) and (c) respectively.

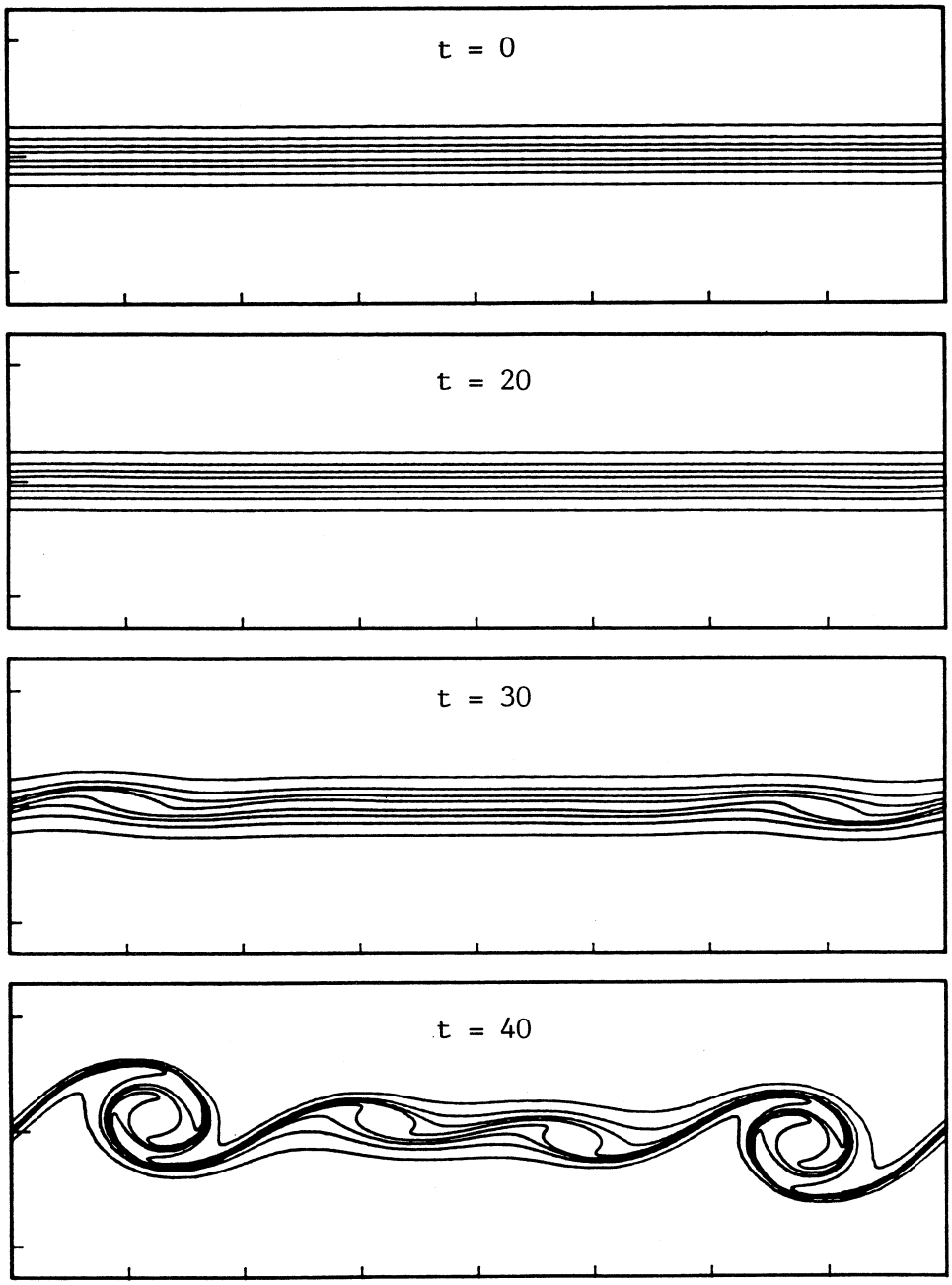

Figure 7.6 : Evolution of an initially undisturbed layer with thickness $\delta_\omega/\lambda_{comp} = 0.24/2\,\pi$. A 32-bit implementation of code-version B was used for the computation. Times t as shown.

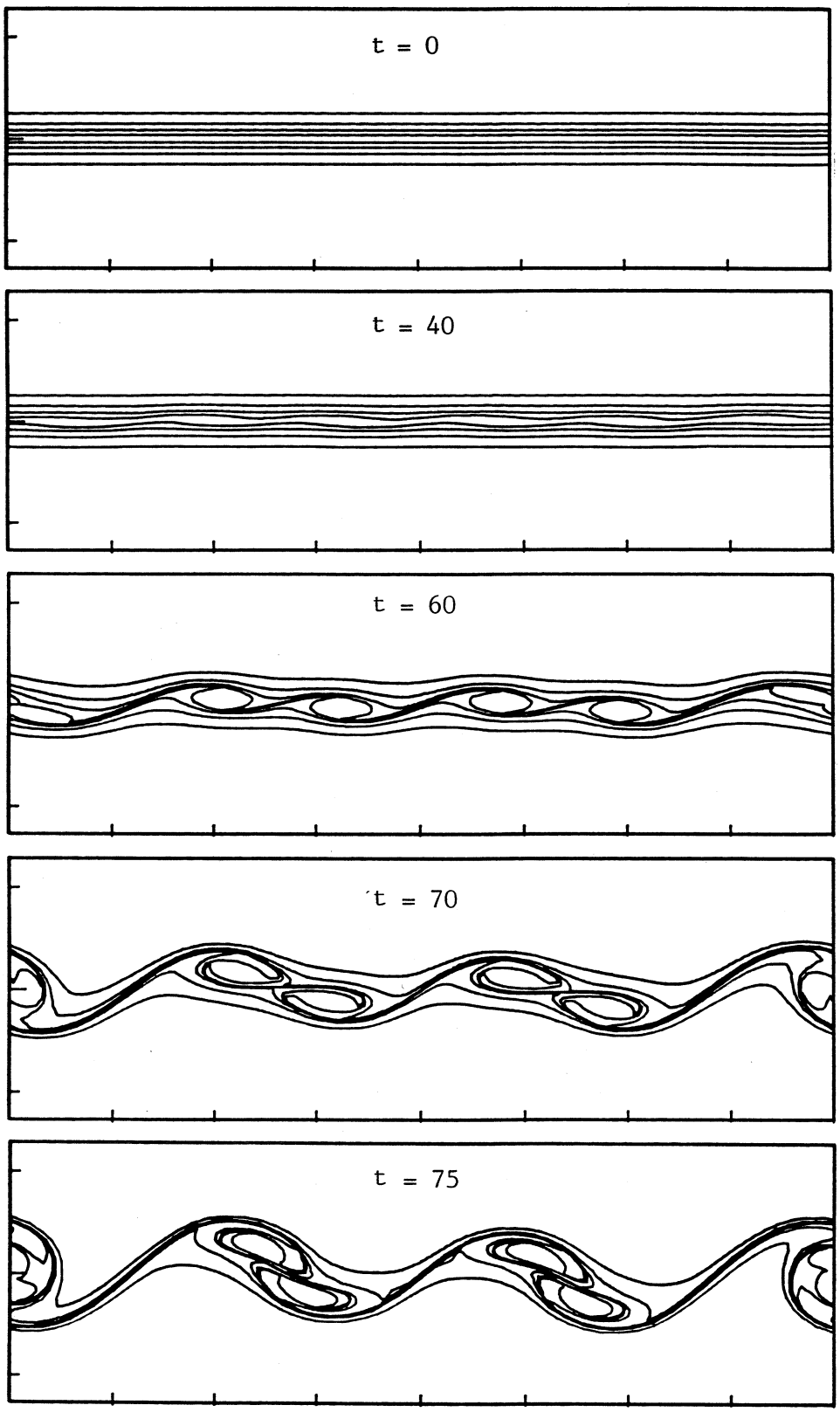

Figure 7.7 : Evolution of an initially undisturbed layer with $\delta_\omega/\lambda_{comp} = 0.24/2\pi$. A 32-bit precision implementation of code-version C was used for this calculation. Times t as shown.

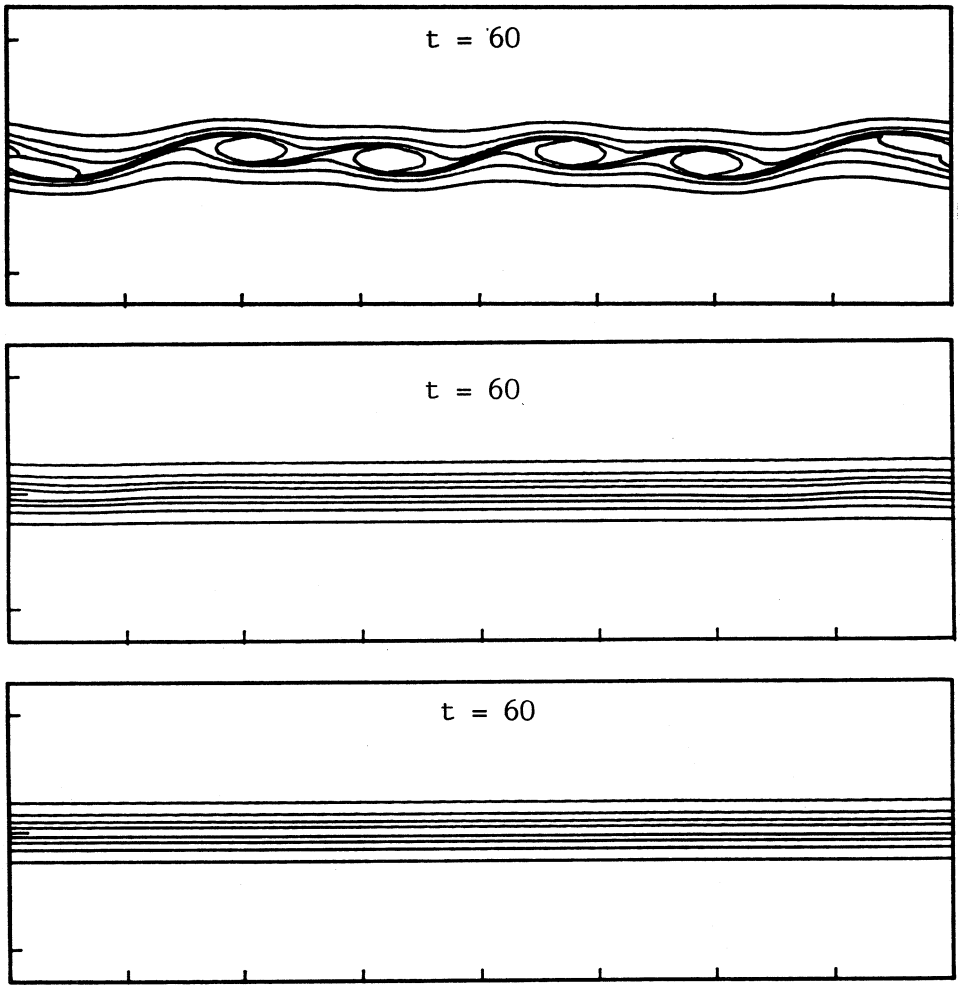

Figure 7.8 : State of the δ_ω = 0.24 layer at t = 60 for three separate computations.
(a) code-version C (table 4.1), 32- bit precision, numeric quadrature plus analytic patch. (figure 7.7)
(b) code-version D, 32-bit precision, numeric quadrature only.
(c) code-version C, 64-bit precision, numeric quadrature plus analytic patch.

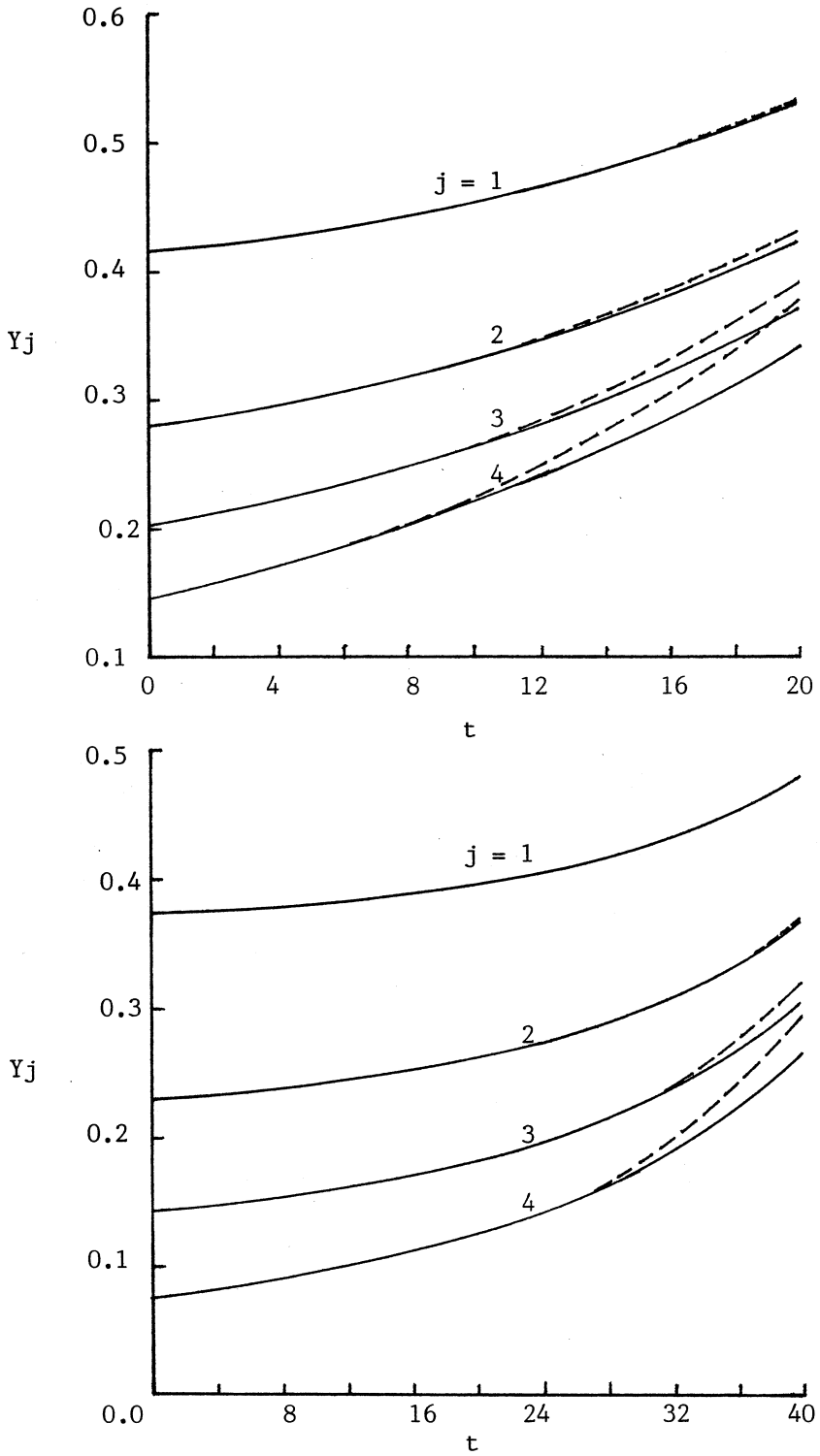

Figure 7.9 : Variation of maximum contour height for perturbation $\alpha_0 f_1^{(4)} + \alpha_0 f_2^{(4)}$ to the M =4 vorticity profile
(a) $\alpha_0/\lambda_1 = 0.05/\pi$,
(b) $\alpha_0/\lambda_1 = 0.01/\pi$.
Solid lines show the CD solution while dashed lines show the linear sloution. Times, t are in computational units with $\Gamma_{comp} = 1$, $\lambda_{comp} = 2\pi$.

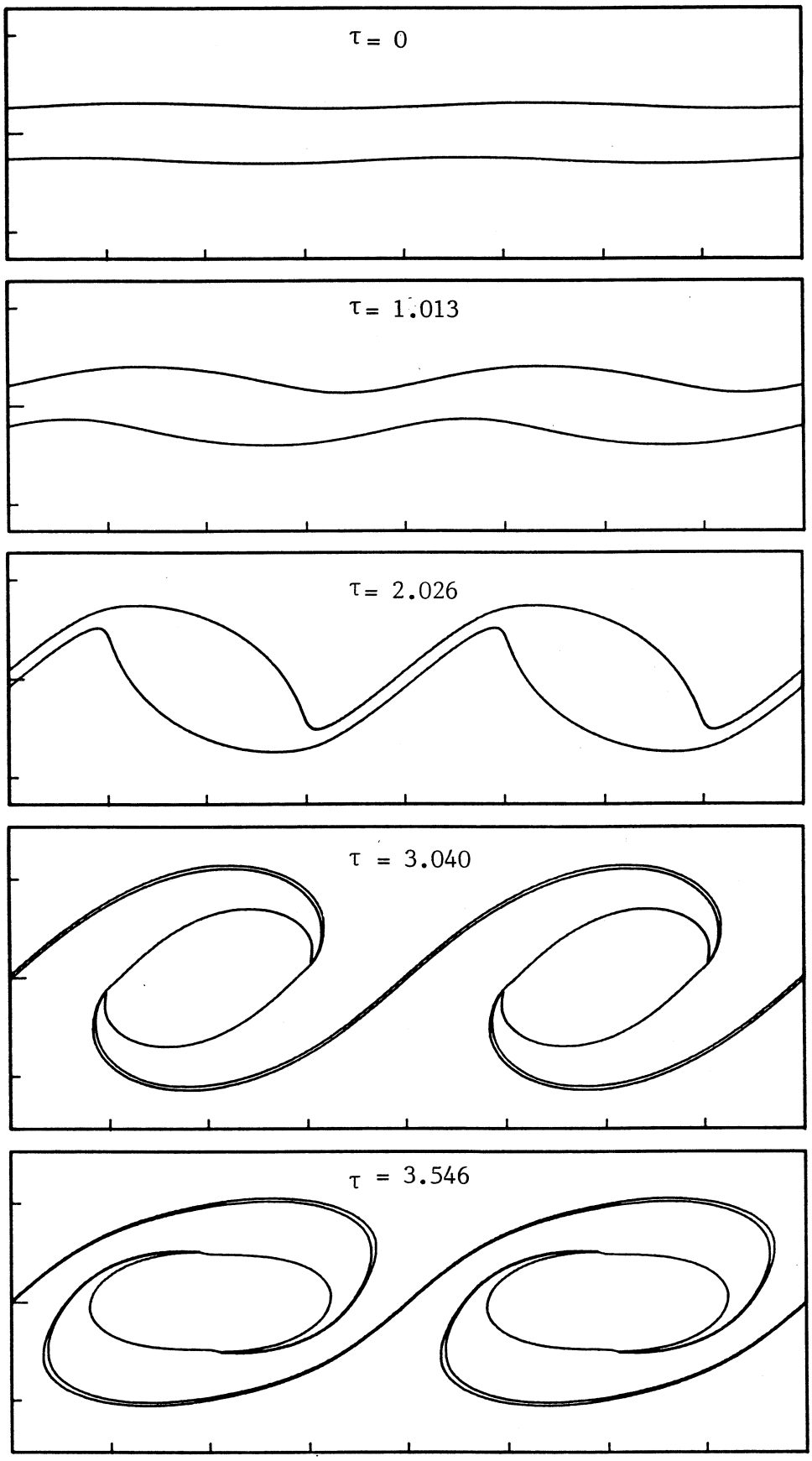

Figure 7.10 : For caption see over.

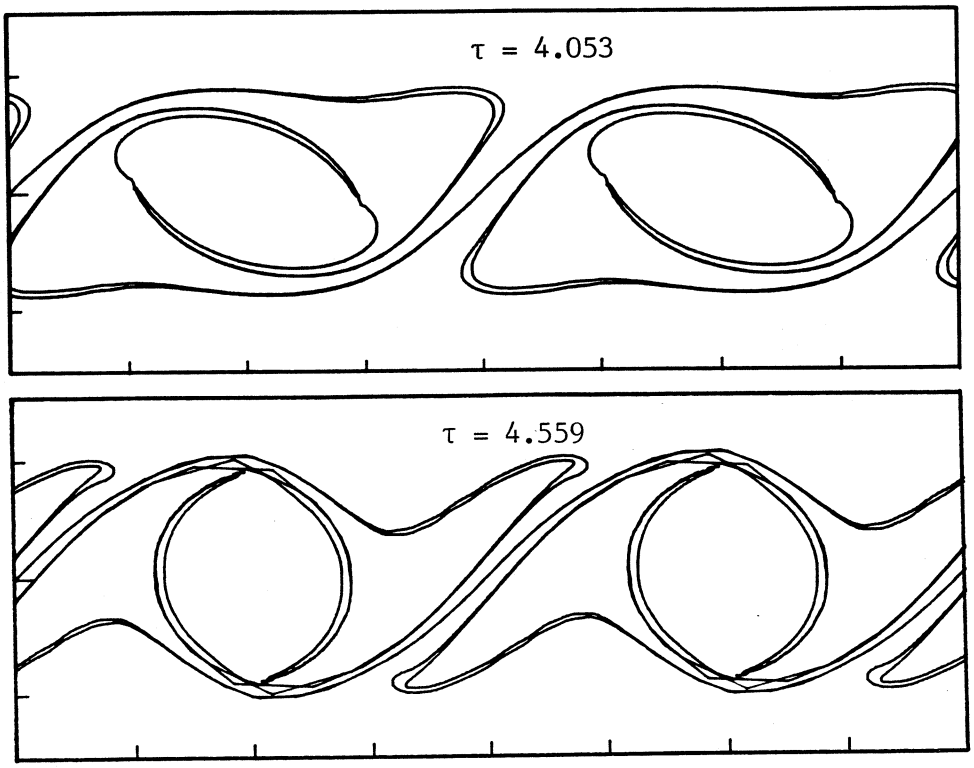

Figure 7.10 : Evolution of a uniform-vorticity layer disturbed by a single mode perturbation , $\delta_\omega / \lambda_1 = 0.875/2\pi$, $a_0/\lambda_i = 0.05/2\pi$. Initial disturbance f_1 (case 1, table 7.5). Times τ as shown.

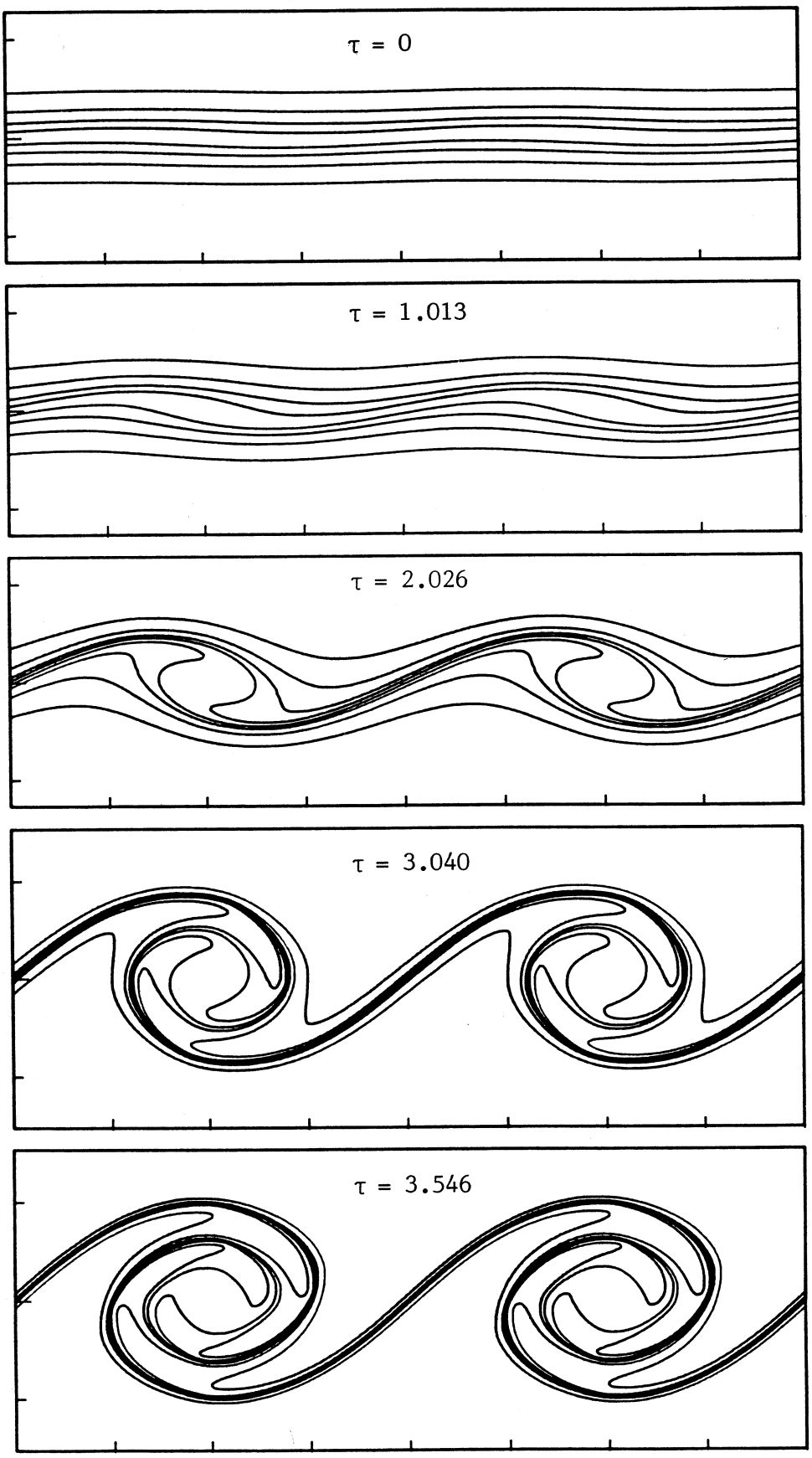

Figure 7.11 : for caption see over.

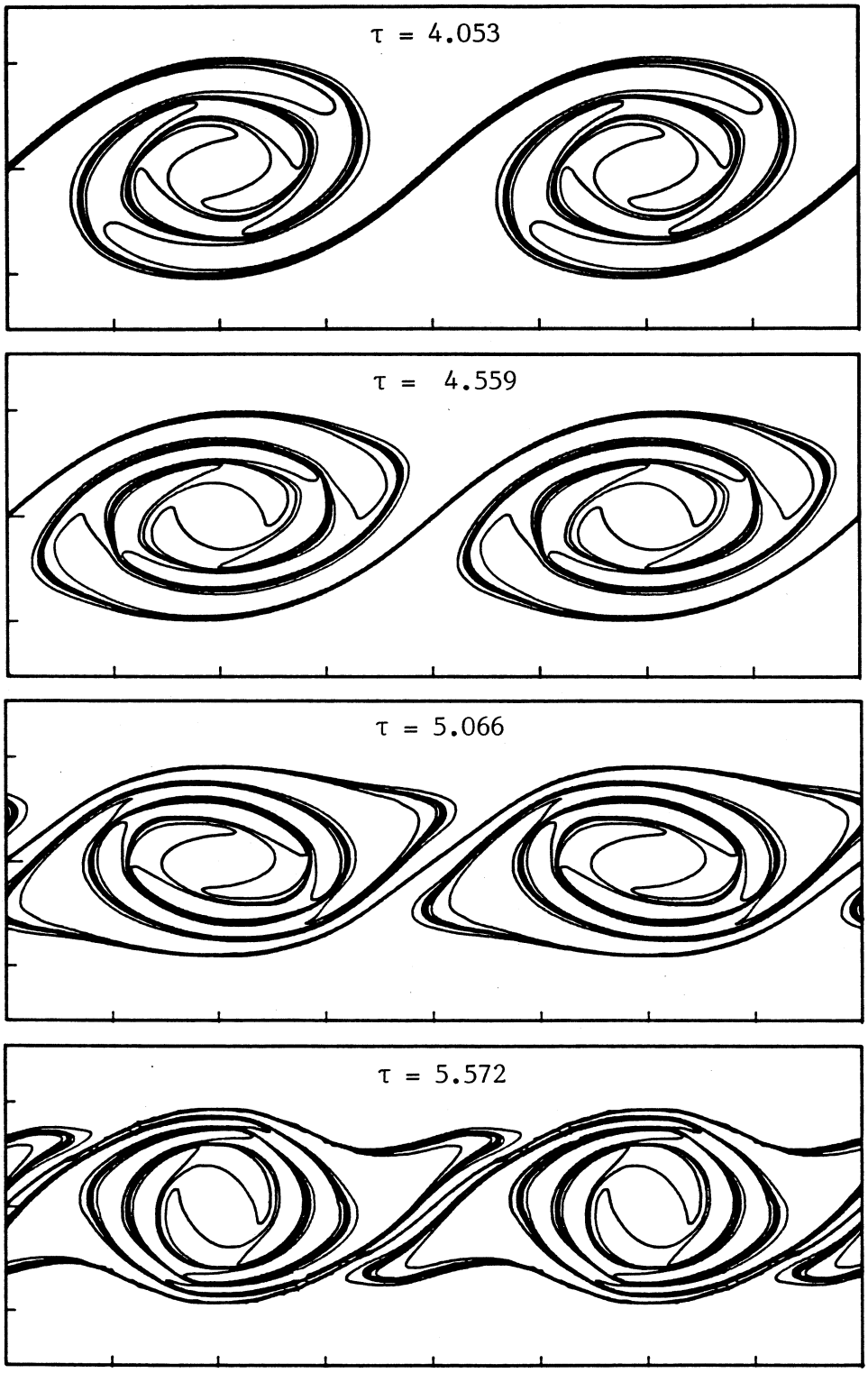

Figure 7.11 : Evolution of the M = 4 layer disturbed by a single mode perturbation, $\delta_\omega/\lambda_1 = 0.875/2\pi$, $a_0/\lambda_1 = 0.052\pi$. Initial disturbance $f_1^{(4)}$, (case 2, table 7.5). Times τ as shown.

(a)

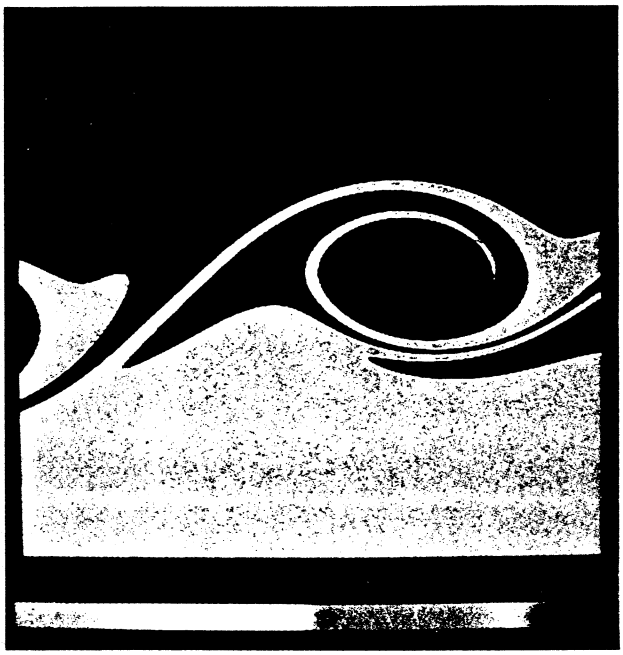

(b)

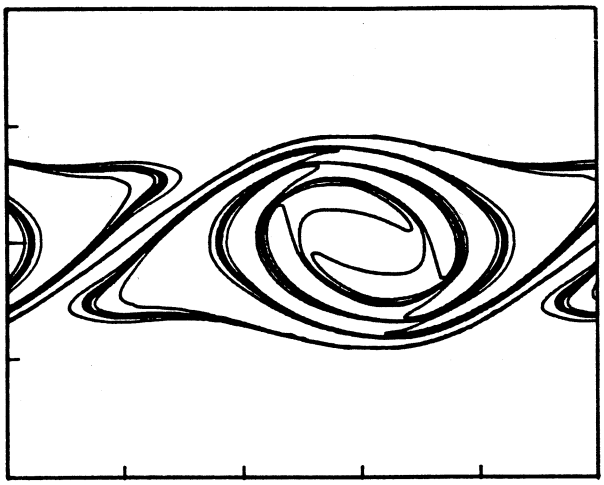

Figure 7.12 : Comparison of CD solution with experimental observation.
(a) Digital Laser-Induced-Fluorescence picture of the plane mixing layer showing a single vortex structure. This figure is a reproduction of figure 7a from Koochesfahani & Dimotakis (1986). (The original figure was in colour.)
(b) CD solution (case 2) at τ = 5.284 (t= 210)

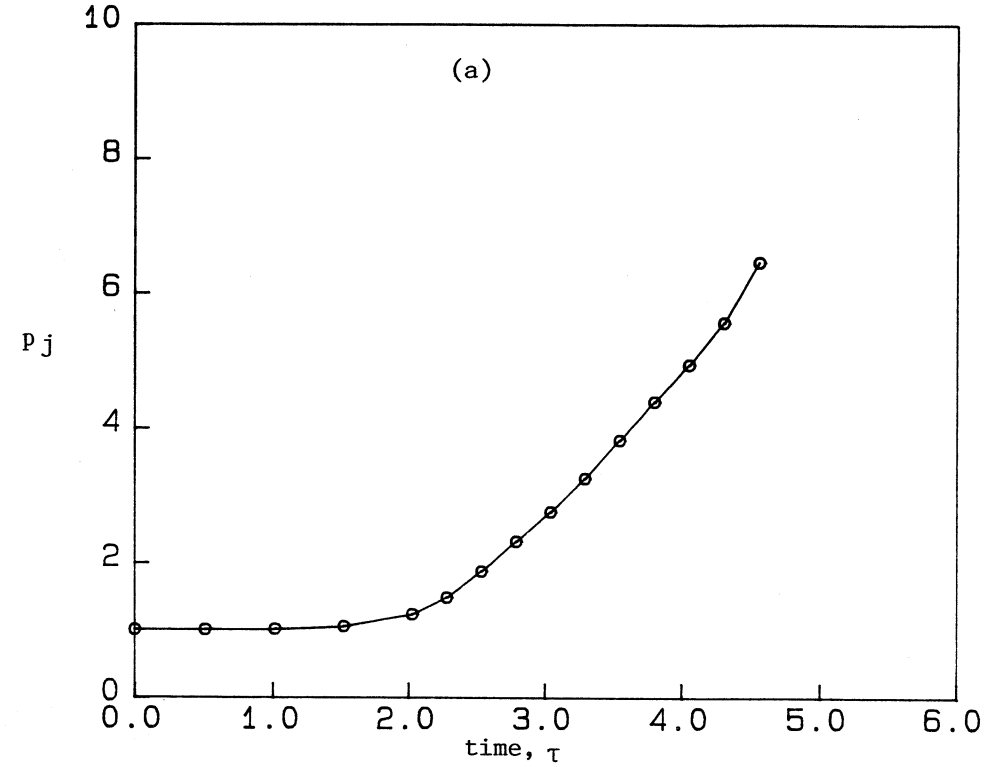

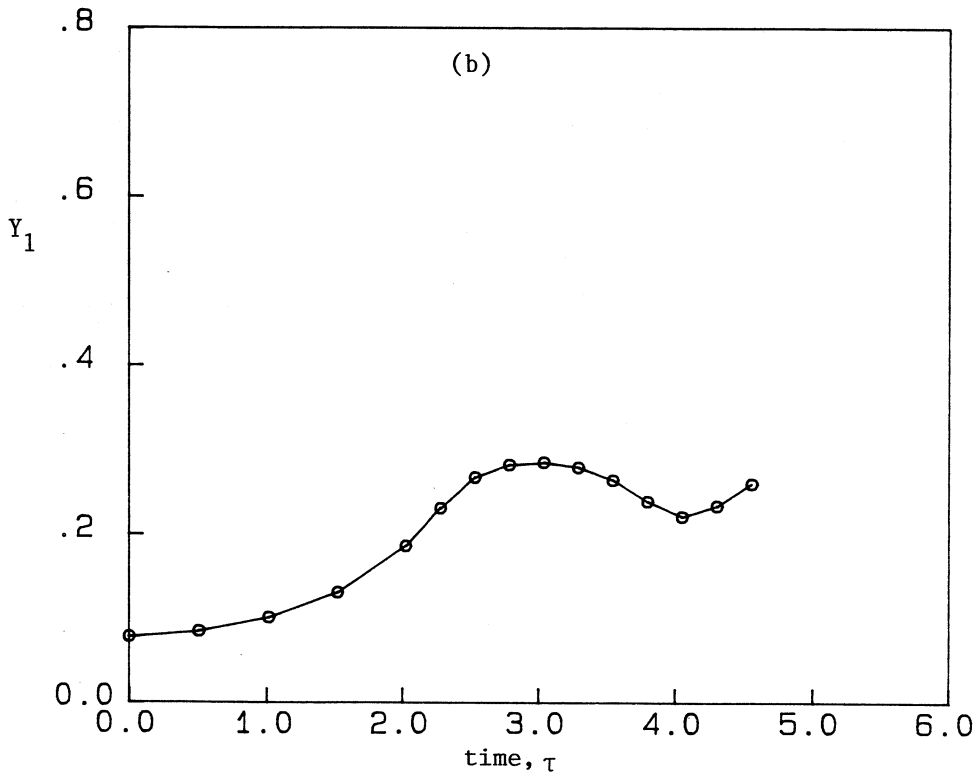

Figure 7.13 : (a) Growth of contour length p_1 for case 1 (table 7.5).
(b) Variation of Y_1 for case 1.

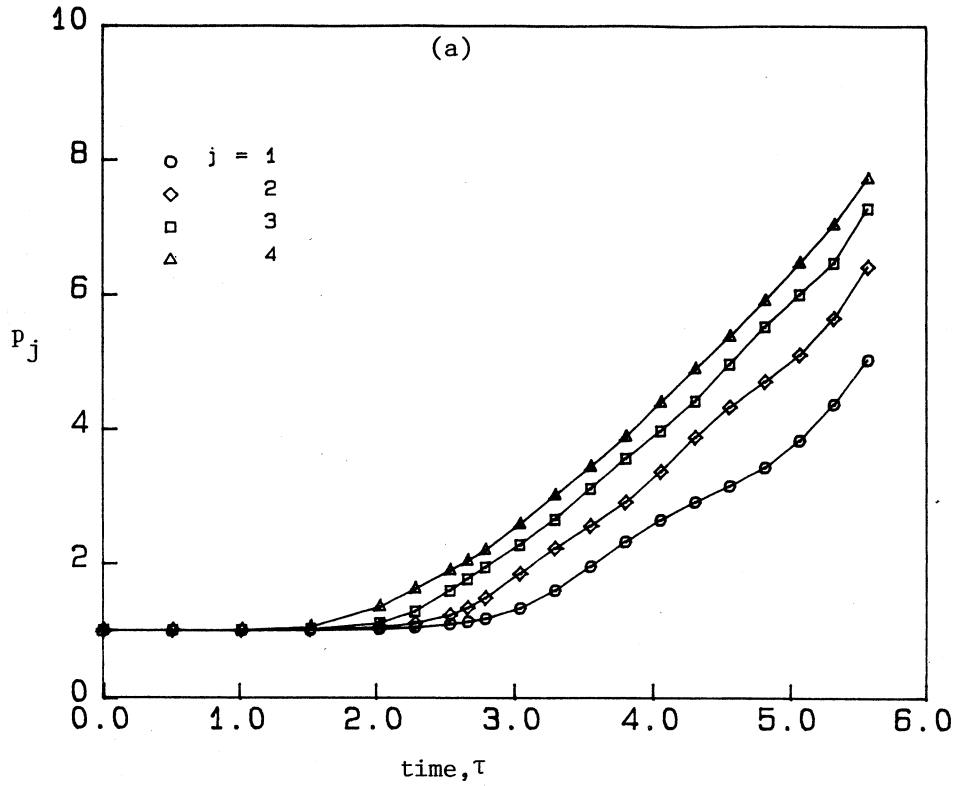

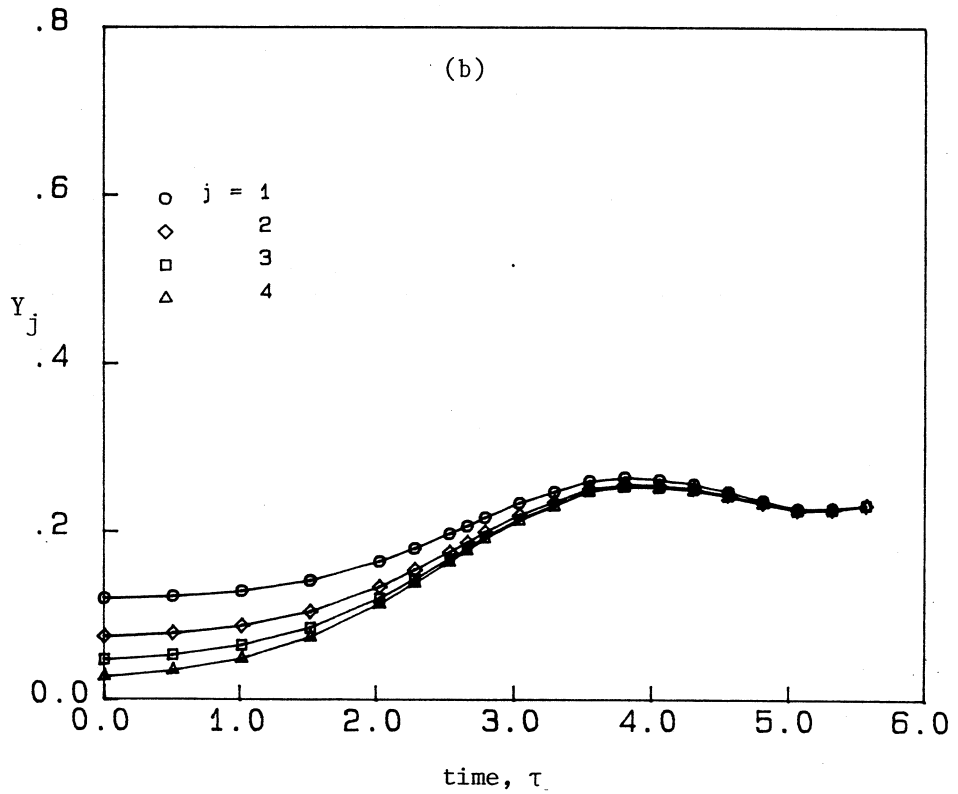

Figure 7.14 : (a) Growth of contour length p_j for nonlinear roll-up (case 2, table 7.5).
(b) Variation of Y_j for case 2.

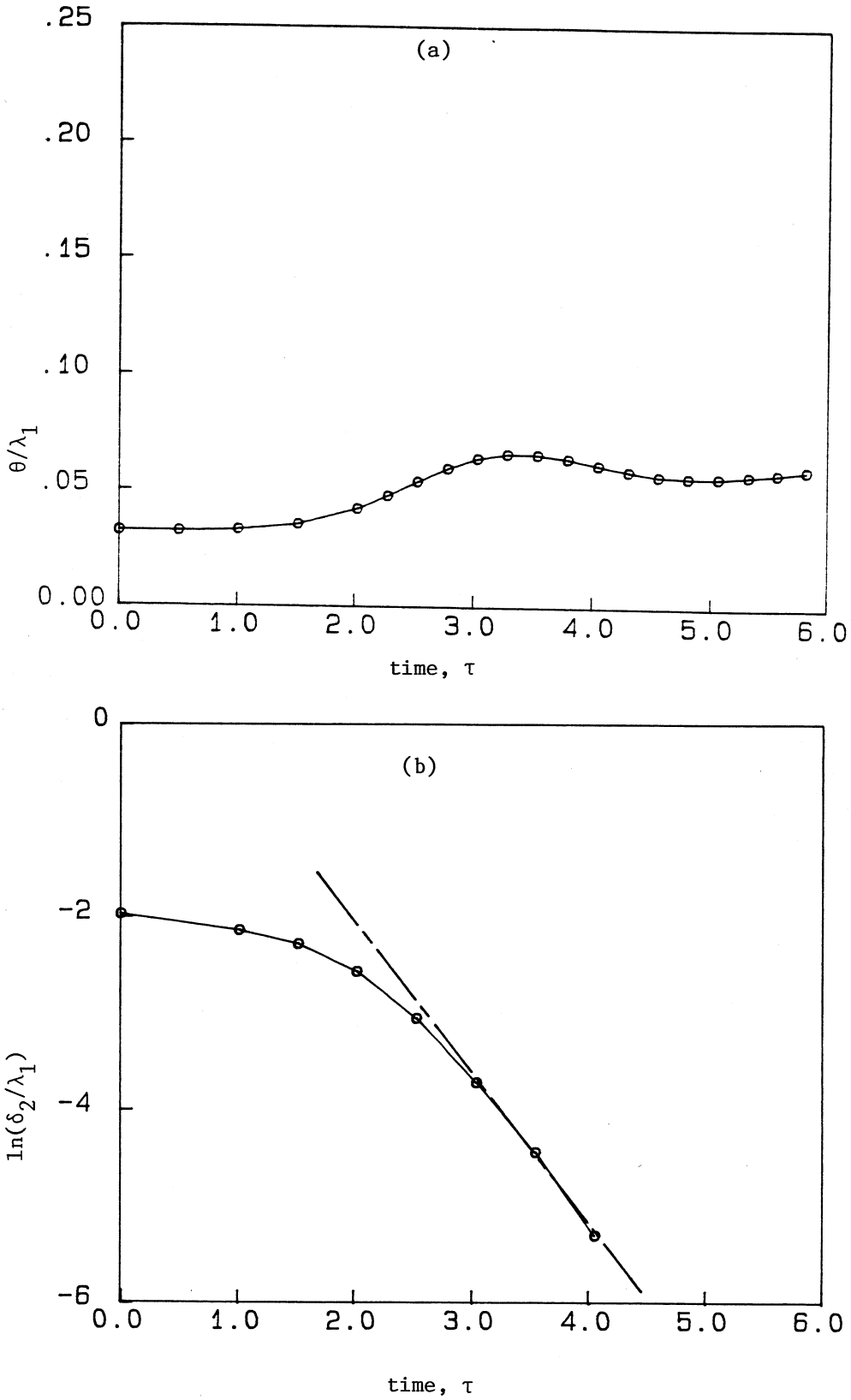

Figure 7.15 : (a) Variation in momentum thickness for case 2. (b) Variation in braid thickness plus asymptotic limit superimposed as a dashed line.

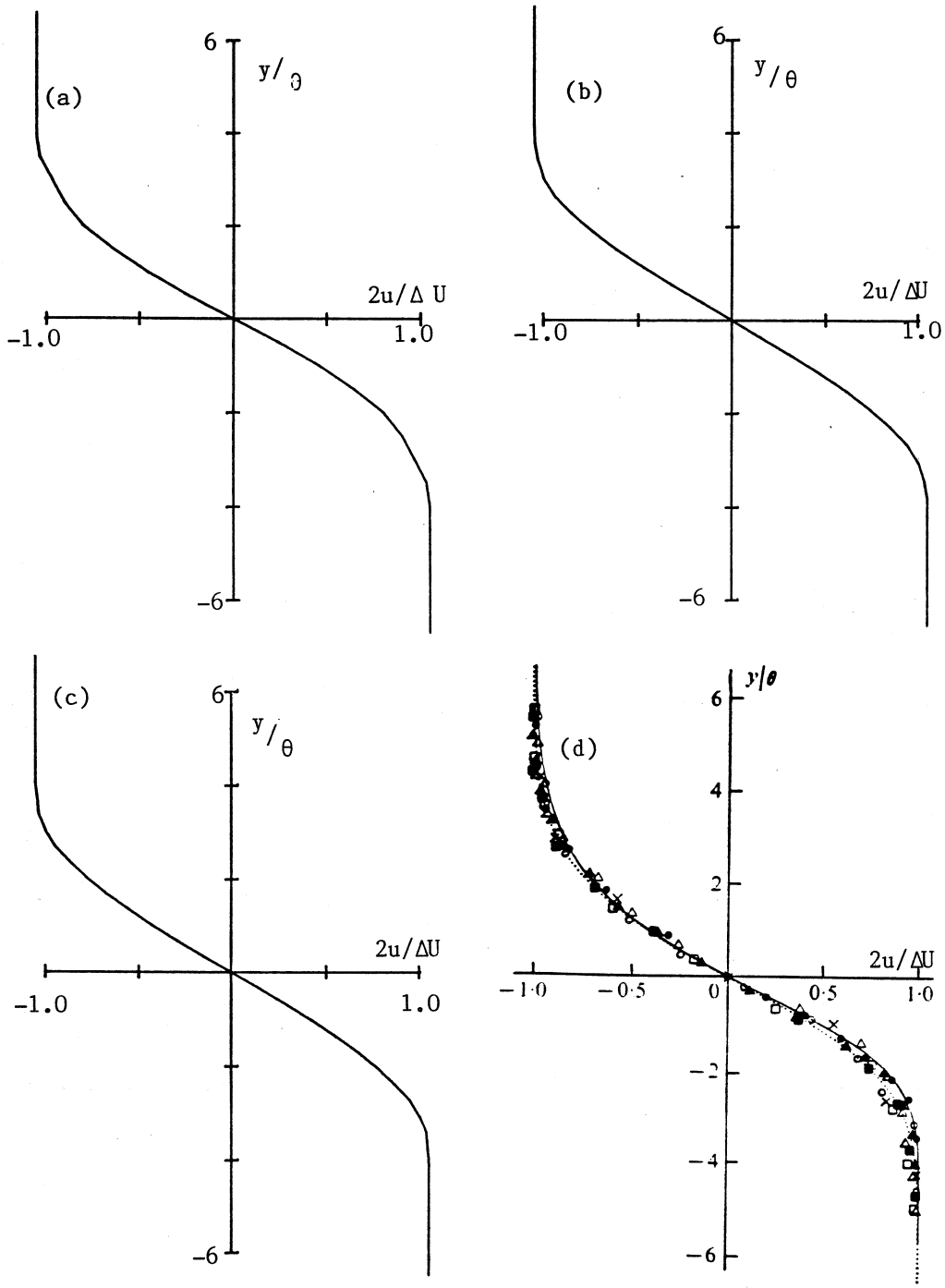

Figure 7.16 : Mean-velocity profiles $\langle u_x \rangle$ at various times during the nonlinear roll-up of the shear layer, case 2, (table 7.5) compared with experimental measurements from Winant and Browand (1974).
(a) $\tau = 0$, (b) $\tau = 2.026$, (c) $\tau = 5.066$
(d) Experimentally measured mean velocity profile in the nonturbulent region of a plane mixing layer. (Winant & Browand 1974).

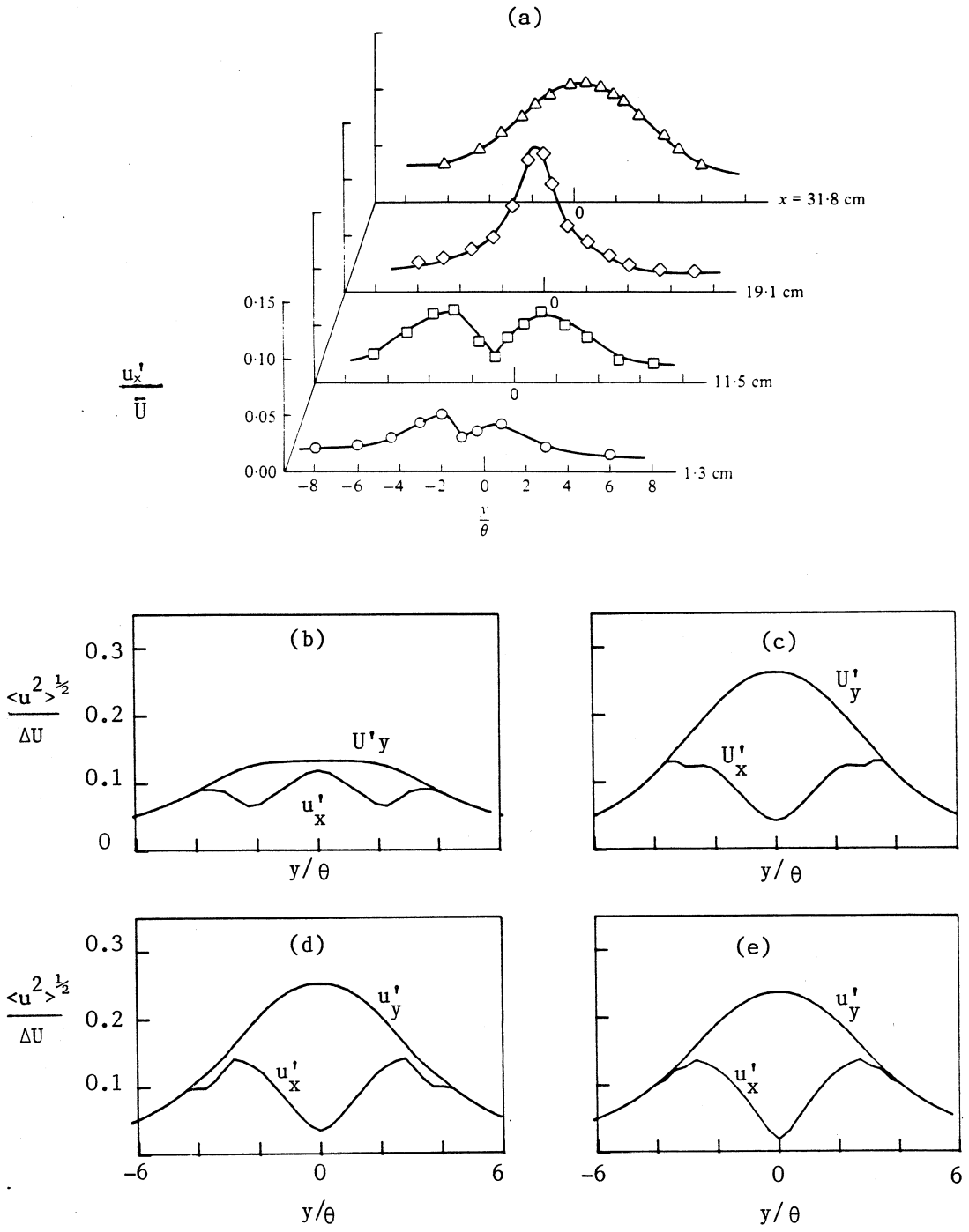

Figure 7.17 : Velocity fluctuation intensities for a single mode roll-up
(a) Experimental measurements of the longitudinal velocity fluctuations reproduced from figure 28 in Ho & Huang, 1982.
CD calculation, case 2:
(b) τ = 2.026 (c) τ = 3.040 (d) τ = 4.053 (e) τ = 5.066.

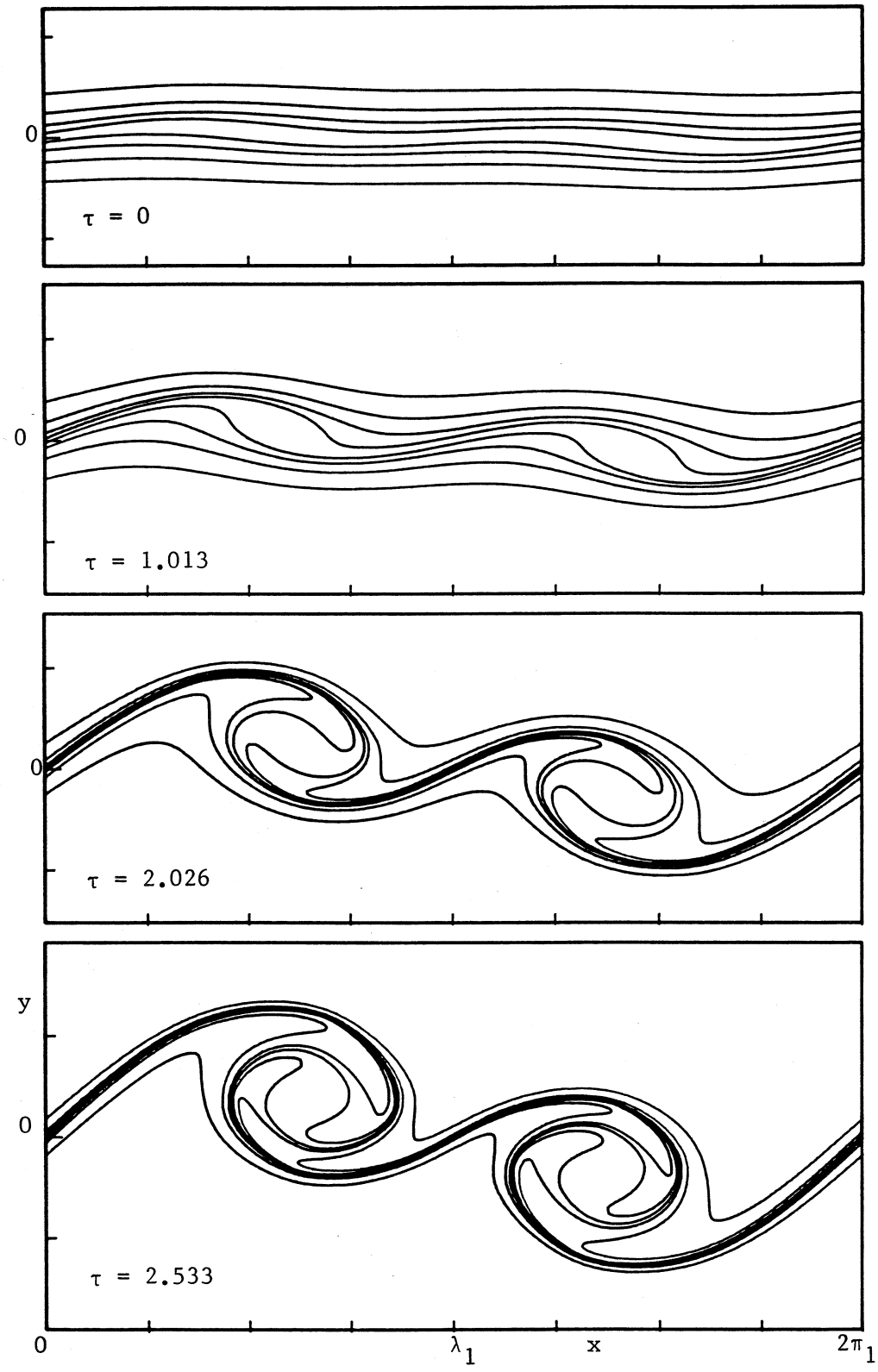

Figure 7.18 : Evolution of the M = 4 shear layer showing a single pairing event $\delta_\omega/\lambda_1 = 0.875/2\pi$ $a_0/\lambda_1 = 0.05/\pi$, initial disturbance $f_1^{(4)} + f_2^{(4)}$. (Case 3, table 7.5.)

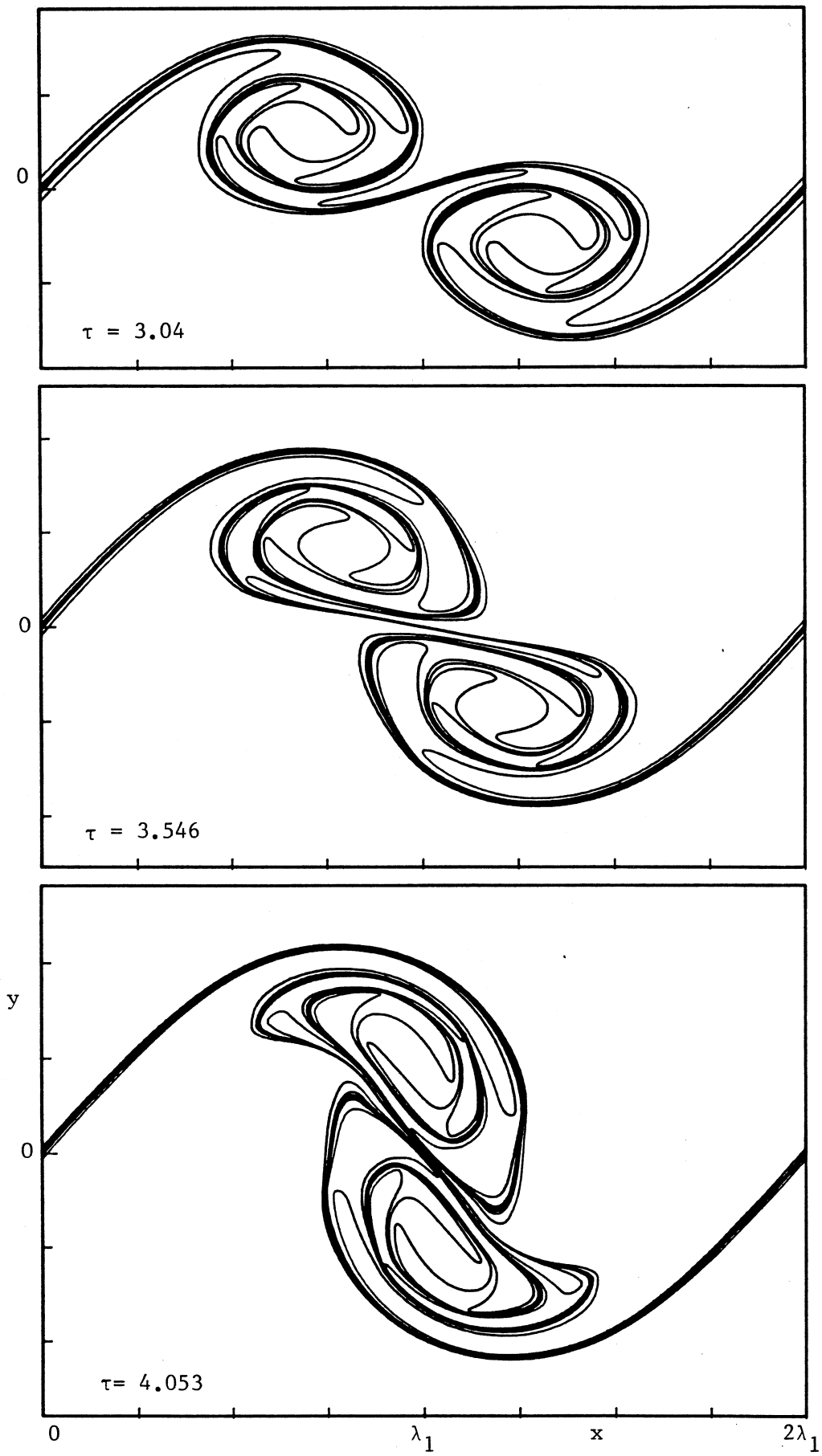

Figure 7.18 : continued.

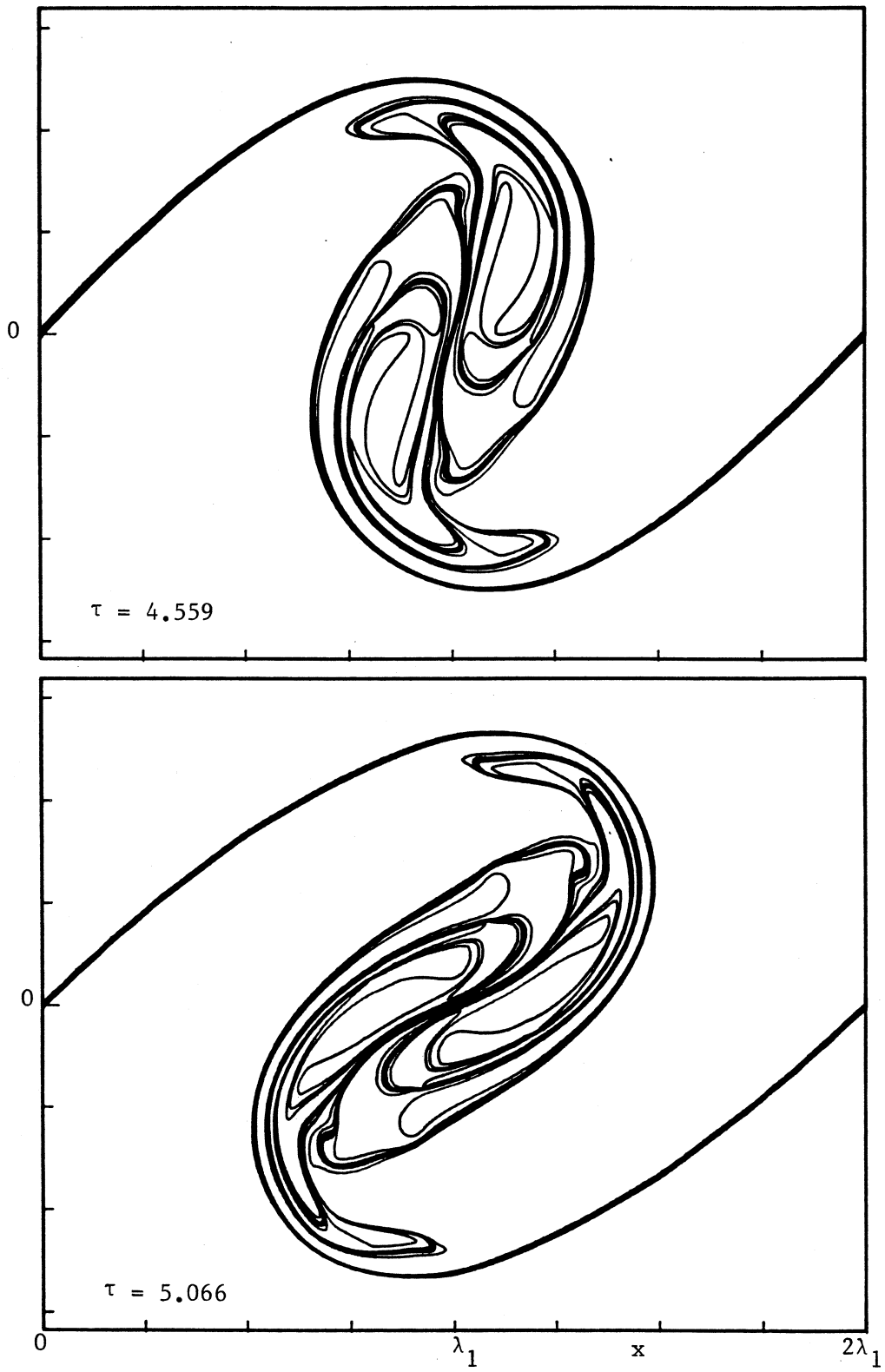

Figure 7.18 : continued.

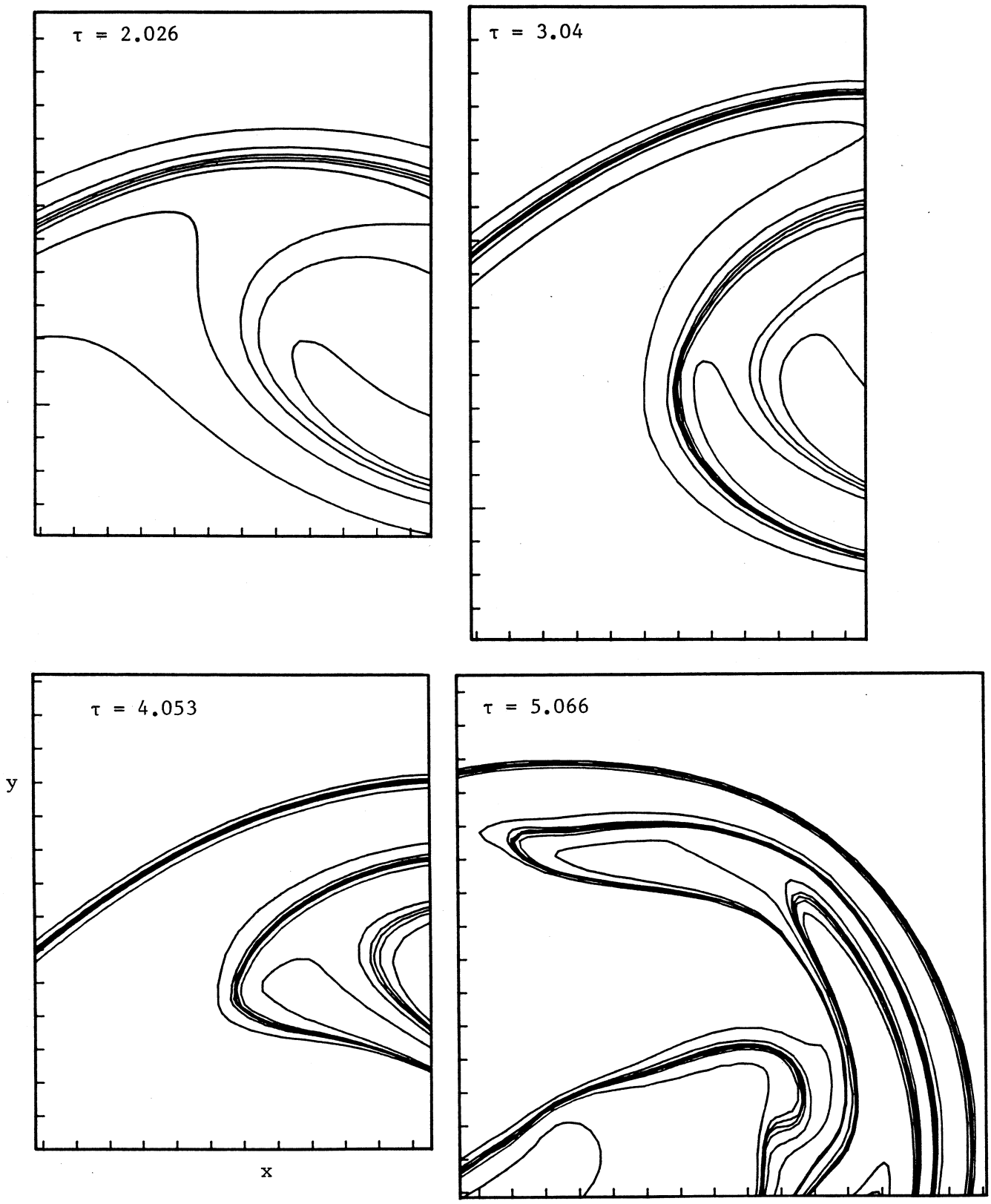

Figure 7.19 : Four magnified views of the contours for the pairing calculation in figure 7.18 (case 3). Times τ as shown.

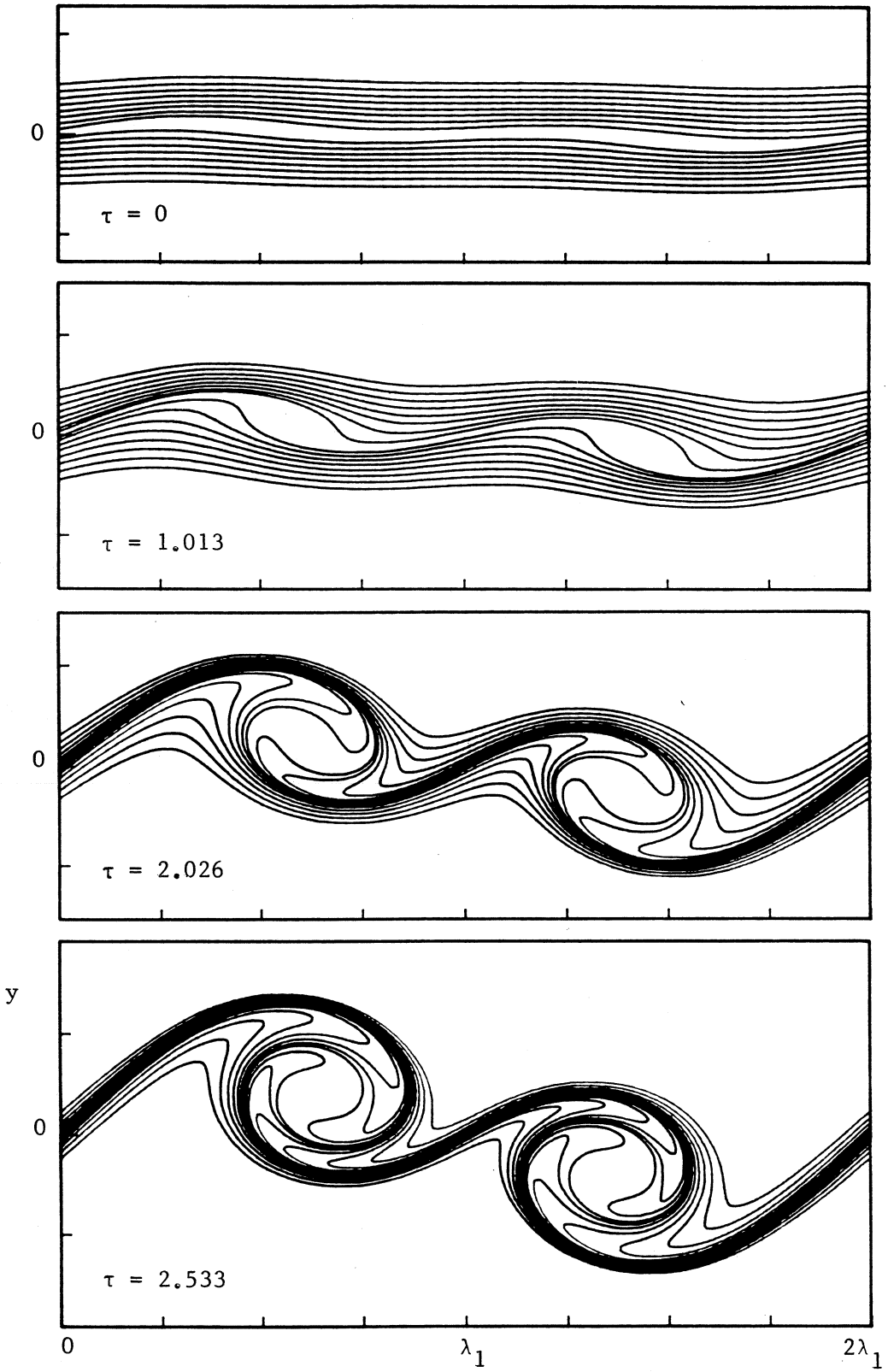

Figure 7.20 : Evolution of an M = 8 shear layer showing a single pairing event $\delta_\omega/\lambda_1 = 0.875/2\pi$, $a_0/\lambda_1 = 0.05/\pi$ initial disturbance $f_1^{(8)} + f_2^{(8)}$. Case 4, table 7.5

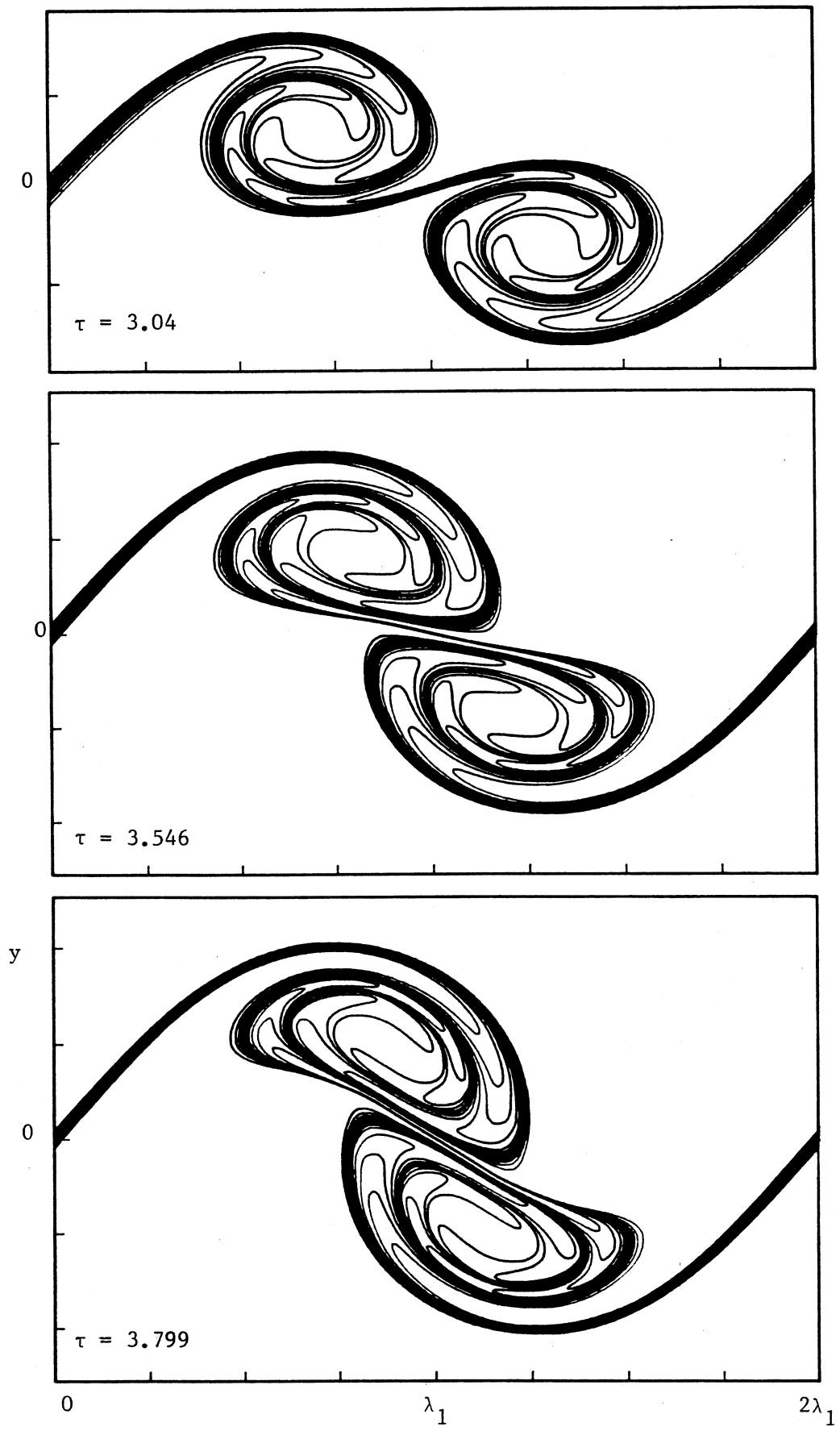

Figure 7.20 : continued.

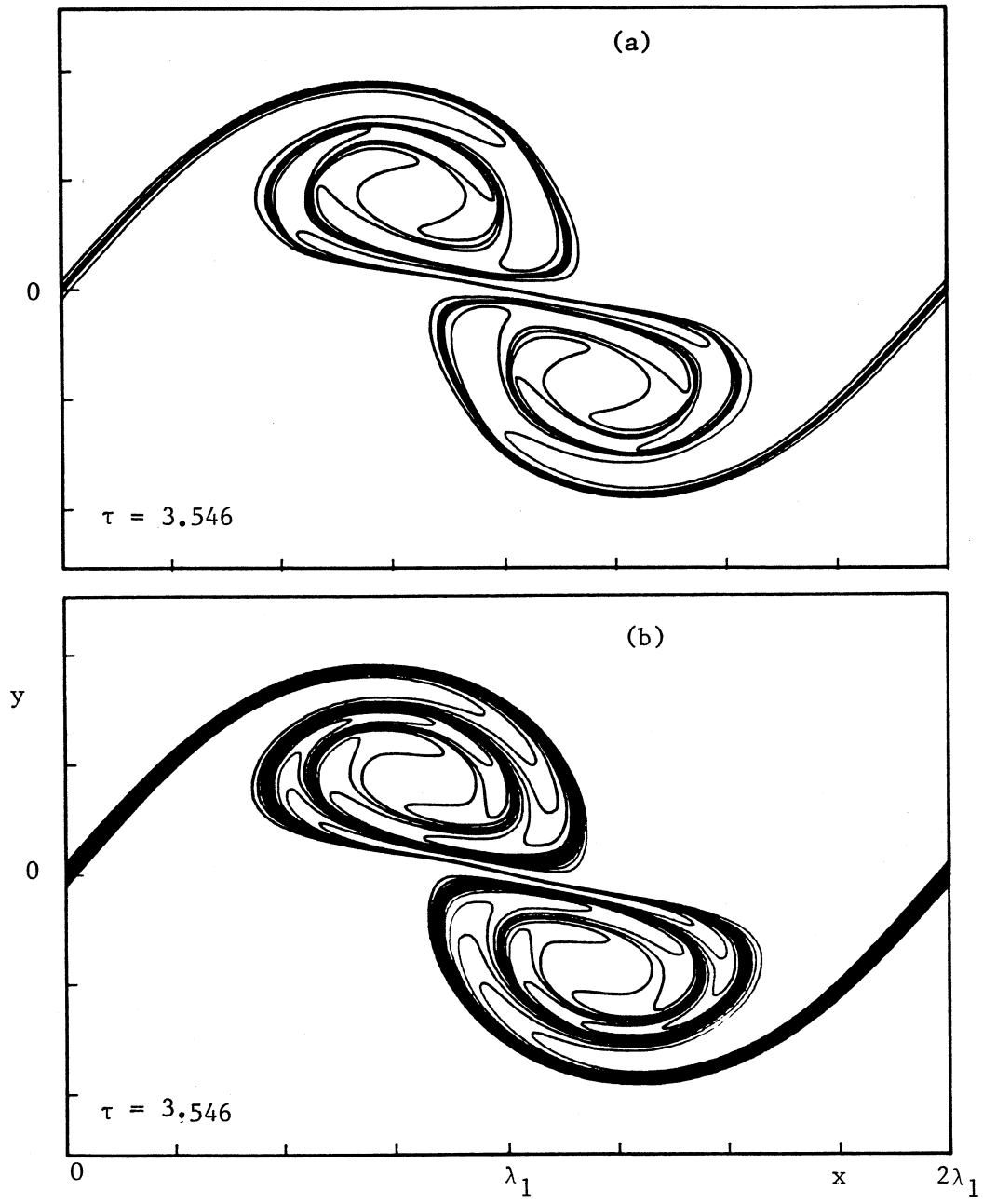

Figure 7.21 : Comparison of (a) the M = 4 layer (case 3) and (b) the M = 8 layer (case 4) at τ= 3.546.

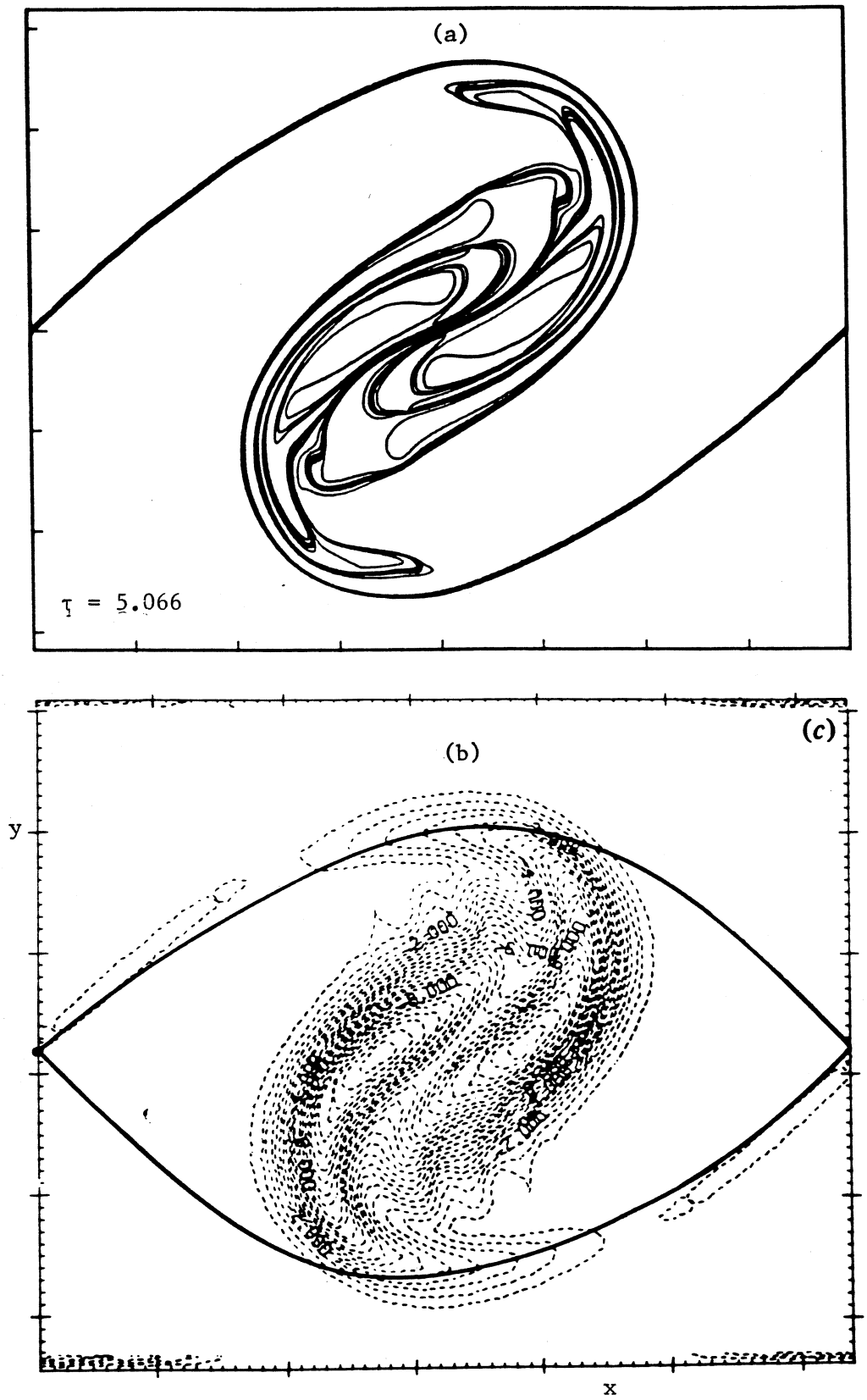

Figure 7.22 : Comparison of layer evolutions involving a pairing event :
(a) CD simulation of an inviscid shear layer (case 3, figure 7.17)
(b) finite-difference calculation at $Re_\delta \simeq 100$ reproduced from figure 8 of Corcos & Sherman (1984).

(c)

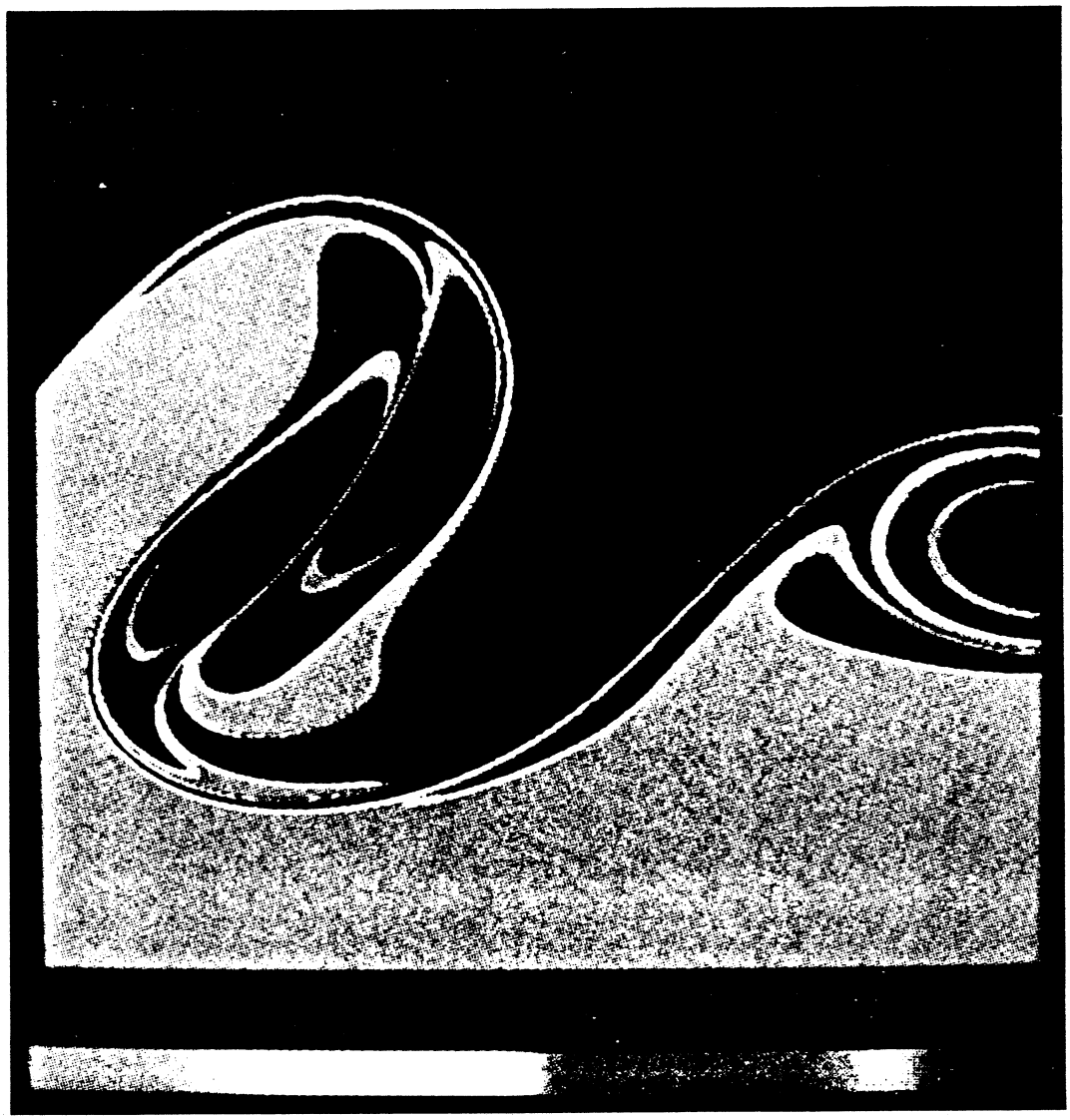

Figure 7.22 : (c) Digital Laser-Induced-Fluorescence picture of the plane mixing layer at Re_δ = 1750 showing the coalescence of two vortices into a single structure. This figure is a reproduction of figure 7b from Koochesfahani & Dimotakis (1986).

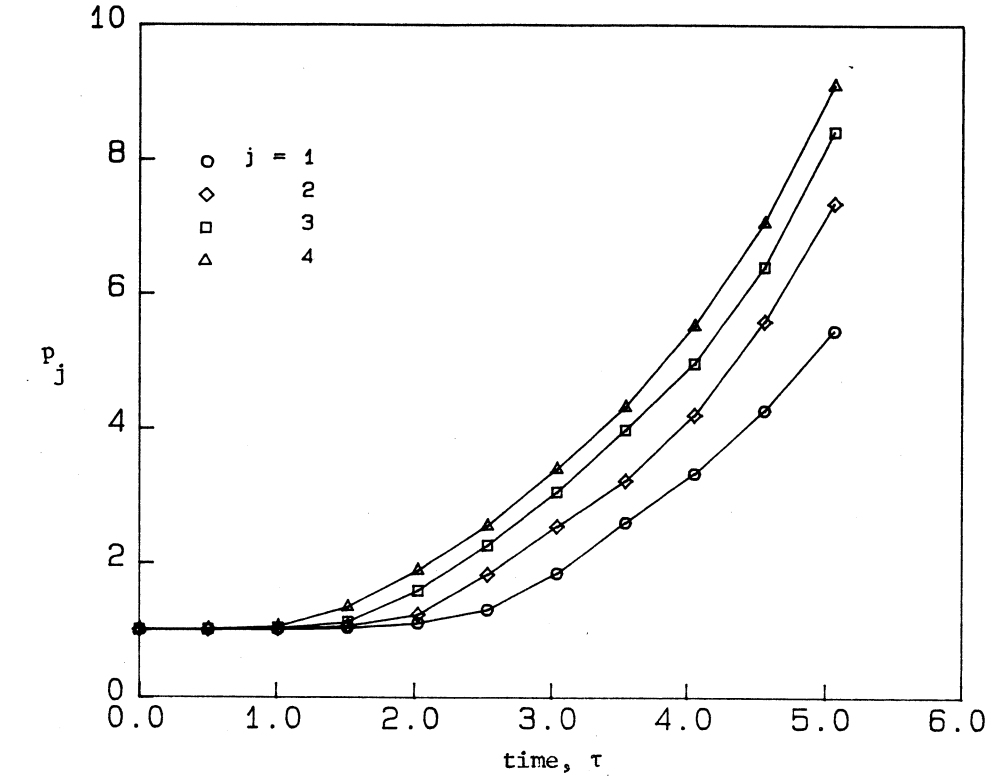

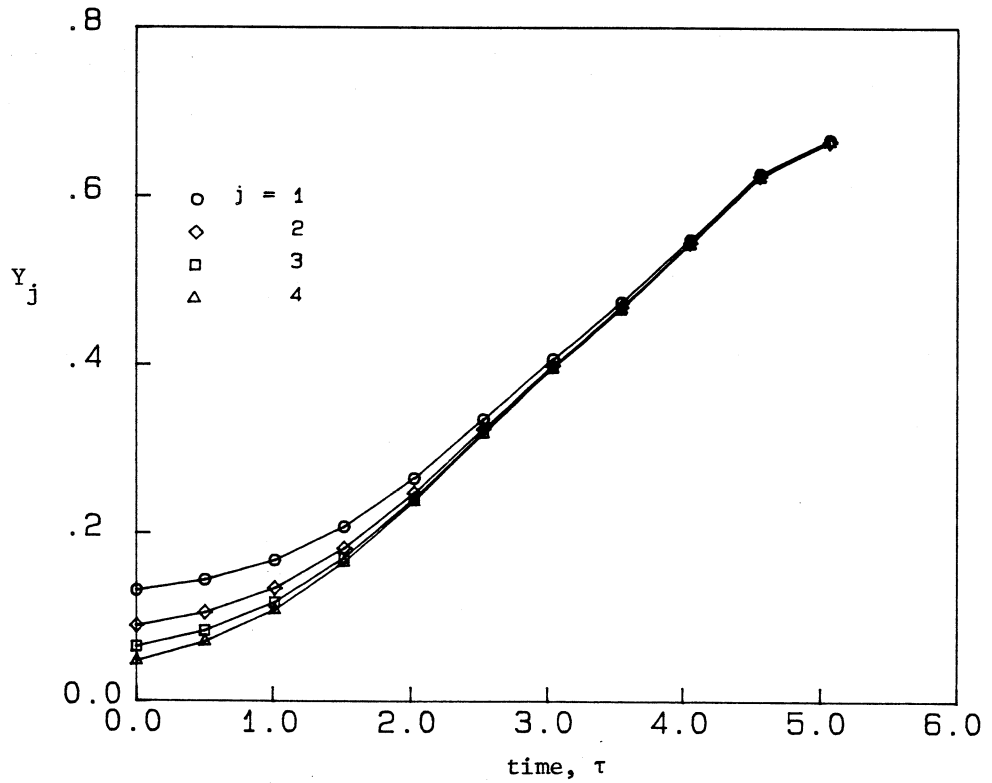

Figure 7.23 : (a) Growth of contour length p_j for pairing event (case 3)
(b) Variation of Y_j for pairing event (case 3).

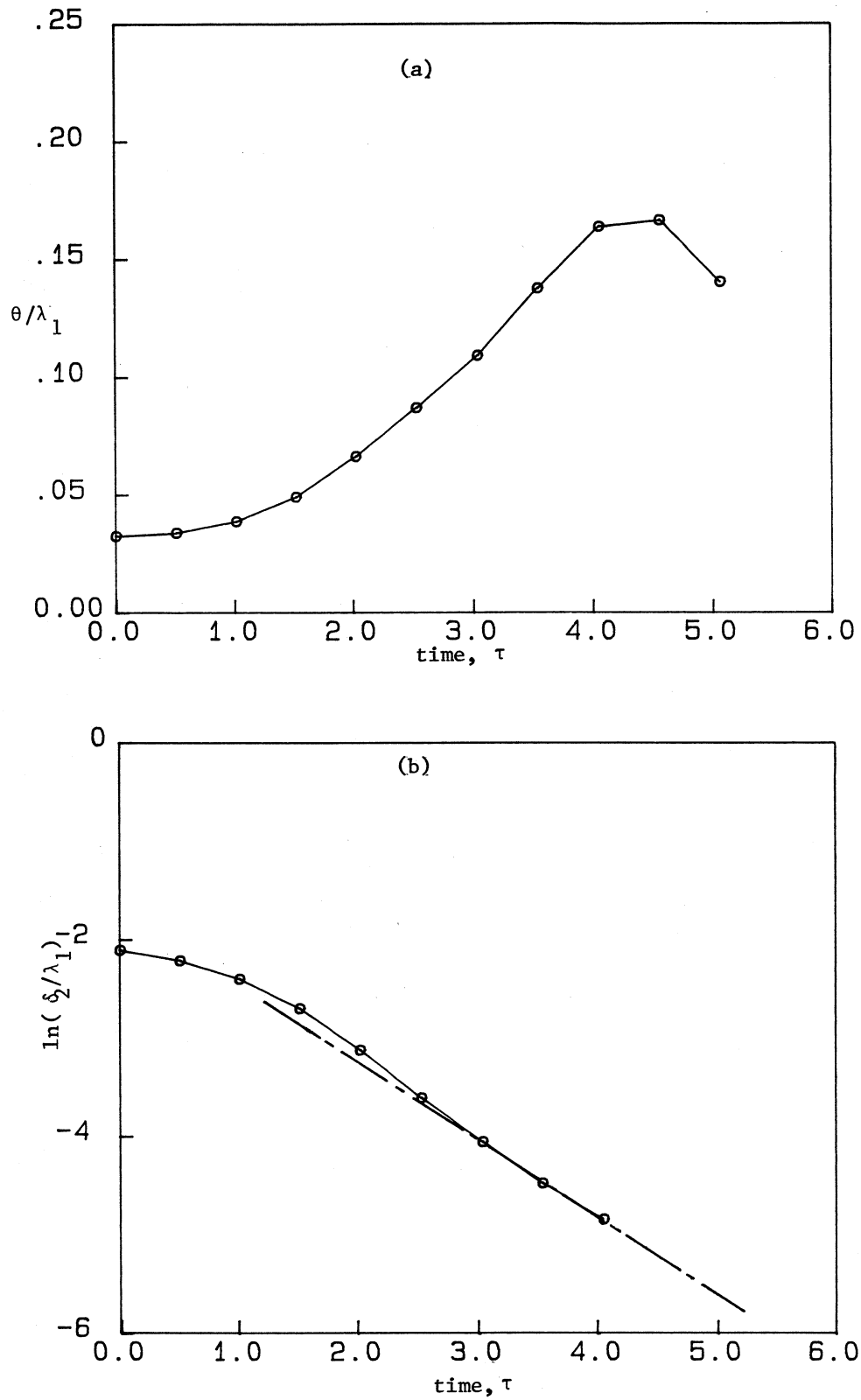

Figure 7.24 : (a) Variation of layer momentum thickness, θ, for pairing event (case 3)
(b) Variation in braid thickness for case 3. The asymptotic limit is superimposed as a dashed line.

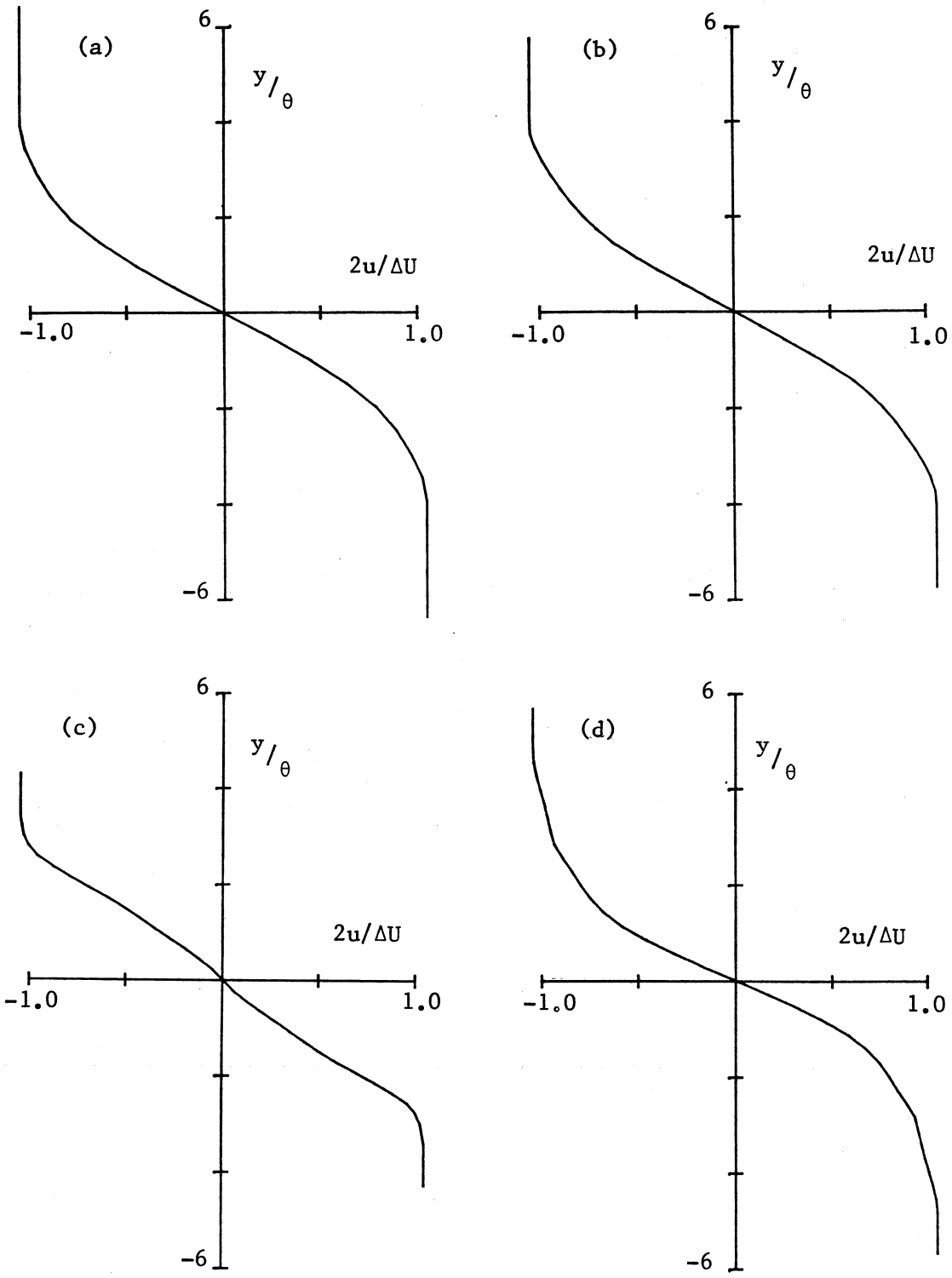

Figure 7.25 : Mean velocity profiles for the pairing event (case 3).
(a) τ = 2.026 (b) τ = 3.04 (c) τ = 4.053 (d) τ = 5.066.

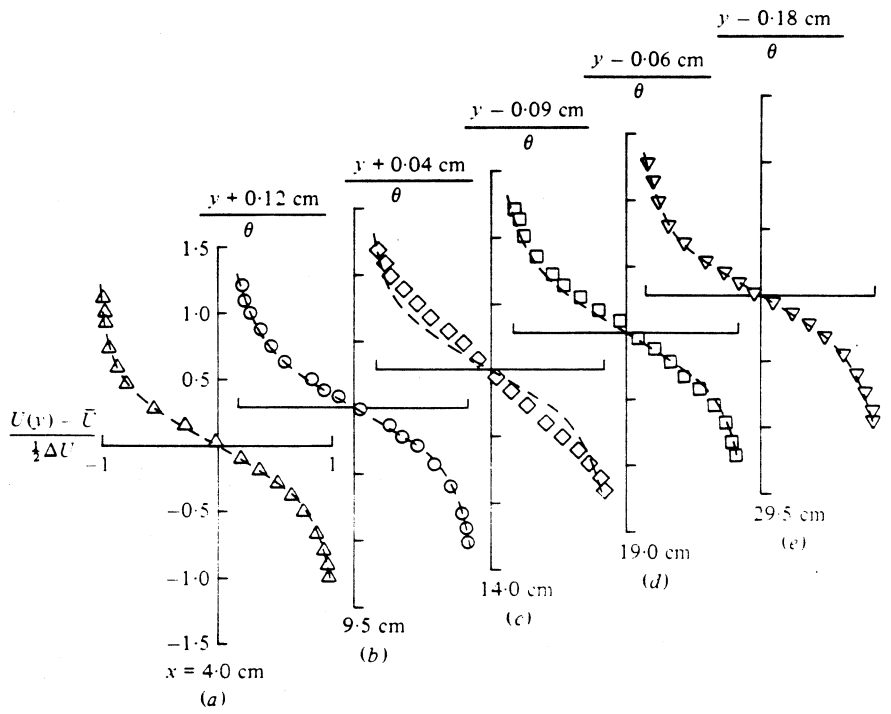

Figure 7.25 continued : (e) Mean velocity profiles for the mode II mixing layer (equivalent to the pairing simulation, case 3) measured at various streamwise stations. This figure is reproduced from figure 23 in Ho and Huang (1982).

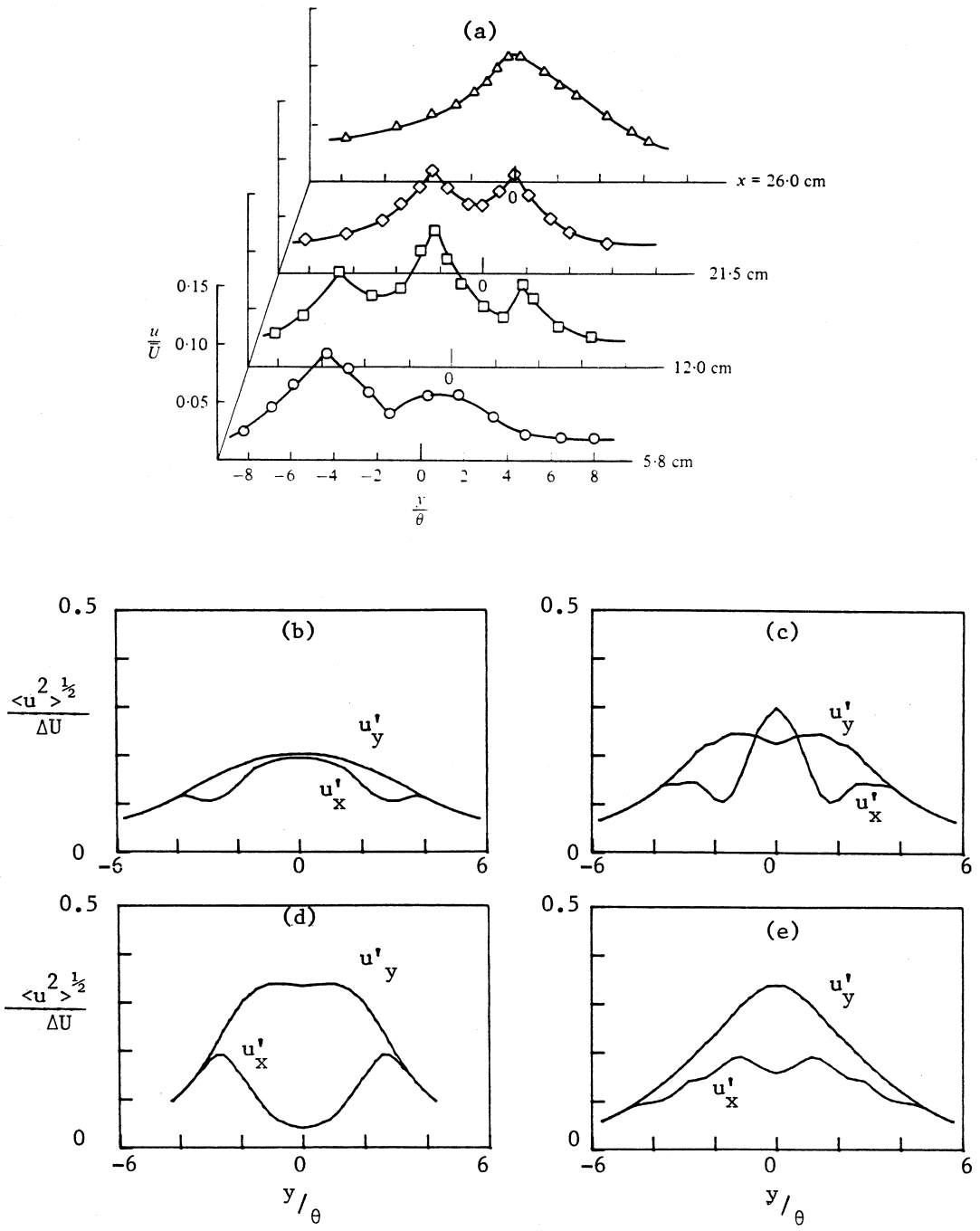

Figure 7.26 : Velocity fluctuation intensities for the pairing event (case 3)

(a) Experimental measurements of the longitudinal velocity fluctuations in the mode II mixing layer reproduced from figure 29 in Ho and Huang (1982).

(b-e) CD calculation : (b) $\tau = 2.026$ (c) $\tau = 3.04$ (d) $\tau = 4.053$ (e) $\tau = 5.066$.

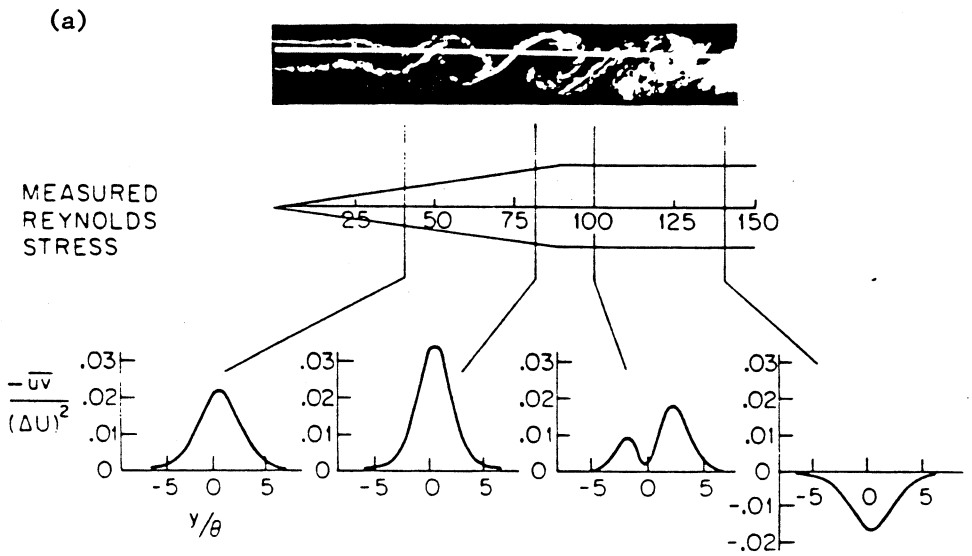

Figure 20 Evolution of Reynolds-stress cross-stream distribution with downstream distance in a forced turbulent mixing layer (from Oster & Wygnanski 1982 and Browand & Ho 1983). $f_1 \ll f_n$. The measurements were performed at $R = 0.25$, but the visualization refers to $R = 0.43$. Comparison is only qualitative.

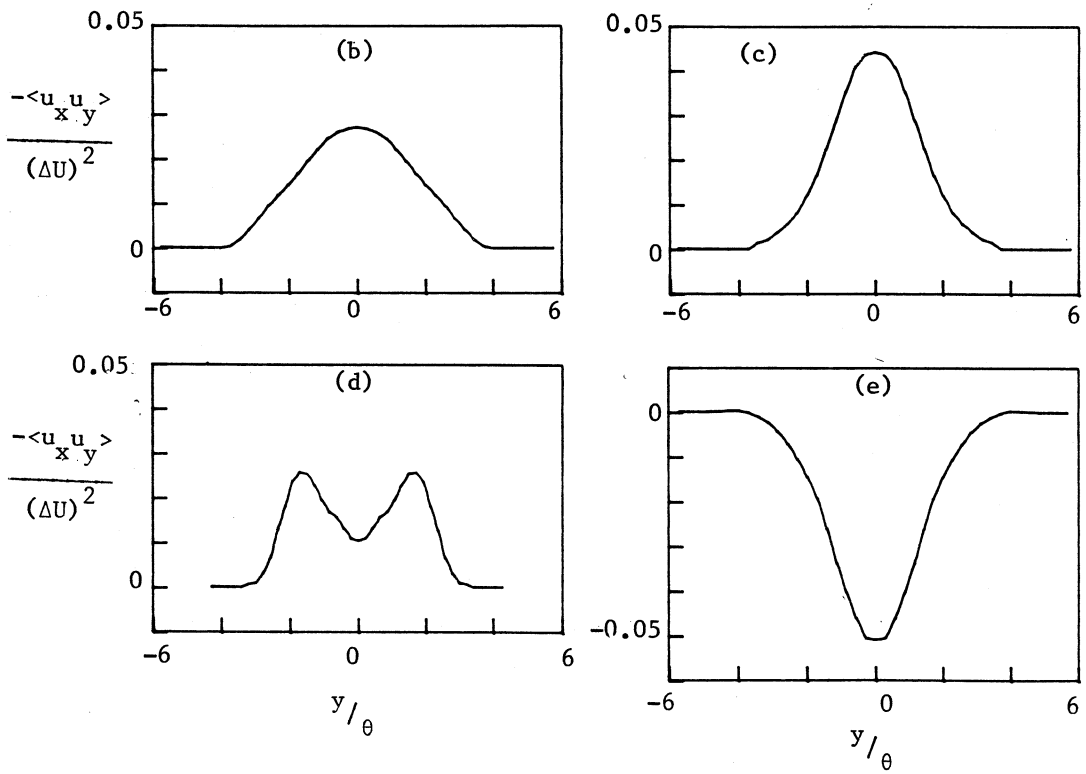

Figure 7.27 : Reynolds stresses for the pairing event (case 3)
(a) Experimental measurements from Oster and Wygnanski (1982). This figure has been reproduced from Ho & Huerre (1984).
(b-e) CD calculation : (b) $\tau = 2.026$ (c) $\tau = 3.04$
(d) $\tau = 4.053$ (e) $\tau = 5.066$.

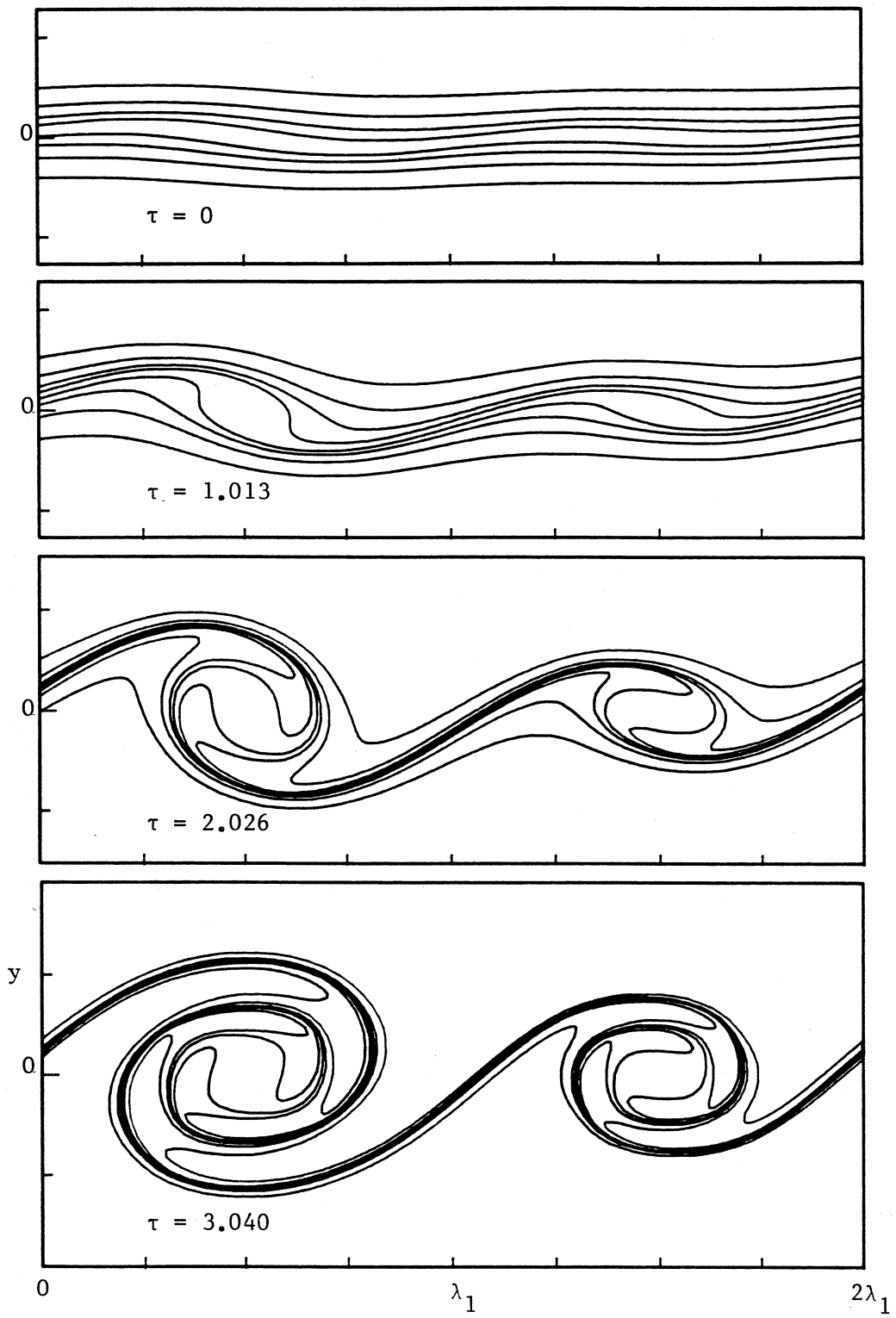

Figure 7.28 : Evolution of an M = 4 shear layer showing a tearing event $\delta_\omega/\lambda_1 = 0.875/2\pi$ $a_0/\lambda_1 = 0.05/\pi$, initial perturbation $f_1^{(4)} + e^{i\pi/2} f_2^{(4)}$ (case 5, table 7.5).

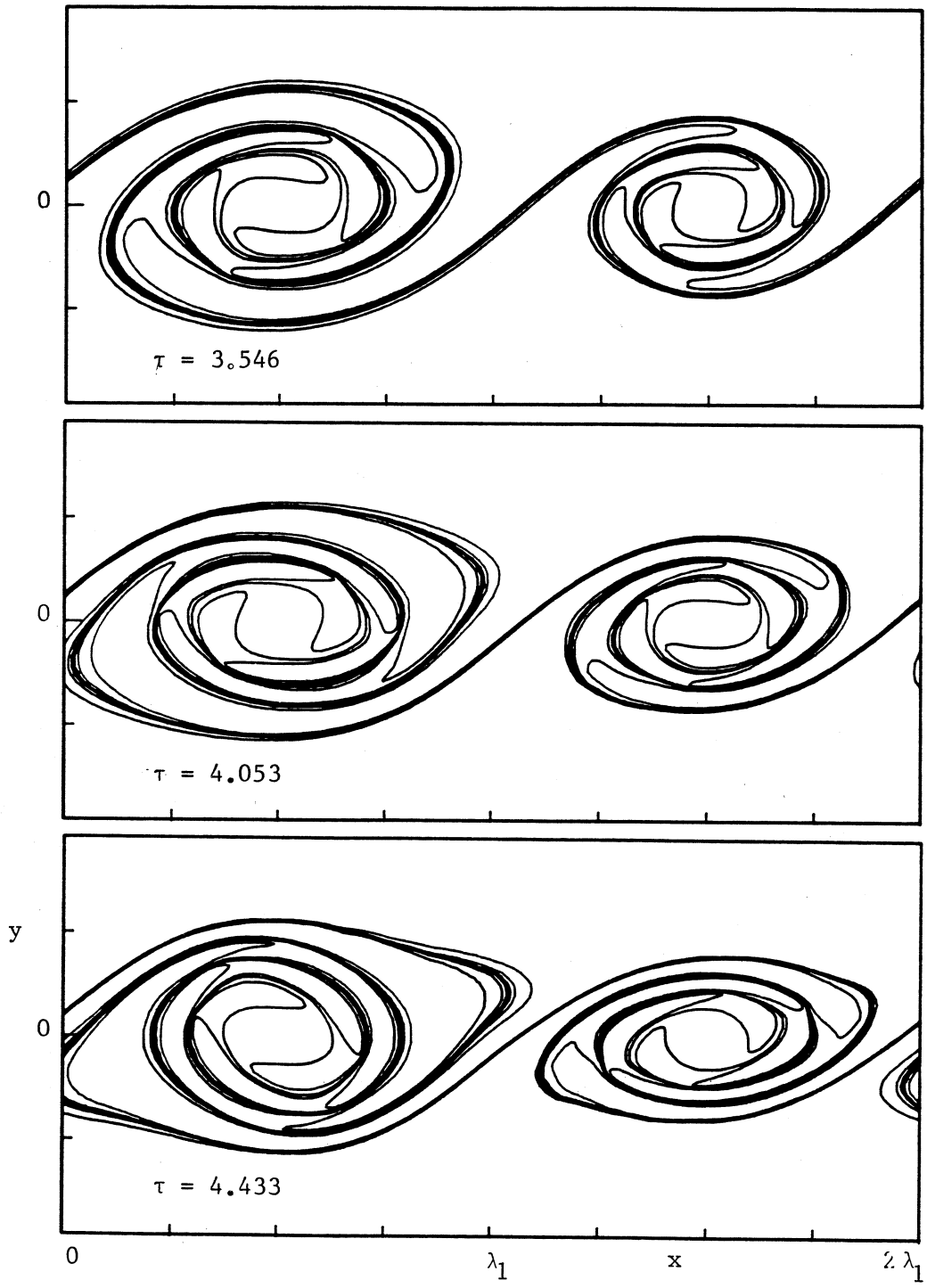

Figure 7.28 : continued.

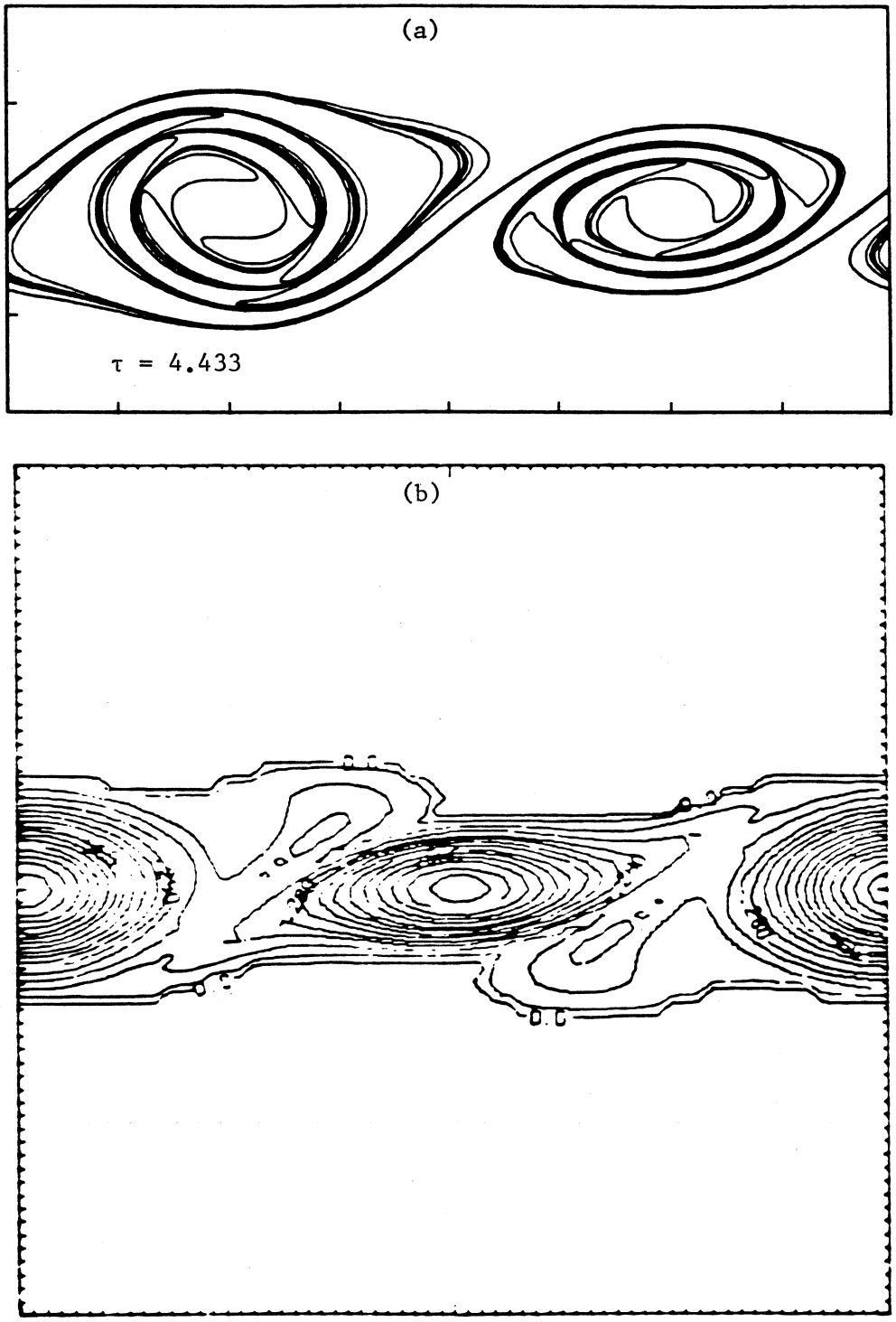

Figure 7.29 : Comparison of the CD calculation (tearing mode, case 5) with a calculation at Re= 400
(a) τ = 4.433 solution from case 5 (figure 7.26)
(b) Spectral method solution at t = 24 reproduced from Riley & Metcalfe (1980), figure 14 c.

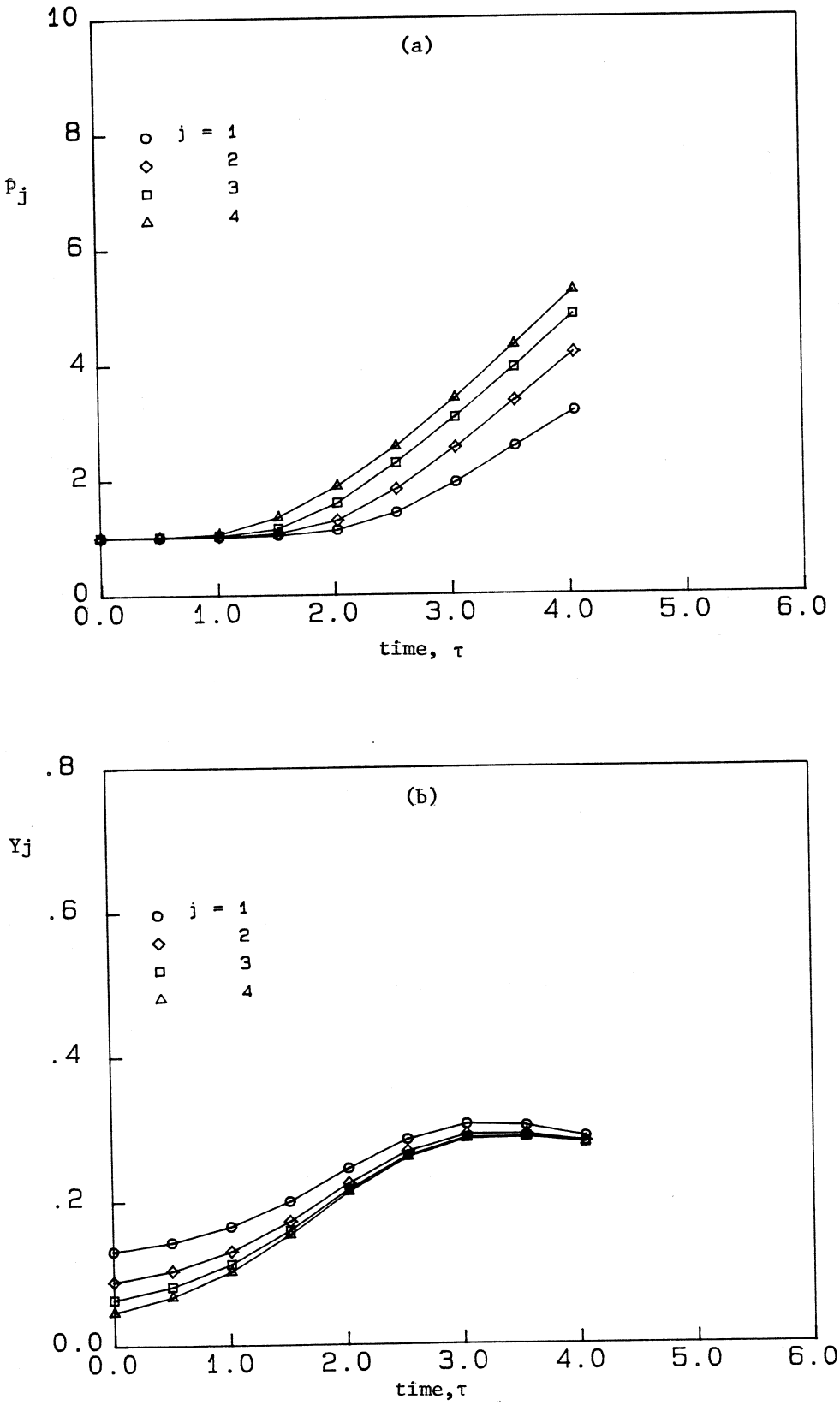

Figure 7.30 : (a) Growth of contour length p_j, for a tearing event (case 5).

(b) Variation of Y_j for tearing event.

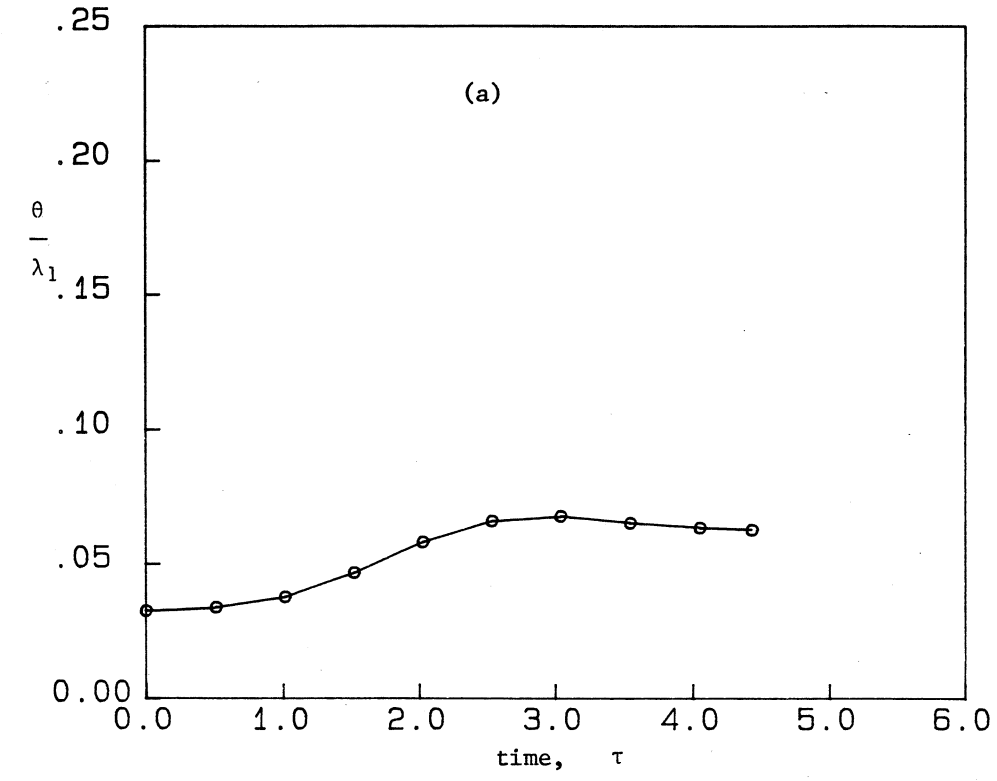

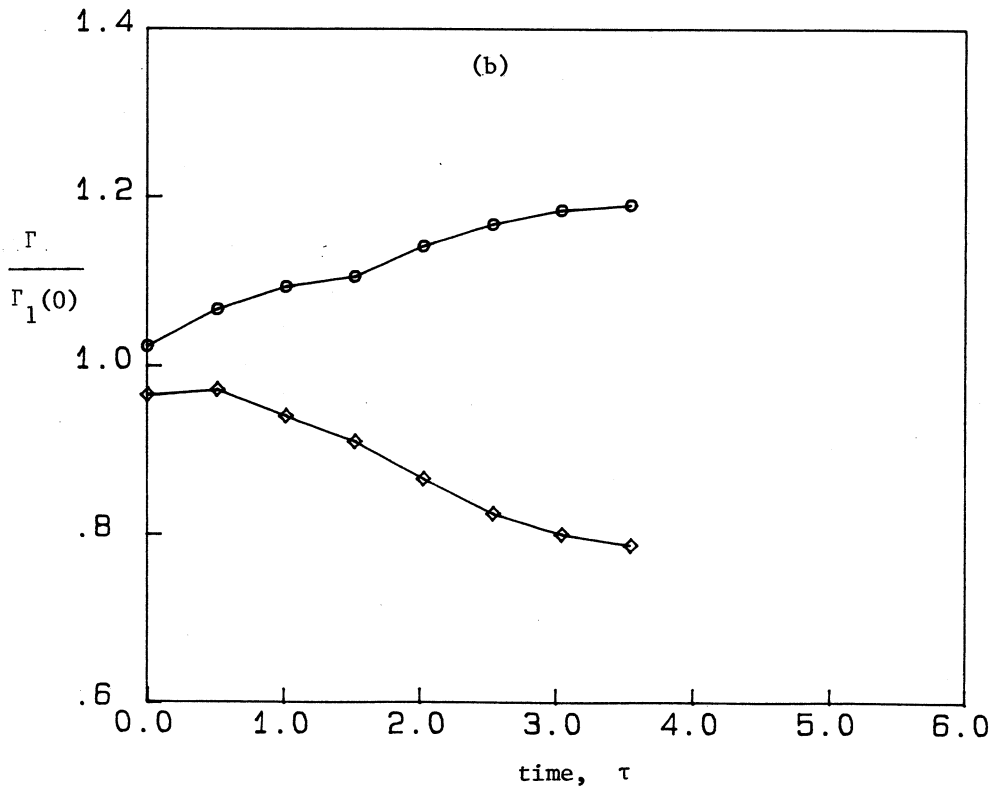

Figure 7.31 : (a) Variation of momentum thickness for tearing event (case 5).
(b) Variation of vortex strengths $\Gamma/\Gamma_1(0)$ for vortex 1 and 2 for the tearing event. Vortex 1 is defined as being the vorticity in $0 < x < \lambda_1$, while vortex 2 is the vorticity in $\lambda_1 < x < 2\lambda_1$ where $\lambda_{comp} = 2\pi$.

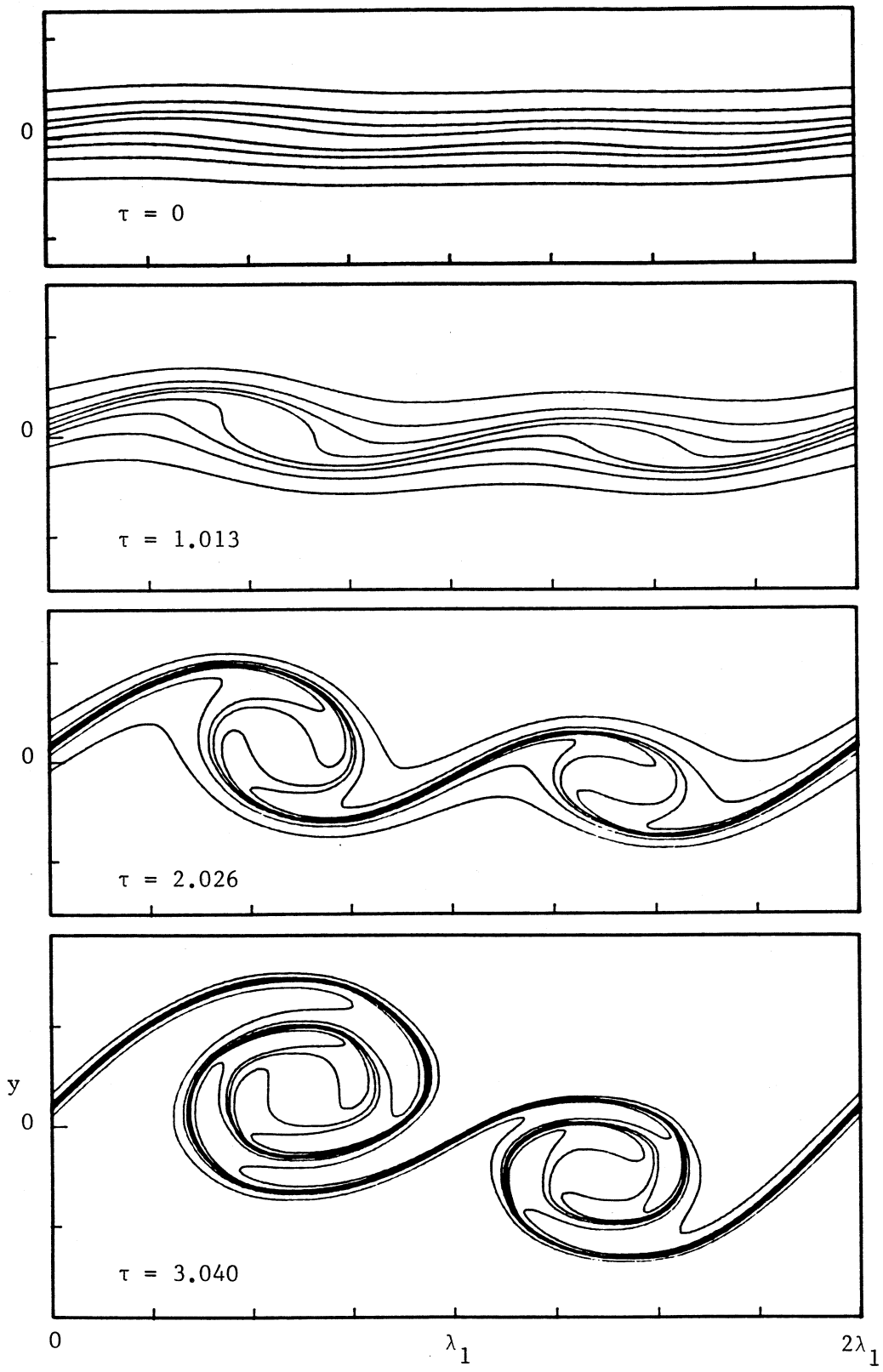

Figure 7.32 : Layer evolution for a combined pairing/tearing event, $\delta_\omega/\lambda_1 = 0.875/2\pi$ $a_0/\lambda_1 = 0.05/\pi$, initial disturbance $f_1^{(4)} + e^{i\pi/4} f_2^{(4)}$ (case 6, table 7.5)

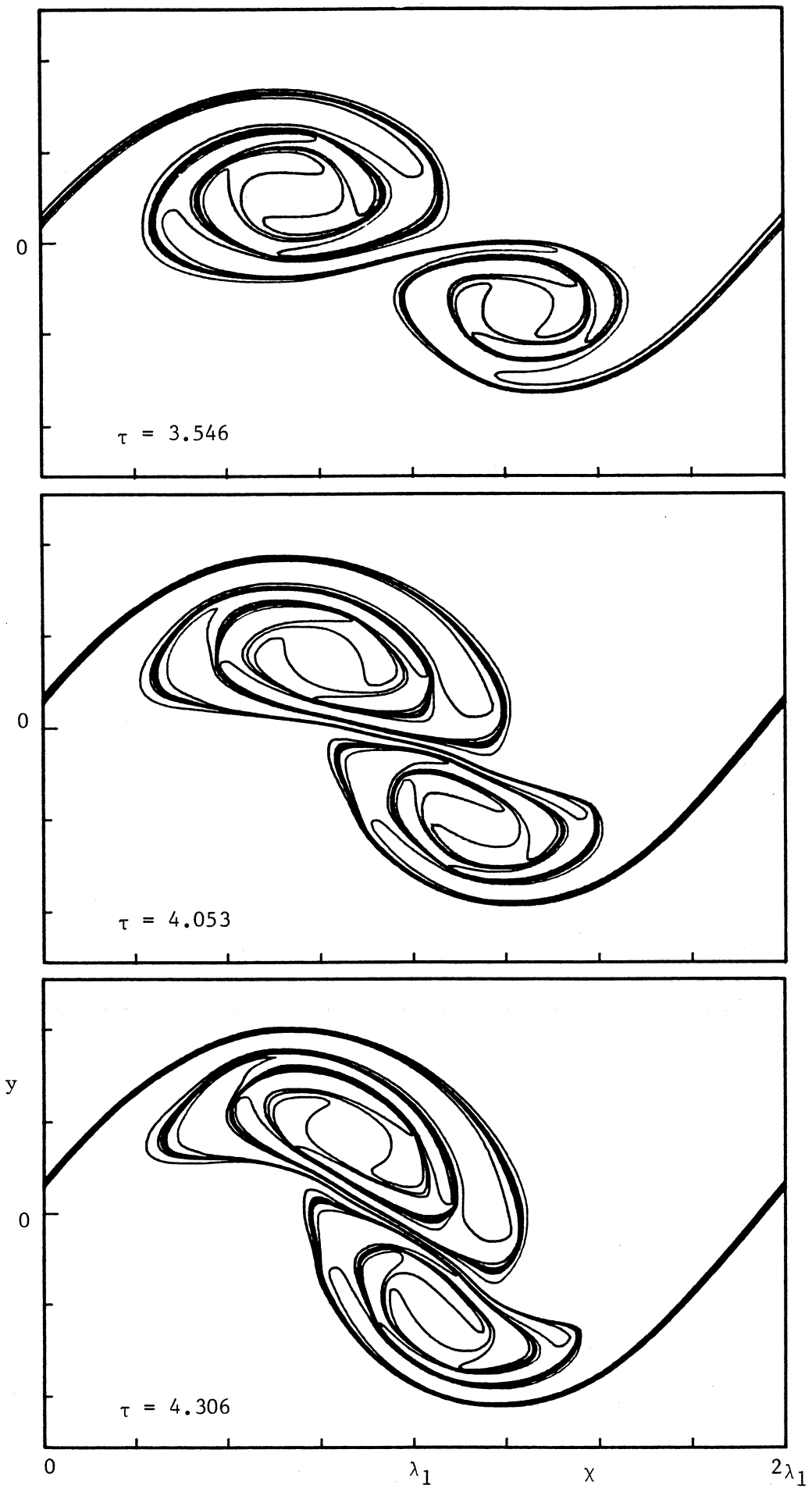

Figure 7.32 : continued.

(a)

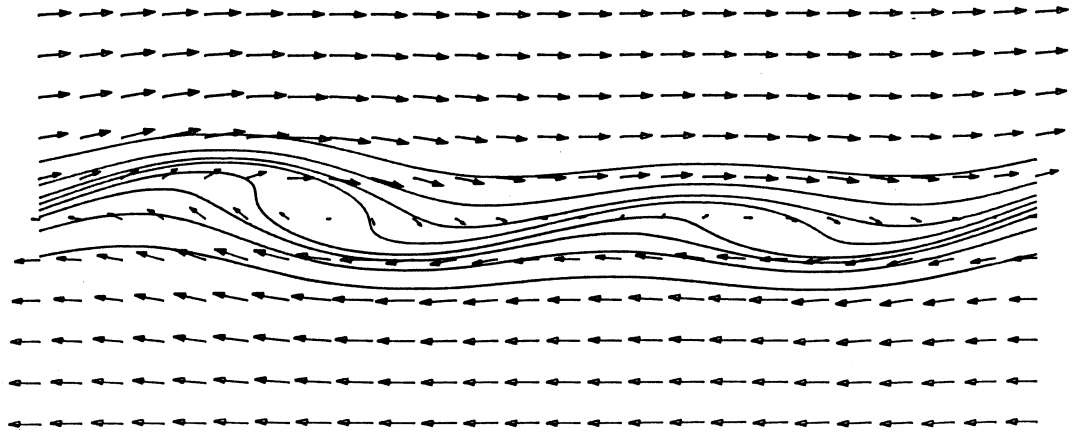

(b)

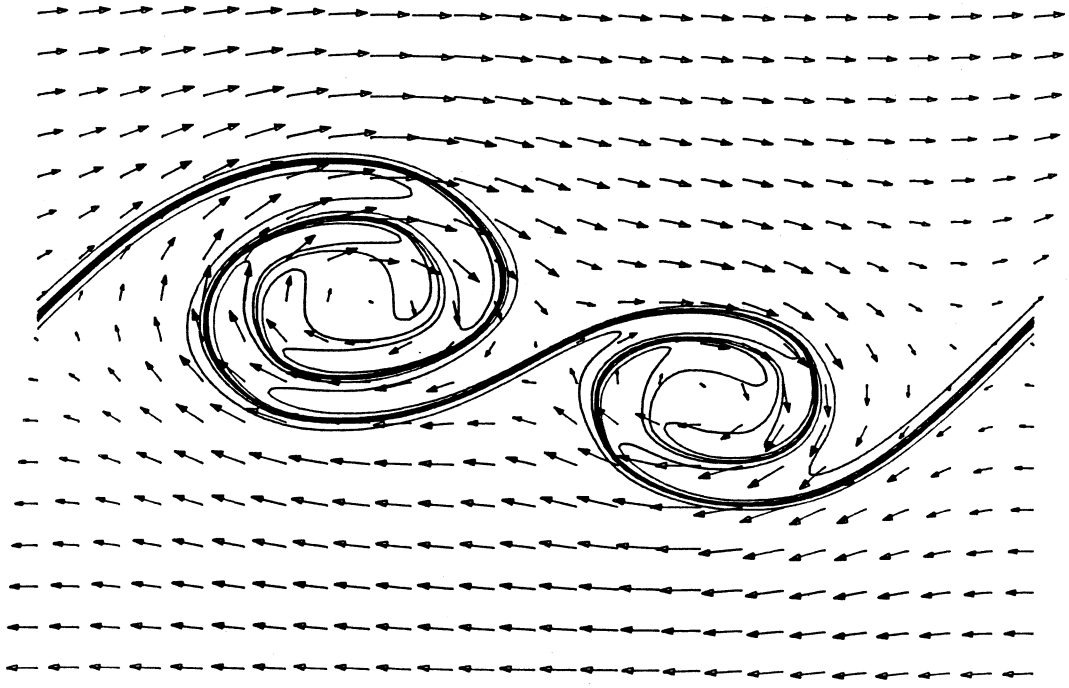

Figure 7.33 : Vector velocity plots for the combined tearing/ pairing event, (case 6).
(a) τ = 1.013
(b) τ = 3.040

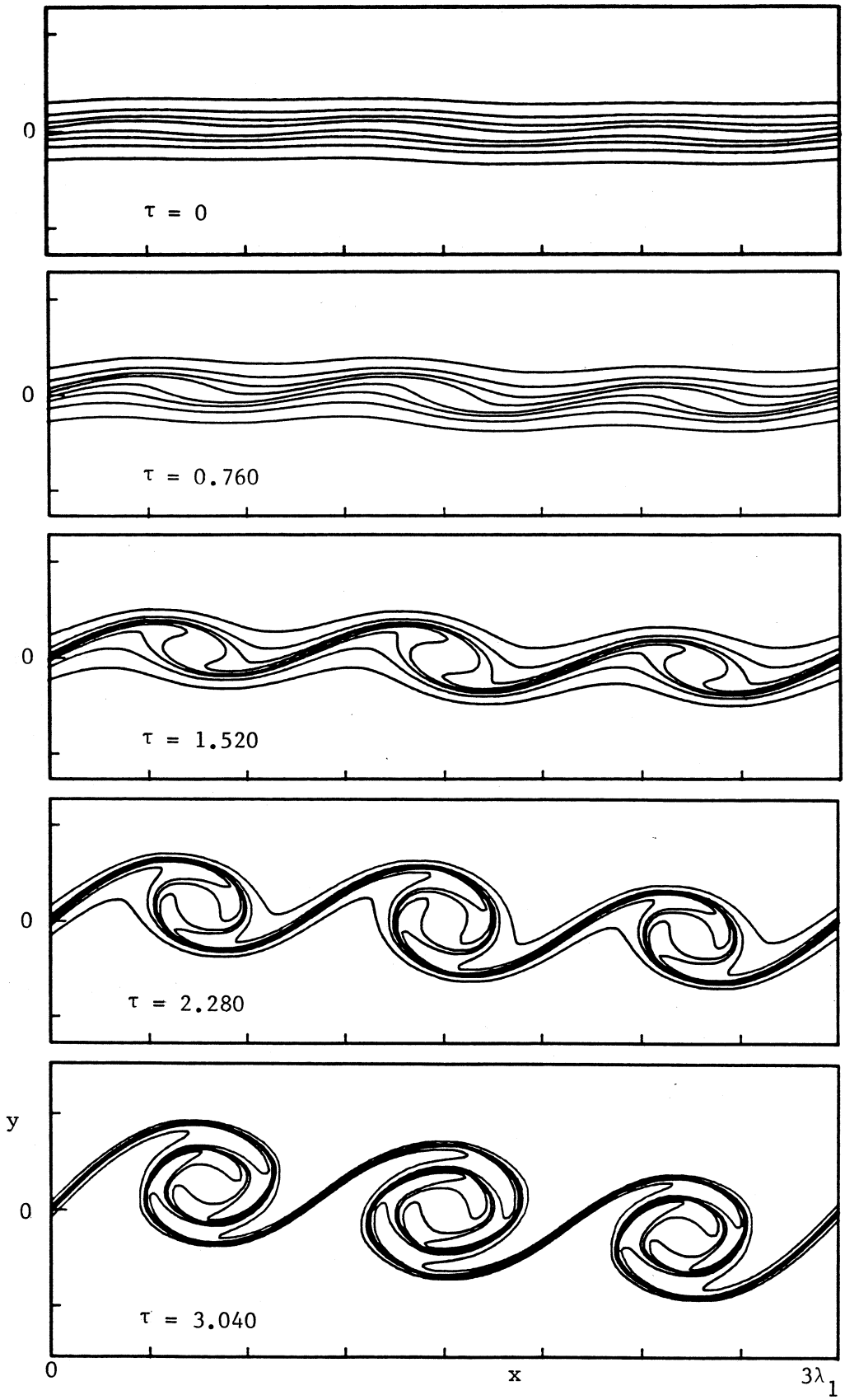

Figure 7.34 : Evolution of an M = 4 layer showing a three vortex coalescence. $\delta\omega/\lambda_1 = 0.875/2\pi$ $a_0/\lambda_1 = 0.05/\pi$, initial disturbance $f_1^{(4)} + f_3^{(4)}$ (case 7, table 7.5) Tic mark spacing is $3\lambda_1/8$.

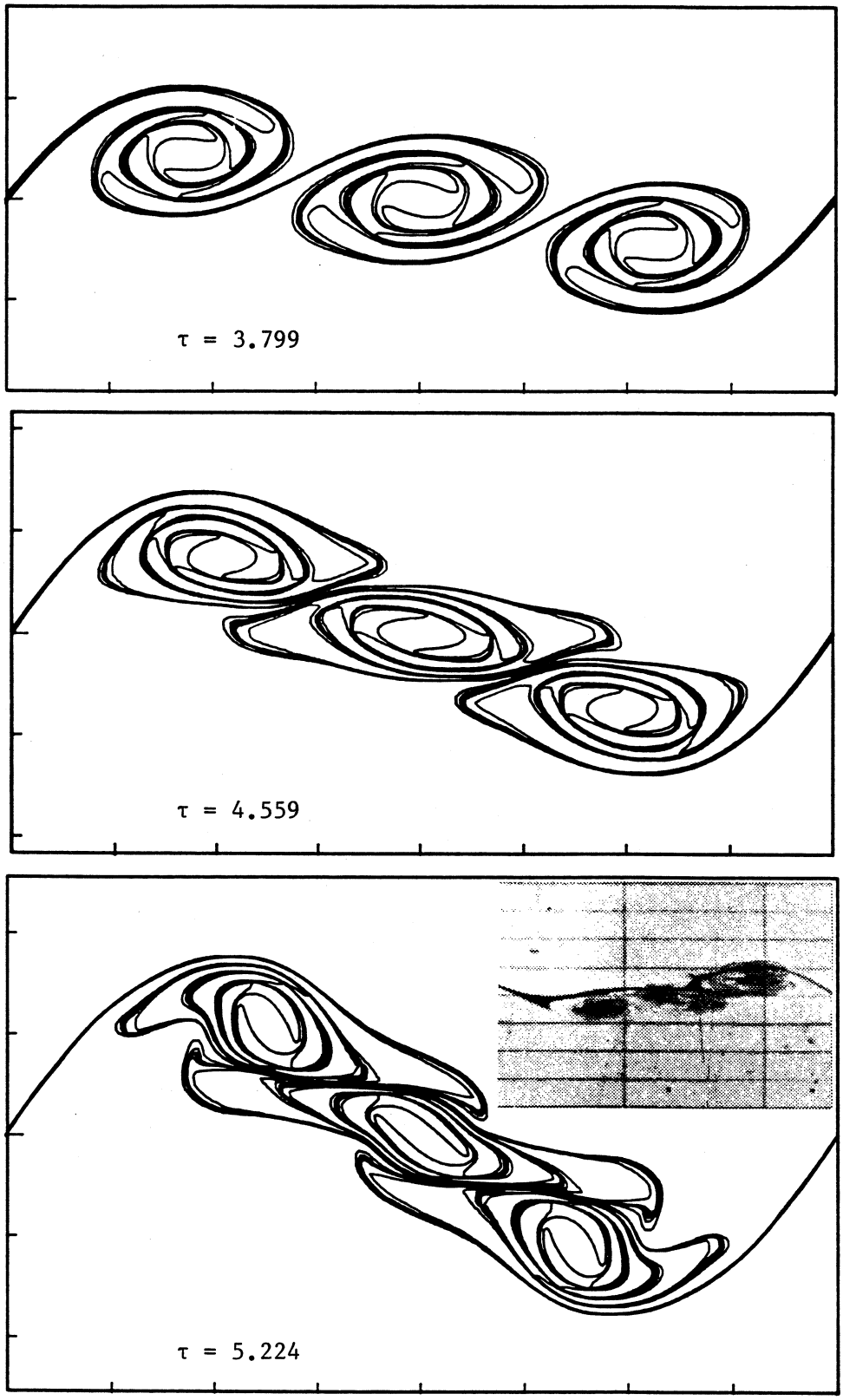

Figure 7.34 continued : Inset on the solution at τ= 5.224 is a reproduction of part of figure 6a (x = 21.0) from Winant & Browand (1974). Note that the shear across the layer is in the opposite sense.

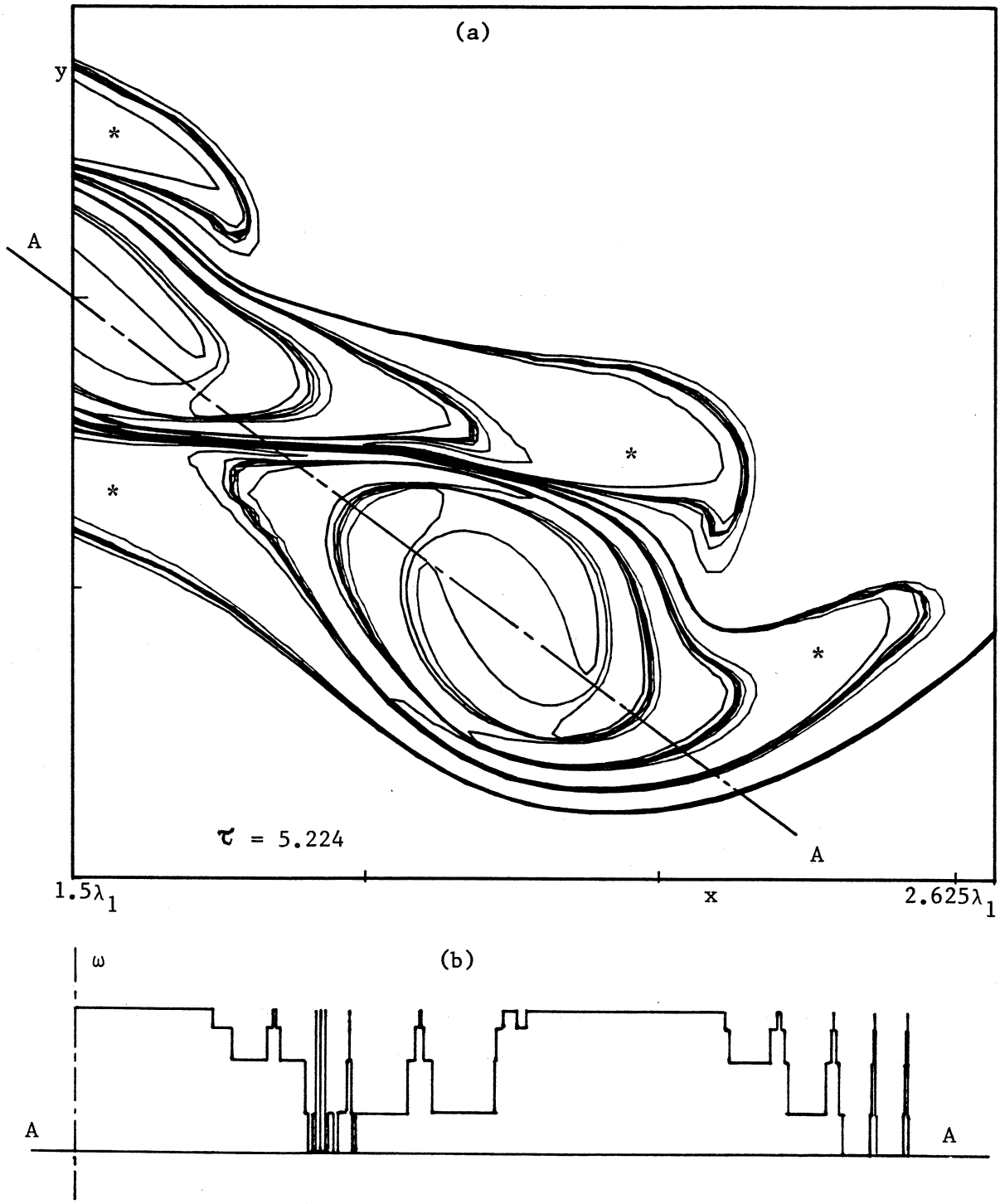

Figure 7.35 : (a) Magnified view of the vortex contours for case 7 (figure 7.32) at $\tau = 5.224$. Tic mark spacing is $3\lambda_1/8$.
(b) Vorticity profile along the section AA.

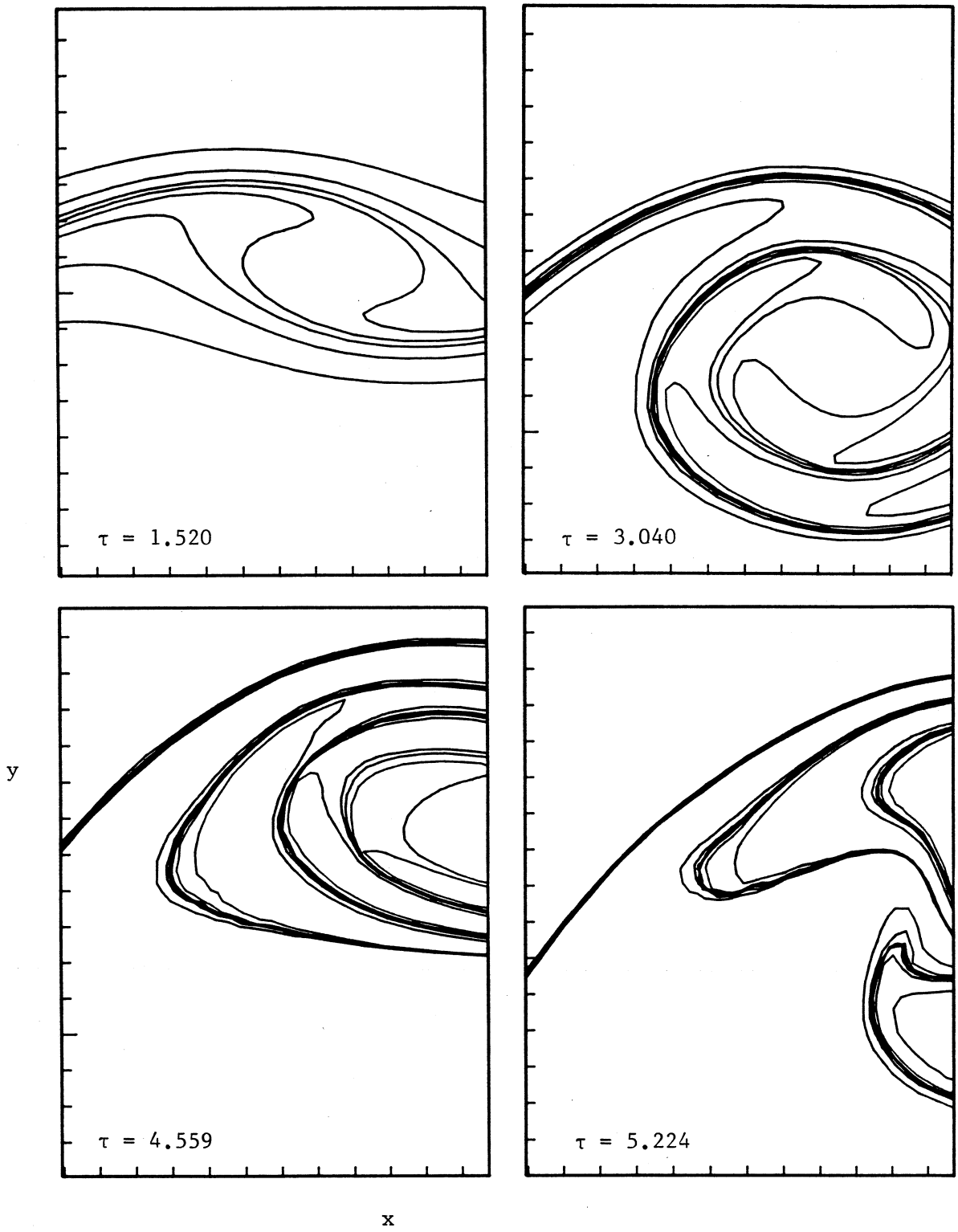

Figure 7.36 : Four magnified views of the contours in case 7 (figure 7.32). Times τ as shown, tic mark spacing = $3\lambda_1/20\pi$

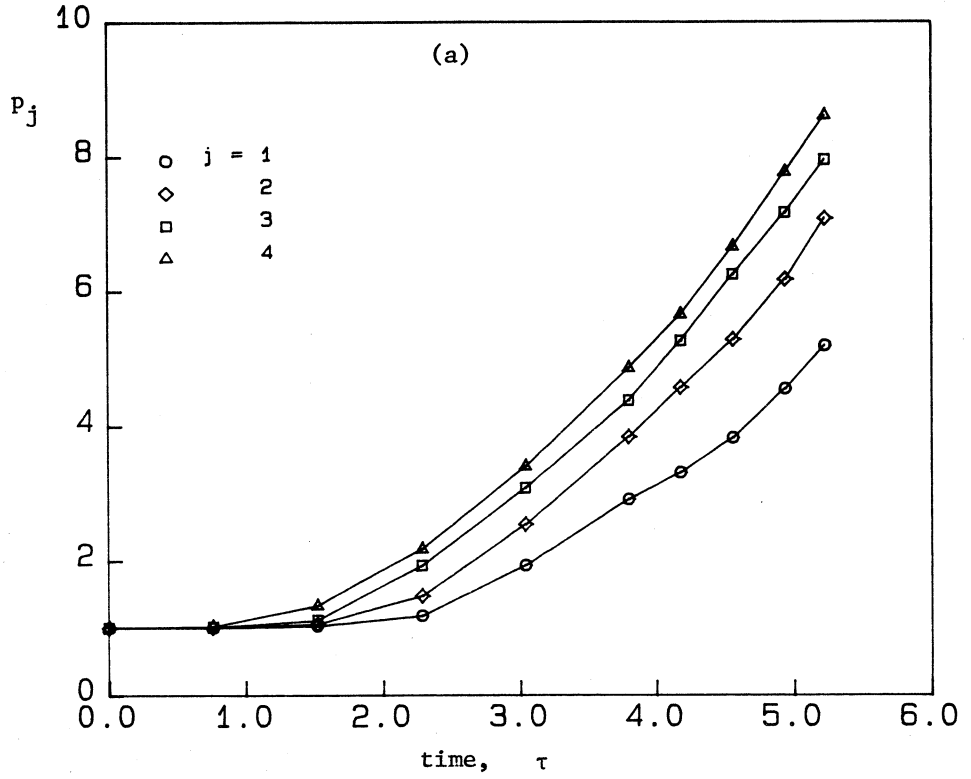

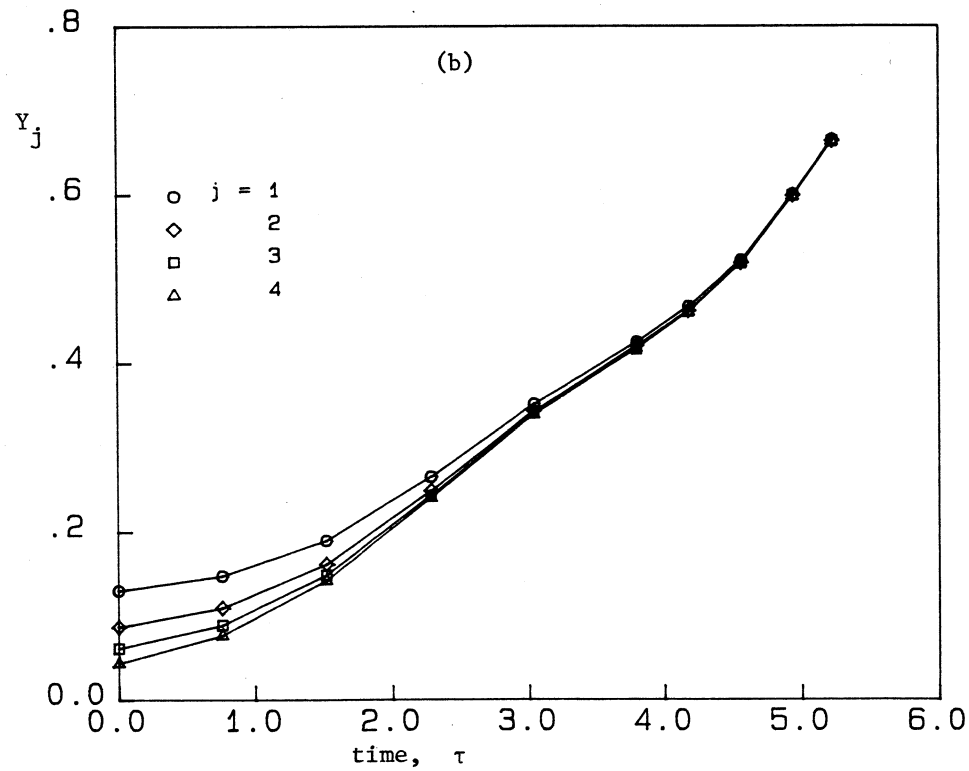

Figure 7.37 : (a) Growth of contour length p_j for three-vortex-event (case 7).

(b) Variation of Y_j with time (case 7).

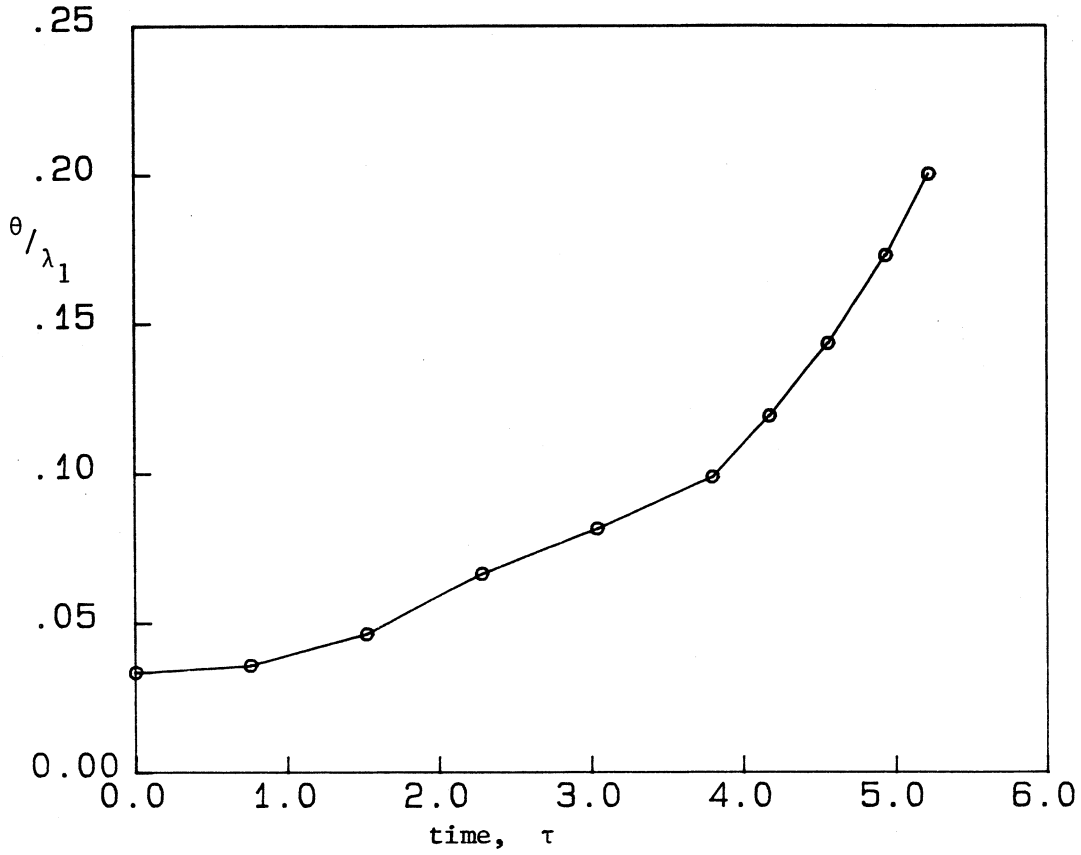

Figure 7.38 : Growth of layer momentum thickness θ for the three-vortex-event (case 7).

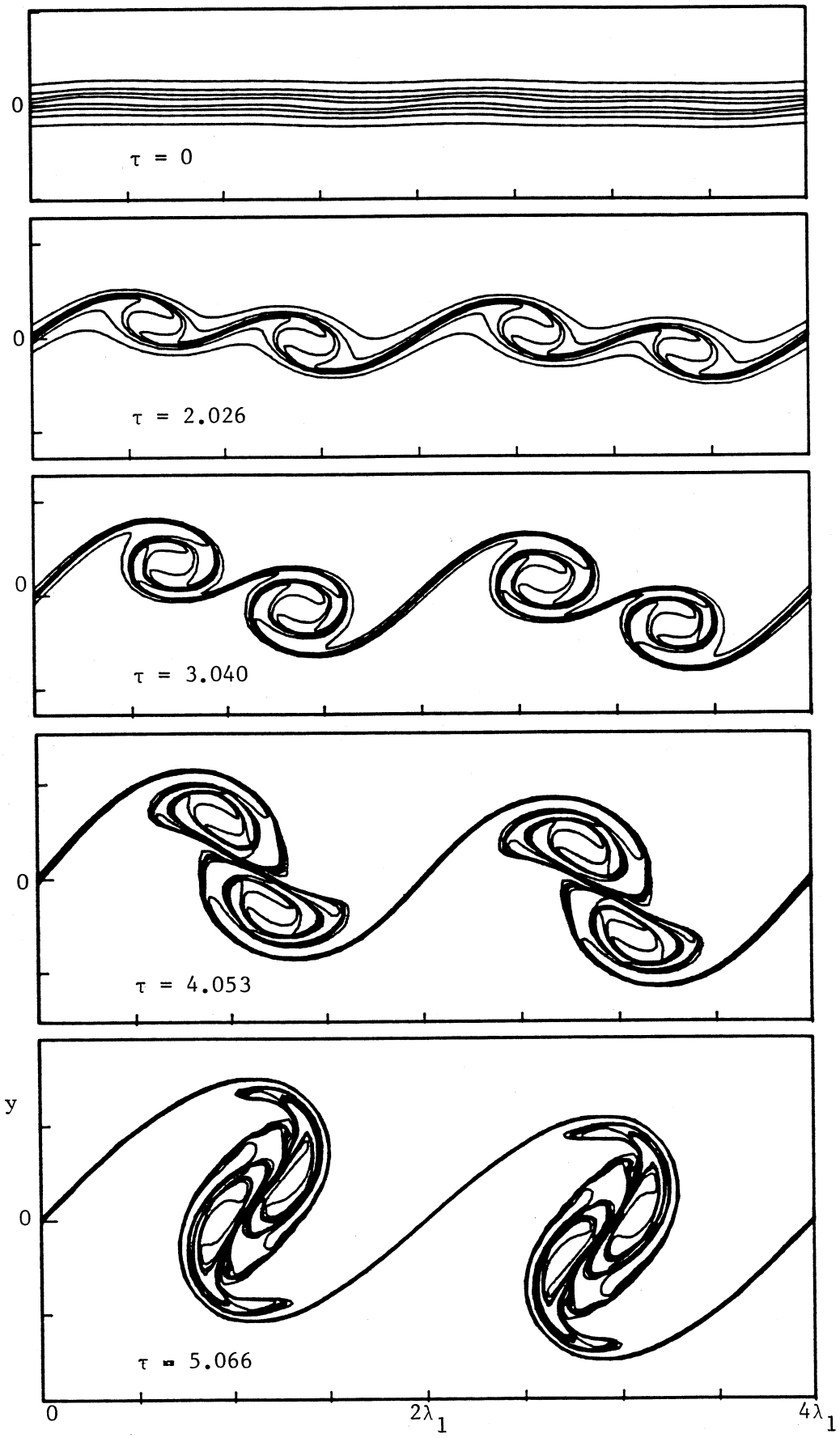

Figure 7.39 : Evolution of an M = 4 shear layer $\delta_\omega/\lambda_1 = 0.875/2\pi$ $a_0/\lambda_1 = 0.04/\pi$, initial disturbance $f_1^{(4)} + f_2^{(4)} + f_4^{(4)}$, (case 8, table 7.5).

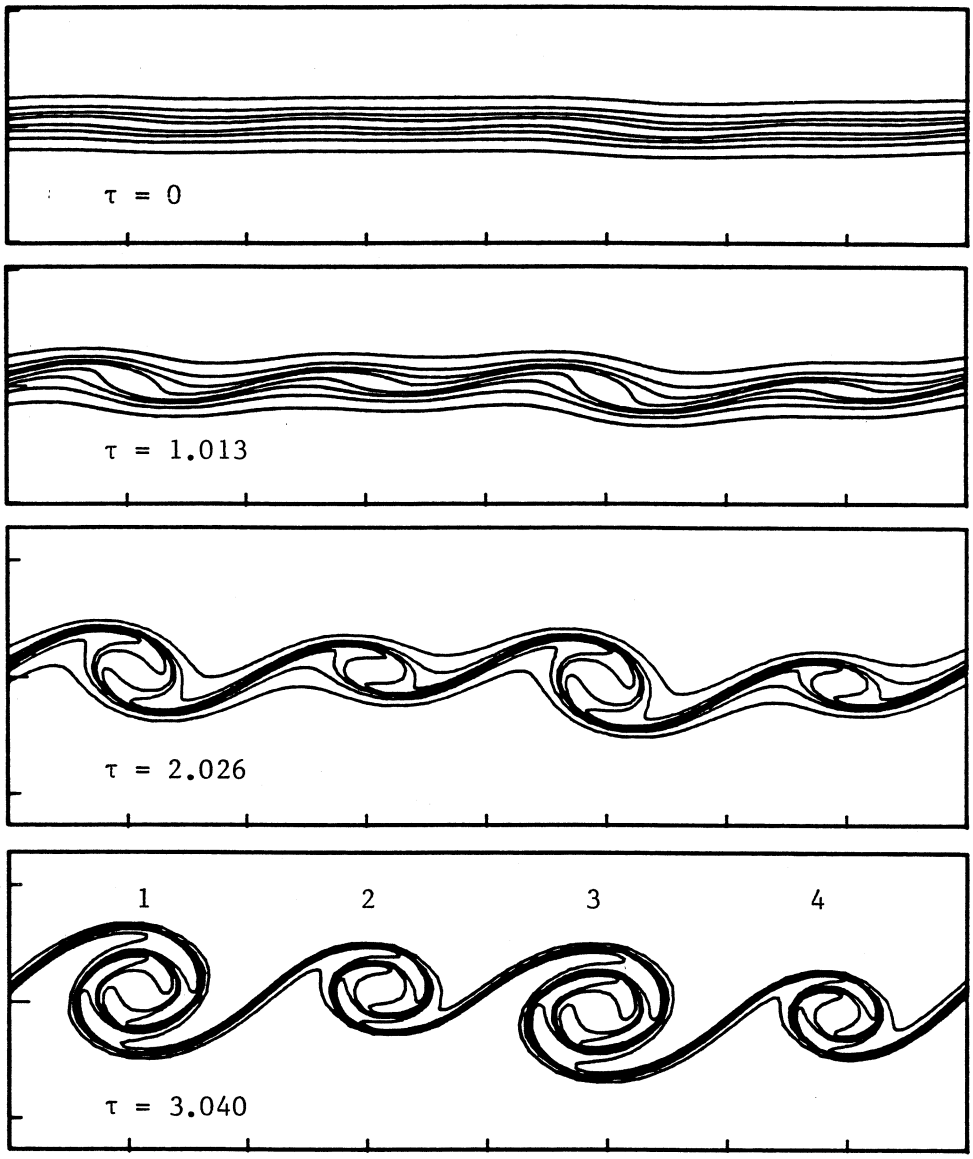

Figure 7.40 : Evolution of an M = 4 shear layer $\delta_\omega/\lambda_1 = 0.875/2\pi$ $a_0/\lambda_1 = 0.04/\pi$, initial disturbance $f_1^{(4)} + e^{i\pi/2} f_2^{(4)} + f_4^{(4)}$, (case 9, table 7.5).

8.0 SECONDARY STREAMWISE VORTICES

We now explore the evolution of prototype structures for the streamwise vorticity superimposed upon the quasi-two-dimensional base flow of spanwise vortices. Here, we will take the Corcos-Lin model of the secondary vortices as starting point and eschew further consideration of the (unknown) formation mechanism. This CLS model assumes that the secondary vortices consist of an array of highly flattened, ribbon-like vortices with alternating circulations of magnitude Γ_2. Locally, the vortices are aligned with the braid and evolve in the ambient three-dimensional stretching strain field provided by the primary (spanwise) vortices. The model (cylindrically-symmetric) flow is exactly periodic in the spanwise direction and consists of rectilinear vortices whose axes are aligned with the extensional axis of a uniform plane stretching strain.

Previous simulations by Corcos & Lin (1984) have simulated the secondary vortex flow configuration up to $Re_2 = O(500)$ where $Re_2 = \Gamma_2/\nu$. However, we are interested in high resolution simulations at the nominal limit $Re_2 = \infty$ and so use the CD method to provide evolutionary histories for selected piecewise-constant vorticity distributions. Corcos & Lin find that the vorticity distribution collapses into compact, nearly-axisymmetric cases on two length scales; one on the wavelength of the vortex array (λ_2) and another on the thickness of the individual vortices (δ_2).

8.1 Flow Configuration

Consider the interaction of an array of nonuniform inviscid vortices (the secondary vortices) with an applied stretching-strain field. In Cartesian (x, y, z)-coordinates, the full unsteady velocity field, $\underline{u}$, has components

$$u_x = V_x(x,y,t) \quad , \tag{8.1a}$$

$$u_y = V_y(x,y,t) - \gamma(t)\, y \quad , \tag{8.1b}$$

$$u_z = \gamma(t)\, z \quad , \tag{8.1c}$$

Here, the terms containing $\gamma(t)$ define the uniform (y, z)-plane-strain field induced externally by the primary vortices and V_x, V_y are the components of the self-induced velocity field of the secondary vortices. Referring to figure 8.1, z is directed locally along the braid of the nominally two-dimensional primary vortex motion, x lies in the spanwise direction and y is normal to (x,z). Note that these coordinate directions are not the same as those defined for the primary, quasi-two-dimensional motions. The only nonzero component of the vorticity field is $\omega_z(x,y,t)$. The velocity and vorticity fields of equations (8.1), (8.2) are such that vortex lines are of infinite extent and are always parallel to the z-axis.

The secondary vortex structure at the midpoint of the braid is modelled here as an infinite x-wise periodic array consisting of one row of identical vortices with centroids at $y = 0$, $x = (p + 1/4)\lambda_2$, $p = -\infty \ldots \infty$ and circulation $-\Gamma_2$, and of a second row of identical vortices with centroids at $y = 0$, $x = (p - 1/4)\lambda_2$, $p = -\infty \ldots \infty$ and circulation Γ_2. Figure 8.2 shows two members of the array corresponding to $p = 0$, which we denote by vortex 1 (right hand) and vortex 2 (left hand) respectively. Geometrically, vortex 2 is the mirror image of vortex 1 in $x = 0$, and it has circulation equal in magnitude, but opposite in sign, to that of vortex 1. At time t each vortex appears in (x, y) cross-section as a nested set of M nonintersecting contours which delineate discontinuities in the piecewise-constant ω_z field. We denote the contours of vortex 1 by the counterclockwise running curves $C_j(t)$, counting $j = 1 \ldots M$ from the outermost contour inwards. The domain of the (x, y)-plane bounded by $C_j(t)$ and $C_{j+1}(t)$ is denoted by $R_j(t)$ and has area $A_j(t)$. $R_M(t)$ is interior to $C_M(t)$ while $R_0(t)$, $0 \le x \le \lambda_2/2$ is exterior to $C_1(t)$. The initial vorticity distribution for vortex 1 is

$$\omega_z(x,y,0) = \begin{cases} \omega_0(x,y,0) = 0 \text{ in } R_0(0) \quad , \\ \omega_j(0) = \text{const in } R_j(0), \; j = 1 \ldots M \end{cases} \tag{8.2}$$

Hence from equation (3.24) for $t \geq 0$

$$\omega_z(x,y,t) = \omega_j(t), \text{ in } R_j(t) \quad , \tag{8.3a}$$

$$\omega_j(t) = \omega_j(0) \exp[Q(t)] \; , \; j = 1 \ldots M, \tag{8.3b}$$

also

$$A_j(t) = A_j(0) \exp[-Q(t)] \quad , \tag{8.4}$$

$$\Omega_j(t) = \omega_j(t) \; A_j(t) = \omega_j(0) \; A_j(0) \quad , \tag{8.5}$$

where Ω_j is the magnitude of the circulation contained in R_j. The Ω_j, $j = 1 \ldots M$ are invariants of the vortex motion and $\Gamma_2 = \sum_j \Omega_j$ is the magnitude of the total circulation of vortex 1.

8.2 Initial Conditions and Parameters

The initial conditions refer to the geometrical shape of the C_j and the values of the $\omega_j(0)$, $j = 1 \ldots M$. For most simulations the C_j were initially elliptically shaped as illustrated, for example, in the first frame of figure 8.3. The dimensions of the major and minor ellipse axes $(r_1)_j$ and $(r_2)_j$ respectively, and the values of $\omega_j(0)$ were chosen to model a nearly sinusoidal distribution of vorticity along $y = 0$, and a normal vorticity distribution along $x = \pm \lambda_2/2$. We define the initial vorticity thickness δ_ω for each vortex as

$$\delta_\omega = \frac{2 \sum_{j=1}^{M} \omega_j(0) [(r_2)_j - (r_2)_{j+1}]}{\omega_{max}} \quad , \tag{8.6a}$$

where $(r_2)_{M+1} = 0$ and $\omega_{max} = \omega_M(0)$. This is equivalent to the vorticity thickness definition for the two-dimensional shear layer (see equation (7.11d)). The vortex aspect ratio is defined as

$$a_2 = \lambda_2/(2\delta_\omega) \quad . \tag{8.6b}$$

One example of a nonelliptical vorticity distribution was tried to check the sensitivity of the vortex dynamics to small changes in the vorticity distribution. The definition of the contour shape for C_1 in the first quadrant is given by the (x, y)-coordinate pairs in table 8.4.

Since the formation mechanism which initially produces the secondary vortices is not fully understood (see section 6.3), their strength and typical geometry at the time when nonlinear self-interaction begins to influence their evolution remains uncertain. We therefore considered three initial configurations corresponding to a_2 = 12.7, 25.8 and 51.7, for the M = 4 profile, a_2 = 14.5 for the M = 8 profile, and one nonelliptical case with a_2 = 12.7. The M = 4 cases were combined with several values of the strain parameter γ.

The respective ellipse and vorticity parameters are summarized in tables 8.1 and 8.2 for M = 4 and M = 8 respectively. The initial number of nodes, distributed on C_1 were $N_1(0)$ = 60 (a_2 = 12.7, 14.5), $N_1(0)$ = 60 (a_2 = 25.8) and $N_1(0)$ = 100 (a_2 = 51.7). For the nonelliptical profile, $N_1(0)$ = 80. Proportionally smaller $N_j(0)$, j = 2,3,4 were used on the inner contours.

The only further parameter (the local strain environment) is the dimensionless stretching strain rate

$$\gamma_2 = \gamma\lambda_2{}^2/(4\pi^2\Gamma_2) \quad . \tag{8.7}$$

Using the mixing layer parameters from section 6.4, $\gamma \approx \pi\Delta U/(2\lambda_1)$, $\lambda_2 = \lambda_1$ and $\Gamma_1 \approx \Delta U\lambda_1$, gives

$$\gamma_2 \approx (8\pi\beta)^{-1} \quad , \tag{8.8}$$

where $\beta = \Gamma_2/\Gamma_1$. The hot wire measurements of Jimenez (1983) (see also Jimenez et al 1985) indicate that $\beta = 0(1)$. Using β = 0.25 and 0.5 gives $\gamma_2 \approx$ 0.16 and 0.08 respectively.

Presently we take $\gamma_2 = 0,\ 0.1,\ 0.2$ and 0.4. This last value is large but is of interest as an extreme case. A characteristic time-scale for the flow can be defined by

$$T_c = \frac{\lambda_2^2}{4\pi^2\Gamma_2} \quad , \tag{8.9}$$

so that the nondimensional time

$$\tau = t \ / \ T_c \quad , \tag{8.10}$$

where t is the physical time. Lengths and times are normalized by setting $\lambda_2 = 2\pi$ and $\Gamma_2 = 1$.

8.3 Simulation Results and Discussion

Sequences of evolving contour portraits which depict the timewise deformation of typical vortex pair for the range of a_2 and γ_2 treated are shown in figures 8.3 - 8.4 and 8.10 - 8.23. Table 8.5 contains a summary of the full set of simulations performed.

We regard the simulations as quantitatively reliable in $0 \le \tau \le \tau_{max}$ where, for most cases displayed, τ_{max} is a value somewhat larger than those indicated in the final frame of each sequence. Computations were generally performed with code-version B (table 4.1) and node-adjustment-parameter set 3 (table 4.3). Individual calculations were finally terminated for $\tau \ge \tau_{max}$ when either *(i)* $\max_j[\Delta(\Omega_j)] \ge \varepsilon^{(2)}$, where presently $\varepsilon^{(2)} = 0(10^{-2})$ and/or *(ii)* $\max_j[N_j(\tau)] \ge N_{max}$, where the value $N_{max} = 1000$ was determined by available computing resource limitations of a 2Mb virtual machine on the University of Queensland's IBM 3083. The onset of *(i)* was usually accompanied by the appearance of substantial spatial oscillations in the shape of the C_j of the order of the local node spacing. These oscillations were taken to indicate insufficient resolution. $\mathrm{Max}_j[N_j(\tau)]$ invariably occurred on C_1, with a typical value of 600 and $\Sigma_j N_j(\tau) = 0(1500)$.

Figures 8.3 and 8.13 show the array evolution with $\gamma_2 = 0$, (i.e., no out-of-plane stretching) for $a_2 = 12.7$ and $a_2 = 25.8$ respectively. These cases are of interest since first they provide solutions against which the influence of $\gamma_2 > 0$ can be evaluated, and second, variations in E(t) given by equations (4.23-4.25) may be used as a global check on accuracy.

At $\tau = 4$ in the sequence of figure 8.3, the differential rotation of the C_j induced by the initial vorticity concentration towards the centre of each vortex is clearly evident. Later, for $\tau \geq 12$, this results in the formation of a central vortex core. Simultaneously, the vortex tails (those regions of the initial vortex closest to neighbouring vortices) are drawn out into thin, curved vortex layers whose thickness is small compared to the local radius of curvature. The overall result, by $\tau = 16$, is the generation of a rolled-up double spiral vortex similar to those found in vortex coalescence computations (Zabusky et al 1979; Overman & Zabusky 1982; Jacobs & Pullin [1]). Note that the inner contours C_3 and C_4 which contain roughly 25% of Γ_2 at $\tau = 16$ in figure 8.3 quickly collapse into the vortex core. In contrast, the outer contours C_1 and C_2 undergo continuous and large deformation both within the vortex core and as part of the spiral filament, resulting in large vorticity gradients at the outer edge of the core.

The sequence of figure 8.4 with $a_2 = 12.7$, $\gamma_2 = 0.1$ shows the expected exponential reduction in the $A_j(\tau)$ as vortex lines are stretched longitudinally by the z-component of the strain. With $\gamma_2 = 0.2$ and 0.4 in figures 8.10 and 8.11 respectively, the increased spin induced by the vorticity amplification is strong enough to substantially reduce the time-scale of the initial vortex core roll-ups, when compared with the $\gamma_2 = 0$ evolution. Although the model flow is highly idealized, the simulations indicate that the interface between the two free streams of the mixing layer becomes highly corrugated in the braid region (see also the perspective view obtained by Jimenez et al 1985) and, in cross-section, the

braid has been distorted into mushroom-shaped vortical structures, similar to those photographs taken by Bernal (1981). The most striking example is shown in figure 8.7.

By analogy with the roll-up of the primary shear layer (chapter 7), we assume that the dimensional roll-up time-scale for $\gamma_2 = 0$ is order λ_2/σ_0, where σ_0 is the velocity jump across the flattened vortex at its centroid at $t = 0$. Using a vortex-sheet model with $\sigma(x) = \sigma_0 \sin(2\pi x/\lambda_2)$, where $\sigma_0 = \pi\Gamma_2/\lambda_2$, in conjunction with a similarity transformation (equation 3.28 here; Lundgren 1982) which relates stretched and equivalent unstretched two-dimensional vortex flows, we estimate the dimensionless roll-up time-scale for $\gamma_2 > 0$ as

$$T_r \approx \gamma_2^{-1} \ln(1 + 4\pi\gamma_2) \quad , \qquad (8.11)$$

in broad agreement with the trends shown in figures 8.3 - 8.4 and 8.10 - 8.11. In figure 8.11 at $\tau = 5$, the beginning of a local shear instability may be seen on each flattened spiral vortex arm. This instability occurs at the tip of C_2 presumably because of the contour shape perturbations caused locally by the vorticity gradient along the vortex sheet. (The vorticity thicknesses, however, are in the range resulting in high growth rates of perturbations according to the linear theory discussed in section 7.2 and appendix 5.) Thus, the actual site of the local instability is determined by the artificial and nonsmooth character of the piecewise-constant vorticity field. However, a continuous initial vorticity field will generally contain local nonuniformities qualitatively similar to those modelled presently by vorticity discontinuities. We therefore expect the appearance of local or tertiary instabilities dynamically equivalent to those produced in the CD simulations shown here.

A check on the sensitivity of the vortex dynamics to the number of contours defining the piecewise-constant vorticity profile was undertaken by performing a simulation with $M = 8$, $a_2 = 14.5$ and $\gamma_2 = 0.1$. The evolution is displayed in figure 8.7 and is effectively a higher resolution simulation of the

case shown in figure 8.4 which has the same initial outer contour, timescale and strain environment. The computation was performed on the CSIRO's Cyber 205 using code-version C (table 4.1) and node-parameter set 2 (table 4.3). There is little difference between the major features of the two cases but the M = 8 case results in a slightly faster roll-up into a more compact core and also generates smoother spiral arms that wind about the core.

The sensitivity of the dynamics to contour shape was partly explored by performing a simulation with a nonelliptical contour shape as the initial condition. The arbitrarily selected shape (defined in table 8.4) provides a vorticity profile that is closer to being continuous in the spanwise direction than that provided by the initially elliptic contours. Figure 8.9 shows the evolution of such a vorticity distribution. The gross features of this case are very similar to those developed by the corresponding elliptical initial condition of figure 8.4. However, there is *(i)* a slightly slower roll-up of the vortex core due to the reduction of circulation in the region near the centroid of the vortex and *(ii)* the formation of bulbous tips on the spiral arms.

The trend of the simulations with $a_2 = 25.8$ ($\gamma_2 = 0$, 0.1, 0.2, 0.4) in figures 8.13 - 8.19 and with $a_2 = 51.7$ ($\gamma_2 = 0.1$, 0.2) in figures 8.20 - 8.23 shows some resemblance to those for $a_2 = 12.7$ but with notable differences in detail. The more flattened initial vortex shape leads to enhancement of a shear instability. In some cases, for example figures 8.17 and 8.20, these local instabilities dominate the evolution to the extent that each vortex history is perhaps best viewed as a series of local roll-ups of the type which were shown by Lin & Corcos (1984, §4) to evolve on infinite, stretched shear layers subject to periodic streamwise perturbations. The stretched periodic shear layer will be the subject of discussion in chapter 9. These (tertiary) vortex cores are connected by their own system of thin braids, each undergoing biaxial stretching caused by the combined strain fields of the

primary and secondary vortices. By analogy with the (uncertain) formation mechanism for the secondary vortices, we might speculate that this new braid system may provide sites for the production of still higher-order structure orthogonal to and acting as an energy sink to the secondary vortices.

In figures 8.12, 8.15, 8.18 - 8.19, and 8.21 - 8.22 we show magnified views of the vortex core regions at selected times. These views illustrate the fine structure that has evolved in the vorticity field. Shown inset in figure 8.12 and 8.15 are vorticity distributions obtained along cuts through the vortex centroid. Notice the reversal in sign of the vorticity gradient produced near the outer edge of the core by roll-up of contour C_3 interior to the vortex. On a long time scale we would expect that the accelerating differential-rotation in the vortex core would wind these gradient reversals into a spiral embedded within weaker ambient core vorticity, thus producing even finer scales of motion than those generated on the "outer" spiral.

The details of figures 8.19 and 8.22 reveal corrugations of the C_j on the scale of the local node spacing which are not visible in the corresponding larger-scale plots of figures 8.17 and 8.20 respectively. This is a purely numerical instability which signals the breakdown of the computation. It appears because the node-adjustment scheme is ultimately unable to provide, within the bound $\max [N_j(t)] < N_{max}$, the small-scale node spacing required for the resolution of the very finest scales of motion. For figure 8.19 we find $\Delta(\Omega_1) \sim 0.003$, $\Delta(\Omega_2) \sim 0.01$, $\Delta(\Omega_3) \sim 0.04$, $\Delta(\Omega_4) \sim 0.08$ (recall the definition in equation 4.22) at $\tau = 3.8$ while for figure 8.22 we find $\Delta(\Omega_1) \sim 0.005$, $\Delta(\Omega_2) \sim 0.01$, $\Delta(\Omega_3) \sim 0.003$, $\Delta(\Omega_4) \sim 0.01$ at $\tau = 3.8$. For these extreme cases (i.e., large a_2) the values of $\Delta(\Omega)$ indicate that the respective solutions are losing quantitative accuracy, and that they provide only a qualitatively faithful picture of the tendency towards the formation of a series of vortex cores through local instabilities. In figure 8.22, we indicate the division of the vortex into core and braid segments at $\tau =$

3.8. The respective fractions of the total circulation in each segment are $\Omega_A \approx .11\Omega$, $\Omega_B \approx .07\Omega$, $\Omega_C \approx 0.35\Omega$, $\Omega_D \approx 0.12\Omega$, $\Omega_E \approx 0.3\Omega$, $\Omega_F \approx 0.27\Omega$ and $\Gamma_2 = 2(\Omega_A + \Omega_B + \Omega_C + \Omega_D + \Omega_E) + \Omega_F$.

A comparison fo the final frame of each simulation suggests that the vortex tails appear to approach a nearly stationary state. This may be understood as follows; in the vicinity of the vortex tails the velocity field may be well approximated by a point vortex model obtained by assuming that the circulation $\pm \Gamma_2$ of each finite area vortex is concentrated at the vortex centroid (see appendix 4). The (x, y)-plane velocity field for this point-vortex array coupled with the stretching strain is

$$u_x - iu_y = \frac{\Gamma_2}{2i\lambda_2}\left\{\cot\left[\frac{\pi}{\lambda_2}(x+iy+\frac{\lambda_2}{4})\right] - \cot\left[\frac{\pi}{\lambda_2}(x+iy-\frac{\lambda_2}{4})\right]\right\} + i\gamma y. \tag{8.12}$$

when $\gamma > 0$, (8.12) exhibits stagnation points at $x_m = \pm m\lambda_2/2$, $y_m = (-1)^m Y\lambda_2/(2\pi)$, $m = 0,1,2...$ where Y is a solution of

$$Y \cosh(Y) - (2\pi\gamma_2)^{-1} = 0 \quad . \tag{8.13}$$

For $\gamma_2 = 0.1$, 0.2 and 0.4, $Y \approx 1.018$, 0.652 and 0.372 respectively. The dimensionless velocity field from equation (8.12) ($\Gamma_2 = 1$, $\lambda_2 = 2\pi$) with $\gamma_2 = 0.1$ is shown in figure 8.5 superimposed on the contour shapes for $a_2 = 12.7$, $\gamma_2 = 0.1$ at $\tau = 10$ from figure 8.4. Also shown in figure 8.5 and in the final frame of each of Figures 8.4, 8.6 - 8.11, 8.14, 8.16, 8.17, 8.20, and 8.23 are segments of the (x, y)-plane stagnation streamlines of (8.12) for the left hand vortex (vortex 2). As the vortex tilts in the anticlockwise direction, it appears that the tips of the flattened vortex tails approach and become trapped in the respective stagnation regions. The competition between this tendency and the contracting vortex core sustains the spiral arms by subjecting the outer filaments to (x, y)-plane extensional strain, while the core is compressed near its centre by a local strain field which is the sum of the (y, z)-plane stretching strain and the

(x, y)-plane strain induced near the vortex centroid by all other members of the secondary vortex array. The agreement with this model is less convincing for the $a_2 = 51.7$ results of figures 8.20 and 8.23 firstly because the point vortex approximation loses accuracy near the vortex tails owing to the extended vortex geometry, and secondly, since the simulation is terminated before the vortex tails have fully rotated into the stagnation region.

In figure 8.6 we show the vortex array evolution calculated using a single contour (M = 1) uniform vorticity model. The total circulation and initial shape of C_1, and hence the mean vorticity is the same as the simulation of figure 8.4. By comparison, we show also on figure 8.6 the evolution of an isolated uniform elliptical vortex subject to a (y, z)-plane stretching-strain field with $\gamma_2 = 0.1$ (see equation 5.1). The initial aspect ratio and strength are the same as those for the left hand member (vortex 2) of the pair shown at $\tau = 0$. Hence, the differences in the subsequent shapes may be attributed to the influence of the array on vortex 2. By $\tau = 10$ both vortex 2 and the isolated vortex have tilted and have changed their shape to some extent, but the array pair exhibit no fine structure remotely comparable to that depicted in the $\tau = 10$ frame of figure 8.4. At $\tau = 16$, which is beyond the range of the present nonuniform vortex computation, the vortices of figure 8.6 have decreased in both area and in effective aspect ratio. This is an example of the Neu (1984a,b) strain induced collapse mechanism for isolated elliptical vortices, modified for vortex 2 by the (x, y)-plane strain of all other members of the array. Lin & Corcos (1984) give an estimate of the collapse time for isolated vortices (their equation 8.8) by assuming collapse following a local balance between the self-induced velocity at the vortex tip and the y-component of the strain velocity. In our notation, this is

$$T_n \approx 60(1 + \eta)^4 \cos^2\theta_e \gamma_2 \quad . \tag{8.14}$$

where η^{-1} is the ellipse aspect ratio and θ_e may be identified with the angle of tilt at t = 10 in figure 8.6. With the parameters of figure 8.6, $T_n \approx 7.5$ which is somewhat less than $T_n \approx 16$ suggested by the results of figure 8.6. For the present nonuniform vortex evolution, the collapse mechanism appears to be only partly effective, since the nonlinear self-induction of the flattened vortices generates a rolled-up and dominant vortex core before substantial local focusing of vorticity by the γ-component of strain can become operative. We note that this result appears to cast some doubt on the relevance of uniform vortex models to the inviscid dynamics of nonuniform vortices at least for those initial distributions that will produce a rapid distortion of the vorticity field.

In figures 8.24 and 8.25 we have plotted the energy associated with vortex array induced fluid velocities in the (x, y)-plane as calculated from equations (4.23-4.25) with a = 12.7 and 25.8 respectively. When $\gamma_2 = 0$, $E(\tau)$ is sensibly constant with errors $(E(\tau_{max}) - E(0))/E(0) \approx 0.005$ in both cases. When $\gamma_2 > 0$, $E(\tau)$ increases because of energy transfer from the stretching strain field to kinetic energy in the (x, y)-plane vortex motion. Further transfers to smaller scales given by the spiral vortex turn spacing and by shear layer instability scales may be expected but these transfers have not been presently resolved in quantitative detail. In a real viscous fluid this energy is eventually dissipated in both the vortex sheet and rod structures generated by the nonlinear vortex evolution.

A quantitative measure of individual vortex deformation during its evolution is shown in figures 8.26 - 8.28, where we have plotted the perimeters of the nested vortex contours against τ. In their flow visualization study, Lasheras, Cho & Maxworthy (1986) indicate that the chemical reaction producing the visible dye is confined to a very thin but highly distorted interface even after the appearance of three-dimensional motions. Hence, we use the growth of the outer contour (C_4) perimeter as a measure of the enhancement of the growth of the interfacial area due to the secondary vortices.

In figures 8.26 - 8.28, C_3 and C_4 both show a sudden reduction near the time of formation of the central vortex core. By contrast C_1 and C_2 exhibit an explosive increase in length as they are advected into and undergo rapid distortion within the spiral vortex arms.

The $Re_2 = \infty$ simulations here are complementary to the moderate Re_2 results of Lin & Corcos (1984) but contain some notable differences. The calculations depicted in figures 4, 7 and 11 of Lin & Corcos at $Re_2 = 508$, 508 and 1950 with $a_2 = 8$, $\gamma_2 = 0.08$, $a_2 = 11.3$, $\gamma_2 = 0.16$ and $a_2 = 18$, $\gamma_2 = 0.11$ respectively, are the results most nearly comparable to ours. The beginnings of the spiral shear-layer formation can be seen in figures 4(c-d) and 11 while the onset of the local shear instability is evident in the highest Re_2case of figure 8. In the moderate Re_2 simulations the intensification of vorticity by the strain field and the consequent balance effected by the enhanced viscous diffusion appear to attenuate the radial vorticity oscillations characteristic of spiral shear layers. This attenuation results in the vortex tail remaining ,as for example in figure 4(d), only as an appendage to the well formed nearly axisymmetric Burgers vortex. By comparison, the results here indicate that the $Re_2 = \infty$ roll-up of individual vortex influenced by the induced strain due to the rest of the array can effectively lead to the formation of new spiral vortex layers containing several turns on a time scale comparable with both γ^{-1} and the vorticity focusing time scale. At large but realistic Re_2, these results together suggest a mechanism whereby vortex sheets may be continually created by spiral production following roll-up associated with nonlinear secondary or higher-order instabilities, and destroyed by relaxation via the Lundgren (1982) mechanism towards the asymmetric Burgers vortex of Robinson and Saffman (1984).

Table 8.1 : Initial geometry and vorticity distribution for vortex 1 of the 4 contour (M = 4) simulations for three initial geometries. Values of δ_ω are 0.248, 0.122, 0.0608.

j	$(r_1)_j$	a_2 = 12.7 $(r_2)_j$	$\omega_j(o)$	a_2 = 25.8 $(r_2)_j$	$\omega_j(o)$	a_2= 51.7 $(r_2)_j$	$\omega_j(o)$
1	1.53	0.208	-0.63	0.102	-1.29	0.0512	-2.57
2	0.918	0.125	-1.48	0.0612	-3.02	0.0306	-6.037
3	0.535	0.0728	-2.00	0.0357	-4.08	0.01785	-8.159
4	0.247	0.0336	-2.30	0.0165	-4.69	0.00824	-9.382

Table 8.2 : Vorticity profile for the 8 contour secondary vortex. Initial geometry and vorticity distribution for vortex 1 of the 8 contour(M = 8) simulations for two initial geometries. Values of δ_ω are 0.217 and 0.106.

j	$(r_1)_j$	a_2 = 14.5 $(r_2)_j$	$\omega_j(0)$	a_2 = 29.6 $(r_2)_j$	$\omega_j(0)$
1	1.53	0.208	-0.2121	0.102	-0.4326
2	1.316	0.179	-0.4899	0.0877	-1.000
3	1.117	0.152	-0.8601	0.0745	-1.754
4	0.933	0.127	-1.320	0.0622	-2.692
5	0.750	0.102	-1.780	0.0500	-3.630
6	0.581	0.0541	-2.230	0.0388	-4.548
7	0.398	0.0541	-.2720	0.0265	-5.548
8	0.214	0.0291	-3.000	0.0143	-6.119

Table 8.3 : Initial geometry and vorticity distribution for vortex 1 of the nonelliptical vorticity distribution for $\delta_\omega = 0.248$, $M = 4$.

j	$a_2 = 12.7$		
	$(r_1)_j$	$(r_2)_j$	$\omega_j(0)$
1	1.53	0.208	-0.535
2	0.0918	0.125	-1.256
3	0.535	0.0728	-1.697
4	0.247	0.0336	-1.952

Table 8.4 : Coordinates defining the initial nonelliptical profile of the C_1 in the first quadrant $x \geq 0$, $y \geq 0$.

x	y	x	y	x	y
1.53	0	1.408	0.157	0.960	0.200
1.522	0.042	1.360	0.171	0.880	0.201
1.520	0.056	1.320	0.181	0.760	0.201
1.513	0.084	1.260	1.190	0.640	0.202
1.500	0.107	1.200	0.196	0.500	0.203
1.472	0.128	1.120	0.190	0.360	0.204
1.442	0.143	1.060	0.200	0.2	0.260
				0	0.208

Table 8.5 : Summary of secondary vortex simulations showing aspect ratio, stretching strain strength, version-of-code (table 4.1) and node-parameter set (table 4.3) used.

Case	a_2	γ_2	M	τ_{max}	Version of code	Node Parameters
1	12.7	0	4	16	B	3
2	12.7	0.1	4	10	B	3
3	8	0.1	1	16	B	3
4	14.5	0.1	8	10	C	2
5	12.7	0.1	4*	12	C	2
6	12.7	0.2	4	8	B	3
7	12.7	0.4	4	5	B	3
8	25.8	0.0	4	8	B	3
9	25.8	0.1	4	6	B	3
10	25.8	0.2	4	5	B	3
11	25.8	0.4	4	3.8	B	3
12	51.7	0.1	4	3.8	B	3
13	51.7	0.2	4	2.5	B	3

* nonelliptic contours.

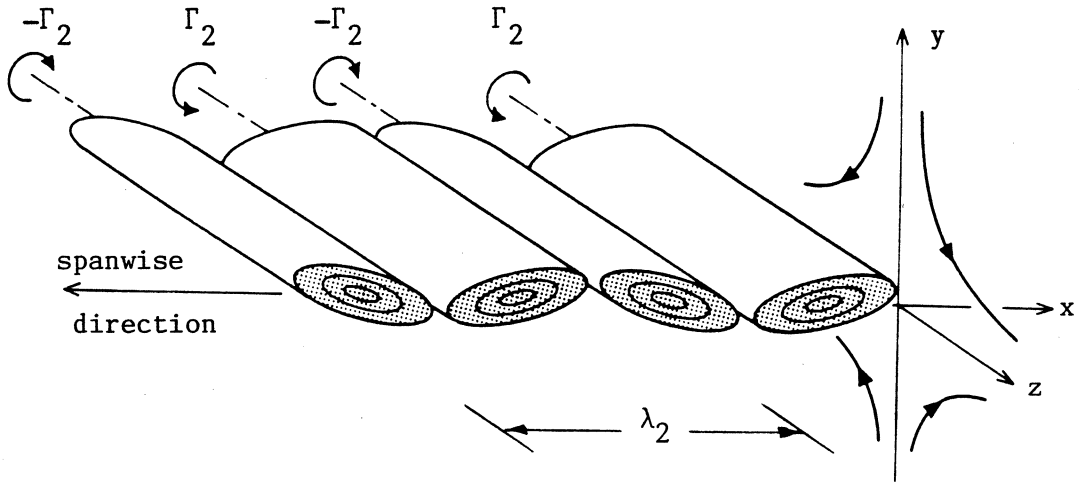

Figure 8.1 : The Corcos-Lin model of secondary vortices (near the midpoint of the braid) subject to locally-uniform three-dimensional strain induced by the primary (spanwise) vortices.

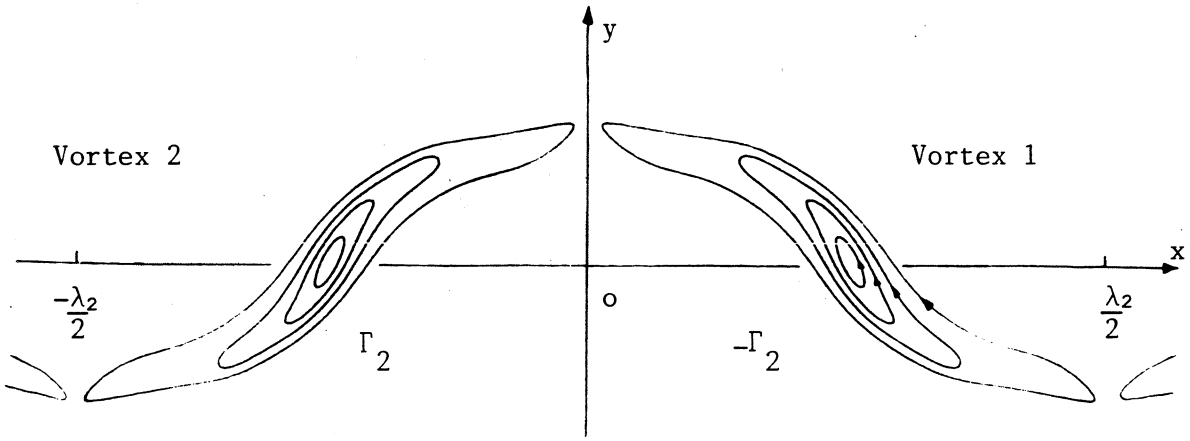

Figure 8.2 : Pair of counter-rotating vortices in (x, y)-plane. The contours describing vortex 1 are C_j, j = 1, 4 where j = 1 for the outermost contour. $\omega_j(0)$ is the initial uniform vorticity in R_j bounded by C_j and C_{j+1}. The flow is irrotational outside of the vortices.

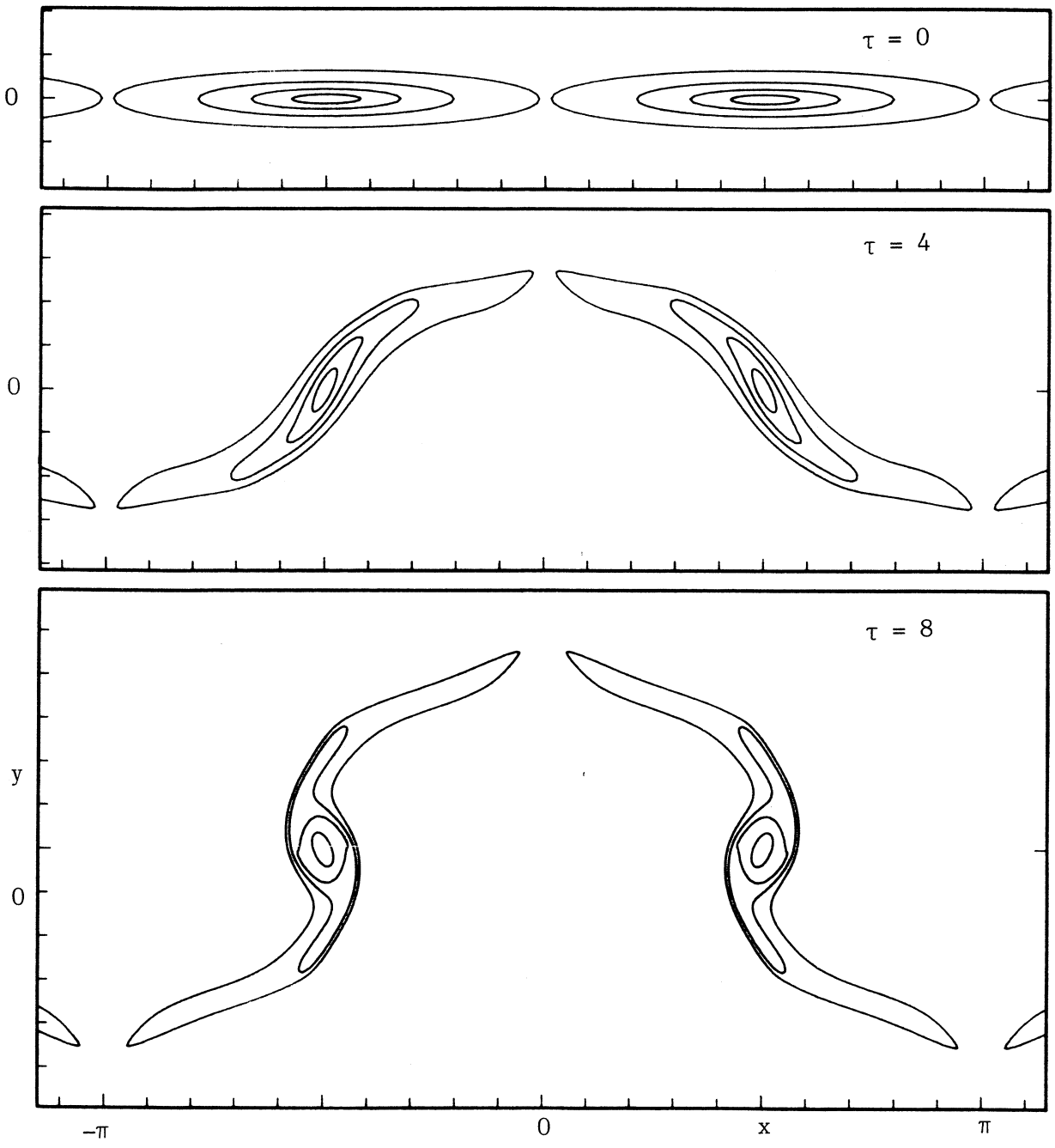

Figure 8.3 : Case 1, for legend see over page.

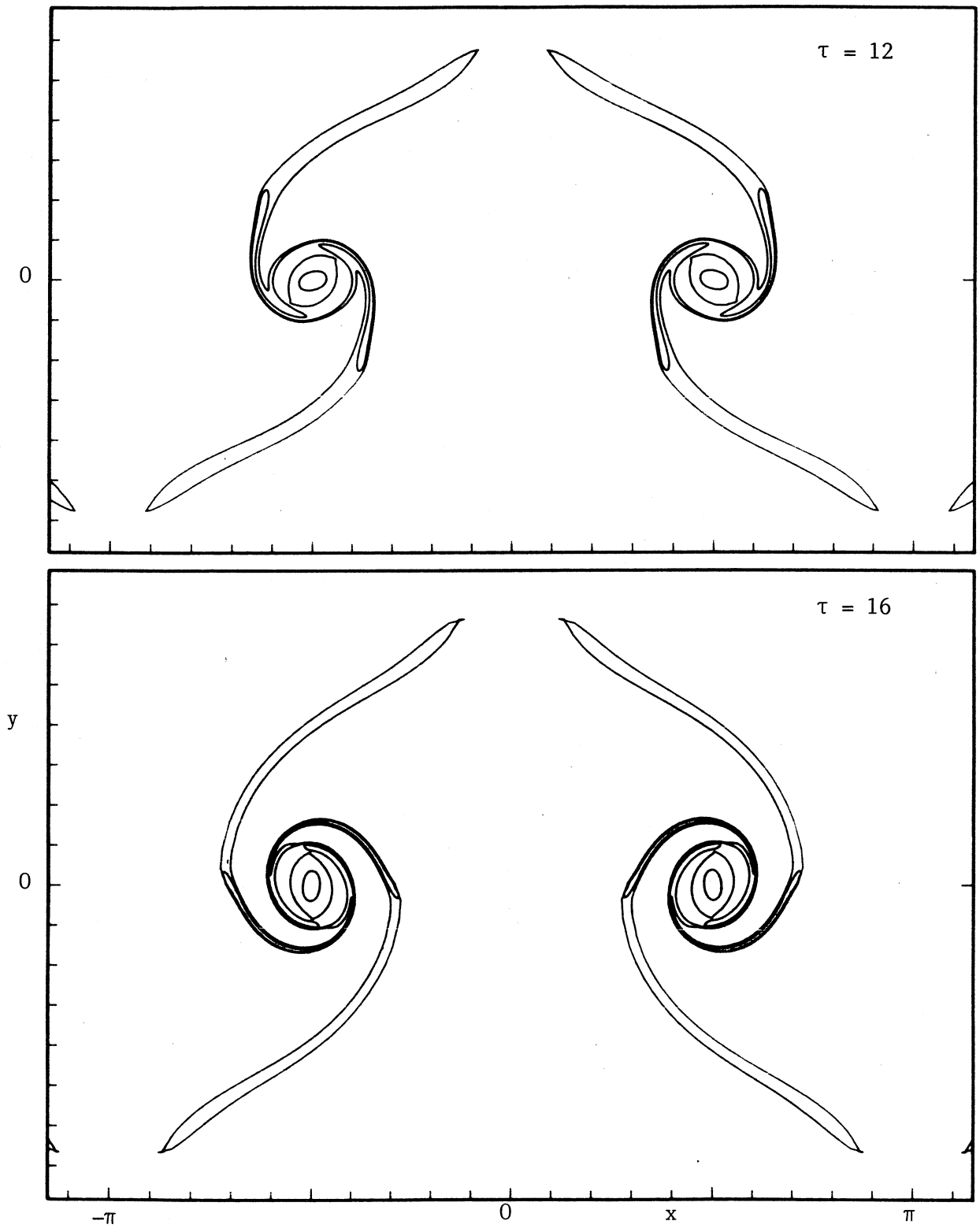

Figure 8.3 : Evolution of vortex array, $a_2 = 12.7$, $\gamma_2 = 0$, case 1 (table 8.5)
Dimensionless times τ as shown.

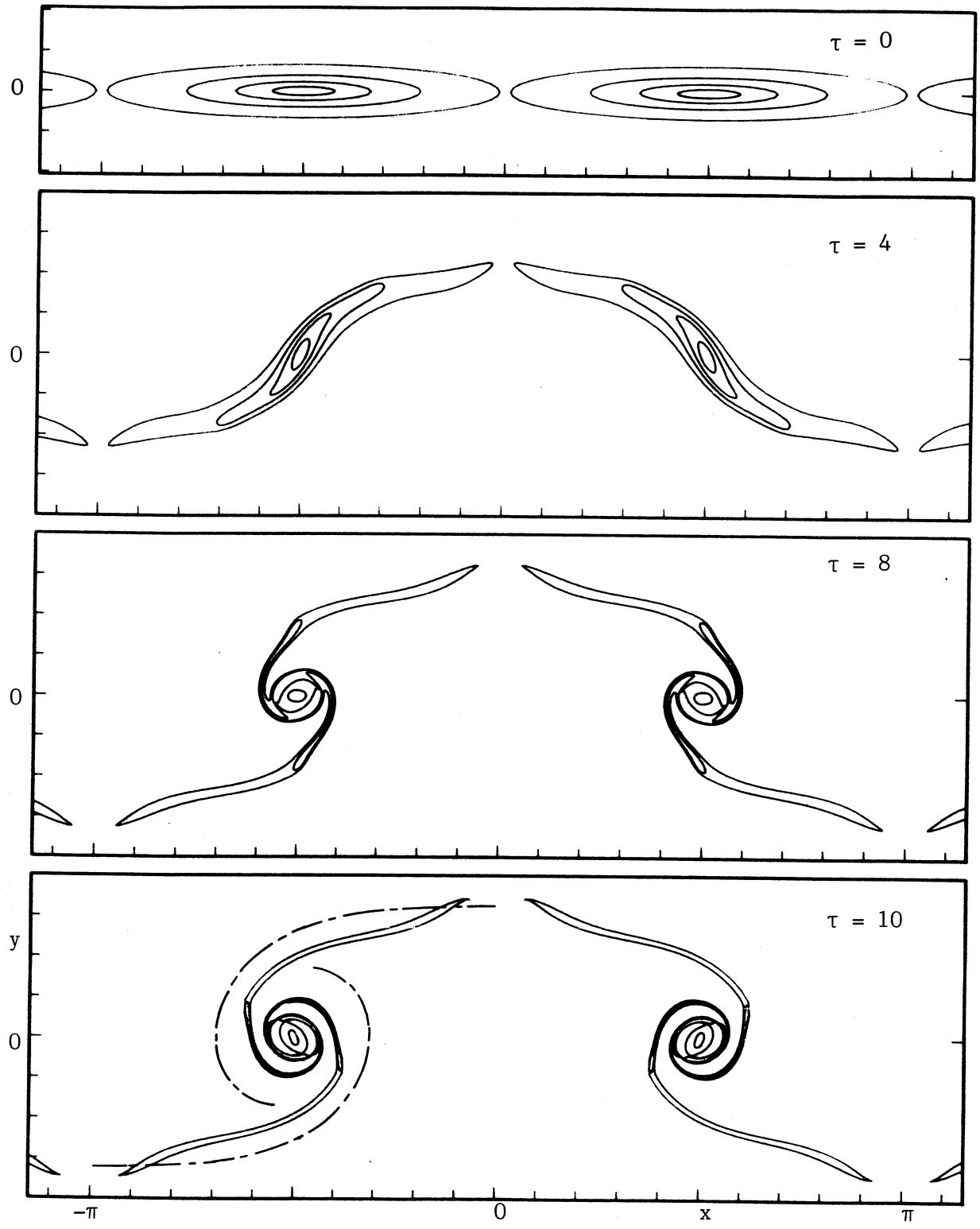

Figure 8.4 : Evolution of vortex array, $a_2 = 12.7$, $\gamma_2 = 0.1$ case 2 (table 8.5). Dot-dashed lines show the (x, y)-plane projection of the stagnation stream surface for a point vortex approximation to the secondary array. Dimensionless times τ as shown.

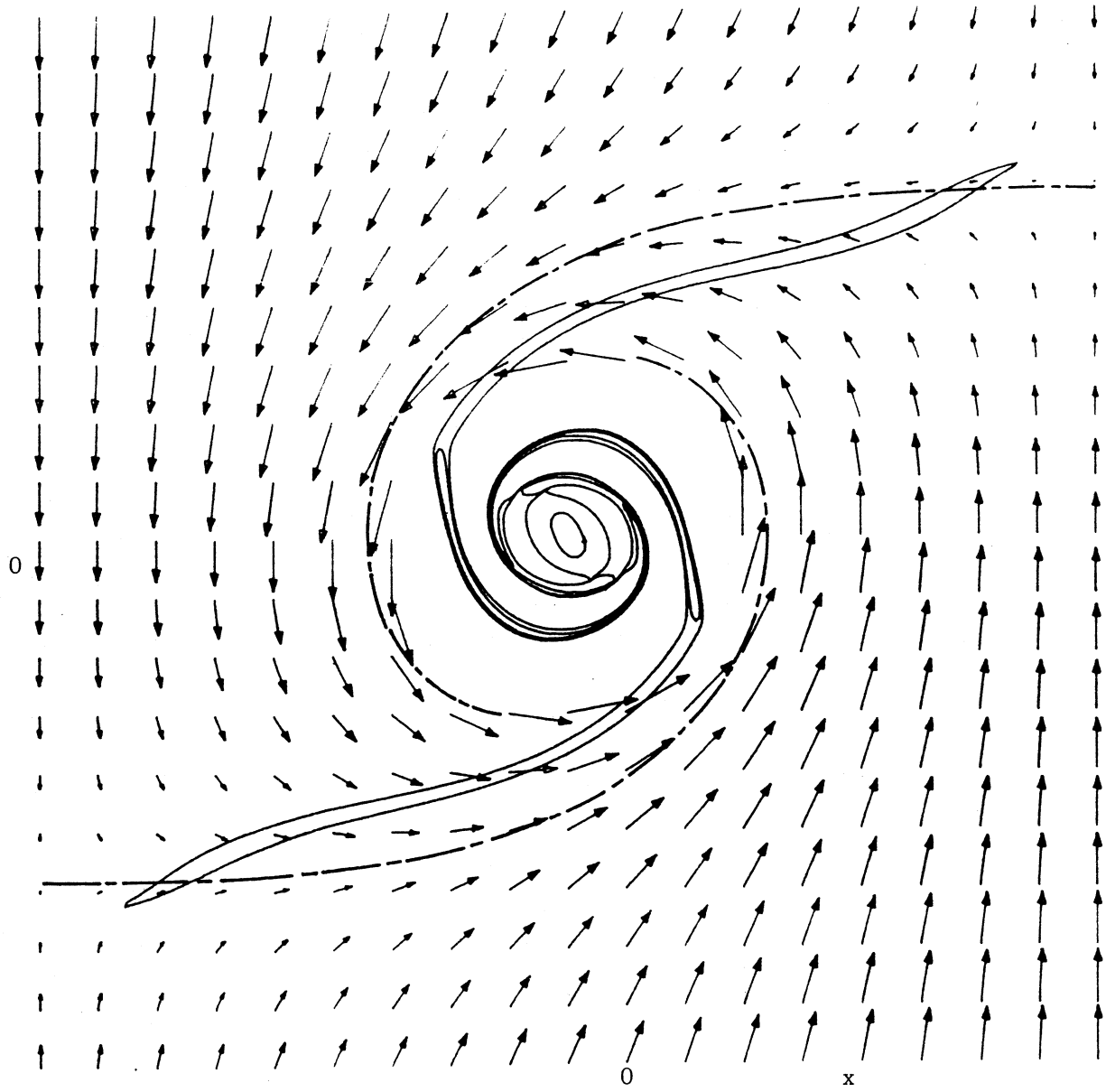

Figure 8.5 : Magnified view of vortex contours, $a_2 = 12.7$, $\gamma_2 = 0.1$, $\tau = 10.0$, case 2. Arrows indicate the x-y velocity field of a point-vortex array in the (y, z)-plane stretching strain field with $\gamma_2 = 0.1$. Dot-dashed lines represent the (x, y)-projection of the stagnation stream surface for this velocity field.

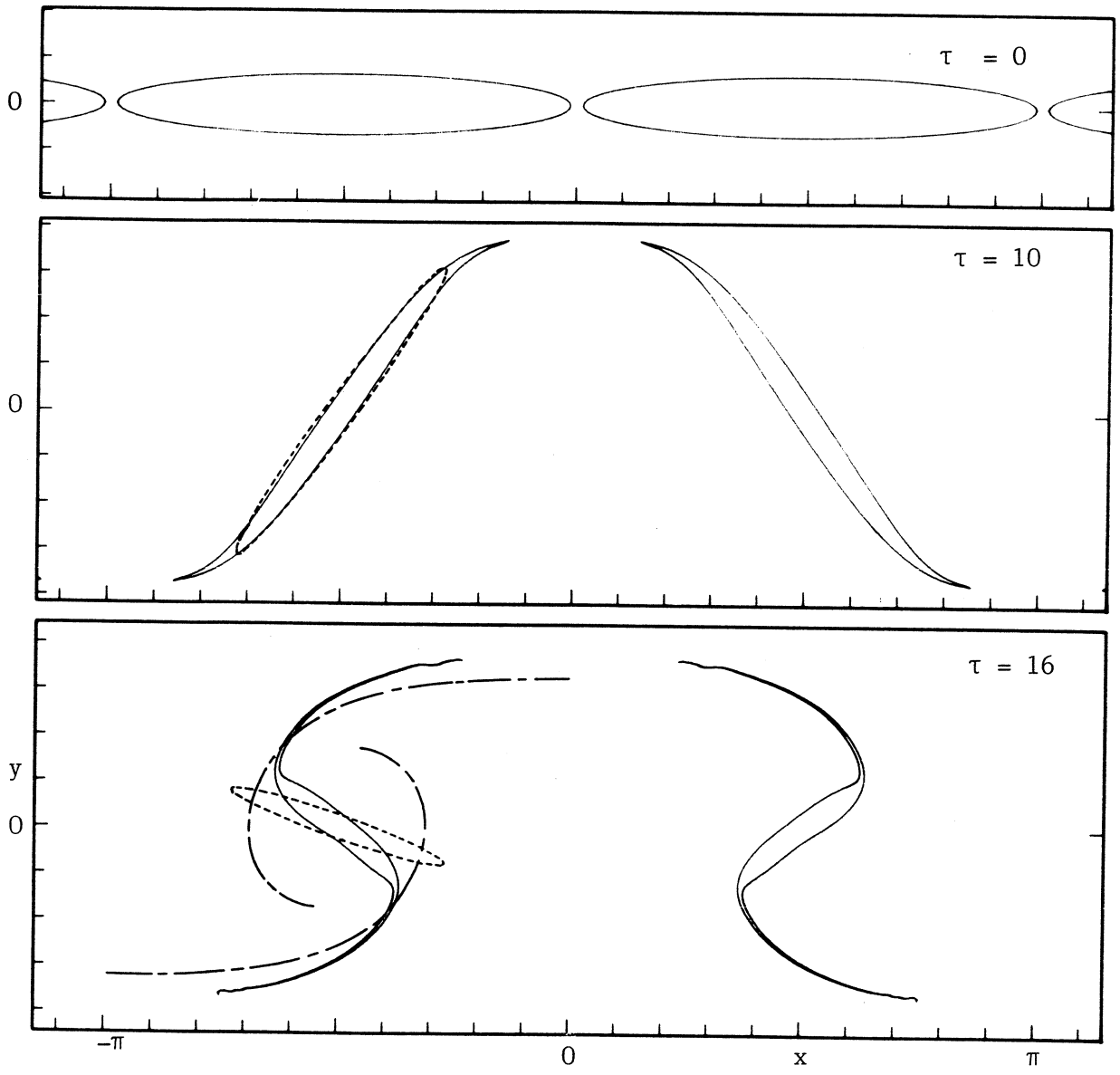

Figure 8.6 : Evolution of vortex array, $a_2 = 8$, $\gamma_2 = 0.1$, case 3. The vorticity is uniform in each vortex. Dashed contours indicate the evolution of an isolated elliptical vortex embedded in a (y, z)-plane stretching strain field $\gamma_2 = 0.1$.

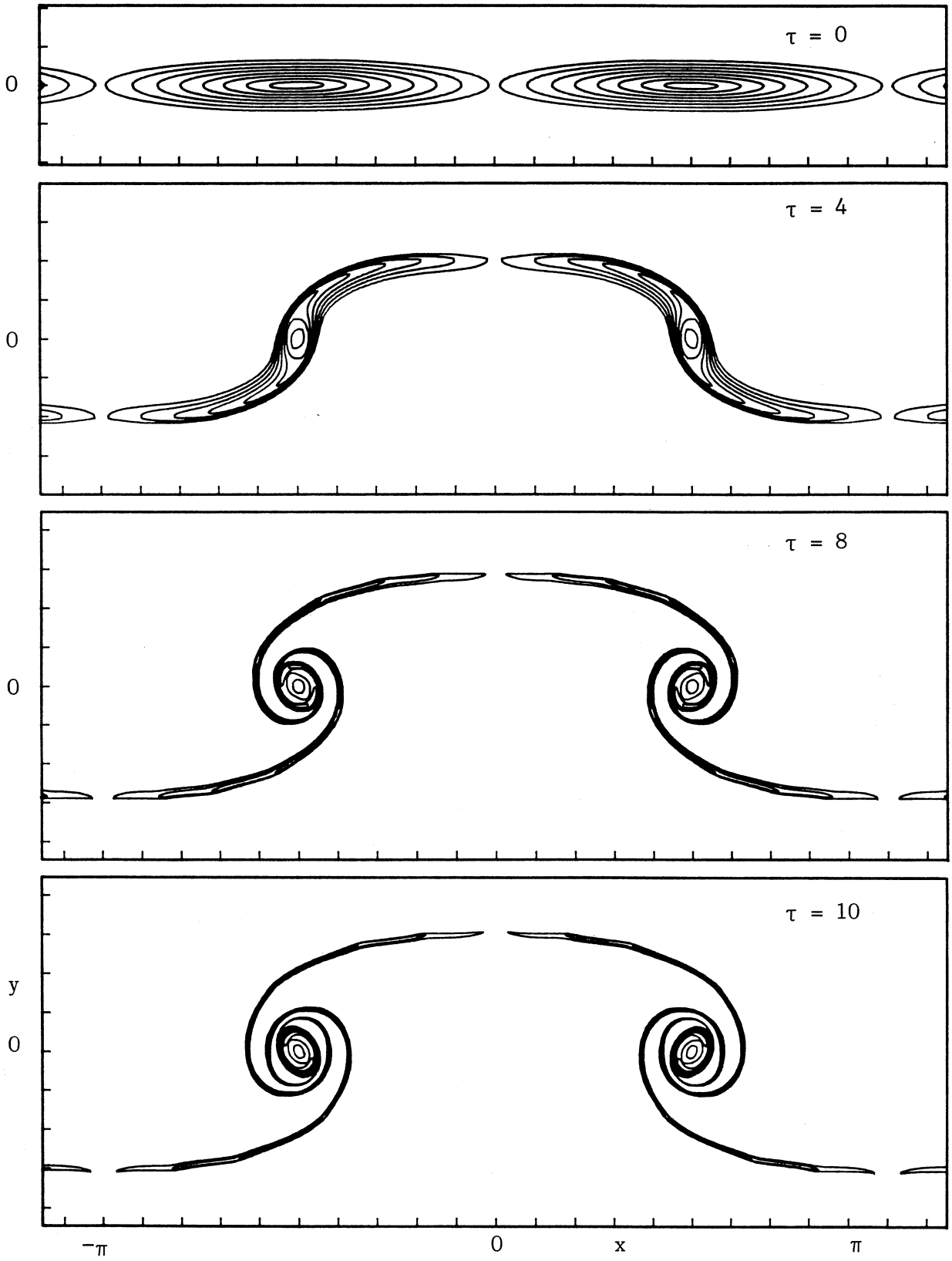

Figure 8.7 : Evolution of a vortex array, a_2 = 14.5, M = 8, γ_2 = 0.1, case 4.

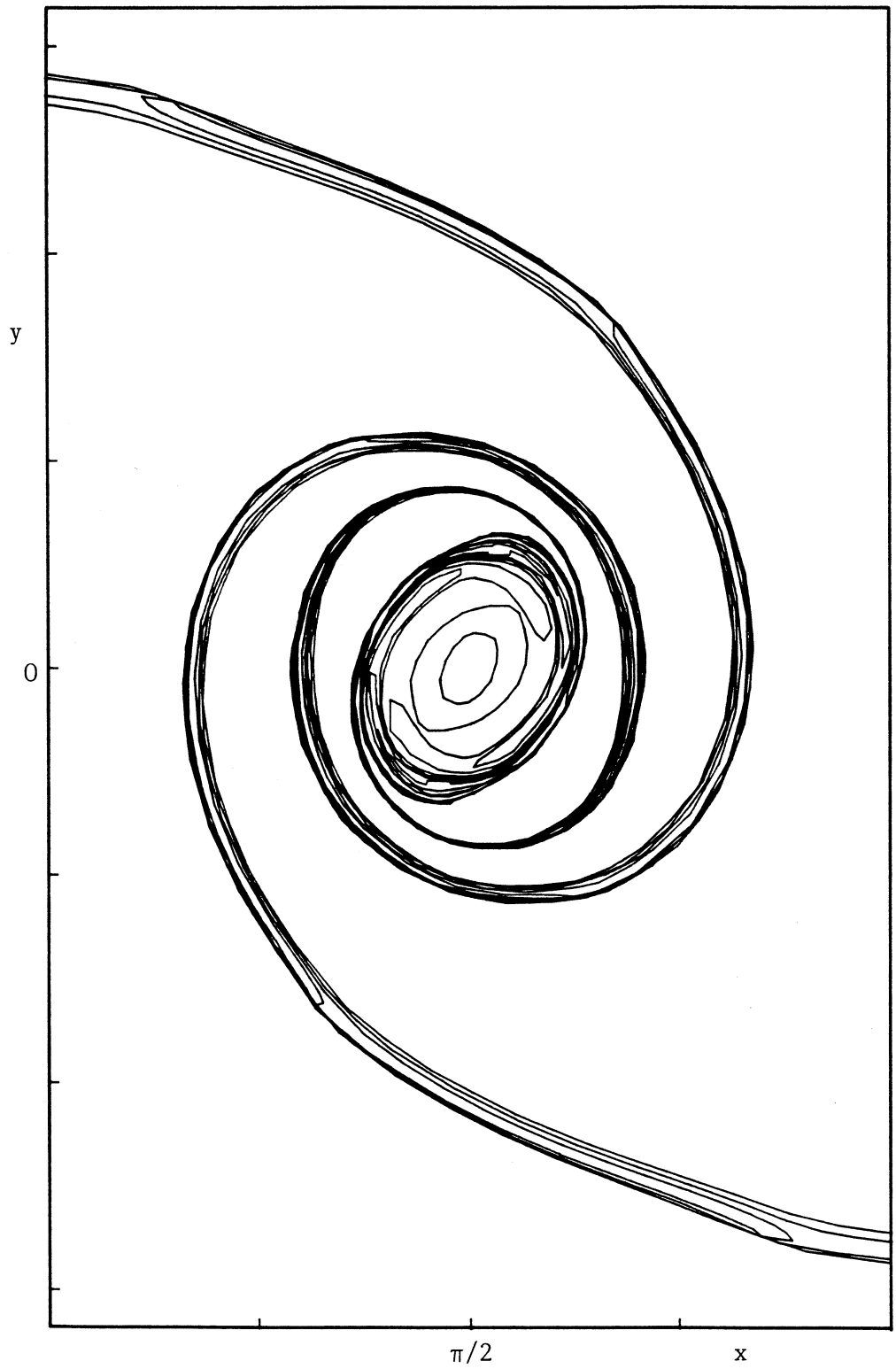

Figure 8.8 : Magnified view of the vortex contours, $a_2 = 14.5$, $M = 8$, case 4 at $\tau = 10$.

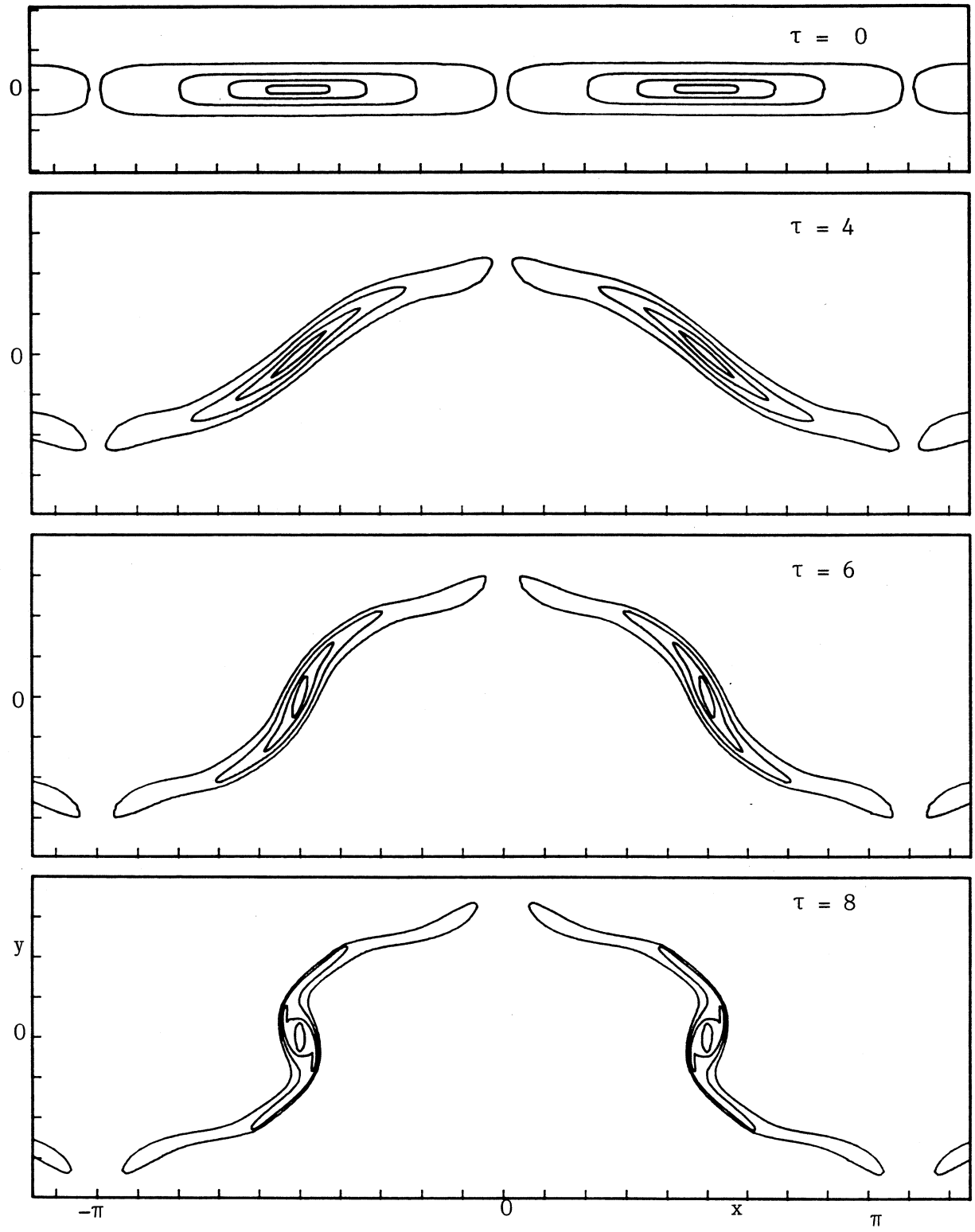

Figure 8.9 : Evolution of vortex array, $a_2 = 12.7$, $\gamma_2 = 0.1$, nonelliptic initial contours, case 5 (table 8.5).

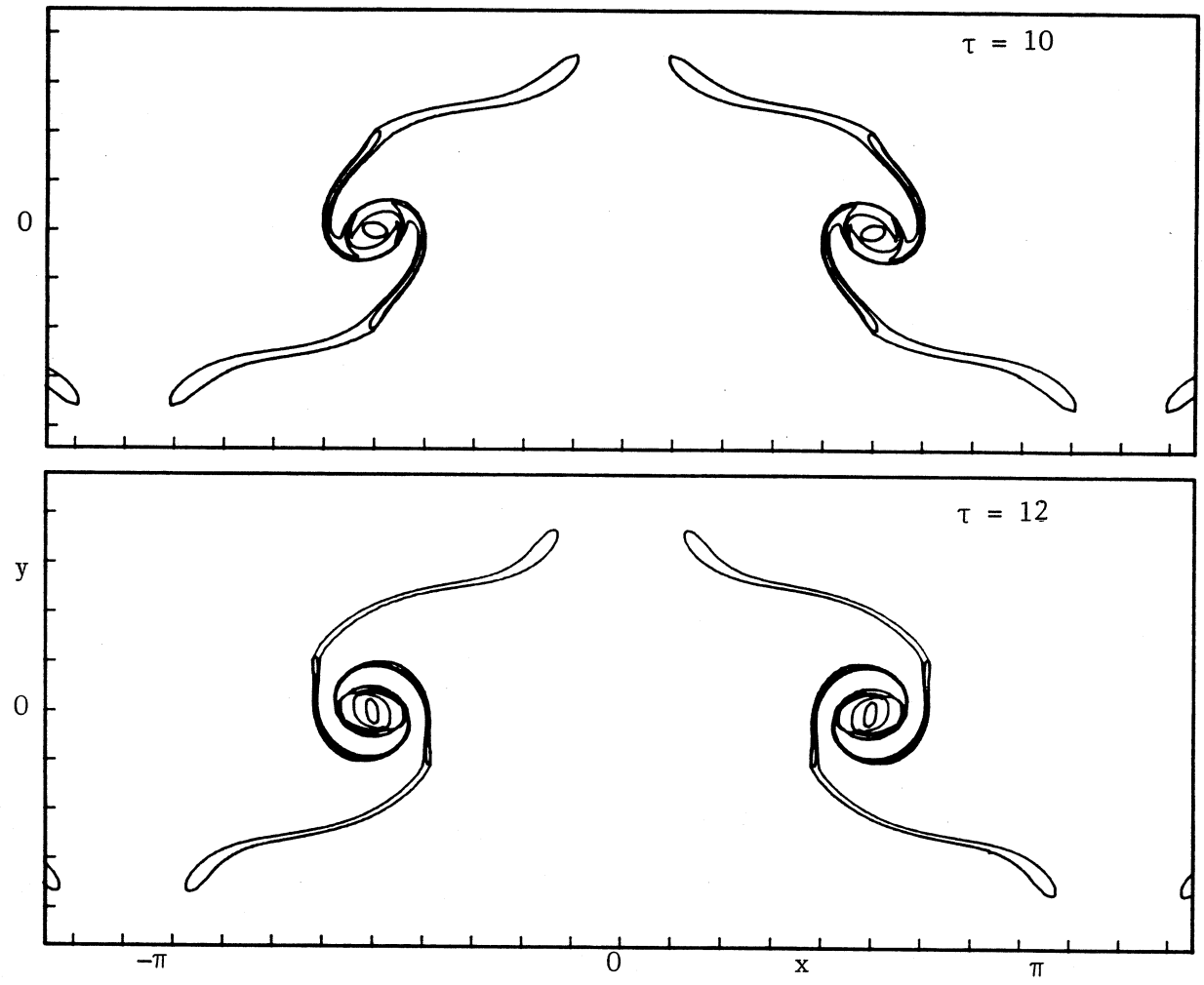

Figure 8.9 continued.

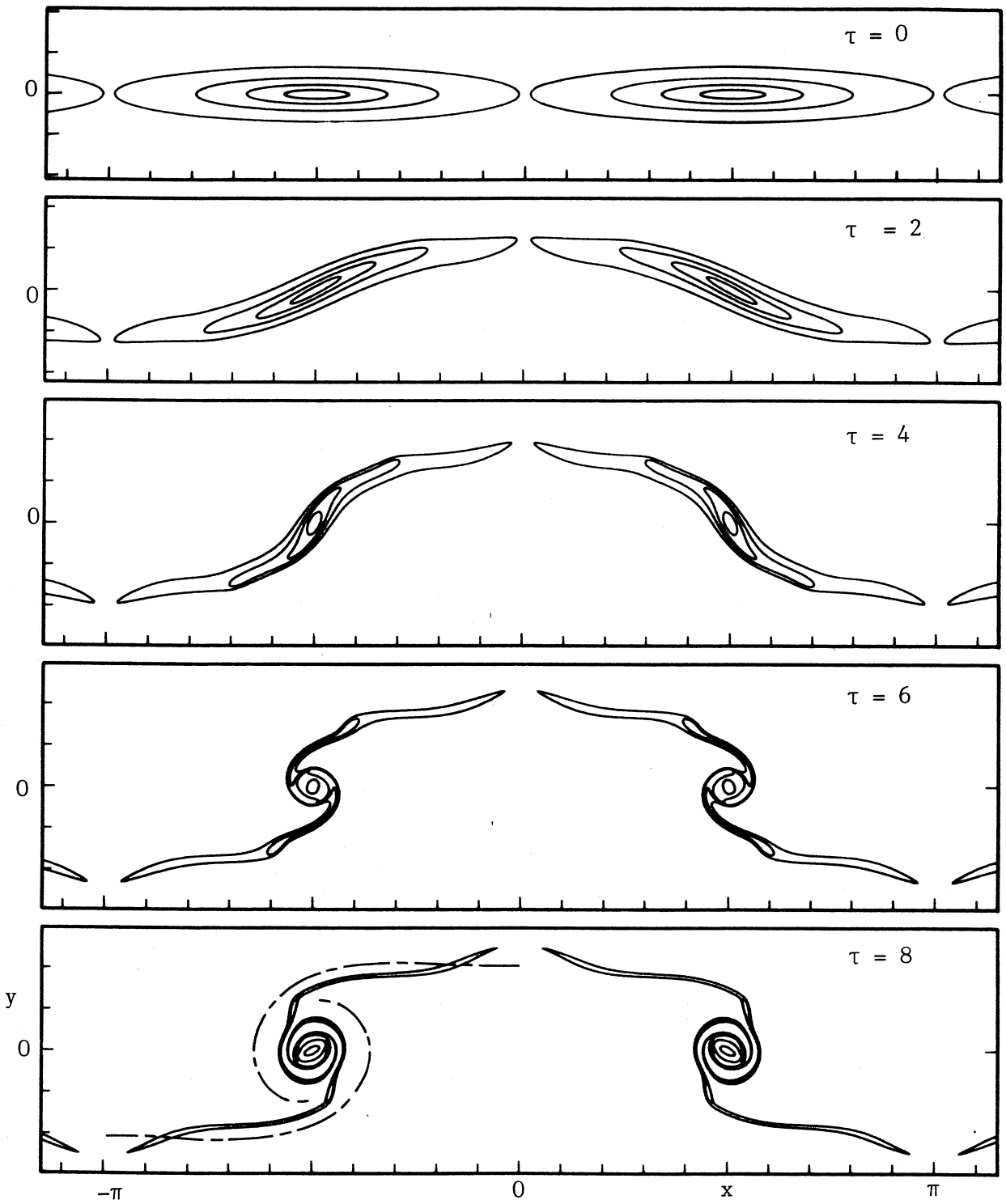

Figure 8.10 : Evolution of vortex array, $a_2 = 12.7$, $\gamma_2 = 0.2$, case 6. Dimensionless times τ as shown.

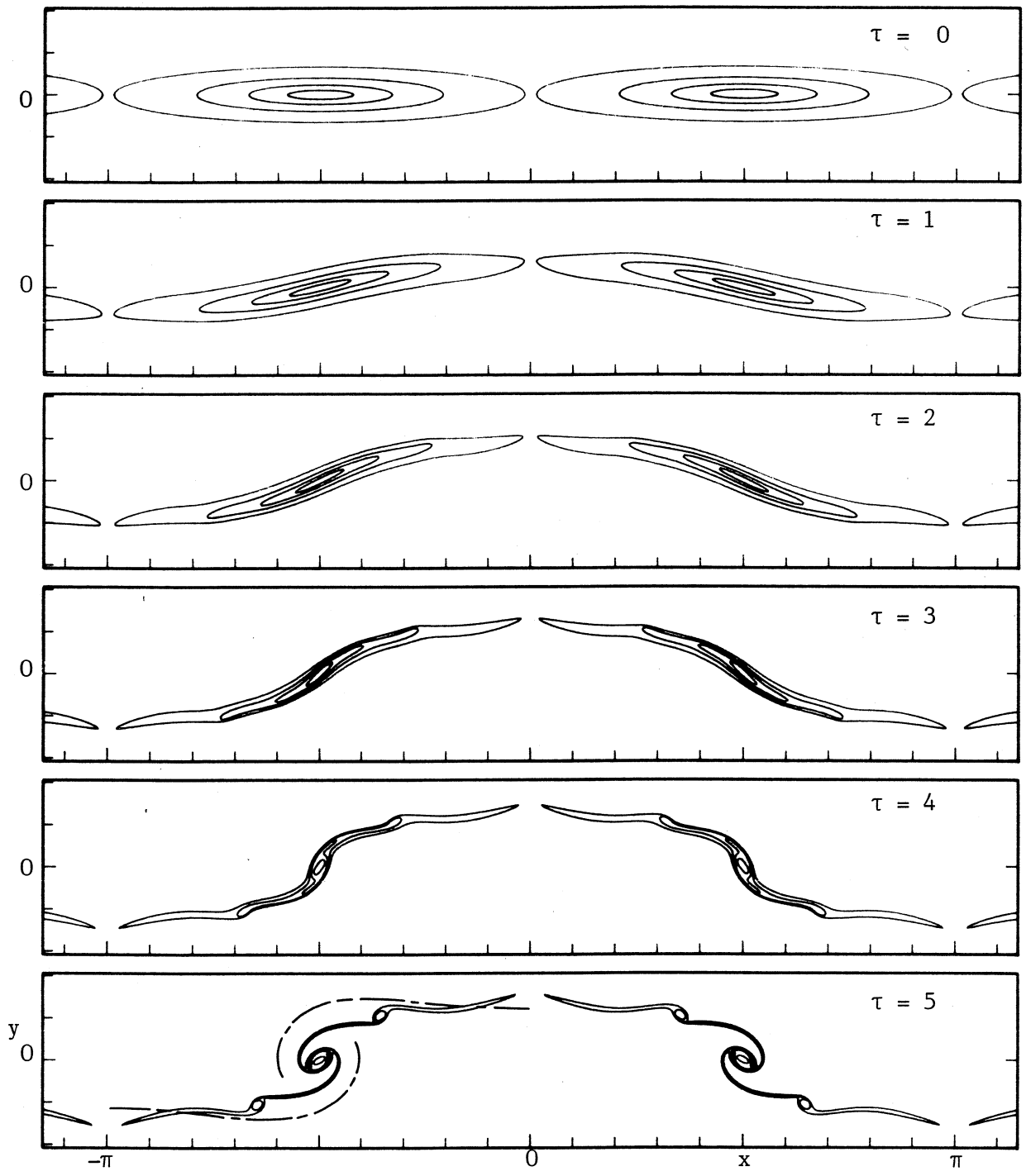

Figure 8.11 : Evolution of vortex array, $a_2 = 12.7$, $\gamma_2 = 0.4$, case 7. Dimensionless times τ as shown.

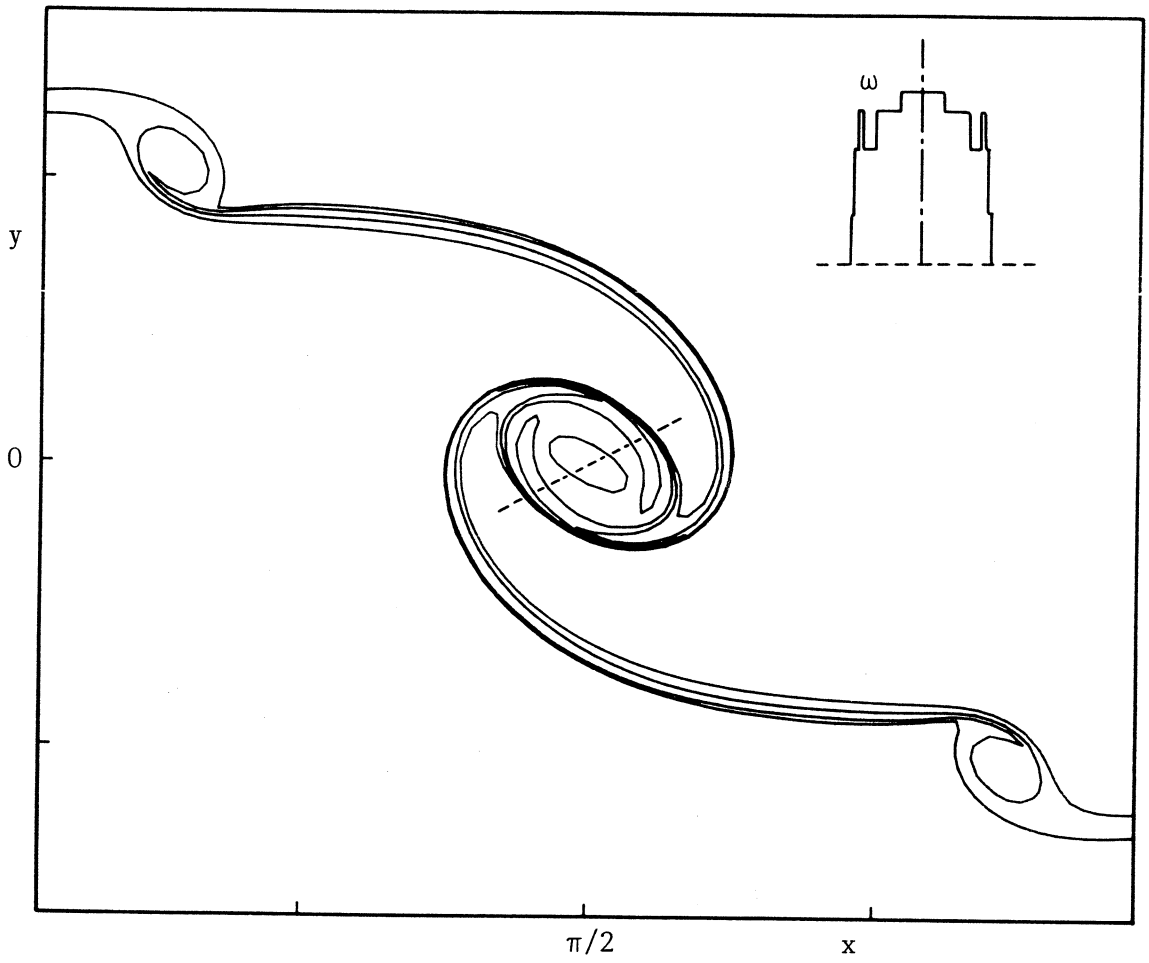

Figure 8.12 : Magnified view of vorticity contours, $a_2 = 12.7$, $\gamma_2 = 0.4$, $\tau = 5$, case 7. Inset; vorticity distribution in vortex core.

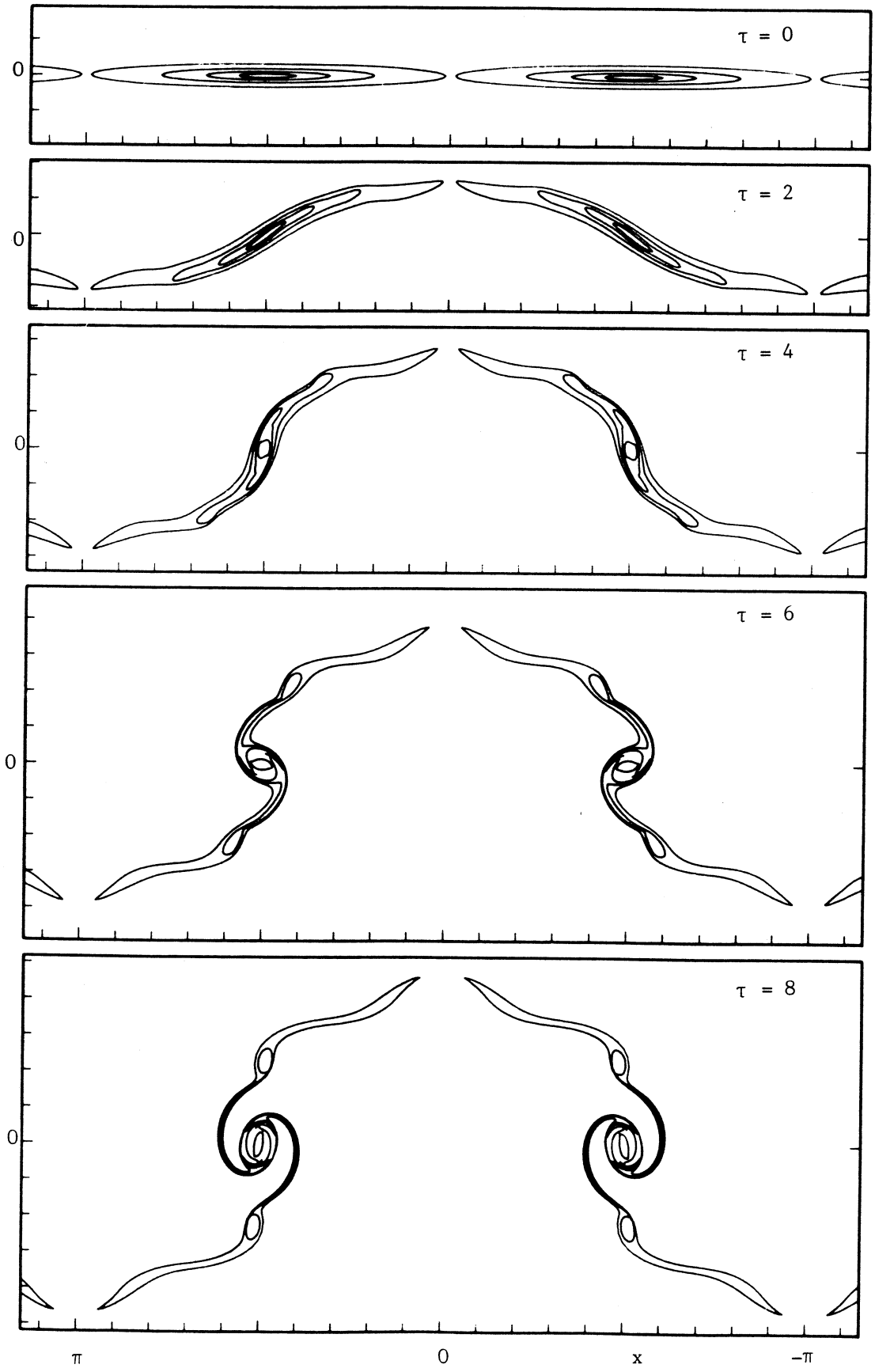

Figure 8.13 : Evolution of vortex array, $a_2 = 25.8$, $\gamma_2 = 0$, case 8. Dimensionless times τ as shown.

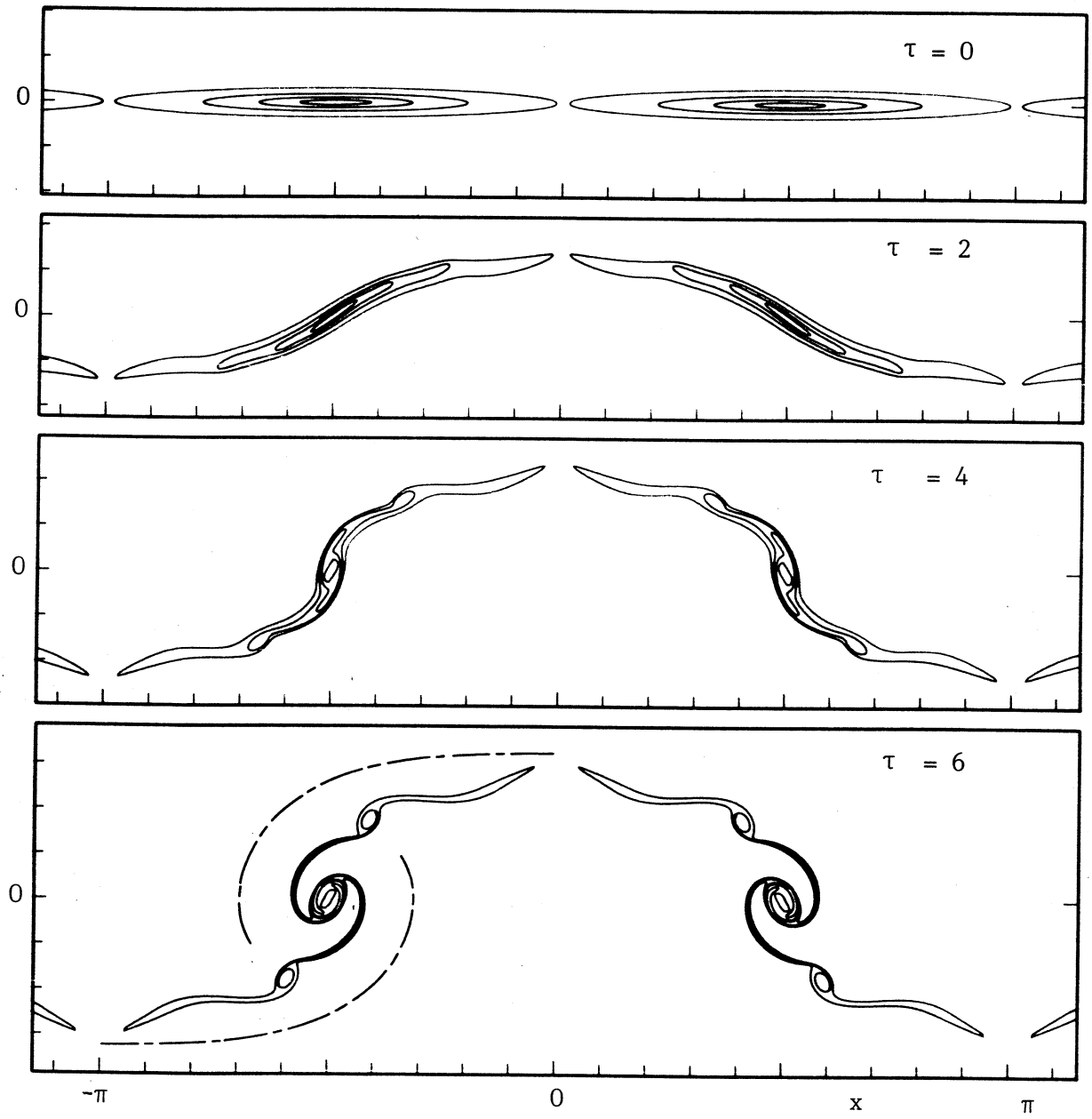

Figure 8.14 : Evolution of vortex array, $a_2 = 25.8$, $\gamma_2 = 0.1$, case 9. Dimensionless times τ as shown.

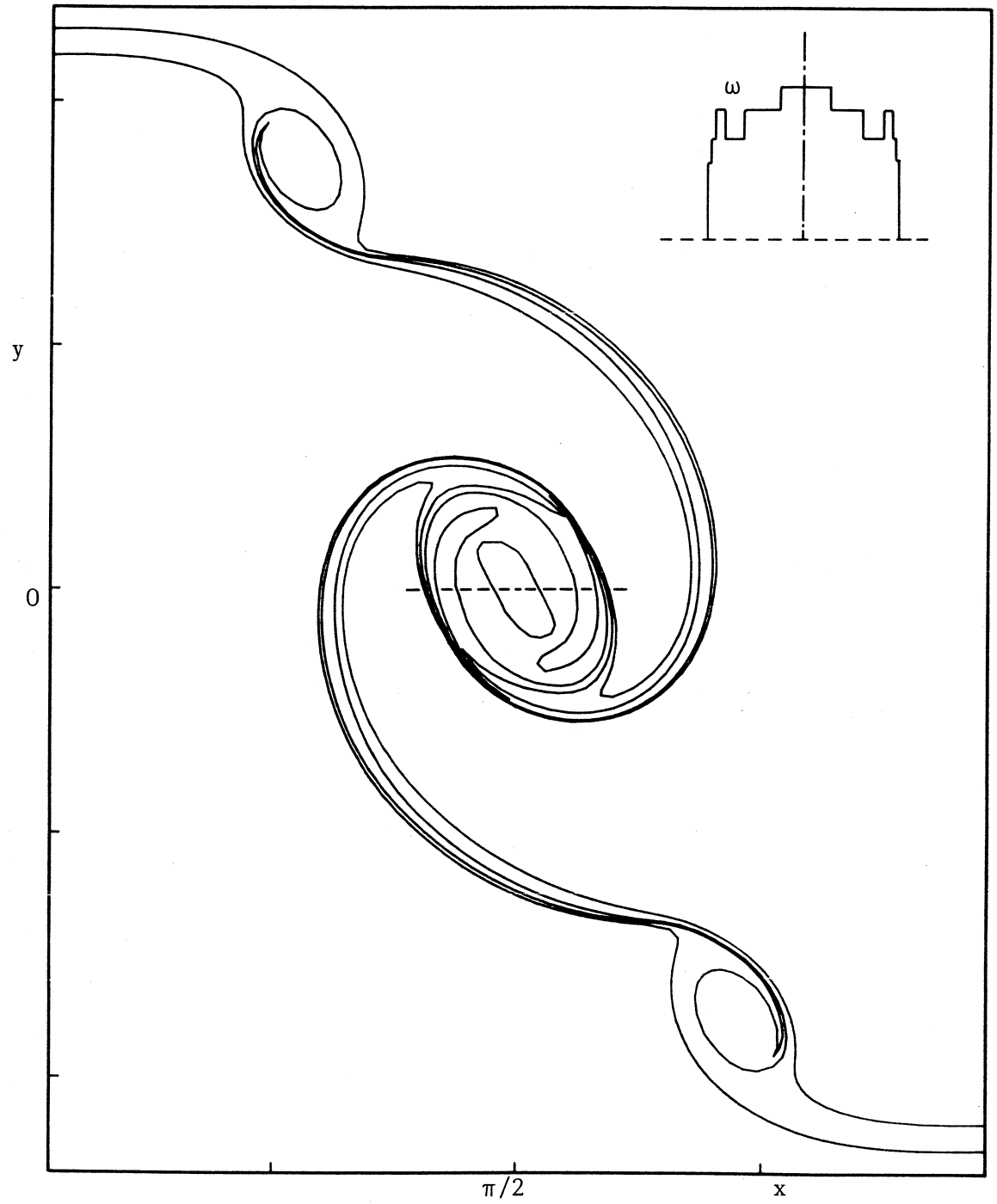

Figure 8.15 : Magnified view of vortex contours, $a_2 = 25.8$, $\gamma = 0.1$, $\tau = 6$, case 9. Inset: vorticity distribution in vortex core.

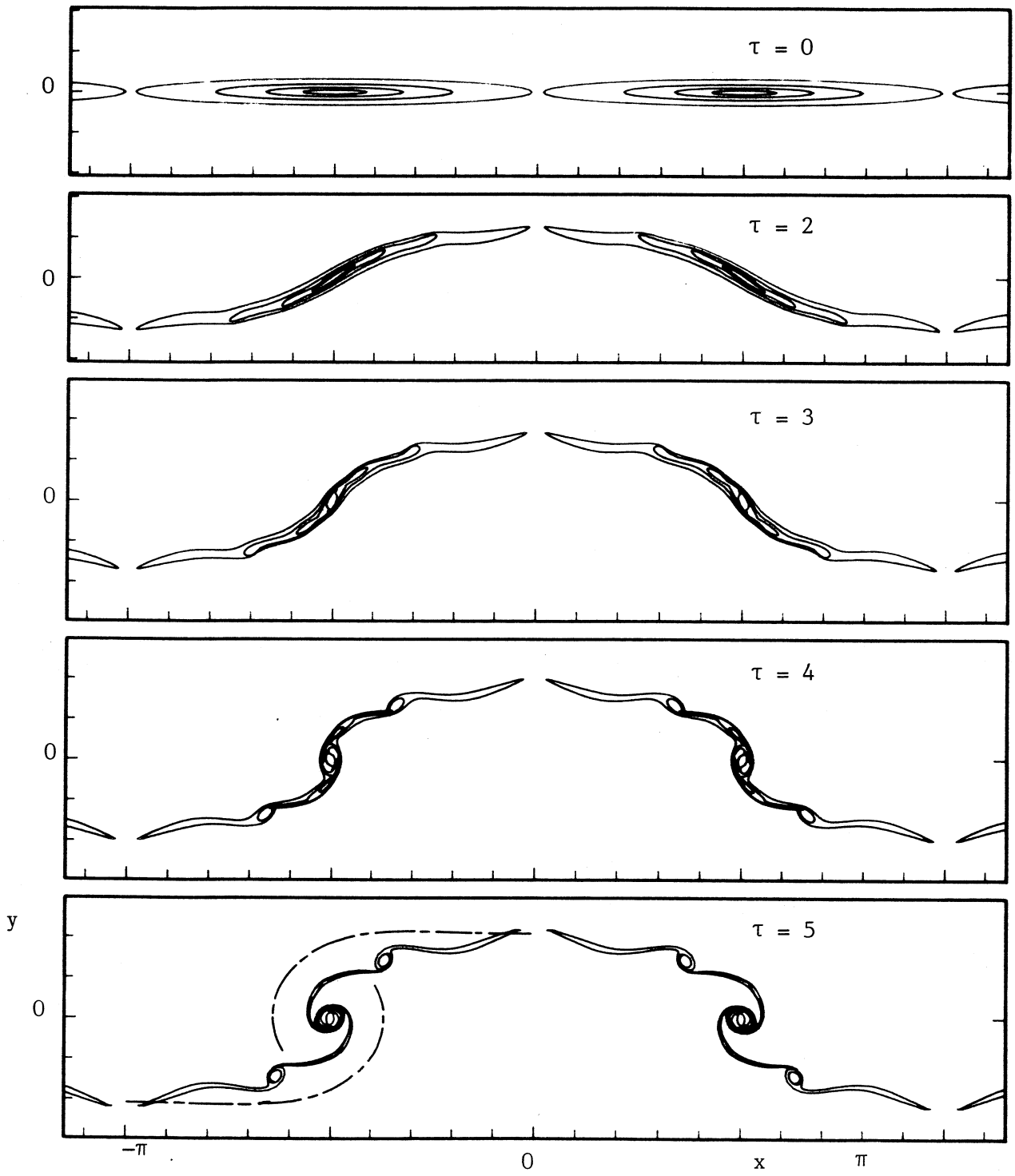

Figure 8.16 : Evolution of vortex aray, $a_2 = 25.8$, $\gamma_2 = 0.2$, case 10. Dimensionless times τ as shown.

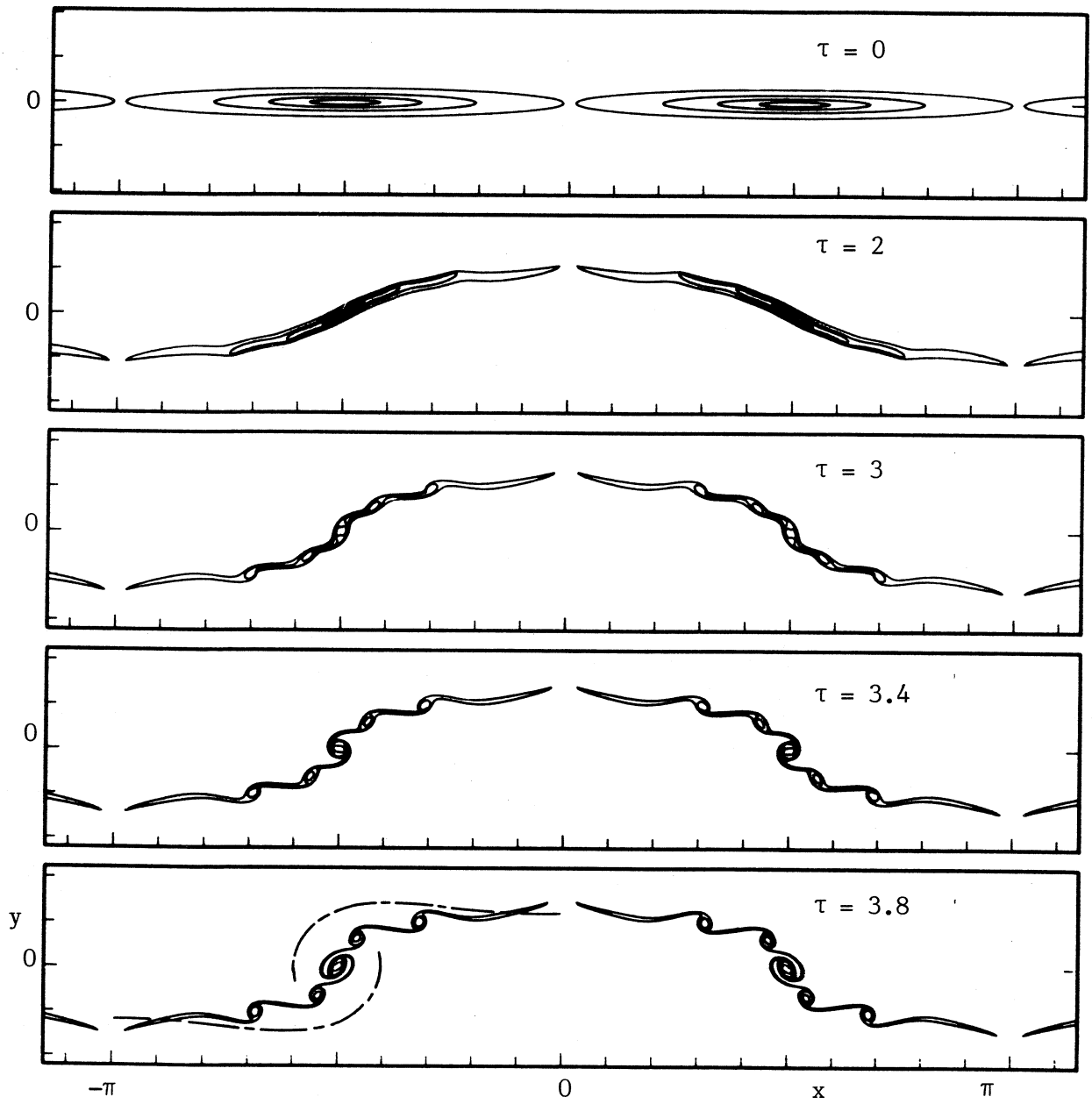

Figure 8.17 : Evolution of vortex array, $a_2 = 25.8$, $\gamma_2 = 0.4$, case 11. Dimensionless times τ as shown.

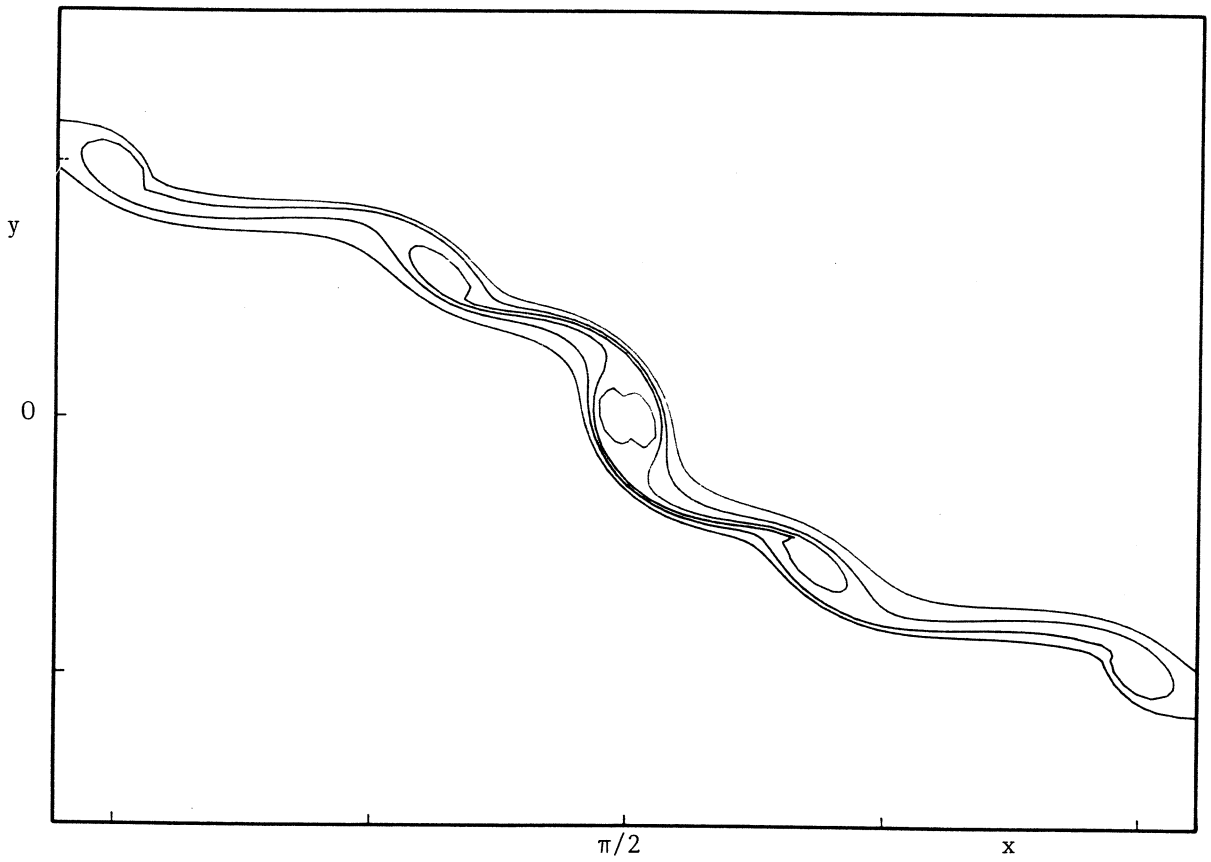

Figure 8.18 : Magnified view of vortex contours, $a_2 = 25.8$, $\gamma_2 = 0.4$, $\tau = 3$, case 11.

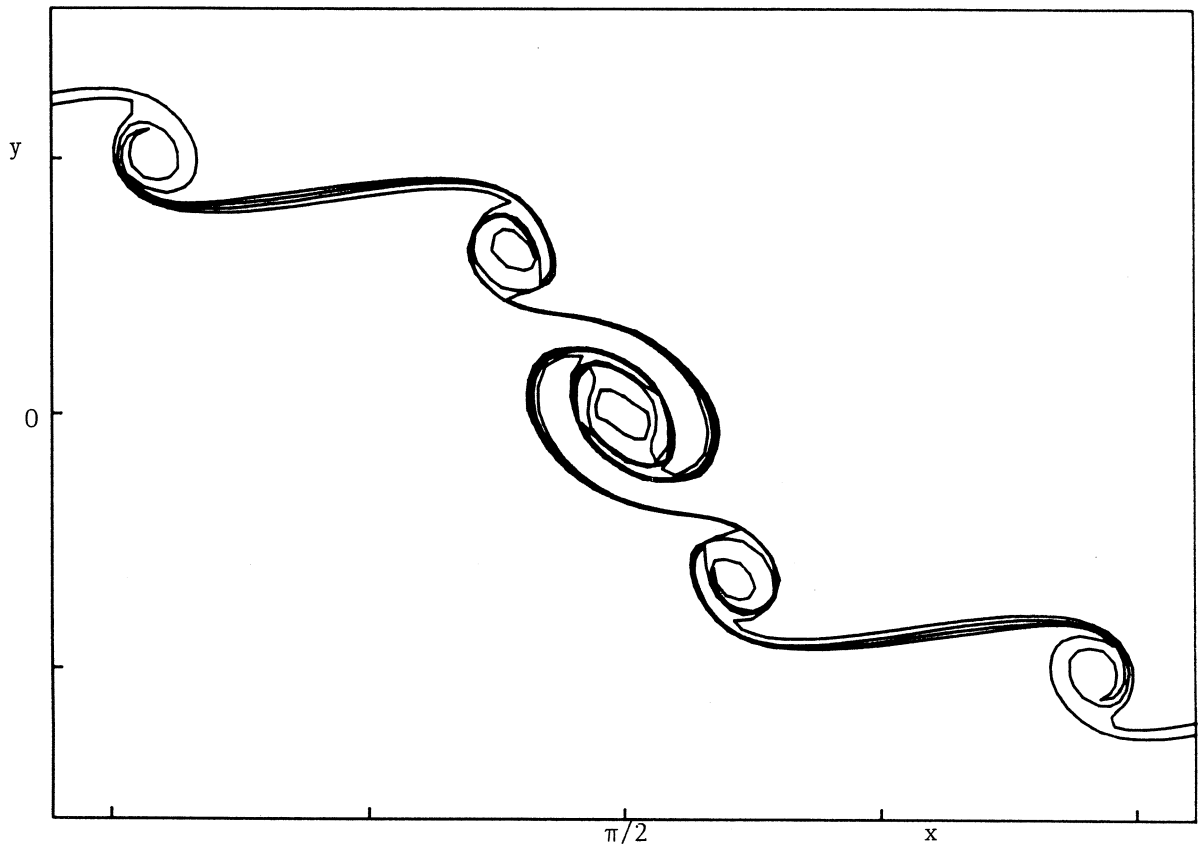

Figure 8.19 : Magnified view of vortex contours, $a_2 = 25.8$, $\gamma_2 = 0.4$, $\tau = 3.8$, case 11.

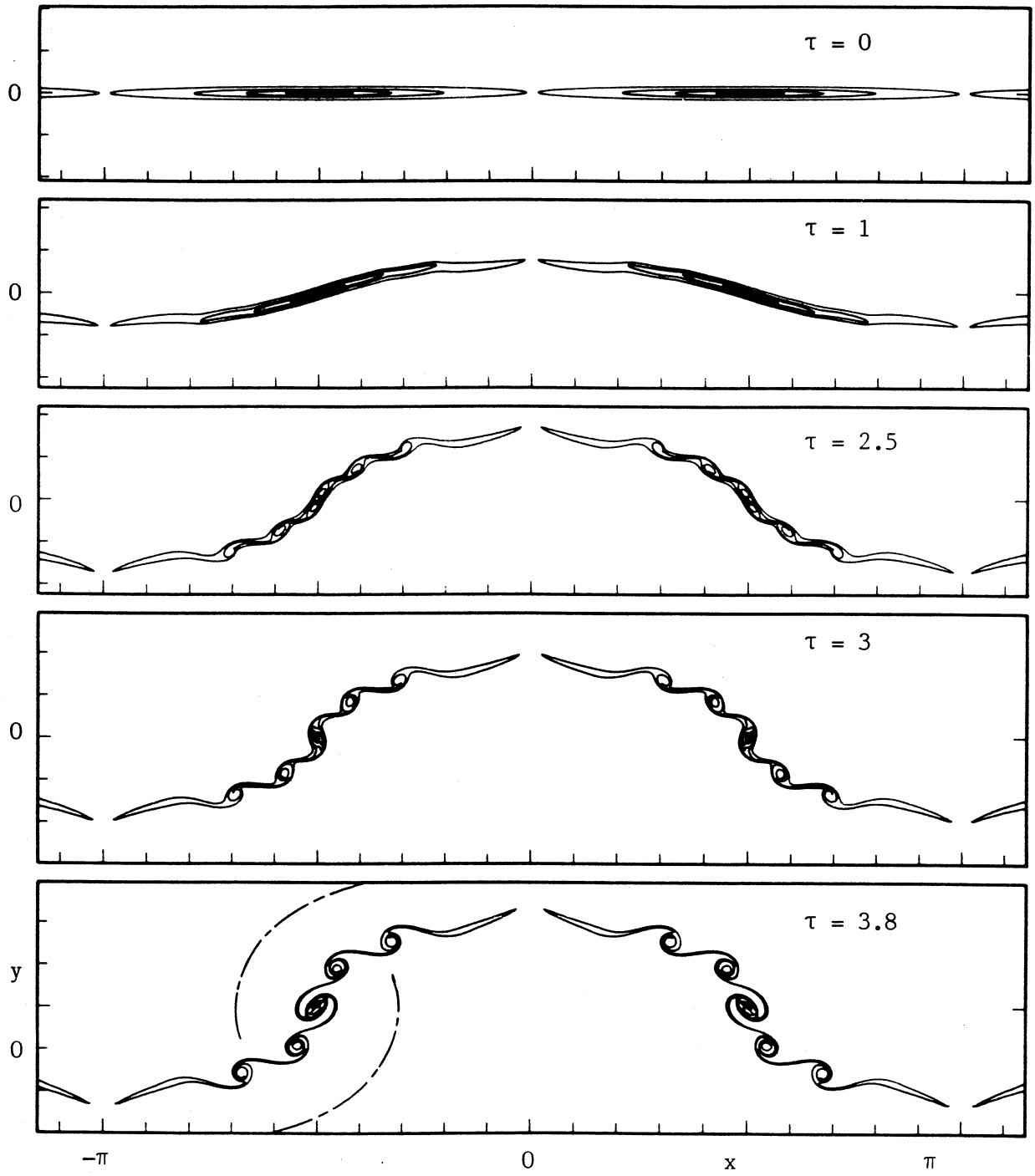

Figure 8.20 : Evolution of vortex array, $a_2 = 51.7$, $\gamma_2 = 0.1$, case 12. Dimensionless times τ as shown.

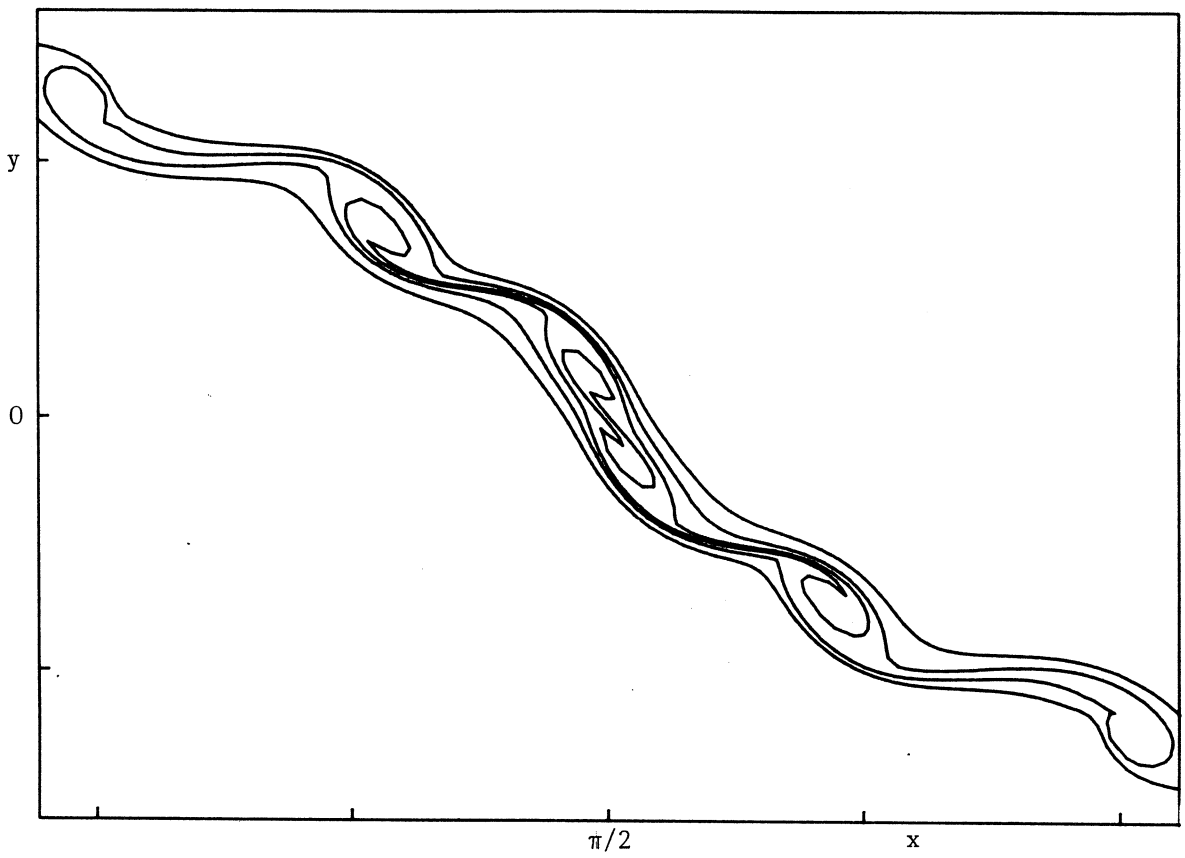

Figure 8.21 : Magnified view of vortex contours, $a_2 = 51.7$, $\gamma_2 = 0.1$, case 12, $\tau = 2.5$.

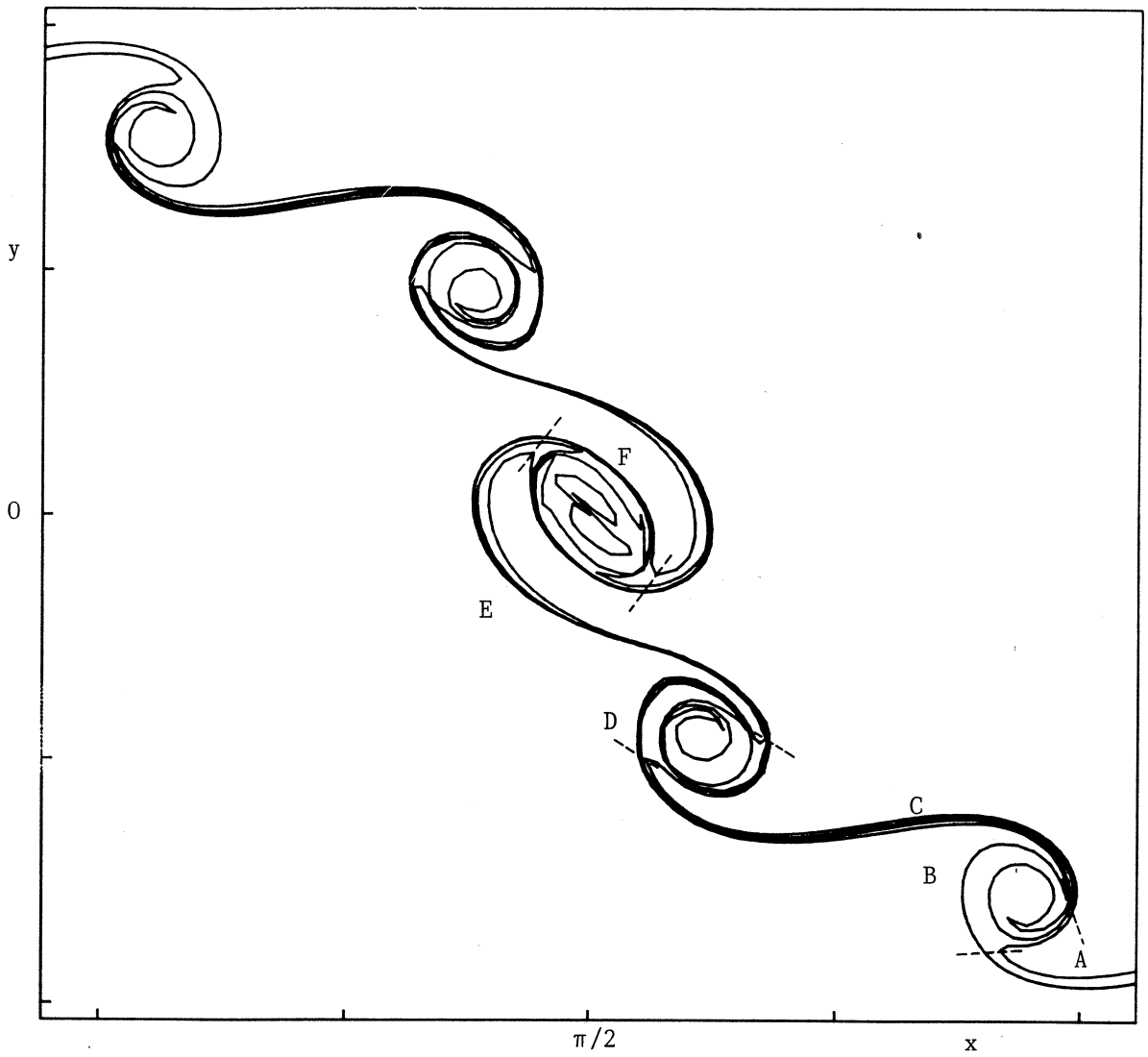

Figure 8.22 : Magnified view of vortex contours, $a_2 = 51.7$, $\gamma_2 = 0.1$, $\tau = 3.8$. Dashed lines indicate division of vortex into a system of cores and connecting braids. Section A extends to the end of vortex tail.

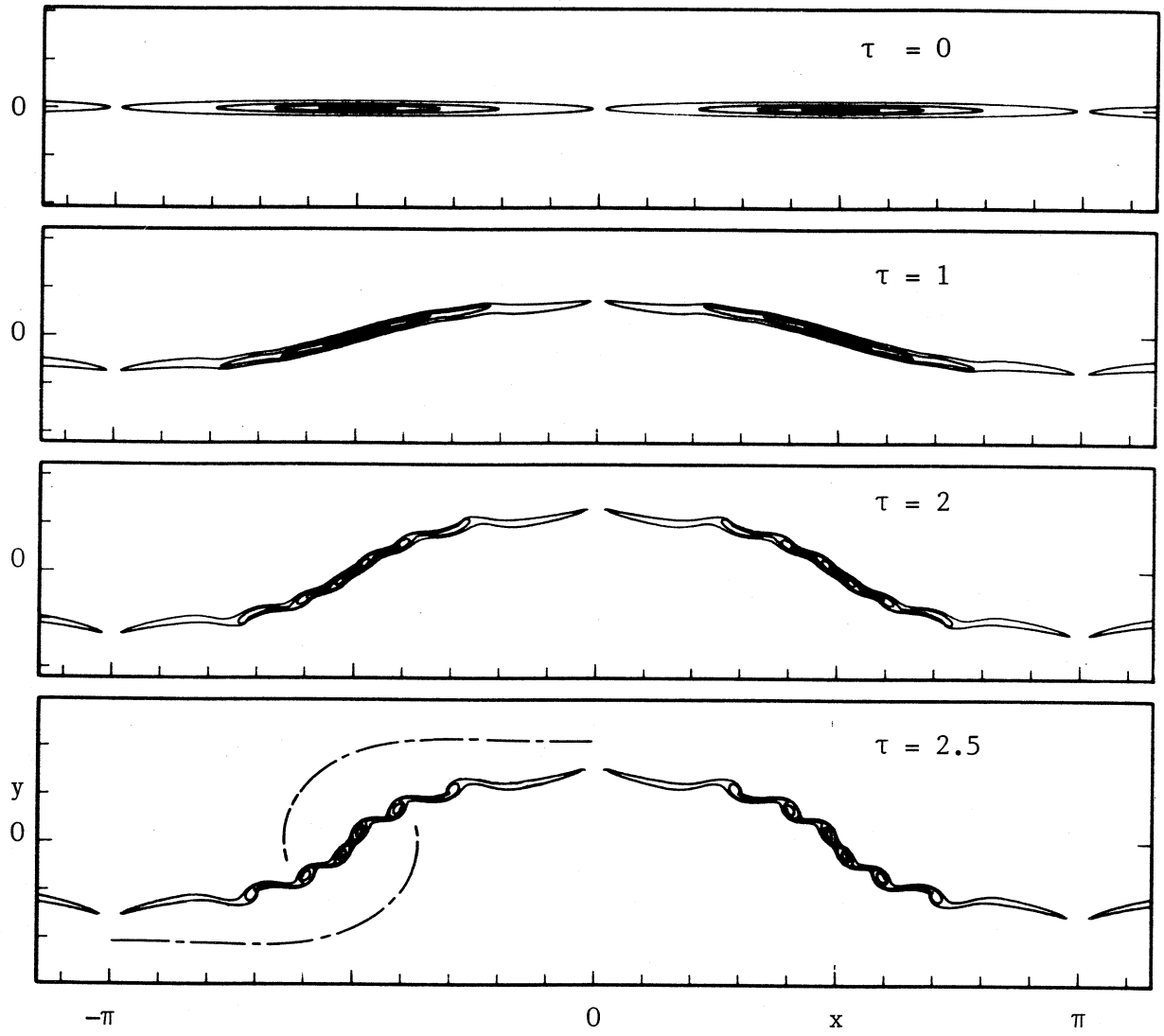

Figure 8.23 : Evolution of vortex array $a_2 = 51.7$, $\gamma_2 = 0.2$, case 13. Dimensionless times τ as shown.

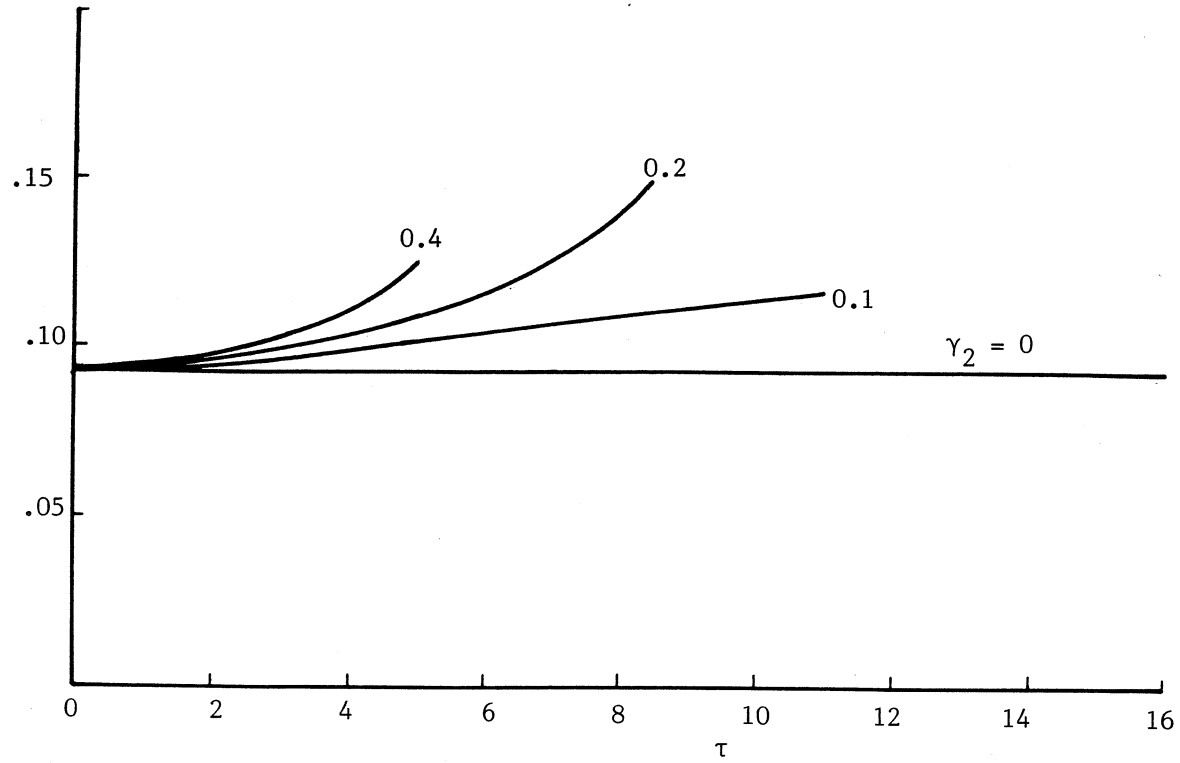

Figure 8 24 : Energy of the vortex array per member, $a_2 = 12.7$. Values of γ_2 as shown.

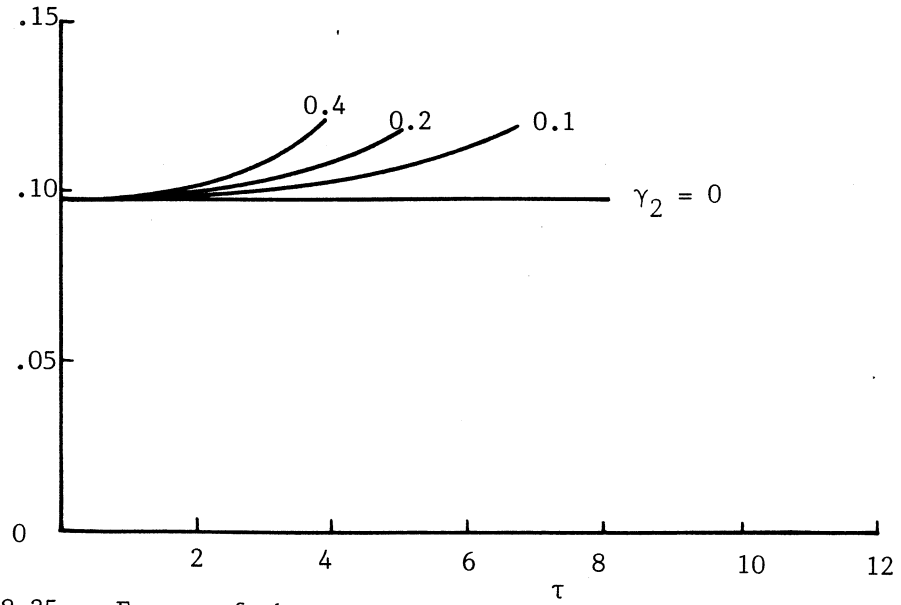

Figure 8.25 : Energy of the vortex array per member, $a_2 = 25.8$. Values of γ_2 as shown.

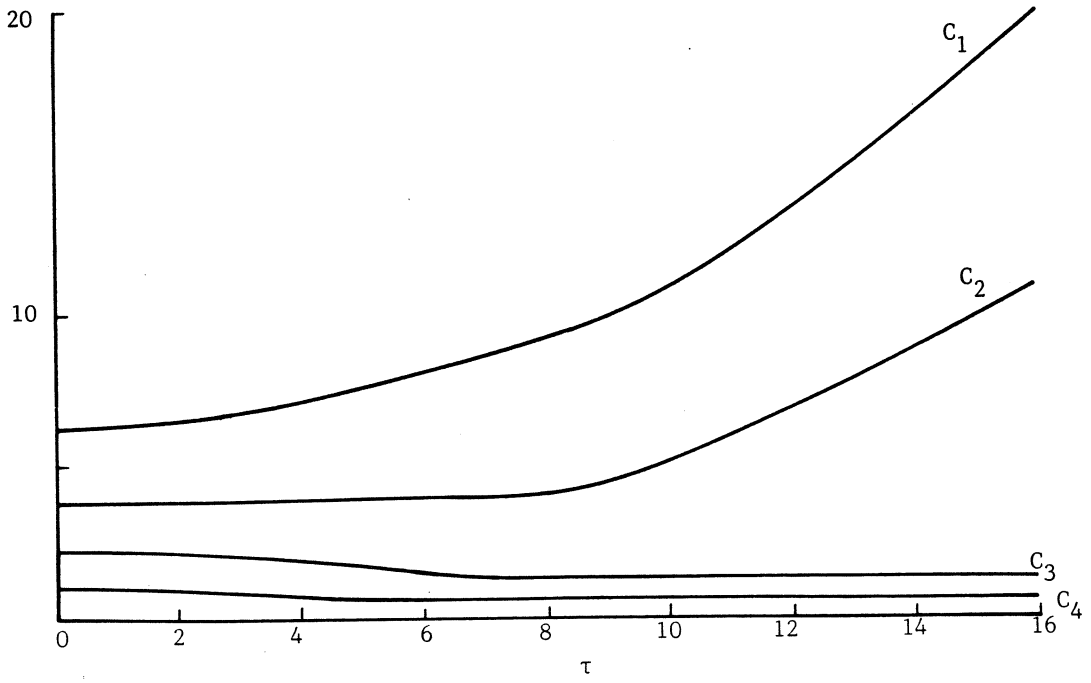

Figure 8.26 : Variation of contour perimeter with time τ, $a_2 = 12.7$, $\gamma_2 = 0.$

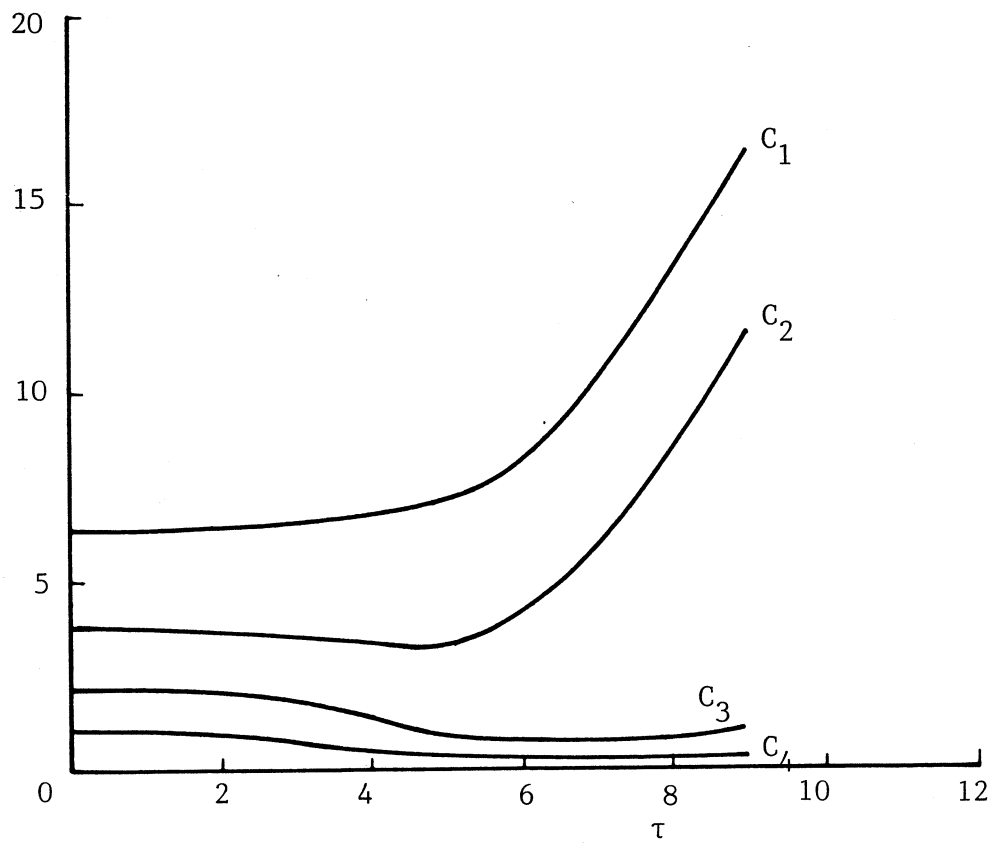

Figure 8.27 : Variation of contour perimeter with time τ, $a_2 = 25.8$, $\gamma_2 = 0.2.$

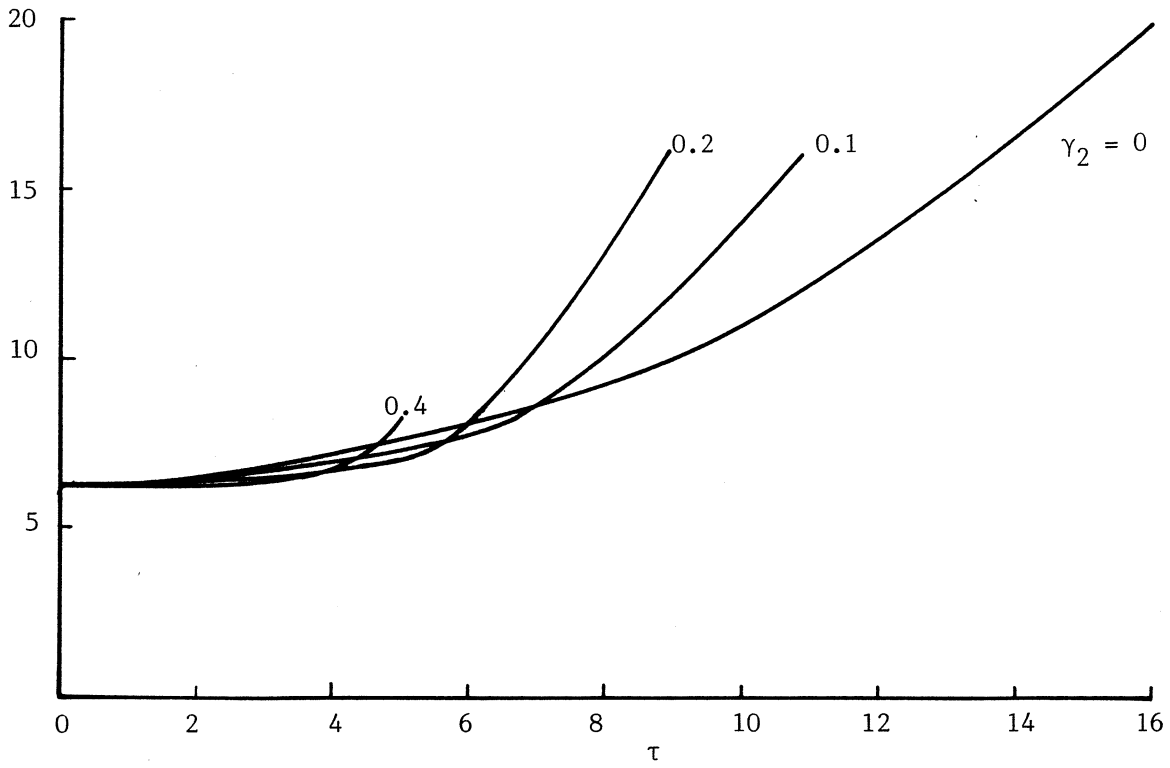

Figure 8.28 : Variation of perimeter of outermost contour with time, τ
$a_2 = 12.7$, values of γ_2 as shown.

9.0 STRETCHED SHEAR LAYERS

Some of the secondary vortex simulations (especially those with high aspect ratios) exhibit a Kelvin-Helmholtz type instability which results in each secondary vortex evolving into a string of compact vortex cores connected by braids of streamwise vorticity. A clear example is shown in figure 8.20 with M = 4, a_2 = 51.7 and γ_2 = 0.1, two frames of which are reproduced in figure 9.1. Locally, that is within the dashed box of figure 9.1, the evolution is similar to the purely two-dimensional roll-up of the primary (or spanwise) vortices investigated in chapter 7.

These small-scale vortices, which we associate with the tertiary motions of the CLS model, evolve in the ambient strain environment provided by the primary vortices. Given the similarities with the two-dimensional layer evolution, it appears profitable to study the behaviour of a stretched shear layer as a model of the secondary vortices in the limit of $a_2 \rightarrow \infty$.

The stretched shear layer has been studied by Lin & Corcos (1984) at moderate Re_δ using a finite difference technique. They used a Burgers vortex layer as an initial condition and found roll-up and, in some cases, pairing similar to that for the purely two-dimensional layer but substantially modified by the ambient strain environment.

9.1 Flow Configuration

In figure 9.2 we show a conceptual view of the flow model. A nonuniform unidirectional vorticity profile is approximated by a piecewise-constant distribution in the same way as for the purely two-dimensional layer defined in section 7.1. The imposed stretching strain (defined in section 8.1) is represented by the four streamline segments in the (y, z)-plane. The layer is periodic in the (spanwise) x-direction and the extensional axis of the strain is aligned with the

vortex lines along the z-axis (i.e., parallel to the braids in the primary motion). The circulation contained in one wavelength λ_3 of the fundamental eigenfunction (i.e., spacing of the rolled-up vortex cores) is Γ_3 giving $\Delta U_3 = \Gamma_3/\lambda_3$ as the velocity jump across the layer. By analogy with the two-dimensional evolution, the characteristic time for roll-up is $T_c = \lambda_3^2/\Gamma_3$.

Note that, unlike the viscous simulations of Lin & Corcos (1984), the Re = ∞ flow here has no equilibrium state. (The initially unperturbed layer decreases monotonically in thickness as $\exp(-\gamma t)$.) In simulations presented here, we effectively "turn on" the dynamics at $\tau = 0$.

9.2 Initial Conditions and Parameters

For the numerical simulations, the wavelength of the computational domain $\lambda_{comp} = 2\pi$ and the total circulation contained in the domain was set to $\Gamma_{comp} = 1$. The stretching parameter γ_3 was scaled to achieve the same local conditions for the vortex roll-up as experienced in the dashed box shown in figure 9.1. Measuring the circulation and spacing of the vortex cores, we obtain the approximate values (in terms of the secondary vortex simulation units) of $\lambda = 0.15\pi$ and $\Gamma = 0.15$ with a strain strength $\gamma_2 = 0.1$. These values give a characteristic time for roll-up of $T_c = 1.48$. Hence, for $\Gamma_3 = 0.5$ and $\lambda_3 = \pi$, the stretching parameter becomes $\gamma_3 = 0.0075$. As there is some variation in the strengths and spacing of the small vortex cores in figure 9.1, we attempt to bracket the effective strain environment by generally using two values of γ_3 for each vorticity distribution.

We have not determined the stability characteristics for this nonequilibrium layer. Instead, we start from the same initial conditions (ie., we apply perturbations consisting of the same eigenfunctions and amplitudes to the layer) as for the purely two-dimensional simulations shown in chapter 7.

9.3 Simulation Results and Discussion

The computations were performed on a Cyber 205 supercomputer using (code-version C, table 4.1) and node-parameter sets 1 and 2, (table 4.3). The only extra features of the numerical implementation were *(i)* the addition of a y-component of velocity due to the imposed strain field and *(ii)* the intensification of the vorticity as specified in equation (3.24). We have selected three vorticity configurations to illustrate the effects of vortex stretching. These correspond to the pure-pairing, pure-tearing and three-vortex coalescence cases (cases 3, 5, and 7 respectively) in section 7.4. A preliminary result showing the stretched pure-pairing evolution was included in Jacobs & Pullin [4]. Table 9.1 contains a summary of the full set of computations.

Figures 9.3 and 9.4 show the evolution of a stretched layer which is initially perturbed to produce the pure-pairing interaction of case 3 in section 7.4.2. Two values of stretching chosen to model the local conditions in the secondary vortex simulations (γ_3 = 0.0075, 0.015 for figures 9.3 and 9.4 respectively) were investigated to indicate the trends with increasing γ_3 and, in figure 9.5, we show the individual frames taken at roughly equivalent times near the end of each simulation.

The intensification of vorticity combined with the conservation of circulation leads to a reduction in the area enclosed by the bounding contours (equation 3.27). This intensification of vorticity also accelerates the roll-up into compact cores and enhances the production of the spiral filaments that wind around these cores. Figure 9.6a shows the variation of contour lengths with time. Once the spiral filaments have formed, there is a rapid increase in the contour length as occurred in the two-dimensional simulations. However, the stretching induces a higher rate of growth. For the higher strain rates (γ_3 = 0.015) of the simulation in figure 9.4 and its associated plot of contour length in figure

9.7a, these effects are more pronounced. At $\tau = 3.5$ in the pairing simulations, $p_1/\lambda_1 = 2.6$, 3.2 and 4.0 for $\gamma_3 = 0.0$, 0.0075, 0.015 respectively.

In general, the simulations of the stretched layer could not be taken to as large a time, τ, as the equivalent, purely two-dimensional simulations of section 7.4. This limitation is due to the enhanced spiral production and the associated increase in numbers of nodes, $N_j(\tau)$. The numbers of nodes on each of the upper four contours are shown on the plots of figure 9.5. For $\gamma_3 = 0.015$, $N_4(\tau=3.8) = 960$ which is quite close to the limit of $N_{max} = 1000$.

The stretching strain also has a marked effect upon the interaction of the subharmonic. First, it inhibits the rotation of the centroids of the vortex cores about each other and, secondly, the reduction in area of the vortex cores inhibits coalescence of the rolled-up cores. More evidence for the inhibition of rotation of the centroids is contained in figures 9.6b and 9.7b which show that, for any particular time, the maximum-height-reached is reduced with increasing strain. For example, at $\tau = 3.5$, $Y_j/\lambda_1 = 0.468$, 0.40, 0.352 for $\gamma_3 = 0.0$, 0.0075, 0.015 respectively. However, in both plots having $\gamma_3 > 0$, Y_j still has a high growth rate at the final times shown. The extent to which the pairing interaction is inhibited may be explained via Lundgren's transformation (3.28) to an equivalent purely two-dimensional flow (i.e., $\gamma_3 = 0$) which has an in-plane strain

$$\underline{u}_s = \gamma_3/2 \exp[-Q(t(T))] \quad (x\underline{i} - y\underline{j}) \quad . \qquad (9.1)$$

With the line joining the vortex centroids nearly aligned with the x-axis, the purely two-dimensional strain (9.1) tends to separate the vortex cores thus slowing and/or inhibiting the tendency for the cores to merge. (See also the discussion in chapter 10.) In the stretched layer simulations, however, the velocity vector (consisting of the stretching strain plus the induced field due to the rest of the vortex array) at the centroid of a vortex core includes a component towards the

centre of symmetry of the vortex pair (Lin & Corcos 1984). Thus, although the pairing process may be initially inhibited, the stretched vortices will always approach each other if they are initially perturbed in an alternating fashion.

Two simulations involving the pure-tearing interaction are displayed in figures 9.8 and 9.9 for $\gamma_3 = 0.0075$ and 0.015 respectively. Again the vorticity intensification leads to increased speed of rotation of the cores and enhanced production of spiral filaments but the effect on the tearing interaction appears to be minimal. For both values of stretching investigated the tearing interaction proceeded to a point where the larger vortex circulation was 1.5 times that of the smaller vortex (see figure 9.11), in much the same time as for the $\gamma_3 = 0$ case (see figure 7.31b). Solution frames at roughly equivalent times near the final times for each of the tearing simulations are shown in figure 9.10. Another feature inhibited by vortex stretching is the migration of the thick braid formed around the larger core. In the relatively long-time, $\gamma_3 = 0$, simulations of the single mode perturbation (case 2, section 7.4.1), the fluid contained in the braids migrated along the layer. However, for the finite γ_3 here, the spiral filaments are rapidly tightened about the concentrated cores and do not migrate.

As a final example, we show the effect of stretching on the three-vortex interaction. Figure 9.12 displays the evolution of the layer while figure 9.13 compares this stretched result with the equivalent two-dimensional result (case 7, section 7.4.3). As discussed above the following stretching-induced effects are present *(i)* the formation of compact cores with reducing area *(ii)* enhanced spiral production *(iii)* inhibition of coalescence of the cores and *(iv)* inhibition of the migration of fluid contained in the braids/filaments.

Table 9.1: Summary of stretched shear layer simulations.

Case	δ_ω	λ_{comp}/λ_1	γ_3	perturbation	T_c	τ_{max}	Code-Version	Node-Parameters	CPU-time seconds
1	0.438	2	0.0075	$0.05(f_1^{(4)} + f_2^{(4)})$	19.74	4.306	C	2	12100
2a	0.438	2	0.015	$0.05(f_1^{(4)} + f_2^{(4)})$	19.74	3.673	C	1	8030
2b	0.438	2	0.015	$0.05(f_1^{(4)} + f_2^{(4)})$	19.74	3.799	C	2	12300
3	0.438	2	0.0075	$0.05(f_1^{(4)} + e^{i\pi/2} f_2^{(4)})$	19.74	3.799	C	2	12100
4	0.438	2	0.015	$0.05(f_1^{(4)} + e^{i\pi/2} f_2^{(4)})$	19.74	3.483	C	2	12800
5	0.292	3	0.011	$0.033(f_1^{(4)} + f_3^{(4)})$	13.16	4.654	C	2	12300

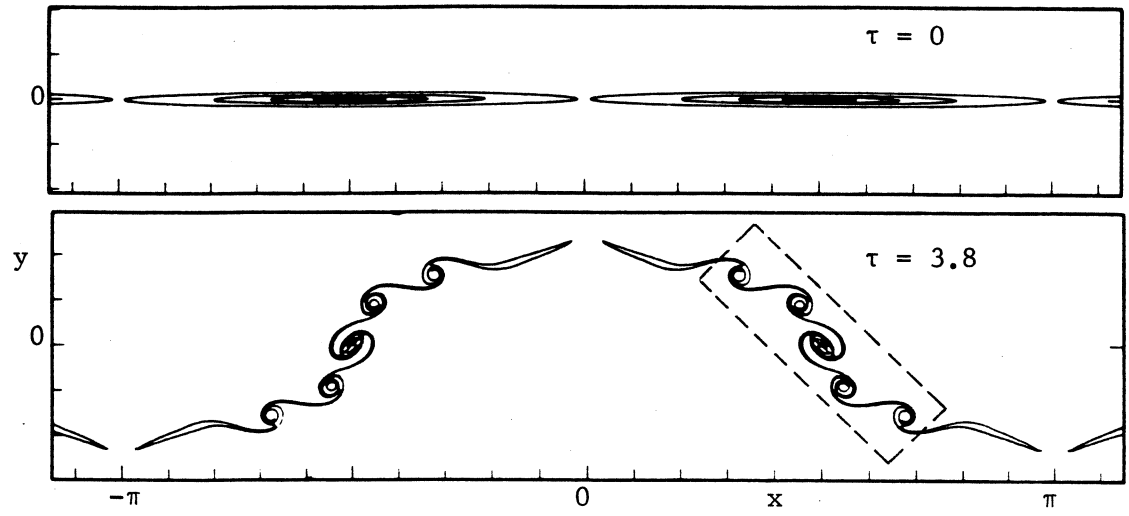

Figure 9.1 : Initial and final solution frames for the evolution of the secondary vortex array, $a_2 = 51.7$, $\gamma_2 = 0.1$ figure 8.20. The dashed box denotes the region where the vortex dynamics is similar to that for a periodic layer.

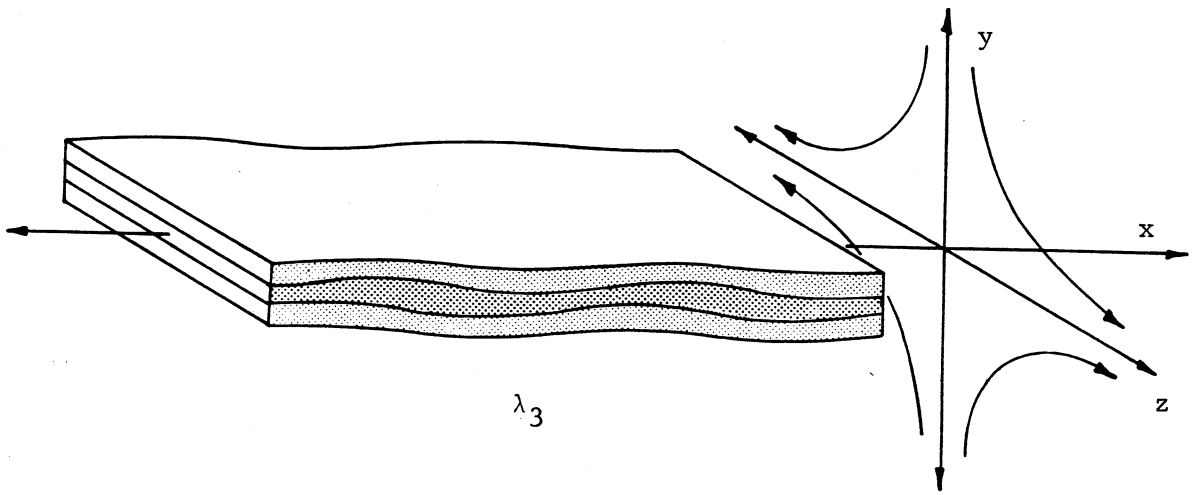

Figure 9.2 : A section of an x-periodic shear layer subject to locally-uniform three-dimensional strain. The layer shown here consists of three regions of uniform vorticity ω_z.

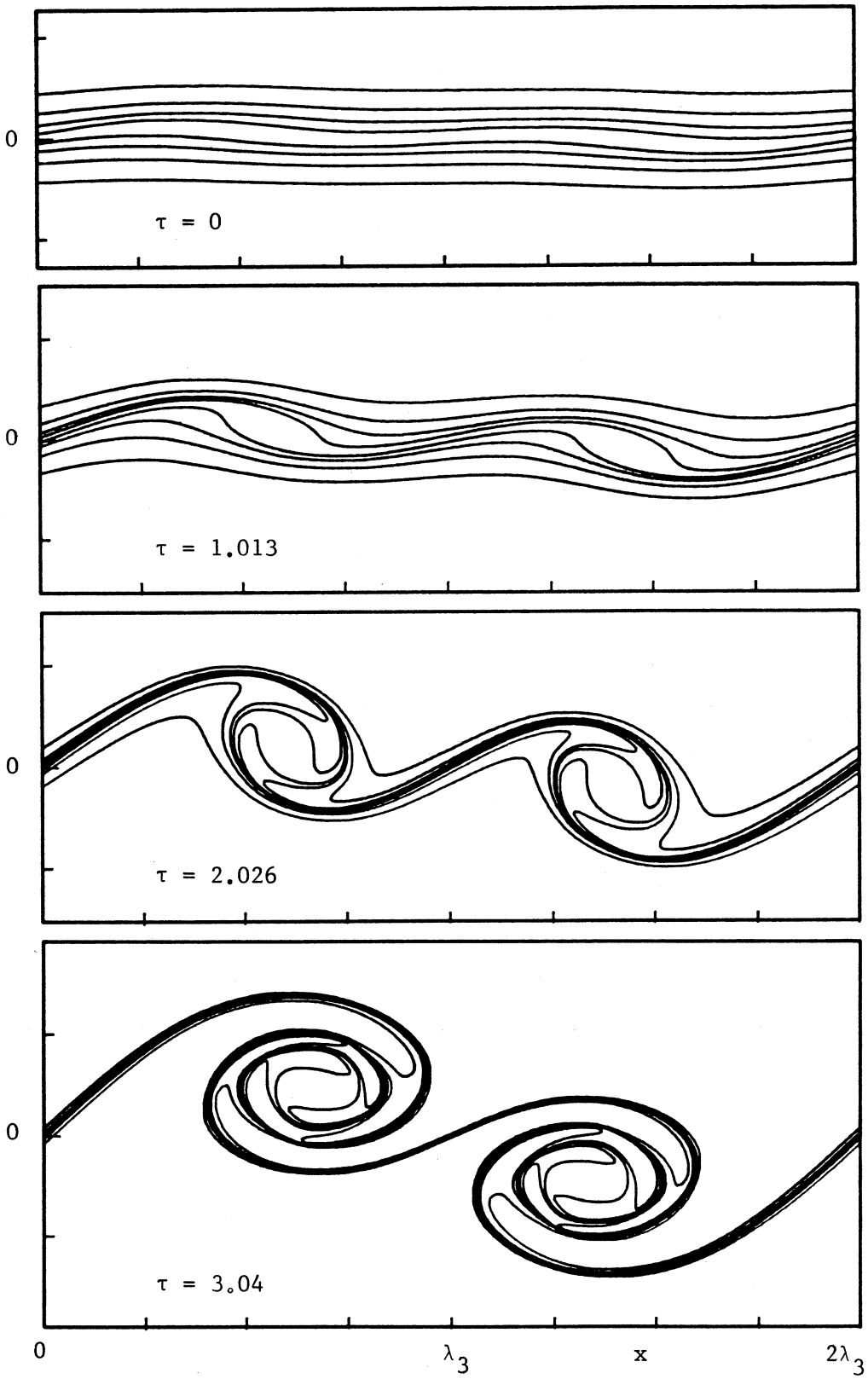

Figure 9.3 : Evolution of a stretched shear layer showing a single pairing event, $\gamma_3 = 0.0075$, $\delta_\omega/\lambda_3 = 0.875/2\pi$, $a_0/\lambda_3 = 0.05/\pi$, initial disturbance $f_1 + f_2$, case 1 (table 9.1). Times τ as shown.

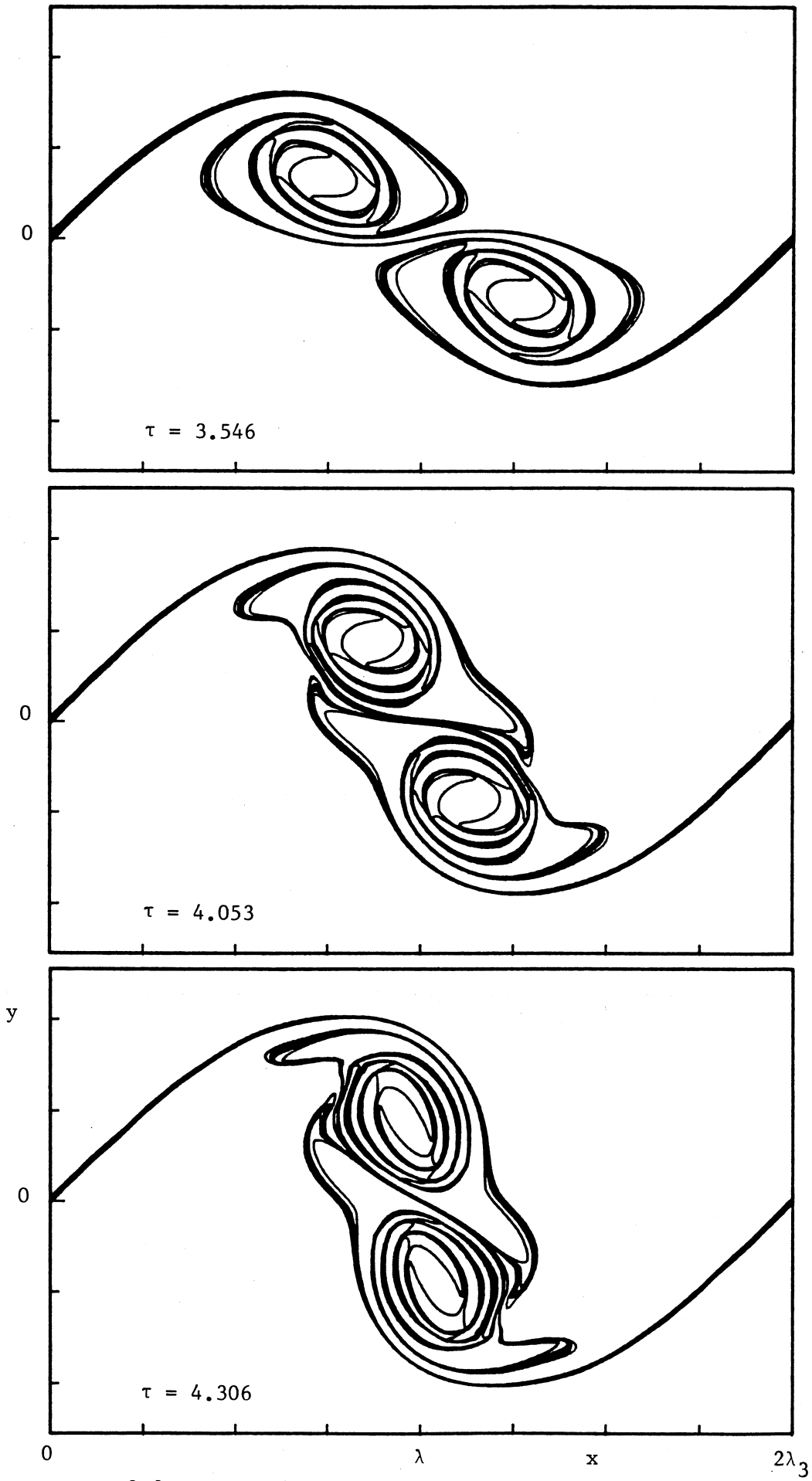

Figure 9.3 continued.

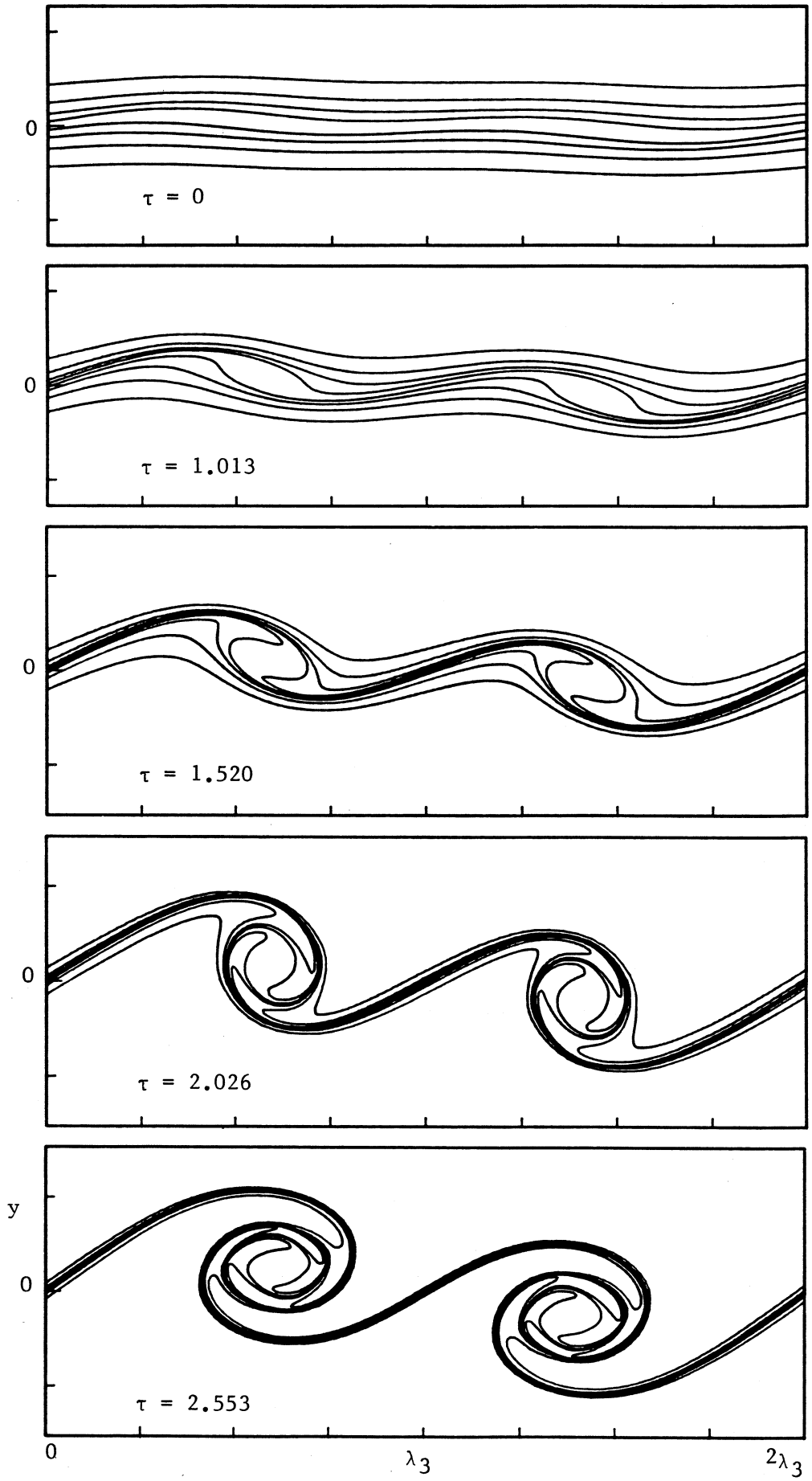

Figure 9.4 : for caption see over page.

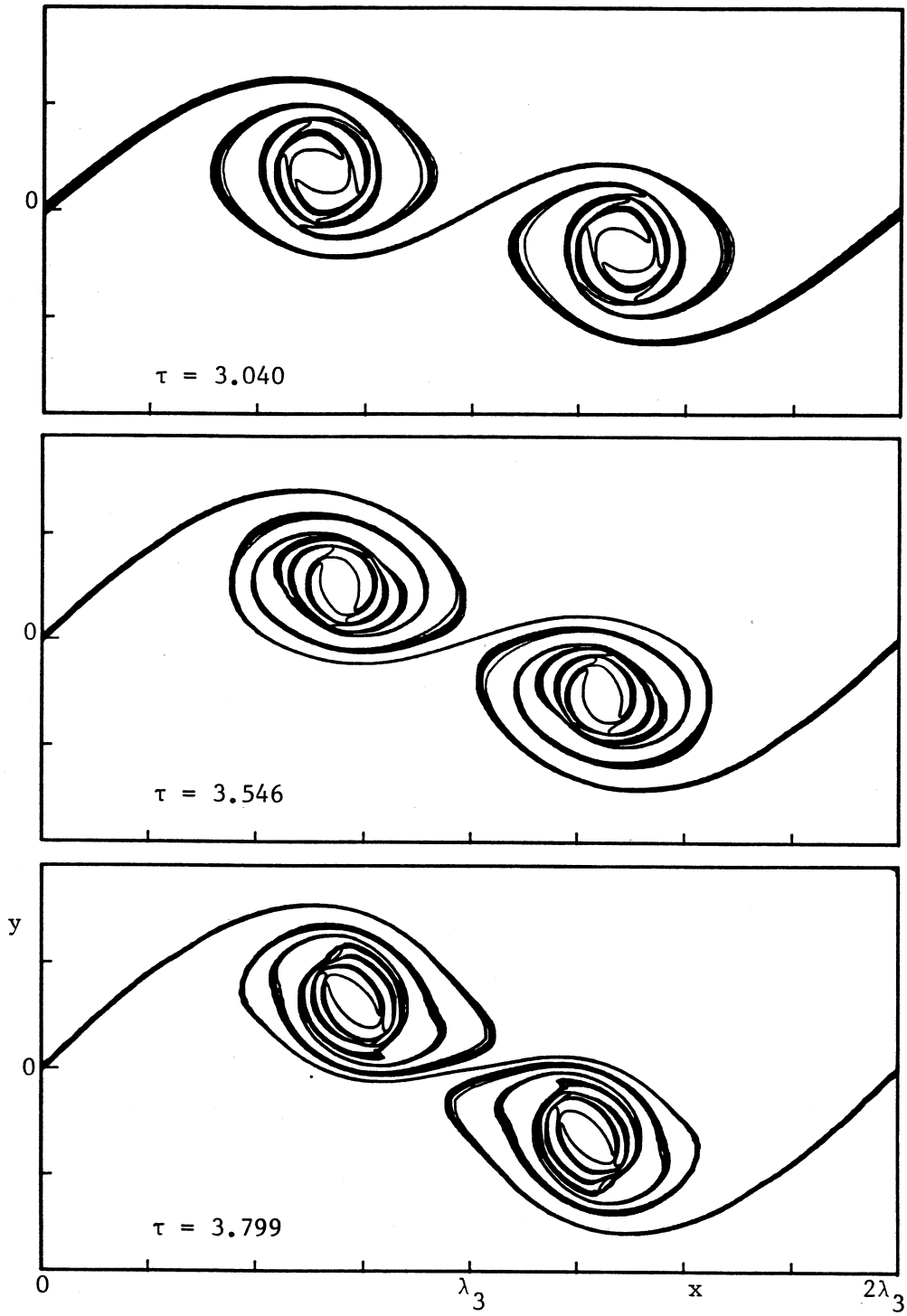

Figure 9.4 : Evolution of a stretched shear layer showing a single pairing event, $\gamma_3 = 0.015$, $\delta_\omega/\lambda_3 = 0.875/2\pi$, $a_0/\lambda_1 = 0.05/\pi$, initial disturbance $f_1 + f_2$, case 2b (table 9.1). Times τ as shown.

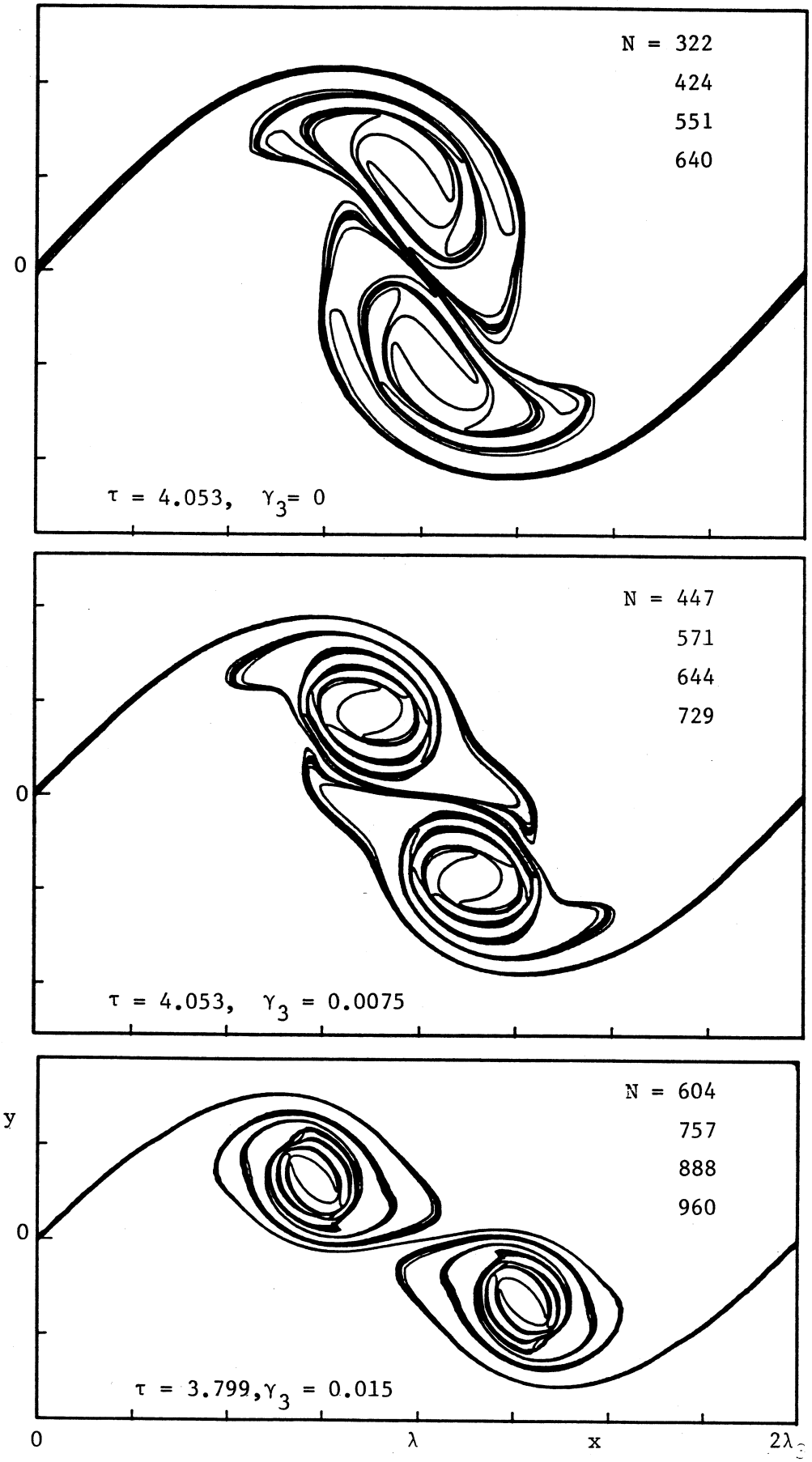

Figure 9.5 : Comparison of late-time solutions for the pairing event with 3 values of stretching, γ_3. Times τ, stretching strain strength γ_3 and numbers of nodes defining C_j, j = 1...4 as shown.

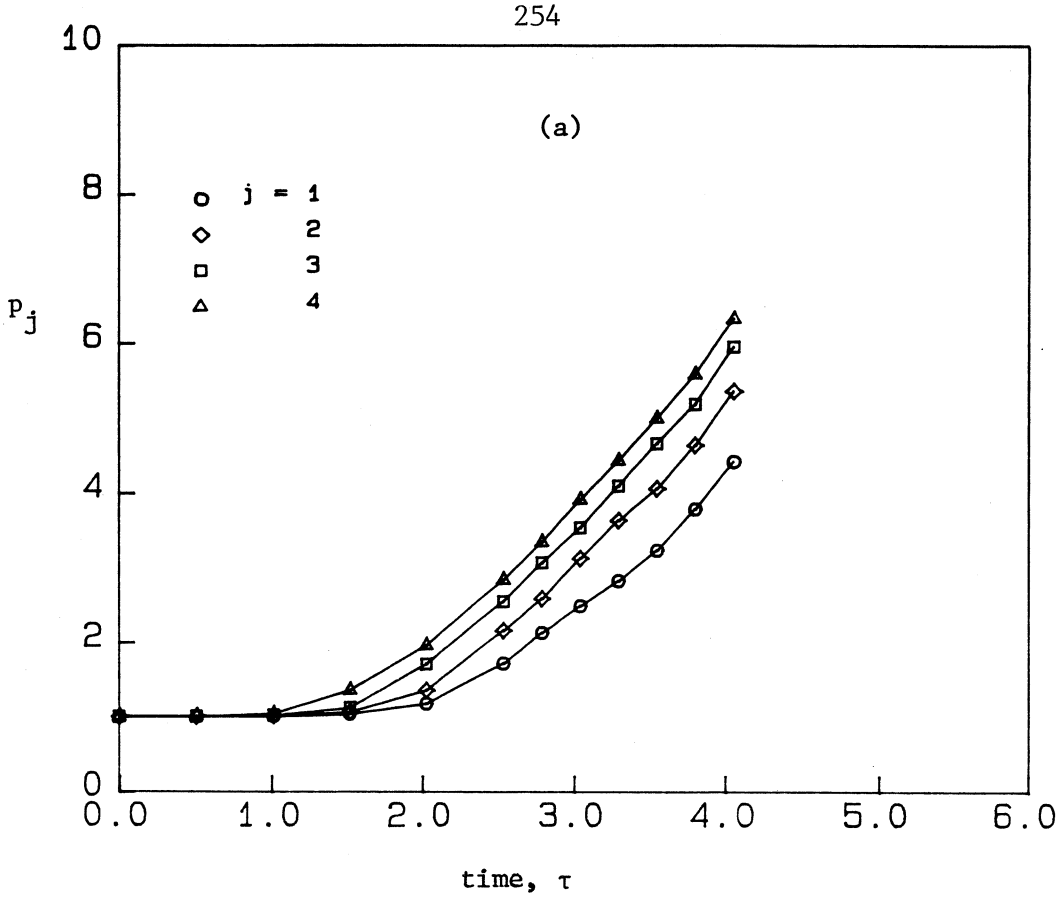

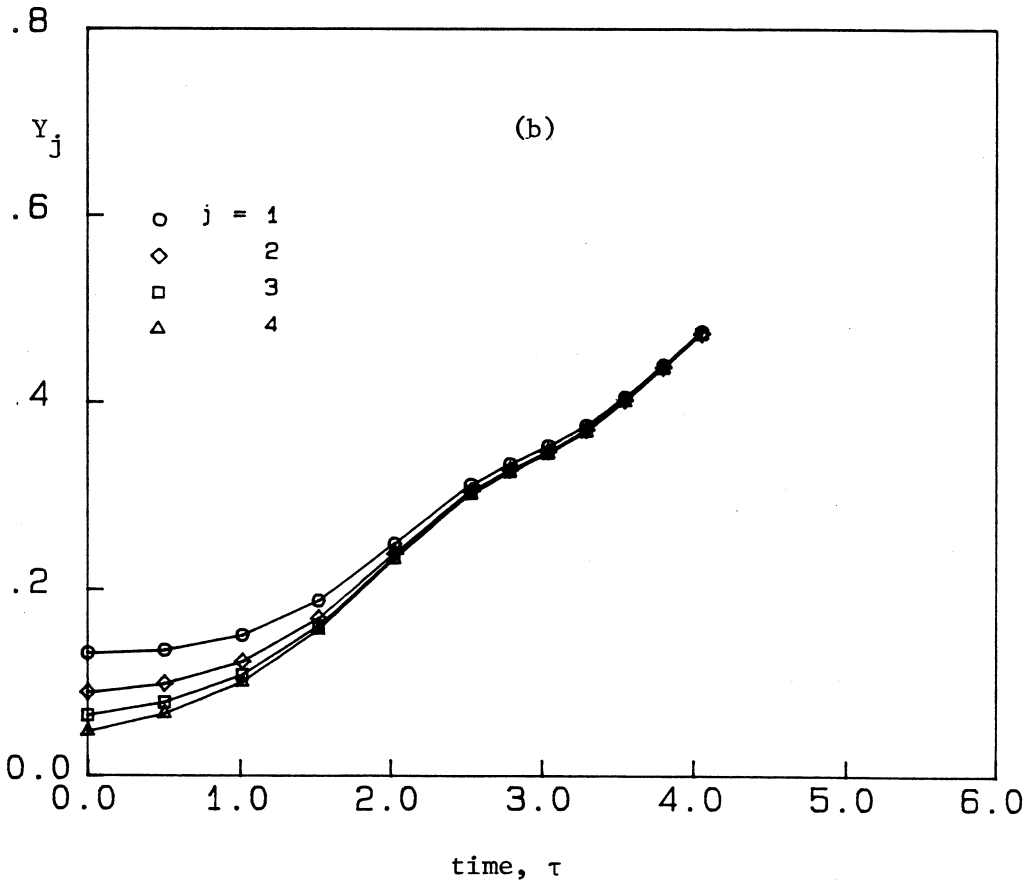

Figure 9.6 : (a) Growth of contour length, p_j, for the pairing event with $\gamma_3 = 0.0075$, case 1 (table 9.1).
(b) Variation of contour height, Y_j, for case 1.

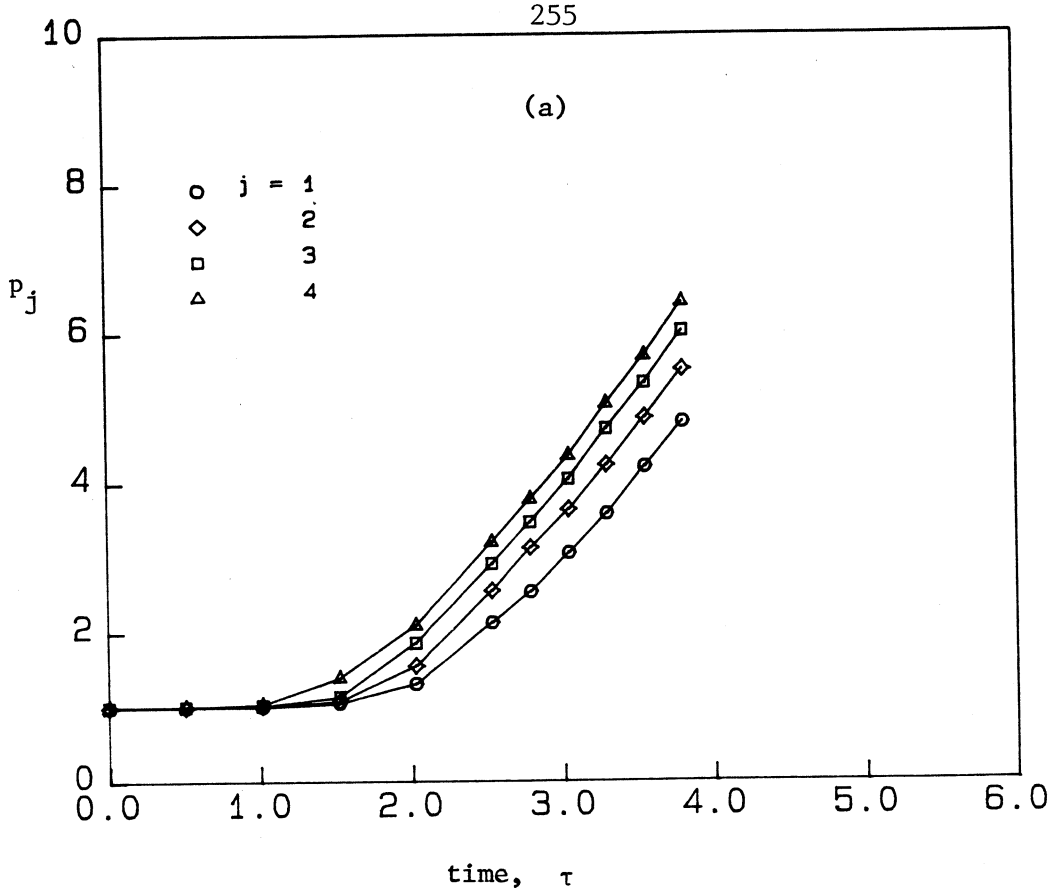

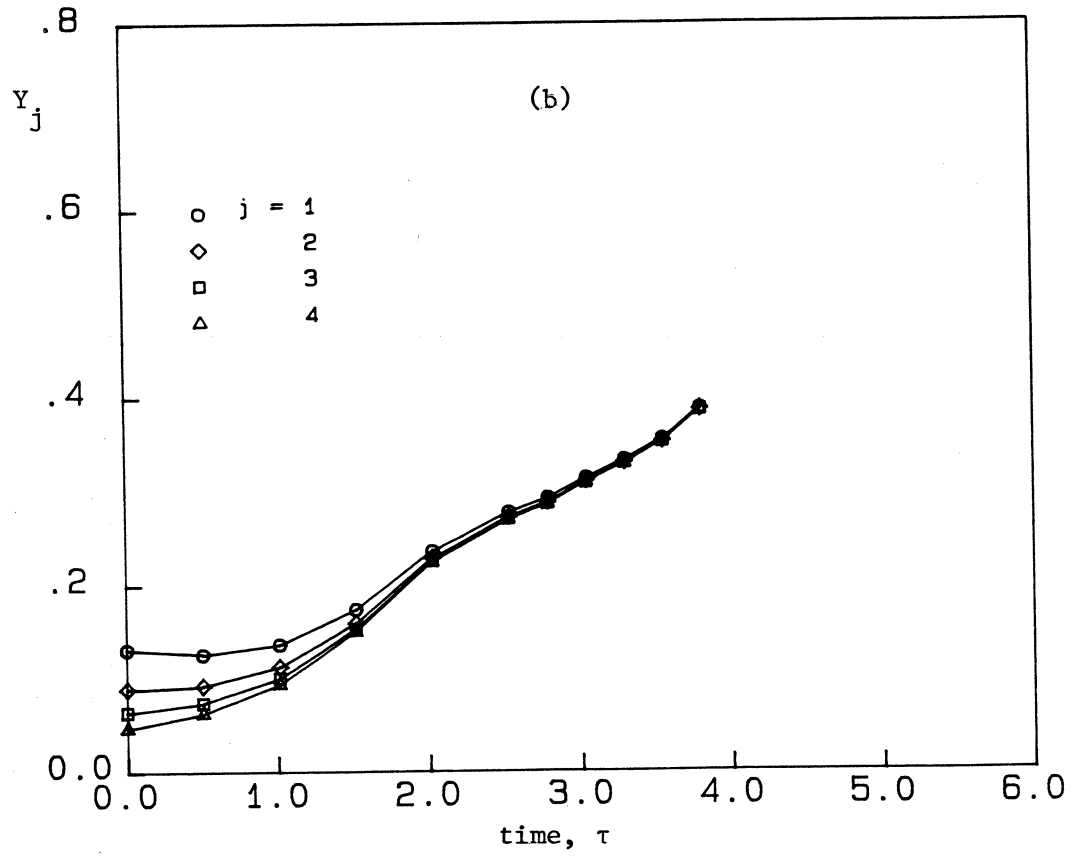

Figure 9.7 : (a) Growth of contour length, p_j, for the pairing event with $\gamma_3 = 0.015$, case 2b (table 9.1).
(b) Variation of contour length, Y_j, for case 2b.

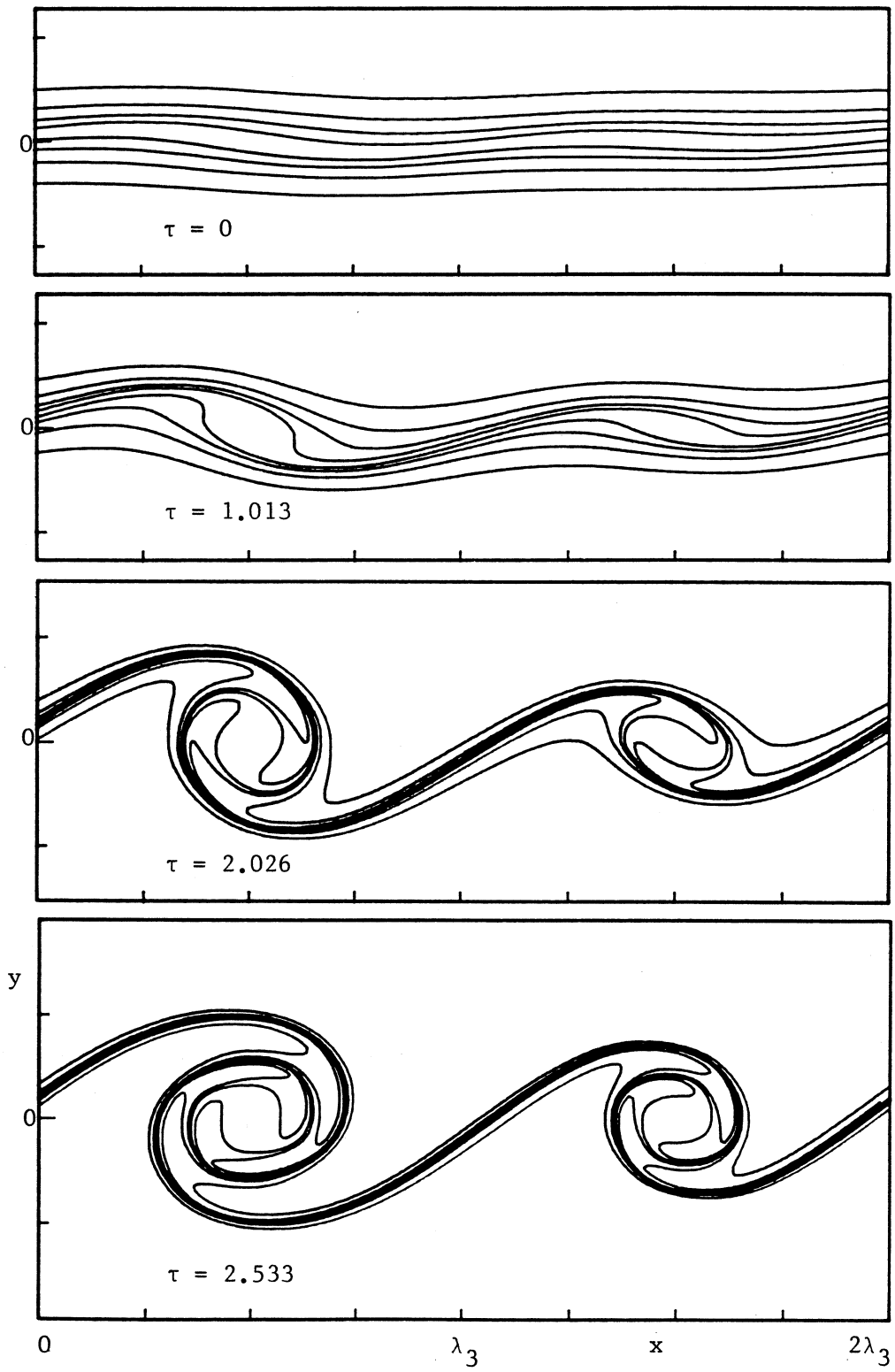

Figure 9.8 : Evolution of a stretched shear layer showing a tearing event, $\gamma_3 = 0.0075$, $\delta_\omega/\lambda_3 = 0.875/2\pi$, $a_0/\lambda_1 = 0.05/\pi$, initial disturbance $f_1 + e^{i\pi/2} f_2$, case 3 (table 9.1). Times τ as shown.

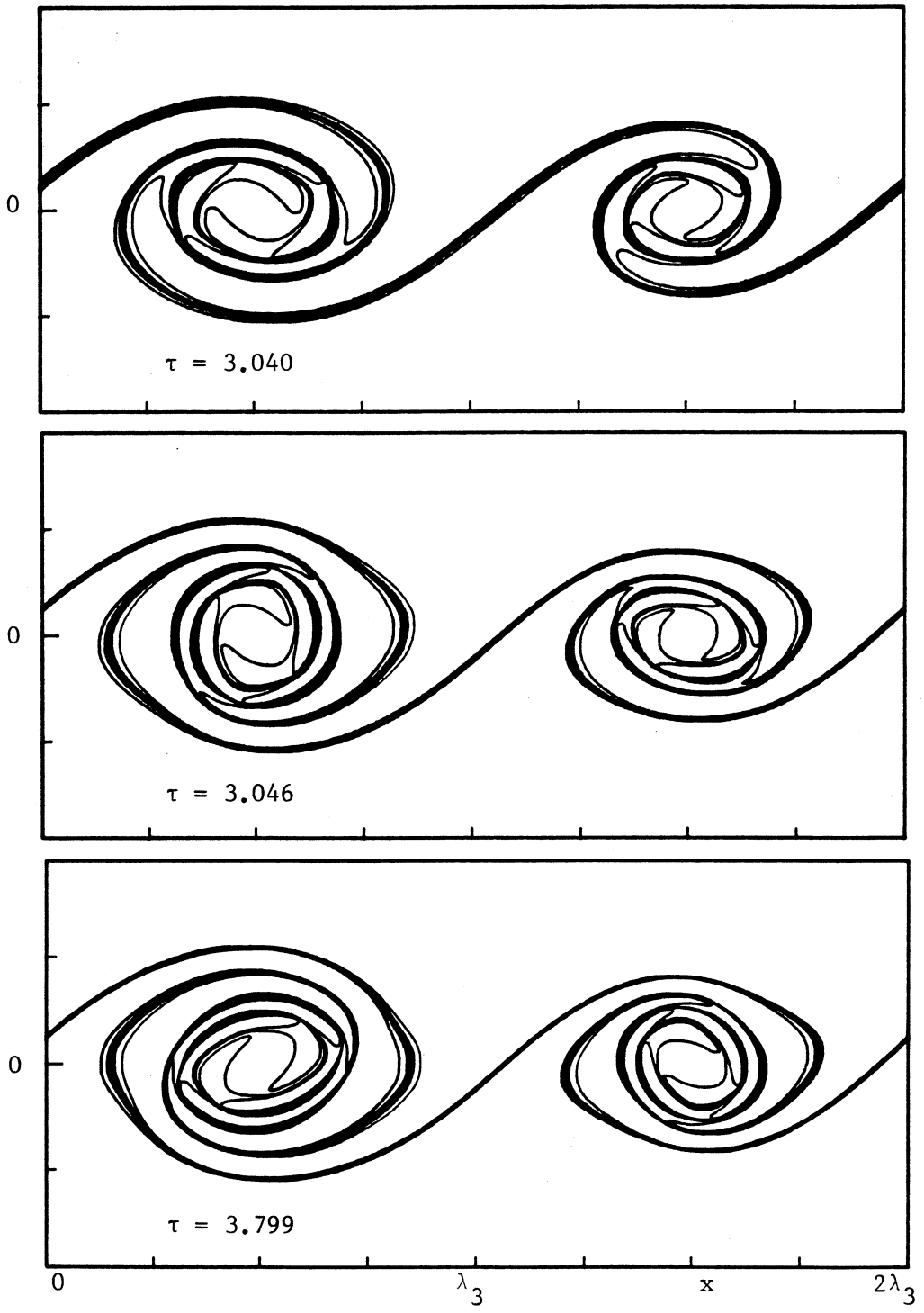

Figure 9.8 continued.

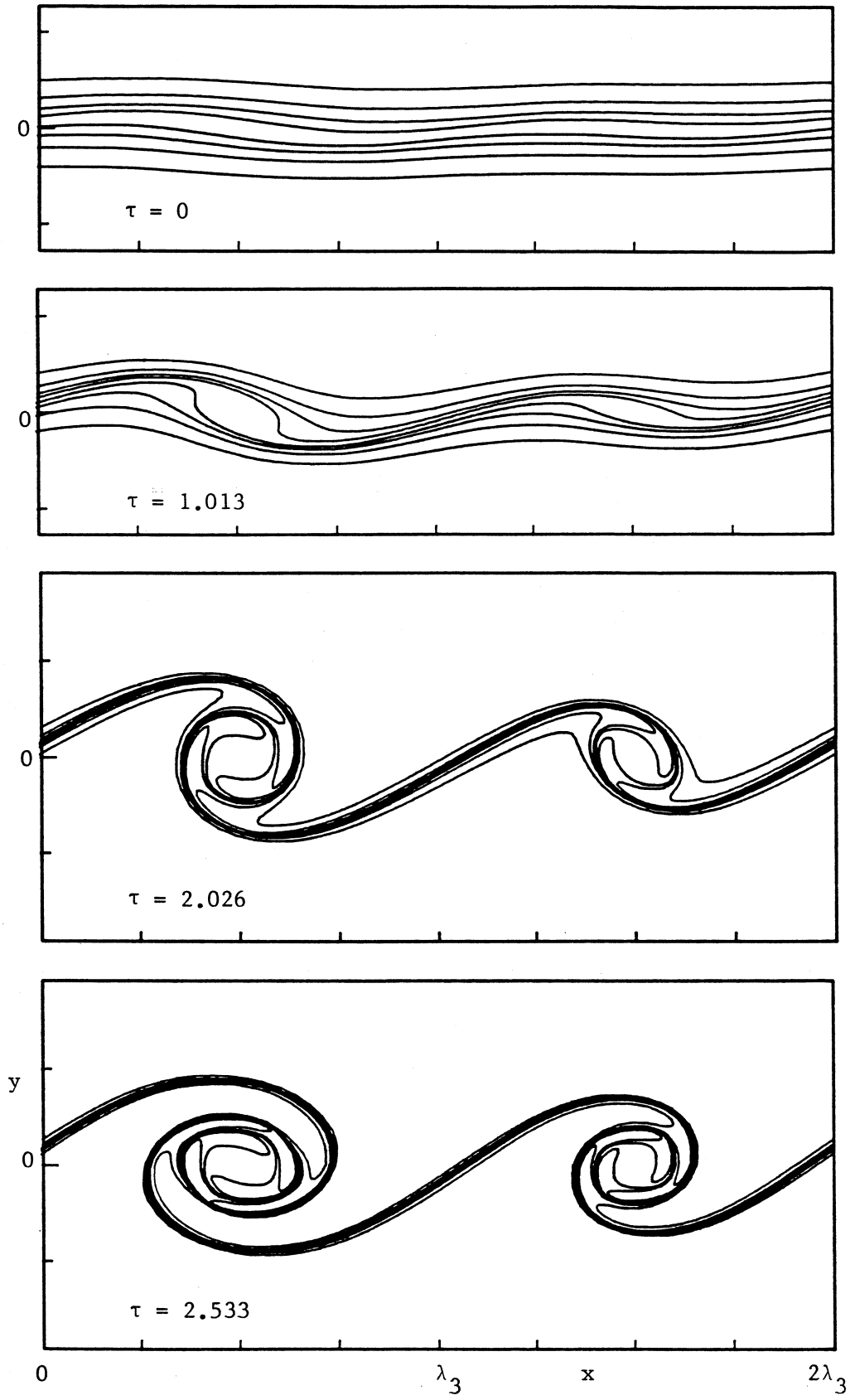

Figure 9.9 : for caption see over page.

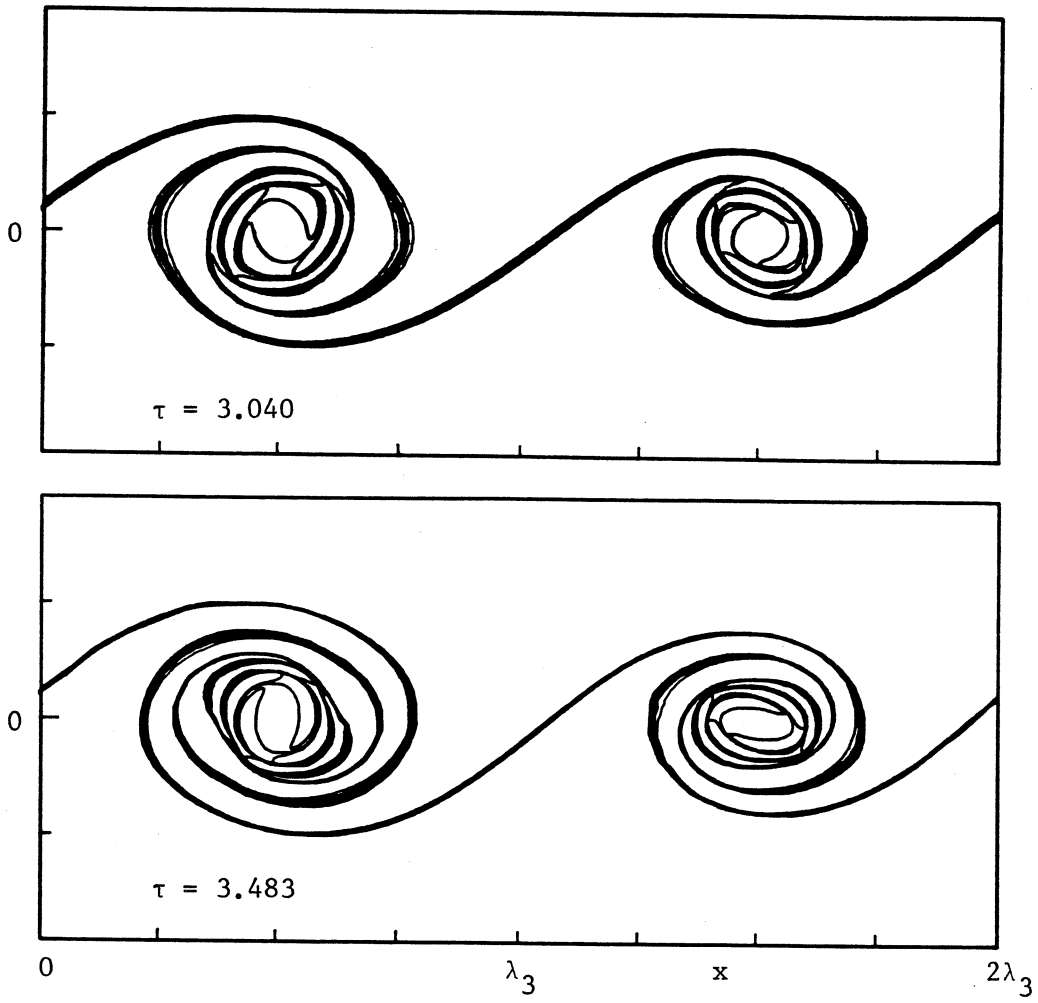

Figure 9.9 : Evolution of a stretched shear layer showing a tearing event, $\gamma_3 = 0.015$, $\delta_\omega/\lambda_3 = 0.875/2\pi$, $a_0/\lambda_3 = 0.05/\pi$, initial disturbance $f_1 + e^{i\pi/2} f_2$, case 4 (table 9.1). Times τ as shown.

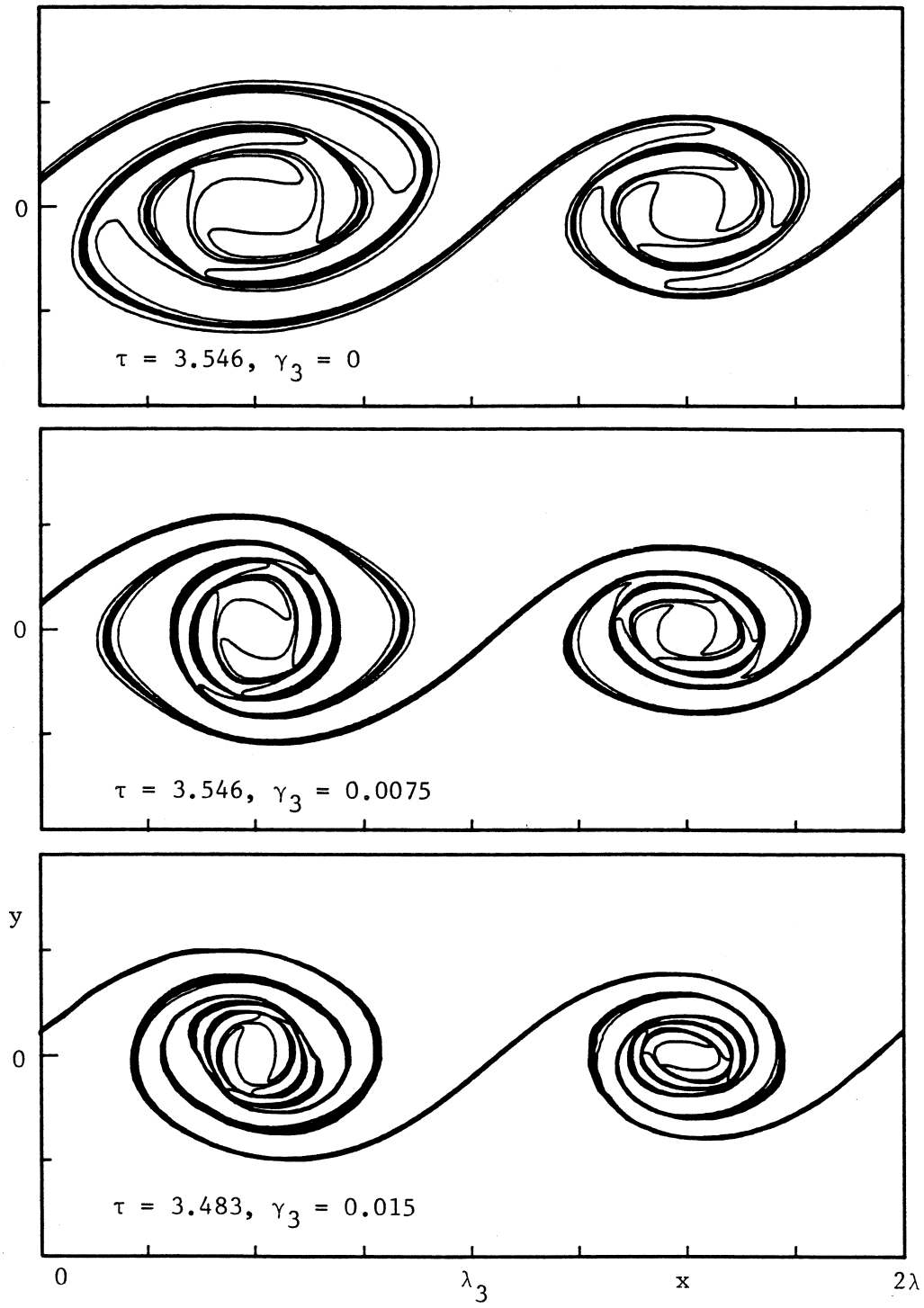

Figure 9.10 : Comparison of late-time solutions for the tearing event with 3 values of stretching, γ_3,. Times τ and stretching strain strength γ_3 as shown.

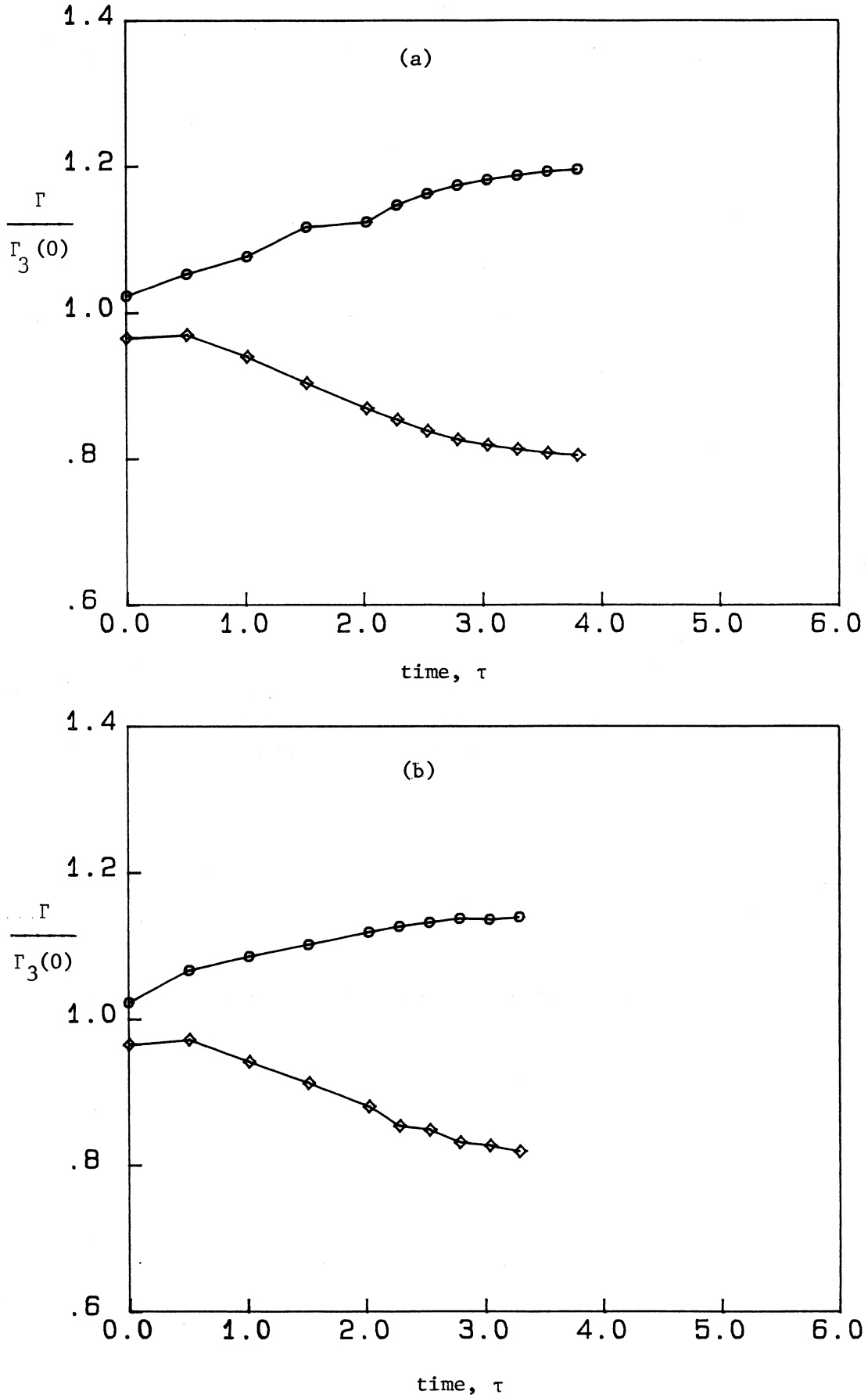

Figure 9.11 : Variation of circulations in vortex 1 and 2 in the stretched "tearing" simulation (a) $\gamma = 0.0075$, case 3 (b) $\gamma = 0.015$, case 4 (table 9.1). $\Gamma_3(0)$ is the nominal circulation for a rolled-up vortex.

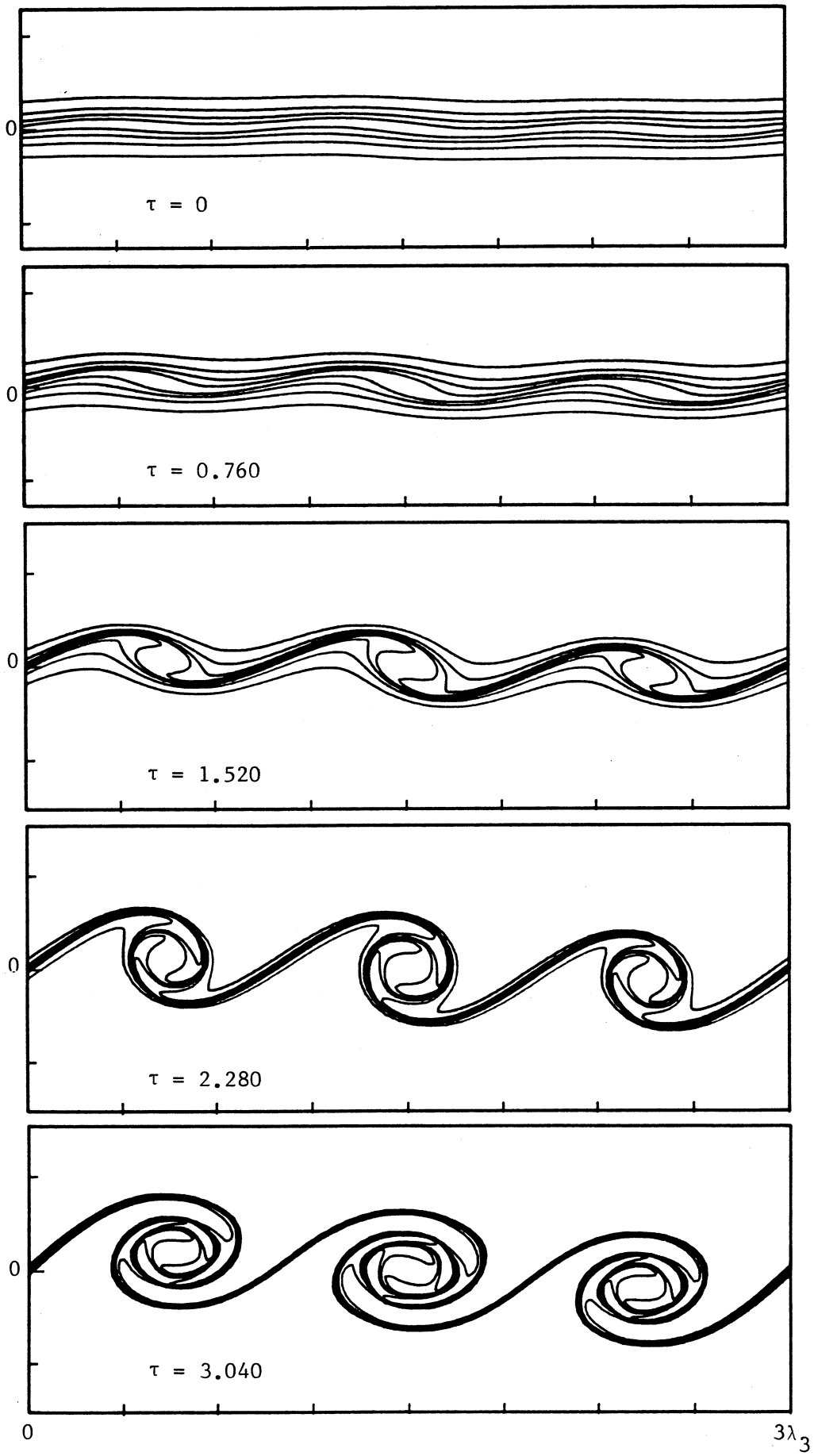

Figure 9.12 . for caption see over.

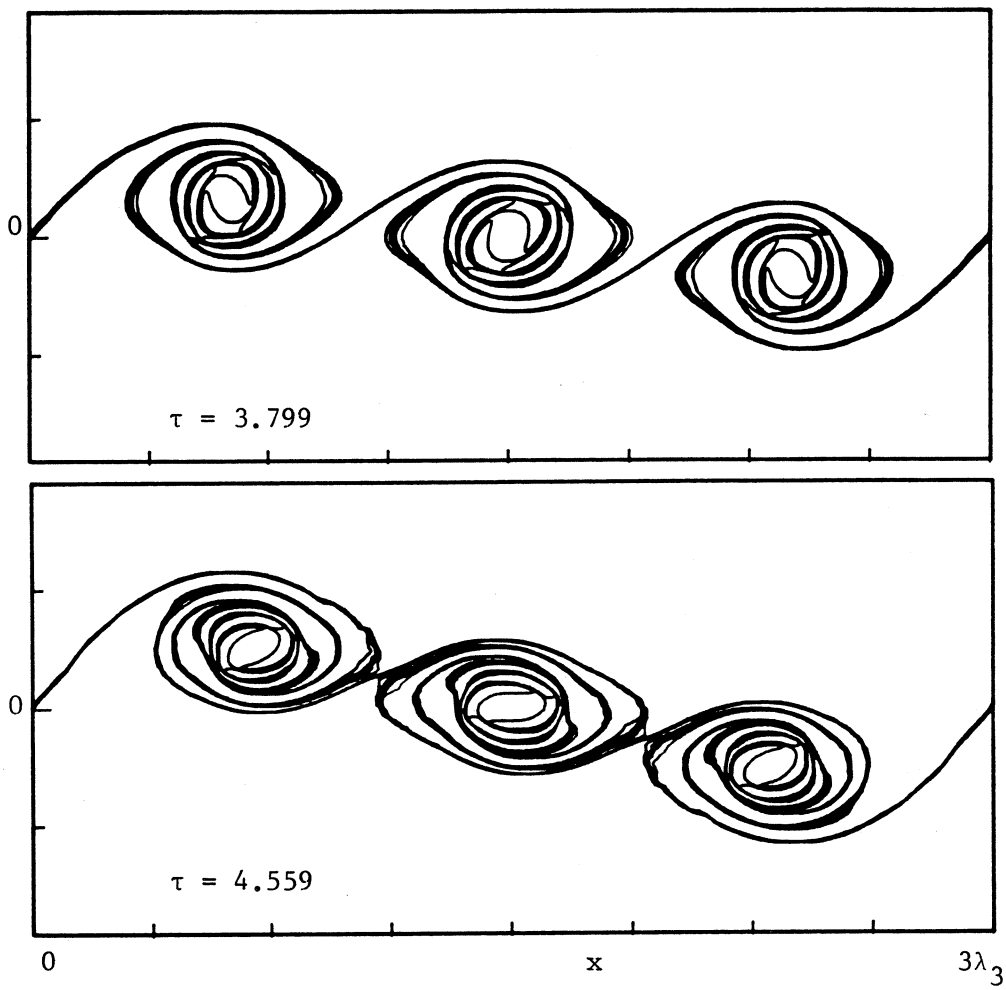

Figure 9.12 : Evolution of a stretched shear layer showing three-vortex event, $\gamma_3 = 0.011$, $\delta_\omega/\lambda_3 = 0.875/2\pi$, $a_0/\lambda_3 = 0.05/\pi$, initial disturbance $f_1 + f_3$, case 5 (table 9.1). Times τ as shown.

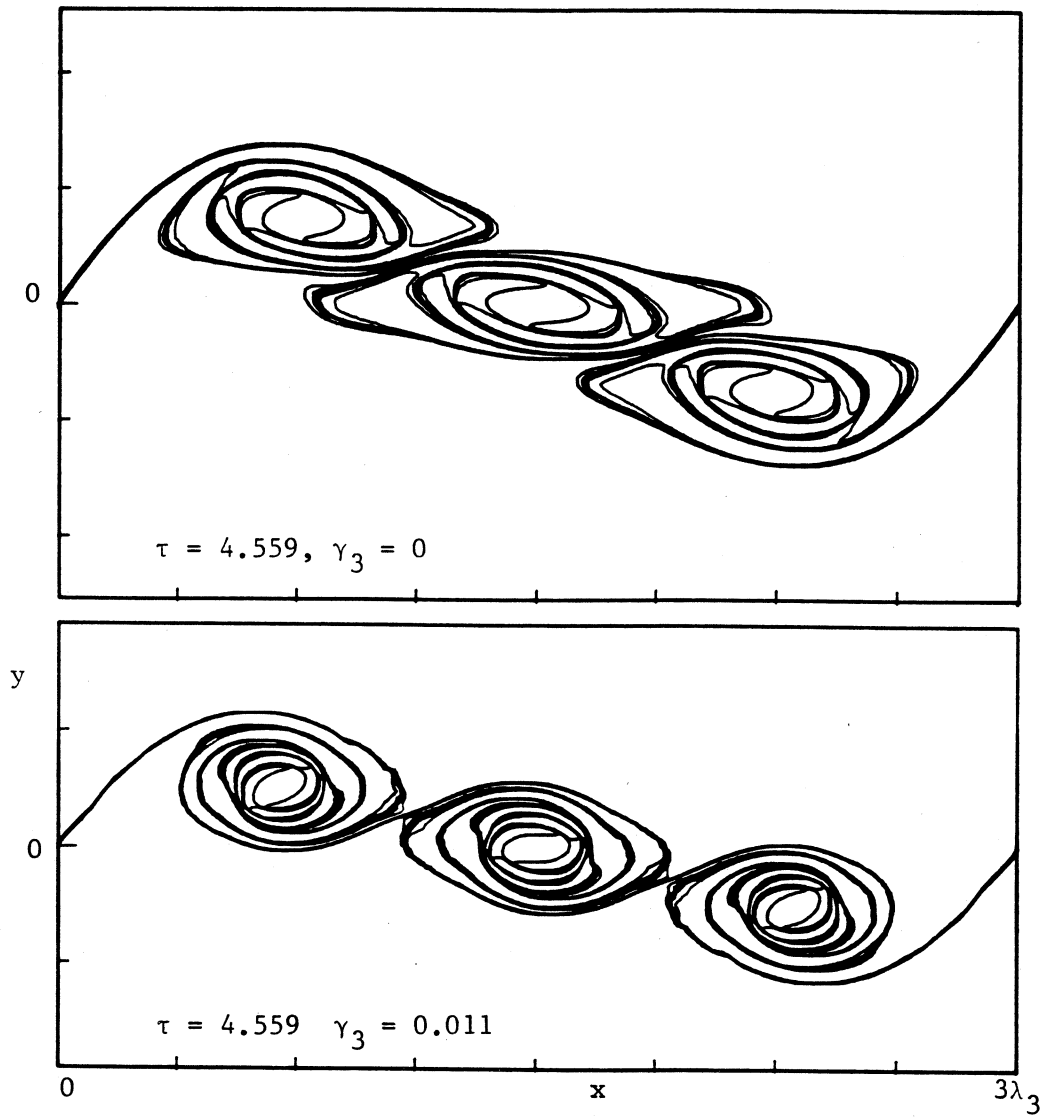

Figure 9.13 : Comparison of late time solutions for the three-vortex event with different strain rates, γ_3. Times τ and stretching strain strength γ_3 as shown.

10.0 THE EFFECT OF STRETCHING ON VORTEX COALESCENCE

In this section we describe qualitatively the influence of plane three-dimensional stretching strain (3.20) on the inviscid coalescence or merging process of two equal vortices. The terms "coalescence" and "merging" are used synonymously to describe a process by which the boundaries of the interacting FAVRs approach closely and the regions fold together into a single structure.

Both uniform vorticity FAVRs and nonuniform piecewise constant vorticity FAVRs are studied. The results from the former have been published in Jacobs & Pullin [1] while the nonuniform vorticity results appeared in Jacobs & Pullin [2].

One situation approximated by an isolated pair of interacting vortices is the long time behaviour of the rolled-up vortices of the stretched shear layer undergoing pairing. In some of the shear layer simulations there is pairing for small values of stretching but, for larger strains, the results are inconclusive as the computation could not be taken to long enough simulation times. The main reason for the expense of the shear layer computations is the rapidly increasing length of the braids that wrap around, and join, the rolled-up vortex cores. Here, we can start the calculation afresh with a pair of the rolled-up vortex cores being approximated by two circular vortices, diameter d, separated by a distance D.

Another application is Lundgren's (1982) strained spiral vortex model of the fine structure of turbulence at high Re. In this model, the mere existence of non-axisymmetric vortex sheets leads to the -5/3 law for the turbulence energy spectrum. The coalescence of like signed vortices is a possible mechanism for the generation of such spiral filaments. In nearly all two-dimensional simulations the merging process results in the ejection of vortex arms presumably to conserve angular momentum (Zabusky, Hughes & Roberts, 1979).

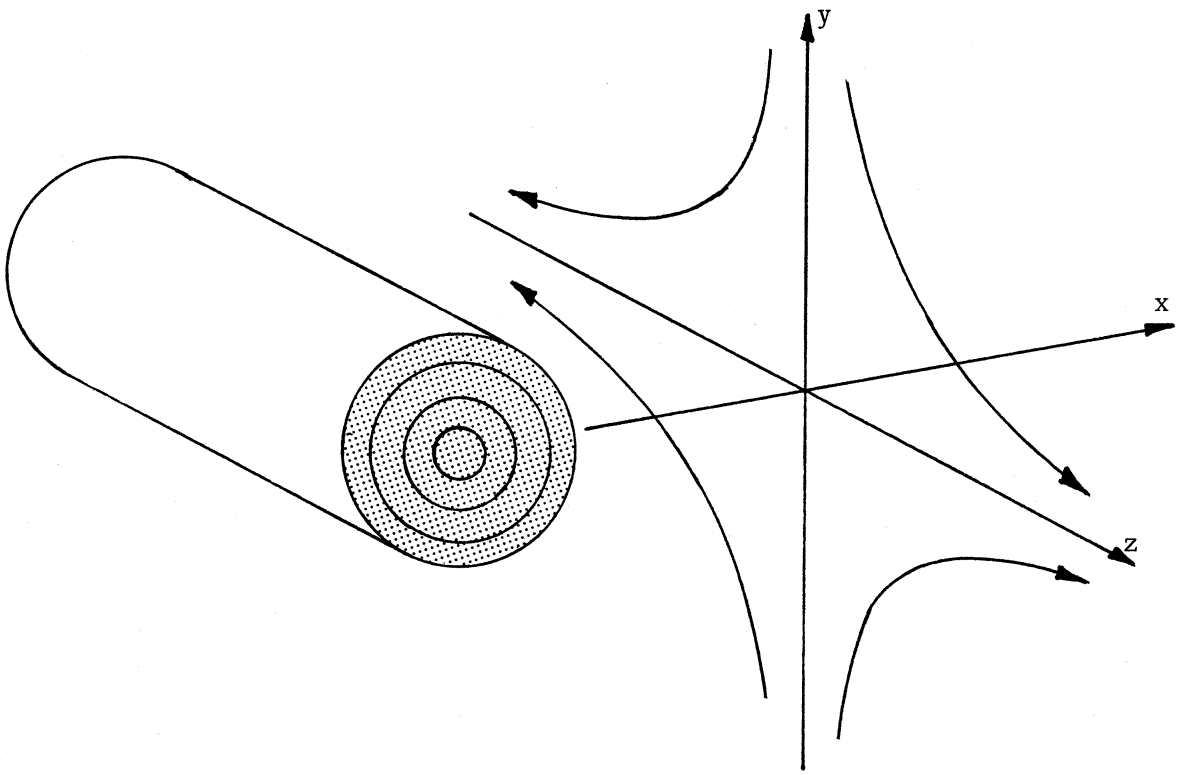

Figure 10.1 : Sectional view of a rectilinear vortex tube embedded in a stretching strain field. The vortex region consists of M = 4 regions of uniform vorticity. The imposed strain field is represented by the four curved streamlines in the (y, z)-plane.

Table 10.1 : Normalized vorticity profile for M = 1.

j	ω_j	q_j
1	0.274	1.0
2	0.643	0.600
3	0.870	0.350
4	1.0	0.162

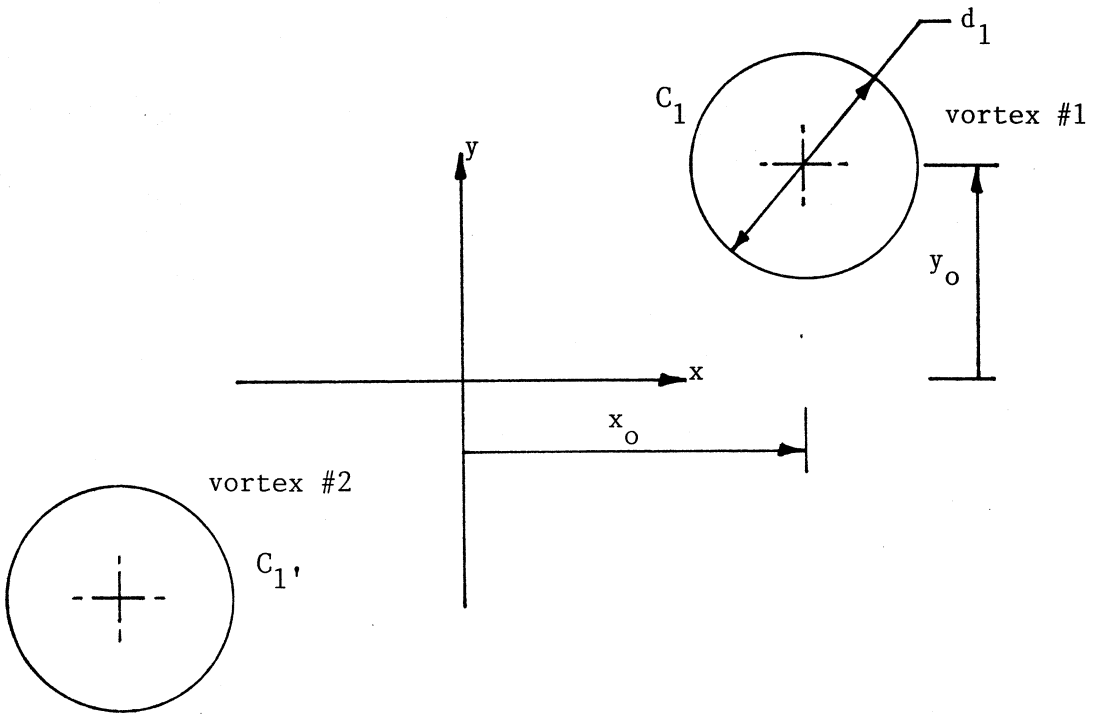

Figure 10.2 : Initial vortex configuration showing two uniform-vorticity FAVRs. The centre of vortex #1 is located at (x_o, y_o) and has diameter d_1. Vortex #2, bounded by C_1', is the image of vortex #1 rotated about the origin by π radians.

Previous simulations of this flow configuration include those by Christiansen (1973) and Christiansen & Zabusky (1973) using a Cloud-in-Cell technique in which the FAVR was approximated by a "cloud" of point vortices. These studies showed that there were large deformations in the vortex regions as they interacted and that there was a maximum initial separation beyond which coalescence would not occur. Later, the CD method was introduced by Zabusky, Hughes & Roberts (1979) and applied to essentially the same uniform vortex pair. When the initial separation is sufficiently large, the vortices simply rotate about each other but may either *(i)* have wave-like deformations travelling around the bounding contours or *(ii)* be a steady state solution of the Euler equations: the rotating V-states (Deem & Zabusky 1978). For an experimental investigation of vortex merging (in a rotating system) see Griffiths & Hopfinger (1986).

10.1 Flow Configuration

Consider a rectilinear FAVR embedded in a three-dimensional plane strain field as shown in figure 10.1. A section of the vortex tube is shown with the (x,y)-plane contours delineating the discontinuities in the ω_z vorticity field. The (y,z)-plane component of the plane strain field is represented by the four curved streamlines with their extensional axis aligned with the vortex lines in the z-direction.

In the (x,y)-plane, the initial vorticity distribution of vortex 1 is specified by a set of M concentric circular contours C_1 to C_M with centre (x_0, y_0). Vortex 2 is constrained to be an image of vortex 1 through a rotation of π radians. Thus we calculate the motion of only one vortex explicitly. The diameter of C_j is d_j and we define

$$q_j = \frac{d_j}{d_1} \quad , \tag{10.1}$$

The total area of the FAVR, $A = \Sigma_j A_j$, is set to unity so that $d_1 = (4/\pi)^{1/2}$. (Here A_j is the area of each uniform vorticity region R_j.) The circulation of each FAVR is then

$$\Gamma = \sum_{j=1}^{M} \omega_j (q_j^2 - q_{j+1}^2) \frac{\pi d_1^2}{4} \quad , \tag{10.2}$$

and the vorticity is normalized to give $\Gamma = 1$. Table 10.1 gives values of q_j and ω_j for both the uniform vorticity (M=1) FAVR and a nonuniform case (M=4). These profiles are the essentially same normalized vorticity profiles as used in chapters 7 to 9. The initial separation is

$$D = 2\sqrt{(x_0^2 + y_0^2)} \quad , \tag{10.3}$$

and a characteristic time is

$$T_c = \frac{A^{1/2}}{\Gamma} \quad , \tag{10.4}$$

The equation governing the motion of C_j is given in (3.15) (with corresponding discretized form (4.2), (4.3)). Computation were performed using code-version 1 (table 4.1) and node-parameter set 4 (table 4.3). Calculations were terminated either when $N_1 = O(500)$ (800 in cases 13 -15) or when the time step for the ODE solver became unacceptably small (and the calculation progressed slowly) except where marked in table 10.2.

10.2 Simulation Results and Discussion

Results are shown as sequences of contour evolution for $\beta_0 = 0$ and $0 \le \gamma_0 \le 0.2$. Table 10.2 summarizes all of the cases presented in this section giving the initial vorticity distribution, stretching and final time reached. Other cases where β_0 is nonzero are shown in section 5.1 as test cases to prove the method. The values of D have been chosen to approximately match the two-dimensional simulations of

Table 10.2 : Summary of simulations for the two vortex interaction. The starred times indicate cases for which the simulation proceeded to the indicated time without encountering the limits for nodes or computer processing time.

Case	M	γ	x_0	y_0	t_{max}
1	1	0.0	0.75	0.0	27.5
2	1	0.05	0.75	0.0	17.5
3	1	0.10	0.75	0.0	12.5
4	1	0.15	0.75	0.0	10.0
5	1	0.0	0.85	0.0	25.0
6	1	0.05	0.85	0.0	20.0
7	1	0.10	0.85	0.0	17.5
8	1	0.15	0.85	0.0	17.5*
9	1	0.0	0.96	0.0	25.0
10	1	0.05	0.96	0.0	25.0*
11	1	0.10	0.96	0.0	25.0*
12	1	0.15	0.96	0.0	25.0*
13	1	0.05	0.0	0.96	20.0
14	1	0.10	0.0	0.96	17.5
15	1	0.15	0.0	0.96	12.5
16	4	0.10	0.75	0.0	12.5
17	4	0.20	0.75	0.0	8.5

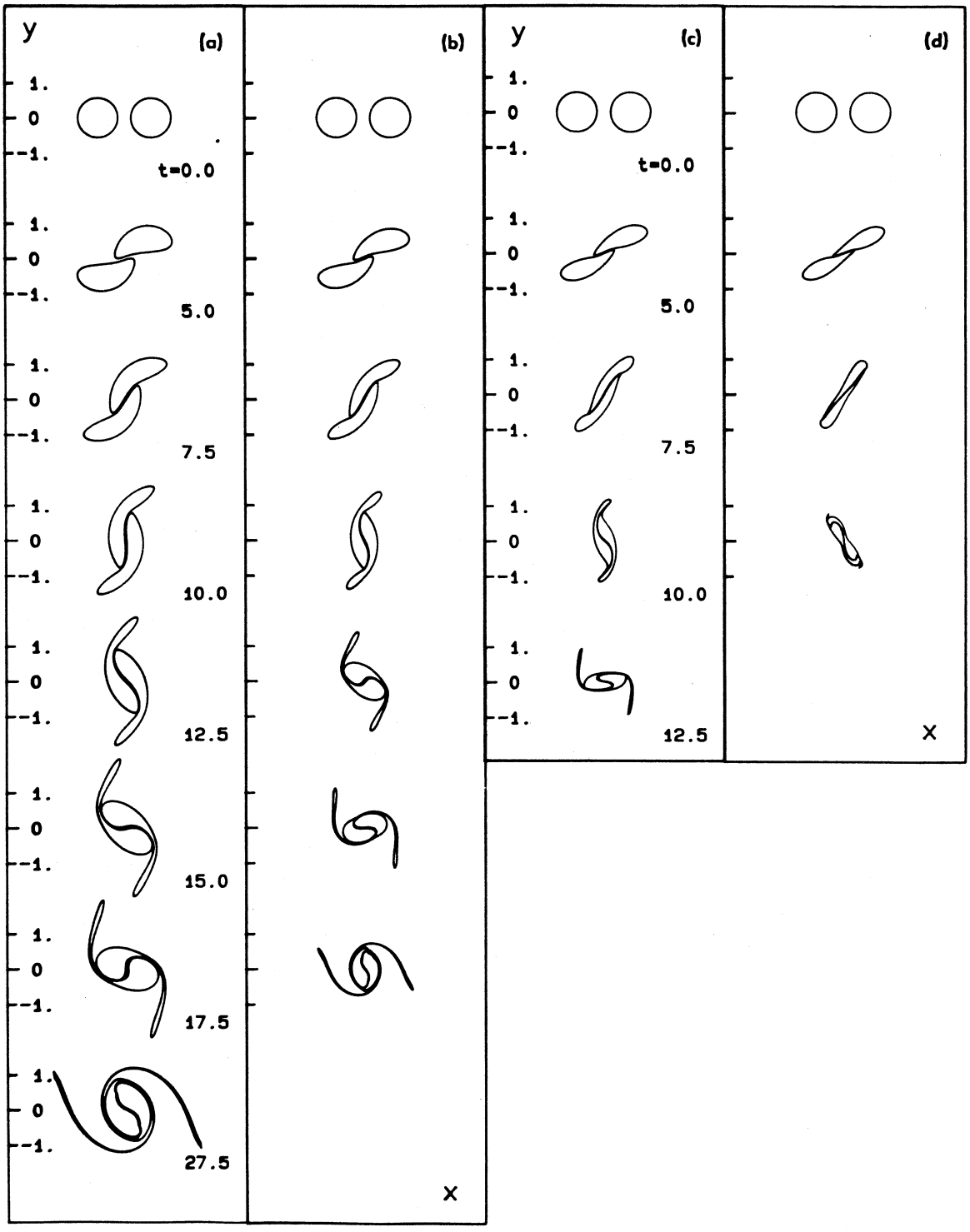

Figure 10.3 : Coalescence of equal uniform vortices (M = 1) with D = 1.5 in a stretching strain field $\gamma_o \geq 0$, $\beta_o = 0$. Times t as shown. (a) $\gamma_o = 0$, case 1, (b) $\gamma_o = 0.05$, case 2, (c) $\gamma_o = 0.10$, case 3, (d) $\gamma_o = 0.15$, case 4.

Zabusky, Hughes & Roberts (1979). A sensitivity test demonstrating convergence of contour shapes with increasing N_1 for the M=1, D=1.5 case is also described in chapter 5. In the final frame of each sequence, the fractional error in A_1 is $O(10^{-3})$. Figures 10.3 through 10.5 show the qualitative effect of stretching strain and different initial separation, D, for M = 1. In these figures the vortices are initially oriented so that the line joining their centres is perpendicular to the compressive axis of the stretching strain. Figure 10.6 shows the effect of orienting the vortices so that the line joining the centres is parallel to the compressive axis while figure 10.7 illustrates the difference between uniform and nonuniform FAVR interactions for a single initial separation.

Two principal effects of stretching are apparent from the D = 1.50 sequences of figure 10.3. First, there is a slight increase in the speed of angular rotation of the merged structure with increasing γ_0 caused by the vorticity intensification, and second, the vortex stretching is seen to substantially inhibit the formation of spiral sheets of vorticity. At low or zero γ_0, these sheets are ejected from the main vortex core and subsequently remain stable to local Kelvin-Helmholtz instability because of the stabilizing effect of the two-dimensional (x, y)-plane strain induced by the merged central vortex (Moore & Griffith-Jones 1974; Moore 1976).

For the highest stretching rate (γ_0 = 0.15), the two FAVR's coalesce into an elongated "perturbed elliptical" shape with much attenuated embryo-spiral arms containing little circulation. In fact, each of the vortex sheets shown for γ_0 = 0.10 and 0.15 is actually a double sheet, one from each primary vortex core. The formation of the inner sheet (nearer the vortex centre) appears to be connected with apparent cusp formation in the bounding contour, C_1. This cusp formation can be seen, for example, in figure 10.3(c) at t = 7.5. At the later time of t = 12.5, the inner sheet is of negligible thickness with the bulk of material being contained in the

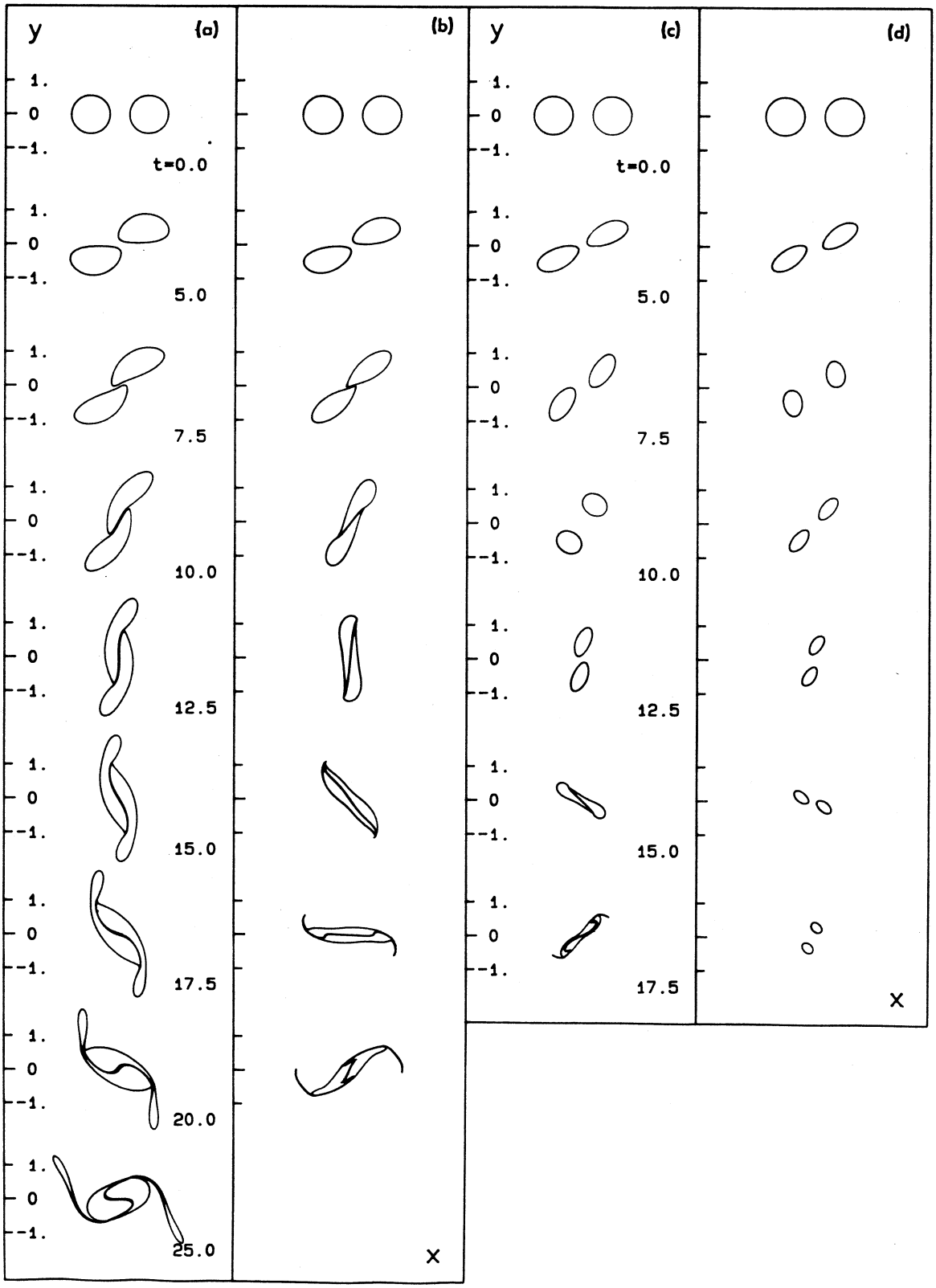

Figure 10.4 : Coalescence of equal uniform vortices (M = 1) with D = 1.70 in a stretching strain field $\gamma_o \geq 0$, $\beta_o = 0$. Times t as shown. (a) $\gamma_o = 0.0$, case 5, (b) $\gamma_o = 0.05$, case 6, (c) $\gamma_o = 0.10$, case 7, (d) $\gamma_o = 0.15$, case 8.

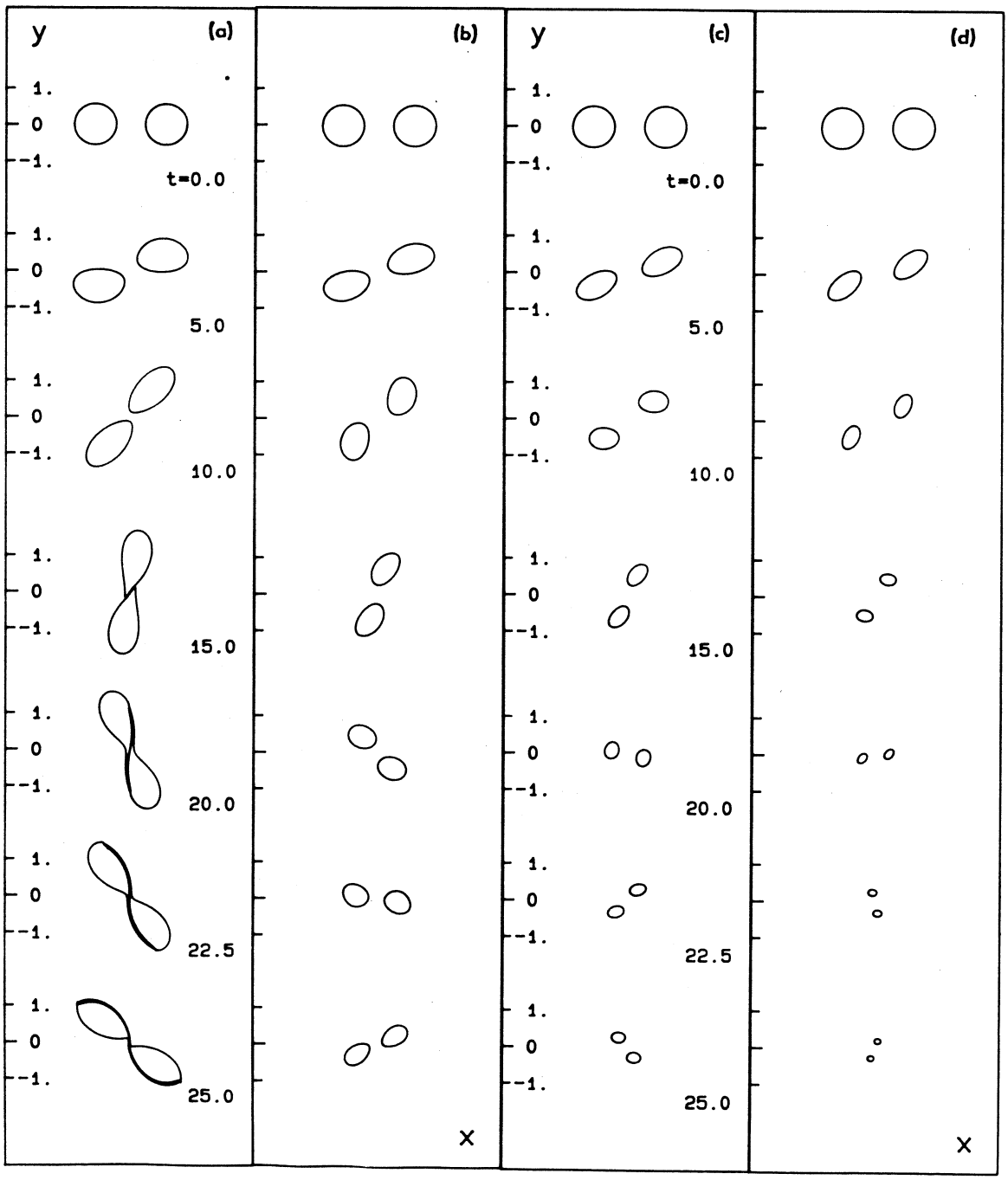

Figure 10.5 : Coalescence of equal uniform vortices (M = 1) with D = 1.92 in a stretching strain field $\gamma_o \geqq 0$, $\beta_o = 0$. Times t as shown. (a) $\gamma_o = 0.0$, case 9, (b) $\gamma_o = 0.05$, case 10, (c) $\gamma_o = 0.10$, case 11, (d) $\gamma_o = 0.15$, case 12.

sheets ejected at the tails of the merging vortex cores. This breaking of the vortex contours and the formation of filaments is further discussed in section 5.3.

Figures 10.4(a,b,c) with D = 1.70 and γ_0 = 0.0, 0.05 and 0.10 show that the vortex merging process is qualitatively similar to that shown for D = 1.50 with the difference that, for larger initial separation, spiral vortex-sheet formation is suppressed at lower values of γ_0. Increasing γ_0 further to γ_0 = 0.15 in figure 10.4(d) inhibits vortex coalescence completely for $t \leq 17.5$. Continuation of this case past t = 25.0 (not shown) produced no indication of coalescence at a later time. Increasing the initial separation to D = 1.92 in figures 10.5(a-d) gives only a weak merging interaction for γ_0 = 0. Coalescence in $t \leq 25$ is completely inhibited for $\gamma_0 > 0.05$, with each uniform FAVR stretching ultimately to a line vortex while moving in an inwardly directed spiral trajectory.

The evolutionary tendencies for this initial orientation agree qualitatively with those of the stretched vortex layer studied in chapter 9. For an initial layer perturbation consisting of the primary mode and its first subharmonic in phase (pairing) we obtained coalescence for small values of γ_0 but there was no tendency towards merging for the larger value. This agreement may be fortuitous however, since in the x-periodic configuration, there is effectively an extra component of strain present due to the rest of the array. This strain is absent in these two vortex calculations but would be equivalent to finite $\beta_0 \sim 0(\gamma_0)$.

The tendency toward strain-induced suppression of vortex merging seen in these two vortex simulations, may be understood qualitatively by considering the two-dimensional $\sigma(\tau)$ flow equivalent to each sequence in figures 10.3 - 10.5. From 3.29 these have $b(T) = -\gamma_0/2$. See figure 5.3 for the two-dimensional $\sigma(T)$ simulation equivalent to the D = 1.50, γ = 0.15 case in figure 10.3 (d). Since $\gamma_0 > 0$, the vortex centres initially lie on the principal extension axis (ξ) of

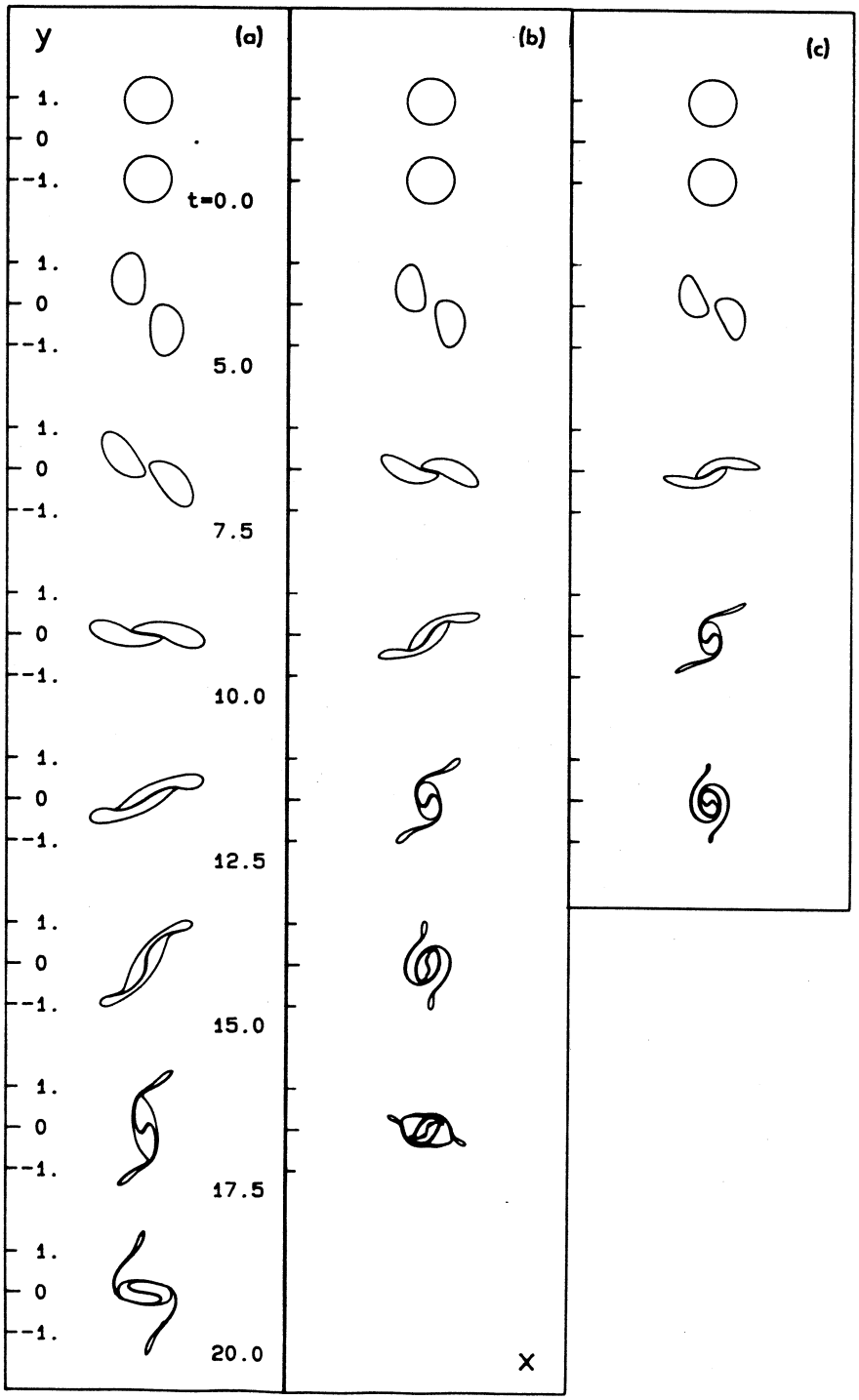

Figure 10.6 : Coalescence of equal uniform vortices (M = 1) with D = 1.92 in a stretching strain field $\gamma_o \geq 0$, $\beta_o = 0$. The line joining the vortex centres is initially aligned with the compressive axis (y) of the stretching strain. Times t as shown. (a) $\gamma_o = 0.05$, case 13, (b) $\gamma_o = 0.10$, case 14, (c) $\gamma_o = 0.15$, case 15.

strain for the $\sigma(t)$ flow. Hence the strain field tends to increase the ratio $D/A_1(0)^{1/2}$ for small T, thus inhibiting coalescence. This interpretation immediately suggests that positioning the vortex centres initially on the y-axis (i.e the principal compression axis of strain for both the $\sigma(T)$ and $\zeta(t)$ flows with $\gamma_0 > 0$) would alter the qualitative effect of stretching. This is clearly demonstrated in figures 10.6(a-c) where D = 1.92 and γ_0 = 0.05, 0.01 and 0.15. Comparing these sequences with the equivalent cases in figure 10.5 shows that stretching now enhances coalescence, leading to a well developed spiral sheet structure for all γ_0.

To illustrate the effect of vortex nonuniformity on the two vortex interaction, figure 10.7 displays three simulations with initial configuration equivalent to the D = 1.5 uniform vorticity FAVR pair which produce a strong merging interaction for γ_0 = 0. Figure 10.7(a) is an extract from the sequence in figure 10.3(c) having M = 1. Sequences (b) and (c) have initial configurations D = 1.5. $d_1 = (4/\pi)^{1/2}$, Γ = 1 and the M = 4 initial vorticity profile defined in table 10.1. The time scales are the same in each sequence. Figure 10.7(b) compared to 10.7(a) shows that the concentration of vorticity toward the vortex geometrical centre partially inhibits, but does not stop, coalescence of the FAVR's. For t = 7.5 the vortices are again essentially separate. At this time however, they are aligned with the compression axis of strain (y-axis) leading consequently to a strong coalescence by t = 12.5. The larger strain γ_0 = 0.2 of figure 10.7(c) appears to further inhibit the onset of merging as for the uniform FAVR simulations. It is interesting to note that for cases (b), (c) the C_1 contours are subject to extreme distortion leading to resolution difficulties but, in contrast, the C_2 - C_4 contours undergo only small perturbations.

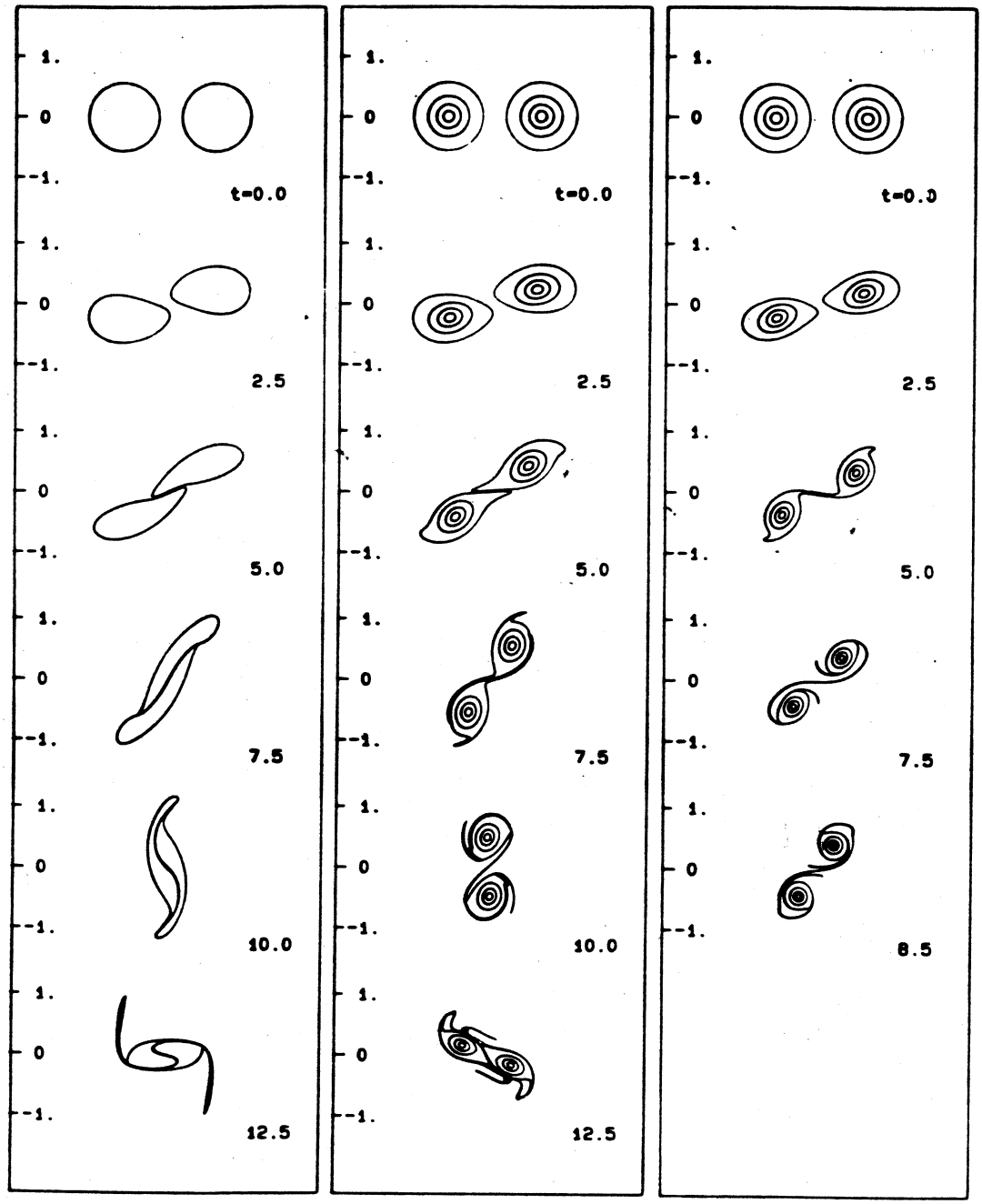

Figure 10.7: Coalescence of equal vortices with D = 1.50 in a stretching strain field, $\gamma_o > 0$, $\beta_o = 0$. Times t as shown. (a) uniform vortex, M = 1, $\gamma_o = 0.1$, case 3, (b) non-uniform vortex, M = 4, $\gamma_o = 0.1$, case 16, (c) non-uniform vortex, M = 4, $\gamma_o = 0.2$.

11.0 CONCLUSIONS

We have developed a Contour-Dynamic algorithm and an associated numerical implementation suitable for the simulation of essentially two-dimensional flows of an inviscid, incompressible fluid but with the added feature of vortex stretching. Being a Lagrangian technique, the CD algorithm allowed the natural evolution of fine-scale motions and, being based on a piecewise-continuous vorticity distribution, could attain a resolution not previously achieved using vortex methods. The numerical implementation included quadratic interpolating elements and an "analytic-patch" procedure to improve the solution accuracy in situations where the contours approached closely. The code could handle both *(i)* the evolution of several isolated vorticity patches and *(ii)* the evolution of spatially periodic vorticity distributions.

There are, however, several aspects of the technique that need further work. The current implementation is limited to short or moderate time simulations as the number of nodes increases rapidly with the formation of filaments on the contours. The formation of cusps and filaments needs to be explored, possibly using a Fourier decomposition of the contour descriptions (Moore 1976; Krasny 1984), while filament truncation could be implemented in much the same manner as Dritschel (1986a) but with consideration given to the changing topology of the contours (say, from a continuous layer to an array of discrete FAVRs). Also, there is need for improvement in *(i)* the node-adjustment algorithm to reduce truncation errors while maintaining robustness and *(ii)* the contour interpolation for the same reasons.

We have applied the CD method to the vortex modelling of various eddy scales of the plane turbulent mixing layer. Several numerical simulations, based on the hierarchical model of Corcos, Lin and Sherman (Corcos & Sherman 1984; Corcos & Lin 1984; Lin & Corcos 1984), produced evolutionary scenarios that represent plausible structures of the flow at the nominal limit of Re = ∞, for moderate times.

For the nominally two-dimensional instability and roll-up of the plane shear layer, we examined the influence of the initial vorticity profile and the presence of various subharmonic disturbances on the layer evolution. In all cases, the inviscid simulations lead to the production of much fine scale detail which usually resulted in termination of the computation. Overall, the simulations showed that variations in the initial vorticity field had only a minor effect on the flow evolution but that the subharmonic content of the initial perturbation greatly influenced the post-rolled-up evolution. Disturbing the layer with a perturbation consisting of a combination of the fundamental eigenfunction and its first subharmonic resulted in a range of post-rolled-up evolutions for differing values of phase angle ϕ. For $\phi = 0$, adjacent vortex pairs rotated about each other and coalesced into an array of larger vortical structures with a larger wavelength. Comparisons with finite Re simulations and experimental observations provide supporting evidence for the hypothesis that the large-scale vortex-dynamics for the roll-up and pairing processes are only weakly dependent upon Re (Zabusky & Deem 1971). Setting $\phi = \pi/2$ resulted in a tearing interaction in which the roll-up of the layer produces adjacent vortex cores of different strengths. Unlike previous moderate Re simulations, the smaller cores produced in the $Re = \infty$ simulation here were not completely absorbed by the larger vortices on either side. Disturbing the layer with a combination of the fundamental eigenfunction resulted in the roll-up and subsequent interaction of subsets of three adjacent vortices in a manner similar to that observed in the forced mixing layer experiments of Ho & Huang (1982).

Several parameters of the primary motion were not explored. In particular, other values of the relative amplitude and phase of the subharmonic components need to be tried. The domain could be extended to include a disturbance involving several different wavelengths but this requires the layer thickness to be quite small in order to include integral numbers of wavelengths for all components. In the limit, a

pseudo-random disturbance should be investigated as we are not sure just what type of perturbation is introduced by the truncation error of the single precision calculations in section 7.2.

The stretching-strain / vortical interaction studied in the secondary vortex simulations provided an example of an energy transfer mechanism (relevant to the turbulent energy cascade) from the large-scale motions (plane strain field) to the smaller-scale vortex motions. The main features displayed by the simulations of the secondary vortices include *(i)* the rapid formation of an intense rolled-up vortex core with companion double-arm vortex spirals, *(ii)* the presence of weak sheet-like vorticity tails terminating the spirals, which are maintained by the local velocity induction of all members of the secondary vortex array coupled with the y-component of the strain velocity and *(iii)* incipient tertiary instabilities embedded in the spiral filaments and containing in some cases, their own smaller-scale vorticity spirals. A comparison of corresponding M = 1 and M = 4 simulations illustrated the flow sensitivity to nonuniform vorticity distribution (or concentration) with the concentration accelerating the roll-up process. There is also a suggested dependency on Re_2 as the spiral shear layers and local shear instabilities that developed in our $Re_2 = \infty$ simulations did not appear in the moderate Re calculations of Lin & Corcos (1984) where viscous effects promoted the formation of nearly axisymmetric Burgers vortex cores with much attenuated vortex arms.

Features that have been omitted by the secondary vortex simulations include *(i)* the timewise decay of the stretching strain strength caused by the successive amalgamation events of the spanwise vortices *(ii)* strong random variations to the perfect spanwise periodicity of the array that are clearly indicated by experimental observations (e.g., Bernal 1981; Roshko 1980) and *(iii)* fully three-dimensional instabilities involving the interaction of the primary (spanwise) and secondary (streamwise) vorticity. These instabilities may destroy the flow coherence on a time-scale comparable with

that found for the evolution of the fine structure in either the primary or secondary vortex simulations.

The evolution of the stretched vortex layer was not explored in depth but the calculations performed indicated some of the effects of stretching. In particular, the stretching enhanced the production of spiral filaments but inhibited the coalescence of the rolled-up vortex cores for the pairing simulations. In simulations of the interaction of two equal vortices (otherwise isolated) showed that the inhibition of vortex coalescence was strongly dependent upon the initial orientation of the vortex cores with respect to the compression and extension axes of the stretching strain field. In fact, orienting the vortex cores so that they are initially aligned with the compressive axis of the strain resulted in a significant enhancement of the merging process.

12.0 REFERENCES

Abernathy, F.H. & Kronauer, R.E. 1962: "The formation of vortex streets". *J. Fluid Mech.* **13**, 1-20.

Abramowitz, M. & Stegun, I.A. 1965: "Handbook of Mathemtical Functions". Dover, New York.

Acton, E. 1976: "The modelling of large eddies in a two-dimensional shear layer". *J. Fluid Mech.* 76, 561-92.

Alvarez, C. & Martinez-Val, R. 1984: "Visual measurement of streamwise vorticity in the mixing layer". *Phys. Fluids.* **27**, 2367-2371.

Amsden, A. A & Harlow, F. H. 1964: "Slip instability". *Phys. Fluids.* **7**, 327-334.

Aref, H. 1983: "Integrable, chaotic and turbulent vortex motion in two dimensional flows". *Ann. Rev. Fluid Mech.* **15**, 345-389.

Aref, H. and Siggia, E.D. 1980: "Vortex dynamics of the two-dimensional turbulent shear layer". *J. Fluid Mech.* **100**, 705-737.

Aref, H. & Siggia, E. D. 1981: "Evolution and breakdown of a vortex street in two dimensions". *J. Fluid Mech.* **109**, 435-463.

Ashurst, W.T. 1977: "Numerical simulation of turbulent mixing layers via vortex dynamics" in *Turbulent Shear Flows I* edited by F. Durst et al, p 402, Springer.

Batchelor, G.K. 1967: *An Introduction to Fluid Dynamics.* Cambridge University Press.

Benny, D.J. 1961: "A nonlinear theory for oscillations in a parallel flow". *J. Fluid Mech.* **10**, 209-236.

Berk, H.L. & Roberts, K.V. 1970: "The water bag model". *Methods in Computational Physics.* **9**, 88-134.

Berk, H.L., Nielsen, C.E. & Roberts, K.V. 1970: "Phase space hydrodynamics of equivalent nonlinear systems: experimental and computational observations". *Phys. Fluids.* **13**, 980-995.

Bernal, L. 1981: "The coherent structure of turbulent mixing layers. I. Similarity of the primary vortex structure. II. Secondary streamwise vortex". Ph.D Thesis, Calif, Inst. Tech.

Bernal, L.P. & Roshko, A. 1986: "Streamwise vortex structure in the plane mixing layers". *J. Fluid Mech.* **170**, 499-525.

Bradshaw, P. 1979: "Introduction to the section of 'Coherent Structures'". in *Turbulent Shear Flows 2*, edited by Bradbury et al. Springer-Verlag, Berlin. pp 259-262.

Breidenthal, R. 1981: "Structure in turbulent mixing layers and wakes using a chemical reaction". *J. Fluid Mech.* **109**, 1-24.

Browand, F.K. & Troutt, T.R. 1980: "A note on spanwise structure in the two dimensional mixing layer". *J. Fluid Mech.* **97**, 771-781.

Browand, F.K. & Troutt, T.R. 1985: "The turbulent mixing layer: geometry of large vortices". *J. Fluid Mech.* **158**, 489-509.

Browand, F.K. & Weidman, P.D. 1976: "Large scales in the developing mixing layer". *J. Fluid Mech*, **76**, 127-144.

Brown, G.L. & Roshko, A. 1974: "On density effects and large structure in turbulent mixing layers". *J. Fluid Mech.* **64**, 775-816.

Burgers, J.M. 1948: "A mathematical model illustrating the theory of turbulence". *Adv. Appl. Mech.* **1**, 171-196.

Calder, A.C. & Laframboise, J.G. 1986: "Multiple-water-bag simulation of inhomogenous plasma motion near an electrode". *J. Comput. Phys.* **65**, 18-45.

Cantwell, B.J. 1981: "Organized motion in turbulent flow". *Ann. Rev. Fluid Mech.* **13**, 457-515.

Chandrsuda, C., Mehta, R.D., Weir, A.D. & Bradshaw, P. 1978: "Effect of free-stream turbulence on layer structure in turbulent mixing layers". *J. Fluid Mech.* **85**, 693-704.

Chapman, G.T. & Tobak, M. 1985: "Observation, theoretical ideas and modeling of turbulent flows- Past present and future". in *Theoretical approaches to turbulence*, edited by D.L. Dwoyer et al. Applied Mathematical Sciences, **58**, Springer-Verlag.

Chorin, A.J. 1973: "Numerical studies of slightly viscous flows". *J. Fluid Mech.* **57**, 785-796.

Chorin, A.J. 1982: "The evolution of a turbulent vortex". *Commun. Maths Phys.* **83**, 517-535.

Christiansen, J.P. 1973: "Numerical Simulation of hydrodynamics by the method of point vortices". *J. Comput. Phys.* **13**, 363-379.

Christiansen, J.P. & Zabusky, N.J. 1973: "Instability, coalescence and fission of finite-area vortex structures". *J. Fluid Mech.* **61**, 219-243.

Corcos, G.M. 1979: "The mixing layer: Deterministic models of a turbulent flow". Reseach Report, University of Calfornia, Berkeley.

Corcos, G.M. & Lin, S.J. 1984: "The mixing layer: Deterministic models of a turbulent flow. Part 2. The origin of three-dimensional motion". *J. Fluid Mech.* **139**, 67-96.

Corcos, G.M. & Sherman, F.S. 1984: "The mixing layer: deterministic models of a turbulent flow. Part 1. Introduction and the two dimensional flow". *J. Fluid Mech.* **139**, 29-66.

Couet, B., Buneman, O. & Leonard, A. 1981: "Simulation of three dimensional incompressible flows with a vortex in cell method". *J. Comp. Phys.* **39**, 305-328.

Couet, B. & Leonard, A. 1980: "Mixing layer simulation by an improved three-dimensional vortex-in-cell algorithm". In *Proc 7th Intl. Conf. on Numerical Methods in Fluid Dynamics.* Stanford, Ames.

Damms, D.M. & Kuchemann D. 1974: "On the vortex sheet model for the mixing between two parallel streams I; description of the model and experimental evidence". *Proc Roy Soc Lond.* A339 451.

Davis, R.W. & Moore, E.F. 1985: "A numerical study of vortex merging in mixing layers". *Phys. Fluids.* **28**, 1626-1635.

Deem, D.S. & Zabusky, N.J. 1978: " Vortex waves: stationary "V-states", interactions, recurrences, and breaking". *Physical Review Letters.* **40**, 859-862.

Dimotakis, P & Brown, G. L. 1976: "The mixing layer at high Reynold's number: large structure dynamics and entrainment". *J. Fluid Mech,* **78**, 535-560.

Dritschel, D.G. 1985: "The stability and energetics of co rotating uniform vortices". *J. Fluid Mech.* 157, 95-134.

Dritschel, D.G. 1986a: "Contour Surgery: a contour-dynamics method for the long time behaviour of a two-dimensional, inviscid, rotational flow". submitted to *J. Comput. Phys.*

Dritschel, D.G. 1986b: "The non-linear evolution of rotating configurations of uniform vorticity". *J. Fluid Mech.* **172**, 157-182.

Dwoyer, D.L., Hussaini, M.Y. & Voigt, R.G. 1985: "Theoretical Approaches to Turbulence". *Applied Mathematical Sciences* **58**. Springer Verlag, New York.

Floating Point Systems (Author Unknown) 1986: "Notes on Supercomputers". *Eng. Comput.* **3**, 254-258.

Forsythe, G.E., Malcolm, M.A., & Moler, C.B. 1977: "Computer methods for mathematical computations". *Prentice-Hall, Englewood Cliffs, N.J.*

Freymuth, P., Bank, W. & Palmer, M. 1984: "First experimental evidence of vortex splitting". *Phys. Fluids,* **27**, 1045-1046.

Garbow, B.S. : "Algorithm 535: the QZ algorithm to solve the generalized eigenvalue problem for complex matrices". *Collected Algorithms fo the ACM.*

Gradshteyn, I.S. & Ryzhik, I.M. 1980: "Table of Integrals , series and products". Academic Press, New york.

Griffiths, R.W. & Hopfinger, E.J. 1986: "Experiments with baroclinic vortex pairs in a rotating fluid". *J. Fluid Mech.* **173**, 501-518.

Hernan, M.A. & Jimenez, J. 1982: "Computer analysis of a high speed film of the plane turbulent mixing layer". *J. Fluid Mech.* **119**, 323-345.

Higdon, J.J.L. & Pozrikidis, C. 1985: "The self-induced motion of vortex sheets". *J. Fluid Mech.* **150**, 203-231.

Hinze, J.O. 1975: "Turbulence". 2nd Edition, McGraw Hill, New York.

Ho, C.M. & Huang, L.S. 1982: "Subharmonics and vortex merging in mixing layers". *J. Fluid Mech.* **119**, 443-473.

Ho, C.M. & Huerre, P. 1984: "Perturbed free shear layers". *Ann. Rev. Fluid Mech.* **16**, 365-424.

Hussain, A.K.M.F. 1986: "Coherent structures and turbulence". *J Fluid Mech.* **173**, 303-356.

Hussain, A.K.M.F. & Zaman, K.B.M.Q. 1985: "An experimental study of organized motions in th turbulent plane mixing layer". *J. Fluid Mech.* **159**, 85-104.

Inoue, O. 1985: "Vortex simulation of a turbulent mixing layer". *AIAA Journal.* **23**, 367-373.

Jimenez, J. 1983: "A spanwise structure of the plane shear layer". *J. Fluid Mech.* **132**, 319-36.

Jimenez, J. & Cogollos, M. & Bernal, L.P. 1985: "A perspective view of the plane mixing layer". *J. Fluid Mech.* **152**, 125-143.

Kadomtsev, B.B & Kostomarov, D.P. 1972: "Turbulent layer in an ideal two-dimensional fluid". *Phys Fluids.* **15**, 1-3.

Konrad, J.H. 1976: "An experimental investigation of mixing in two-dimensional turbulent shear flows with applications to diffusion-limited chemical reactions". PhD Thesis. Calif. Inst. Tech.

Koochesfahani, M.M. & Dimotakis, P.E. 1986: "Mixing and chemical reactions in a turbulent liquid mixing layer". *J. fluid Mech.* **170**, 83-112.

Krasny, R. 1984: "A numerical method for periodic vortex sheet roll up". Research Report, Centre for Pure and Applied Mathematics, University of California, Berkeley.

Krasny, R. 1986: "Desingularization of periodic vortex sheet rollup". *J. Comput. Phys.* **65**, 292-313.

Lamb, H. 1932: *Hydrodynamics*. 6th Ed. Dover Publications, New York.

Lasheras, C., Cho, J.S & Maxworthy, T. 1986: "On the origin and evolution of streamwise vortical structures in a plane, free shear layer". *J. Fluid Mech.* **172** 231-258.

Leonard, A. 1980a: "Vortex simulation of three dimensional spotlike disturbances in a laminar boundary layer". in *Turbulent Shear Flows 2*, pp 66-77 Springer-Verlag,Berlin .

Leonard, A. 1980b "Vortex methods for flow simulation". *J. Comp. Phys.* **37**, 289-335.

Leonard, A. 1985: "Computing three-dimensional incompressible flows with vortex elements". *Ann. Rev. Fluid Mech.* **17**, 523-559.

Liepmann, H.W. 1979: "The rise and fall of ideas in turbulence" *American Scientist*. **67**, 221-228.

Lin, S.J. & Corcos, G.M. 1984: " The mixing layer: deterministic models of a turbulent flow. III. The effect of plasma strain on the dynamics of streamwise vortices". *J. Fluid Mech.* **141**, 139-178.

Love, A.E.H. (1893): "On the stability of certain vortex motions". Proceedings of the London Mathematical Society. **25**, 18-42.

Lundgren, T.S. 1982: "Strained spiral vortex model for turbulent fine structure". *Phys. Fluids.* **25**, 2193-2203.

Matsui, T. & Okude, M. 1982: "Formation of the secondary vortex street in the wake of a circular cylinder". in *Structure of Complex Turbulent Shear Flow*. IUTAM Symposium, Marseille. Eds, R. Dumas, L. Fulachier. Springer, Berlin.

Melander, M.V., Overman II, E.A. & Zabusky, N.J. 1986: "Computational vortex dynamics in two and three dimensions". *Technical Report ICMA-86-93*, Jan 1986.

Metcalfe, R.W., Orszag, S.A., Bratchet, M.E., Meiron, S. & Riley, J.J. 1986: "Secondary instability of a temporally growing mixing layer". to appear in *J. Fluid Mech.*

Michalke, A. 1964: "On the inviscid instability of the hyperbolic-tangent velocity profile". *J. Fluid Mech.* **19**, 543-556.

Milne-Thomson, L.M. 1968: *Theoretical Hydodynamics*. 5th ed MacMillan and Co., London.

Moin, P. & Kim, J. 1982: "Numerical investigation of turbulent channel flow". *J. Fluid Mech.* **118**, 341-377.

Moin, P. & Kim, J. 1985: "The structure of the vorticity field in turbulent channel flow. Part 1. Analysis of instantaneous fields and statistical correlations". *J. Fluid Mech.* **155**, 441-464.

Moore, D.W. 1976: "The stability of an evolving two-dimensional vortex sheet". *Mathematika*, **21**, 35-44.

Moore, D.W. 1978: "The equation of motion of a vortex layer of small thickness". *Studies in Appl. Math.* **58**, 119-140.

Moore, D.W. 1979: "The spontaneous appearance of a singularity in the shape of an evolving vortex sheet". *Proc. R. Soc. Lond. A.* **365**, 105 - 119.

Moore, D.W. & Griffith-Jones, R. 1974: "The stability or an expanding circular vortex sheet". *Mathematika*, **21**, 128-133.

Moore, D.W. & Saffman, P.G. 1975: "The density of organized vortices in a turbulent mixing layer". *J. Fluid Mech.* **69**, 465-473.

Nakamura, Y. & Leonard, A. & Spalart, P. 1982: " Vortex simulation of an inviscid shear layer". *AIAA/ASME 3rd joint Thermophysics, Fluids, Plasma and Heat Transfer Conference*. St. Louis, Missouri. AIAA paper 82-0948.

Neu, J. 1984a: "The dynamics of stretched vortices". *J. Fluid Mech.* **143**, 253-276.

Neu, J. 1984b: "The dynamics of a columnar vortex in an inposed strain". *Phys. Fluids*, **27**, 2397.

Orszag, S.A & Israeli, I. 1974: "Numerical simulation of viscous incompressible flows". *Ann. Rev. Fluid Mech.* **6**, 281-318.

Oster, D. & Wygnanski, I. 1982: "The forced mixing layer between parallel streams". *J. Fluid Mech.* **123**, 91-130.

Overman, E.A. & Zabusky, N.J. 1982: "Evolution and merger of isolated vortex structures". *Phys. Fluids.* **25**, 1297-1305.

Patnaik, P.C. & Sherman, F.S. & Corcos, G.M. 1976: "A numerical simulation of Kelvin-Helmholtz waves of finite amplitude". *J. Fluid Mech.* **73**, 215-240.

Paterson, D. 1986: "Computation of wind flows over three-dimenstional buildings". PhD thesis, University of Queensland.

Perry, A.E. 1986: "A description of eddying motions and turbulence". 9th Australasian Fluid Mechanics Conference, Auckland 8-12 December, 1986. pp 7-12.

Perry, A.E. & Hornung, H. 1984: "Some aspects of three dimensional separation, part 2: Vortex skeletons". *Z. Flugwiss. Weltraumforsch.* **8**, 155-160.

Perry, A.E. & Chong, M.S. 1982: "On the mechanism of wall turbulence". *J. Fluid Mech.* **119**, 173-217.

Pierrehumbert, R.T. 1980: "A family of steady, translating vortex pairs with distributed vorticity". *J. Fluid Mech.* **99**, 129-144.

Pierrehumbert, R.T. & Widnall, S.E. 1982: "The two and three-dimensional instabilities of a spatially periodic shear layer". *J. Fluid Mech.* **114**, 59-82.

Pozrikidis, C. & Higdon, J.J.L. 1985: "Non-linear Kelvin-Helmholtz instability of a finite vortex layer". *J. Fluid Mech.* **157**, 225-263.

Pullin, D.I. 1981: "The nonlinear behaviour of a constant vorticity layer at a wall". *J. Fluid Mech.* **108**, 401-421.

Rayleigh, Lord 1880: "On the stability, or instability, of certain fluid motions". *Proc. Lond. Math. Soc.* **11**, 57-70.

Reynolds, O. 1895: "On the dynamical theory of incmpressible viscous fluid and the determination of the criterion". *Phil. Trans. R. Soc. London.* Ser A **186**, 123-161.

Riley, J.J. & Metcalfe, R.W. 1980: "Direct simulation of a perturbed turbulent mixing layer". AIAA paper 80-0274.

Roache, P.J. 1976: *Computational Fluid Dynamics.* Hermosa.

Roberts, K.V. & Christiansen, J.P. 1972: "Topics in computational physics". *Computer Physics Communications.* **3**, suppl, 14-32.

Roberts, F.A., Dimostakis, P.E. & Roshko, A. 1982: "Kelvin-Helmholtz instability of superposed streams". Figure 146 in *Album of Fluid Motion*, M. Van Dyke, p 85. Stanford Caifornia, Parabolic.

Robinson, A.C. & Saffman, P.G. 1984: "Stability and structure of stretched vortices". *Stud. Appl. Math.* **70**, 163-181.

Rosenhead, L. 1932: "The formation of vortices from a surface of discontinuity". *Proc Roy Soc London* series A. **134**, 170-192.

Roshko, A. 1976: "Structure of turbulent shear flows: A new look". *AIAA Journal* **14**, 1349-1357.

Roshko, A. 1980: "The plane mixing layer: Flow visualization and three dimensional effects". *Lecture notes in Physics*, **136, 208-217**. The role of coherent structures in modelling of turbulence. J. Jiminez (ed). Springer-Verlag.

Saffman, P.G. 1977: "Problems and progress in the theory of turbulence". in *Structure and Mechanisms of Turbulence*. Springer-Verlag.

Saffman, P.G. 1981: "Dynamics of vorticity". *J. Fluid Mech.* **106**, 49-58.

Saffman, P.G. 1985: "Vortex dynamics". in *Theoretical Approaches to Turbulence* edited by D.L. Dwoyer et al. Applied Mathematical Sciences, **58**, Springer-Verlag, New york.

Saffman, P.G. & Baker, G.R. 1979: "Vortex Interactions". *Ann. Rev. Fluid Mech.* **11**, 95-122.

Saffman, P.G. & Meiron, D.I. 1986: "Difficulties with three dimensional weak solutions for inviscid incompressible flow". *Phys. Fluids*, **29**, 2373-2375.

Saffman, P.G. & Schatzman, J.C. 1981: "Properties of a vortex street of finite vortices". *SIAM J. Sci. Stat. Comput.* **2**, 285-295.

Saffman, P.G. & Schatzman, J.C. 1982: "Stability of a vortex street of finite vortices". *J. Fluid Mech.* **117**, 171-185.

Saffman, P.G. & Szeto, R. 1980: "Equilibrium shapes of a pair of equal uniform vortices". *Phys. Fluids* **23**, 2339-2342.

Saffman, P.G. & Szeto, R. 1981: "Structure of a linear array of uniform vortices". *Stud. Appl. Math.* **65**, 223-248.

Temperton, C. 1979: "Direct methods for the solution of the discrete Poisson equation: some applications". *J. Comput. Phys.* **31**, 1-20.

Teng, Z.H. 1986: "Variable elliptic vortex method for incompressible flow simulation". 10th *Intl. Conf. Numerical Methods in Fluid Dynamics*. pp 369-374.

Thorpe, S.A. 1971: "Experiments on the stability of stratified shear flows: Immicible fluids". *J. Fluid Mech.* **46**, 299-319.

Tokunaga, H. & Yasui, Y. 1985: "Numerical analysis of two-dimensional unsteady turbulent shear flow by discrete vortex model". *Bulletin of JSME*, **28**, 62-67.

Van Dyke, M. 1982: *An Album of Fluid Motion*. Parabolic Press, Stanford, California.

Wan. Y.H. 1984: "On the nonlinear stability of circular vortex patches". in *Fluids and Plasma: Geometry and Dynamics*. Contemporary Mathematics. **28**, edited by J.E. Marsden, American Mathematical Society. pp215-219.

Wu, H.M., Overman, E.A. & Zabusky, N.J. 1984: "Steady-state solution of the Euler equations in two dimensions: rotating and translating V-states with limiting cases. 1. Numerical algorithms and results". *J. Comput. Phys.* **53**, 42-71.

Winant, C.D. & Browand, F.K. 1974: "Vortex pairing, the mechanism of turbulent mixing-layer growth at moderate Reynolds number". *J. Fluid Mech.* **63**, 237-255.

Wygnanski, I., Oster, D., Fieldler, H & Dziomba, B. 1979: "On the perserverance of a quasi-two-dimensional eddy-structure in a turbulent mixing layer". *J. Fluid Mech*, **93**, 325-335.

Yih, C.S. 1979: *Fluid Mechanics: A concise introduction to the theory*. West River Press, Ann Arbor.

Zabusky, N.J. & Deem, G.S. 1971: "Dynamical evolution of two-dimensional unstable shear flows". *J. Fluid Mech.* **47**, 353-379.

Zabusky, N.J. & Hughes, M.H. & Roberts, K.V. 1979: "Contour dynamics for the Euler equations in two dimensions". *J. Comput. Phys.* **30**, 96-106.

Zabusky, N.J. & Overman, E.A. 1983: "Regularization of contour dynamical algorithms. I. Tangential Regularization". *J. Comput. Phys.* **52**, 351-373.

APPENDIX 1 : Contour-Dynamic Formulation using Green's Theorem

In chapter 3 the inviscid model is formulated by considering distributions of singularities around the contours C_j. Alternatively, we could start with the velocity field due to a point-vortex and generalize to a finite area, two-dimensional region. (Only regions of uniform vorticity are considered here.) This velocity field can be calculated using the Biot-Savart law and, for a purely two-dimensional flow may be expressed in complex coordinates as

$$V_x - iV_y = \frac{\Gamma}{2\pi i (Z - \zeta_o)} \quad , \qquad \text{(A1.1)}$$

where $Z = X + iY$ is the complex coordinate of the point at which the velocity is calculated and Γ is the strength (circulation) of the point vortex at ζ_o. Integrating over a finite area region R_1 containing uniform vorticity ω_1, the velocity field becomes

$$V_x - iV_y = \frac{1}{2\pi i} \iint_{R_1} \frac{\omega \, dx_o \, dy_o}{Z - \zeta_o} \quad , \qquad \text{(A1.2)}$$

where the zero subscripts indicate integration variables over R_1. The area integral (A1.2) over R_1 may now be converted into a line integral around the enclosing contour C_1 using a complex form of Green's theorem

$$\iint_{R_1} \frac{dF(Z, \zeta_o)}{d\zeta_o} \, dx_o \, dy_o = \frac{1}{2} i \oint_{C_1} F(Z, \zeta') \, d\zeta^{*\prime} \quad , \qquad \text{(A1.3)}$$

where * denotes the complex conjugate and primed quantities are integration variables around C_1 (Pullin 1981). Thus the velocity expression (A1.2) becomes

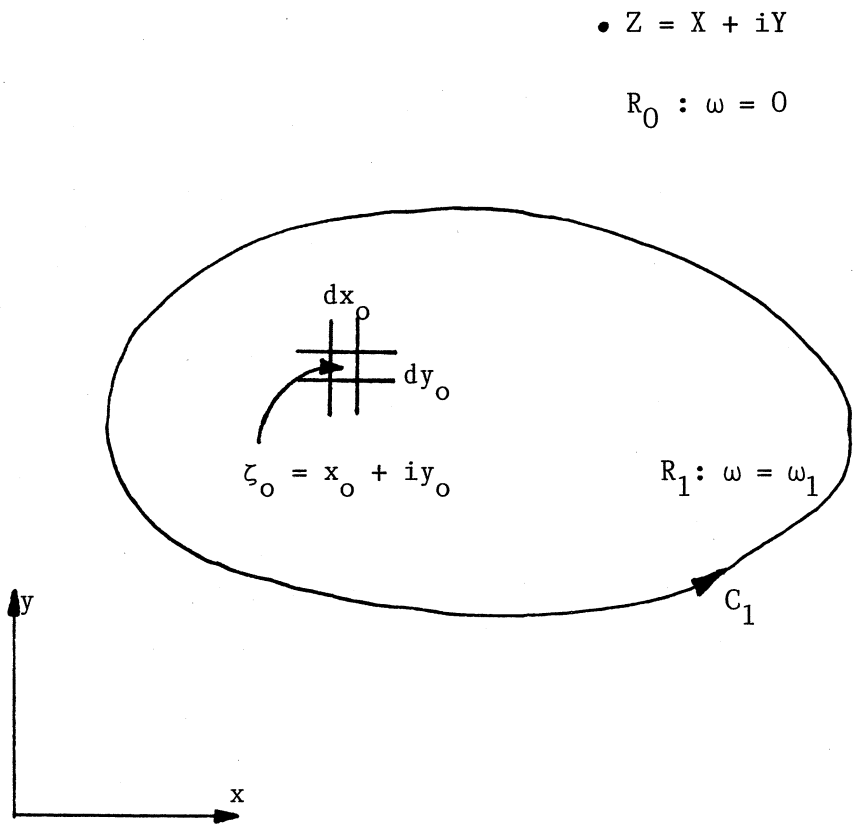

Figure A1.1 : A single uniform vorticity FAVR consisting of a simply connected region R_1 bounded by contour C_1. Z is a general point in the plane while ζ_o is a point in R_1.

$$V_x - iV_y = \frac{-\omega_1}{4\pi} \oint_C \ln(Z - \zeta') \, d\zeta^{*\prime} \quad . \tag{A1.4}$$

Making the substitution $d\zeta^{*\prime} = d\zeta' - 2i\, dy'$ gives

$$V_x - iV_y = \frac{\omega_1 i}{2\pi} \oint_C \ln(Z - \zeta') \, dy' \quad , \tag{A1.5}$$

for Z external to R_1. Integrating (A1.5) by parts results in

$$V_x - iV_y = \frac{-\omega_1}{2\pi i} \oint_C y' \, \frac{1}{Z - \zeta'} \, d\zeta' \quad . \tag{A1.6}$$

The velocity expression in (A1.6) now has the same form as that in (3.10). We may check the far-field velocity expression for large Z/ζ' by expanding the denominator of (A1.6) in terms of ζ'/Z to give

$$V_x - iV_y \approx \frac{\omega_1}{2\pi i} \frac{1}{Z} \oint_{C_1} \left\{ 1 + \frac{\zeta'}{Z} + O[(\zeta'/Z)^2] \right\} d\zeta' \quad . \tag{A1.7}$$

Retaining only first order terms in the integral gives

$$V_x - iV_y \approx \frac{\omega_1}{2\pi i} \frac{1}{Z} \oint_{C_1} y' \, d\zeta' + O[(\zeta'/Z)^2] \quad , \tag{A1.8}$$

which reduces to

$$(V_x - iV_y) = \frac{\omega_1 \, A_1}{2\pi i} \frac{1}{Z} + O[(\zeta'/Z)^2] \quad , \tag{A1.9}$$

where A_1 is the area of the vortex region enclosed by C_1. Hence, for large Z, the velocity field given by (A1.6) approaches that due to a point-vortex of strength $\omega_1 A_1$.

APPENDIX 2 : The "Delta-Model" Applied to Contour Dynamics

The "δ-model" for the vortex sheet works in much the same way as the vortex blob approach where the singular velocity field of a point vortex $(-y, x)/(2\pi |\zeta|^2)$ is replaced by that of a vortex blob $(-y, x)/(2\pi(|\zeta|^2 + \delta^2))$. Krasny (1984, 1986) applied the δ-model to the problem of the roll-up of a vortex sheet and was able to obtain solutions beyond the critical time for $\delta > 0$. Here we apply the δ-model to the Contour-Dynamic formulation with the aim of modifying the the cusp and filament formation processes.

Taking the CD equation (3.25), and using $-\omega\zeta^*/2$ instead of $-\omega y$ for the rotational part of the flow field in equation (3.9), the motion of a particle on the contour C_j is given by

$$\frac{\partial \zeta_j^*}{\partial t} = -\beta(t)\ x + i\ [\gamma(t) - \beta(t)]\ y_j + \frac{\exp[Q(t)]}{4\pi i} \sum_{m=1}^{M} \Delta\omega_m \oint_{C_m} \frac{\zeta_j^* - \zeta_m^{*\prime}}{\zeta_j - \zeta_m'}\, d\zeta_m' \quad , \qquad \text{(A2.1)}$$

We now desingularize the integrand of (A2.1) to obtain the "δ-equation" for CD

$$\frac{\partial \zeta_j^*}{\partial t} = -\beta(t)\ x + i\ [\gamma(t) - \beta(t)]\ y_j + \frac{\exp[Q(t)]}{4\pi i} \sum_{m=1}^{M} \Delta\omega_m \oint_{C_m} \frac{(\zeta_j^* - \zeta_m^{*\prime})^2}{|\zeta_j - \zeta_m'|^2 + \delta^2}\, d\zeta_m' \quad , \qquad \text{(A2.2)}$$

where δ is a small positive real number. The effect for the CD method is to "smudge" to the vorticity jump (delineated by the contours) over a finite layer of characteristic thickness δ. The δ-equation conserves area but does not satisfy the Helmholtz conditions. Its local effect is to add a dispersion

velocity component that is tangential to the contour (Pullin, unpublished manuscript).

We have not analysed the effect of δ nor fully investigated the $\delta = 0$ limit but we have performed a few exploratory computations to illustrate the influence of $\delta > 0$. Figure A2.1 shows the evolution of two interacting FAVRs with $d = (\pi/4)^{1/2}$, $D = 1.50$ and $\gamma = 0.1$ (case 3 in chapter 10) for $\delta = 0.0$, 0.1, 0.2 and 0.3. The computations proceed forward in time to $t = 12.5$ and then the time-step reversed to see if the initial configuration can be faithfully reproduced. The $\delta = 0$ case displays an obvious problem with filamentation, however, the results for $\delta > 0$ do not show any marked improvement (reduced filamentation) until δ has become relatively large (i.e., roughly the thickness of the merged core). Although the $\delta = 0.3$ case has the "cleanest" result the overall vortex dynamics has been significantly affected. Note the presence of very curved arms and a more nearly elliptical central vortex core.

A set of simulations based on case 9 of chapter 10 is shown in figure A2.2. Although the overall rotational speeds of the merging structures are not affected, the local evolutionary features appear to be retarded with increasing δ. In particular, the shape of the vortex structure at $t = 30$ for $\delta = 0.3$ is similar to that at $t = 20$ for $\delta = 0$.

In summary, it appears that the marginal benefit we obtain by applying the δ-model is not as great as that obtained by Krasny (1984, 1986) for the vortex sheet problem. This may be due to the vorticity discontinuity having only a "weak" effect when compared to that induced by the velocity discontinuity of the vortex sheet.

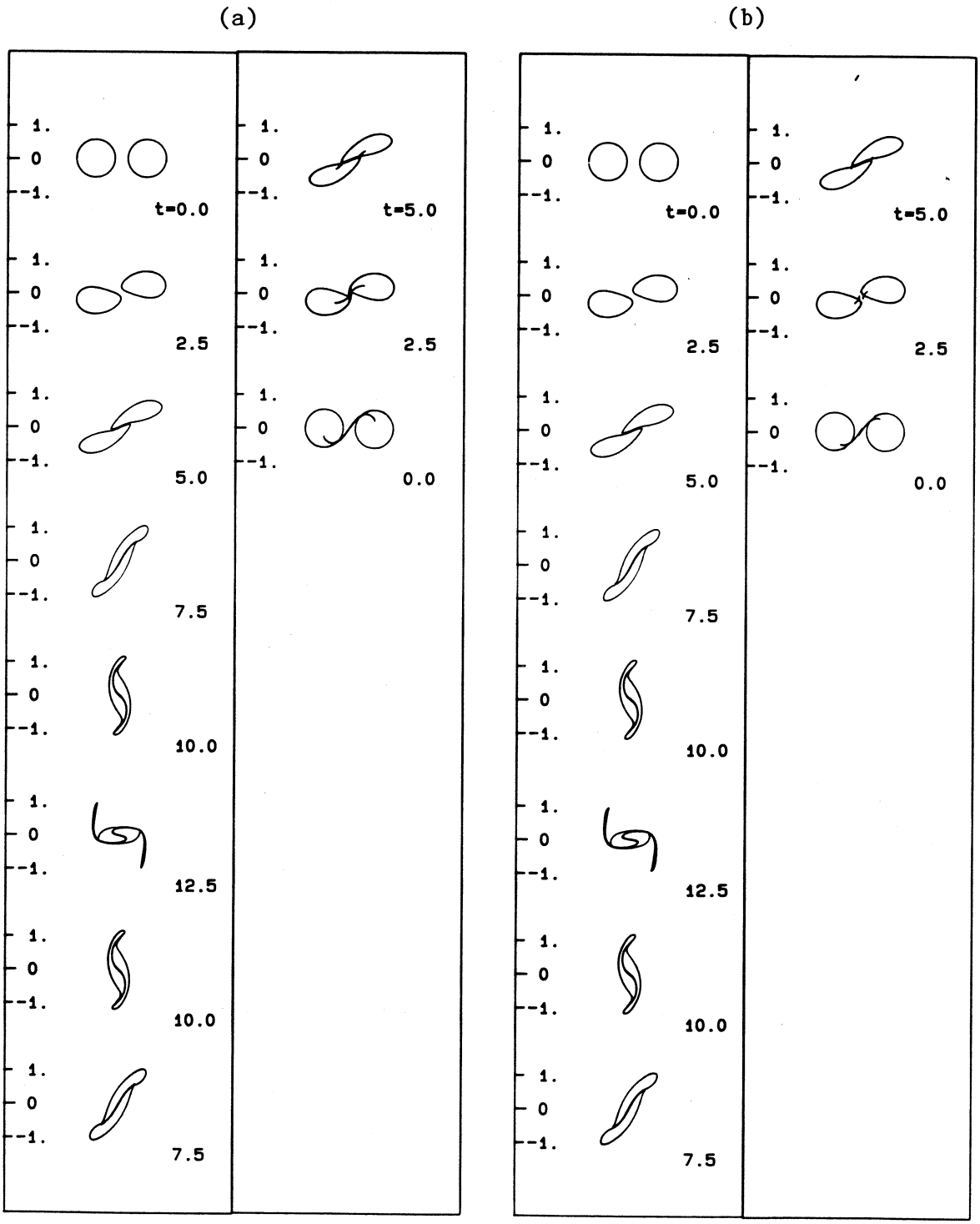

Figure A2.1 a,b : Merging of two, equal uniform vorticity FAVRS, $d = (\pi/4)^{\frac{1}{2}}$, $D = 1.5$, $\gamma = 0.1$ with (a) $\delta = 0$, (b) $\delta = 0.1$. Times t as shown.

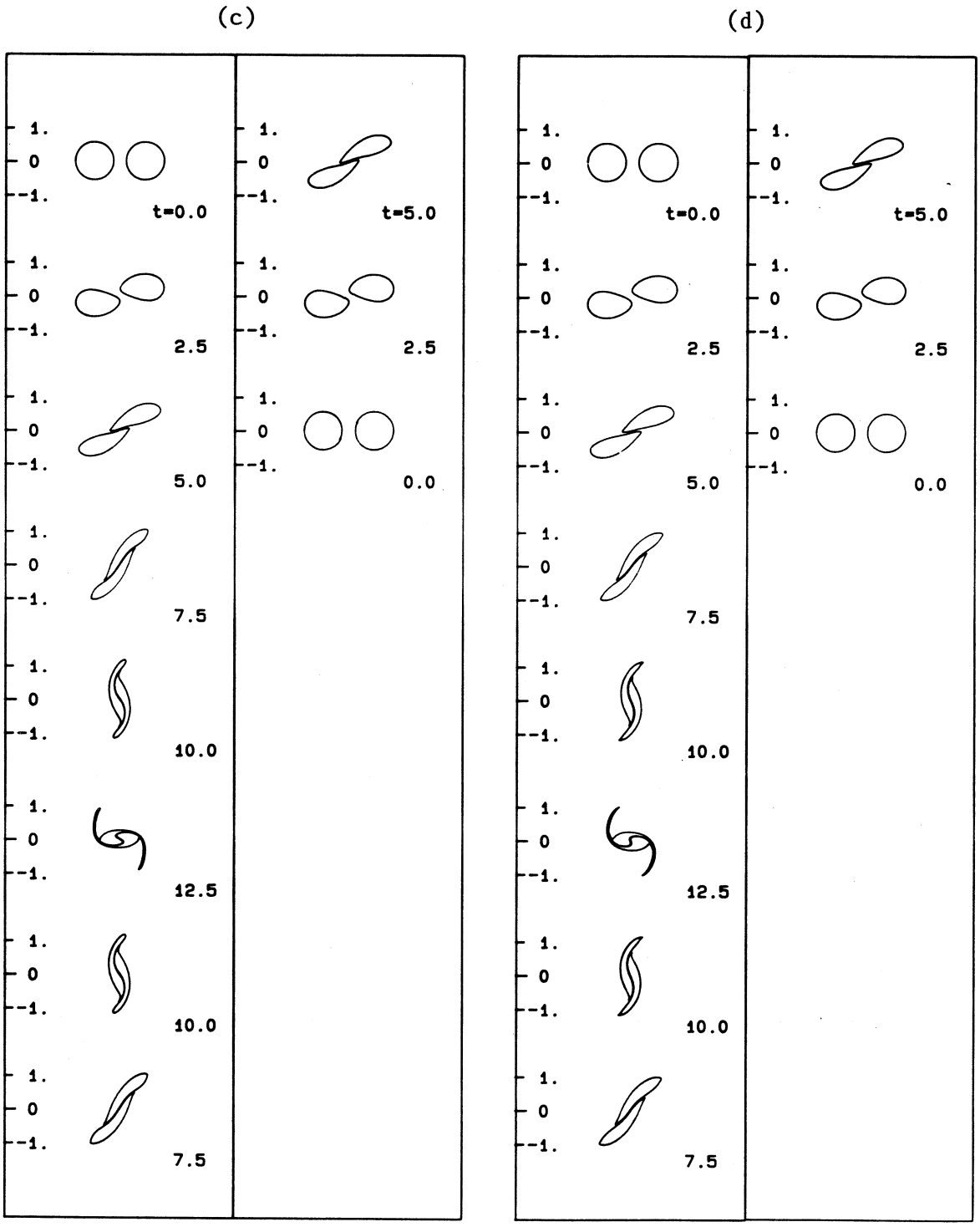

Figure A2.1 c,d : (c) $\delta = 0.2$, (d) $\delta = 0.3$

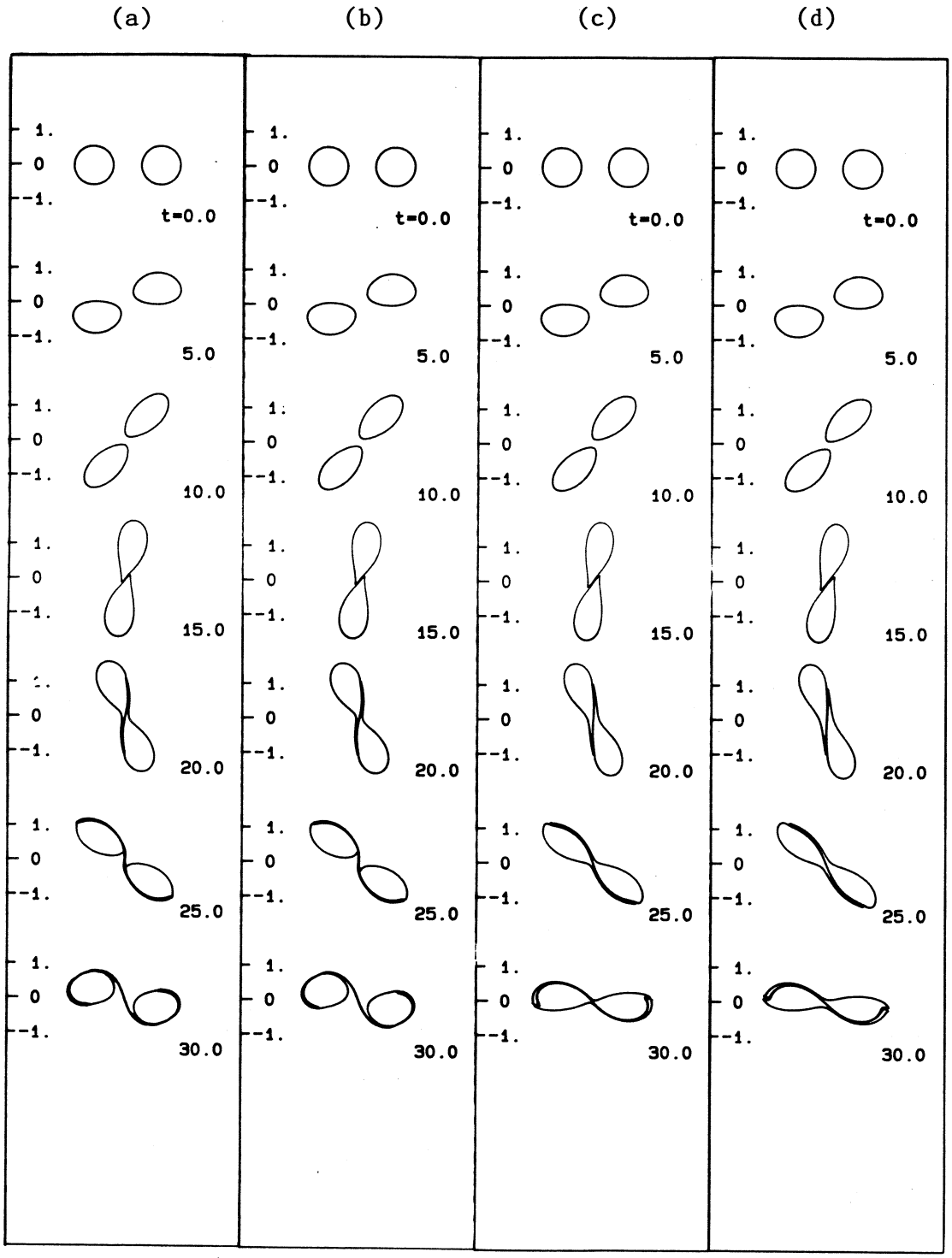

Figure A2.2 : Merging of two equal, uniform-vorticity FAVRS, $d = (\pi/4)^{\frac{1}{2}}$, $D = 1.92$, $\gamma = 0$ with (a) $\delta = 0$, (b) $\delta = 0.1$, (c) $\delta = 0.2$, (d) $\delta = 0.3$.

APPENDIX 3 : Analytic Patch Procedure for the Velocity Calculation

The governing equations (4.7) for the spatially periodic CD formulation contain an integrand of the form

$$I_{total} = (Y - y') \cot\left[\frac{1}{2}(Z - \zeta')\right] \frac{d\zeta'}{de'} \quad , \qquad (A3.1)$$

which is not well behaved over contour segments that approach very closely but, do not coincide with, the velocity point Z = X + iY.

Consider the contour segment defined by

$$\zeta'(e) = Ae^2 + Be + \zeta_0 \quad , \qquad (A3.2)$$

where $\zeta'(-1) = \zeta_{-1}$ and $\zeta'(1) = \zeta_1$. For the segment in figure A3.1, $\zeta_{-1} = 0.5 - i$, $\zeta_0 = 1.0$, $\zeta_1 = 1.0 + 2i$. The weakly singular behaviour of (A3.1) over the segment is illustrated in figures A3.2 (a, b, c) where the real (labelled "R") and imaginary parts of the integrand I_{total} are plotted for Z = 1.3, 1.1 and 1.01 respectively. The smaller the distance

$$d = \min_{-1 \le e \le +1} |Z - \zeta'(e)| \quad , \qquad (A3.3)$$

becomes, the more difficult the integrand behaviour. For these examples, the fixed rule (4 point) Gaussian quadrature (4.10) cannot produce an accurate estimate of

$$J = \int_{-1}^{1} I_{total}\, de' \quad , \qquad (A3.4)$$

using a single panel. The estimate of J can, however, be improved by breaking the segment into N smaller panels, applying the quadrature (4.10) to each panel, and summing the result. Just how many panels are required to produce a specified accuracy depends on d. Figure A3.3 shows the variations in the estimate for Im(J) with the number of panels used, N. The panels here have been specified as having equal ranges of the interpolation parameter, e. Both parts, (a) and

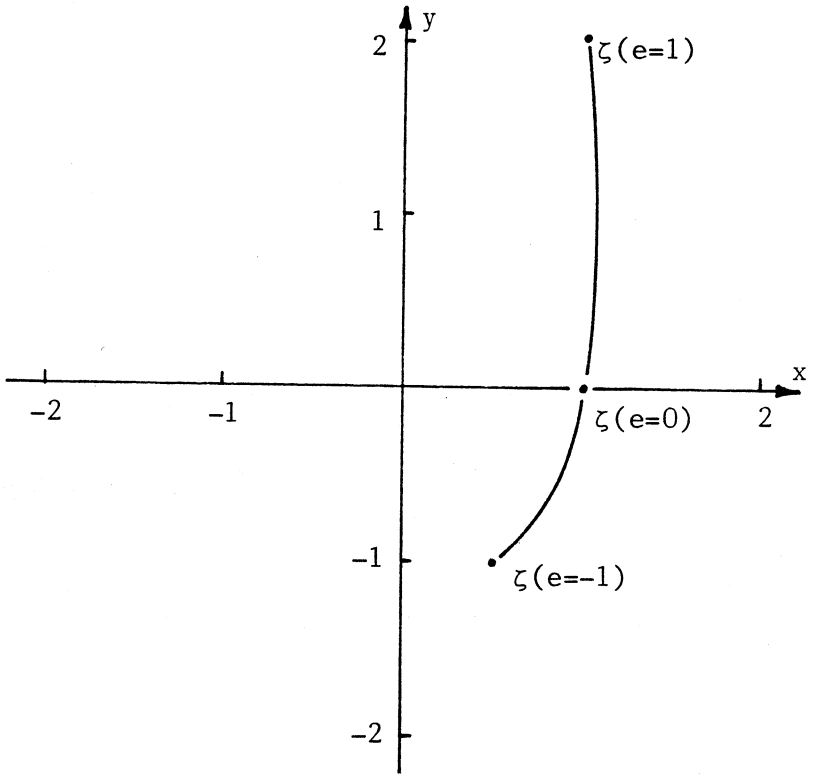

Figure A3.1 : A single parabolic segment $\zeta(e) = Ae^2 + Be + C$ defined by the subset of three nodes

$\zeta(-1) = (\zeta_m)_{n-1} = 0.5 - i$,

$\zeta(0) = (\zeta_m)_n = 1.0$,

$\zeta(1) = (\zeta_m)_{n+1} = 1.0 + 2.0i$.

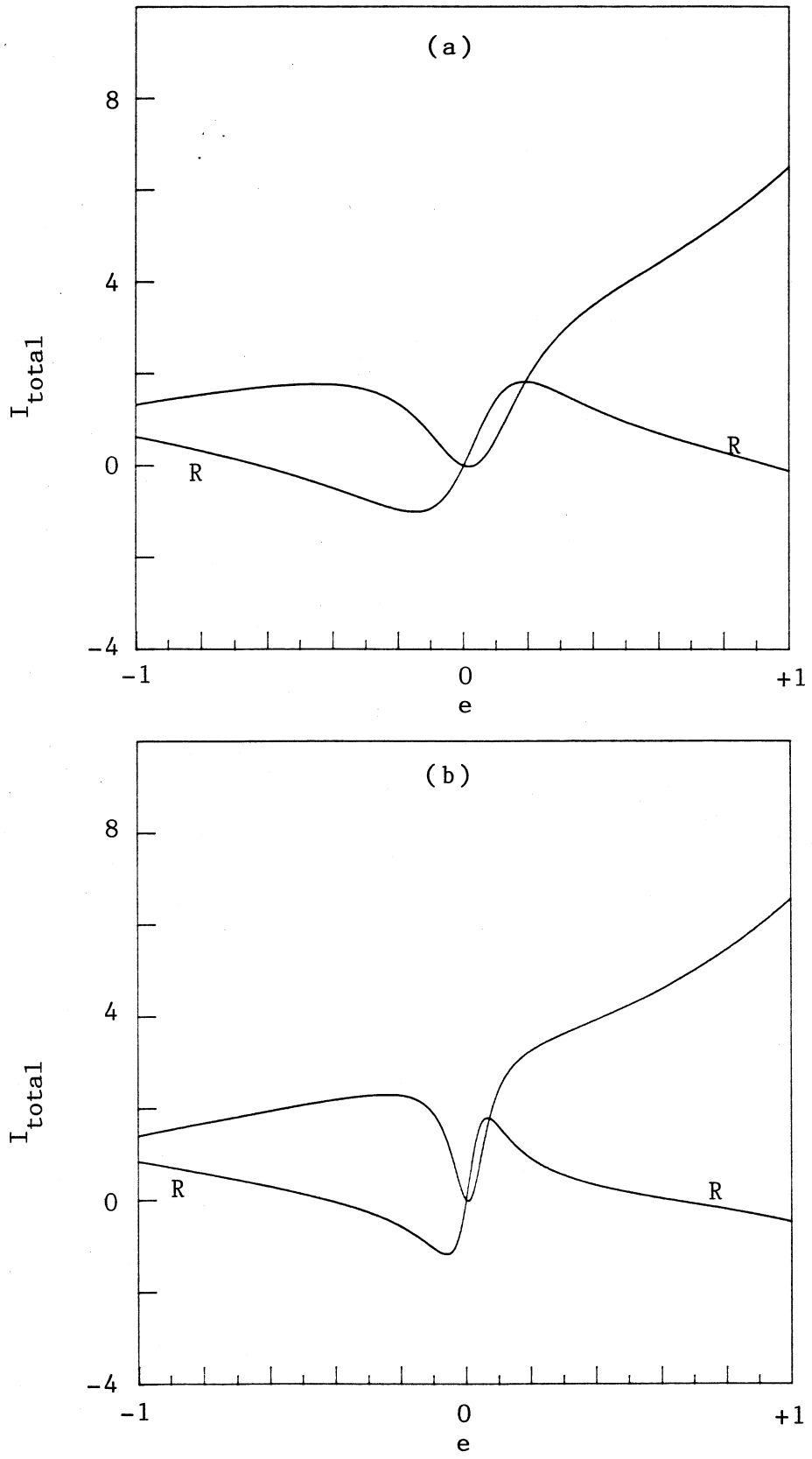

Figure A3.2 : For caption see opposite.

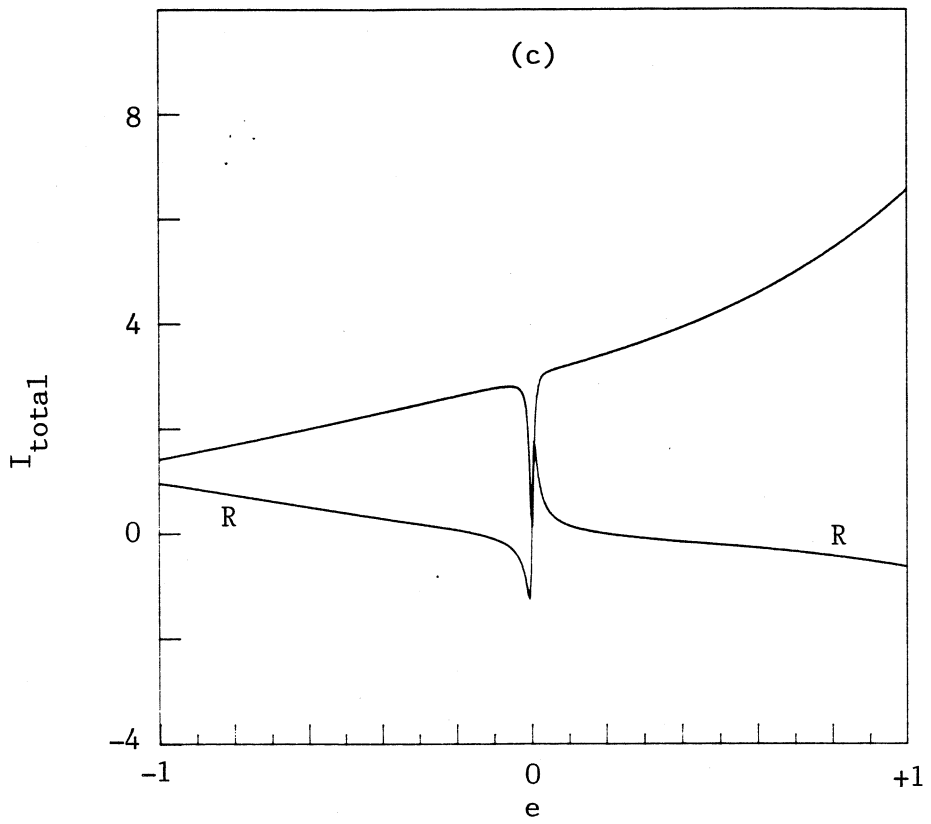

Figure A3.2 : Real parts (labelled R) and imaginary parts of the integrand I_{total} (A3.1) as functions of the interpolation parameter (e) over the segment defined in figure A3.1. The weakly singular behaviour becomes more pronounced as Z approaches the contour segment.

(a) Z = 1.3

(b) Z = 1.1

(c) Z = 1.01

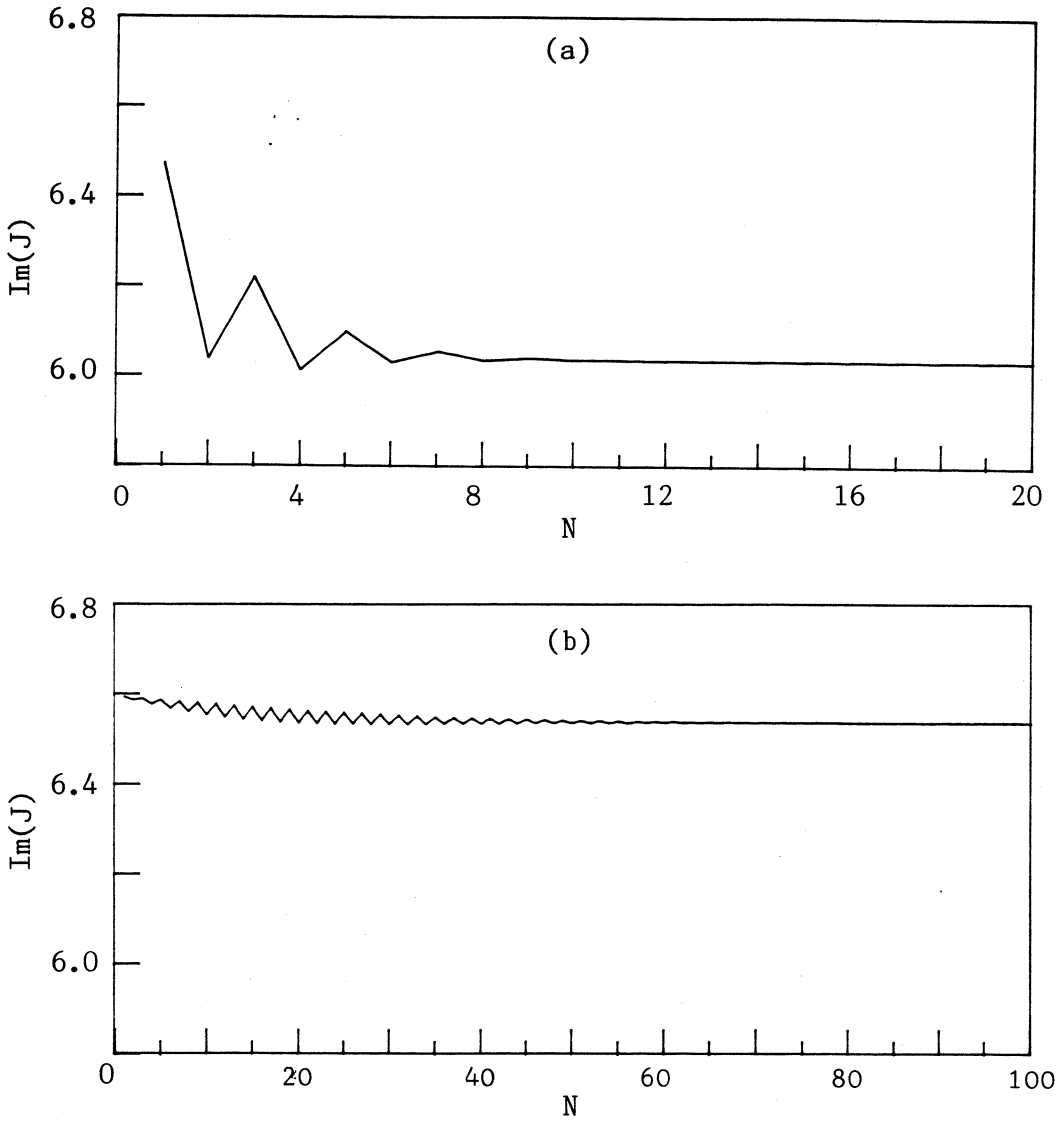

Figure A3.3 : Variation of the imaginary part of the integral J (A3.4) with the number of panels used in the numerical quadrature over the segment defined A3.1. The real parts are nearly zero hence they are not displayed here.
(a) Z = 1.1
(b) Z = 1.01

(b), show that the estimate converges, for sufficiently large N.

The velocity calculation is the most computationally expensive part of the CD implementation even with a fixed rule quadrature. The implementation of an adaptive scheme would result in a lot more work being done if the contours approach each other very closely and, as d becomes small, the progress of the calculation would greatly reduced.

To avoid this problem we propose to decompose the full integrand, I_{total}, into a rapidly varying part, I_{fast}, and a slowly varying part, I_{slow}. The slowly varying part may be integrated accurately using our fixed rule quadrature (4.10) with only one panel per contour segment. I_{fast} should have a simple form so that it may be analytically integrated over the segments but the complexity I_{slow} is of little consequence as the implementation of the numerical quadrature is relatively insensitive to integrand form.

To obtain an integrand which is similar in behaviour to I_{total}, we expand (A3.1) for small $|\, Z - \zeta' \,|$. Retaining only first order terms we have

$$I_{fast} = 2\frac{(Y - y')}{(Z - \zeta')}\frac{d\zeta'}{de'} \quad . \tag{A3.5}$$

Subtracting (A3.5) from (A3.1) leaves

$$I_{slow} = \left\{(Y - y') \cot\left[\frac{1}{2}(Z - \zeta')\right] - 2\frac{(Y - y')}{(Z - \zeta')}\right\}\frac{d\zeta'}{de'} \quad . \tag{A3.6}$$

Figures (A3.4a,b) show the variation of I_{fast} and I_{slow} respectively along the segment defined in figure (A3.1) with Z = 1.01. The small magnitude of I_{slow} indicates that the total integrand is closely approximated by I_{fast} especially in the region close to Z (i.e., e ≈ 0).

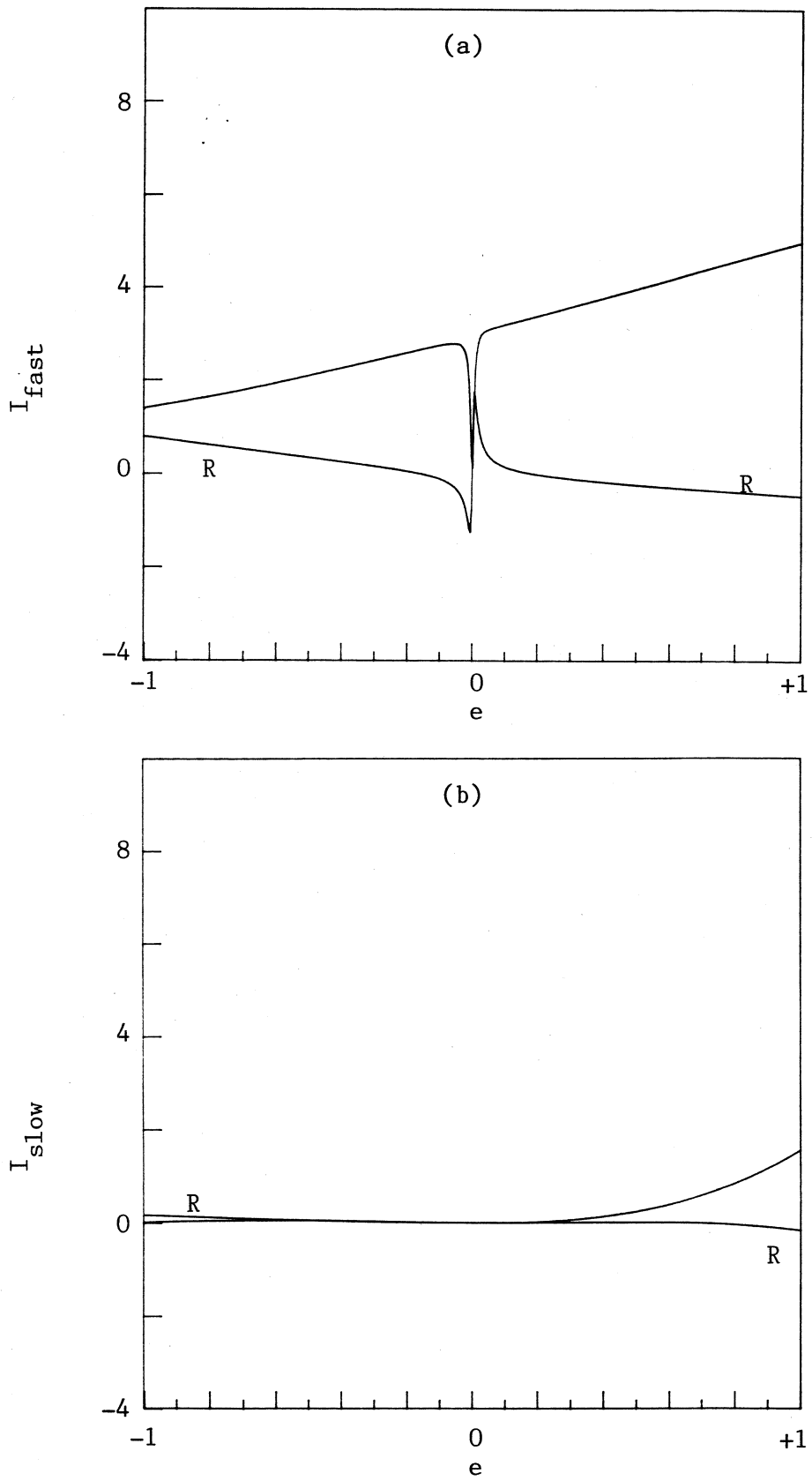

Figure A3.4 : Real parts (labelled R) and imaginary parts of the integrands (a) I_{fast} and (b) I_{slow} as functions of the interpolation parameter (e) over the contour segment defined in figure A3.1. Z = 1.01.

With I_{slow} smooth, the integral

$$J_{slow} = \int_{-1}^{1} I_{slow}\, de' \quad , \tag{A3.7}$$

may be approximated accurately with just one panel. The analytic integration of I_{fast}

$$J_{fast} = \int_{-1}^{1} \frac{I_{fast}}{2}\, de' \quad , \tag{A3.8}$$

can be done either for straight line interpolation between the points defining the segment

$$\zeta'(e) = \begin{cases} \zeta_0 - e\,(\zeta_{-1} - \zeta_0) \quad , \quad -1 \le e \le 0 \quad , & \text{(A3.9a)} \\ \zeta_0 + e\,(\zeta_1 - \zeta_0) \quad , \quad 0 \le e \le 1 \quad , & \text{(A3.9b)} \end{cases}$$

or for parabolic interpolation (A3.2). Both cases are needed as the parabolic result breaks down for $|A| \le$ machine-precision.

First we give the result for straight line interpolation. The total expression for J_{fast} is composed of contributions from each of the straight line segments $\zeta_{-1} \to \zeta_0$ and $\zeta_0 \to \zeta_1$,

$$J_{fast} = J_{-1} + J_1 \quad , \tag{A3.10}$$

where

$$J_{-1} = (y_0 - y_{-1}) + \left\{ -(Y - y_{-1}) + (Z - \zeta_{-1})\frac{(y_0 - y_{-1})}{(\zeta_0 - \zeta_{-1})} \right\} \times \left[\ln(Z - \zeta_0) - \ln(Z - \zeta_{-1}) \right] \quad , \tag{A3.11a}$$

and

$$\lim_{\substack{Z \to \zeta_0 \\ Z \to \zeta_{-1}}} J_{-1} = (y_0 - y_{-1}) \quad , \tag{A3.11b}$$

The expression for J_1 is similar but has the translation $\zeta_0 \to \zeta_1$ and $\zeta_{-1} \to \zeta_0$.

The difference of the logarithms can be rewritten as

$$\ln(Z - \zeta_0) - \ln(Z - \zeta_{-1}) = \ln\frac{|z_0|}{|z_{-1}|} + i(\angle z_0 - \angle z_{-1}) \quad , \tag{A3.12}$$

where $\zeta_0 = (Z - \zeta_{-1})$, $\zeta_{-1} = (Z - \zeta_{-1})$ and $\angle$ represents the angle argument. There is no difficulty with the real part of equation (A3.12) but, to select the correct branch for the imaginary part, we force a branch cut to lie along the straight line segment $\zeta_1 \rightarrow \zeta_0$. This numerical evaluation can be achieved in more than one way but we choose to evaluate (A3.12) as

$$\ln(Z - \zeta_0) - \ln(Z - \zeta_{-1}) = \ln[t^*(Z - \zeta_0)] - \ln[t^*(Z - \zeta_{-1})] \quad , \tag{A3.13a}$$

where

$$t = \frac{(\zeta_0 - \zeta_1)}{|\zeta_0 - \zeta_1|} \quad . \tag{A3.13b}$$

These are essentially the same expressions as used in the isolated FAVR calculations (equations (4.3a-c)).

We now consider the expressions for J_{fast} using parabolic interpolation (A3.2). Defining

$$T = Z - \zeta_0 \quad , \tag{A3.14}$$

and denoting real and imaginary parts by the subscripts R and I respectively, the integral may be written

$$J_{fast} = \int_{-1}^{1} \left\{ \frac{(T_I - B_I e - A_I e^2)(B + 2Ae)}{T - B\,e - A\,e^2} \right\} de \quad . \tag{A3.15}$$

Expanding the numerator and using integral-table 2.17 of Gradshteyn & Ryzhik (1980), the integral can be evaluated as

$$J_{fast} = term_1 + coeff_2.term_2 + coeff_3.term_3 \quad , \tag{A3.16a}$$

where

$$\text{term}_1 = 2(2B_I - A_I B/A) \quad , \tag{A3.16b}$$

$$\text{coeff}_2 = -T_I + [A_I T + B/2\ (-B_I + A_I B/A)]\ /\ A \quad , \tag{A3.16c}$$

$$\text{term}_2 = \ln(Z - \zeta_1) - \ln(Z - \zeta_{-1}) \quad , \tag{A3.16d}$$

$$\text{coeff}_3 = -2B_I T + \frac{B}{A}\left[2A_I T + B/2(-B_I + A_I B/A)\right] \quad , \tag{A3.16e}$$

$$\text{term}_3 = \frac{1}{\sqrt{(-\Delta)}}\left\{\ln\left[\frac{-B - 2A - \sqrt{(-\Delta)}}{-B - 2A + \sqrt{(-\Delta)}}\right] - \ln\left[\frac{-B + 2A - \sqrt{(-\Delta)}}{-B + 2A - \sqrt{(+\Delta)}}\right]\right\} \tag{A3.16f}$$

and

$$\sqrt{(-\Delta)} = (B^2 + 4AT)^{1/2}. \tag{A3.16g}$$

Special care must be exercised when selecting the branch cuts for term_2 and term_3.

The real part of term_2 is straight forward and may be calculated as in equation (A3.12). The imaginary part corresponds to the angle enclosed by the two lines $Z - \zeta_{-1}$, $Z - \zeta_0$ and the contour segment. For the three examples Z_I, Z_{II} and Z_{III} in figure A3.5 these angles are θ_I, θ_{II} and θ_{III} respectively.

The logic for determining θ has the following steps.
(i) Evaluate the magnitude of θ using the cosine rule

$$\theta = \text{acos}[(L_{-1}^2 + L_1^2 - |\Delta z|^2)/(2L_{-1}L_1)] \quad , \tag{A3.17a}$$

where

$$\Delta z = \zeta_1 - \zeta_{-1} \quad , \tag{A3.17b}$$

$$L_1 = |Z - \zeta_1| \quad , \tag{A3.17c}$$

$$L_{-1} = |Z - \zeta_{-1}| \quad . \tag{A3.17d}$$

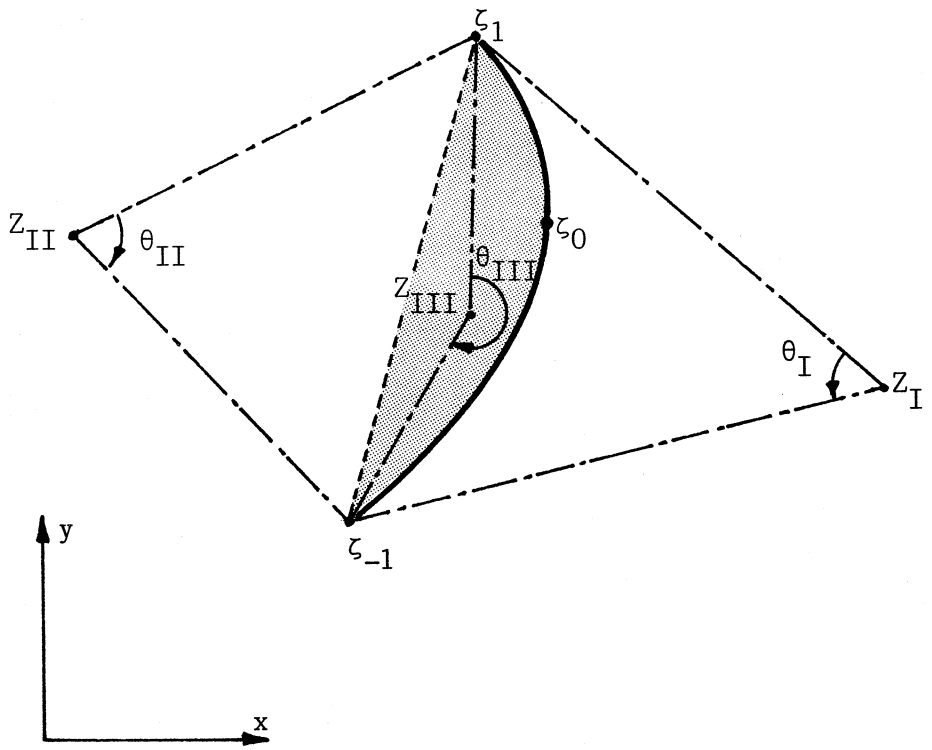

Figure A3.5 : Three examples of the evaluation of the imaginary part of $term_2$ (A3.16d). θ is always the angle enclosed by the two straight lines $Z - \zeta_1$, $Z - \zeta_{-1}$ and the curved contour segment. In the shaded region $\theta = 2\pi - \theta_{cos}$ where θ_{cos} is evaluated using the cosine rule (A3.17).

(ii) Determine where on the ζ-plane Z lies by computing an indicator, λ, which is the parameter of a straight line joining Z and D. The line is defined by

$$\zeta(\lambda) = D + \lambda(Z - D) \quad , \tag{A3.18a}$$

$$D = 0.5(\zeta_{-1} + \zeta_1) \quad , \tag{A3.18b}$$

We search for the intersection of the line (A3.18) with the parabolic curve (A3.2) given by the solution of the two equations

$$A_R e^2 + B_R e + x_0 = D_R + \lambda(X - D_R) \quad , \tag{A3.19a}$$

$$A_I e^2 + B_I e + y_0 = D_I + \lambda(Y - D_I) \quad , \tag{A3.19b}$$

in the unknowns λ and e. In general, there will be two solutions

$$e = \frac{-\beta \pm \sqrt{(\beta^2 + 4\alpha^2)}}{2\alpha} \quad , \tag{A3.20a}$$

where

$$\alpha = A_R - A_I \left[\frac{X - D_R}{Y - D_I} \right] \quad , \tag{A3.20b}$$

$$\beta = B_R - B_I \left[\frac{X - D_R}{Y - D_I} \right] \quad , \tag{A3.20c}$$

with one solution being in the range $-1 < e < 1$. We choose this solution and calculate λ using

$$\lambda = (A_I e^2 + B_I e - A_I)/(Y - D_I) \quad , \tag{A3.21}$$

If $\lambda > 1.0$ then Z is inside the speckled region of figure A3.6, else it is outside.

(iii) Determine the orientation of the triad Z, ζ_1, ζ_{-1} on the ζ plane using a cross product

$$C = \Delta x.y - \Delta yx \quad , \tag{A3.22a}$$

where

$$\Delta Z = \Delta x + i\Delta y \quad , \tag{A3.22b}$$

$$D = x + iy \quad , \tag{A3.22c}$$

(iv) Combine the magnitude and sign using

$$\begin{aligned} &\text{if } (\lambda < 1.0) \text{ then} \\ &\quad \theta = \text{sign } (\theta_{cos}, D) \\ &\text{else} \\ &\quad \theta = \text{sign } (2\pi - \theta_{cos}, -D) \quad , \end{aligned} \tag{A3.23}$$

where the function sign transfers the sign from the second argument to the first.

The evaluation of $term_3$ is best done in the w-plane where

$$w = (B^2 + 4AT)^{1/2} \quad . \tag{A3.24}$$

Substituting the parabolic segment equations(A3.2) into (A3.24) gives

$$w(e) = \pm(2Ae + B) \quad , \tag{A3.25}$$

which indicates that the parabolic segment maps to two straight line segments in th w-plane, one being the image of the other through the origin (see figure A3.6). Hence, the evaluation of $term_3$ can be done in much the same way as in equation (A3.13)

$$\begin{aligned} term_3 = &\frac{1}{w}\left\{ \ln[t^*(c_1 - w)] - \ln[t^*(c_2 - w)] \right\} \\ &+ \frac{1}{w}\left\{ \ln[t^*(c_2 + w)] - \ln [t^*(c_1 + w)] \right\} \quad , \end{aligned} \tag{A3.26a}$$

where

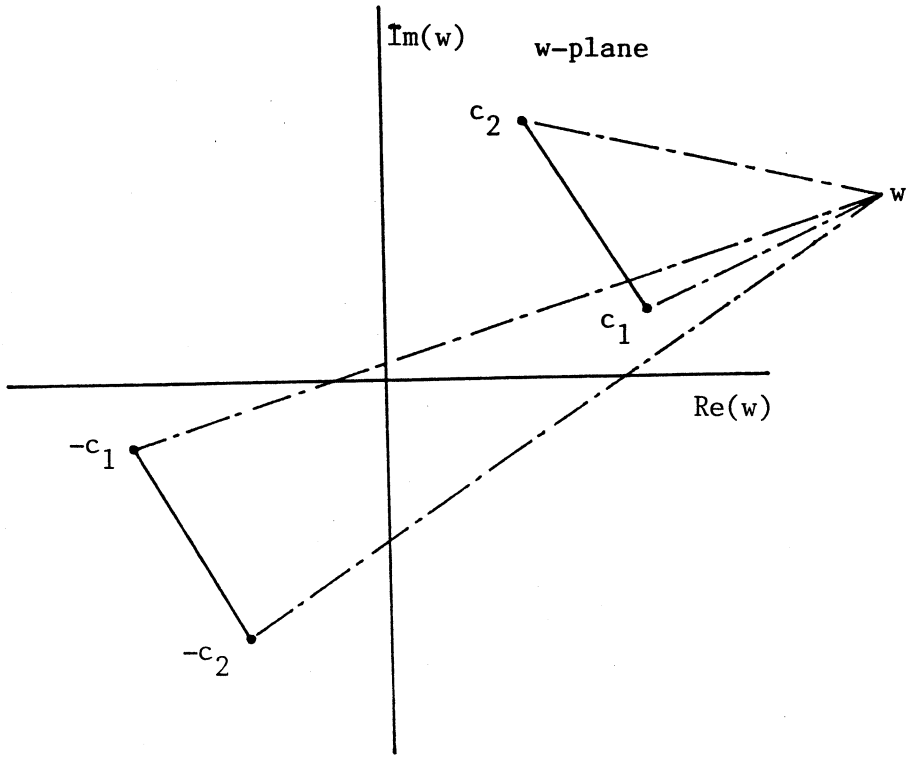

Figure A3.6 : The parabolic segment in the ζ-plane maps to two straight lines in the w-plane as defined by equation (A3.25).

Table A3.1 : Number of panels required to achieve four digit accuracy in the numerical quadrature of J_{total}. d is the distance of closest approach of the segment to Z.

Z	# panels required	effective panel size p	p/d
1.01	70	0.032	0.31
1.02	40	0.056	0.36
1.05	20	0.112	0.45
1.1	12	0.112	0.54
1.2	7	0.319	0.63
1.5	4	0.560	0.89
2.0	2	1.120	0.89

$$c_1 = -B - 2A \quad , \tag{A3.26b}$$

$$c_2 = -B + 2A \quad , \tag{A3.26c}$$

$$t = A \,/\, |A| \quad , \tag{A3.26d}$$

The end points of the two w-plane lines are c_1, c_2 and $-c_1$, $-c_2$ while t is parallel to them.

When compared with the numerical quadrature, the "analytic-patch" procedure is extremly expensive to implement. Hence it has to be used only where required. For an indication of the relative computing effort see the shear layer described in (figures 5.5, 5.6 of) section 5.2. In order to determine a simple criteria for the application the procedure, we carried out a numerical experiment in which we found the number of panels, N, required to produce an accurate (precise to 4 digits in 32-bit arithmetic) estimate for J using the numerical quadrature (4.10) only. The results are summarized in table A3.1. Taking the worst case, and including an "ignorance factor", we set the criteria for applying the patch as

$$\min(|Z - \zeta(e_i)| , i = 0...3) \leq \text{segsize} \quad , \tag{A3.27a}$$

where

$$\text{segsize} = |\zeta_1 - \zeta_0| + |\zeta_0 - \zeta_{-1}| \quad , \tag{A3.27b}$$

approximates the length of the segment. The e_i, i = 0...3 are the integration points for the numerical quadrature. Although this test is rough, especially for segments with high curvature, it has the advantage of being simple and relatively inexpensive.

APPENDIX 4 : Point Vortex Models of Some Simple Flows

We can describe some of the features of the finite area vorticity distributions by approximating the rolled-up vortex cores as point vortices. Here we will use point vortex models to

(i) calculate the stretching strain induced by the primary vortices on the secondary vortices at the midpoint of the braid,

(ii) find the stagnation point of the axis of symmetry and its associated streamline in the stretching secondary-vortex simulations.

For an isolated point with circulation Γ and position ζ_o (figure A4.1) the complex potential is

$$W(\zeta) = \frac{\Gamma}{2\pi i} \ln(\zeta - \zeta_o) \quad , \tag{A4.1}$$

and the associated velocity field is

$$u - iv = \frac{dW}{d\zeta} = \frac{\Gamma}{2\pi i} \frac{1}{\zeta} \quad , \tag{A4.2}$$

where $\zeta = x + iy$.

Extending this to a periodic array of point vortices with circulations Γ and period λ (figure A4.2) we have a complex potential

$$W(\zeta) = \frac{\Gamma}{2\pi i} \ln\left\{ \sin\left[\frac{\pi}{\lambda} (\zeta - \zeta_o) \right] \right\} \quad , \tag{A4.3}$$

and associated velocity field

$$u - iv = \frac{\Gamma}{2\lambda i} \cot\left[\frac{\pi}{\lambda} (\zeta - \zeta_o) \right] \quad , \tag{A4.4}$$

(Milne-Thomson §13.71, 1968)

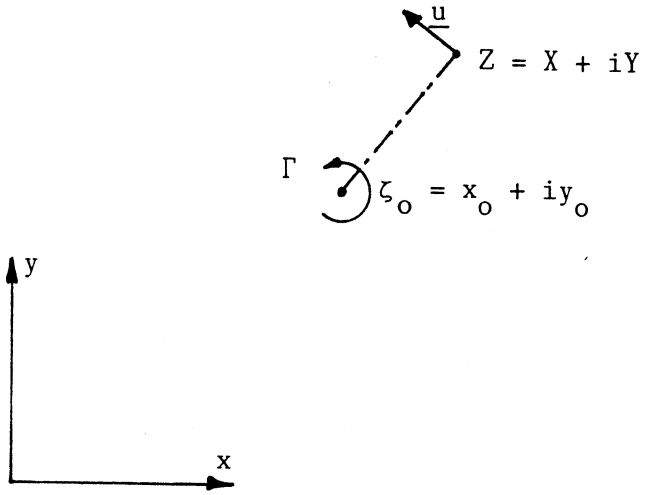

Figure A4.1 : An isolated point vortex located at ζ_o with circulation Γ induces a velocity $\underline{u} = u\underline{i} + v\underline{j}$ at point Z.

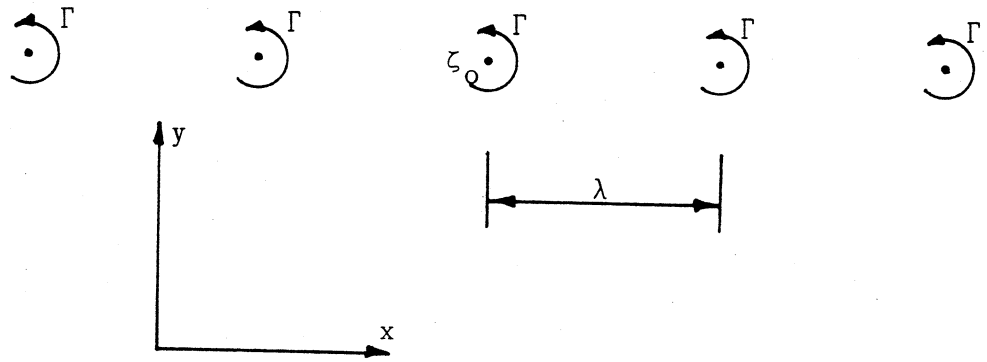

Figure A4.2 : A periodic array of point vortices with circulations Γ and spacing λ. One member of the array is located at ζ_o.

Case (i)

Approximate the rolled-up primary vortices by concentrated point vortices and set $\zeta_o = 1/2$ so that the braid connecting the primary vortices would be at $\zeta = 0$. The velocity field is

$$u - iv = \frac{\Gamma}{2\lambda i} \cot\left[\frac{\pi}{\lambda}\zeta - \frac{\pi}{2}\right] , \qquad \text{(A4.5a)}$$

$$= \frac{-\Gamma}{2\lambda i} \tan\left[\frac{\pi}{\lambda}\zeta\right] . \qquad \text{(A4.5b)}$$

Expanding (A4.5b) for small ζ and retaining only the first order terms gives a velocity field

$$u - iv = \frac{i\Gamma\pi}{2\lambda^2}\zeta . \qquad \text{(A4.6)}$$

By rotating into a new frame of reference given by

$$\zeta' = \zeta e^{-i\theta} , \qquad \text{(A4.7)}$$

we obtain the velocity field

$$u' - iv' = \frac{dW}{d\zeta'} = (u - iv).e^{i\theta} . \qquad \text{(A4.8)}$$

Substituting (A4.6) gives

$$u' - iv' = \frac{\pi\Gamma}{2\lambda^2} i\, e^{2i\theta}\, \zeta' , \qquad \text{(A4.9)}$$

which, for $\theta = -\pi/4$, becomes

$$u' - iv' = \frac{\pi\Gamma}{2\lambda^2}\zeta' . \qquad \text{(A4.10)}$$

This is a plane-strain field of strength $\gamma = \pi\Gamma/(2\lambda^2)$ with principal axes orientated at 45^o to the (x, y)-axes as shown in figure A4.3.

Each rolled up vortex contains the vorticity redistributed from one period, λ_1, of the initially perturbed shear layer with velocity jump ΔU across the layer. The circulation of each vortex core is then

$$\Gamma = \lambda_1 \Delta U \quad , \tag{A4.11}$$

giving a stretching field

$$u' - iv' = \frac{\Delta U \pi}{2\lambda_1} \zeta' \quad . \tag{A4.12}$$

Case (ii)

Approximate the rolled-up primary vortices by a double array with period λ as shown in figure A4.4. The circulations Γ_1, Γ_2 are not necessarily equal. The velocity induced by these two arrays minus that due to the point vortex at the origin is

$$u - iv = \frac{\Gamma_1}{2\lambda i} \cot\left[\frac{\pi}{\lambda}\zeta\right] + \frac{\Gamma_2}{2\lambda i} \cot\left[\frac{\pi}{\lambda}\zeta - \frac{\pi}{2}\right] - \frac{\Gamma_1}{2\pi i}\frac{1}{\zeta} \quad , \tag{A4.13a}$$

$$= \frac{\Gamma_1}{2\lambda i}\left\{\cot\left[\frac{\pi}{\lambda}\zeta\right] - \frac{\lambda}{\pi\zeta}\right\} - \frac{\Gamma_2}{2\lambda i} \tan\left[\frac{\pi}{\lambda}\zeta\right] \quad . \tag{A4.13b}$$

Expanding (A4.13b) for small ζ and retaining only first order terms gives

$$u - iv = \frac{i\pi}{2\lambda^2}\left\{\frac{\Gamma_1}{3} + \Gamma_2\right\}\zeta \quad . \tag{A4.14}$$

By rotating into a new frame of reference (A4.7), and setting $\theta = -\pi/4$, we obtain

$$u' - iv' = \frac{\pi}{2\lambda^2}\left\{\frac{\Gamma_1}{3} + \Gamma_2\right\}\zeta' \quad . \tag{A4.15}$$

which is again a plane-strain field orientated at 45^{o} to the (x, y)-axes as shown in figure A4.3.

Case (iii)

To approximately locate the stagnation point in the secondary vortex simulations, consider the point vortex model in figure A4.4. Set $\Gamma_1 = \Gamma$, $\Gamma_2 = -\Gamma$ and add the stretching strain field (3.20). The total (x, y)-plane velocity is

$$u - iv = i\gamma y + \frac{\Gamma}{2\lambda i}\left\{\cot\left[\frac{\pi}{\lambda}\zeta\right] - \cot\left[\frac{\pi}{\lambda}\zeta - \frac{\pi}{2}\right]\right\} . \tag{A4.16}$$

At the line of symmetry, $x = \lambda/4$, the velocity is

$$u - iv = i\gamma y - \frac{i\Gamma}{\lambda}\frac{1}{\cosh\left[\frac{2\pi y}{\lambda}\right]} , \tag{A4.17}$$

so that, at the stagnation point,

$$0 = y\cosh\left[\frac{2\pi}{\lambda}y\right] - \frac{\Gamma}{\lambda\gamma} . \tag{A4.18}$$

This can be nondimensionalized, as done in the secondary vortex simulations, by setting

$$Y = \frac{2\pi}{\lambda}y , \tag{A4.19a}$$

$$\frac{4\pi^2}{\lambda^2}\Gamma = 1 , \tag{A4.19b}$$

to give

$$0 = Y\cosh Y - (2\pi\gamma)^{-1} . \tag{A4.20}$$

Solutions to equations (A4.20) are given in table A4.1 for the values of the nondimensional strain, γ_2, used in the full nonlinear simulation (chapter 8). The corresponding

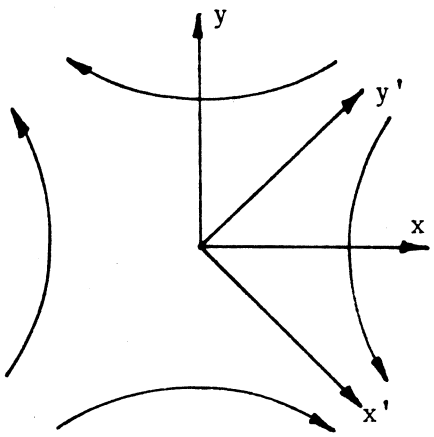

Figure A4.3 : A plane strain field represented by four curved streamlines. The principal axes (x', y') are oriented at 45^{o} to the (x, y) axes.

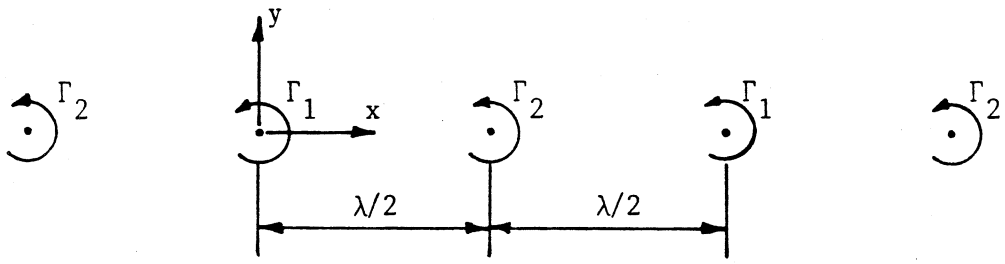

Figure A4.4 : A double periodic array of point vortices with circulations Γ_1 and Γ_2. The wavelength of the array is λ.

Table A4.1 : Solutions to equation (A4.20)

γ	Υ
0.1	1.018
0.2	0.652
0.4	0.372

stagnation streamlines in figure A4.5 are obtained by starting at a point "just off" the stagnation point and numerically integrating (A4.16) in (x, y)-space.

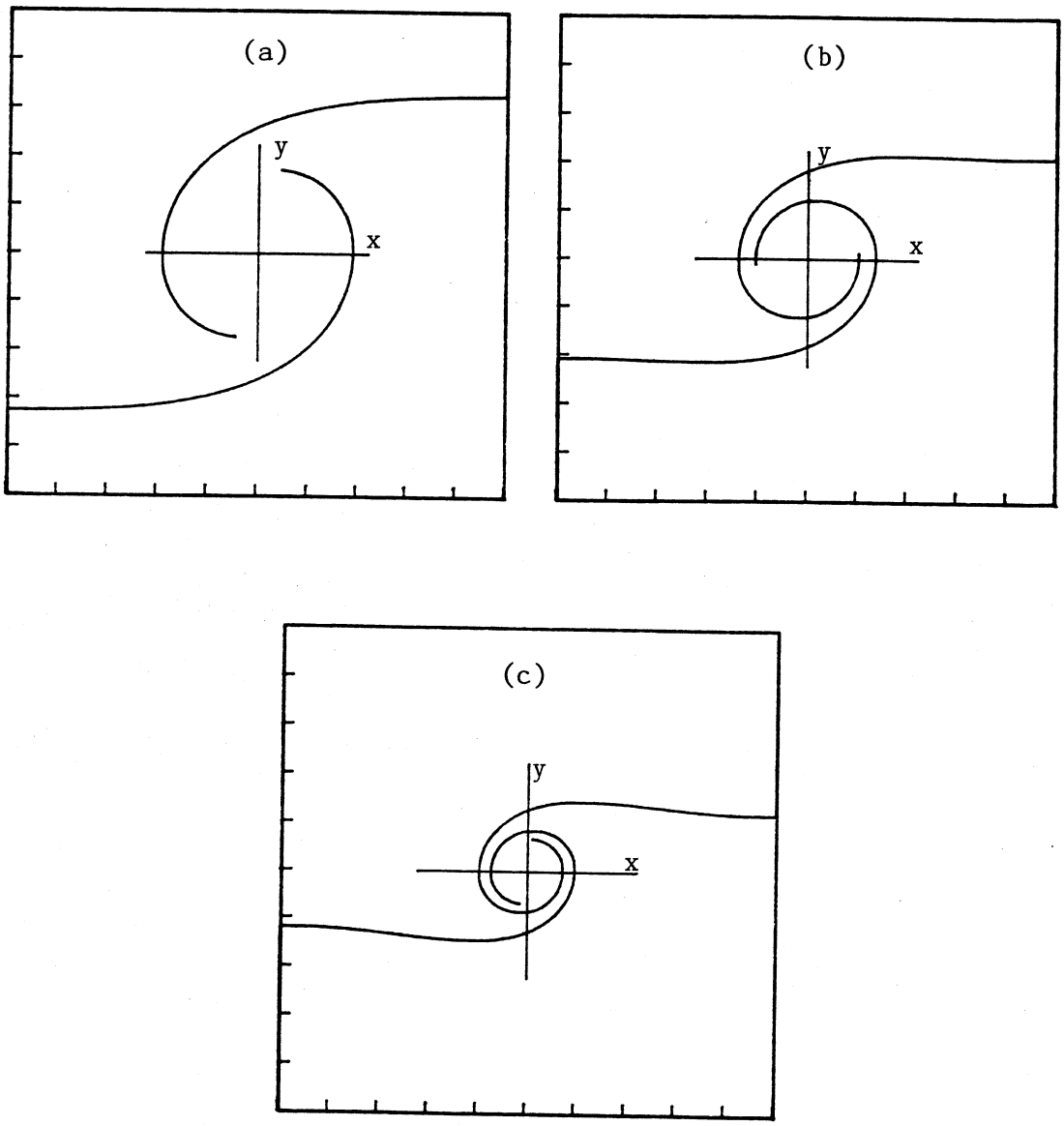

Figure A4.5 : Parts of the stagnation streamlines for three values of stretching strain γ. Tic spacing is $\pi/10$.

(a) $\gamma = 0.1$

(b) $\gamma = 0.2$

(c) $\gamma = 0.4$

APPENDIX 5 : Linear Stability Analysis for the Free Shear Layer

The undisturbed flow consists of a piecewise-constant vorticity layer between two counter-flowing but parallel streams. The contours C_j, $j = 1...M, M'...1'$ delineate the vorticity discontinuities in the (x, y)-plane and the associated velocity field is piecewise-linear as shown in figure A5.1. The regions of uniform vorticity are labelled as $R_1...R_{M'}$, $R_{M'}...R_1$, with primed subscripts indicating contours below the x-axis. To determine the stability of the shear layer to small amplitude two-dimensional perturbations, we search for vorticity preserving solutions to the Euler equations. First we specify the equations governing the flow at contours C_j and $C_{j'}$, and then combine the sets of equations for the 2M contours to form an eigenvalue problem.

Consider the partial layer shown in figure (A5.2) with contours defined as

$$\eta_j(x, t) = q_j \frac{h_1}{2} + \alpha_j \exp(ikx) \exp(i\sigma t) , \qquad \text{(A5.1a)}$$

$$\eta_{j'}(x, t) = -q_j \frac{h_1}{2} + \alpha_{j'} \exp(ikx) \exp(i\sigma t), \qquad \text{(A5.1b)}$$

where η_j is the y-coordinate of C_j, h_j is the mean height, $\alpha_j = \alpha_{rj} + i\alpha_{ij}$ is the complex amplitude of the perturbation, $\sigma = \sigma_r + i\sigma_i$ is the complex growth rate, and $k = 2\pi/\lambda$ is the wavenumber. The vorticity profile is normalized by setting $\max | \omega_j | = 1.0$ and defining $q_j = h_j/h_1$. See table 5.1 for the normalized vorticity profiles for M = 1, 4 and 8.

The regions and corresponding vorticities associated with contours C_j and $C_{j'}$, are

$$R_{j-1} : \eta_{j-1} > y > \eta_j , \quad \omega = \omega_{j-1} , \qquad \text{(A5.2a)}$$

$$R_{j-1'} : \eta_{j-1'} < y < \eta_{j'} , \quad \omega = \omega_{j-1} , \qquad \text{(A5.2b)}$$

$$R_j : \eta_j > y > \eta_{j+1} , \quad \omega = \omega_j , \qquad \text{(A5.2c)}$$

$$R_{j'} : \eta_{j'} < y < \eta_{j-1'} , \quad \omega = \omega_j . \qquad \text{(A5.2d)}$$

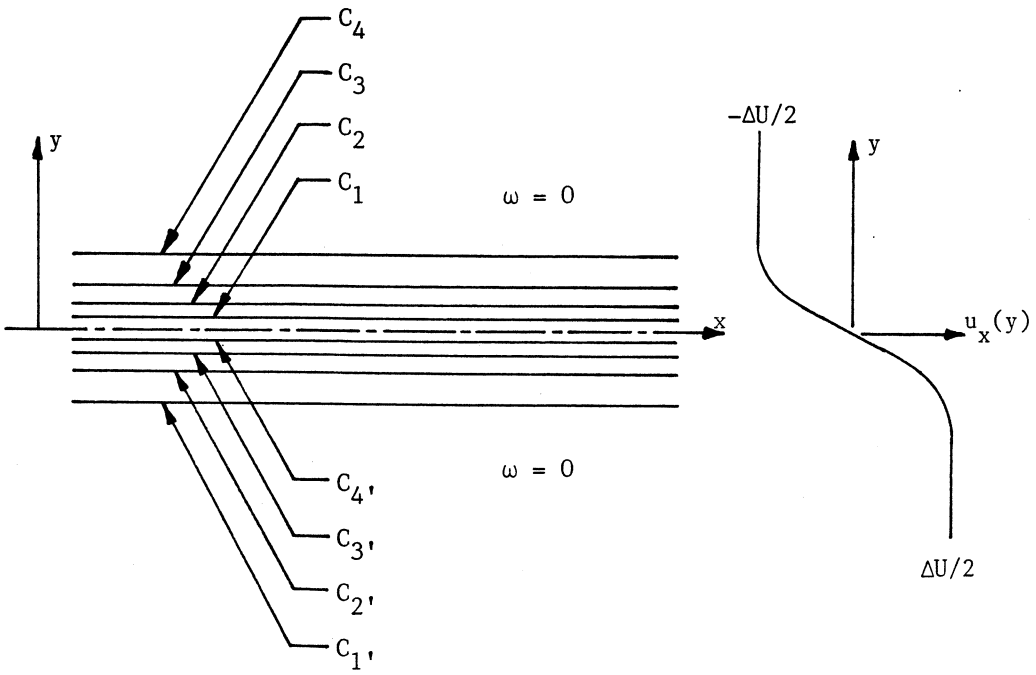

Figure A5.1 : The undisturbed, nonuniform vorticity shear layer for M = 4. For positive ω_j, j = 1 ... 4, the corresponding velocity profile $u_x(y)$ is shown to the right. The upper contours are labelled C_1 ... C_4 while the lower contours are labelled C_1' ... C_4'.

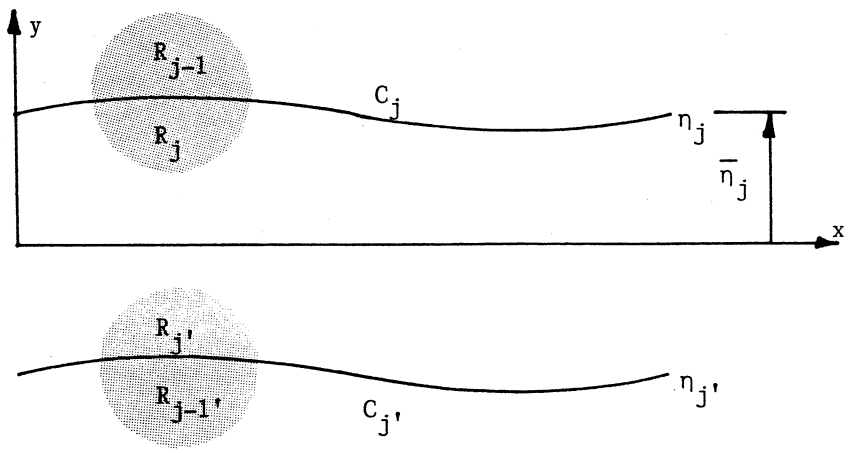

Figure A5.2: A partial view of the shear layer showing contours C_j and C_j', slightly perturbed from their mean position. The average y-position of C_j is $\bar{\eta}_j = q_j h_1/2$.

Table A5.1 : Normalized vorticity profiles with $\delta_\omega = 1.0$ and $\omega_{max} = 1.0$.

j	M = 1, h_1 = 1.0		M = 4, h_1 = 1.667		M = 8, h_1 = 1.92	
	ω_j	q_j	ω_j	q_j	ω_j	q_j
1	1.0	1.0	0.274	1.0	0.071	1.0
2			0.643	0.6	0.161	0.86
3			0.870	0.35	0.287	0.73
4			1.0	0.162	0.440	0.61
5					0.593	0.49
6					0.743	0.38
7					0.907	0.26
8					1.0	0.14

The velocity in each region is defined as the gradient of a flow potential, ϕ, superimposed on the rotational part of the undisturbed parallel flow. The velocity vector

$$\underline{u} = u_x\underline{i} + u_y\underline{j} \quad , \tag{A5.3a}$$

is given by

$$R_{j-1} : \underline{u}_{j-1} = \nabla\phi_{j-1} - \omega_{j-1}\left[y - q_j\frac{h_1}{2}\right]\underline{i} + u_j\underline{i} \ , \tag{A5.3b}$$

$$R_{j-1'} : \underline{u}_{j-1'} = \nabla\phi_{j-1'} - \omega_{j-1}\left[y + q_j\frac{h_1}{2}\right]\underline{i} - u_j\underline{i} \ , \tag{A5.3c}$$

$$R_j : \underline{u}_j = \nabla\phi_j - \omega_j\left[y - q_{j+1}\frac{h_1}{2}\right]\underline{i} + u_{j+1}\underline{i} \ , \tag{A5.3d}$$

$$R_{j'} : \underline{u}_{j'} = \nabla\phi_{j'} - \omega_j\left[y + q_{j+1}\frac{h_1}{2}\right]\underline{i} - u_{j+1}\underline{i} \ , \tag{A5.3e}$$

where $\underline{i}$ and $\underline{j}$ are the unit vectors in the x- and y-directions. The velocities

$$u_j = \sum_{n=M}^{j} \omega_n(\eta_{n+1} - \eta_n) \quad , \quad j = 1...M \ , \tag{A5.4}$$

are the undisturbed velocities at the contours C_j, $j = 1...M$. The flow potentials are defined as

$$\phi_{j-1} = e^{ikx}\, e^{i\sigma t}\,(Q_{j-1,1}\, e^{ky} + Q_{j-1,2}\, e^{-ky}) \quad , \tag{A5.5a}$$

$$\phi_{j-1'} = e^{ikx}\, e^{i\sigma t}\,(Q_{j-1',1}\, e^{ky} + Q_{j-1',2}\, e^{-ky}) \quad , \tag{A5.5b}$$

$$\phi_j = e^{ikx}\, e^{i\sigma t}\,(Q_{j,1}\, e^{ky} + Q_{j,2}\, e^{-ky}) \quad , \tag{A5.5c}$$

$$\phi_{j'} = e^{ikx}\, e^{i\sigma t}\,(Q_{j',1}\, e^{ky} + Q_{j',2}\, e^{-ky}) \quad . \tag{A5.5d}$$

The form of the flow potentials in (A5.5) have been chosen to satisfy continuity with the Q's being complex constants (yet to be determined). Note that, when considering the whole layer, η_0 , $\eta_{0'}$, $Q_{0',2}$, $Q_{M,2}$ and $Q_{M',2}$ do not exist and $\omega_0 = 0$.

We can differentiate the flow potentials (ϕ's) to obtain the velocity directly in terms of the complex constants (Q's) using the relationships

$$u_x = \frac{\partial \phi}{\partial x} \quad , \tag{A5.6a}$$

$$u_y = \frac{\partial \phi}{\partial y} \quad , \tag{A5.6b}$$

The equations defining the stability characteristics of the layer may be derived by applying the following constraints at each interface.

(i) The u_x and u_y velocities across the interface are continuous.

(ii) Particles that are initially on the interface always remain on the interface. That is

$$\frac{\partial \hat{\eta}}{\partial t} + \bar{u}_x \frac{\partial \hat{\eta}}{\partial x} - \hat{u}_y = 0 \quad , \tag{A5.7}$$

where the bar indicates a mean quantity (undisturbed layer), the hat, a perturbation quantity. This gives us six equations for every pair of contours C_j and $C_{j'}$, which, in matrix form, may be expressed as

$$\underline{\underline{A}}\ \underline{Q} = \underline{0} \tag{A5.8a}$$

where $\underline{\underline{A}}$ and $\underline{Q}$ are

$$\underline{Q} = [\, Q_{j-1,1} \quad Q_{j-1,2} \quad Q_{j-1',1} \quad Q_{j-1',2} \quad Q_{j,1} \quad Q_{j,2} \quad Q_{j',1} \quad Q_{j',2} \quad \alpha_j \quad \alpha_{j'} \,]^T \tag{A5.8b}$$

$$\underline{\underline{A}} = \begin{bmatrix} ikp & ik/p & 0 & 0 & -ikp & -ik/p & 0 & 0 & (\omega_j - \omega_{j-1}) & 0 \\ p & -1/p & 0 & 0 & -p & 1/p & 0 & 0 & 0 & 0 \\ 0 & 0 & 0 & 0 & -kp & k/p & 0 & 0 & i\sigma + u_j ik & 0 \\ 0 & 0 & ik/p & ikp & 0 & 0 & -ik/p & -ikp & 0 & (\omega_j - \omega_{j-1}) \\ 0 & 0 & 1/p & -p & 0 & 0 & -1/p & p & 0 & 0 \\ 0 & 0 & 0 & 0 & 0 & 0 & -k/p & kp & 0 & i\sigma - u_j ik \end{bmatrix} \tag{A5.8c}$$

For a uniform vorticity layer (M = 1) we set $Q_{0,1} = Q_{0',2} = 0$, $Q_{1,1} = Q_{1',1}$ and $Q_{1,2} = Q_{1',2}$, thus reducing (A5.8b,c) to

$$\underline{Q} = [Q_{0,2} \quad Q_{0',1} \quad Q_{1,1} \quad Q_{1,2} \quad \alpha_1 \quad \alpha_{1'} \quad] \tag{A5.9b}$$

$$\underline{\underline{A}} = \begin{bmatrix} ik/p & 0 & -ikp & ik/p & \omega_1 & 0 \\ -1/p & 0 & -p & 1/p & 0 & 0 \\ 0 & 0 & -kp & k/p & i\sigma - i\frac{\eta_1 k}{2}\omega & 0 \\ 0 & ik/p & -ik/p & -ikp & 0 & \omega_1 \\ 0 & 1/p & -1/p & p & 0 & 0 \\ 0 & 0 & -k/p & kp & 0 & i\sigma + i\frac{h_1 k}{2}\omega_1 \end{bmatrix} \tag{A5.9c}$$

$$p = \exp(h_1 k/2) \quad . \tag{A5.9d}$$

This can be rearranged into the form of a standard eigenvalue problem

$$\underline{\underline{C}}\ \underline{Q} = \sigma\ \underline{\underline{B}}\ \underline{Q} \quad , \tag{A5.10}$$

where σ is the eigenvalue and $\underline{\underline{A}} = \underline{\underline{C}} - \sigma\underline{\underline{B}}$. We can solve the M = 1 problem "by hand" to find the range of σ which have $\sigma i < 0$ but for M > 1 we resort to a numerical solution using the QZ algorithm (Garbow, ACM).

For a shear layer with M > 1, we have to assemble the six equations from each pair of contours C_j and $C_{\bar{j}}$, into a single set of equations. As there are common Q's between adjacent regions R_j, some of the elements of the eigenvector are shared between adjacent sets of six equations. The arrangement for assembling the full eigenvector is shown in figure A5.3. Although we have 6M equations, there are only 2M finite eigenvalues as there is a degree of degeneracy built into the formulation of the contour perturbation (A5.1) and the velocity potentials (A5.5). These extra degrees of freedom

Figure A5.3 : Assembling the eigenvector for the M pairs of contours. The general case for j = 2...M - 1 is shown with its elements overlapping the special cases j = 1 and j = M. N is the number of elements in the eigenvector after adding the contour pair C_{j-1} and $C_{j-1'}$; N = 8 + (j-1).6. For contours C_1 and $C_{1'}$; $Q_{0,1} = 0$, $Q_{0',1} = 0$ and for C_M and $C_{M'}$, $Q_{m',1} = Q_{M,1}$ and $Q_{M',2} = Q_{M,2}$.

j = 1		j = 2...M-1		j = M	
element #	quantity	element #	quantity	element #	quantity
-	$Q_{0,1} = 0$				
1	$Q_{0,2}$				
2	$Q_{o',1} = 0$				
-	$Q_{0'2}$				
3	$Q_{1,1}$	N - 5	$Q_{j-1,1}$		
4	$Q_{1,2}$	N - 4	$Q_{j-1,2}$		
5	$Q_{1',1}$	N - 3	$Q_{j-1',1}$		
6	$Q_{1',2}$	N - 2	$Q_{j-1',2}$		
7	$\alpha_{\perp}$	N - 1	-		
8	$\alpha_{\perp'}$	N	-		
		N + 1	$Q_{j,1}$	N - 5	$Q_{M-1,1}$
		N + 2	$Q_{j,2}$	N - 4	$Q_{M-1,2}$
		N + 3	$Q_{j',2}$	N - 3	$Q_{M-1',1}$
		N + 4	$Q_{j',2}$	N - 2	$Q_{M-1',2}$
		N + 5	α_j	N - 1	-
		N + 6	$\alpha_{j'}$	N	-
				N + 1	$Q_{M,1}$
				N + 2	$Q_{M,2}$
				N + 1	$Q_{M',1} = Q_{M,1}$
				N + 2	$Q_{M',2} = Q_{M,2}$
				N + 3	α_M
				N + 4	$\alpha_{M'}$

are present because we did not utilize all of the symmetries of the physical problem. To check the final numerical code for this stability analysis, the uniform-vorticity layer was studied using M = 1, M = 2 and M = 4 with $\omega_j = 1$, j = 1...4. No difference was observed in the computed results.

The solution space $0 < kh_1 < \infty$ was searched by selecting a vorticity profile with $\omega_{max} = 1$ and h_1 set to give $\delta_\omega = 1.0$ (see table A5.1). We then obtain particular solutions to the eigenvalue problem (A5.10) for selected values of k. The results are summarized in figure (A5.4) which show the perturbation growth rates, s_i/ω_{max}, over a range of $k\delta_\omega$ for four vorticity profiles. The layer is stable outside this range. If we let $M \rightarrow \infty$ then we expect the computed solution to approach that of the Rayleigh equation (Yih § 19) for an inviscid properly-continuous vorticity layer. The plots of growth rate in figure A5.4 support this conjecture as the M = 4 and M = 8 curves provide reasonable approximations to the continuous result (curve 4) except for short waves with wavelength of order the contour seperation. This continuous vorticity profile

$$\omega(y) = -0.5\Delta U \, \mathrm{sech}^2(y) \quad , \tag{A5.11}$$

corresponds to a hyperbolic-tangent velocity profile

$$u_x(y) = 0.5\Delta U \tanh(y) \quad . \tag{A5.12}$$

as studied by Michalke (1964). We find that the wavenumber $k\delta_\omega$ of the perturbation with the largest growth rate decreases with decreasing momentum thickness θ/δ_ω (table A5.2), as observed by Nakamura, Leonard & Spalart (1982). The same trend is seen with the highest wavenumber for an unstable perturbation.

The contour shapes are obtained from the α elements in the eigenvector, $\underline{Q}$. We are only interested in the real part of η (A5.1) so we define the contour shape for C_j as

$$\eta_j(x) = q_j \frac{h_1}{2} + \alpha_{rj} \cos(kx) - \alpha_{ij} \sin(kx) \quad . \tag{A5.13}$$

As numerical results computed using QZ are not normalized to any particular phase and amplitude, hence we impose the constraints

$$(\alpha_r)_j = -(\alpha_r)_{j'} \quad , \tag{A5.14a}$$

$$(\alpha_i)_j = -(\alpha_i)_{j'} \quad , \tag{A5.14b}$$

$$|\alpha_M| = 1.0 \quad , \tag{A5.14c}$$

which induce the symmetry $C_{j'} = 2\pi - C_j$ and set the maximum amplitude of (any of) the contours to one. Figure A5.5 illustrates the normalization procedure for the piecewise-constant vorticity profile M = 4 with $k\delta_\omega = 0.875$ (i.e., the mode with the highest growth rate). The values of the α_j produced by the numerical code are plotted on a graph with axes "Old Re" and "Old Im". A new set of axes ("New Re" and "New Im") satisfying the constraints (A5.15) is overlaid and the normalized values for the α_j recorded. Values of normalized α's for all vorticity profiles and wavenumbers used in the numerical simulations of chapters 7 and 9 are given in tables 7.3 (M = 4) and 7.4 (M = 8).

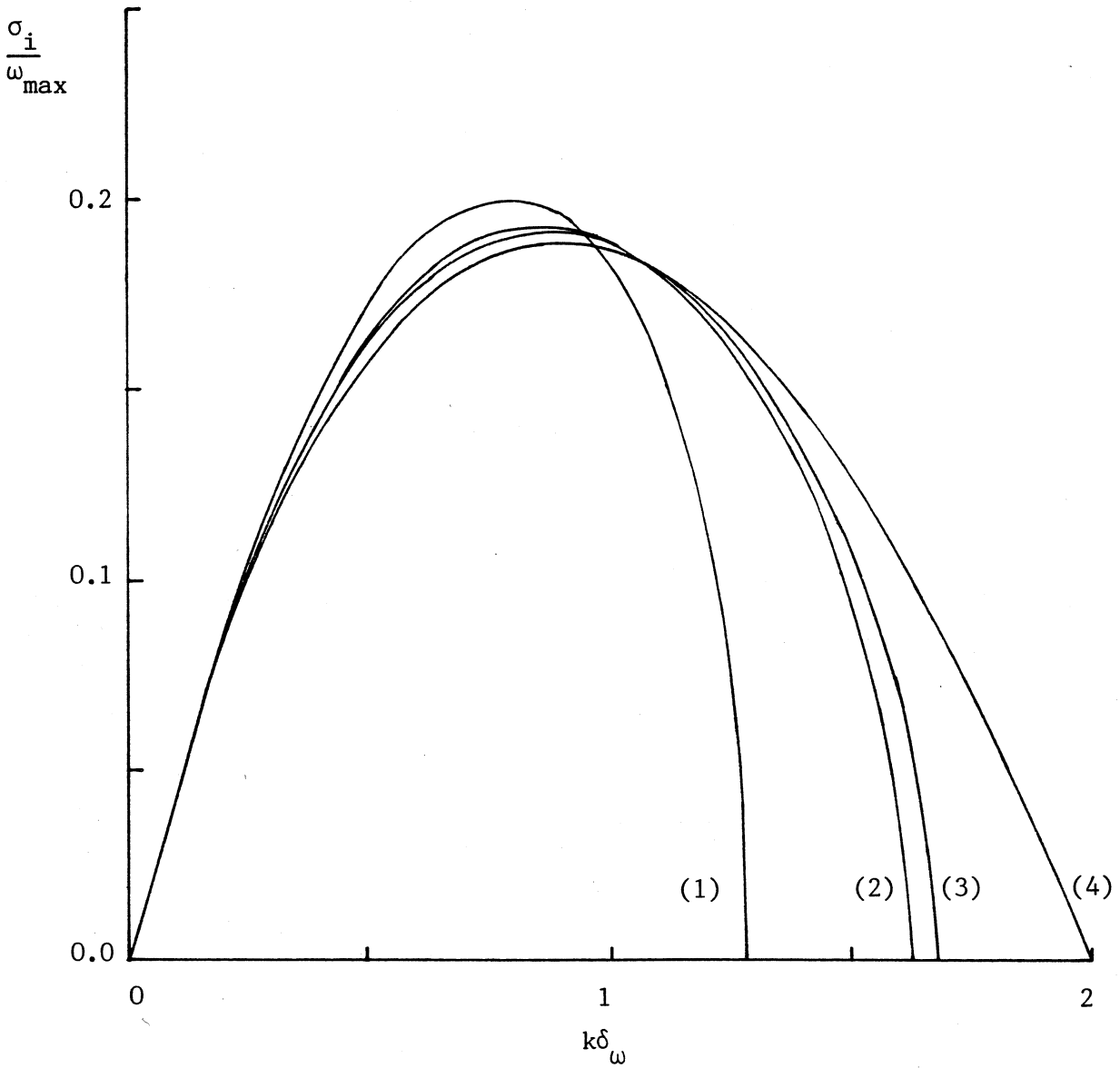

Figure A5.4 : Normalized growth rates for four vorticity distributions.

(1) single region, M = 1, of uniform vorticity

(2) M = 8 piecewise-constant vorticity profile as defined in table A5.1

(3) M = 4 piecewise-constant vorticity profile as defined in table A5.1

(4) the continuous vorticity profile (A5.11) corresponding to the hyperbolic-tangent velocity profile (Michalke, 1964)

Table A5.2 : Extreme values of the parameters in the stability analysis for each vorticity profile.

Vorticity Profile	$\frac{\theta_v}{\delta_\omega}$	$\frac{h_1}{\delta_\omega}$	Perturbation with max growth $k\delta_\omega$	σ_i/ω_{max}	highest unstable wavenumber $\kappa\delta_\omega$
uniform vorticity (M = 1)	0.167	1.0	0.795	0.2012	1.279
piecewise constant (M = 4)	0.228	1.67	0.875	0.1926	1.675
piecewise constant (M = 8)	0.215	1.92	0.857	0.1938	1.626
$\omega = -\frac{1}{2}\sec^2(y)$	0.25	-	0.889	0.1898	2.0

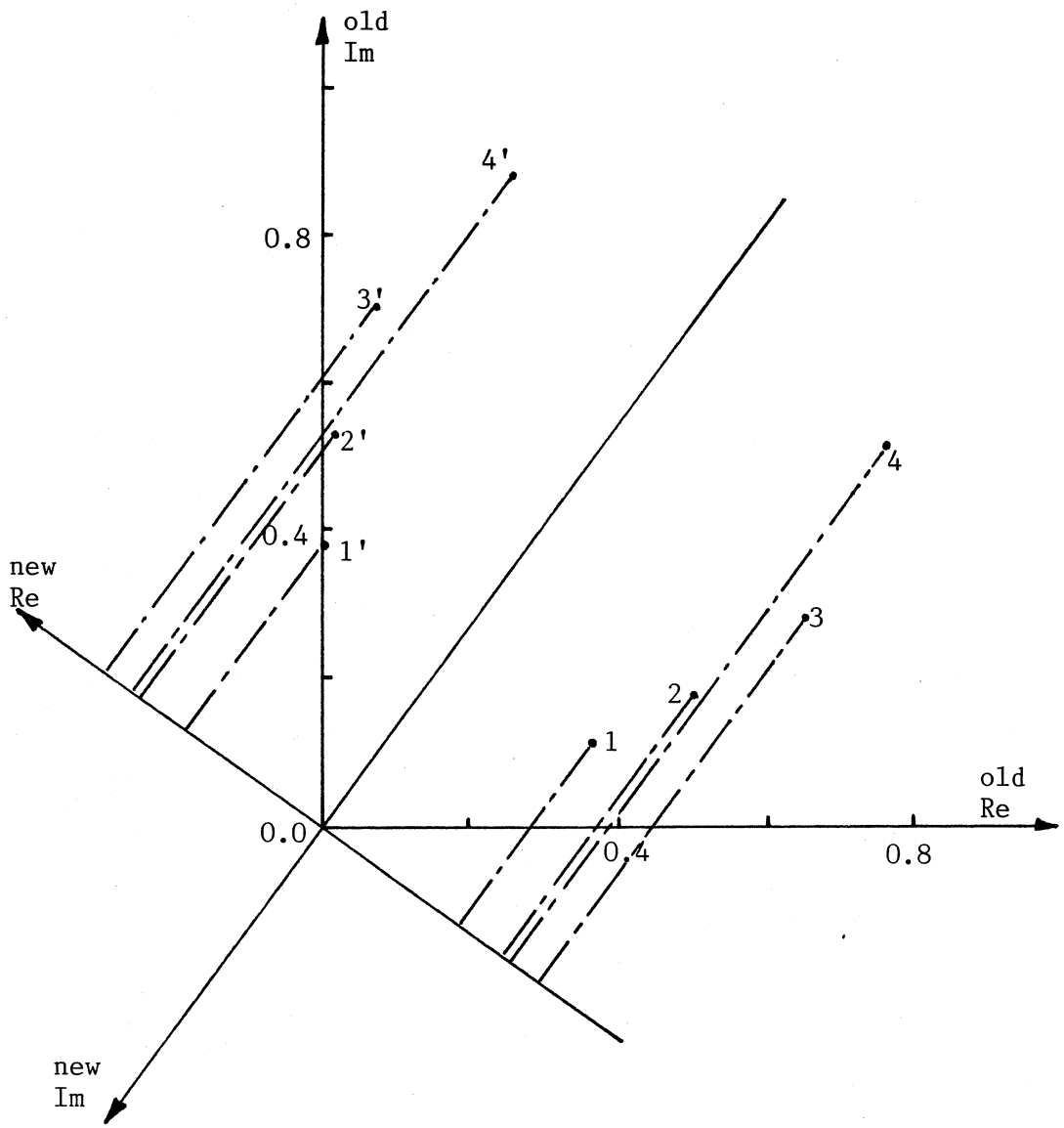

Figure A5.5 : Plot of α_j, j = 1 .. 4 for the non uniform vorticity profile (M = 4) and wavenumber $k\delta_\omega = 0.875$.
Old axes - results as computed by the QZ algorithm.
New axes - results normalized as per (A5.14).